NREL/CP-570-25315

Proceedings of the 1998 U.S. DOE Hydrogen Program Review

April 28-30,1998 Alexandria, Virginia

Volume I

Sponsored by the
Office of Solar Thermal, Biomass
Power and Hydrogen Technologies
U.S. Department of Energy

National Renewable Energy Laboratory
1617 Cole Boulevard
Golden, Colorado 80401-3393
A national laboratory of the U.S. Department of Energy
Operated by Midwest Research Institute
for the U.S. Department of Energy
Under Contract No. DE-AC36-83CH10093

Prepared under Task No. HY811010

August 1998

Forward

The Department of Energy's Office of Utility Technologies Hydrogen Program conducts R&D and technology validations for the development of safe, cost-effective hydrogen energy technologies that support and foster the transition to a hydrogen economy. In order to enable a future that includes hydrogen energy, the DOE Hydrogen Program supports a strong core R&D effort, including near-, mid-, and long-term strategies.

Today, fossil fuels, particularly natural gas, serve as the feedstock for the production of hydrogen. Improvements in these technologies are expected to reduce the cost of hydrogen, improving the economics of widespread hydrogen use, particularly in the transportation sector. Soon, hydrogen could be produced from the thermal processing of biomass, providing hydrogen at competitive prices from a renewable resources. In the future, hydrogen will be produced directly from sunlight and water by biological organisms or by using semiconductor-based systems similar to photovoltaics (PV). These renewable-based production technologies have the potential to produce essentially unlimited quantities of hydrogen in a sustainable manner.

Storage of hydrogen is an important area for research, particularly when considering transportation as a major user, and the need for efficient energy storage for intermittent renewable power systems. Although compressed gas and liquid hydrogen storage systems have been used in vehicle demonstrations worldwide, the issues of safety, capacity, and energy consumption have resulted in a broadening of the storage possibilities to include metal hydrides and carbon nanostructures. Stationary storage systems that are high efficiency with quick response times will be important for incorporating large amounts of intermittent PV and wind into the grid as base load power.

In addition to the extensive fuel cell development programs in other offices within DOE, the Hydrogen Program conducts fuel cell research focused on development of inexpensive, membrane electrode assemblies, and the development of reversible fuel cells for stationary applications. The Program also supports research in the development of hydrogen/ methane blends and hydrogen-fueled internal combustion engines and generator sets.

A large hurdle to expanded use of hydrogen is public perception. Widespread hydrogen use represents an extraordinary educational challenge, as well as the absolute requirement that safety be intrinsic to all processes and systems. The development of reliable, low-cost hydrogen sensors is an important aspect of the Program, as is the development of codes and standards for the safe use of hydrogen.

This document contains technical progress reports on 42 research projects funded by the DOE Hydrogen Program in Fiscal Year 1998, in support of its mission to make hydrogen a cost-effective energy carrier for utility, building, and transportation applications. Each year, the Program conducts a rigorous review of its portfolio of projects, utilizing teams of experts to provide vital feedback on the progress of research. These proceedings serve as an important technology reference for the DOE Hydrogen Program.

Catherine E. Gregoire Padró
Hydrogen Program Manager
National Renewable Energy Laboratory
Golden, Colorado

TABLE OF CONTENTS

Volume I

Biological Systems

Electrochemical Systems

Process and Systems Analysis

Volume II

Storage and Separation Systems

Transportation Systems

Biological H_2 from Fuel Gases and from H_2O

P. Weaver, P.-C. Maness, C. Rhodes, J. Scahill, S. Dundorf, and S. Martin
National Renewable Energy Laboratory
Golden, Colorado 80401

Summary

The two stand-alone objectives of the research are to economically produce H_2 in the near term from biomass (thermally gasified to syngas) and in the mid term from H_2O using cyanobacteria or algae with an oxygen-tolerant bacterial hydrogenase.

Photosynthetic bacteria have four different terminal enzymes that mediate their H_2 metabolisms—nitrogenase, uptake hydrogenase, fermentative hydrogenase, and carbon monoxide-linked hydrogenase. Each has been microbiologically and biochemically examined for their potential to specifically generate H_2 in large-scale processes. Based on measurements of maximal activities, stabilities, energy requirements, equilibria, and partial pressures of the H_2 producing reactions, the CO-linked hydrogenase is easily the most suited for practical applications. The enzyme mediates H_2 production from CO at rates up to 3 $mmol \cdot min^{-1} \cdot g$ cell dry $weight^{-1}$ at near ambient temperature and pressure. At biological temperatures, equilibrium for the CO shift into H_2 lies far towards H_2 production. Less than 0.1 ppm of CO remains after a 20% CO gas phase is acted upon by bacteria. The necessary contact time between CO and bacteria is approximately ten seconds. Similar biological activities are observed with thermally generated fuel gases. The product gas can be directly used in fuel cells. New bacterial isolates from nature and mutant strains are being selected to further improve the novel technology. Oxygen-resistant enzymes identified in some bacterial strains could lead to a more general, second generation technology mediating the solar production of H_2 from H_2O.

Presently, mass transfer of gaseous CO limits the bacterial production of H_2 from fuel gases. New bioreactor designs have significantly enhanced shift rates. Vapor-phase and bubble-train bioreactors employing immobilized or suspended bacteria are being scaled up. A User Facility has been established for the safe engineering scale up and validation of solar or dark technologies for the Hydrogen Program. The first system to be tested at the site will integrate fuel gas generators with biological shift reactors and a PEM fuel cell.

Introduction: An economic process for producing hydrogen, whether biologically or chemically based, would ideally be (1) H_2O derived, (2) solar driven, (3) highly efficient, (4) durable, (5) insensitive to hydrogen partial pressure, and (6) inexpensive to build and operate. A complete system fulfilling all of these goals is not currently available. Of the biological options, systems employing intact cells of photosynthetic bacteria are the most advanced. Unlike cyanobacteria or algae, however, photosynthetic bacteria do not oxidize water and therefore do not directly fulfill criterion (1). They do, however, evolve H_2 from biomass (previously photosynthetically generated from H_2O and CO_2). These bacteria employ several different enzymatic mechanisms that may have commercial potential for possible near term applications of H_2 production from biomass. One mechanism that incorporates thermal and biological processes appears particularly promising: thermally generated fuel gases derived from biomass can be sufficiently conditioned by bacterial catalysts in a one-step process that they may be directly injected into platinum-electrode, hydrogen fuel cells.

A complete system of sustained hydrogen production based on the direct photooxidation of water is more difficult to achieve. Oxygen production is inherent in the oxidation of water, and the hydrogen-evolving enzymes of cyanobacteria and algae are usually rapidly inactivated by oxygen. A number of newly isolated photosynthetic bacterial strains contain an O_2-resistant, evolving hydrogenase enzyme. This hydrogenase has been partially purified from two strains of bacteria, where it is found tightly bound to membrane fractions. The enzymes require an additional electron mediator for H_2 production. Genetic transfer and expression of the oxygen-resistant, bacterial hydrogenase enzyme and cofactor in a cyanobacterial or algal host could provide a method for the linkage of photoreduced ferredoxin to an evolving hydrogenase, even in the simultaneous presence of photoevolved oxygen. This type of genetic construct could grow naturally when CO_2 was present, but would concomitantly photoevolve H_2 and O_2 from water in the absence of CO_2. Creation of a recombinant microbe to fulfill all of the ideal criteria listed above is considered an early mid-term goal.

Approach: The two stand-alone objectives of the research are to economically produce H_2 in the near term from biomass (thermally gasified to syngas) using ambient temperature bacteria as catalysts and in the mid term from H_2O using cyanobacteria or algae with an oxygen-tolerant bacterial hydrogenase.

Past Results: Photosynthetic bacteria have four different terminal enzymes that mediate their H_2 metabolisms—nitrogenase, uptake hydrogenase, fermentative hydrogenase, and carbon monoxide-linked hydrogenase. Each has been microbiologically and biochemically examined for their potential to specifically generate H_2 in large-scale processes.

Of the intact cell metabolisms of phototrophs that evolve hydrogen, the nitrogenase-mediated reactions have been the most studied. Nearly all isolates of photosynthetic bacteria have a nitrogenase enzyme complex (Weaver et al. 1975), which, in the absence of ammonium ion or dinitrogen gas and in the presence of oxidizable organic materials, functions to reduce protons and evolve hydrogen. A large variety of soluble organic acids, alcohols, and sugars can be nearly totally photoconverted into H_2 and CO_2 by this metabolism. Rates of 131 μmol H_2 evolved/min·g cell dry weight have been obtained in saturating light. Hydrogen evolution is largely light dependent (Schultz et al. 1985) and strongly exergonic. The hydrolysis of about 4 ATP (largely synthesized

in light) is required to generate each H_2 and can drive the gas production to equilibrium pressures in excess of 100 atmospheres. Radiant energy conversion efficiencies (ignoring the chemical energy of the organic substrate) are about 5.3% for the most active strains of photosynthetic bacteria. The best outdoor, solar-driven efficiency is 3.4%. Cultures grown on glutamate as the nitrogen source produced H_2 at linear rates for 7-10 days before *nif*$^-$ strains began to dominate the cultures. Experiments with weekly feedings of N_2 maintained the *nif*$^+$ wild-type genotype dominant and active H_2 production could be observed for more than 30 days. Even with the assumption that the best strains and conditions could be maintained, the maximum solar conversion efficiencies that could be expected are probably less than 10%, however, due to the large energy expenditure of the bacteria in performing this H_2-evolving metabolism. Non-sterile, solar-driven cultures (200-300 liter scale) were susceptible to contamination by sulfate-reducing and methanogenic bacteria growing on the evolved H_2 plus CO_2. Limiting the available fixed nitrogen, including that present in sedimented photosynthetic bacteria, is necessary to limit H_2S and CH_4 evolution by the contaminants. Algal growth is similarly inhibited by this method and also by the strongly reducing conditions. An in-house cost analysis of the process has been performed (Herlevich and Karpuk). First year costs for H_2 production, clean-up, and compression are estimated at \$24.40 per 10^6 Btu at 5% solar energy conversion and \$15.70 per 10^6 Btu at 10% conversion efficiency.

Many strains of photosynthetic bacteria also produce hydrogen from organic substrates by way of a fermentative hydrogenase enzyme when grown in intermittent or low, continuous light (Schultz and Weaver 1982). High, continuous light represses synthesis of the enzyme. The enzyme does not require ATP. It can mediate hydrogen production at rates more than 3-fold those of nitrogenase, or about 440 μmol H_2/min·g cells. However, it equilibrates at low partial pressures of about 0.1 atmospheres of H_2. The active rates of hydrogen production can thus only be maintained by sparging with inert gas, by vacuuming, or by scavenging with a hydrogen-consuming process. Sparging or vacuuming are considered prohibitively expensive, although closed-loop, sparged systems connected to fuel cells may be effective. Methanogenic bacteria strongly contaminate non-sterile cultures. In fact, methanogenic bacteria naturally scavenge the H_2 to such low levels that they are extremely effective in maintaining the H_2 partial pressure considerably below the equilibrium pressure, which functions to "pull" the conversion of organic materials into H_2 and CO_2 and then into CH_4. This apparently natural process is the basis for an NREL patent on solar-enhanced anaerobic digestion (Weaver, 1990).

A unique type of hydrogen producing activity was found in a strain of photosynthetic bacteria by Uffen (1976) that functioned only in darkness to shift CO (and H_2O) into H_2 (and CO_2). We have isolated more than 450 strains of photosynthetic bacteria from local sites that perform this shift reaction in darkness, as does the Uffen strain, but will also quantitatively assimilate CO into new cell mass in light, unlike the Uffen strain, which makes them easy to grow. We have tested many of our strains for CO shift activity and growth with crude (water-scrubbed only) synthesis gas (primarily CO and H_2) generated from thermally gasified wood chips. In light, the novel photosynthetic bacteria assimilate the CO and H_2 components and a portion of the trace gases. In darkness, all of the isolates respond similarly by shifting the CO component of synthesis gas into additional H_2, thereby leaving a product gas highly enriched in H_2 (with CO_2 and trace pyrolysis gases). No inhibitory effects of synthesis gas on long-term photosynthetic growth were noted. At ambient temperature and pressure conditions and starting from 200,000 ppm of CO in the gas phase, less than 0.1 ppm of CO remained at equilibrium. The product gas could be fed directly into a phosphoric

acid fuel cell with generation of electrical power. No harmful effects to the fuel cell were noted.

Bacterial catalyzed shift rates as high as 1.5 mmol H_2 produced from CO per min per g cell dry weight were obtained from vigorously agitated cultures at low cell density. Less actively stirred cells at more normal cell densities (2-6 g cells per liter) exhibit H_2 production rates of 10-100 μmol per min per g cells, reflecting a limiting mass transfer of CO into solution. Gas pressures (10% CO) of more than 12 atmospheres strongly increased shift rates but were still limiting.

A variety of bioreactor designs that show enhanced mass transport of CO (at near ambient pressure) were built and tested (Markov et al. 1996; Markov et al. 1997). Hollow-fiber reactors (0.5 m^2 surface area) with bacterial cells immobilized on the outer fiber surfaces evolved H_2 at rates of about 0.3-0.7 $mmol \cdot min^{-1} \cdot g\ cdw^{-1}$. One such reactor produced H_2 from CO (10% in N_2) continuously over a 15 month period with only occasional changes of medium. No detectable levels of CO remained in the effluent gas stream.

Bacterial cultures grown in light with 20% CO in the gas phase are probably not maximally induced for CO shift activity. The specific activity for CO shift activity increased by a factor of six when light-grown cultures were incubated in darkness in a Paar cell at seven atmospheres of 20% CO gas pressure. This indicates that increased availability of CO to the cells causes a further derepression of shift activity enzymes. The capability of running syngas shift reactors at a few atmospheres of pressure is being incorporated into new reactor designs.

Due to limiting mass transfer of CO during assay conditions, it has been difficult to compare bacterial shift activities between the wild-type and mutant strains that we have isolated to-date. A new assay was developed that is independent of mass transfer. Bubbles of CO were added to suspensions of the bacterial strains in syringes and agitated vigorously. At time zero the bubble was expelled from the syringe and liquid samples of the bacterial suspension were injected at precise time intervals into an anaerobic solution of reduced hemoglobin. The hemoglobin rapidly quenches further shift activity by binding the remaining CO in solution to form carboxyhemoglobin, which has a distinctive spectral absorbance that can be readily quantitated from difference spectra. All of the bacterial strains exhibit a linear uptake of CO from solution until the dissolved CO approaches the K_s value (the CO concentration at which shift rates are one-half maximal). Different strains tested have K_s values of 3-8 μM. At normal suspended cell densities, CO concentrations in solution would drop to the K_s value in 3-5 seconds. CO concentrations would drop to 0.2μM (the assay limit of resolution) in 6-8 seconds. This value of CO in solution is equivalent to about 200 ppm of CO in an equilibrated gas phase. Kinetic rates for the further shift of remaining CO below 200 ppm and the time necessary to generate a conditioned gas with less than 10 ppm residual CO are currently unknown; however, FTIR analysis after long-term contact with a bacterial suspension at 30°C indicate the conditioned gas contained less than 0.1 ppm CO.

A mutant strain of photosynthetic bacteria was selected by growing a culture on CO in light in the presence of 5% O_2. Strain CBS-2 responded to the imposed culturing conditions by synthesizing 340% of the hydrogenase activity of its parent. Of particular importance, the O_2-resistant hydrogenase exhibited no oxy-hydrogenase activity in the presence of H_2 and O_2. This is a necessary property if the bacterial hydrogenase is to be integrated into an oxygenic host.

Current Results: The equilibrium constant of the CO shift reaction is strongly dependent upon temperature. At 400°C the calculated K_{eq} is 12, meaning that even with a chemical shift catalyst the CO concentrations in thermally generated fuel gases remains far too high for fuel cell use. At 35°C, where most of the bacterial shift strains function the K_{eq} is about 60,000; at 50°C the K_{eq} is still about 28,500, providing sufficient driving force to ensure the product gas contains less than 1 ppm residual CO.

Most bacterial strains exhibit enhanced shift rates with increasing temperature, up to a sharp maximum temperature. Strain CBS-2 exhibits a maximal shift temperature of 50°C where the shift rate is about 1.3 mmol CO shifted $\cdot min^{-1} \cdot g\ cdw^{-1}$. In at least one instance rates have exceeded 3 $mmol \cdot min^{-1} \cdot g\ cdw^{-1}$. The higher temperature for shift activity may be of additional value in requiring less temperature quenching of the fuel gases. Twenty-four hot springs sites with temperatures between 45-75°C were sampled. Twelve of the cultures gave biological shift activity. A number of strains exhibiting shift activity have been isolated in pure culture, and all appear to be clostridial species, although photosynthetic bacteria and cyanobacteria dominate the hot springs biomass.

The oxygen tolerance of the evolving hydrogenase in strain CBS-2 was examined in considerable detail. This strain was isolated by forcing it to grow photosynthetically with CO as the only carbon source while in the presence of 5% O_2. It could only survive and grow if it could evolve H_2 from CO even in the presence of O_2. This strain retained 50% of its evolving hydrogenase activity after seventeen hours stirring in air (21% O_2). The membrane-bound enzyme was extracted and highly purified. It was found to have a molecular weight of about 56,000 daltons by gel exclusion chromatography. The half-life of the purified hydrogenase stirred in air was about five hours. This compares very favorably with other evolving hydrogenases which have half-lives of about two minutes in air.

Although the hydrogenase appears to be relatively oxygen resistant, it is possible that the enzyme became inactivated but protected during the time it was aerated. In order to determine whether the enzyme could functionally evolve H_2 while O_2 was simultaneously present, different assays had to be employed. The purified enzyme was placed in a 50/50 D_2O/H_2O solution under an H_2 atmosphere with varying amounts of O_2, and the rate of appearance of HD in the gas phase was measured using mass spectrometry. A. Dillon and M. Heben of the Basic Sciences Center at NREL kindly supplied their expertise and apparatus for these measurements. With 3.3% O_2 in the gas phase, the hydrogenase enzyme retained 82% of its deuterium exchange activity. At 13% O_2, the enzyme was about 55% active. Better than 90% activity was regained with subsequent removal of O_2. These data surprisingly indicate that the hydrogenase is partially active under aerobic conditions and partially reversibly inactivated.

A second assay was developed which placed the purified hydrogenase with methyl viologen in a chamber with a clark hydrogen electrode. The enzyme is slightly reversible (at about 2.5% of the evolution rate). With the addition of 4.3% O_2, the kinetic rate of H_2 consumption was instantaneously reduced to about 35% of the anaerobic rate, but remained constant thereafter for the duration of the assay. Once again, better than 90% activity was regained upon return of the solution to anaerobic conditions.

Continuous-flow bioreactors were established with 10% CO in N_2 as the sole carbon source for the

bacteria. Cultures of strain EB21 were typical in that after 7-10 days the pH dropped and after 20 days the pH was below 6.0 and became inhibitory to shift activity. The acidity could not be attributed to carbonic acid and could not be gas stripped. Analysis of spent culture medium indicated there was only 0.7 mm phosphate remaining from the 20 mm added. It is surmised, though not identified, that medium phosphate is converted into intracellular polyphosphate under these conditions. Carr and Sandhu (1966) previously demonstrated that polyphosphate is often synthesized in the absence of fixed carbon substrates. When we added 5g/6 sodium malate, a non-fermentable substrate, to the anaerobic, dark cultures, the pH and CO shift activity of the culture remained constant.

Bubble-tower bioreactors 90 cm tall were inoculated with strain CBS-2 in a malate medium with 10% CO bubbled through a glass frit in the bottom of the columns. Bubble contact time with the bacterial suspension was 6-8 seconds. In a ¾ inch diameter, 90 cm column at flow rates of 14 ml per minute, about 90% of the CO was shifted over periods of a few weeks with no drop in pH. With the addition of Tween 80, a surfactant, 100% of the CO became shifted but the effect lasted only for a day or so. Presumably, the Tween partioned into the cell fraction and the stimulation of mass transfer was lost. A 3" diameter, 90 cm column performed similarly at 140 ml per minute gas flow provided that gas bubbles do not exceed 3-4 mm in diameter.

Gas phase bioreactors have been constructed that immobilize bacteria on high-surface-area solid supports. Most promising is a low cost, low energy input bioreactor made by immobilizing bacteria on the 30 μm diameter fibers of an upside-down nylon carpet that was glued to the inside surface of a 3.2 cm diameter, 115 cm long clear plastic tubing. The carpet forms a semicircle within the upper portion of the horizontal tubing with the nylon extending downward and contacting an aqueous reservoir of medium filling the lower half of the tubing. The fibers wick water and minerals to the immobilized bacteria in the upper half of the tubing volume. A 10% CO gas stream at 40 ml per minute passes through the carpet nap above the reservoir and is shifted into H_2 within the first 60 cm. Most of the product CO_2 enters the reservoir as bicarbonate ion, which should be gas strippable through an external reservoir loop, thereby leaving the reactor effluent gas highly enriched in H_2. Scanning electron micrographs of the fiber surfaces indicate that bacteria colonize only a small portion of the fiber surface, which leaves opportunity for considerable increases in activity.

The Outdoor Photobiology Test Area has been expanded and soon will be considerably enhanced in capability. Both a steam reformer and a biomass gasifier are being constructed to thermally generate authentic fuel gases on a continuous basis for use as feedstock for the bacterial shift reactor. A 50W PEM fuel cell will complete the technology validation. The system will initially run at 300 ml per minute.

Future Work: Further mutant selections should result in significantly increased specific activities in the CO shift reaction. Thermophiles will also be selected. Strains with a lower K_s for CO will be sought. Necessary co-factors for the O_2-tolerant hydrogenase will be characterized. The Outdoor Photobiology Test Area will be re-established with both a propane steam reformer and a small downdraft biomass gasifier to generate fuel gases at the rate of 0.3-14 liters per minute. Scaled-up shift bioreactors will operate continuously on the fuel gases and long-term operation will be automated and monitored. Production of polyhydroxyalkanoates or single-cell protein as side products will be maximized, quantified and incorporated into economic analyses.

Economic Evaluation/Systems Analysis: A FY96 analysis was performed on a separate task in the Hydrogen Program. The bacterial shift reaction is being examined as a possible low cost, single-step gas conditioning process for crude syngas. The projected cost of hydrogen is $17/GJ using a base case of purchased biomass at $46/ton and thermal gasification with biological shift (15% ROI). If biomass is purchased at $22/ton, the price of H_2 drops to $13.5/GJ, well within current market prices. A 10-fold increase in specific shift activity (from 1.5 $mmol \cdot min^{-1} \cdot g\ cdw^{-1}$) will decrease the cost by $4.70/GJ. If further gas purification is not needed to remove the remaining trace gases CO_2, the selling price is further reduced another $3.80/GJ. For many gas uses, such as in PEM or phosphoric acid fuel cells, it is only necessary that the gas stream be free of CO and H_2S, while not necessarily totally free of CO_2. In these applications the cost of further gas purification can be automatically discounted from the base case.

Projected Goals: The equilibrium constant of the CO shift reaction at room temperature is sufficiently large to generate a bacterially conditioned syngas stream with sub-ppm concentrations of CO remaining. Assuming there is no appreciable sulfide present as well, the gas stream is clean enough (with or without CO_2 diminishment) to be directly injected into phosphoric acid or PEM fuel cells. This would effectively eliminate the costs (see Economics) for pressure-swing absorption (or similar gas clean-up process) to yield H_2 for fuel cell use. Our near-term goal will be for this type of fuel cell application.

A genetic construct containing an O_2-tolerant hydrogenase would create an inexpensive photobiological catalyst that would switch in the absence of CO_2 from a growth mode to a H_2-producing mode at nearly maximal solar conversion efficiency. The successful construction and testing of such an oxygenic phototroph is our mid-term goal to photobiologically produce H_2 from H_2O in a single-stage bioreactor.

Major Barriers: The long-term effects on bacteria of trace components in syngas have not been examined and may necessitate more frequent change-out of bacteria. Mass transfer of CO to the bacteria remains rate limiting and needs to be enhanced. Genetic enhancement can easily match any large increase in mass transfer rates. There are a few more unknowns in the photobiological process to produce H_2 from H_2O. The O_2-tolerant hydrogenase must be genetically transferred and expressed in a biophotolytic host and shown to be active in linking to photoreductants. This has been demonstrated in mixed extracts, however, where spinach chloroplasts and bacterial hydrogenase photoproduced H_2 from H_2O in the presence of the redox mediator, methyl viologen.

References:

Carr, N.G., and G. R. Sandhu. 1966. *Biochem. J. 99*, 29P.

Herlevich, A., and M. Karpuk. 1982. SERI/TP-235-1548, 12 pp.

Markov, S.A., P.F. Weaver, and M. Seibert. 1996. *Hydrogen Energy Progress XI*, T.N. Vizeroglu et al. (Eds.) Vol. 3, Schön & Wetzel GmbH, Frankfurt, 2619-24.

Markov, S.A., P.F. Weaver, and M. Seibert. 1997. *Applied Biochem. Biotechnol., 63-65*, 577-84.

Schultz, J.E., and P.F. Weaver. 1982. *J. Bacteriol.*, 149:181-190.

Schultz, J.E., J.W. Gotto, P.F. Weaver, and D.C. Yoch. 1985. *J. Bacteriol.*, 162:1322-1324.

Uffen, R.L. 1976. *Proc. Nat. Acad. Sci.*, 73:3298-3302.

Weaver, P.F. U.S. Patent #4,919,813, issued April 24, 1990.

Weaver, P.F., J.D. Wall, and H. Gest. 1975. *Arch. Microbiol.*, 105:207-216.

SUSTAINABLE BIOREACTOR SYSTEMS FOR PRODUCING HYDROGEN

Oskar R. Zaborsky[1], JoAnn C. Radway[1], Brandon A. Yoza[1],
John R. Benemann[2], and Mario R. Tredici[3]
[1]Hawaii Natural Energy Institute
School of Ocean and Earth Science and Technology, University of Hawaii at Manoa
2540 Dole St. - Holmes Hall 246, Honolulu, Hawaii 96822, U.S.A.
808-956-8146; 808-956-5308; email: ozabo@hawaii.edu
[2] Department of Plant and Molecular Biology, University of California, Berkeley
[3] Dipartimento di Scienze e Tecnologie Alimentari e Microbiogiche,
University of Florence, Italy

Abstract

The overall goal of Hawaii's BioHydrogen Program is to generate hydrogen from water using solar energy and microalgae under sustainable conditions. Specific bioprocess engineering objectives include the design, construction, testing and validation of a sustainable photobioreactor system. Specific objectives relating to biology include investigating and optimizing key physiological parameters of cyanobacteria of the genus *Arthrospira (Spirulina)*, the organism selected for initial process development. Another objective is to disseminate the Mitsui-Miami cyanobacteria cultures, now part of the Hawaii Culture Collection (HCC), to other research groups.

Our approach is to use a single organism for producing hydrogen gas from water. Key stages are the growth of the biomass, the dark induction of hydrogenase, and the subsequent generation of hydrogen in the light. The biomass production stage involves producing dense cultures of filamentous, non-heterocystous cyanobacteria and optimizing biomass productivity in innovative tubular photobioreactors. The hydrogen generation stages entail inducing the enzymes and metabolic pathways that enable both dark and light-driven hydrogen production. The focus of Year 1 has been on the construction and operation of the outdoor photobioreactor for the production of high-density mass cultures of *Arthrospira*. The strains in the Mitsui-Miami collection have been organized and distributed to other researchers who are beginning to report interesting results. The project is part of the International Energy Agency's biohydrogen program.

Introduction

Over the past 25 years, advances have been made in the elucidation of the complex physiological, biochemical, and genetic processes underlying the hydrogen evolution capabilities of microalgae and bacteria. In the area of engineering research and system integration, however, little progress has been made. In fact, no hydrogen-evolving process that showed promise has been demonstrated in the field for any length of time, let alone commercialized. Even those processes that have shown promise in the laboratory have not been evaluated in field performance. Importantly, the solar conversion efficiencies of these systems were below 3%.

Objective

The overall goal of Hawaii's BioHydrogen Program is to generate hydrogen from water using solar energy and microalgae under sustainable conditions. Specific bioprocess engineering objectives include the design, construction, testing and validation of a sustainable photobioreactor system. Objectives relating to biology include investigating and optimizing key physiological parameters of cyanobacteria of the genus *Arthrospira (Spirulina)*, the primary organism of choice. Another objective is to disseminate the Mitsui-Miami cyanobacteria cultures, now part of the Hawaii Culture Collection (HCC), to other research groups.

The effort is a 3-year project. Several areas of research and tasks need to be pursued. These include: (1) sustainable bioreactor system design; (2) hydrogen-producing microbes for the bioprocess; and (3) maintenance of the HCC. The realization of the envisioned process will require the joint development of both the hardware, namely reliable and inexpensive bioreactors, and system "software," namely the cyanobacterial strains that are able to grow and produce hydrogen effectively.

Approach

Our approach uses a single organism for producing hydrogen gas from water. Key stages are the growth of the biomass, the dark induction of the hydrogenase system, and the subsequent generation of the hydrogen in light. The biomass production stage involves producing dense cultures of filamentous, non-heterocystous cyanobacteria and optimizing biomass in innovative tubular photobioreactors, work being done in collaboration with M. Tredici, University of Florence (Tredici and Materassi, 1992). The hydrogen generation stages entail inducing the enzymes and metabolic pathways that enable both dark and light-driven hydrogen production. Our system is also amenable to a single-stage indirect process whereby hydrogen can be produced in the same bioreactor configuration.

Cyanobacteria, like other algae, induce a hydrogen-evolving system under dark anaerobic conditions. Cyanobacteria can accumulate large quantities of carbohydrates when limited for nitrogen. The ability to grow cyanobacteria in large-scale (> 10 ha) has already been demonstrated. This project will initially utilize the HCC as the primary source of cyanobacteria that should be suitable for the process. Strains will be screened for key characteristics such as carbohydrate accumulation (total, productivity), dark-anaerobic hydrogenase induction (rate, maximal), and light-driven hydrogen evolution (effects of light, extent of utilization of stored carbohydrates, inhibition by oxygen).

Technical Goals

Technical goals include: (1) Designing, constructing, and testing tubular photobioreactors that offer superior operational characteristics yet are inexpensive to construct and operate for hydrogen production. Specific goals are demonstrating high productivities, effective mass transfer and outdoor hydrogen production. (2) Understanding and manipulating the physiological parameters of the microalgae to optimize for hydrogen production. The main near-term technical goal is to test the tubular bioreactors performance with *Arthrospira* strains

Major Barriers to Meeting Technical Goals

Major barriers: (1) Understanding the physiological aspects of hydrogen production by these strains to permit developing protocols for effective hydrogen production in the lab; (2) Applying and adapting such protocols to photobioreactors, i.e., integrating the biology with engineering.

Past Results

This research on photobioreactor systems and cyanobacterial hydrogen production has completed its initial year. A previously supported project involved the transfer of the Mitsui-Miami collection to Hawaii.

Current Year Accomplishments and Status

This project was initiated in February 1997 with the design and construction of the prototype photobioreactors at the Kewalo Basin site in Honolulu. An automated monitoring and control system for culture temperature and pH was designed and implemented. Dissolved oxygen and light intensity are also automatically monitored and recorded. The photobioreactors and key components of the monitoring and control systems are shown in Figures 1 and 2. Further improvements in bioreactor design and operations are in progress. An engineering analysis of reactor performance has been initiated; for example, Figure 3 shows sample data for the relationship between holdup and gassing rate. Analyses of mass transfer coefficients and hydraulic dispersion coefficients are planned.

The operational characteristics of the tubular photobioreactors in Hawaii were tested with *Arthrospira*, an organism known to contain hydrogenase and produce hydrogen in the dark. The initial work developed protocols for high-density, high-productivity cultures under local conditions of light and temperature and compared these with prior experience in Italy. *Arthrospira* cultures have been successfully adapted to full sunlight by means of a stepwise process using shade cloth. Culture densities of at least 7.5 g/L were achievable during batch growth of adapted cultures (Figure 4). Semicontinuous culture growth was maintained within specified density ranges by varying the replacement rate of the culture medium; this was accomplished by means of an appropriate daily dilution with fresh medium. Biomass production (dry weight) averaged 0.43 g/L/d (1.03 g/L/d maximum) within the biomass ranges 2.6 - 3.5 g/L and 5.1 - 6.1 g/L (Figure 5). Similar productivities were achieved whether dilution was performed in the morning or late afternoon (Table 1).

Figure 6 shows a typical day's insolation curve and culture growth, and illustrates two factors which act to decrease biomass production. A growth slowdown is apparent during the 2-h period in which maximal sunlight intensities were observed, reflecting inhibition of photosynthesis by

high light intensities. An even larger decrease in productivity was caused by the large nighttime biomass loss, amounting to 20% of dry weight in the sample data shown (Fig. 6). Dark respiratory losses of this magnitude would substantially decrease carbohydrate reserves available for hydrogen production. An experiment designed to test whether dark biomass losses could be decreased by means of oxygen limitation at night is shown in Figure 7, while results are summarized in Table 2. Results suggest that oxygen deprivation at night reduced biomass loss, but also decreased production during subsequent illuminated periods. Thus, net 24-hour production was unaltered by nighttime bubbling with nitrogen. Work is underway to determine whether the treatment increased the carbohydrate/protein ratio or otherwise affected cellular composition. Additionally, laboratory research on the physiology of hydrogen production by *Arthrospira* is being initiated.

Table 1. Effect of morning versus afternoon dilution on daily dry weight production by semicontinuously grown cultures.

Day	AM Dilution	PM Dilution
1	0.622	0.514
2	0.518	0.395
3	0.275	0.251
4	0.589	0.667
5	0.149	0.165
6	0.782	0.336
7	0.079	0.560
8	0.359	0.368
9	0.160	0.448
Mean	0.392	0.412

Table 2. Effect of nighttime N_2 gassing on culture productivity and biomass losses.

Nighttime Bubbling	Daylight Production, g/l/d	Dark Biomass Loss, g/l/d	Net Production, g/l/d
N_2	0.547	0.155	0.392
Air	0.659	0.256	0.403
n	5	5	5
P (T <= t)	0.06	0.02	0.82

Data produced by the outdoor experiments will be used in economic and systems analysis. A preliminary analysis of the two-stage biophotolysis process has been carried out that indicated the overall cost of hydrogen production would be below $15/MMBTU, if certain research goals can be met such as the achievement of very high photosynthetic efficiencies (Benemann, 1995). A key issue is the cost of the photobioreactors, both capital and operating. This project will develop information to allow a more detailed cost analysis, in particular for Hawaii which because of favorable environmental conditions is a likely location for the development and application of such systems.

This project has just finished its first year. A manuscript has been prepared and accepted for publication (Szyper et al., 1998). An invited paper to *Trends in Biotechnology* is in preparation. The research was reported at BioHydrogen '97 and at several workshops and meetings. The work was presented at the American Society for Microbiology meeting in May 1998 (Radway et al., 1998). Interest in the tubular photobioreactors and the culture collection is evident. During the year, discussions have been held with various firms and additional contacts are being pursued.

Plans for Future Work

Major actions for Year 2 include the following:

Task 1. Physiology of Hydrogen Production by *Arthrospira.* Specific subtasks include: (a) Hydrogenase induction of light and N-limited cultures (effects of carbohydrate on dark fermentations); (b) Hydrogen evolution in the light by anaerobically adapted cultures.

Task 2. Sustainable Bioreactor System Design. Subtasks include: (a) continuing performance evaluation of the tubular photobioreactors with several cyanobacterial strains; and (b) development of protocols for induction of hydrogenases and hydrogen production in the photobioreactors.

Task 3. Maintenance of HCC Subtasks include: (a) maintenance and curation of the Mitsui-Miami strains and (b) distribution of strains to qualified researchers and groups.

This project contributes to the International Energy Agency (IEA) Hydrogen Program Annex 10B on biological hydrogen production. The project is also a part of a general U.S.-Japan understanding that fosters binational cooperative research in biological hydrogen production. DOE is providing funding for the transfer of the Mitsui-Miami collection, the establishment of a scientific base for the HCC collection, and for the dissemination of the Mitsui-Miami strains to other qualified researchers at national laboratories and industry. Funding from the Research Institute of Innovative Technology for the Earth (RITE) is being used to evaluate photosynthetic bacteria in the Mitsui-Miami collection for active hydrogen production.

Acknowledgment

This material is based on work supported by the Department of Energy, Hydrogen Program, under award No. DE-FC36-97GO10202, O.R. Zaborsky, principal investigator. Any opinions, findings and conclusions or recommendations expressed in this publication are those of the authors and do not necessarily reflect the views of the Department of Energy. We thank Gerald Cysewski, Cyanotech Corporation, for *Arthrospira* sp. starter cultures.

During the past year, Mitsufumi Matsumoto, a visiting student from Tokyo University of Agriculture and Technology being funded by Japan's Ministry of Education, participated in the project. Andrew Kato, an undergraduate, is currently associated with the project.

References

Benemann, J. R., Photobiological Hydrogen Production, Report to the Pittsburgh Energy Technology Center (1995).

Radway, J. C., Yoza, B. A., Benemann, J. R., Tredici, M. R., and Zaborsky, O. R., Evaluation of an Outdoor Tubular Photobioreactor System in Hawaii, in ASM Proceeding Abstracts, 1998, accepted.

Szyper, J. P. , Yoza, B. A., Benemann, J. R., Tredici, M. R. and Zaborsky, O. R., Internal Gas Exchange Photobioreactor: Development and Testing in Hawaii, in BioHydrogen: Proceedings of the International Conference on Biological Hydrogen Production, June 23-26, 1997, Waikoloa, Hawaii; O. R. Zaborsky, Editor; J. R. Benemann, J. Miyake, T. Matsunaga and A. San Pietro, Associate Editors, Plenum Publishing Corporation, New York, NY, 1998, accepted.

Tredici, M. R. and Materassi, R., From Open Ponds to Vertical Alveolar Panels: The Italian Experience in the Development of Reactors for the Mass Cultivation of Phototrophic Microorganisms, Journal of Applied Phycology, 4, 221-231 (1992).

Figures

Figure 1. Tredici-design tubular photobioreactor at Kewalo Basin, Honolulu, Hawaii. Two eight-tube bioreactors are shown on the research platform. The bioreactors are 20 m long, with a 4 cm diameter tubing. The formation of bubbles is caused by the injection of compressed air.

Figure 2. Photobioreactor components. a) Degassers, b) Sensor assembly (light, temperatures, pH probe), c) temperature control with automated sprinkler, d) air/CO_2 injection manifold.

Figure 3. Holdup (total air bubble volume in all eight reactor tubes) vs. air input rate. Input air pressure was 3 psi.

Figure 4. Batch growth of *Arthrospira* sp. during adaptation to full sunlight.

Figure 5. Daily production by *Arthrospira* sp. maintained within selected density ranges by means of semicontinuous dilution.

Figure 6. 24-hour light and dry weight curve for semicontinuously maintained culture.

Figure 7. Effect of nighttime N_2 gassing on culture growth.

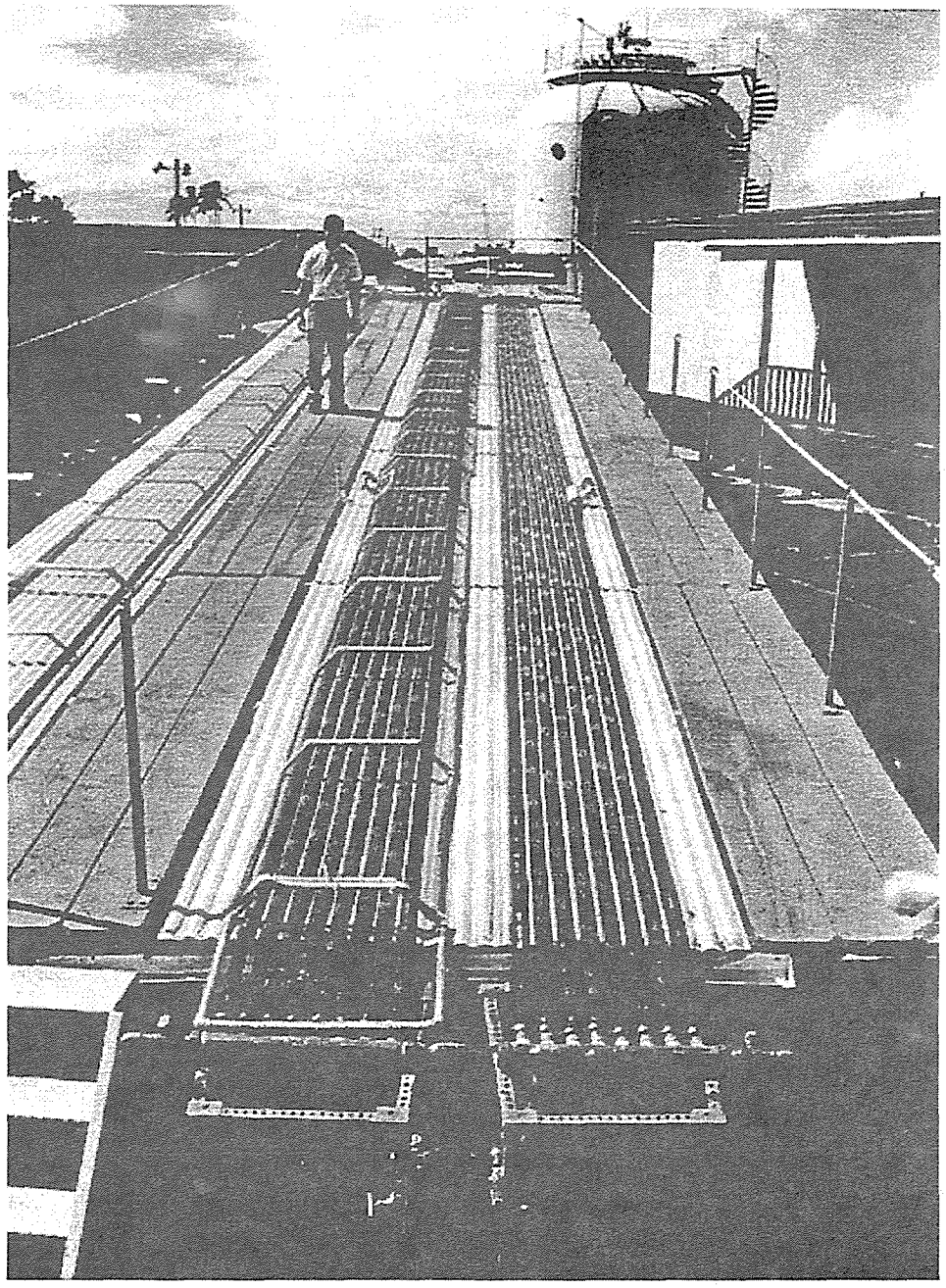

Figure 1

Figure 2

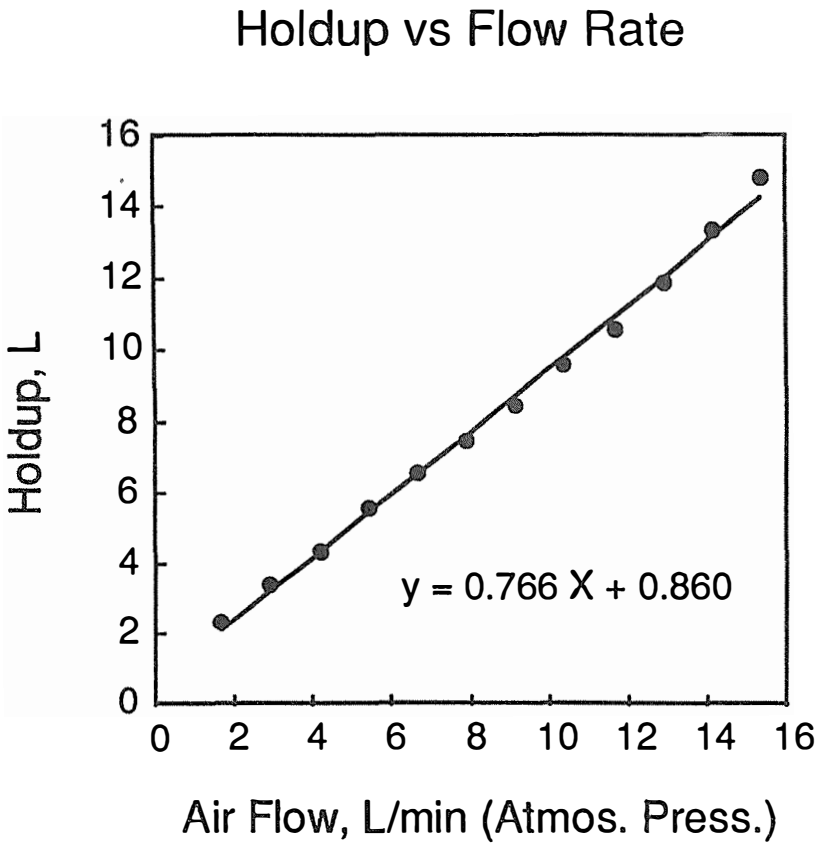
Holdup vs Flow Rate
Holdup, L
Air Flow, L/min (Atmos. Press.)
y = 0.766 X + 0.860
0
2
4
6
8
10
12
14
16

Figure 3

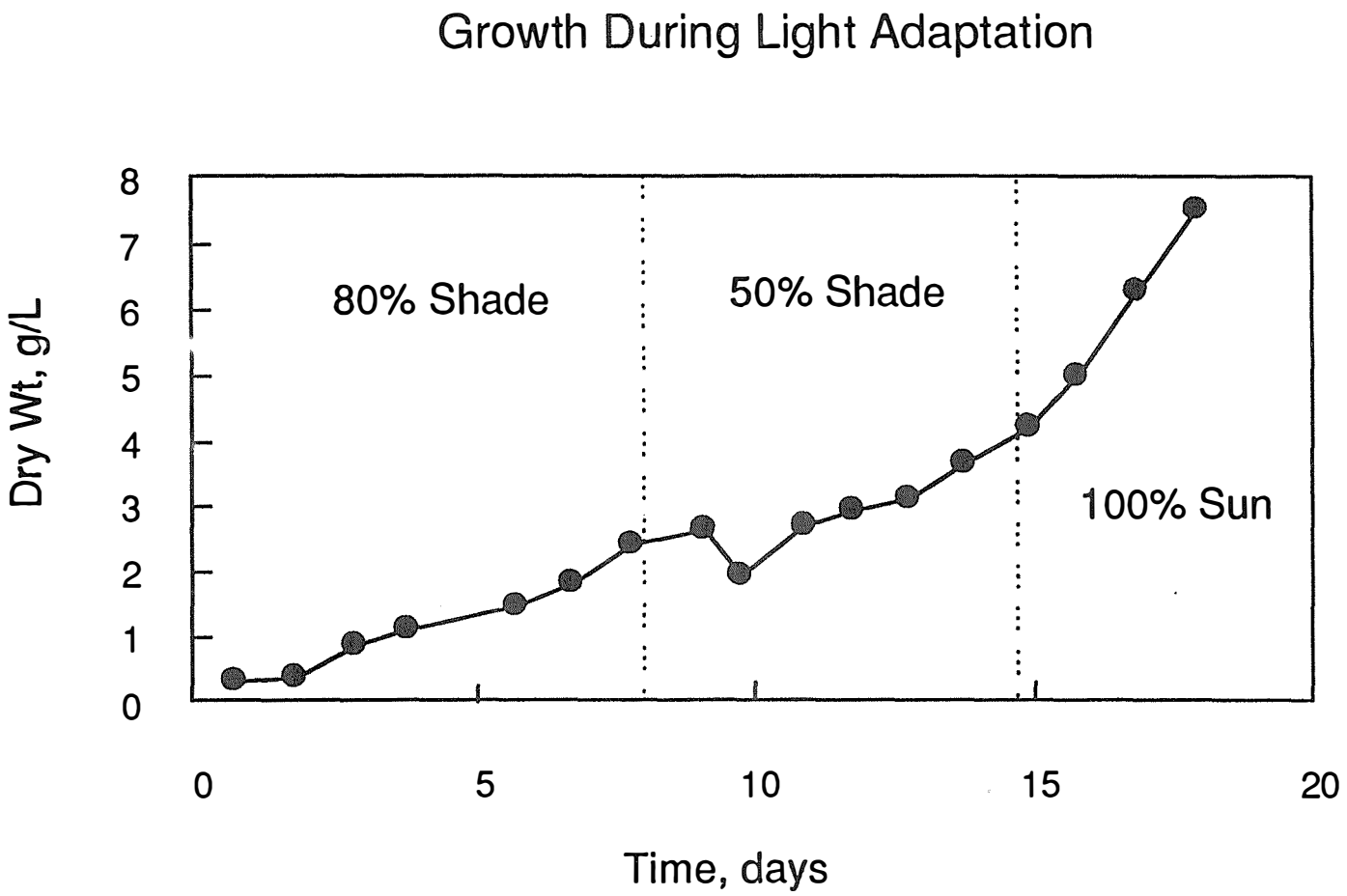
Growth During Light Adaptation
Dry Wt, g/L
0
1
2
3
4
5
6
7
8
80% Shade
50% Shade
100% Sun
0
5
10
15
20
Time, days

Figure 4

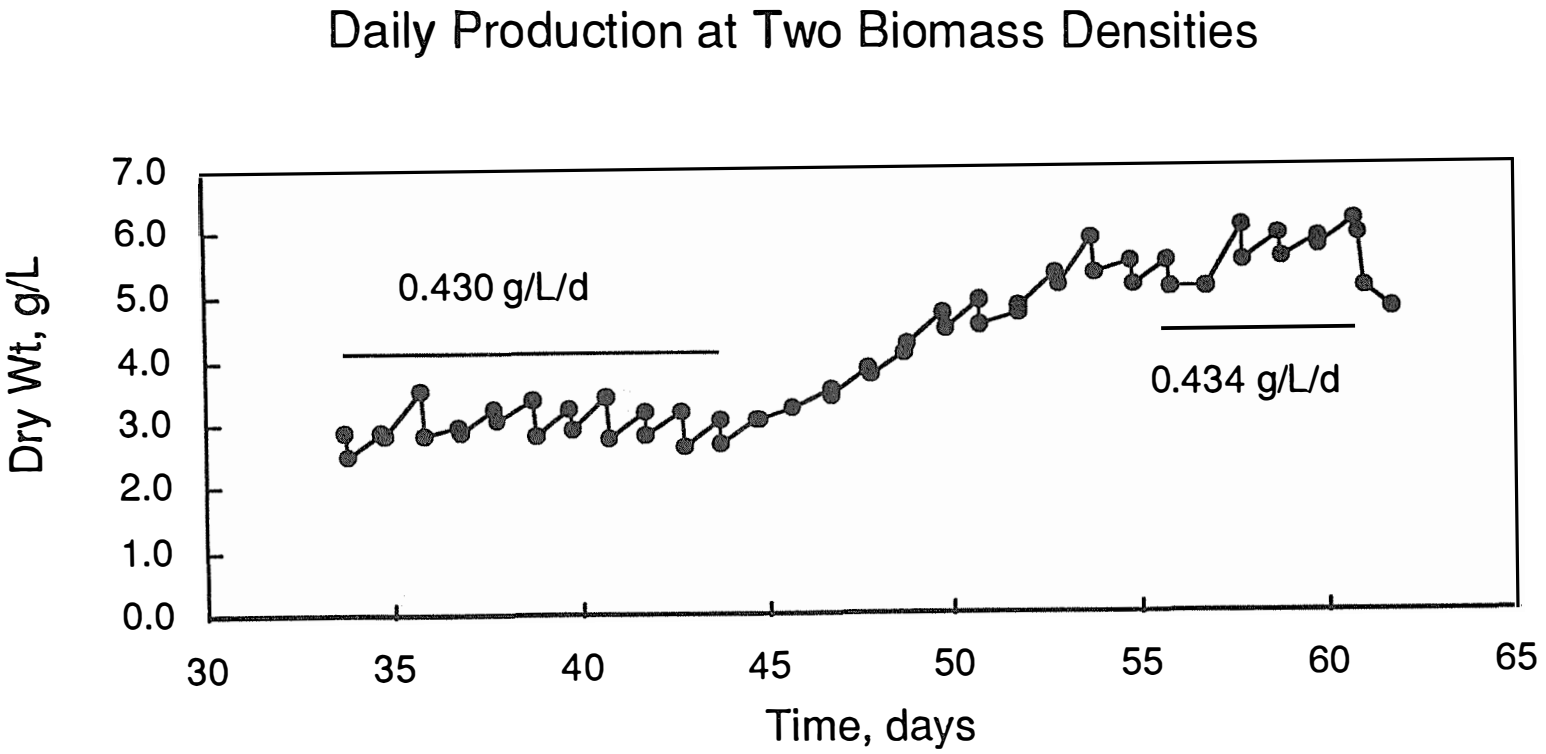
Daily Production at Two Biomass Densities
Dry Wt, g/L
7.0
6.0
5.0
4.0
3.0
2.0
1.0
0.0
0.430 g/L/d
0.434 g/L/d
30
35
40
45
50
55
60
65
Time, days

Figure 5

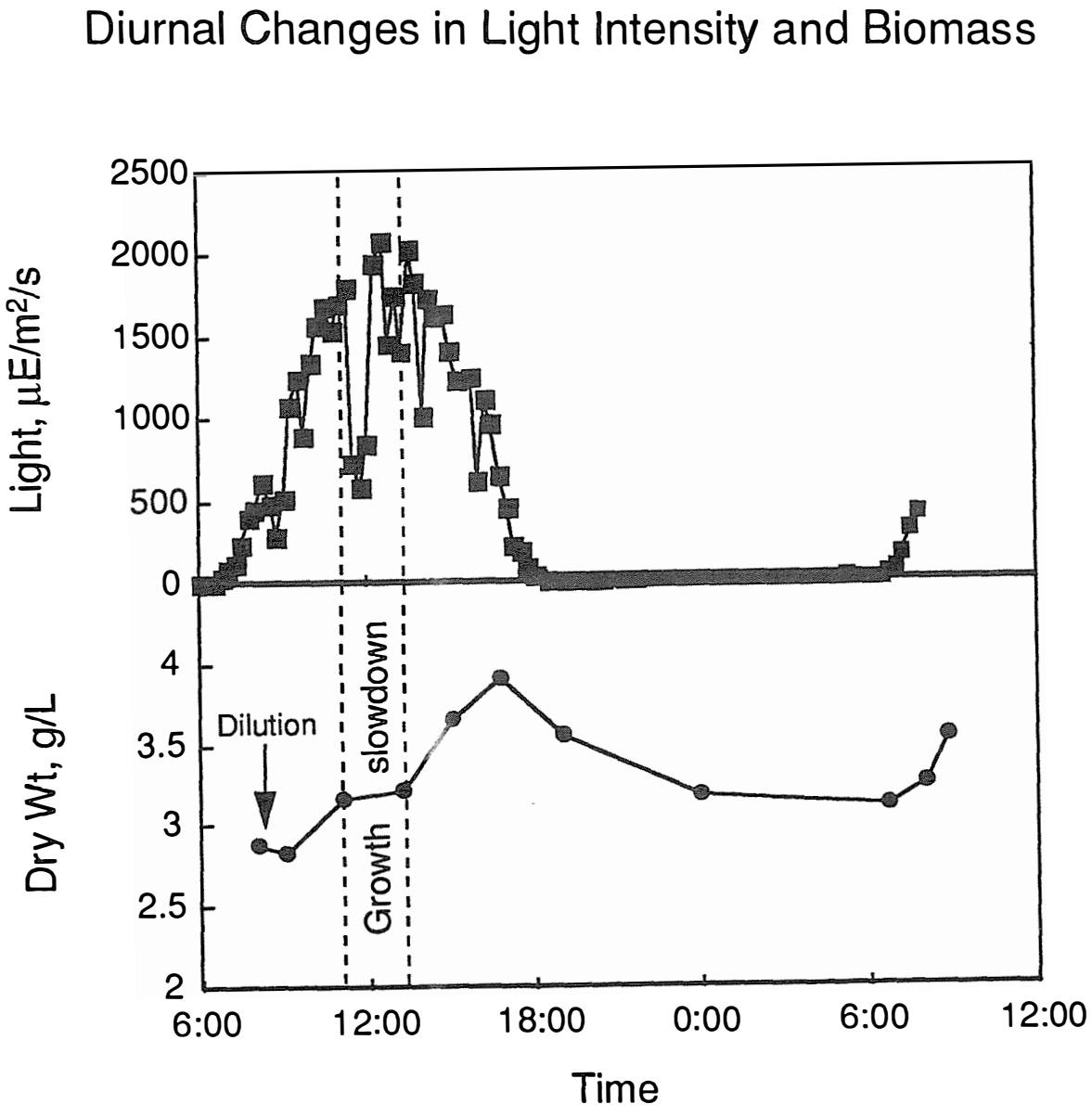
Diurnal Changes in Light Intensity and Biomass
Light, µE/m²/s
2500
2000
1500
1000
500
0
Dry Wt, g/L
4
3.5
3
2.5
2
Dilution
Growth
slowdown
6:00
12:00
18:00
0:00
6:00
12:00
Time

Figure 6

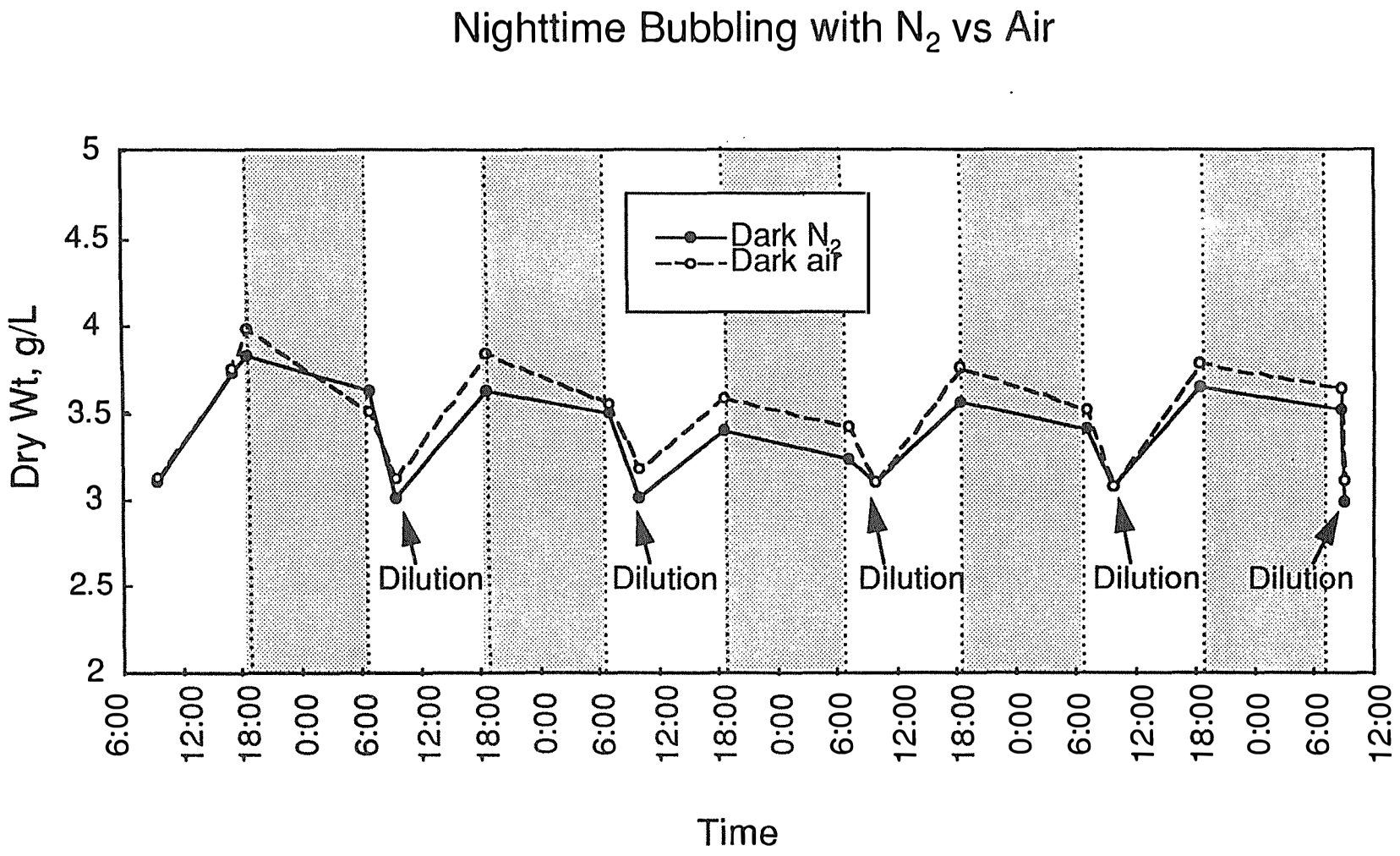
Nighttime Bubbling with N_2 vs Air
Dry Wt, g/L
5
4.5
4
3.5
3
2.5
2
Dark N_2
Dark air
Dilution
Dilution
Dilution
Dilution
Dilution
6:00
12:00
18:00
0:00
6:00
12:00
18:00
0:00
6:00
12:00
18:00
0:00
6:00
12:00
18:00
0:00
6:00
12:00
18:00
0:00
6:00
12:00
Time

Figure 7

MAXIMIZING PHOTOSYNTHETIC PRODUCTIVITY AND SOLAR CONVERSION EFFICIENCY IN MICROALGAE BY MINIMIZING THE LIGHT-HARVESTING CHLOROPHYLL ANTENNA SIZE OF THE PHOTOSYSTEMS

Anastasios Melis*, John Neidhardt and John R. Benemann
Department of Plant and Microbial Biology, 411 Koshland Hall, University of California, Berkeley, CA 94720-3102

Abstract

The solar conversion efficiency and productivity of photosynthesis in light-acclimated *Dunaliella salina* (green algae) were analyzed. Cells were grown under continuous low-light (LL; 100 μmol photons m^{-2} s^{-1}) or high-light (HL; 2,000 μmol photons m^{-2} s^{-1}) conditions. HL-grown cells exhibited signs of chronic photo-inhibition, i.e., a lower pigment content, a highly truncated chlorophyll (Chl) antenna size for the photosystems, and accumulation of photodamaged photosystem-II (PSII) reaction centers in the chloroplast thylakoids. In spite of these deficiencies, high-light-grown cells showed photosynthetic productivity (300 mmol O_2 (mol Chl)$^{-1}$ s^{-1}) that was ~3 times greater than that of the normally pigmented LL-grown cells (~100 mmol O_2 (mol Chl)$^{-1}$ s^{-1}). Recovery from photoinhibition in the HL-grown cells, induced in the absence of a light-harvesting Chl antenna size enlargement, increased photosynthetic productivity further to ~650 mmol O_2 (mol Chl)$^{-1}$ s^{-1}. It is shown that, under moderate to high light conditions, *D. salina* with a highly truncated Chl antenna size will display superior photosynthetic productivity, solar conversion efficiency and H_2 production when compared to the normally pigmented control cells. Estimates of H_2 production in mass culture suggest an average of 220 L H_2 m^{-2} d^{-1} for the cells with the truncated Chl antenna, and less than 50 L H_2 m^{-2} d^{-1} for the normally pigmented cells.

Introduction

Microalgal cultures growing under full sunlight are believed to have lower solar-to-biomass energy conversion efficiencies than when growing under low light intensities. The reason for this inefficiency is that, at moderate to high photon flux densities, the rate of photon absorption by the antenna chlorophylls far exceeds the maximal rate of photosynthesis, resulting in dissipation of the excess photon energy as fluorescence or heat. More than 80% of absorbed photons could thus be wasted, reducing solar conversion efficiencies by these cells and culture productivity to unacceptably low levels. Under bright incident sunlight, fully pigmented cells are also subject to photoinhibition [Powles 1984, Melis 1991, Baroli and Melis 1998], further lowering solar conversion efficiencies and photosynthetic productivity. To make the situation worse, cells deeper in the algal culture are deprived of much needed sun-light as this is strongly attenuated due to filtering by the first layer of cells in the culture container [Naus and Melis 1991, Neidhardt et al. 1998].

Variation in the level of irradiance during plant growth brings about reversible structural and functional adjustments in their photosynthetic apparatus [Anderson 1986, Melis 1991]. It has been demonstrated that the Chl antenna size of green algae such as *Chlorella vulgaris* [Ley and Mauzerall 1982], *Dunaliella tertiolecta* [Sukenik et al. 1988], *Dunaliella salina* [Smith et al. 1990] and *Chlamydomonas reinhardtii* [Neale and Melis 1986, Melis et al. 1996] changes in response to the level of irradiance during cell growth. In general, LL promotes larger Chl antenna size for the photosystems (up to 500 Chl molecules for photosystem-II). HL elicits a smaller Chl antenna size (as low as 60 Chl molecules for this photosystem) [Smith et al. 1990, Melis 1996].

Exposure of plants and algae to high irradiance may cause photoinhibition of photosynthesis [Powles 1984, Barber and Andersson 1992]. When grown under continuous illumination of high intensity (HL=2,000 µmol photons m^{-2} s^{-1}) in the presence of $NaHCO_3$ as the sole carbon source, *D. salina* chloroplasts assemble ~7% of the PSI complexes and ~65% of the PSII complexes compared to low-light (LL=100 µmol photons m^{-2} s^{-1}) controls. However, of the PSII present in the thylakoid of HL-grown cells, only about 20-25% were photochemically competent, the rest occurring as photodamaged centers containing an irreversibly inactive PSII reaction center (D1) protein [Smith et al. 1990, Vasilikiotis and Melis 1994]. Thus, in HL-acclimated, $NaHCO_3$-grown *D. salina*, photosynthesis and growth depend solely on ~7% of the PSI and ~15% of the PSII centers that are operational in LL-grown cells.

Theoretically, a truncated chlorophyll (Chl) antenna size of the photosystems (PS) in the chloroplast of microalgae could alleviate these difficulties because it will minimize absorbance of bright incident sunlight and wasteful dissipation of excitation energy, prevent photoinhibition, diminish mutual cell shading, permit for greater transmittance of light through the culture and, thus, result in a more uniform illumination of the cells. Overall, this would result in greater solar conversion efficiencies and photosynthetic productivity in mass microalgal cultures.

It is predicted that, under bright light intensities, a smaller Chl antenna size will result in a relatively higher light intensity for the saturation of photosynthesis in individual cells but, concomitantly, in a much greater solar conversion efficiency and cellular productivity on a per Chl basis. These theoretical considerations may appear to be a paradox and their validity has not yet been tested in the laboratory. This manuscript presents the results of a feasibility study and experimental demonstration of these concepts. The work in this paper builds upon recent research in this laboratory [Smith et al. 1990, Kim et al. 1993, Neidhardt et al. 1998, Melis et al. 1998]. It presents a comparative analysis of the photosynthetic productivity and solar conversion efficiency of normally pigmented and Chl antenna deficient *D. salina*. The results support the notion that, in mass culture, cells with a highly truncated Chl antenna size will exhibit superior photosynthetic productivity and solar conversion efficiencies compared to that of normally pigmented control cells.

Materials and Methods

Growth of Dunaliella salina cultures

The unicellular green alga *Dunaliella salina* was grown in a hypersaline medium containing 1.5 M NaCl, 0.2 M Tris-HCl (pH 7.5), 0.1 M KNO_3, 0.1 M $MgSO_4$, 6 mM $CaCl_2$, 2 mM KH_2PO_4, 40 μM $FeCl_3$ dissolved in 400 μM EDTA [Pick et al. 1986]. Bicarbonate was added to the medium as the ever present carbon source to a concentration of 25 mM. Supplemental CO_2 was provided by bubbling the culture with a mixture of 3% CO_2 in air. The medium also contained a mixture of micronutrients in the following concentrations: 150 μM H_3BO_3, 10 μM $MnCl_2$, 2 μM Na_2MoO_4, 2 μM $NaVO_3$, 0.8 μM $ZnCl_2$, 0.3 μM $CuCl_2$, 0.2 μM $CoCl_2$.

Growth media were inoculated with several ml of a stock suspension of *D. salina* cells and were cultivated in flat bottles (about 4 cm thick) at a temperature between 26 and 29°C. The cells grew exponentially in the density range between 0.15-1.5x10^6 cells/ml [Naus and Melis 1991]. Measurements were performed with cultures having a cell density between 0.8-1.3x10^6 cells/ml.

The cultures were grown under either low light (incident irradiance of ~100 μmol photons m^{-2} s^{-1}) or high light conditions (irradiance of ~2,000 μmol photons m^{-2} s^{-1}). The incident irradiance was measured with a LI-COR, Model LI-185B radiometer. Shaking of the cultures along with the use of light reflectors ensured a uniform illumination of the cells.

Cell count and chlorophyll quantitation

The cell density in the cultures was obtained upon counting with a Hemacytometer (improved Neubauer chamber) and by use of an Olympus BH-2 compound microscope at a magnification of x100. For the counting, cells were

immobilized and stained by addition of several µl of Utermoehl oil to 0.25-1 ml aliquot of the culture.

Chlorophyll concentrations were measured upon pigment extraction in 80% acetone after removal of cell debris by centrifugation, and by measuring the absorbance of the solutions at 663 and 645 nm. The amount of chlorophyll was calculated by use of Arnon's equations [1949].

Photosynthesis measurements

Photosynthetic activity of the cells was measured by a Clark-type oxygen electrode. An aliquot of 5 ml cell suspension was applied to the oxygen electrode chamber. In order to compare the relative quantum yield of photosynthesis between the different samples, about the same Chl concentration (2-3 mM) was loaded in the oxygen electrode. To ensure that oxygen evolution was not limited by the carbon source available to the cells, 100 µl of a 0.5 M sodium bicarbonate solution (pH 7.4) was added prior to the oxygen evolution measurements. Samples were illuminated with increasing light intensities under stirring and at a temperature of 25°C. The rate of oxygen evolution under each of these light intensities was recorded continuously for a period of 2.5 min. The results were plotted to show the light saturation curves of photosynthesis either on a per chlorophyll or on a per cell basis.

The concentration of the photosystems in thylakoid membranes was estimated spectrophotometrically from the amplitude of the light *minus* dark difference at 700 nm (P700) for PSI, and 320 nm (Q_A) for PSII [Melis 1989]. The light-harvesting Chl antenna size of PSI and PSII was measured from the kinetics of P700 photo-oxidation and Q_A photoreduction, respectively [Melis 1989].

Results and Discussion

Information about the efficiency and productivity of photosynthesis can be obtained directly from the light-saturation curve of photosynthesis (the so-called "P vs I" curve) in which the rate of O_2 evolution, or CO_2 assimilation, is measured and plotted as a function of the actinic light intensity. In such a presentation, the rate of photosynthesis first increases linearly with light intensity and then levels off as the saturating light intensity (I_s) is approached. The slope of the initial, linear, increase defines the quantum yield of photosynthesis (O_2 evolved per photon absorbed) [Björkman and Demmig 1987, Neale et al. 1993]. The rate of photosynthesis is saturated at light intensities higher than I_s. This light-saturated rate (P_{max}) provides a measure of the capacity of photosynthesis for the particular sample [Powles and Critchley 1980]. The three parameters (quantum yield, I_s, and P_{max}), measured with dilute cultures under conditions of little mutual shading, define the vital signs and photosynthetic properties of the algal cells.

It was of interest to compare the optical properties and performance characteristics of LL and HL-acclimated *D. salina.* The objective of this work was to assess the organization and function of the photosynthetic apparatus and to test for the hypothesis that a truncated Chl antenna size would actually help cells to achieve a higher *per chlorophyll* capacity of photosynthesis and greater solar energy conversion efficiencies under moderate to high light intensities.

Optical properties, photosynthetic apparatus organization and performance in LL and HL-grown Dunaliella salina

Cells grown under continuous LL or HL in the presence of 25 mM $NaHCO_3$ as the sole carbon source, had similar doubling times (8-8.5 h, Table 1). However, compared to the LL-, HL-grown cells had only 25% of the cellular Chl content, a much higher Chl *a*/Chl *b* ratio and a substantially truncated Chl antenna size for both photosystem-I (PSI) and photosystem-II (PSII) in their chloroplast (Table 1).

Table 1. Effect of growth irradiance on pigment content, photosystem Chl antenna size, and rate of photosynthesis in *Dunaliella salina.* Cells were grown at low-light (100 μmol photons m^{-2} s^{-1}) or at high-light (2,000 μmol photons m^{-2} s^{-1}).

	Low-light grown	**High-light grown**
Cell doubling time (h)	8.0	8.5
Chl/cell (molecules/cell)	$0.41*10^9$	$0.10*10^9$
Chl *a*/Chl *b* (mol:mol)	4.5:1	12:1
N_{PSI}	230	105
N_α	560 (65%)	---
N_β	140 (35%)	130 (05%)
N_{core}	---	60 (95%)
P_{max} mmol O_2 (mol Chl)$^{-1}$ s^{-1}	100	320
Quantum yield, rel. units	1.0	0.37

The number of Chl (*a* and *b*) molecules specifically associated with PSI (N_{PSI}) was lowered from 230 in LL to 105 in HL. In LL-cells, about 65% of the functional PSII centers were $PSII_\alpha$ with an antenna size N_α of approximately 500 Chl *(a* and *b)*

molecules. The remaining 35% of the functional PSII were of the PSIIβ-type with an antenna size N_β of ~140 Chl *(a* and *b)* molecules. This well-known PSII α–β antenna heterogeneity [Melis 1991] was essentially absent in the HL-cells. In the latter, 95% of all functional PSII centers possessed a small antenna composed of ~60 Chl molecules. These results are consistent with the notion that HL-cells grown in the presence of $NaHCO_3$ exist in a state of chronic irradiance stress as photosynthesis is limited by the slow carbon supply [Smith et al. 1990, Vasilikiotis and Melis 1994, Baroli and Melis 1996]. Such alterations in the pigment and photosystem content of the cells brought about significant changes in the optical properties of the respective cultures. Figure 1 shows the transmittance of light through a LL-grown and a HL-grown *D. salina* culture. For the same cell density 10^6 cells/ml) , it is evident that transmittance of light is attenuated strongly as a function of distance from the surface in the fully pigmented cells. At 5 cm below surface, the level of irradiance is less that 20% of that incident to the culture (Fig. 1). On the contrary, the HL-grown cells with the truncated Chl antenna size permit more than 70% of the incident irradiance to reach the 5 cm mark below the culture surface. It is evident from these considerations that illumination of the culture will be more uniform in cells with a truncated Chl antenna size.

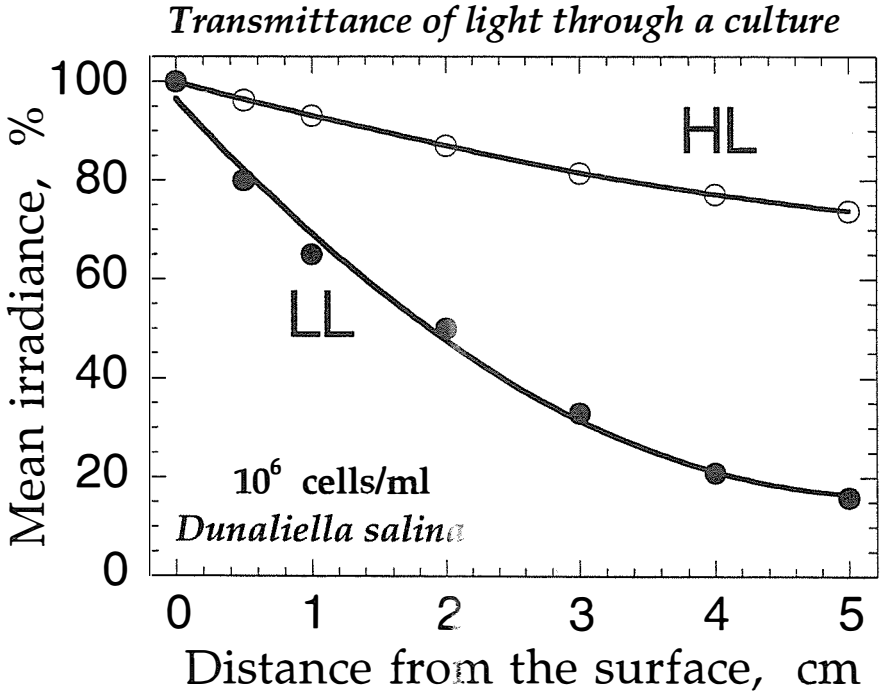

Figure 1. Mean irradiance as a function of distance from the surface in *Dunaliella salina* cultures. Fully pigmented cells were grown under low-light (LL). Cells with a truncated Chl antenna size were grown under high irradiance (HL).

The effect of the truncated Chl antenna size and chronic photoinhibition status on the quantum yield and rate of photosynthesis were assessed. Figure 2A shows the light-saturation curves of LL and HL $NaHCO_3$-grown *D. salina.* It is

evident that LL-grown cells, in which the rate of light absorption limits photosynthesis, have a light-saturated rate (P_{max}) of ~100 mmol O_2 (mol Chl)$^{-1}$ s^{-1}. The HL-cells with the truncated Chl antenna size and chronic photoinhibition condition reached a light-saturated rate of photosynthesis (P_{max} =~320 mmol O_2 (mol Chl)$^{-1}$ s^{-1}) that is ~3 times greater than that of the normally pigmented cells. This difference is attributed to the much smaller Chl antenna size for the HL-grown cells, translating into higher per Chl productivity. Consistent with this interpretation is also the difference in the I_s values which is 8-10 times greater for the HL grown than for the LL-grown cells, suggesting an average 8-10 times greater effective Chl antenna size for the latter (Table 1, [Herron and Mauzerall 1972]).

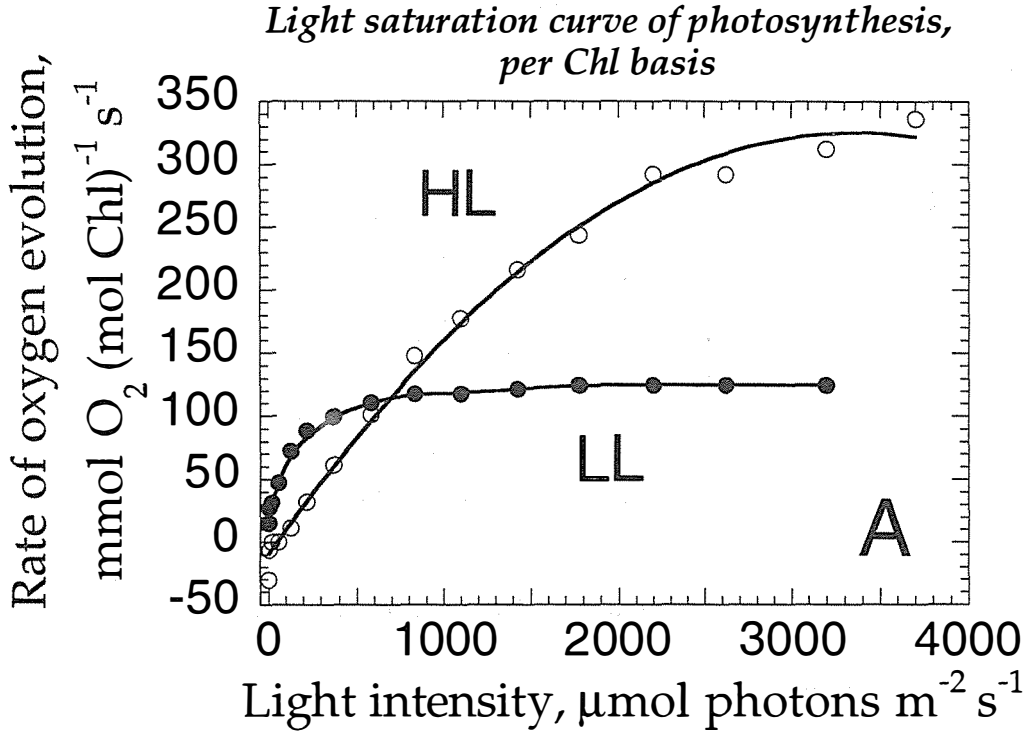

Figure 2A. The light-saturation curve of photosynthesis in $NaHCO_3$-grown *Dunaliella salina.* Cells were grown either at ~100 µmol photons m^{-2} s^{-1} (LL) or at ~2,000 µmol photons m^{-2} s^{-1} (HL). Rates of oxygen evolution on a *per chlorophyll* basis were measured as a function of incident intensity to the cell suspension.

The same results, plotted on a per cell basis (Fig. 2B), show a greater cellular productivity for the LL-grown cells (~75 pmol O_2 10^{-6} cells s^{-1}), compared with the HL-grown cells in which the cell productivity was at ~55 pmol O_2 10^{-6} cells s^{-1}. Again, this difference underscores the chronic photoinhibition status of the HL-grown cells where, in addition to the truncated Chl antenna size, a significant fraction of PSII centers are photochemically inert due to photodamage [Vasilikiotis and Melis 1994]. This configuration of the photosynthetic apparatus in the HL-cells resulted in about similar growth rates with the LL-cells (Table 1). Clearly, however, both rates of growth are below those that can be achieved under optimal growth conditions [Smith et al. 1990, Baroli and Melis 1996].

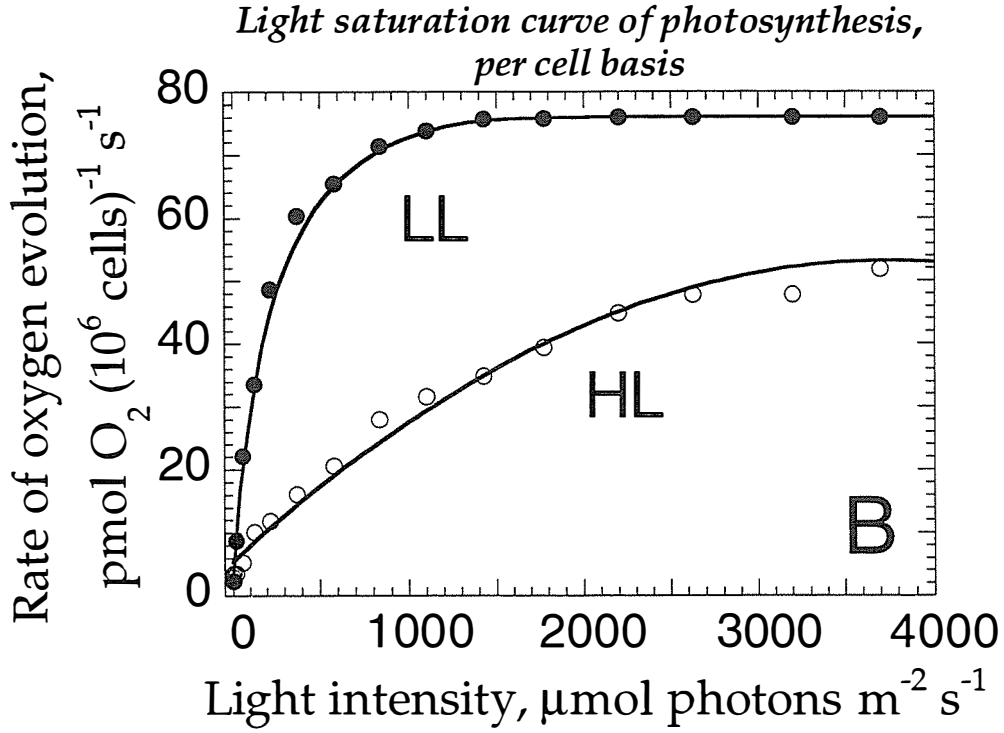

Figure 2B. The light-saturation curve of photosynthesis in $NaHCO_3$-grown *Dunaliella salina.* Cells were grown either at ~100 µmol photons m^{-2} s^{-1} (LL) or at ~2,000 µmol photons m^{-2} s^{-1} (HL). Rates of oxygen evolution on a *per cell* basis were measured as a function of incident intensity to the cell suspension.

It is also evident from the results of Fig. 2A that the initial slopes of the light-saturation curves (which provide a measure of the quantum yield of photosynthesis) are different for the two samples. This is better shown in Fig. 3, which shows the initial portions of the curves in Fig. 2A. We estimated that the initial slope of the light-saturation curve (quantum yield of photosynthesis) of the LL-grown cells (=0.42 rel. units) was steeper than that of the HL-grown cells (=0.15 rel. units). This difference shows that not all Chl molecules are photochemically competent in the HL-grown cells due to the chronic photoinhibition of photosynthesis that prevails in these cells [Smith et al. 1990, Kim et al. 1993, Baroli and Melis 1996]. On the basis of the relative quantum yield in these two measurements (Table 1), it would appear that only about 37% of the Chl molecules are photochemically competent in the HL, the rest being photochemically inert due to the accumulation of photodamaged and, therefore, inactive PSII centers in the HL-thylakoids. In principle then, the P_{max}=~300 mmol O_2 (mol Chl)$^{-1}$ s^{-1}) and the cellular productivity of the HL-grown *D. salina* with a truncated Chl antenna size could be even higher (by a factor of about 3) if there was a way to repair the photodamaged PSII centers while preserving the small Chl antenna size of the HL-grown samples.

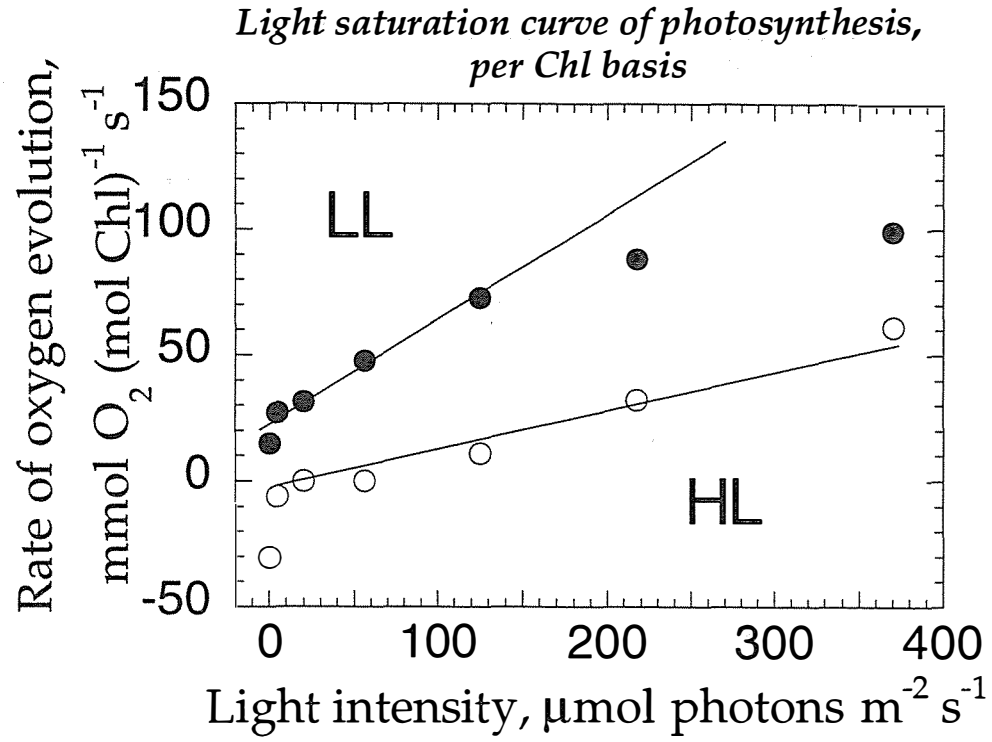

Figure 3. The light-saturation curve of photosynthesis in $NaHCO_3$-grown *Dunaliella salina.* Cells were grown either at ~100 μmol photons m^{-2} s^{-1} (LL) or at ~2,000 μmol photons m^{-2} s^{-1} (HL). The initial slope of the rate of photosynthesis *versus* irradiance (relative quantum yield on a Chl basis) in the LL-and HL-grown cells.

These results suggested that a truncated Chl antenna size for the photosystems will enhance the solar conversion efficiency and productivity of photosynthesis. To further illustrate the effect of Chl antenna deficiency, it was important to correct for the effect of chronic photoinhibition on the cellular photosynthesis. To this end, we devised an experimental approach that would promote the repair of photodamaged PSII centers without the induction of a concomitant significant increase in the Chl antenna size of the photosystems. We performed "light shift" experiments in which HL-grown cultures, with cells in the exponential phase of growth, were shifted to LL-growth conditions. We reasoned that upon a HL--->LL transition, both recovery from photoinhibition and an increase in the Chl antenna size will occur. However, the PSII repair from photoinhibition reportedly occurs with a half-time of about 60 min [Vasilikiotis and Melis 1994, Baroli and Melis 1996], whereas the increase in the Chl antenna size occurs with slower kinetics having a half time of ~4 hours. Thus, in the early stages of a HL--->LL shift, one would encounter a situation where significant recovery from photoinhibition would have occurred with only a minimal increase in the Chl antenna size of the photosystems.

Light shift experiments

Figure 4A shows the adjustment of the light-saturated rate of photosynthesis (P_{max}) in $NaHCO_3$-grown cells following a HL--->LL transition. It is evident that P_{max} increases promptly as a function of time upon the HL--->LL transition, from ~310 mmol O_2 (mol Chl)$^{-1}$ s^{-1}, measured at zero time, to a transient maximum of ~475 mmol O_2 (mol Chl)$^{-1}$ s^{-1}, attained within the first 2 h under LL conditions. This change reflects chloroplast recovery from photoinhibition, i.e., the repair of photodamaged PSII centers and the *de novo* biosynthesis/assembly of PSI centers, both of which bring about a greater capacity for photosynthetic electron transport in the thylakoid membrane [Neidhardt et al. 1998]. Subsequent incubation (> 2h) under LL-conditions caused a gradual decline in the value of P_{max}, reflecting the significant accumulation of Chl in the chloroplast, and an increase in the light-harvesting Chl antenna size which resulted in a lower per Chl P_{max} value for the cells.

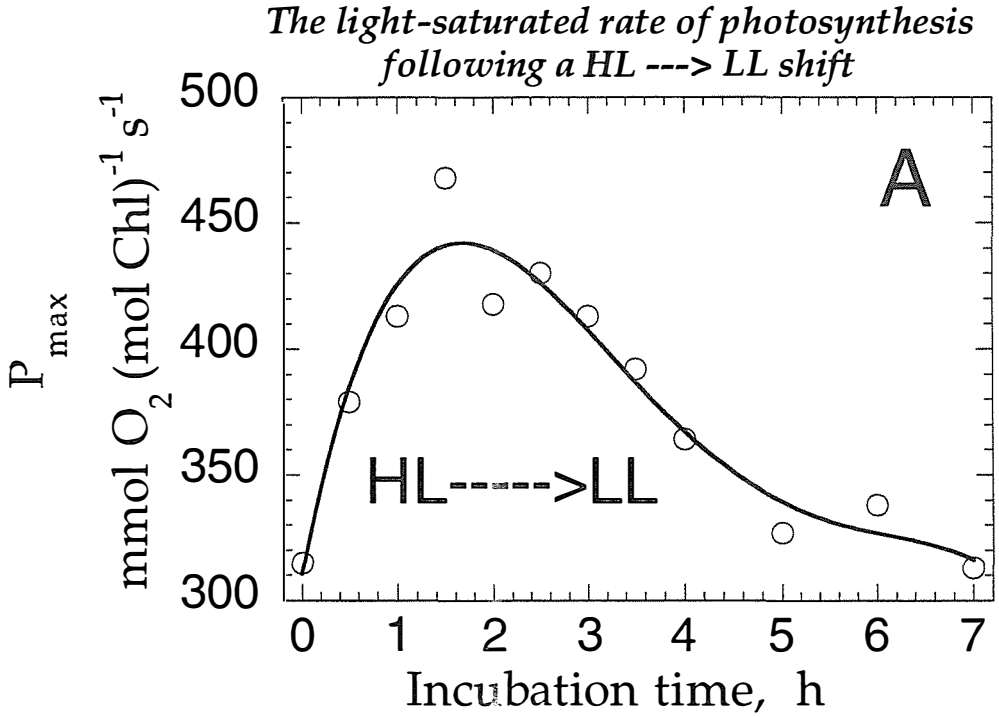

Figure 4A. Changes in the light-saturated rate of cellular photosynthesis (P_{max}) in *D. salina* following a switch of HL-grown cells to LL-growth conditions. The switch in growth irradiance occurred at zero time.

Figure 4B shows the change in the Chl/cell ratio following a HL--->LL transition. Within 7 hours, the Chl/cell ratio increased from less than 4 to about $9x10^{-16}$ mol cell^{-1}. Concomitantly, the Chl *a*/Chl *b* ratio of the cells decreased from ~12/1 to a low value of ~6/1 over the same time period (not shown). The lowering of the Chl *a*/Chl *b* ratio reflects accumulation of Chl *b* and the ensuing increase in the auxiliary light-harvesting chlorophyll antenna size of the photosystems. Both

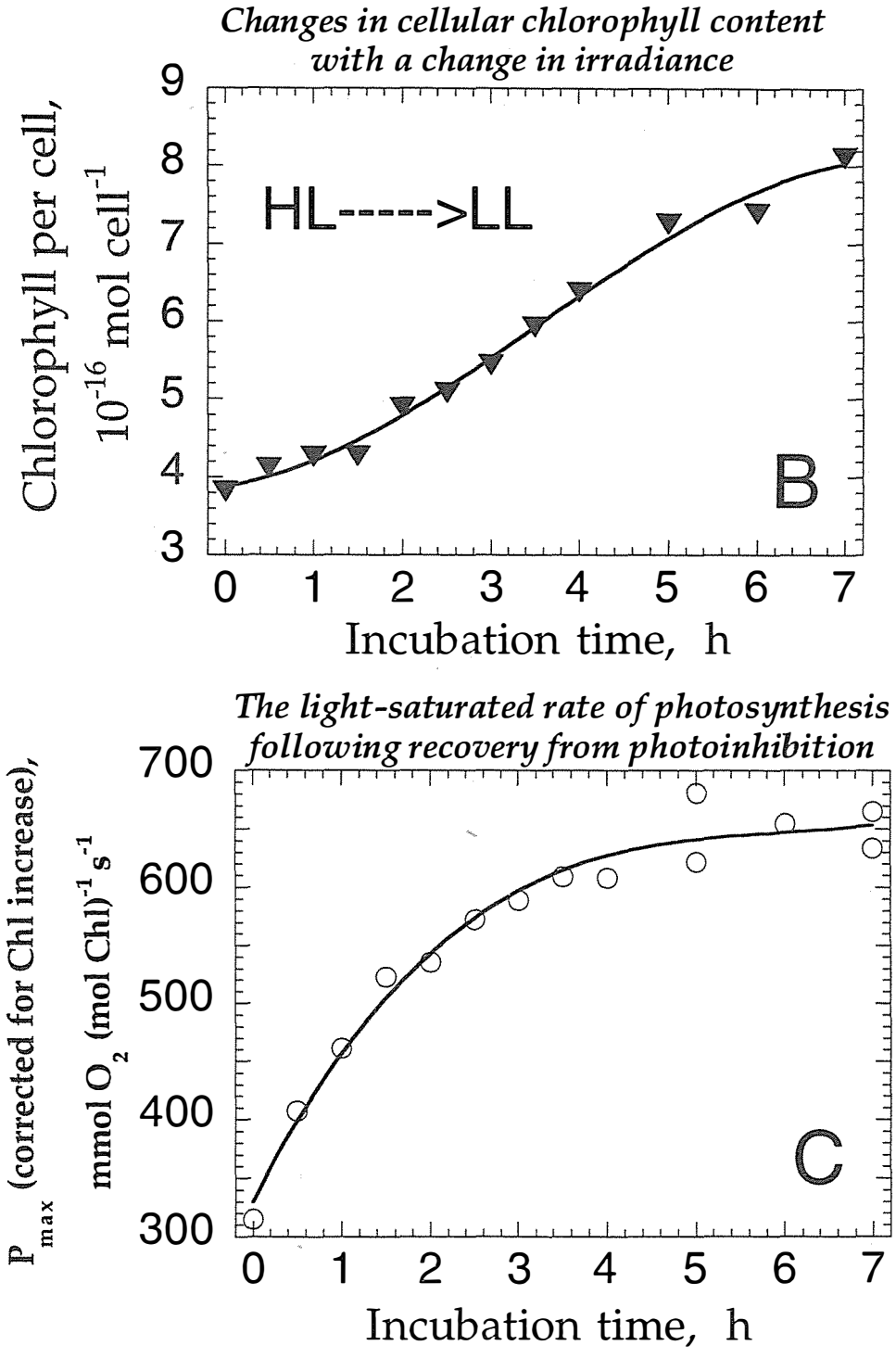

Figure 4. **(B)** Changes in Chl/cell ratio in $NaHCO_3$-grown *D. salina* following a switch of HL-grown cells to LL-growth conditions. The switch in growth irradiance occurred at zero time. **(C)** Light-saturated rates of photosynthesis (P_{max}), corrected for the Chl/cell increase of (B), as a function of incubation under LL. Note the 2.5-fold increased capacity of photosynthesis upon recovery from photoinhibition.

changes are consistent with earlier measurements of the Chl antenna size increase upon a HL--->LL transition [Kim et al. 1993].

Figure 4C shows estimated values of P_{max} as a function of incubation time following a HL--->LL transition. This presentation depicts the P_{max} values that would have been attained upon recovery from photoinhibition in the absence of a concomitant Chl antenna size increase. Results in Fig. 4C were obtained from those of Fig. 4A by correcting for the Chl/cell increase shown in Fig. 4B. Fig. 4C shows that, following recovery from photoinhibition, P_{max} in HL-grown *D. salina* would have increased from ~310 to over 650 mmol O_2 $(mol\ Chl)^{-1}\ s^{-1}$. The exponential increase in the value of P_{max} following the HL--->LL transition mainly reflects the kinetics of the repair of photodamaged PSII centers. The measured half time of ~1 h (Fig. 4C) is consistent with earlier findings on the half time of the PSII repair from photodamage [Vasilikiotis and Melis 1994, Baroli and Melis 1996].

In principle then, in the absence of photoinhibition, the photosynthetic performance of *D. salina* with a truncated light-harvesting antenna size, would be greater by a factor of ~2.5 than that shown in Fig. 2A (HL). Fig. 5 compares the light-saturation curve of photosynthesis of LL-grown cells with the calculated light-saturation curve of HL-grown cells, after the correction of the latter for the effect of photoinhibition. It is evident from the results of Fig. 5 that photosynthetic productivity, on a per Chl basis, would be greater by a factor of ~6 in the cells with a

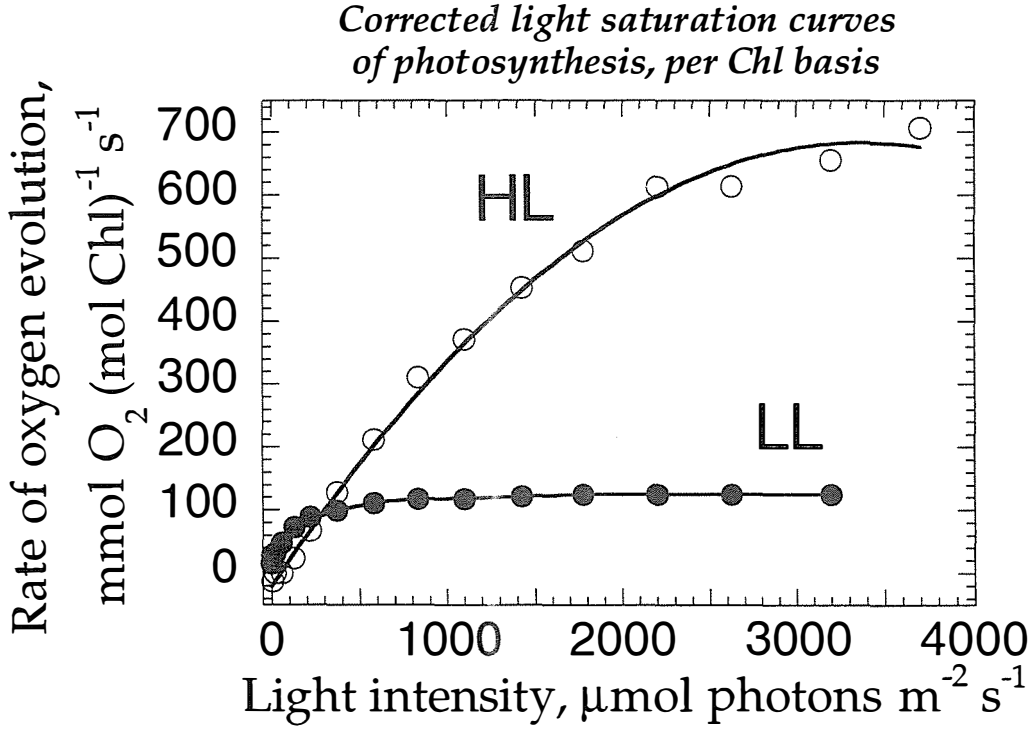

Figure 5. Light-saturation curves of photosynthesis in $NaHCO_3$-grown *D. salina.* (LL) Rates of oxygen evolution on a *per chlorophyll* basis were measured as a function of incident intensity to the suspension of low-light-grown cells. (HL) Rates of oxygen evolution on a *per chlorophyll* basis were estimated from the results of Fig. 2 (HL) upon correction for the effect of photoinhibition (Fig. 4C).

truncated Chl antenna (HL) than in the normally pigmented cells (LL). Moreover, the initial slopes of the light-saturation curves among the two cell types were similar, suggesting that under light-limiting conditions, the quantum yield of photosynthesis would be about the same in the normally pigmented cells (LL) and in the cells with a truncated Chl antenna size (HL).

A significant difference between the two cell types, however, is the fact that photosynthesis in the LL-grown cells saturates at an intensity of about 400 μmol photons m^{-2} s^{-1}, whereas photosynthesis in the cells with the truncated Chl antenna does not quite saturate even at 3,500 μmol photons m^{-2} s^{-1}. This difference has important implications for the solar conversion efficiency in the two cell types. It is predicted that both cell types will absorb sunlight in direct proportion to the incident intensity. However, only the cells with the truncated Chl antenna size will be able to sustain high solar conversion efficiencies at all irradiances. The normally pigmented cells will be unable to utilize intensities exceeding 400 μmol photons m^{-2} s^{-1}. Thus, under bright sunlight conditions, LL-grown cells will dissipate as heat the majority of the absorbed irradiance. A quantitative analysis of the solar conversion efficiency of normally pigmented and Chl antenna deficient cells is given below.

Solar conversion efficiencies and estimates of hydrogen production

It is possible to estimate solar conversion efficiencies in the fully pigmented cells (LL) versus that of the truncated Chl antenna cells (HL). This derivation is based on the observation that the quantum yield of photochemistry, measured under light-limiting conditions, is greater than 0.8 in vascular plants and green algae of diverse origins [Avron and Ben-Hayyim 1969, Sun and Sauer 1971, Thielen and Van Gorkom 1981, Ley and Mauzerall 1982, Bjorkman and Demmig 1987]. Fig. 6 shows photosynthetic solar conversion efficiencies as a function of incident irradiance in normally pigmented (LL) and Chl antenna deficient cells (HL). It is evident that, at low intensities (less than 200 μmol photons m^{-2} s^{-1}), both cell types would perform with a relatively high solar conversion efficiency (normalized to 0.85 for both cell types at 0 μmol photons m^{-2} s^{-1}). At higher incident intensities, however, solar conversion efficiencies for the fully pigmented cells declined sharply, reaching a value of ~0.05 (5%) at full sunlight (2,500 μmol photons m^{-2} s^{-1}). The Chl antenna deficient cells (Fig. 6, HL) also exhibited a decline in solar conversion efficiency with incident irradiance. However, this was noticeable only at intensities greater than 500 μmol photons m^{-2} s^{-1}, reaching a solar conversion efficiency of ~0.45 at full sunlight. From the results of Fig. 6, it was estimated that the integrated solar conversion efficiency over the entire physiological light intensity range (0-2,500 μmol photons m^{-2} s^{-1}) was 65% for the Chl antenna deficient (HL) and only 17% for the normally pigmented cells (LL).

It is evident from the above considerations that overall photosynthetic solar conversion efficiency in green algal cultures will strongly depend on the Chl antenna size of the photosystems and on the level of the solar intensity in the course of the day. Fig. 7 shows the profile of the daily solar radiation received at mid-latitudes during the spring in the North Hemisphere [Bjorkman and Ludlow

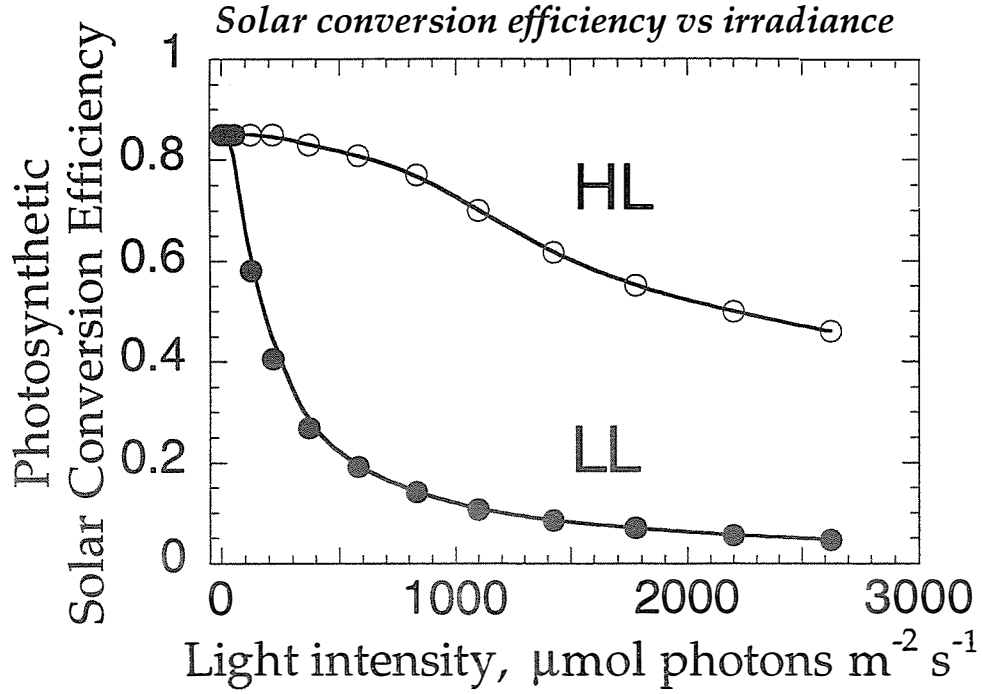

Figure 6. Photosynthetic solar conversion efficiency as a function of incident light intensity in normally pigmented (LL) and Chl antenna deficient (HL) *D. salina.*

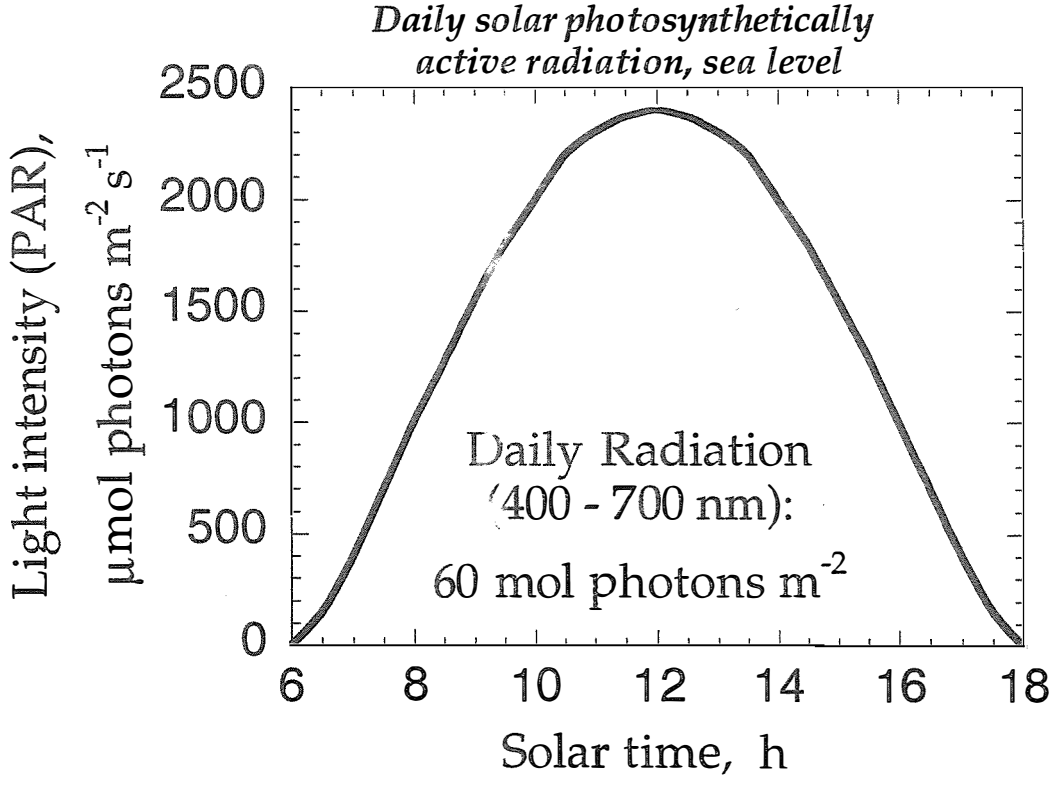

Figure 7. Profile of the daily solar photosynthetically active radiation at sea level.

1972, Kirk 1983]. The integrated area under the daily radiation curve indicated a total daily dosage of about 60 mol photons m^{-2}. This daily radiation could be slightly higher during the summer months and lower during the winter months in the north hemisphere. Moreover, it could be significantly attenuated by cloud cover and other weather conditions that affect solar luminosity. Important in the daily solar radiation profile (Fig. 7) is the observation that an intensity of 500 μmol photons m^{-2} s^{-1} was exceeded soon after 7:00 h. The solar intensity did not recede to that level until just before 17:00 h. Thus, for a period of time equal to about 10 hours, photosynthetic solar conversion efficiency in the fully pigmented cells would be less than 20% (Fig. 6, LL) whereas Chl antenna deficient cells will operate with a conversion efficiency in the range between 85-45% (Fig. 6, HL).

On the basis of these considerations, it is possible to calculate the upper limit of hydrogen production by fully pigmented and Chl antenna deficient cells grown in a photobioreactor under mass culture conditions. This calculation assumes that 60 mol photons m^{-2} (Fig. 7) will be received and absorbed by the respective green algal cultures and that electrons in the photosynthetic apparatus will quantitatively be transferred to form hydrogen in a direct biophotolysis process [Weaver et al. 1980, Greenbaum 1984, 1988, Ghirardi et al. 1997, Benemann 1997]. Table 2 summarizes the parameters involved in these calculations. It is shown that fully pigmented cells will generate at most 25% of the hydrogen (mass or volume) generated by the Chl antenna deficient cells.

Table 2. Solar conversion efficiencies and hydrogen production estimates. The optical properties and pigment contents of fully pigmented and Chl antenna deficient cells are given in Table 1 and Fig. 1.

	Fully pigmented cells	**Chl antenna deficient cells**
Daily incident PAR, mol photons m^{-2}	60	60
Minimum number of mol photons required to produce 1 mol H_2	4	4
Integrated daily photosynthetic solar conversion efficiency	17%	65%
Upper limit of H_2 mass produced (mol H_2 m^{-2} d^{-1})	2.55	9.75
Upper limit of H_2 volume produced (L H_2 m^{-2} d^{-1})	~57	~218

In all certainty, however, hydrogen yields will be lower from those shown in Table 2. Reasons for such attenuation include:

- competition for reduced ferredoxin (electrons) between the hydrogen producing pathway (via the bi-directional hydrogenase) and other metabolic pathways in the chloroplast.
- photoinhibition of green algal photosynthesis under bright sunlight [Baroli and Melis 1996]. In general, this adverse phenomenon lowers photosynthetic productivity [Powles 1984]. Photoinhibition will be significantly more pronounced in the fully pigmented than in the Chl antenna deficient cells [Baroli and Melis 1998].
- mutual cell shading in a mass algal culture, a phenomenon that is significantly more pronounced in the fully pigmented than in the Chl antenna deficient cells (Fig. 1).

The combined effect of the above mentioned attenuations in the production of hydrogen will depend on the case-by-case environmental and physiological conditions prevailing. A precise assessment of the effect of these parameters is, however, beyond the scope of this feasibility study.

Conclusions

Results in this feasibility study demonstrated a novel method for maximizing solar conversion efficiencies and photosynthetic productivity in microalgae by minimizing the number of the light-harvesting antenna pigments of the photosystems. Direct experimental evidence showed that a highly truncated light-harvesting Chl antenna size in the green alga *Dunaliella salina* could result in a

- >6-fold greater photosynthetic productivity (on a per Chl basis), compared to that of normally pigmented cells (Fig. 5)
- >4-fold greater yield of hydrogen production under mass culture, compared to that of normally pigmented cells (Table 2)

In summary, microalgae with a truncated Chl antenna size will be ideal for a variety of commercial applications including CO_2 mitigation, and rare biochemical, biomass or hydrogen production. Cultivation of green algae under continuous illumination of high irradiance resulted in the formation of a highly truncated Chl antenna size. However, this condition readily reverts to that of the fully pigmented cells upon lowering of the light intensity (Fig. 4B) or upon the fall of darkness [Polle and Melis, unpublished]. On the contrary, fully pigmented cells do not readily downscale their Chl antenna size whenever they encounter a HL condition, suggesting that once assembled, the Chl antenna is stable and that minimizing it could occur only over time during further growth and development of the

organism [Kim et al. 1993, Melis 1998]. Thus, HL-acclimated cells, although instrumental in this feasibility study, cannot be used outside the laboratory., For purposes of industrial application and hydrogen production, it would be desirable to develop microalgal mutants with a permanently truncated light-harvesting Chl antenna size, i.e., a cell-type with a photosynthetic unit size that is similar to that of the HL-acclimated cells under all growth irradiances.

Acknowledgment

The work was supported by DOE Cooperative Agreement Number DE-FC36-98GO10278.

References

Anderson JM (1986) Photoregulation of the composition, function and structure of thylakoid membranes. Annu Rev Plant Physiol 37: 93-136

Arnon D (1949) Copper enzymes in isolated chloroplasts. Polyphenol oxidase in *Beta vulgaris*. Plant Physiol 24: 1-15

Avron M and Ben-Hayyim G (1969) Interaction between two photochemical systems in photoreactions of isolated chloroplasts. In, Progress in Photosynthesis Research (H Metzner, ed), Vol. III, pp. 11-85-1196. H. Laupp Jr., Tubingen

Barber J and Andersson B (1992) Too much of a good thing: light can be bad for photosynthesis. Trends Biochem. Sci. 17: 61-66

Baroli I and Melis A (1996) Photoinhibition and repair in *Dunaliella salina* acclimated to different growth irradiances. Planta 198: 640-646

Baroli I and Melis A (1998) Photoinhibitory damage is modulated by the rate of photosynthesis and by the photosystem II light-harvesting chlorophyll antenna size. Planta 205: 288-296

Benemann JR (1997) Feasibility analysis of photobiological hydrogen production. International Journal of Hydrogen Energy 22: 979-987

Björkman O and Demmig B (1987) Photon yield of O_2 evolution and chlorophyll fluorescence characteristics at 77 K among vascular plants of diverse origins. Planta 170: 489-504

Björkman O and Ludlow MM (1972) Characterization of the light climate on the floor of a queensland rainforest. Carnegie Institution Yearbook 71: 85-94

Demmig B and Björkman O (1987) Comparison of the effect of excessive light on chlorophyll fluorescence (77K) and photon yield of O_2 evolution in leaves of higher plants. Planta 171: 171-184

Ghirardi ML, Togasaki RK and Seibert M (1997) Oxygen sensitivity of algal hydrogen production. Appl. Biochem. Biotech. in press

Greenbaum E (1984) Biophotolysis of water: the light saturation curves. Photobiochem. Photobiophys. 8: 323-332

Greenbaum E (1988) Energetic efficiency of hydrogen photoevolution by algal water splitting. Biophys. J. 54: 365-368

Herron HA and Mauzerall D (1972) The development of photosynthesis in a greening mutant of *Chlorella* and an analysis of the light saturation curve. Plant Physiol. 50: 141-148

Kim JH, Nemson JA and Melis A (1993) Photosystem II reaction center damage and repair in *Dunaliella salina* (green alga): Analysis under physiological and irradiance-stress conditions. Plant Physiol. 103: 181-189

Kirk JTO (1983) Light and photosynthesis in aquatic ecosystems. Cambridge University Press, Cambridge

Ley AC and Mauzerall DC (1982) Absolute absorption cross sections for photosystem II and the minimum quantum requirement for photosynthesis in *Chlorella vulgaris.* Biochim Biophys Acta 680: 95-106

Melis A (1989) Spectroscopic methods in photosynthesis: photosystem stoichiometry and chlorophyll antenna size. Phil. Trans. R. Soc. Lond. B 323: 397-409

Melis A (1991) Dynamics of photosynthetic membrane composition and function. Biochim. Biophys. Acta (Reviews on Bioenergetics) 1058: 87-106

Melis A (1996) Excitation energy transfer: Functional and dynamic aspects of *Lhc* (*cab*) proteins. In: Oxygenic Photosynthesis: The Light Reactions, (DR Ort, CF Yocum, eds), pp. 523-538. Kluwer Academic Publishers, Dordrecht, The Netherlands

Melis A (1998) Photostasis in plants: mechanisms and regulation. In: Photostasis (TP Williams and A Thistle, eds), pp. *in press.* Plenum Publishing Corporation, New York, NY.

Melis A, Murakami A, Nemson JA, Aizawa K, Ohki K and Fujita Y (1996) Chromatic regulation in *Chlamydomonas reinhardtii* alters photosystem stoichiometry and improves the quantum efficiency of photosynthesis. Photosynth. Res. 47: 253-265

Melis A, Neidhardt J, Baroli I and Benemann JR (1998) Maximizing photosynthetic productivity and light utilization in microalgae by minimizing the light-harvesting chlorophyll antenna size of the photosystems. In, BioHydrogen '97. Proceedings of the International Conference on Biological Hydrogen Production. Waikoloa-Hawaii, pp. *in press.* Plenum Publishing Corporation, New York, NY

Naus J and Melis A (1991) Changes of photosystem stoichiometry during cell growth in *Dunaliella salina* cultures. Plant Cell Physiol. 32: 569-575

Neale PJ and Melis A (1986) Algal photosynthetic membrane complexes and the photosynthesis-irradiance curve: a comparison of light-adaptation responses in *Chlamydomonas reinhardtii.* J. Phycol. 22: 531-538

Neale PJ, Cullen JJ, Lesser MP and Melis A (1993) Physiological bases for detecting and predicting photoinhibition of aquatic photosynthesis by PAR and UV radiation. In, Photosynthetic Responses to the Environment (HY Yamamoto, CM Smith, eds). Current Topics in Plant Physiology, an ASPP Series, Volume 8, pp. 61-77.

Neidhardt J, Benemann JR, Zhang L and Melis A (1998) Photosystem-II repair and chloroplast recovery from irradiance stress: relationship between chronic photoinhibition, light-harvesting chlorophyll antenna size and photosynthetic productivity in *Dunaliella salina* (green algae). Photosynth. Res. in press

Pick U, Karni L and Avron M (1986) Determination of ion content and ion fluxes in the halotolerant alga *Dunaliella salina*. Plant Physiol 81: 92-96

Powles SB (1984) Photoinhibition of photosynthesis induced by visible light. Annu. Rev. Plant Physiol. 35: 15-44

Powles SB and Critchley C (1980) Effect of light intensity during growth on photoinhibition of intact attached bean leaflets. Plant Physiol. 65: 1181-1187

Smith BM, Morrissey PJ, Guenther JE, Nemson JA, Harrison MA, Allen JF and Melis A (1990) Response of the photosynthetic apparatus in *Dunaliella salina* (green algae) to irradiance stress. Plant Physiol 93: 1433-1440

Sukenik A, Bennett J and Falkowski PG (1988) Changes in the abundance of individual apoproteins of light harvesting chlorophyll a/b-protein complexes of photosystem I and II with growth irradiance in the marine chlorophyte *Dunaliella tertiolecta*. Biochim Biophys Acta 932: 206-215

Sun ASK and Sauer K (1971) Pigment systems and electron transport in chloroplasts. Biochim. Biophys. Acta 234: 399-414

Thielen APGM and van Gorkom HJ (1981a) Quantum efficiency and antenna size of photosystem II_α, II_β and I in tobacco chloroplasts. Biochim Biophys Acta 635: 111-120

Thielen APGM and van Gorkom HJ (1981b) Energy transfer and quantum yield in photosystem-II. Biochim Biophys Acta 637: 439-446

Vasilikiotis C and Melis A (1994) Photosystem II reaction center damage and repair cycle: chloroplast acclimation strategy to irradiance stress. Proc Nat Acad Sci USA 91: 7222-7226

Weaver PF, Lien S and Seibert M (1980) Photobiological production of hydrogen. Solar Energy 24: 3-45

DEVELOPMENT OF AN EFFICIENT ALGAL H_2-PRODUCTION SYSTEM

Maria L. Ghirardi, Timothy Flynn, Marc Forestier and Michael Seibert
National Renewable Energy Laboratory, Golden, CO 80401

Abstract

Two major problems facing the development of a commercial photobiological algal H_2-producing system are the low rates of H_2 evolution and the sensitivity of the H_2-evolving enzyme system to O_2, a by-product of the photosynthetic water-splitting process. The objective of our project is to generate O_2-tolerant mutants from the green alga *Chlamydomonas reinhardtii* that are high producers of H_2 for use in a photobiological water-splitting, H_2-producing system that is cost effective, renewable, scalable, and non-polluting.

We are currently employing a dual approach to address the O_2-sensitivity problem. The first approach, based on classical mutagenesis and selection procedures, depends on the ability of a mutagenized population of algal cells to survive under conditions that require them to either produce (H_2-production selection) or consume (photoreductive selection) H_2 in the presence of controlled amounts of O_2. The second approach, based on molecular genetic strategies, involves the cloning of the hydrogenase gene from *C. reinhardtii* and identification of expression factors required for optimal H_2-evolution activity. The latter approach will complement the first in our future goal of generating a commercial organism suitable for use in the private sector.

Our previous work established conditions for application of the H_2-production and photoreductive selective pressures, as well as for the quantitative determination of the rates and O_2 sensitivity of the H_2-producing system in selected organisms. This estimation is done by measuring the V_0 (initial rate of H_2 evolution in the absence of O_2) and the I_{50} for O_2 inactivation of H_2 evolution (the concentration of O_2 in the gas phase that inhibits the rate of the reaction to 50% of the V_0 value) in algal cells. Mutants with an increased O_2 I_{50} were obtained by application of the H_2-production

pressure to cell wall-less *C. reinhardtii* cells in the presence of increasing amounts of added O_2. However, those mutants were not stable and reverted to a WT phenotype. Our most important accomplishment last year was demonstrating the feasibility of a proprietary chemochromic sensor screening procedure for quickly identifying individual algal clones on agar plates that photoproduce H_2 (but only under anaerobic conditions).

Our accomplishments for the past year include: (a) improvement of the specificity of the photoreductive pressure by including atrazine in addition to DCMU in the selection medium to prevent the selection of mostly herbicide-resistant mutants; (b) improvement of the H_2-production selection by adding acetate to the induction medium and pre-exposing the algal cells to O_2 prior to selective pressure; (c) construction and testing of a glove-box system for screening algal mutants on agar plates in the presence of controlled amounts of O_2 (the current set-up allows us to screen 72 clones/day) using the chemochromic sensor; (d) isolation of mRNA from induced and non-induced algal cells to be used in the construction of a subtraction expression library; and (e) successful generation of antibodies against the algal hydrogenase. In our first round of selection/screening of about 2000 mutant algal clones, we isolated a stable *C. reinhardtii* clone that evolves H_2 at a rate 4 times (greater than 70% of maximum electron transport capacity of the organism) that of the WT. This represented an unanticipated breakthrough that underscores the fact that we have been able to successfully address one of the major problems facing algal H_2 production systems. This was possible due to the way we have been selecting and screening for mutants. However, this particular procedure may not select for mutants with more than about a 3 times increase in tolerance to oxygen. Improving the O_2-tolerance of our mutant strains demonstrated to be high producers of H_2 will be one of the focus points of our research during the next year. This will involve adjustments in our current selection and screening process, and a search for additional assays for O_2 sensitivity of the H_2-production pathway. Concomitantly, we will finish the construction of the subtractive library and will start to probe it with the hydrogenase antibody to attempt to identify transformants carrying hydrogenase cDNA.

Introduction

Photobiological H_2-production from water by green algae is catalyzed by a chloroplast stromal enzyme, the reversible hydrogenase, that catalyzes both hydrogen production and uptake. The enzyme is induced by the anaerobic incubation of algal cells in the dark, but is inhibited by the presence of very low concentrations of O_2. The latter property, coupled with the low rates of H_2 evolution in WT cells and the low light saturation level of algal photosynthesis in general, has precluded the use of algae in applied H_2-producing systems.

Commercialization of a cost-effective, algal H_2-production system will ultimately depend on the availability of strains that produce H_2 directly from water under aerobic conditions at high rates. Previous work aimed at identifying O_2-tolerant, H_2-producing algal mutants was based on a photoreductive selection procedure involving the H_2-uptake activity of the reversible hydrogenase (McBride et al., 1977). We have used McBride's experimental conditions and applied the selection to WT *C. reinhardtii* cells. However, the resultant mixed population of cells exhibited only slightly

higher tolerance to O_2 (Ghirardi et al., 1997a) and initial rates of H_2 evolution in the absence of O_2 (i.e., the V_0) similar to those of the parental WT. These results suggested that the selective pressure was not very specific for O_2-tolerant organisms, but that desired mutants could be obtained if an effective secondary screening procedure could be identified.

We also developed a novel selective pressure to isolate O_2-tolerant, H_2-producing mutants of *C. reinhardtii*, which depends on the role of metronidazole (MNZ) in algal photosynthetic electron transport (Ghirardi et al., 1996). Experimental conditions for this second selective pressure include the addition of O_2 to inhibit O_2-sensitive hydrogenases. This should favor the selection of O_2-tolerant, H_2-producing clones. The effect of MNZ concentration, light intensity, activation state of the hydrogenase, and added O_2 concentration were studied, and parameters for application of the selective pressure were previously determined. An algal variant (D5) with increased O_2 I_{50} (the concentration of O_2 in the gas phase that inhibits the rate of the reaction to about 50% of the V_0) for H_2 evolution activity (0.98% O_2 compared to 0.30% O_2 for the parental cell wall-less cw15 strain) was isolated by application of H_2-production selective pressure in the presence of 2.8% added O_2 (Ghirardi et al., 1996, 1997b). Subsequently, an unstable mutant (IM6) with an even higher O_2 I_{50} (1.4% O_2) was isolated by application of the selective pressure to the D5 variant under 5% O_2 (Ghirardi et al., 1997a, Seibert et al., 1997).

The work done up until last year suggested that neither of the above two selective pressures was specific enough to generate stable O_2-tolerant, H_2-producing mutants at desirable levels. Furthermore, the measurement of an O_2 I_{50} for H_2 evolution to confirm the O_2 tolerance of clones surviving either of the two selective pressures required many time-consuming steps and had become a severely limiting factor for rapidly identifying useful mutants. It became clear that a new secondary screening procedure was required to speed up the mutant identification process. A very sensitive thin-film, membrane detector for H_2 was recently developed at the National Renewable Energy Laboratory, and it is based on the chemochromic properties of a WO_3/Pd film upon direct exposure to H_2 (Benson et al., 1996). This film was adapted in a proprietary manner (U.S. patent pending) for biological use, and its potential utility for detecting H_2 production by individual algal colonies grown on agar plates was demonstrated under anaerobic conditions (Ghirardi et al., 1997b). Progress using the selection/screening process will be discussed in this paper, and we will also describe some improvements made on the application of the two selection pressures in order to improve their selectivity.

Finally, in order to speed up the production of a commercial organism, it will be useful to more specifically mutate specific amino acid residues on the hydrogenase (the enzyme that releases molecular H_2) that are found to be involved in the O_2 sensitivity problem. Unfortunately, the algal hydrogenase gene has not been cloned yet, and does not seem to have sequence homology to prokaryote hydrogenases. Also, the nature of the residues involved in conferring O_2-sensitivity to hydrogenases are not known (however, see McTavish et al., 1995). As a consequence, it is not currently possible to improve the production rates and O_2 sensitivity of the hydrogenase enzyme by site-directed mutagenesis. Given the fact that the expression of the hydrogenase activity requires anaerobic induction, we have initiated a molecular biological approach to clone the algal hydrogenase gene, based on the construction of a subtraction expression library using induced and non-induced cells. This strategy depends on the assumption that the hydrogenase enzyme is

transcriptionally-regulated in *C. reinhardtii*, which should be the case, since the hydrogenase is a photosynthetic protein that is encoded by a nuclear gene (Taylor, 1989). Moreover, an expression library of subtracted genes between induced and non-induced cells can also be used to identify other proteins that may be required for the expression and stability of hydrogenase activity under anaerobic conditions. With the successful cloning of the algal WT hydrogenase gene, we will be able to compare its sequence to those of the mutants that we are currently generating by the classical genetics approach. This sequence comparison will serve as a guide for site-directed mutagenesis that should further stabilize the hydrogenase in the presence of O_2 and increase the rates of H_2 evolution.

Results and Discussion

Mutagenesis

Mutations in *C. reinhardtii* cells were induced by treatment with ethylmethane sulfonate (EMS) for different periods of time. EMS is an alkylating agent that chemically tautomerizes guanines or thymines and alters their base-pairing affinities and thus causes mutations. We chose to use EMS instead of nitrosoguanidine, as in previous experiments, to minimize the occurrence of multiple-linked mutations. We also shifted the research from the cw15 cell wall-less strain to a WT *C. reinhardtii* strain because the cw15 cells were too fragile to survive chemochromic screening on agar plates (see later). In order to maximize the frequency of a single-point mutation in each surviving cell, we

Table I. Effect of time of exposure to 5 μg/ml EMS on the number of surviving WT *C. reinhardtii* cells

Time of exposure (min)	Number of surviving cells	Percentage of survivors
0	3.50×10^7	100
5	2.77×10^7	79
10	2.07×10^7	59
15	1.72×10^7	49
20	1.19×10^7	34
25	1.02×10^7	29
30	7.70×10^6	22

attempted to achieve about 50% survival level with the mutagen treatment (Prof. Walter Niehaus, personal communication). Table I shows the number of surviving WT *C. reinhardtii* cells following treatment with 5 μg/ml EMS for different periods of time (see also Fig. 1, Flynn et al., submitted). The number of surviving organisms was determined by counting the number of green surviving colonies on agar plates 2-3 weeks after mutagenesis. Three EMS-treatment populations yielding 66%, 56% and 42% surviving organisms were chosen for subsequent application of the two selective pressures described in the Introduction and below.

Photoreductive Selection

Wild-type populations of cells were submitted to photoreductive selection in the presence of 10% O_2 and 3 μM DCMU for 3 weeks. The Chl concentration of the culture decreased significantly during the first 2 weeks, but started increasing again on the third week (not shown). The resulting mixed population, PRS1, had an estimated O_2 I_{50} of 0.60% O_2, which is about 1.5 times as high as that of the WT population (Ghirardi et al., 1997; Flynn et al., submitted), and a V_0 similar to the WT. The relatively small increase in the O_2 I_{50} observed after photoreductive selection suggested that the selective pressure might not be specific for O_2-tolerant organisms. One of the possibilities was that DCMU-tolerant mutants were being co-selected by the procedure. This would explain the rapid recovery in Chl concentration of the culture if a herbicide-tolerant population of mutants took over the culture. The possibility of DCMU-tolerance was investigated by determining the effect of DCMU on the viability of both the WT and the PR3 (derived from the PRS1) populations. The two populations were replica-plated onto agar containing different amounts of DCMU. The plates were then incubated in a growth chamber for 3 weeks under photoautotrophic conditions and the surviving colonies were counted. Figure 1 clearly demonstrates that randomly-selected clones from the PR3 population (closed circles) contained a large number of organisms that exhibited an increased tolerance to DCMU when compared to the WT population (open triangles), as hypothesized (see also Flynn et al., submitted).

DCMU, an urea-type herbicide, inhibits O_2 evolution and electron transport through photosystem II. It works by binding to amino acid residues on the reducing side of the D1 reaction center protein. Another group of photosystem II herbicides, the triazines, shares some but not all binding residues with DCMU. We attempted to increase the specificity of photoreductive selection for O_2-tolerant organisms by applying the selective pressure in the presence of both DCMU and atrazine. This should eliminate herbicide-resistant mutants which survive photoreductive selection but do not exhibit O_2-tolerance to H_2 production. Given the lack of complete overlap between the binding residues for the two herbicides, few of the survivors (single-point mutants) are expected to have a double resistance phenotype. The two herbicides were shown to completely inhibit cell growth at less than 10 μM total herbicide concentration in WT cells (Flynn et al., submitted). Therefore, we chose to add 15 μM DCMU + 15 μM atrazine to subsequent photoreductive selection experiments to ensure complete inhibition of photoautotrophic growth, an absolute requirement for success of this selective procedure.

The application of photoreductive pressure to a mutagenized population of WT cells in the presence of the two herbicides resulted in a population of survivors, PR10, that did not show an increase in the Chl concentration after 4 weeks of selection (data not shown), demonstrating that very few clones survived the pressure. The O_2 I_{50} for H_2 evolution of selected clones from this population was about the same as that for the WT population, but this time the V_0 increased about two-fold over the estimated V_0 for the WT population (not shown). More importantly, very few of the survivors had increased resistance to DCMU, atrazine, or both herbicides combined (maximum resistance was to less than 5 μM atrazine or 5 μM DCMU), as verified by the effect of different doses of these herbicides on the growth of selected surviving clones on agar (not shown). Moreover, none of the herbicide-resistant surviving clones passed the chemochromic screening. The results are very

encouraging, since many of the surviving clones have much higher rates of H_2 evolution. However, since the selection did not yield mutants with large increases in O_2-tolerance, we will work next under higher O_2 partial pressures to attempt to obtain more desirable mutants. These should have not only higher V_0s but also higher O_2 I_{50}s.

H_2-Production Selection

In order to improve the specificity of the H_2-production selection for O_2-tolerant, H_2-producing mutants, we added 10 mM sodium acetate to the induction medium preceding the selection. Acetate is metabolized by *C. reinhardtii* and serves as a source of energy to promote new protein synthesis. We thus expected that this would result in an increased level of hydrogenase activity. Figure 2 shows that, indeed, the resistance of *C. reinhardtii* cells to MNZ increases when the induction of the enzyme is done in the presence of acetate. We also attempted to improved the specificity of this selection by introducing a 2-minute pre-exposure of the cells to O_2, before the MNZ treatment. The results, shown in Fig. 2 suggest that, as expected, the toxic effect of MNZ can be modulated by pre-inactivation of the O_2-sensitive hydrogenase by oxygen.

The specificity of the H_2-production selection procedure for O_2-tolerant, H_2-producing mutants was determined by analyzing the V_0 and O_2 I_{50} for H_2 evolution in a representative sample of survivors. These clones survived H_2-production selective pressures applied in the presence of either 2.8% or 5% O_2. These two parameters have been used as diagnostic tools in determining whether a survivor is an electron-transport, an antenna, or an O_2-tolerant, H_2-producing mutant (Flynn et al., submitted). Electron transport mutants should have lower rates of ferredoxin reduction than the WT and, thus, lowerrates of H_2 evolution at saturating light intensity. Mutants with a smaller antenna complement should show higher rates of H_2 evolution (per Chl) than the WT at saturating light intensity, since the number of Chl molecules per reaction center is decreased in these mutants. Finally, O_2-tolerant mutants should have an increased O_2 I_{50}, but no significant changes in the V_0 are expected. Out of 24 random clones tested, 15 shows lower rates of H_2 evolution (suggesting that they are electron transport mutants), 6 had higher rates of H_2 evolution per Chl (suggesting that they are antenna mutants), and 3 showed increases in the O_2 I_{50} (characteristic of an O_2-tolerant mutant). It is clear that this type of selection pressure produces at least two different classes of mutants besides O_2-tolerant, H_2-producing clones. The effect of the selection on the kinetic parameters for H_2 evolution of a *mixed population of survivors*, was to slightly increase the O_2 I_{50} and double the V_0 (data not shown). This effect is not what was expected, given that only 6 out of 24 mutants were shown to be antenna mutants (and thus with higher rates of H_2 evolution), while the majority of the survivors (15 out of 24) were expected to exhibit lower rates of H_2 evolution. As was the case with the survivors from the photoreductive selection, it is apparent that this selection procedure requires a secondary screening process to rapidly identify specific desired mutants. These results may also suggest that our assay for O_2 I_{50} should be re-evaluated as a means of measuring O_2 sensitivity.

Secondary Screening

The chemochromic screening procedure is shown in Figure 3, which depicts the steps involved in preparing the selected clones (see also Fig. 4, Flynn et al., submitted). Clones that survived the

selective pressure were transferred to agar and arranged in a grid pattern using sterile tooth picks. The colonies were then allowed to grow on agar for 7-14 days, replica-plated using sterile velveteen cloth, and grown on plates for another 7-14 days. The agar plate was then covered by a piece of filter paper and the cells were anaerobically induced on the plates in the dark for 4 h. At the end of the induction period, the plates were transferred to an anaerobic chamber and preexposed to a controlled amount of O_2 for a fixed period of time. The chemochromic sensor film was applied and the plates were then exposed to light. The H_2 produced by active colonies leaves a blue dot on the film (Ghirardi et al., 1997a; Seibert et al., 1997) that is easily seen by eye. The sensitization reaction on the sensor film is reversible, and the dots fade after a few minutes of exposure of the film to O_2 (Ghirardi et al., 1997a).

The relative intensity of the dots on the chemochromic film (determined visually) was correlated with the capacity for H_2 evolution (V_0) by the individual clones. Two colonies that gave rise to, respectively, very intense and less intense dots on the chemochromic sensor, were grown in liquid medium, anaerobically induced, and then used for H_2-evolution measurements. Figure 4 shows the initial rates of H_2 evolution versus O_2 concentration for cells derived from the clone that originated the intense signal (D2) and from the one that originated a less intense signal (E4). The clear correlation between the estimated V_0 and intensity of the dot confirms that the film responds to the amount of H_2 produced by algal colonies (Flynn et al., submitted).

Chemochromic film screening was then applied to survivors from photoreductive and H_2-production selective pressures done at 5% O_2. A total of about 2,000 clones were screened at 3% O_2, and 32 clones were selected. Figure 5 shows the results from a subsequent screening of the 32 clones (now co-located on the same agar place), in the presence of 8% O_2 (Flynn et al., submitted). The first important outcome of this subsequent screening experiment is the demonstration that, in contrast to our results last year, **mutants that we have select this year are stable** and do not rapidly revert. The first panel in Fig. 5 represents the response of the film when the screen is not preceded by a pre-exposure of the cells to O_2. Most of the pre-selected clones produced some H_2 under these conditions, and generated blue spots on the sensor. The second panel shows the response of the film after a 2-min pre-exposure of the induced cells to 8% O_2. It is clear that pre-exposure to O_2 inactivates a larger number of colonies but still allows H_2 evolution by many of the clones to occur. The last panel shows the reversibility of the film sensitization reaction: the blue dots fade when the sensor is exposed to O_2 for several minutes. V_0 and O_2 I_{50} values for 5 of the 32 clones were determined and are shown in Table II, Columns 3 and 4. It is very encouraging that all of the screened clones that were tested exhibited significantly higher V_0s for H_2 evolution compared to the WT. Indeed, the highest rate reported in Table II, 454 μmoles H_2·mg Chl^{-1}·h^{-1}, is 4 times that of the WT and **by far the highest H_2-production rate reported in the literature for green algae**. It should be emphasized that we are not generating antenna mutants, since the Chl a/b ratio of these clones are unchanged from the WT. The time courses of H_2 evolution of the 24.g1 clone and WT cells are shown in Fig. 6. The cells used in the experiment were exposed to about 1.4% O_2 in the electrode chamber for 2

Table II. Kinetic parameters of selected algal clones

Mutant Isolate	Original selective pressure	V_0 (μmoles H_2·mg Chl^{-1}·h^{-1})	O_2 I_{50} for H_2 evolution (relative units)	Half-life of the rate of H_2 evolution (relative units)
9.c2	mz	245	1.01	0.86
6.b2	mz	224	0.81	1.74
9.b5	mz	226	1.19	2.84
24.g1	pr	454	1.01	2.00
23.i6	pr	370	0.82	1.26
WT	n.a.	111	1.00	1.00

min before the actinic light was turned on. The Y-axis shows the H_2 concentration in the electrode chamber during the experiment. It is evident that, under the experimental conditions of the experiment shown, the rates of H_2 evolution of the isolated clone are substantially higher than that of the WT.

The result described above represents a major break-through in our research, since the 24g.1 mutant demonstrates rates of H_2 evolution that correspond to at least 70% of the maximum electron transport capacity of algal cells (under aerobic conditions), as compared to a much lower value for WT cells. The increases in the estimated O_2 I_{50} observed with the clones in Table II were not consistent, which suggests that either the O_2 I_{50} for H_2 evolution is not be the best method of testing for O_2-tolerant H_2-production under the conditions we are using, that the two pressures are still not optimal for specific selection of O_2-tolerant organisms, or that the current screening procedure is only identifying high H_2-producing mutants but not O_2-tolerant ones. To address the first possibility, we used an alternative approach to estimate the O_2-tolerance of the H_2-producing capacity, based on the half-life of the H_2 evolution activity measured up to 45 s after the onset of illumination. Since illumination also induces O_2 evolution, it was reasoned that the hydrogenase activity in WT cells would decrease more rapidly in the light than the activity of O_2-tolerant clones. The initial rate of H_2 evolution upon illumination (time zero) and the rate after 40-45 s after onset of illumination were measured and a half-life was calculated based on a single exponential decay model. Table II (Column 5) indicates that the rate of H_2 evolution by WT *C. reinhardtii* decays more rapidly than that of most of the tested selected mutant clones (this is a preliminary result at this point and must be confirmed). This does indicate, though, that both selective pressures can identify mutants of *C. reinhardtii* with both higher H_2-production rates and increased O_2 resistance.

With additional rounds of mutagenesis and selection at higher O_2 concentrations, and by tuning both the selection and the screening procedures, we expect to identify much more O_2-tolerant mutants in addition to the high H_2-producers isolated so far.

Generation of antibodies

The hydrogenase enzyme of *C. reinhardtii* was purified by Happe and Naber (1993), and its N-terminus was sequenced up to 24 amino acid residues. The enzyme was shown to contain one subunit of 49 kDa, which was detected only in extracts from induced cells. We synthesized an oligopeptide containing this particular sequence of residues, coupled it to the Rabbit Serum Albumin (RSA) and injected it into rabbits to induce an immunogenic response. The immunized rabbits were bled and their sera tested against the coupled oligopeptide on a sheet of nitrocellulose. A positive reaction was observed with sera from two of the rabbits (not shown). The sera recognized two bands, with molecular weights of just over 66 kDa, and of about 100 kDa, corresponding to 1-2 and 14-15 molecules of oligopeptide per RSA molecule. Extracts from induced and non-induced cells were also challenged with the immune sera, which recognized two bands of about 48 and 49 kDa, present only in extracts from induced cells (not shown). These results suggest that the immunized sera do indeed recognize the algal hydrogenase in cell extracts. However, given the low yield of the reaction and the fact that the sera pick up two protein bands in denaturing gels (and not one band as reported by Happe and Naber [1993]), further work will be required before we can be absolutely sure that the protein bands that we observe correspond to the reversible hydrogenase enzyme.

Subtraction Library

Total RNA and mRNA were extracted from *C. reinhardtii* cells that had been induced for 0, 0.5, 1, and 4 hours, respectively. The quality of the total RNA was shown to be very high, based on the appearance of even the low molecular weight ribosomal RNA bands in an agarose gel, which are present only in a diffuse form when the RNA sample is partially degraded. The translational capacity of the isolated mRNA was determined with a wheat germ *in vitro* translation system. All mRNA isolates were able to direct the synthesis of high molecular weight proteins, which confirms their integrity. The mRNA from non-induced cells was photobiotinylated using the Subtractor kit from Invitrogen. The mRNA from induced cells is being reverse transcribed into cDNA molecules and will be used in the subsequent hybridization step with the photobiotinylated mRNA, followed by purification through an avidin column. This procedure will yield cDNA species that are unique to anaerobically-induced cells. Among them we expect to find the hydrogenase cDNA as well as cDNA encoding for other proteins that may be required for optimal H_2 production by the enzyme.

Conclusions and Future Work

The two selective pressures have been improved and are being used in combination with a secondary chemochromic screening procedure to identify O_2-tolerant mutants of *C. reinhardtii* that are unexpectedly high producers of H_2. We have successfully isolated mutants with greatly increased H_2-production capacity compared to the WT (corresponding to at least 70% of the maximum aerobic electron transport capacity of the organism). However, our current selection/screen design will have to be adjusted to select for much better O_2-tolerant mutants as well. One proposed change is to expose induced selected clones to higher O_2 partial pressures (or for longer periods of time), and then transfer the plates to the anaerobic glove-box for screening in the absence of added O_2. Also, the nature of our assay for O_2-tolerance based on an O_2 I_{50} might be re-evaluated at this point (we suspect technical problems in doing the assay) and perhaps replaced by an alternative procedure based on

the half-life of the initial rate of H_2 evolution, as shown in Table II. Future work will involve using our selection and screening tools to examine large numbers of new mutants in order to identify useful O_2-tolerant, high H_2-producing clones.

The antibodies that we generated by means of a synthetic oligopeptide have shown a positive reaction against protein bands in extracts from induced cells. In contrast to Happe's work (1993), two protein bands were recognized by the immune sera. It is possible that one of them represents a translationally-modified form of the enzyme, or that one of them is a precursor or degradation form of the other. We will confirm that the detected protein bands do indeed represent the hydrogenase enzyme by physiological correlating the activation/inactivation of enzyme activity with the immunological detection of the protein bands on Western blots. If this turns out to be the case, we will have in our hands a powerful tool to (1) perform physiological studies on the expression of the reversible hydrogenase in algal cells, and (2) use in the cloning of the hydrogenase gene by the subtractive library approach.

The subtracted cDNA will be inserted into an expression vector and used to transform *E. coli*. The transformants will be probed with the antibody, as described above, to identify the ones carrying the hydrogenase cDNA, or, alternatively, with a DNA probe. This DNA probe will be constructed based on a nucleotide sequence homologous to that encoding the 24 amino acid residues sequenced by Happe. Finally, the cDNA inserts of other transformants will be sequenced, and we will attempt to identify their potential expression factors in order to gain some understanding on the regulation of the hydrogenase activity under anaerobic conditions.

Acknowledgments

We thank Dave Benson, NREL, for supplying us with the chemochromic sensor films used in the screening procedure, and Dr. Thomas Lutton for continuous help in the development of H_2-evolution measurement and analysis.

References

Benson, D.K., C.E. Tracy, and C. Bechinger. 1996. "Design and Development of a Low-Cost Fiber-Optic Sensor for Hydrogen Detector". In *Proceedings of the 1996 U.S. DOE Hydrogen Program Review*, vol. II, 605-624, NREL/CP-430-21968.

Flynn, T., M.L. Ghirardi, D. Benson, and M. Seibert. "Selecting and Screening for O_2-tolerant Mutants of H_2-Producing *Chlamydomonas reinhardtii*". *Appl. Biochem. Biotechnol.*, submitted.

Ghirardi, M.L., S. Markov, and M. Seibert. 1996. "Development of an Efficient Algal H_2-Producing System". In *Proceedings of the 1996 U.S. DOE Hydrogen Program Review*, vol. I, 285-302, NREL/CP-430-21968

Ghirardi, M.L., T. Flynn, S. Markov, and M. Seibert. 1997a. "Development of an Efficient Algal H_2-Producing System". In *Proceedings of the 1997 U.S. DOE Hydrogen Program Review*, 11-24, NREL/CP-430-23722.

Ghirardi, M.L., R.K. Togasaki, and M. Seibert. 1997b. "Oxygen Sensitivity of Algal H_2-Production". *Appl. Biochem. Biotechnol.* 63-65, 141-151.

Happe, T., and J.D. Naber. 1993. Isolation, Characterization and N-terminal Amino Acid Sequence of Hydrogenase from the Green Alga *Chlamydomonas reinhardtii*". *Eur. J. Biochem.* 214, 475-481.

McBride, A.C., S. Lien, R.K. Togasaki, and A. San Pietro. 1977. "Mutational Analysis of *Chlamydomonas reinhardi*: Application to Biological Solar Energy Conversion". In *Biological Solar Energy Conversion* (A. Mitsui, S. Miyachi, A. San Pietro, and S. Tamura, eds.), Academic Press, New York.

McTavish, H., L. A. Sayavedra-Soto, and D.J. Arp. "Substitution of *Azotobacter vinelandii* Hydrogenase Small-Subunit Cysteines by Serines Can Create Insensitivity to Inhibition by O_2 and Preferentially Damages H_2 Oxidation over H_2 Evolution". *J. Bacteriol.* 177, 3960-3964.

Seibert, M., M. Ghirardi, P.C. Maness and P. Weaver. 1997. "Photobiological Production of Renewable Fuels, Chemicals, and Materials". In *Proceedings of the International AAA BIOTEC Conference* (Ferrara, Italy; Oct. 1996), Vol. IV, pp. 122-136.

Taylor, W.C. 1989. "Regulatory Interactions between Nuclear and Plastid Genomes". *Ann. Rev. Plant Physiol. and Plant Mol. Biol.* 40, 211-233.

Trebst, A. 1987. "The Three-Dimensional Structure of the Herbicide Binding Niche on the Reaction Center Polypeptides of Photosystem II". *Z. Naturforsch.* 42c, 742-750.

Figure Legends

Figure 1. Percentage of the initial population of control WT *C. reinhardtii* (open triangles) and survivors from a photoreductive experiment (PR3) that are viable after 3 weeks on agar plates containing different concentrations of the herbicide DCMU.

Figure 2. Kinetics of population survival after metronidazole selection. A population of mixed *C. reinhardtii* cells derived from EMS treatment was anaerobically induced in the presence of 0 or 5 mM sodium acetate. Following induction but prior to illumination, the induced cells were either preexposed to 5% O_2 for two minutes in the dark or treated directly with 40 mM MNZ in the presence of 5% O_2 and 400 $\mu E \cdot m^{-2} \cdot s^{-1}$ for different periods of time. Aliquots were taken at each time point, the cells were washed and plated for colony counting.

Figure 3. Procedure for preparation of survivors from the two selective pressures for chemochromic screening. Clones that survived the selective pressure were transferred to an agar plate and arranged in a grid pattern using sterile tooth picks. The colonies were grown on agar for 7-14 days, replica-plated using sterile velveteen cloth, and allowed to grow on plates for another 7-14 days. The agar plate was then covered with a piece of filter paper, and the cells were anaerobically induced on the plates in the dark for 4 h. At the end of the induction period, the plates were transferred to an

anaerobic chamber and preexposed to a controlled amount of O_2 for a fixed period of time for screening.

Figure 4. Initial rates of H_2 evolution measured in the presence of different initial concentrations of O_2 in the assay medium. The V_0 was estimated from a single exponential decay fit to the curve. The D2 strain has a higher V_0 and generated a more intense spot in the chemochromic sensor film than the E4 strain.

Figure 5. Response of the chemochromic sensor to H_2 produced by anaerobically activated algal colonies on an agar plate illuminated for 5 min in the presence of 8% O_2. The first panel shows H_2 evolution by colonies that were not pre-exposed to O_2. In the second panel, algal colonies were pre-exposed to 8% O_2 for 2 min before illumination. The last panel indicates that the sensitization of the chemochromic film is reversible because the blue spots fade upon exposure of the sensitized film to O_2 for several minutes.

Figure 6. Change in H_2 concentration as a function of time, measured with WT (lower curve) and with the 24.g1 mutant clone (upper curve). This clone was identified by application of chemochromic screening under 8% O_2 to a population of survivors from a photoreductive selection done in the presence of 5% O_2 and 15 μM each of DCMU and atrazine. Anaerobically-induced cells were added to the electrode chamber, pre-set to about 1.4% O_2. The cells were then incubated in the dark for 2 min before the actinic light was turned on. After monitoring H_2 evolution for 1 min, the lights were turned off, again.

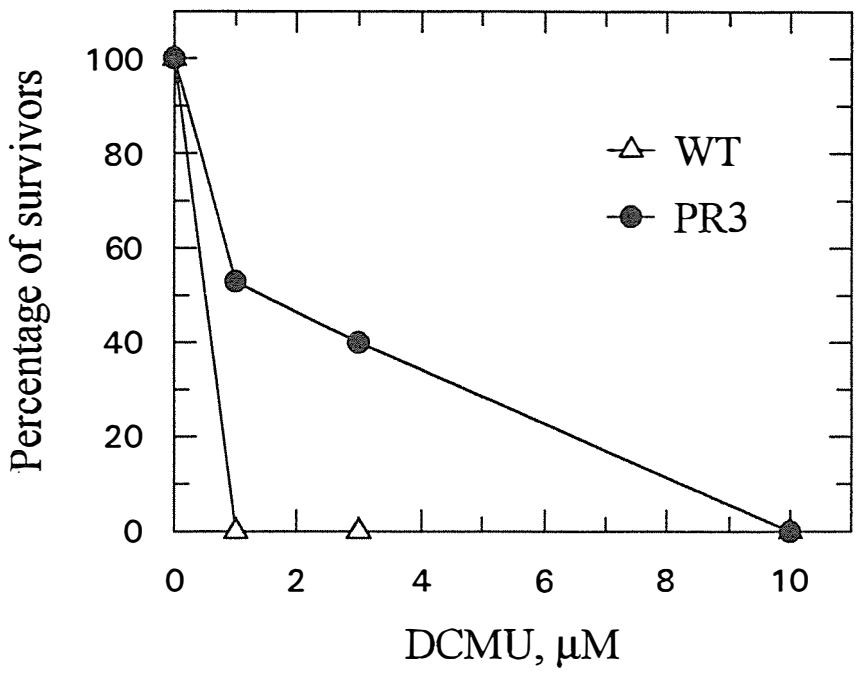
Percentage of survivors
100
80
60
40
20
0
0
2
4
6
8
10
DCMU, μM
WT
PR3

Figure 1

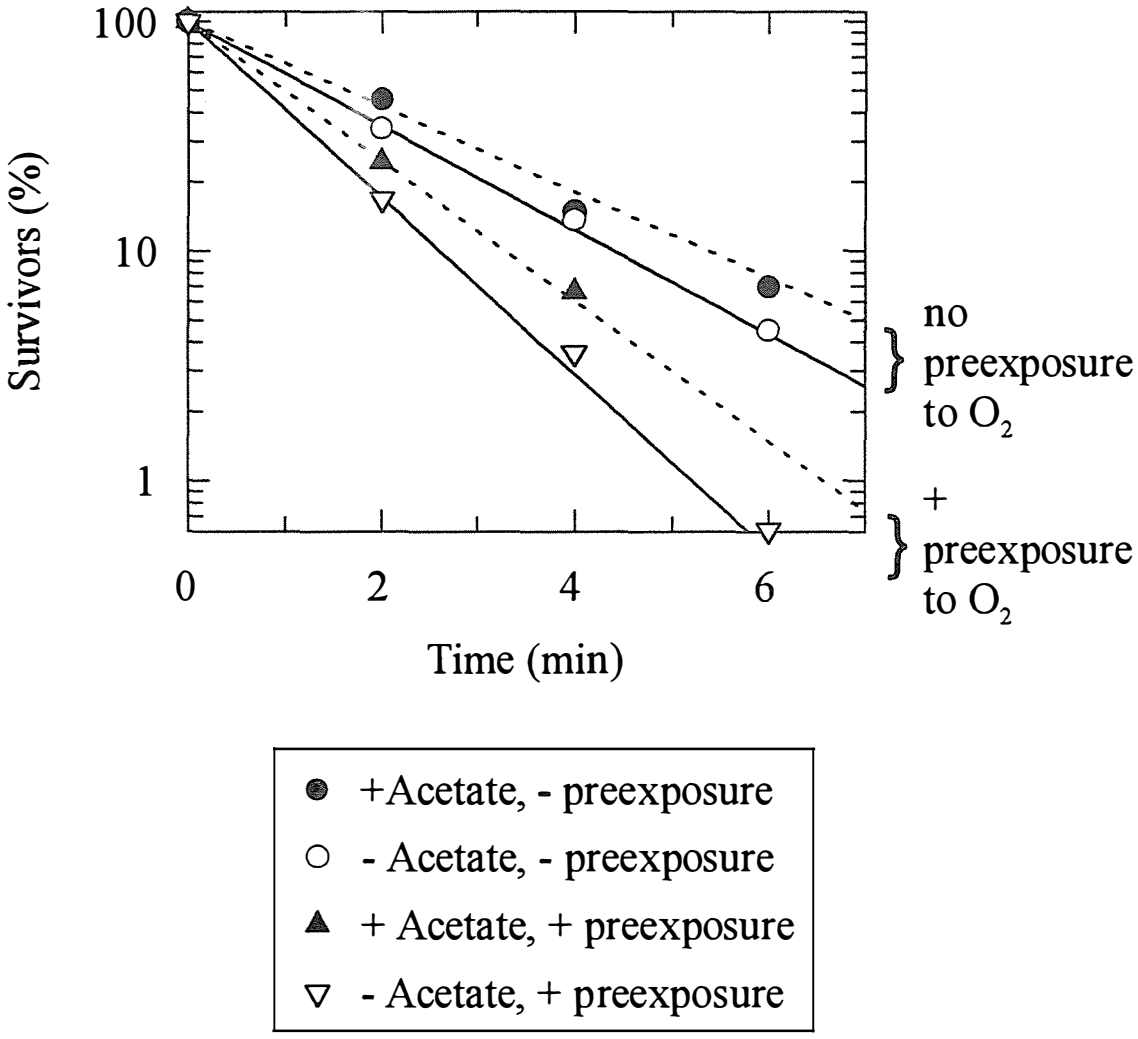
100
10
1
Survivors (%)
0
2
4
6
Time (min)
no preexposure to O_2
+ preexposure to O_2
+Acetate, - preexposure
- Acetate, - preexposure
+ Acetate, + preexposure
- Acetate, + preexposure

Figure 2

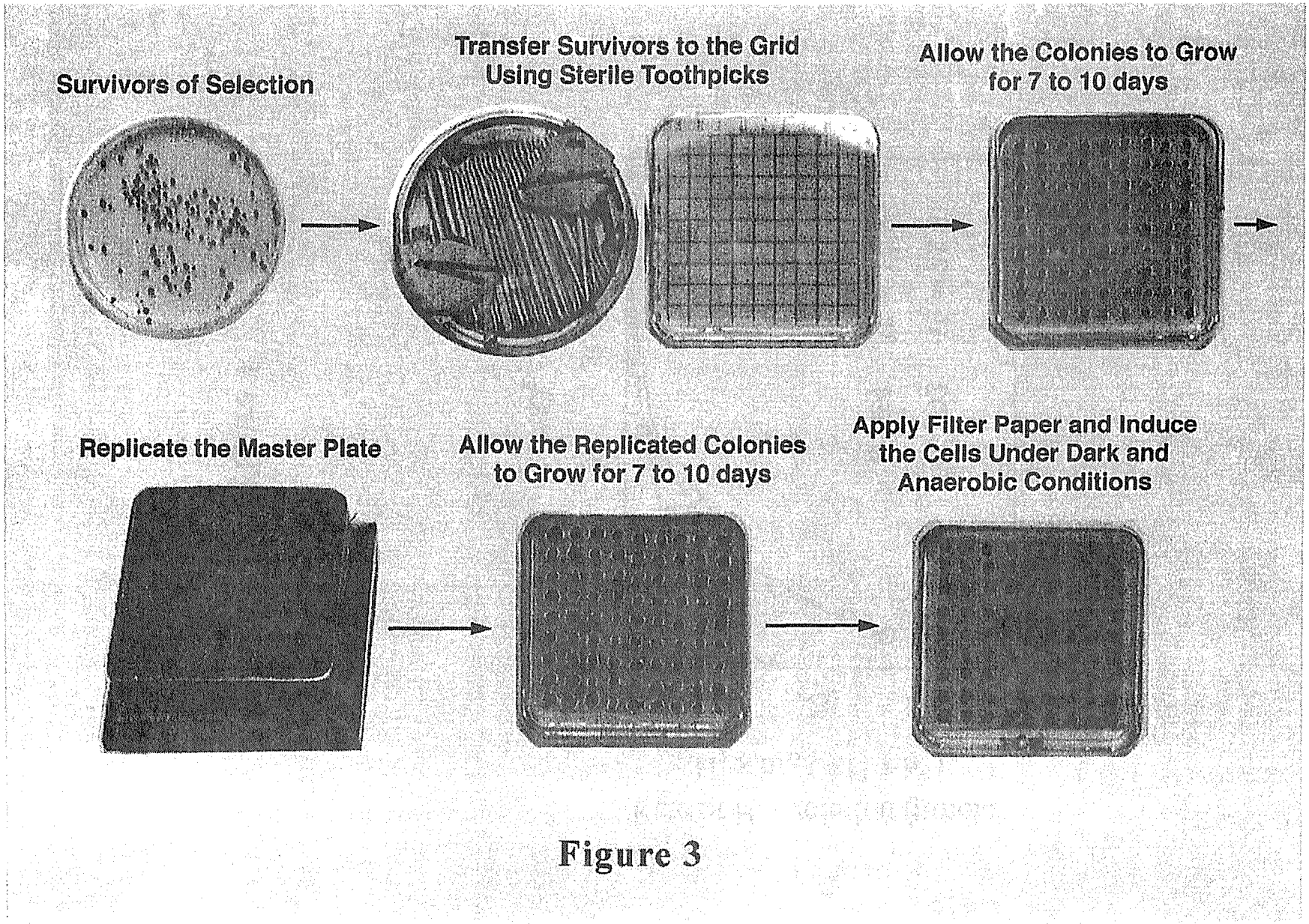
Survivors of Selection
Transfer Survivors to the Grid
Using Sterile Toothpicks
Allow the Colonies to Grow
for 7 to 10 days
Replicate the Master Plate
Allow the Replicated Colonies
to Grow for 7 to 10 days
Apply Filter Paper and Induce
the Cells Under Dark and
Anaerobic Conditions

Figure 3

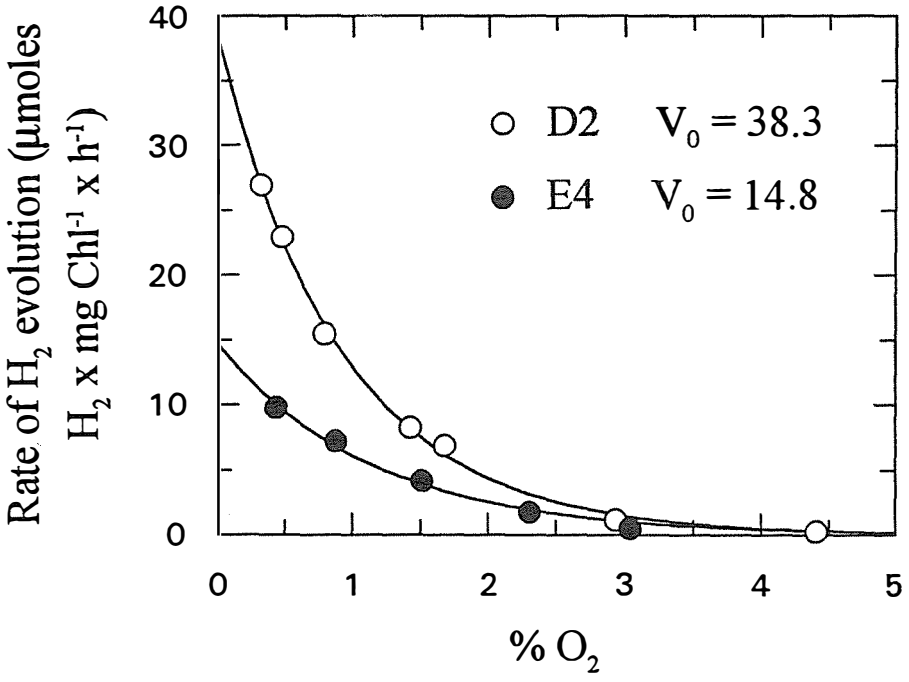
Rate of H_2 evolution (µmoles H_2 x mg Chl^{-1} x h^{-1})
40
30
20
10
0
0
1
2
3
4
5
% O_2
D2 $V_0 = 38.3$
E4 $V_0 = 14.8$

Figure 4

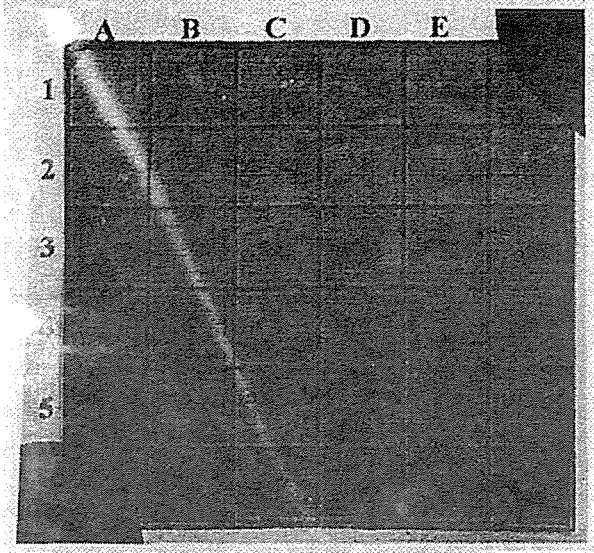

No O_2 pre-exposure

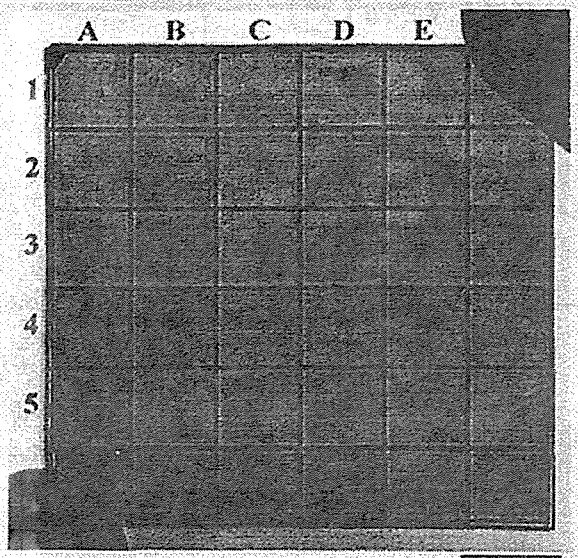

Two min. O_2 pre-exposure

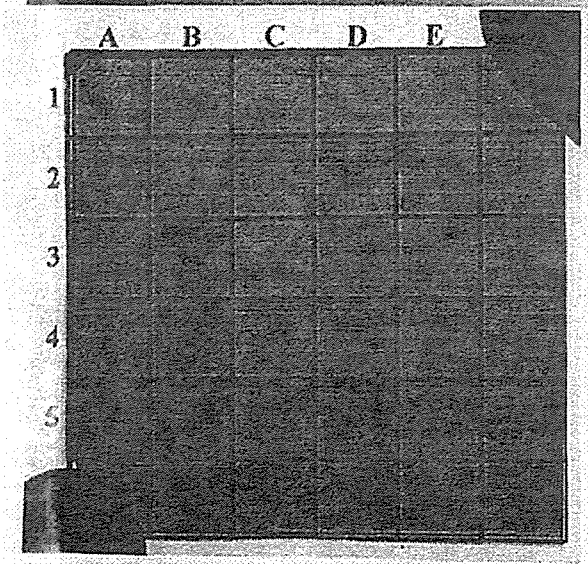

Several min. after O_2 exposure

Figure 5

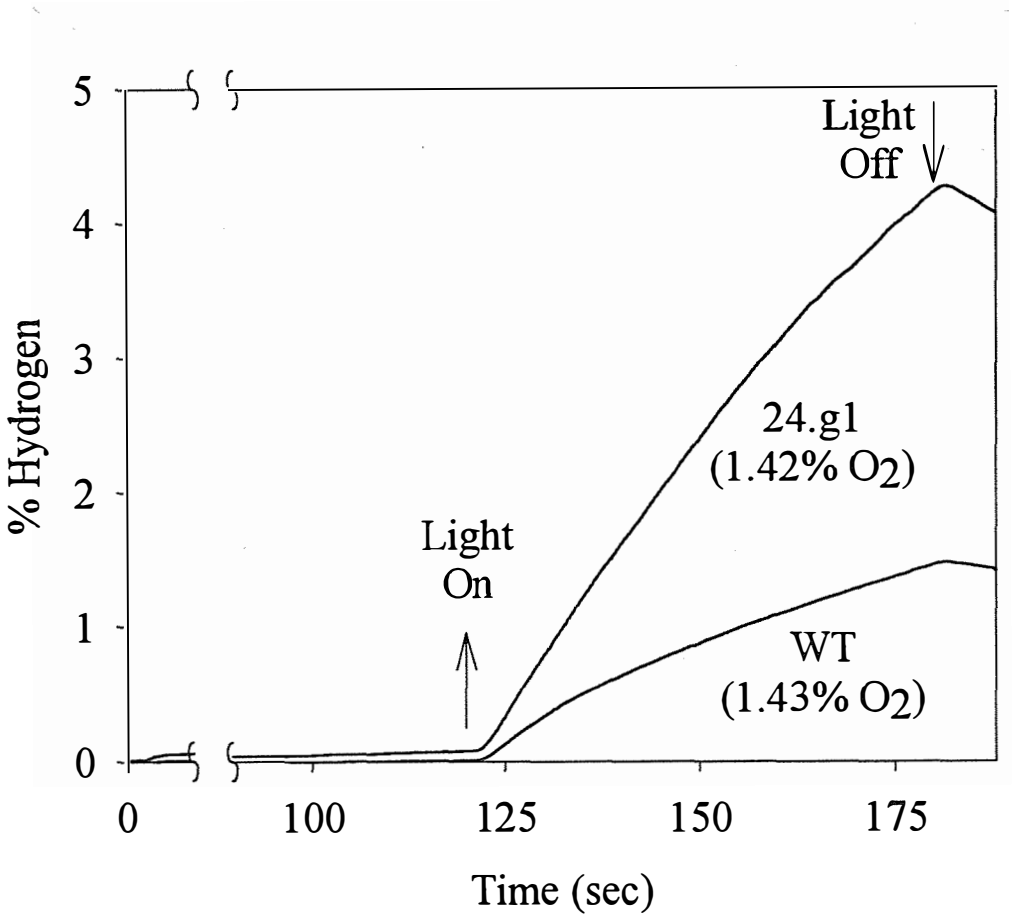
5
4
3
2
1
0
% Hydrogen
Light
Off
24.g1
(1.42% O2)
Light
On
WT
(1.43% O2)
0
100
125
150
175
Time (sec)

Figure 6

RENEWABLE HYDROGEN PRODUCTION BY PHOTOSYNTHETIC WATER SPLITTING

E. Greenbaum and J. W. Lee
Oak Ridge National Laboratory
P.O. Box 2008
Oak Ridge, TN 37831-6194

Abstract

This mission-oriented research project is focused on the production of renewable hydrogen. We have demonstrated (Greenbaum, 1980) that certain unicellular green algae are capable of sustained simultaneous photoproduction of hydrogen and oxygen by light-activated photosynthetic water splitting. It is the goal of this project to develop a practical chemical engineering system for the development of an economic process that can be used to produce renewable hydrogen. There are several fundamental problems that need to be solved before the application of this scientific knowledge can be applied to the development a practical process: (1) maximizing net thermodynamic conversion efficiency of light energy into hydrogen energy, (2) development of oxygen-sensitive hydrogenase-containing mutants, and (3) development of bioreactors that can be used in a real-world chemical engineering process. We are addressing each of these problems here at ORNL and in collaboration with our research colleagues at the National Renewable Energy Laboratory, the University of California, Berkeley, and the University of Hawaii.

Current Status of the Research

During the current year, we have made progress in understanding the limiting aspects of the production of molecular hydrogen and oxygen via light-activated microalgal water splitting. We have focused on item 1 above, an investigation of maximizing the net thermodynamic conversion efficiency of light energy into hydrogen energy. In particular, we have focused on the question of how many light reactions are required to split water to molecular hydrogen and oxygen. We recently reported (Greenbaum et al., 1995; Lee et al., 1996) that certain mutants of the green algal *Chlamydomonas reinhardtii* that lack detectable levels of the Photosystem I reaction center were capable of

simultaneous photoproduction of molecular hydrogen and oxygen, photoassimilation of atmospheric carbon dioxide and photoautotrophic growth. Although the absence of PS I in mutants B4 and F8 for the data reported in the references was confirmed by physical, biochemical and genetic techniques, subsequent analyses in our own laboratories as well as those of colleagues to whom we have sent the mutants indicate that there is variability in the PS I content of the cultures depending on growth conditions. While some strains retain undetectable levels of P700, others contain variable (0-20%) amounts of wild-type P700. This property of mutants B4 and F8 has been communicated to the journals in which the results were initially published (Greenbaum et al., 1997a,b).

In his analysis of this work, Boichenko (1996) postulated a "leaky" model of the Z-scheme, illustrated schematically in Fig. 1. According to this model, under continuous high-intensity light PS I turns over with sufficient rapidity to accommodate reductant generated by multiple PS IIs thereby preserving a key requirement of the Z-scheme: only PS I is capable of generating low-potential reductant that can be used for hydrogen evolution or carbon dioxide fixation.

We are testing the hypothesis of Fig. 1. In these experiments, mutant Fud26 of the green alga *C. reinhardtii* that had a measurable ratio of Photosystem I to Photosystem II of 0.08 was used for our studies. Table 1 summarizes the properties of this mutant. Our preliminary results with the alga characterized in Table 1 suggests that the Z-scheme is not capable of quantitatively accounting for the pulsed yields of hydrogen and oxygen production or photosynthesis under light-limiting conditions. However, in order to be completely certain that this is the case, we feel that it is necessary to perform the Photosystem I, Photosystem II, and antenna size measurements side-by-side with the oxygen and hydrogen measurements rather that shipping the samples offsite for analysis.

We are in the process of acquiring a spectrometer that will enable us to perform our own measurements of Photosystems I and II. This instrument is scheduled for delivery on June 6, 1998. Acquisition of this capability will enable us to perform all measurements necessary to perform a quantitative test of the Z-scheme. This capability will enable us to address the criticism that perhaps the Photosystem I measurements in the mutants of our original work was degraded by the process of shipping or freezing the algae.

Table 1. Photosynthetic Parameters of Mutant Fud26*

Parameter	Value
PSI : PSII Ratio	0.081
PSI Antenna	150
PSII Antenna	320

*Measurements by A. Melis. Frozen samples were pelleted and shipped to the University of California by express courier for analysis.

There is an important practical motivation for determining if evidence can be adduced supporting the possibility that sustained simultaneous photoevolution of hydrogen and oxygen can be driven by a single light reaction because it can, in principle, lead to a doubling of the conversion efficiency of light

energy into hydrogen energy. This result, combined with algae that linearize the light saturation curve and possess oxygen-tolerant hydrogenases, would be the appropriate test organisms for development in bioreactors that can be used in chemical engineering development processes.

Work Plan for FY 1999

It is anticipated that upon receipt of our own spectrometer we will be able to perform, a side-by-side basis, all the measurements that are necessary for performing a quantitative test of the Z-scheme for hydrogen and oxygen production and carbon dioxide assimilation. We will also address the question of how the accumulation of carbon reserves affects the ability of algae to photoproduce hydrogen by a Photosystem I-mediated reaction. This approach has the advantage of spatial separation of hydrogen and oxygen which avoids the oxygen-tolerance problem of the hydrogenase enzyme. We will also work on the important problem of linearizing the light saturation curve of photosynthesis.

References

1. Boichenko, V. A. 1996. "Can Photosystem I be a Photogenerator of Low Potential Reductant for CO_2 Fixation and H_2 Photoevolution?" *Photosyn. Res.*, 47:291-292.

2. Greenbaum, E., J. W. Lee, C. V. Tevault, S. L. Blankinship, T. G. Owens, and L. J. Mets. 1997a. "CO_2 Fixation and Photoevolution of H_2 and O_2 in a Mutant of *Chlamydomonas* Lacking Photosystem I." *Nature*, 376:438-441.

3. Greenbaum, E., J. W. Lee, C. V. Tevault, S. L. Blankinship, T. G. Owens, and L. J. Mets. 1997b. "Photosystem I Measurements in Mutants B4 and F8 of *Chlamydomonas*," *Science*, 277:167-168.

4. Greenbaum,E., J. W. Lee, C. V. Tevault, S. L. Blankinship, and L. J. Mets. 1995. "CO_2 Fixation and Photoevolution of H_2 and O_2 in a Mutant of *Chlamydomonas* Lacking Photosystem I." *Nature*. 376:438-411.

5. Greenbaum, E. 1980. "Simultaneous Photoproduction of Hydrogen and Oxygen by Photosynthesis." *Biotechnol. Bioeng. Symp.*, 10:1-13.

6. Lee, J. W., C. V. Tevault, T. G. Owens, and E. Greenbaum. 1996. "Oxygenic Photoautotrophic Growth Without Photosystem I." *Science*, 273:364-367.

Figure

Fig. 1 Schematic illustration of the "leaky" Z-scheme of photosynthesis. It is postulated that under saturating illumination PS I undergoes multiple turnovers such that it can accommodate all output generated by Photosystem II.

The Leaky Z-Scheme of Photosynthesis

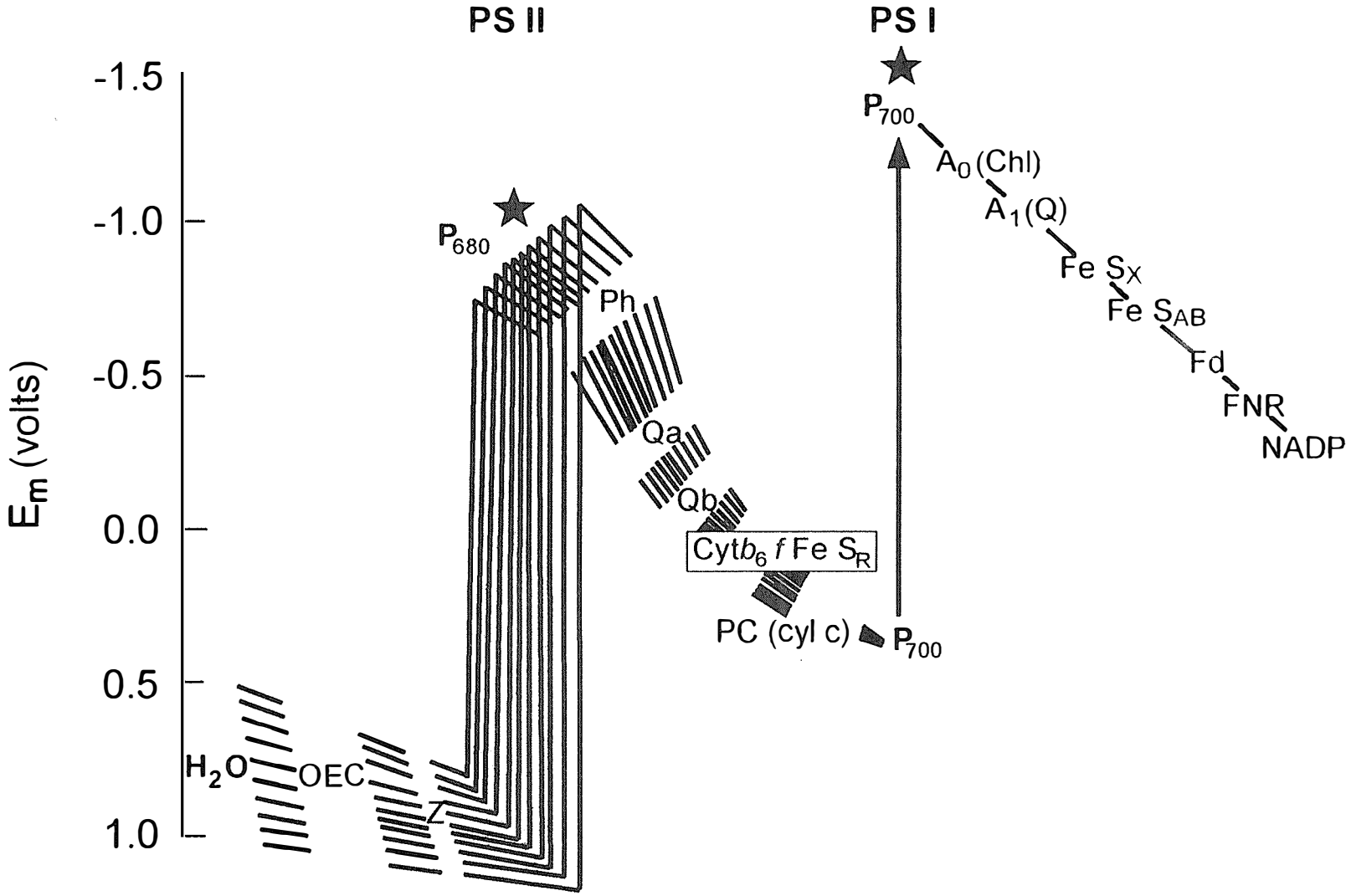

Figure 1

DEVELOPMENT OF NEW MATERIALS AND APPROACHES TO PHOTOCATALYTIC SYSTEMS

Clovis A. Linkous
Darlene K. Slattery
Florida Solar Energy Center
1679 Clearlake Road
Cocoa, FL 32922-5703

Abstract

This work describes our efforts in developing a dual bed photocatalytic system for water-splitting to make H_2. Several potential improvements were investigated: the use of carbonate ion in facilitating the O_2 evolution process, the use of NiO_x as a substitute for Ir on TiO_2, the use of WO_3 as a substitute for TiO_2, and a study of various classes of organic pigments for photocatalytic application. We have also generated some prototype designs for future dual photocatalyst systems that should enable higher efficiencies.

Introduction

We are engaged in a research effort to develop an efficient, affordable, direct photoconversion scheme for generating H_2 from H_2O using sunlight. The approach is to use semiconductors in powdered form in a dual bed configuration, breaking down the energy requirement for water splitting into a 2-photon process, and enabling separate production of H_2 and O_2. A schematic showing how such a system would work is shown in the first row of Figure 1. In this approach, the photocatalytic system would employ two modules, each consisting of a shallow, flat, sealed container, in which micron-sized photocatalytic particles are immobilized. An aqueous solution

containing a redox mediator is pumped between the two chambers. Different photoparticles and catalysts are chosen for their respective modules so as to effect oxidative water-splitting in one vessel to evolve oxygen gas, and reductive water-splitting in the other to evolve hydrogen.

The general chemical mechanism for a dual bed concept photosystem would be as follows:

H_2 photoreactor: $4\,H_2O + 4\,M^\circ \rightarrow 2\,H_2 + 4\,OH^- + 4\,M^+$

O_2 photoreactor: $\underline{4\,OH^- + 4\,M^+ \rightarrow O_2 + 2\,H_2O + 4\,M^\circ}$

net: $2\,H_2O \rightarrow 2\,H_2 + O_2$

M is a "redox mediator", or charge-carrying agent, that shuttles electron equivalents from O_2-evolving photomodule to the H_2 module.

Our inital photocatalysts were TiO_2 in the O_2-evolving bed, and InP in the H_2-evolving bed [Linkous 1996a]. It was soon found that modification with noble metal co-catalysts made for more rapid gas evolution. Iridium was found to facilitate O_2 evolution, and Pt was found to facilitate H_2 evolution. Many candidate redox mediators were screened in order to find the best one [Linkous 1996b]. The alkaline redox couples I^-/IO_3^- and Br^-/BrO_3^- were identified.

Efficiencies were still low because of fundamental limitations with the photocatalysts. The band gap of TiO_2 was too wide (3.0 eV), so that only a small portion of the solar spectrum (in the UV) could be absorbed and utilized. Corrosion was also a problem. H_2 evolution from Pt-InP suspended particulates had slowed considerably after only a few hours of photolysis time. Inspection showed that the originally black powder had become gray, due to oxide formation. It was first thought that photocorrosion was occurring, but subsequently it was found that the InP was reacting with the IO_3^- ion that was forming as a consequence of I^- oxidation.

As a substitute for TiO_2, it was decided to look at WO_3. With a somewhat narrower band gap (2.7 eV), it promised to absorb more of the solar spectrum. The WO_3 became part of an IEA (Internation Energy Agency) collaboration. Dr.'s Jan Augustynski and Martinne Ulmann from the University of Geneva, Switzerland, have been working their own WO_3 preparations as part of a Swiss national collaboration on a tandem photoelectrochemical cell. Their colloidal WO_3 has an effective band gap energy of 2.5 eV, so that it would absorb some 2.5 times as much sunlight as TiO_2 [Augustynski 1996].

The colloids proved to be rather unstable, however. In the presence of a surfactant or other stabilizer, the colloidal state could be maintained, but only at the risk of blocking the surface photochemistry. In the absence of additives, the aqueous colloids could be maintained on their own for several days by continuously stirring in the dark, but the act of performing a photocatalytic evaluation on them accelerated their aggregation. The final material consisted of 1.0 μm particles that were less photoactive than commercial grade WO_3.

We also began to look at organic pigments as alternative photocatalysts. Their high extinction coefficients and good match with the solar spectrum was thought to compensate for comparatively low charge carrier mobilities. Many organic compounds representing the major classes of dyestuffs were evaluated for their suitability as O_2-evolving photocatalysts . Several trends soon emerged. Di- and triarylmethanes, phthalocyanines, polymethines, xanthenes, thioxanthines, and acridines all tended to have insufficiently large ionization potentials. Other classes, such as anthraquinones, perylenes, quinacridones, and pyranthrones reliably gave ionization potentials that should be able to oxidize water. Consideration of water miscibility and light fastness helped narrow the field even further. A field of roughly a dozen structurally related compounds were chosen for experimental evaluation.

Results and Discussion

Effect of CO_3^{2-} on O_2 Evolution

This is another IEA interaction that began only this year. Our collaborators are Dr.'s H. Arakawa and K. Sayama of the National Institute of Materials and Chemical Researach in Tsukuba, Japan. They have observed the stoichiometric, co-evolution of H_2 and O_2 from single pot, photocatalytic powder dispersions of TiO_2 and other photocatalysts in the presence of carbonate ion, CO_3^{2-} [Sayama, 1994]. The presence of carbonate ion had been found to be vital to the O_2 evolution process. Apparently the intermediate surface-adsorbed hydroxyl radicals generated from initial water oxidation are quite reactive, and will oxidize any available redox agent present, even background organic contaminants. The carbonate ion acts as a scavenger for hydroxyl radical, forming a peroxydicarbonate species that ultimately breaks down, releasing O_2[Sayama 1997]. Thus carbonate acts as a catalyst for O_2 evolution.

We decided to see whether the same effect could be observed for the O_2-evolving half of our dual bed system. Accordingly, 250 mg dispersions of various photocatalysts were suspended in 50 ml solution and photolyzed. The relevant data are shown in Table 1. At a 0.5 M CO_3^{2-} concentration, very little improvement was seen; in fact, for the most active Ir-TiO_2 system, a negative effect was apparent. Our interpretation is that the CO_3^{2-} ion adsorbs not only on the TiO_2 surface, but on the co-catalyst as well. For the dual bed approach to work, the redox mediator (IO_3^-) needs open access to the co-catalyst surface. By charge conservation principles, the rate of IO_3^- reduction must match that of O_2 evolution. If the Ir surface is blocked by CO_3^{2-} ion, then any gains made on the TiO_2 surface are lost on the co-catalyst surface. Therefore, in the absence of any kind of favorable preferential adsorption, the use of carbonate ion in directing O_2 evolution in the dual bed system is inadvisable.

Evaluation of NiO_x-TiO_2 Photocatalyst

A black powder consisting of TiO_2 precipitated from $Ti(i\text{-}PrO)_4$ and modified with 3 weight % Ni was given to us by Dr. Arakawa. Part of the agreement was to test the photocatalyst in Florida sunlight. While water-splitting may have occurred, it was at too low a production rate for us to reasonably detect it with our existing gas chromatographic apparatus.

Subsequent testing was done indoors in front of a Xe lamp. In conjunction with our IO_3^- redox mediator, it showed reasonable photoactivity, more than doubling the gas output in comparison to plain TiO_2. On the other hand, Ir-TiO_2 still performs better by an order of magnitude. With an anticipated large scale loading of only 100 mg Ir/m^2, saving money on the cost of the co-catalyst does not justify enlarging the system to accommodate the lower photoactivity level.

Table 1. Evaluation of NiO_x-TiO_2 as Alkaline O_2-Evolution Photocatalyst: Carbonate Effect

All solutions were 1.0 M NaOH

photocatalyst	light source	$[CO_3^{2-}]$	$[IO_3^-]$	O_2 evolved (ml)
NiO_x-TiO_2	sun	0	0	< 0.02
NiO_x-TiO_2	sun	0.5 M	0	< 0.02
NiO_x-TiO_2	Xe	0	0.2 M	0.98
NiO_x-TiO_2	Xe	0.5 M	0.2 M	0.93
TiO_2	Xe	0	0.2 M	0.40
Ir-TiO_2	Xe	0	0.2 M	11.7
Ir-TiO_2	Xe	0.5 M	0.2 M	3.93

Evaluation of Sol/Gel-Deposited WO_3 Photocatalyst

Because of our difficulties in maintaining the colloidal particle size of WO_3 obtained via ion exchange, our Swiss collaborators sent us their own preparations that had been immobilized via sol/gel techniques on ITO. Since their photocatalysts had been painted on a surface and lightly sintered before testing, the original particle size could be preserved. The porous dispersion consisted of 15-30 nm particulates.

We put together a special cell that could hold the WO_3/ITO samples nearly perpendicular to the direction of irradiation while being surrounded by the redox mediator solution. Gas evolution into the head space was analyzed for O_2 via gas chromatography. Data for the photocatalytic behavior of these samples are shown in Table 2. As a comparison, a dispersion of Ir-TiO_2 was cast onto glass and tested in alkaline IO_3^- solution under the same conditions.

Because of the acid/base properties of WO_3, the solutions were made 1.0 M in H_2SO_4. It was seen that only modest concentrations of ferric ion are optimum; the 1.0×10^{-3} M solution actually generated more O_2 than the 0.1 M solution. This is due to an optical absorption effect: the 0.1 M solution was decidedly orange in color, and so absorbed much of the light that the WO_3 could have used. Co-catalysts did not improve the O_2 evolution rate. The iodate ion actually did rather well in the acidic solution, even though the risk of darkening the solution with triiodide at this pH was great. Rather than colorize the solution, there was some evidence that solid I_2 was precipitating onto the WO_3 surface. While from a practical device point of view this would be a prohibitive development, for a short batch photolysis experiment it did not significantly change the results.

Table 2. Evaluation of Sol/Gel-Deposited WO_3 on ITO as an O_2-Evolution Photocatalyst

Solution composition: $[Fe^{3+}]$ = 0.001 M, or $[IO_3^-]$ = 0.2 M; 1.0 M H_2SO_4

photocatalyst	mediator	O_2-evolved (ml)
WO_3	Fe^{3+}	0.04, <0.02[b]
Pt-WO_3	Fe^{3+}	0.03
Ir-WO_3	Fe^{3+}	0.02
WO_3	IO_3^-	0.4
WO_3 (Fisher)	Fe^{3+}	<0.02
Ir-TiO_2 (film)[a]	IO_3^-	2.3

[a] solution was 1.0 M NaOH; [b] $[Fe^{3+}]$ = 0.1 M

The Ir-TiO_2 film was by far the most photoactive. Thus despite the inherent advantages of WO_3 in terms of solar absorption, it still lags TiO_2 in terms of overall photoactivity.

Electronic Structure of Quinacridone and Other Organic Pigments

This year came the business of actually locating and working with some of the pigments we had done calculations on earlier. Not all of them were commercially available. Also, other promising substances were subsequently identified. Ultimately, some 12 structurally related pigments were acquired.

The first step was to characterize their electronic structure. This was attempted electrochemically, but proved to be difficult because the pigments were poorly soluble and resisted sulfonation. Instead, we are going to try and obtain direct ionization potential data to compare to our calculations. The effort now is focused on identifying an apparatus that can work with these involatile, high molecular weight compounds.

Meanwhile, electronic structure information is also available via solid phase spectra. Most of the compounds were amenable to vacuum sublimation, and so solid films on glass could be prepared in this manner. It was intended to derive the effective energy gap of each material from the onset of absorption of its lowest energy transition. Some of the spectra were too broad and diffuse to identify a clear onset of absorption, so sometimes we had to simply mark the peak maximum. A few were soluble in organic solvent, yielding clear absorption maxima.

In Table 3, effective band gap data are given for the 12 organic pigments that we have acquired and tested. A general correlation is seen between the size of the band gap and the magnitude of the calculated ionization potential.

Table 3. Energy Gap and Ionization Potential Data for Organic Pigments

name	band gap energy (eV)	calculated IP (eV)
dimethoxy-violanthrone	2.08[e]	6.93
indanthrene Gold Orange	2.4[p]	7.96
Cromophtal Red 3B	2.2[s]	7.27
isoviolanthrone	2.5, 2.0, 1.9[s]	7.26
indanthrene Yellow GCN	3.2[s]	8.56
indanthrene Black BBN	1.9[s]	7.93
bis-(p-chlorophenyl) DPP	2.17[p], 1.98[e]	7.02
indigo	1.84[p]	7.42
pyranthrone	2.6[s]	7.62
quinacridone	2.16[p], 1.98[e]	6.67
indanthrone	1.89[p]	6.24
perylene TCDA	2.20[p]	8.45

[s]solution; [p]peak; [e]edge

"Tandemizing" the Dual Bed Configuration

Utilization of two photocatalytic beds automatically cuts the overall quantum efficiency in half. This may be considered a negative attribute, but perhaps more accurately it should be thought of as a trade-off between quantum efficiency and the need to make effective use of the solar spectrum. While net water decomposition to H_2 and O_2 has been observed in single component photocatalytic suspensions [Sayama, 1996], the photocatalyst employ typically possessed a band gap energy of > 3.0 eV. Less than 10% of the solar spectrum can be utilized by such materials.

The general strategy of fabricating devices consisting of two or more small band gap materials connected in series for effective absorption of sunlight while generating enough driving force for water splitting has been employed in a number of configurations. Principal among these is the "tandem" cell approach, where two dissimilar materials with different band gap energies are deposited onto one another. The material with the wider band gap is placed forwardmost to the direction of irradiation, so that light of longer wavelength passing through it can be absorbed by the narrower band gap material.

The dual bed photocatalytic system can be "tandemized" by essentially folding the second bed underneath the first one, as shown in Figure 1. If scattering losses in the uppermost module can be minimized, and complementary photocatalysts are employed, then one can achieve the tandem effect, that is, have high energy photons absorbed in the first semiconductor layer, and lower energy photons absorbed in the second layer. The circulating redox electrolyte would then flow from left to right across the top module and right to left across the lower one. The single unit would be tilted slightly so that evolved gases would percolate to a head space at the upper corner. Materials cost savings would also accrue, since the module area is basically cut in half, and the photocatalysts would be immobilized on either side of the same transparent membrane.

Another development in the evolution of the dual bed configuration has to do with the motion of the redox mediator working fluid. It is projected that an efficiency increase may be had by perforating the membrane or transparent support. In this embodiment, the redox mediator effuses through microperforations in the photocatalyst support to reach the other immobilized photocatalyst dispersion. This feature eliminates the need to include a pump to move the redox solution across the surface of the photocatalyst; instead, a hopper supplying make-up water will suffice.

In the various tandem concepts, the photocatalysts are dispersed in layers on either side of a transparent membrane. One then has at least three laminates combining to form a single sheet. It has been demonstrated that the individual particles in each layer can communicate with each other, or in other words, an electron-hole pair generated well within a photocatalyst layer can migrate via particle-particle contact to the working fluid interface and perform redox chemistry. One can then speculate that if the photocatalyst laminates are thickened until they contact each other, there could be charge carrier flow across the membrane to the opposite interface. The optimum thickness of the photocatalyst layers at this point is uncertain, since it would be a trade-off between the penetration depth of the light each layer is expected to absorb, the diffusion lengths of the photogenerated charge carriers, and the mechanical strength of the photocatalyst bilayer.

If the two photocatalyst layers could electronically communicate with each other, then the need for a redox mediator would be obviated. The perforation feature would still have value; instead of having the mediator diffuse through the pores, the protons resulting from water oxidation (assuming acidic media) would be the mobile species. The pores could then be filled with a proton-conducting ionomer or other medium that would be selective toward the solvated species of interest. This would eliminate much of the parasitic gas intermingling that would occur through an open, perforated structure.

Acknowledgements

The authors would like to thank Dr. Harold Freeman, Ciba-Geigy Professor of Dyestuff Chemistry at North Carolina State University, for his many suggestions and support. Financial support from the US Department of Energy, Office of Solar Thermal, Biomass Power, and Hydrogen Technologies is gratefully acknowledged.

References

Augustynski, J., Calzaferri, G., Courvoisier, J.C., Grätzel, M., and Ulmann, M. 1996. "A Two-Photon System for the Cleavage of Water into Hydrogen and Oxygen by Visible Light." *Proceedings on Solar Energy Materials.*

Linkous, C.A. 1996a. "Solar Photocatalytic H_2 Production from Water Using a Dual Bed Photosystem." In *Proceedings of the 1996 U.S. DOE Hydrogen Program Review*, vol. 1, 389-395.

Linkous, C.A., Slattery, D.K., Ouelette, A.J.A., McKaige, G.T., and Austin, B.C.N. 1996b. "Solar Photocatalytic H_2 from Water Using a Dual Bed Photosystem." In *Hydrogen Energy Progress XI: Proceedings of the 11th World Hydrogen Energy Conference*, vol. 3, 2545-2550.

Linkous, C.A. and Slattery, D.K. 1997. "Investigation of WO_3 Powder as an O_2 Evolution Photocatalyst," Minutes of the IEA Annex X Meeting , April 15-18, 1997, Paul Scherrer Institute, Switzerland.

Sayama, K. and Arakawa, H. 1994. "Effect of Na_2CO_3 Addition on Photocatalytic Decomposition of Liquid Water over Various Semiconductor Catalysts." *J. Photochem. Photobiol. A: Chem.*, 77: 243-247.

Sayama, K. and Arakawa, H. 1997. "Effect of Carbonate Salt Addition on the Photocatalytic Decomposition of Liquid Water over Pt-TiO_2 Catalyst." *J. Chem Soc., Faraday Trans.*, 93: 1647-1654.

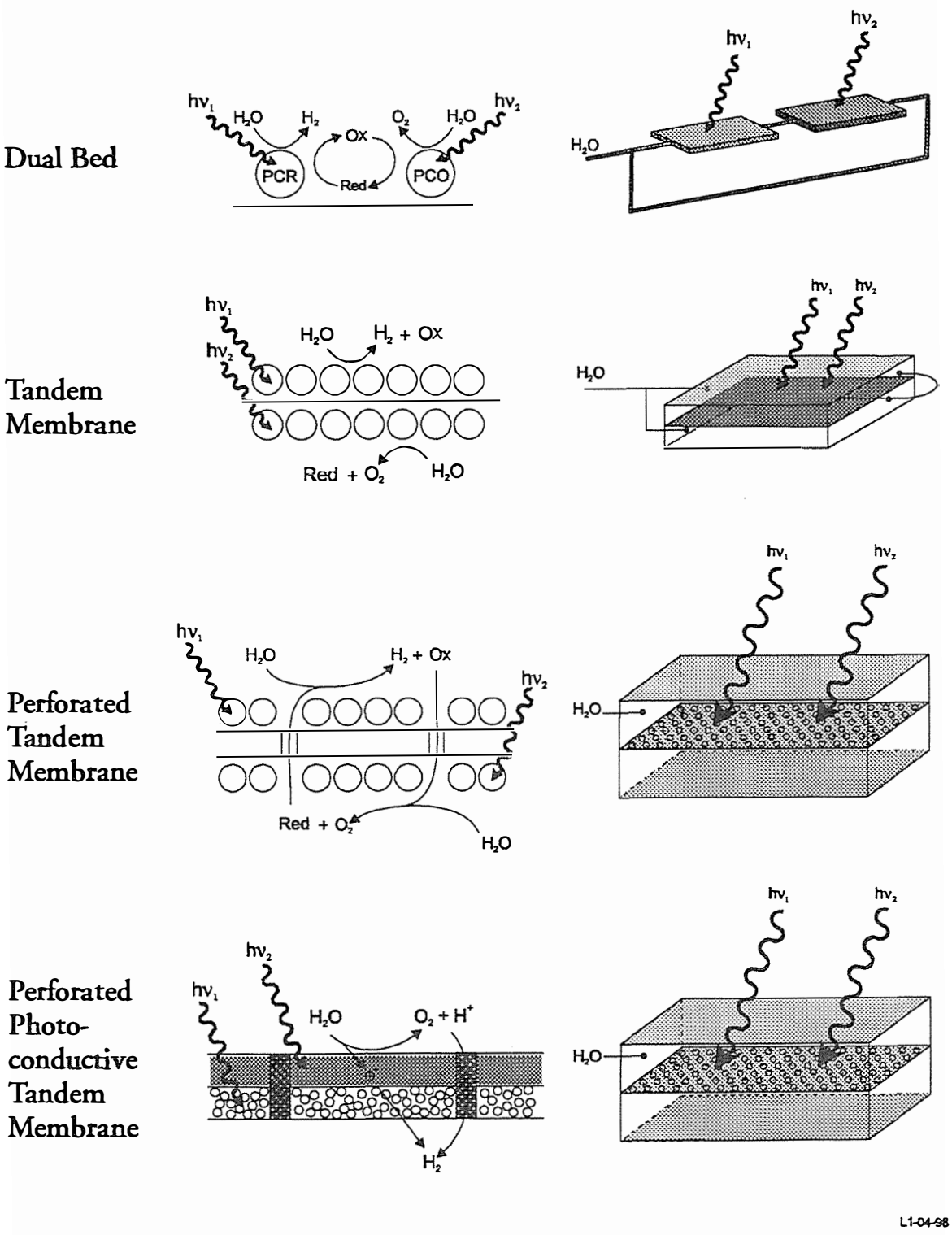

Figure 1. Evolution of Dual Bed Photocatalytic Water-Splitting Systems

GENERATION OF HYDROGEN FROM PHOTOCATALYTIC CLEAVAGE OF WATER

R.G. Mallinson, D. E. Resasco and L. L. Lobban
School of Chemical Engineering and Materials Science

K. M. Nicholas
Department of Chemistry and Biochemistry

Institute for Gas Utilization Technologies
University of Oklahoma
Norman, OK 73019

Abstract

This paper describes the objectives, methods and early results on the US Department of Energy sponsored project to generate hydrogen from splitting of water using photocatalysts. The approach uses organometallic photosensitizers adsorbed onto platinated titania. Platinized titania is a photocatalyst for water splitting, but does not absorb sunlight in the visible range, where most of the sun's energy is contained. Organometallic photosensitizers are synthesized, attached to platinized titania and characterized by UV-Vis spectroscopy, cyclic voltammetry, action spectra and hydrogen generation ability. Thus far, Copper, Iron and Ruthenium catalyst systems have been produced and characterized in this manner. Suitable sensitized systems that have the desriable properties have not yet been found.

Introduction

The cleavage of water to form hydrogen and oxygen would be an ideal source of hydrogen for energy needs. The feedstock, water, is available in virtually inexhaustible supply, and the resulting fuel, hydrogen, burns with no polluting products, the only reaction product being water. The cleavage reaction is endothermic, however, and the energy required to achieve a significant hydrogen production rate is high. Ideally, the energy source must also be available in abundant supply and be nonpolluting. Solar energy meets these requirements, and the use of solar energy to drive the cleavage of water to produce hydrogen is an extremely attractive means to convert solar energy to chemical energy.

There has been extensive investigation of chemical systems that involve the absorption of electromagnetic radiation by chemical agents, followed by reactions leading to the cleavage of water. Photocatalytic cleavage of water by semiconductor photocatalysts is among the most promising techniques since the catalyst is a solid material which is relatively inexpensive, resistant to deactivation, nontoxic and safe to handle. The most promising of these semiconductor systems is a supported catalyst, Pt-RuO_2/TiO_2. The energy of UV light matches the band gap existing in the anatase form of TiO_2. When the surface of the TiO_2 support is illuminated by UV light, electrons in the valence band are excited to the conduction band, leaving an electron hole. The electrons can react with adsorbed water, leading to a sequence of reactions resulting in the production of H_2 and O_2. The Pt and RuO_2 crystallites on the titania surface are believed to catalyze important steps in the subsequent reactions, increasing the rate of product formation.

Despite numerous studies examining this reaction system, the rate of production of hydrogen remains too low for easy commercialization. Significant limiting factors would appear to be (1) the narrow range of wavelengths that are absorbed by titania to initiate the reactions, (2) the difficulty of combining photoaccessibility and reactant accessibility to high surface areas of the photocatalyst, and (3) the efficiency of the subsequent catalytic (versus photocatalytic) steps to form H_2 and O_2. We will investigate novel photocatalytic materials and attempt to alleviate each of the three limitations cited above.

The anatase form of TiO_2 absorbs only a narrow range of solar energy, i.e., wavelengths < 370 nm. More complete utilization of solar energy (to address the first limitation) requires the presence of molecules that will absorb light in the visible wavelength range, i.e., from ~400 to ~850 nm. Among the most efficient are ruthenium complexes such as ruthenium (II) tris-2,2'-bipyridyl cation ($Ru(bpy)_3^{2+}$). These complexes absorb light in the visible wavelength range. The resulting excited complex may lose energy by ejection of an electron if a suitable acceptor is available. The acceptor may be other dyes in the aqueous phase, or the acceptor may be a solid semiconductor, but in either case the acceptor must be located sufficiently close that diffusion to the acceptor is possible within the lifetime of the excited complex (about 300 angstroms for excited $Ru(bpy)_3^{2+}$ in aqueous solution). In this project we plan to explore the binding of photsensitizers to the titania both as a way of isolating the catalyst and, perhaps more importantly, to determine if materials which may have too short an excited lifetime in solution may show activity when bound to the titania directly.

The use of aerogel TiO_2 as the semiconductor support in the Pt-RuO_2 photocatalyst has not been reported. Aerogels have characteristics which address the second limiting factor mentioned above. Aerogels are mesoporous, high specific surface area materials. Mass transfer within the pores of the aerogels is therefore rapid. Because of the very thin pore walls, only a fraction of incident light may be absorbed while the remainder is transmitted. A larger surface area thus may become photocatalytically active. Also because of the structure, a higher fraction of the generated valence electrons and electron holes should react with adsorbed species since the distance to migrate to a solid-liquid interface is very small.

Synthesis of Catalysts/Photosynthesizers

Recent investigations in the laboratories of Grätzel, Ferrere and Meyer (cf. Grätzel and Kalyanasundaram, 1993) indicate that metal complexes with short metal-ligand charge transfer (MLCT) excited state lifetimes are capable of efficient photoinjection of electrons to TiO_2 if covalently bound to the semiconductor surface. Hence we have sought: 1) to prepare iron(II) and copper(I) complexes of substituted diimmine ligands which will allow both modulation of their redox and absorption characteristics and their attachment to TiO_2; and 2) to investigate the ability of the TiO_2-bound complexes to mediate photoinduced water splitting. We have synthesized complexes of the type Fe_2X_2 and CuL_2X (L= -CO_2H and -PO_3H- substituted bipyridyl and biquinoline ligands) in quantities to allow characterization and hydrogen generation experiments. A Ru based complex which has been well studied in solution has also been produced. These are shown in Figure 1. We have also completed the successful adsorption of these sensitizers onto TiO_2 and Pt-TiO_2.

More potential sensitization candidates are to be identified and characterized. Easier and cheaper (e.g. Fe, easier to produce ligands) methods for the synthesis of the selected sensitizer compounds need to be investigated. These second generation complexes in which the photoelectrochemical, redox, and TiO_2 absorption properties of the compounds are "tuned" through variation of ligand substituents to improve their capabilities as visible sensitizers. Strategic introduction of electron-withdrawing or electron donating groups on the bipyridyl, phenanthroline and biisoquinoline ligands will shift the redox potentials and the visible absorption maixima of the complexes. The relative efficacy of ionizable substituents (e.g. CO_2H, PO_3H_2, SO_3H) for binding the sensitizers to titania will also be assessed. The use of Pt/RuO_2/TiO_2 with the sensitizers will also be examined.

Catalyst Characterization

The responsivity of the sensitizers to different wavelengths of light has been examined through diffuse reflectance UV-VIS measurements of the dry catalyst powders and are shown in Figure 2. It may be seen that these compounds display intense MLCT absorptions in the 500-600 nm region. Experiments to determine the properties (photo-electrical and chemical) of the sensitizers and their electron injection capabilities are to be performed. Experiments need to be conducted to determine the Action spectra and photocurrents in order to characterize the sensitizers in terms of quantum efficiencies. Cyclovoltammetric studies are to be done to quantify the ground state potentials of the sensitizers. Figure 3 illustrates the desirable characteristics for the regenerative oxidation and reduction of a photosensitized system. Figure 4 shows the voltage-current characteristics for the Iron

system, which shows the reduction and oxidation peaks as well as the MLCT peak. Figure 5 shows that the reduction potential is satisfactory but the oxidation potential is not. For this system a sacrificial reductant would need to be used. Figure 6 shows the voltage-current data for the copper system and the absence of a reduction peak suggests that the system undergoes an irreversible oxidation. The nature of attachment of the dye to the TiO_2 photocatalyst and the influence of attachment on the characteristics of the photocatalyst are also to be examined. These may include surface areas, chemisorption and temperature programmed desorption. Comparisons of the characterizations between the fresh and spent catalysts will be made as well as an examination of their longevity.

Investigations of electrochemical, photoelectrochemical, and water splitting photochemical properties will continue with the new sensitizer candidates. As part of this we will obtain action spectra of the sensitizers, including the original set. These characterizations will allow correlation and screening of new materials for effective visible light water splitting.

Hydrogen Generation Measurements

A three-phase continuous photocatalytic reactor for testing the catalysts has been designed and built. It is diagramed in Figure 7. Experiments can be performed both in the ultraviolet and the visible regions and the hydrogen production can be continuously monitored. A provision for filtering out specific wavelengths of light has also been made. Results of other researchers on water splitting experiments under UV illumination have been reproduced for validating the reactor system. The system built can give an accurate picture of catalyst life times and turnover numbers in terms of hydrogen production. The system can also be used to determine the effect of different illumination conditions on the hydrogen production capabilities of the sensitizer/photocatalyst systems. Experimental verification of data from the literature has been made with platinized titantia using UV light as shown in Figure 8.

Experiments involving both ultraviolet and visible regions will be performed and the behavior of the sensitizer under the different illumination conditions will be examined. The effects of the following variables on the hydrogen production will be studied: a. effect of intensity of incident light; b. effect of temperature of the bath; c. effect of sacrificial reductants in the reaction mixture; d. role of pH.

A smaller, non-continuous reaction system will also be fabricated. This will allow in-situ UV-Vis spectra to be obtained to examine the distribution and efficiency of the light spectrum used. Headspace GC analysis will characterize the evolved gas by using a recycle loop.

Acknowledgments

This project is funded by the U.S. Department of Energy under grant number: DE-FC36-97GO10141 and the authors gratefully acknowledge this support. The authors also wish to express their appreciation for the assistance and advice of John Turner, Susan Ferrere and their colleagues at the National Renewable Energy Laboratory.

References

Grätzel, M.and K. Kalyanasundaram, Metal Complexes as Photosensitizers in Photoelectrochemical Cells, in Photosensitization and Photocatalysis Using Inorganic and Organometallic Compounds, K. Kalyanasundaram and M. Grätzel, Eds, Kluwer Academic Publishers, the Netherlands, 247-271, 1993.

Figure titles

Figure 1 - Sensitizer Complexes.

Figure 2 - UV-Vis Spectra of Sensitized and Unsensitized Titania.

Figure 3 - Band Edge and Ideal Redox Potential Positions.

Figure 4 - Cyclic Voltammetry of the Iron Sensitized System.

Figure 5 - Redox Potential Positions of Iron Sensitized System.

Figure 6 - Cyclic Voltammetry of the Copper Sensitized System.

Figure 7 - Flow Photoreactor System.

Figure 8 - Comparison of Continuous Hydrogen generation with UV.

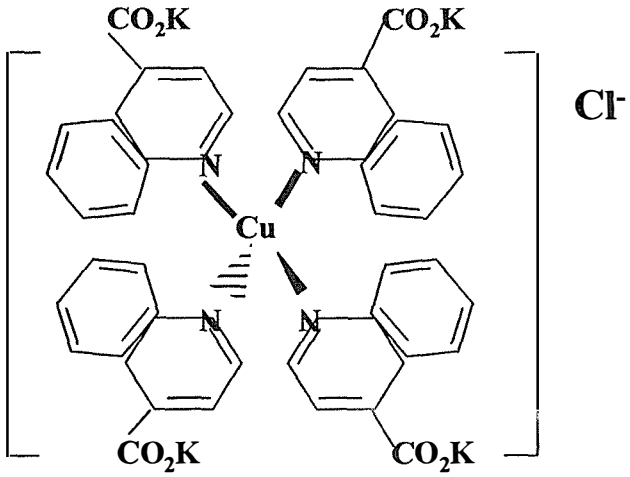

Cl⁻

bis(2,2'-biquinoline-4,4'-dicarboxylate)
Cu(I) chloride

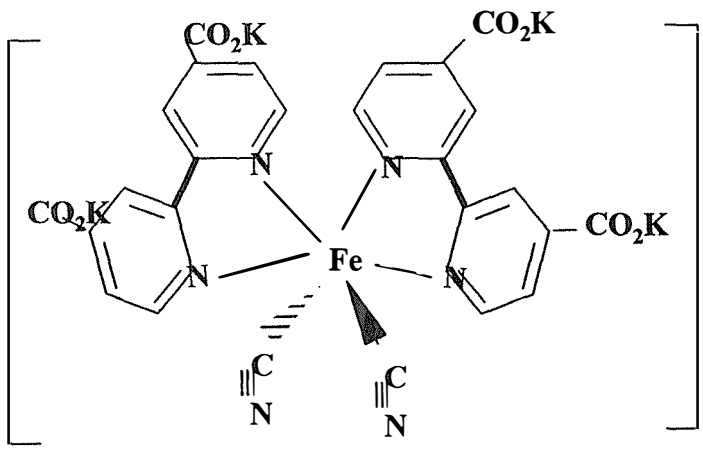

Dicyanobis(2,2'-bipyridine-4,4'-dicarboxylate)iron(II)

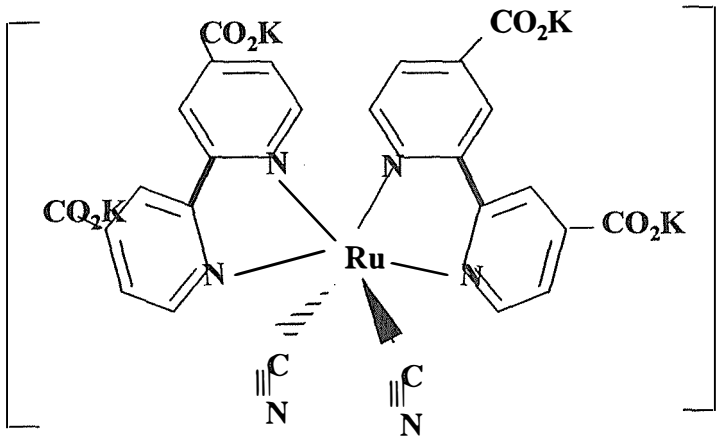

dicyanobis (2,2'-bipyridine-4,4'-dicarboxylate) ruthenium (II)

Figure 1

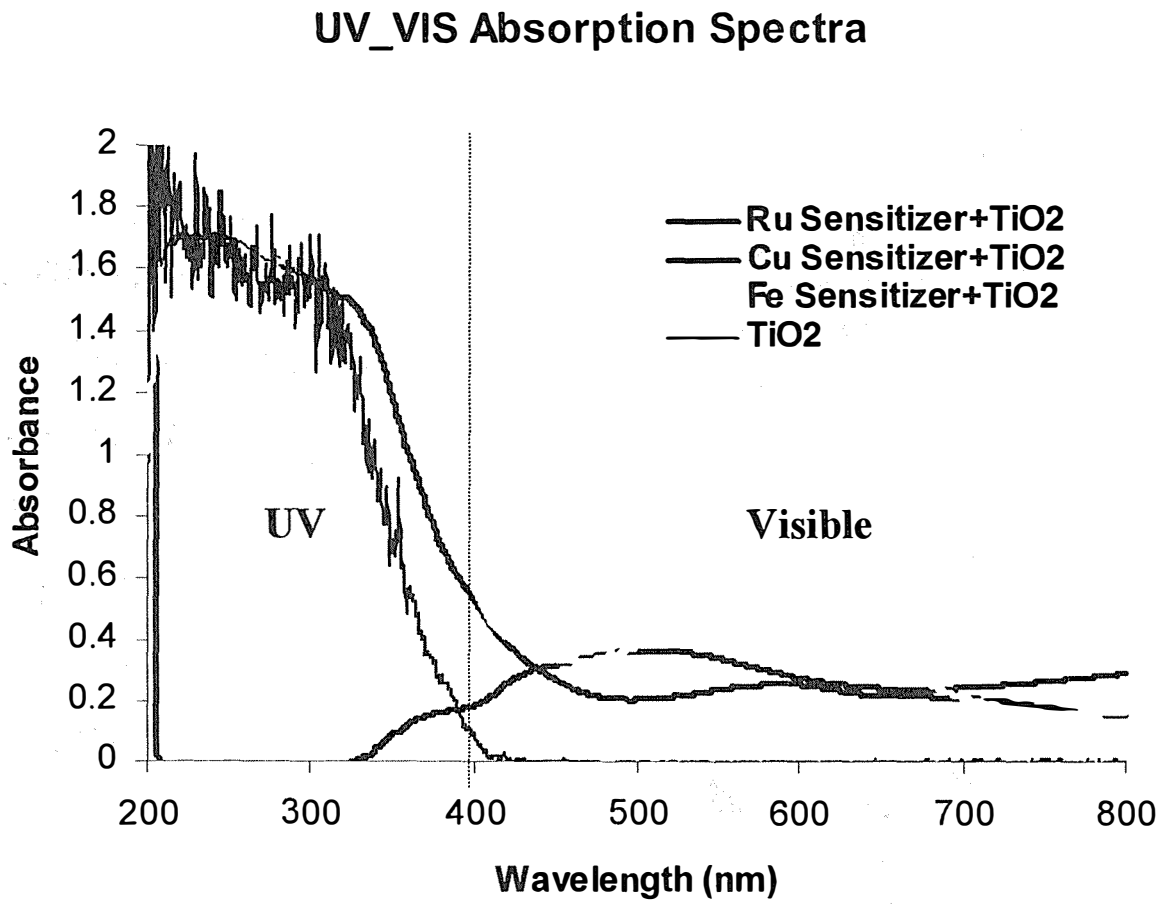
UV_VIS Absorption Spectra
Absorbance
2
1.8
1.6
1.4
1.2
1
0.8
0.6
0.4
0.2
0
200
300
400
500
600
700
800
Wavelength (nm)
UV
Visible
Ru Sensitizer+TiO2
Cu Sensitizer+TiO2
Fe Sensitizer+TiO2
TiO2

Figure 2

For regenerative photosensitization the ground state oxidation potential of the Sensitizer Dye must be more positive the water oxidation potential (+1.23 V vs NHE)

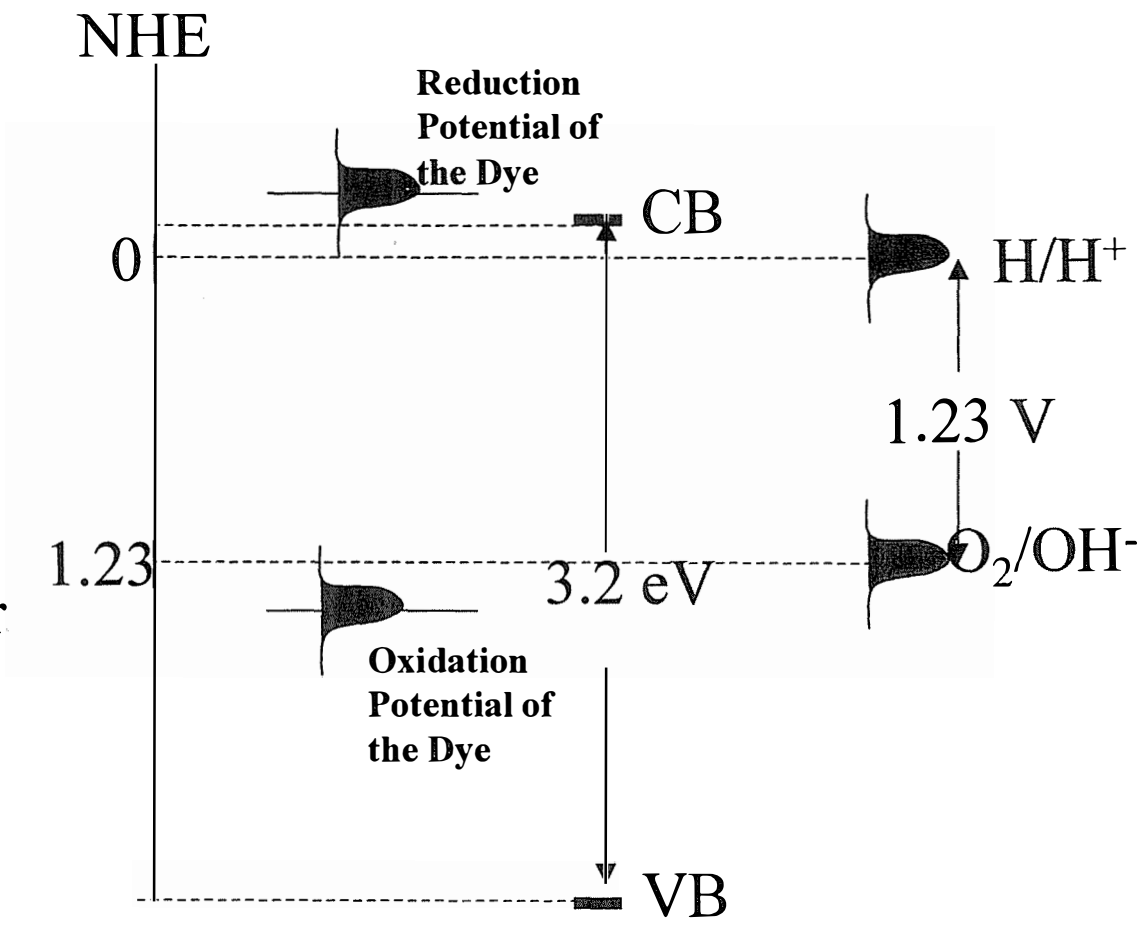

Ideal Band Edge and Redox Potential Positions for water splitting using dye sensitized semiconductors.

Figure 3

Fe[2,2'-bipyridine-4,4'-dicarboxylate)$_2$(CN)$_2$]

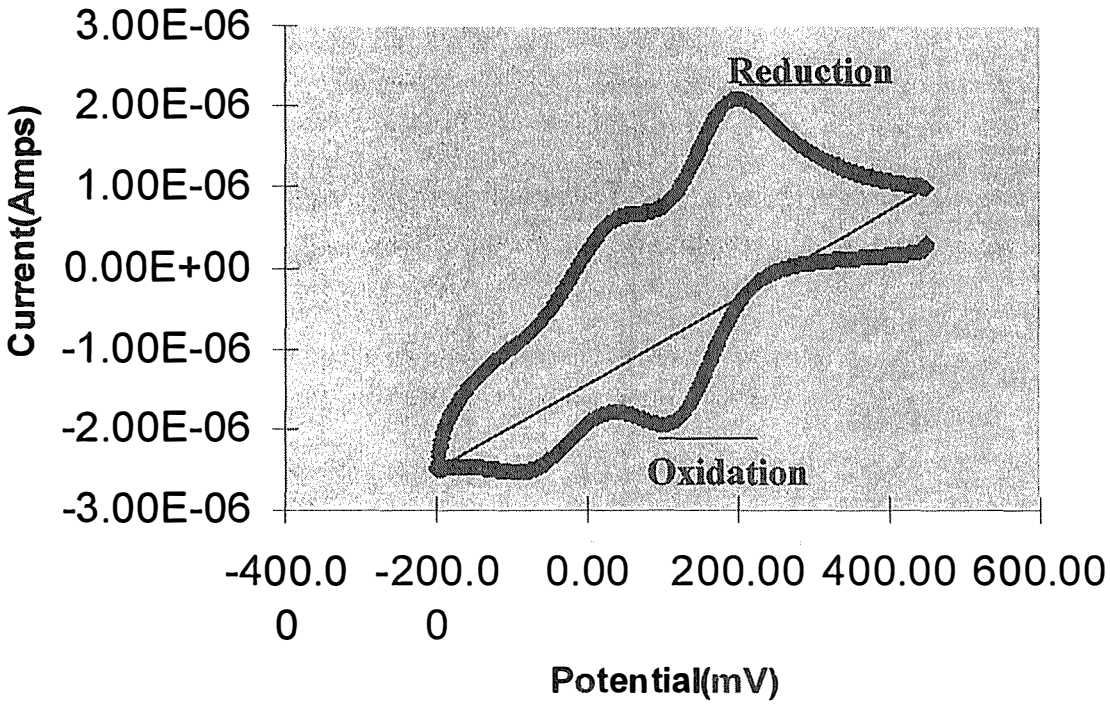

Ag/AgCl Reference

- **Peak at 200mV and the peak at 100mV correspond to the reduction and oxidation potentials of the Dye.**
- **The peak at 25 mV and the trough at -75 mV be attributed to the Metal to Ligand Charge Transfer (MLCT).**
- **The dye may be suitable for systems employing a sacrificial reductant.**

Figure 4

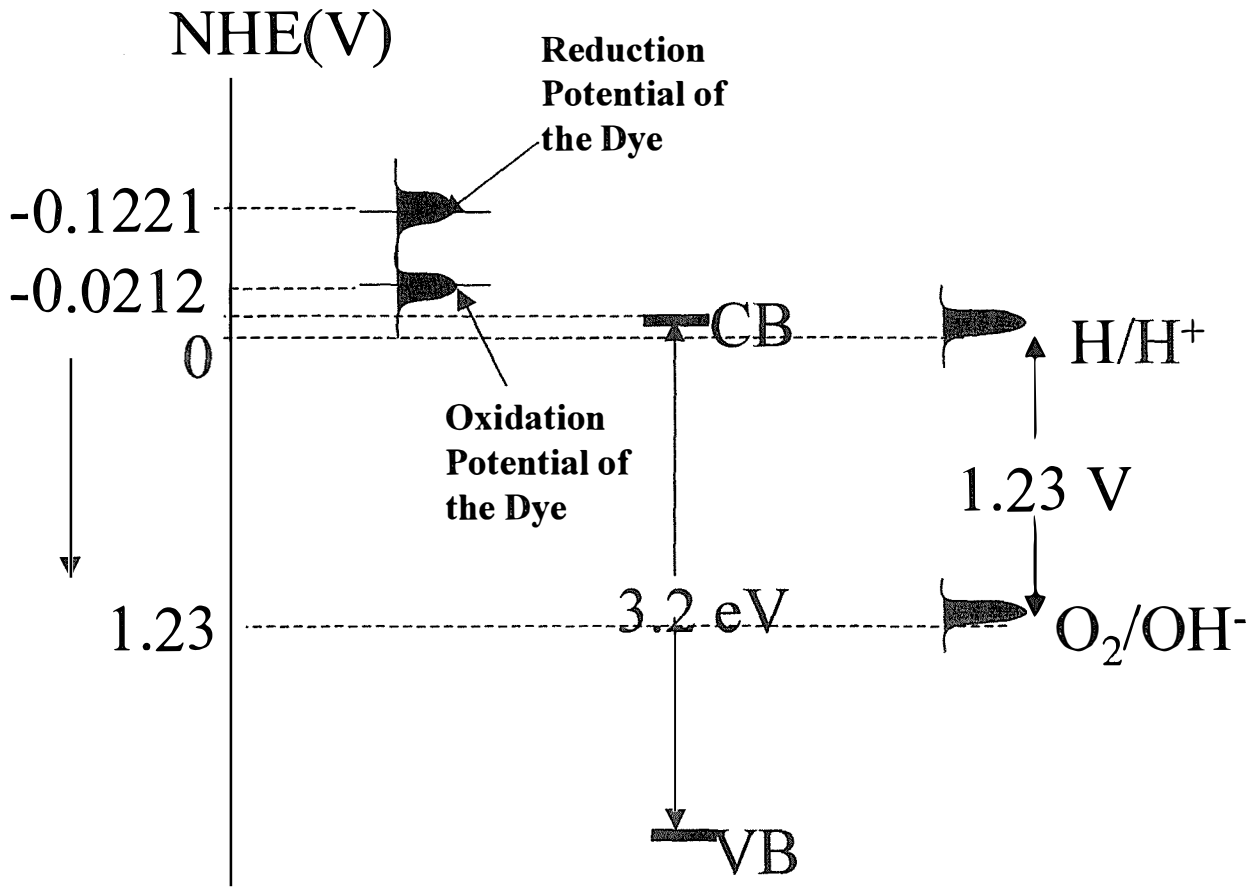
NHE(V)
Reduction Potential of the Dye
-0.1221
-0.0212
0
CB
H/H+
Oxidation Potential of the Dye
1.23 V
1.23
3.2 eV
O2/OH-
VB

Figure 5

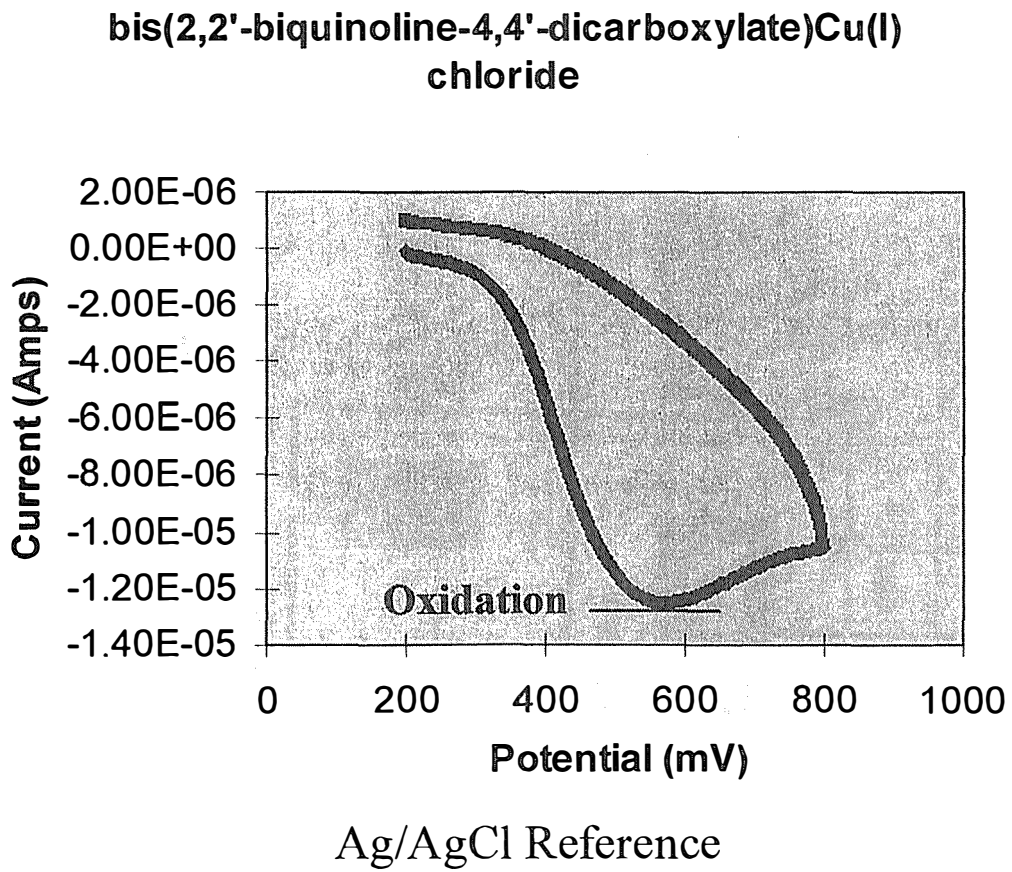

- **The trough at 550 mV corresponds to the oxidation potential of the Dye.**
- **The absence of a reduction potential peak suggests an irreversible oxidation process**

Figure 6

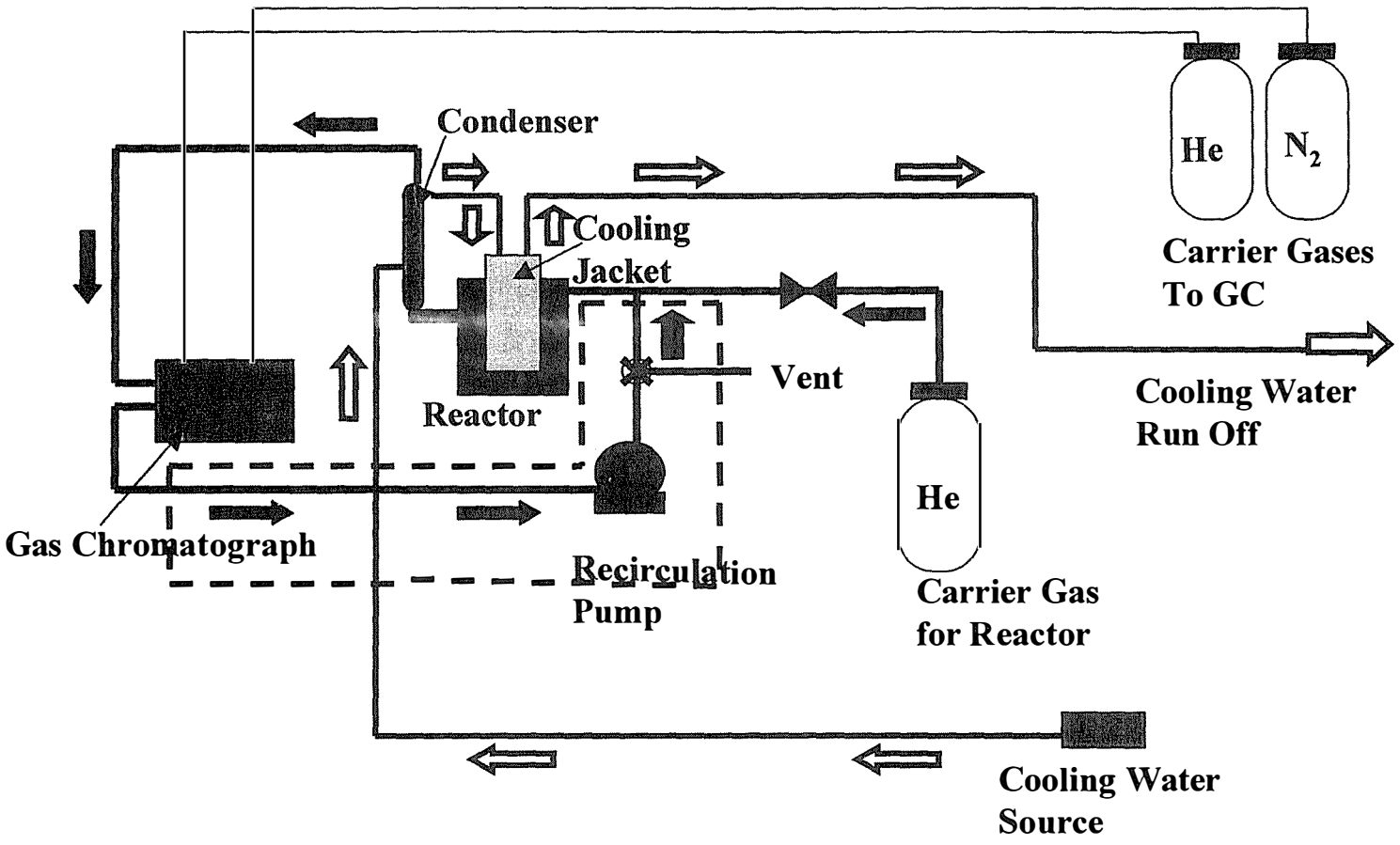
Condenser
Cooling
Jacket
He
N_2
Carrier Gases
To GC
Vent
Reactor
Cooling Water
Run Off
He
Gas Chromatograph
Recirculation
Pump
Carrier Gas
for Reactor
Cooling Water
Source

Figure 7

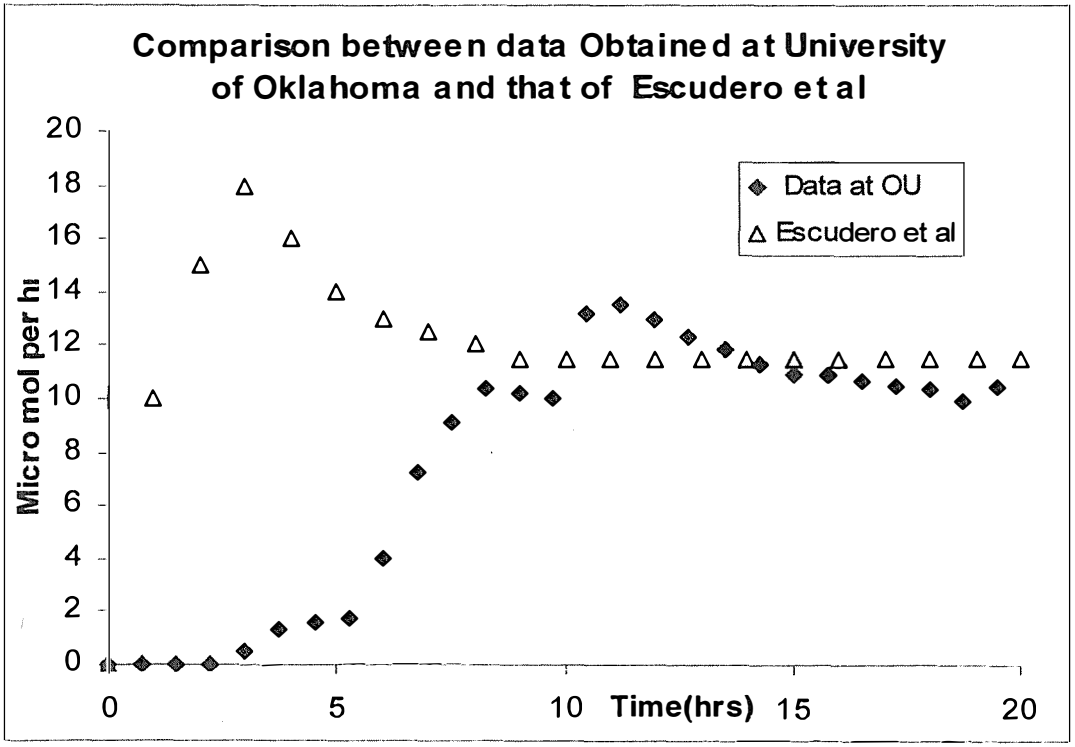

TiO_2-Pt (1 gm) Photocatalyst under UV irradiation

Figure 8

LOW-COST FIBER-OPTIC CHEMOCHROMIC HYDROGEN DETECTOR

D. K. Benson, C. E. Tracy, G. Hishmeh, P. Ciszek, and Se-Hee Lee
National Renewable Energy Laboratory
Golden, CO 80401

Abstract

The ability to detect hydrogen gas leaks economically and with inherent safety is an important technology that could facilitate commercial acceptance of hydrogen fuel in various applications. In particular, hydrogen fueled passenger vehicles will require hydrogen leak detectors to signal the activation of safety devices such as shutoff valves, ventilating fans, alarms, etc. Such detectors may be required in several locations within a vehicle - wherever a leak could pose a safety hazard. It is therefore important that the detectors be very economical. This paper reports progress on the development of low-cost fiber-optic hydrogen detectors intended to meet the needs of a hydrogen-fueled passenger vehicle. In our design, the presence of hydrogen in air is sensed by a thin-film coating at the end of a polymer optical fiber. When the coating reacts reversibly with the hydrogen, its optical properties are changed. Light from a central electro-optic control unit is projected down the optical fiber where it is reflected from the sensor coating back to central optical detectors. A change in the reflected intensity indicates the presence of hydrogen. The fiber-optic detector offers inherent safety by removing all electrical power from the leak sites and offers reduced signal processing problems by minimizing electromagnetic interference. Critical detector performance requirements include high selectivity, response speed and durability as well as potential for low-cost production.

A sensor based on the reversible, palladium-catalyzed reaction of amorphous tungsten oxide with hydrogen was studied extensively. While it was found to be adequately sensitive in a simple reflective sensor configuration, it was too slow. A new sensor configuration was invented and tested. The new design uses the coating in a surface plasmon resonance configuration so that very subtle changes in the refractive index of the coating can be detected at the resonance wavelength. This new design increased the response speed significantly, but introduced other

problems. We found that reversible desorption of water vapor from the amorphous tungsten oxide also changed its refractive index and gave rise to a false hydrogen signal. Increasing the thickness of the palladium catalyst layer to block the water vapor while still allowing the hydrogen to pass through proved to be effective at removing the false signals. However, this solution introduced an unexpected degradation in the sensor sensitivity over time. We eventually explained this degradation by a new interpretation of the reversible hydrogen reaction with the tungsten oxide. We believe that, contrary to conventional wisdom, oxygen is extracted from the tungsten oxide by hydrogen rather than hydrogen being inserted into the tungsten oxide. This reaction is only reversible if the film has access to oxygen. The thick palladium film that is needed to prevent false signals blocks the oxygen and allows mostly irreversible reactions and, hence degradation in sensitivity and response speed.

In view of the problems with the tungsten oxide sensor, we identified a new sensor coating, yttrium hydride and conducted preliminary tests. This material reacts reversibly with hydrogen in air to form a continuous range of compositions between the dihydride and the trihydride with dramatic changes in optical properties that are readily detected in a fiber-optic sensor configuration. Preliminary tests on an unoptimized sensor showed promising sensitivity to hydrogen and response speed much greater than in the tungsten oxide sensors. We plan to optimize the new sensor and evaluate its performance.

Background

The ability to detect hydrogen gas leaks economically and with inherent safety is an important technology that could facilitate commercial acceptance of hydrogen fuel in various applications. In particular, hydrogen fueled passenger vehicles will require hydrogen leak detectors to signal the activation of safety devices such as shutoff valves, ventilating fans, alarms, etc. Such detectors may be required in several locations within a vehicle - wherever a leak could pose a safety hazard. It is therefore important that the detectors be very economical. An optical fiber coated with a thin film chemochromic (a color change induced by a chemical reaction) coating offers the possibility of meeting the objectives of safety and low cost.

The reversible reaction between WO_3 and hydrogen has been well known since Schaefer showed that thin films of WO_3 with a superficial coating of platinum showed several orders of magnitude increases in electrical conductance when exposed to hydrogen in air. The reaction was thought to be the result of proton insertion into the tungsten oxide lattice in analogy to the electrochemical hydrogen insertion thought to occur during electrochromic coloration of tungsten oxide. Ito and coworkers (Ito 1984) showed that this hydrogen reaction also produced a broad optical absorption band just as its does in electrochromic coloration of tungsten oxide. They used the optical absorption as a means to detect hydrogen gas and suggested its possible use in a fiber-optic hydrogen detector. In their suggested detector design, light reflected from the thin film coating on the end of a fiber would be attenuated by the optical absorption band and indicate the presence of hydrogen at the sensor location.

Last year (Benson 1997) we tested the Ito suggestion by studying the reaction of tungsten oxide films in vacuum and in carefully controlled partial pressure mixtures of hydrogen with oxygen and hydrogen with air. Sensor response time constants were measured over a range of temperatures and hydrogen partial pressures. The reactions were shown to be reversible and samples tested over several months showed no evidence of degradation. The time constants, however, were too long - on the order of 30 seconds for response and nearly 30 minutes for recovery under typical room temperature testing conditions.

A new sensor design was invented (Benson 1998) which enhances the sensitivity to subtle changes in the coating. The chemochromic film is configured so that a surface plasmon resonance (SPR) occurs in it at a certain wavelength (Raether 1988). The hydrogen reaction produces a change in the optical index of the tungsten oxide which shifts the wavelength of the resonance absorption peak. The intensity of the reflected light at that wavelength is very sensitive to the shift in refractive index. Detecting the reflected light at or near the resonance wavelength enhances and speeds the hydrogen response signal. The new design also incorporated a means to produce a reference signal at a wavelength away from the resonance in the same optical fiber so that two outputs, a hydrogen-sensitive signal and a hydrogen-insensitive reference signal could be processed. The ratio of the hydrogen-sensitive signal to the reference signal should cancel much of the noise caused by changes in the optical transmittance of the optical fiber, a significant noise problem in a vibrating environment such as a vehicle.

This year's work has focused on testing the new SPR fiber-optic detector design.

Approach

Two parallel activities were pursued. In the first, we focused on the measurement of the hydrogen response characteristics of the sensor films in a configuration which produced a surface plasmon resonance absorption. For this purpose we deposited sensor films on large glass prisms for convenience of handling and measurement. The objective was to optimize the coating design and qualify it for the performance goals of speed, sensitivity, selectivity, and durability.

In the second activity, we designed and fabricated a complete prototype portable fiber-optic detector. This detector used a single, one millimeter diameter optical fiber that was either coated directly with the sensor film or had a small specially designed attachment to the fiber. The prototype instrument was designed to demonstrate the operation of a fiber-optic hydrogen detector and to determine the advantages of certain design features such as the ability to ratio a hydrogen signal to at reference signal for noise reduction.

Experimental Methods

Coatings

Thin film sensor coatings were deposited by thermal evaporation. Tungsten oxide powder (99.9%) was evaporated from a resistively heated tungsten effusion source. Palladium and silver

metals were evaporated from tungsten boats. All depositions were monitored with a quartz crystal deposition rate monitor. Film thicknesses were measured with a stylus gauge.

Chemochromic Response Measurements

Thin films sensors were deposited on 20mm right angle prisms for easier characterization. The test apparatus was designed to seal the coated surface from the surrounding air and expose it to a flow of a predetermined gas mixture. Small percentages of hydrogen in air were simulated by mixing measured flows of oxygen and nitrogen with prepared sources of 10% and 1% hydrogen in nitrogen. A synthetic air source was used for flushing the sample between test runs.

A fiber-optic white light source illuminated the coating through one leg of the prism and a fiber-optic detector picked up reflected light through the other leg of the prism and directed it to a diode array spectrophotometer (Fig. 1). The locations of the ends of the fibers (functioning as entrance and exit apertures) were fixed so that only light internally reflected by the sensor coating at a 45° angle would reach the spectrometer.

Fast toggle valves on the gas mixing manifold and timed acquisition of spectra made it possible to measure the optical reflectance spectra as a function of time and to calculate the response time constant of the sensor.

Optical Modeling

The spectral transmittance, reflectance and other optical characteristics of the sensor films were modeled using software from the Thin Film Center (Macleod 1995). This software also solves the equations for the surface plasmon resonance condition and accurately predicts the reflectance spectra. Most of the optical constants for modeling the various materials used in the sensors were obtained from the American Optical Society (Palik 1995). The optical properties of tungsten oxide thin films with various amounts of hydrogen "inserted" (commonly referred to a H_xWO_3) were modeled using measured optical data from Rubin and von Rottkay for tungsten oxide films with lithium electrochemically "inserted" (Li_xWO_3). It is well known that the optical properties of these two materials are very similar and we found the model calculations using optical data from Li_xWO_3 to agree will enough with measurements on H_xWO_3 to be satisfactory for our design purposes.

Results

Evaluation of Sensor Coatings

Figure 2 shows a theoretical reflectance spectrum for a tungsten oxide sensor film in a surface plasmon resonance configuration. The sensor film consists of a stack of two layers: a 40 nm thick layer of gold and a 600 nm thick layer of WO_3. The shift in this spectrum from curve a to b is the predicted result of the "insertion" of hydrogen to a level of $H_{0.068}$ WO_3. In this model, as in the sensor test configuration, the incident light strikes the film from inside the glass prism at 45° , an

angle which is greater than the angle for total internal reflection. Without the coating, all of the light would be reflected. However, at the resonance wavelength, the electric field of the incident light interacts resonantly with the free electrons in the gold to set up an electrical charge oscillation at the glass/gold interface. This is a so-called surface plasmon resonance (SPR). The wavelength at which the resonance occurs is strictly a function of the optical dielectric constants of the glass and gold. The light energy at this wavelength is dissipated by electrical losses in the gold and by re-radiation of the light by the electrons in all directions.

This SPR condition can be reinforced by the right choice of tungsten oxide thickness such that a constructive interference occurs at the resonance wavelength in the oxide layer. Under these conditions, the gold/WO_3 stack acts like a pair of coupled resonators and both the resonance wavelength and the resonance amplitude depend sensitively upon the optical dielectric constants of the glass, the gold and the WO_3. When the hydrogen reacts with the tungsten oxide, the oxide refractive index decreases and the resonance shifts as indicated in the figure.

The reaction of hydrogen and tungsten oxide is too slow without a catalyst. A thin layer of a catalyst such as palladium must be added. The palladium tends to absorb the resonance wavelength light and dampen the resonance. Figure 3 shows the theoretical reflectance spectrum from a sensor coating consisting of 40 nm gold/ 600 nm WO_3/ 3 nm Pd. For comparison, we show a measured reflectance spectrum from a sensor coating of this same configuration. The spectral characteristics of the light source and the light detector have not been removed, so the measured spectrum contains more structure than the theoretical one, but the SPR can be clearly seen. This resonance wavelength was very stable, with no significant shift detected over the temperature range tested from 24° to 69° C.

Figure 4 shows a set of spectra from a time series taken during exposure to 5% hydrogen in air at room temperature. The inset shows the change in reflected light intensity at the resonant wavelength over time. The change in signal amplitude is approximately exponential with a time constant of about 20 seconds. Similar measurements were made over a range of hydrogen concentrations and the time constant was found to decrease as the concentration increased. Over a range of concentrations up to 5%, the relationship between time constant and partial pressure appeared to be:

$$\tau \propto P_{H2}^{-2}$$

Unfortunately, the tungsten oxide readily exchanges water vapor with the atmosphere. Adsorbed water vapor increases its refractive index. Consequently, exposure of the sensor to dry air causes rapid loss of adsorbed water from the film and a shift in the SPR that mimics exposure to hydrogen! Of course, such a false alarm is unacceptable.

We applied a protective layer of poly-tetrafluoroethylene over the palladium by thermal evaporation. This retarded the exchange of water vapor without significantly affecting the SPR and the sensitivity to hydrogen. However, the sensor SPR was still susceptible to severe drift in changing humidity.

We next considered increasing the thickness of the palladium film to serve both catalytic and protective functions. Since the palladium adsorbs resonance light and tends to broaden the SPR, implementing this design option is tricky. However, if the film thicknesses are chosen correctly, a constructive interference resonance condition can be made to occur between the gold and palladium layers which coincides with the SPR. Figure 5 shows the theoretical and measured reflectance spectra from such a coating in the SPR configuration (45° incidence angle).

Measurements with this sensor film design confirmed that it was only very weakly sensitive to prolonged exposure to humidity while remaining sensitive to hydrogen. Figure 6 shows the response of the sensor during exposure to 0.9% hydrogen in air. The response time constant is a few seconds. Over time, however, this response time increased dramatically. Figure 7 shows the measured response time for such a sensor over a period of two days. The time constant is seen to increase from a few seconds to more than 200 seconds, approximately increasing in proportion to the square root of time the sensor was exposed to the test gases.

Considerable effort was spent in attempting to understand and correct this unexpected degradation. We now believe that the cause of the degradation is a natural result of the mechanism by which hydrogen reacts with the WO_3, a reaction which is commonly misrepresented in the technical literature. This issue is addressed in the Discussion section below.

In view of the inherent difficulties with the tungsten oxide sensor films, we searched for alternatives. Recent research, primarily at the Philips Laboratory (Huiberts 1996, Griessen 1997), has shown that the Lanthanide hydrides and related hydrides undergo reversible transitions between di-hydride and tri-hydride when exposed to hydrogen in air. Thin films of these materials exhibit dramatic changes in optical transmittance that may make them suitable for hydrogen sensing.

Figure 8 shows a very preliminary measurement of the reflectance from a yttrium hydride film during repeated exposure to 0.45% hydrogen in air. The sensor film was not optimized and yet its response time constant was fairly short, about 5.8 seconds. A YH_2 sensor coating incorporating the surface plasmon resonance design should show greater sensitivity and speed. The optical dielectric constants of the di-hydride will have to be determined before an optimized SPR sensor can be designed.

Prototype Sensor

A self-contained, hand-held portable fiber-optic hydrogen sensor was designed and built. The device makes use of off-the-shelf electronic components and analog circuitry (except for a digital voltage readout). It is powered by a 9 V battery. Stabilized voltages for the various components are supplied through DC-DC converters.

The light source is a high brightness, broad spectrum "white" (phosphor enhanced) LED. The light from the LED is projected into the proximal end of a 1 mm diameter polymer optical fiber and transmitted through a 1x2 coupler to an exit port on the instrument. The optical-fiber sensor is plugged into that port with a standard fiber-optic ST connector. Light reflected from the sensor coating on the distal end of the fiber is returned to the instrument and half of its power is directed through one of the coupler legs to a dichroic mirror. The dichroic mirror splits the return light beam into a long wavelength and a short wavelength portion which fall separately on two different photo-diode amplifiers. The voltage signals from the two photo-diodes are divided one by the other in an analog divide circuit. A three-way switch allows the user to monitor the output from either photo-diode separately or their ratio. Figure 9 shows a schematic illustration of the detector's design features.

When used with a WO_3/Pd sensor coating on the end of an optical fiber in a purely reflective mode (no SPR), the light reflected from the sensor is split into a short wavelength component (λ < 500nm) and a long wavelength component (λ > 500nm). When the tungsten oxide film reacts with hydrogen it develops an absorption band in the near infrared portion of the spectrum but remains unaffected in the blue end of the spectrum. Thus the long wavelength portion of the spectrum carries a hydrogen signal, whereas the short wavelength portion does not and can be considered as a "reference" signal.

Since both components of the spectrum follow the same path through the optical fiber, they are both affected similarly by changes in the transmittance through the fiber. Taking the ratio of the "signal" to the "reference" provides a means of canceling some of the changes in fiber transmittance, whatever its cause, and thereby reduces the noise level. Transmittance can be affected by bending in the fiber, by temperature gradients in the fiber and by changes in the light transmittance at the connections.

Figure 10 shows some measurements of the effect of fiber bending. The conditions at the instrument and at the sensor were kept constant and the signals returning to the instrument were recorded as the meter-long polymer optical fiber was intentionally bent through an increasingly sharp radius. The bend in the fiber caused reversible optical losses and attenuated the intensity of the reflected beam. In the figure, the percentage change in the signal voltage from each photo-diode due to fiber bending is shown separately along with the analog ratio of the two voltages. It is clear that the use of a reference signal, greatly decreases the effect of fiber bending.

In order to produce a sharp SPR in the sensor film, the light beam must strike the film at a single angle. In our design, where we want the reflected light to be returned along the same fiber path, the preferred angle is 45 ° and the best shape for the sensor "head" is a 90° prism acting as a retro-reflector. However, an optical fiber transmits a bundle of light rays which emerge from the end of the fiber in a cone of angles. If this cone of rays is used to illuminate the sensor coating on the retro-reflector, no SPR can be seen in the reflected signal. It is necessary to use a component that collimates the diverging bundle of rays before directing them to the sensor coating. The use of such optical components on the end of fiber-optic detectors is common

enough that they have been given the name *optodes*, in analogy to the *electrodes* used in electrochemical sensors.

Remembering that our ultimate goal is a low-cost detector, we chose to design an optode that would be a small, single component that could be mass produced from polymer by low-cost means such as compression molding. A commercial, optical ray-tracing code was used for the design (anon. 1998).

The optode consists of a plano-convex lens integrally combined with a 90° prism. A simple spherical convex lens surface is not sufficient to collimate the emerging broad spectrum beam and focus the reflected light back onto the 1 mm diameter fiber tip. Therefore a conic surface was used in the optimization of the optode (radius of curvature 2.85 mm, conicity -2.055, 5.1 mm FL). Fig. 11 illustrates the optimized optode design assuming that it will be made from PMMA and will be coupled to a polymer optical fiber having a numerical aperture of 0.5.

Because of the expense of fabricating a single component of this design, we also designed a less than optimal optode that could be easily fabricated by cementing a commercially available stock BK7 glass plano-convex lens (10 mm diameter, 15 mm FL, radius of curvature 7.73 mm) to a glass 90° prism. Again, the optical ray-trace code, Zemax was used to design the optode.

Several glass optodes of this design were fabricated and coated with a sensor film (15 nm Ag / 440 nm WO_3 / 35 nm Pd). A holder was made to attach the optode to the optical fiber. [In a commercial polymer design, the attachment would be designed as an integral part of the optode.] Figure 12 shows the of the reflected light assuming an incidence angle of 45°: a, theoretical; and b, the measured spectrum. There is a close correlation between the theoretical reflectance spectrum and the measured spectrum.

Discussion

Sensor Films

The thin-film fiber-optic reflective sensor based on palladium catalyzed WO_3 first suggested by Ito (Ito 1984) appears to work well for detecting hydrogen. However, its response is too slow for critical safety applications. We showed that the sensitivity and the response speed of this sensor could be increased by use of a film configuration which produces a surface plasmon resonance. However this sensor configuration introduces additional problems.

In the SPR configuration, the resonance wavelength depends very sensitively upon the refractive index of the WO_3 film, whereas, in the Ito, purely reflective sensor configuration, only a change in the optical absorption of the film mattered. The amorphous WO_3 is micro-porous and readily exchanges water vapor with the air. Consequently, exposure of the SPR sensor to dry gas causes a decrease in the amount of adsorbed water and a decrease in the WO_3 refractive index. This change shifts the surface plasmon resonance and mimics exposure to hydrogen. Of course, such a false alarm is unacceptable in a safety device.

The conventional interpretation of the reaction between catalyzed WO_3 and hydrogen suggests that it should be possible to block the water vapor while still allowing the hydrogen to pass through simply by increasing the thickness of the palladium film. However, we discovered that such a sensor coating is subject to severe degradation due to irreversible reactions. This observation casts doubt upon the conventional interpretation of the chemochromic reaction between hydrogen and WO_3 thin films.

Most of the understanding of reactions between WO_3 thin films and hydrogen come from the extensive literature on electrochromism in this material and is based on electrochemical "insertion" of hydrogen into the amorphous WO_3 (Granqvist 1995). The hydrogen is thought to be inserted as an ion-electron pair with the proton residing in a WO_3 lattice interstice adjacent to a W^{+5} ion. This is the "double-charge injection model." The characteristic optical absorption is thought to be due to either electron exchange between adjacent W^{+5} and W^{+6} ions or by self-trapped, nearly free electrons called polarons. Most recent evidence favors the polaron absorption model.

Some published results challenge the conventional interpretation. We have recently summarized this evidence and suggested some modification to the electrochromic model including the importance of electron exchange between the W^{+4} and W^{+5} ions rather than W^{+5}-W^{+6} exchange (Zhang 1996). Among other puzzling observations reported in the literature is the inability to find evidence of the added hydrogen after an a-WO_3 film has been colored by hydrogen electrochemical "insertion" (Wagner 1990). Our SPR results are also puzzling in this regard because we observed a shift in resonance with hydrogen reaction that is characteristic of lowered refractive index. A decrease in refractive index suggests a lowering of the molar polarizability which is inconsistent with the *addition* of hydrogen ions within the WO_3 lattice. It is more consistent with the removal of something.

When a-WO_3 films are irradiated with short wavelength light, they become blue just as they do when colored by electrochemical insertion of hydrogen or by chemochromic coloration in hydrogen gas. It has been shown (Bechinger 1993) that this is probably due to photo-dissociation of chemically bound water with resulting "insertion" of the hydrogen as the oxygen radical is either trapped by an oxygen vacancy in the partially reduced WO_3 or escapes as O_2. In the Bechinger photochromic study, the authors found that the coloration was irreversible unless the film was exposed to oxygen.

Our results are consistent with the Bechinger observations and the following model (Zhang 1996). Hydrogen in air reacts with oxygen at the surface of palladium. Part of the hydrogen is oxidized to water and part is dissolved in the palladium where it readily diffuses to the Pd/WO_3 interface. Atomic hydrogen spontaneously reduces the tungsten oxide to form WO_{3-y} plus H_2O that is adsorbed by the WO_3. The reaction is:

$$H + WO_{3-y}.nH_2O = WO_{3-y-x/2}\ [nH_2O\ (x/2)H_2O]$$

If the palladium catalytic layer is thin enough to be incoherent, the excess water readily escapes until equilibrium is reached with the humidity of the surrounding atmosphere and the sensitivity is unaffected. However, if the palladium is thick, the water cannot escape and its build-up over time suppresses the forward reaction and slows the response of the sensor to hydrogen gas. Paradoxically, the thicker palladium film which protects against false hydrogen signals from desorbing water vapor also introduces a reduces hydrogen sensitivity by the same mechanism.

The inherent interference in the SPR detection of hydrogen by pervasive water vapor makes the WO_3 chemochromic sensor a poor choice for this application. A simpler chemical reaction is needed for the reversible chemochromic sensor.

Detector

The use of a fiber-optic hydrogen gas leak detector has advantages of inherent safety (no electrical power in the vicinity of the sensor), reduced EMI, light weight, and (potentially) low cost. The prototype portable fiber-optic hydrogen detector provided a convenient means of demonstrating some of the features of a chemochromic sensor and the advantages of incorporating a reference beam in the design. The prototype incorporates many components such as operational amplifiers, DC-DC converters, an analog divide component as well as photo-diode amplifiers. Most, if not all of these separate components could be integrated into a single application-specific integrated circuit (ASIC) for economical mass-production. If that is done, then it may be more appropriate to use digital rather than analog circuitry for better compatibility with other digital electronics commonly used in vehicles. An analysis (Spath 1997) of the probable manufacturing costs has shown that it should be possible to mass-produce similar detectors for about $5 each (not including the cost of the optical fiber which is proportional to the length required in each application).

Conclusions

The evaluation of a fiber-optic chemochromic hydrogen gas detector has been partially successful, but more work is required to develop a suitable sensor coating. The chemochromic reaction between tungsten oxide and hydrogen in air is too slow to be used in a safety device without some kind of enhancement. The sensitivity and speed of hydrogen detection can be enhanced by using the sensor film in a surface plasmon resonance configuration. However, in such a configuration, the rapid desorption of adsorbed water vapor from the tungsten oxide can cause a false indication of hydrogen whenever the sensor is exposed to a dry gas. Blocking the migration of water vapor by increasing the thickness of a palladium catalytic layer also blocks the migration of oxygen to and from the tungsten oxide. Without access to oxygen, the chemochromic reaction is at least partially irreversible and the sensitivity to hydrogen and response speed degrade over time. For these reasons, the tungsten oxide sensor is now believed to be unsatisfactory for the intended application.

Preliminary experiments with yttrium hydride showed promising speed and sensitivity in a simple sensor configuration. Optimization of the YH_2 sensor design, including the use of surface plasmon resonance, should provide the needed sensitivity and speed. The YH_2 sensor (and related hydrides films) should be evaluated for performance and durability.

A prototype portable fiber-optic hydrogen detector was designed and built to demonstrate the operation of the sensor. The novel design proved to be successful and limited only by the chemochromic sensor used on the optical fiber. The incorporation of a reference beam in the detector's design was shown to reduce signal noise significantly. A potentially low-cost polymer optode was designed to operate with the fiber-optic hydrogen detector in the surface plasmon resonance configuration. Tests of a glass approximation to the optimized optode design showed that the polymer optode should operate well in the surface plasmon sensor configuration.

Acknowledgments

The authors would like to acknowledge valuable assistance provided by M. Rubin and K. von Rottkay at the Lawrence Berkeley National Laboratory. This research was supported by the U. S. Department of Energy's Hydrogen R&D Program under Contract No. DE-AC-36-83CH10093.

References

Anon., 1998, *Zemax Optical Design Program User's Guide, Version 7.0*, Focus Software, Tucson, AZ, 1998.

Bechinger, C., G. Oefinger, S. Herminghaus, and P. Leidered. 1993. "On the Fundamental Role of Oxygen for the Photochromic Effect in WO_3." *J. Appl. Phys.*, 74:4527-4533.

Benson, D.K., C.E. Tracy, and D.S. Bechinger. 1997. "Design and Development of a Low-Cost Fiber-Optic Hydrogen Detector." In *Proceedings of the 1997 U.S. DOE Hydrogen Program Review*, May 21-23, 1997. Herndon, VA.

Benson, D.K., C.S. Bechinger, and C.E. Tracy. "Fiber Optic Device for Sensing the Presence of a Gas. US Patent No. 5,708,735, Jan. 13, 1998.

Granqvist, C.G. 1995. *Handbook of Inorganic Electrochromic Materials.* New York: Elsevier.

Griessen, R., et al. 1997. "Yttrium and Lanthanum Hydride Films with Switchable Optical Properties." *J. Alloys and Compounds*, 253-254:44-50.

Huiberts, J.N., et al. 1996, "Synthesis of Yttriumtrihydride Films for Ex-situ Measurements." J. N. Huiberts, et al, *J. Alloys and Compounds*, 239:158-171.

Ito, K. and T. Kubo. 1984. "Gas Detection by Hydrochromism." In *Proceedings of the 4th Sensor Symposium*, 153-156.

Macleod, A. 1995. *The Essential Macleod Thin-film Design Software User Manual*, Tucson, AS: The Thin Film Center.

Palik, E. D., ed., 1995, *Handbook of Optical Constants Diskette*, Optical Society of America, Washington, DC.

Raether, H. 1988. *Surface Plasmons*, p 21. Berlin: SpringerVerlag.

Spath, P.L. and D.K. Benson. 1997 "An Economical Hydrogen Detector for Passenger Vehicles." In *Proceedings of the Second Hydrogen Power, Theoretical and Engineering Solutions, International Symposium (HYPOTHESIS)*, Aug. 18-22, 1997. Grinstad, Norway.

Wagner, W., F. Rauch, C. Ottermann, and K. Bange Wagner. 1990. *Nuclear Instr. Methods. Phys. Res. B.*, 50:27.

Zhang, J-G., D.K. Benson, C.E. Tracy, S.K. Deb, A.W. Czanderna and C. Bechinger. 1996. "Electrochromic Mechanism in a-WO_3 Films." *J. Electrochem. Soc.*, 96-24:251-259.

Figure Captions

1. Schematic cross-section through the SPR sensor sample holder.

2. Theoretical reflectance spectrum showing the surface plasmon resonance (SPR) absorption at nm: a, before exposure to hydrogen; b, after reaction with hydrogen to form (nominally) $H_{0.068}WO_3$. Coating consists of 40 nm Au / 600 nm WO_3 and is illuminated at 45°.

3. Reflectance SPR spectrum from a coating : 40 nm Au / 600 nm WO_3 / 3 nm Pd: a, theoretical; b, measured.

4. Selected reflectance spectra from a time series during exposure to 5% H_2 in air. Inset shows reflected intensity at 627 nm versus time. Coating is 40 nm Au / 600 nm WO_3 / 3 nm Pd.

5. Reflectance SPR spectra from a coating with a thicker palladium layer: 17 nm Ag / 330 nm WO_3 / 100 nm Pd: a, theoretical; b, measured.

6. Initial response of sensor coating [17 nm Ag / 330 nm WO_3 / 100 nm Pd] to 0.9% H_2 in air.

7. Sensor response time constant for film [17 nm Ag / 330 nm WO_3 / 100 nm Pd] over a period of two days. Sample exposed to 5% H_2 in air for periods of about 2 minutes, then to dry air. Response time constant measured away from SPR, at 800 nm. The fitted curve varies as the square-root of time.

8. Initial response measurements for a yttrium hydride film [17 nm Ag / 100 nm Y / 20 nm Pd] to 0.45% H_2 in air. The first reduction in the signal corresponds to conversion of Y metal to YH_2 and subsequent cycles to increases in hydrogen content toward the tri-hydride, YH_3. The response was measured in reflection (no SPR) at 700 nm. The time constant of the hydrogen response is about 5.7 seconds.

9. Schematic diagram of the prototype portable fiber-optic hydrogen gas leak detector showing selected design features.

10. Detector signal attenuation due to controlled bending of the optical fiber. Note that the attenuation is nearly the same for the hydrogen signal (long wavelength) and the hydrogen-insensitive, reference signal (short wavelength) and consequently the analog ratio of the two signals is only weakly affected by fiber bending.

11. Design for a PMMA SPR optode. The lens portion is a conic section optimized to minimize chromatic aberration and maximize signal return to the optical fiber.

12. SPR reflectance spectrum using a glass optode made by cementing a plano-convex spherical lens to a 90° prism.

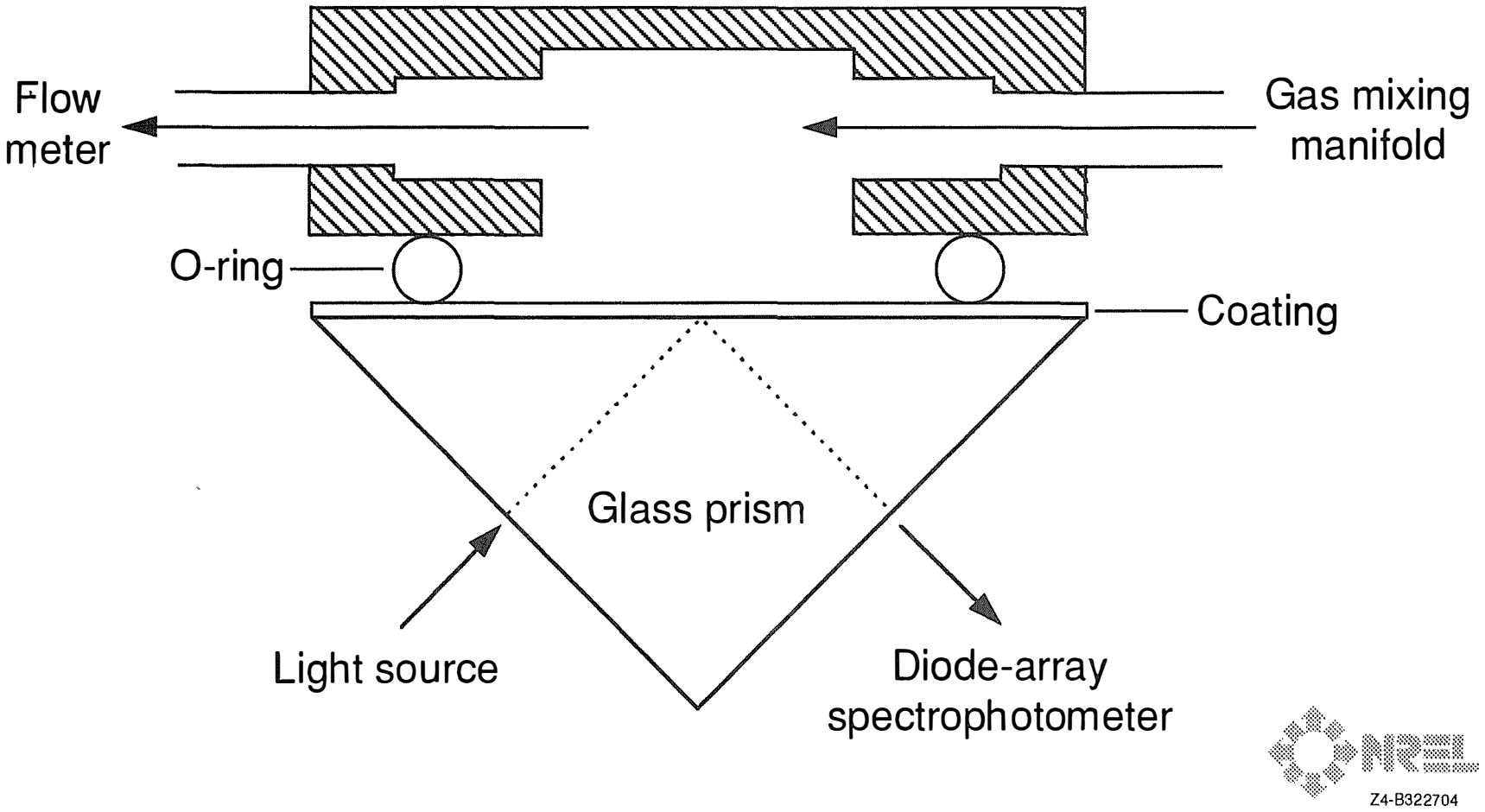
Flow
meter
Gas mixing
manifold
O-ring
Coating
Glass prism
Light source
Diode-array
spectrophotometer
NREL
Z4-B322704

Figure 1

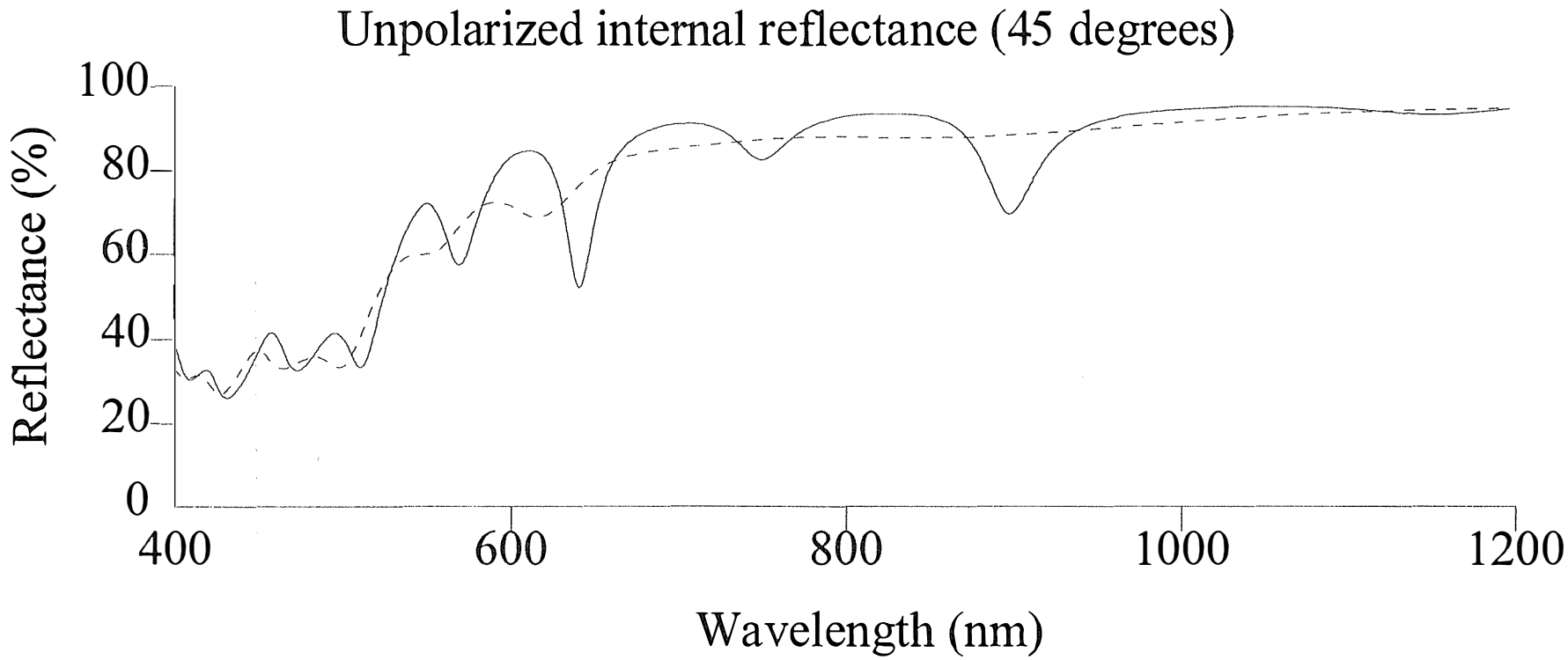
Unpolarized internal reflectance (45 degrees)
Reflectance (%)
100
80
60
40
20
0
400
600
800
1000
1200
Wavelength (nm)

103

Figure 2

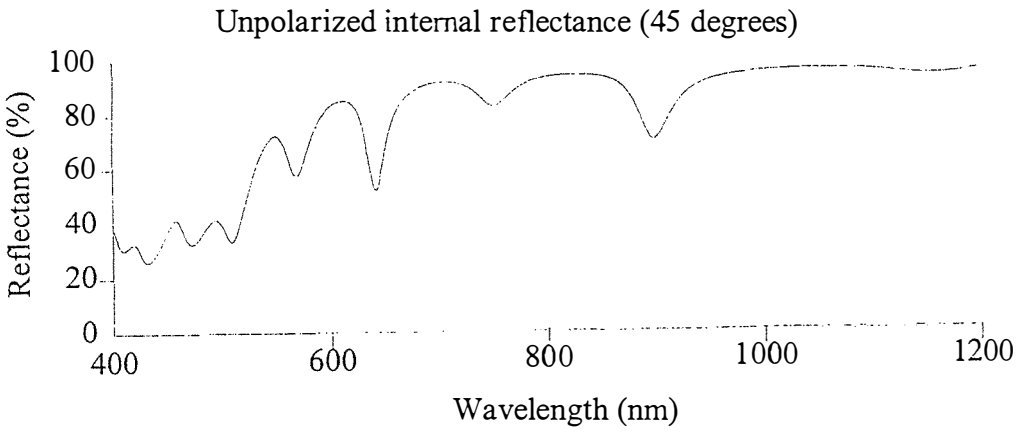
Unpolarized internal reflectance (45 degrees)
Reflectance (%)
100
80
60
40
20
0
400
600
800
1000
1200
Wavelength (nm)

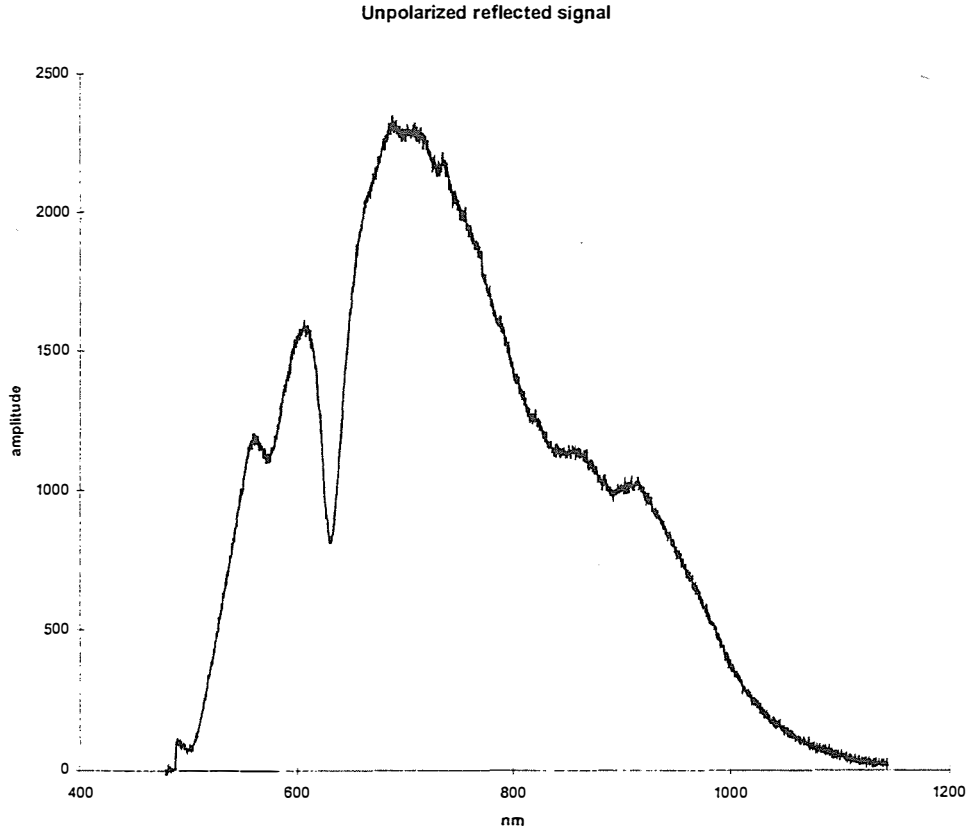
Unpolarized reflected signal
amplitude
2500
2000
1500
1000
500
0
400
600
800
1000
1200
nm

Figure 3

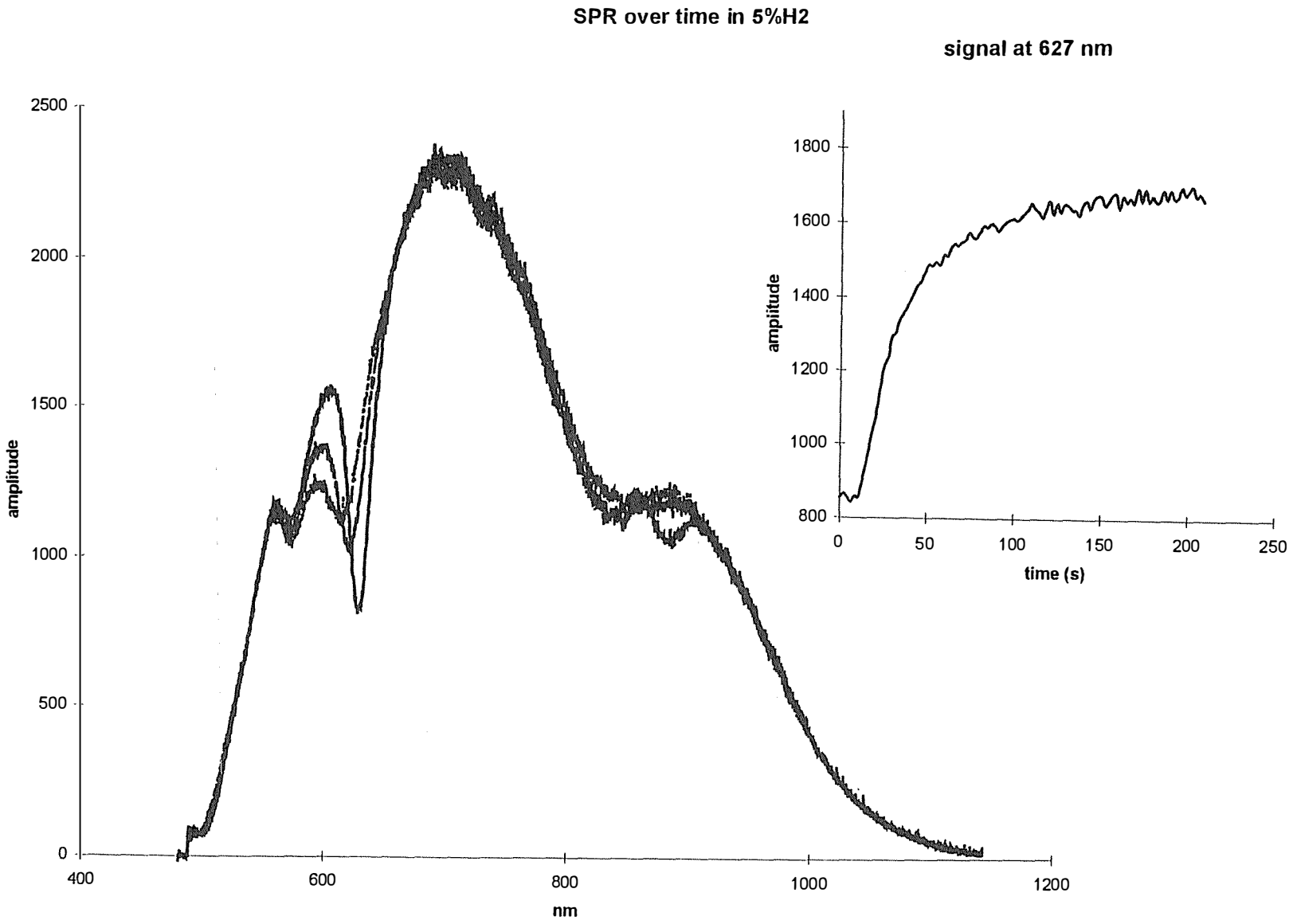
SPR over time in 5%H2
signal at 627 nm
amplitude
nm
time (s)
2500
2000
1500
1000
500
0
400
600
800
1000
1200
1800
1600
1400
1200
1000
800
0
50
100
150
200
250

Figure 4

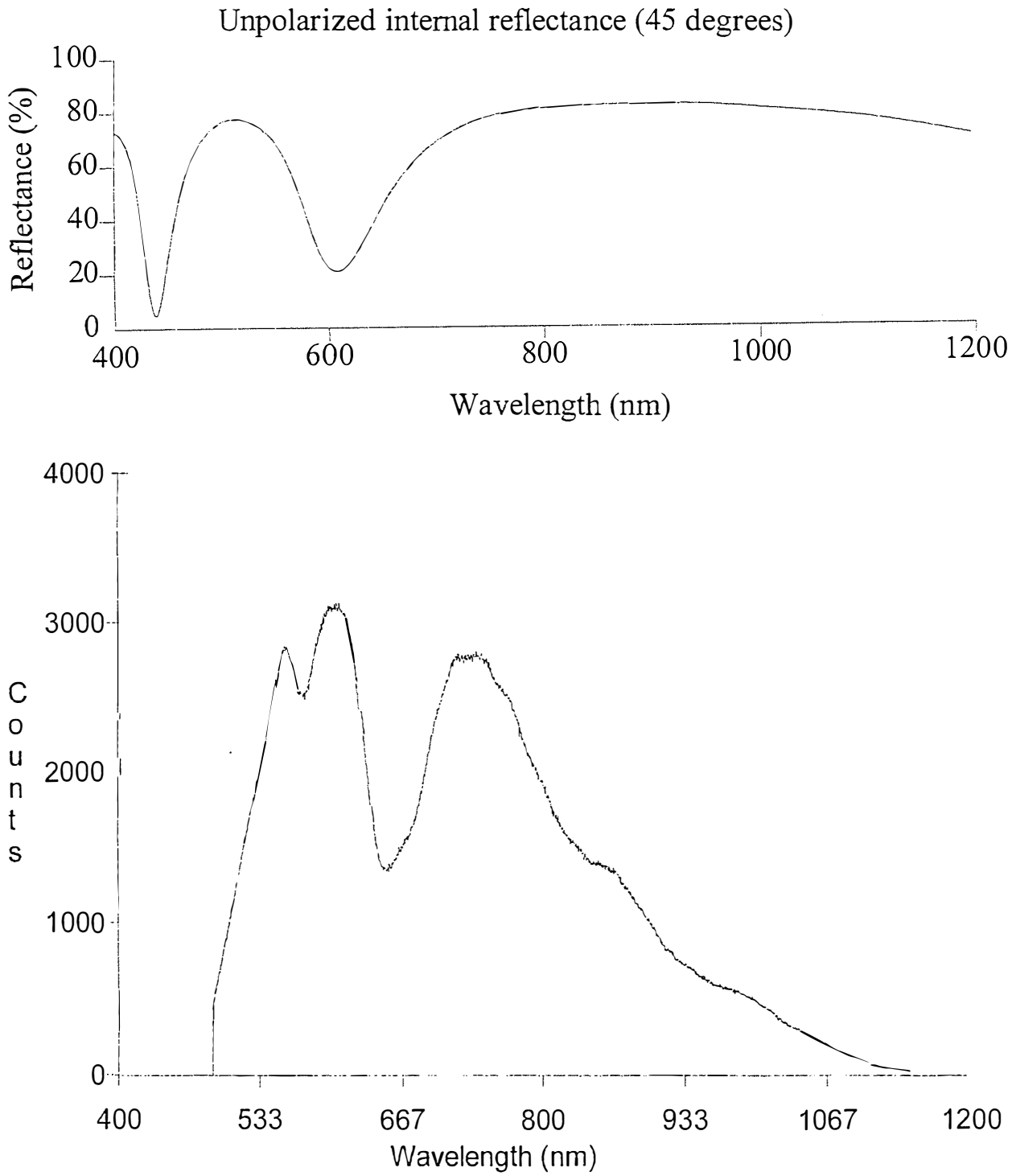
Unpolarized internal reflectance (45 degrees)
Reflectance (%)
100
80
60
40
20
0
400
600
800
1000
1200
Wavelength (nm)
Counts
4000
3000
2000
1000
0
400
533
667
800
933
1067
1200
Wavelength (nm)

Figure 5

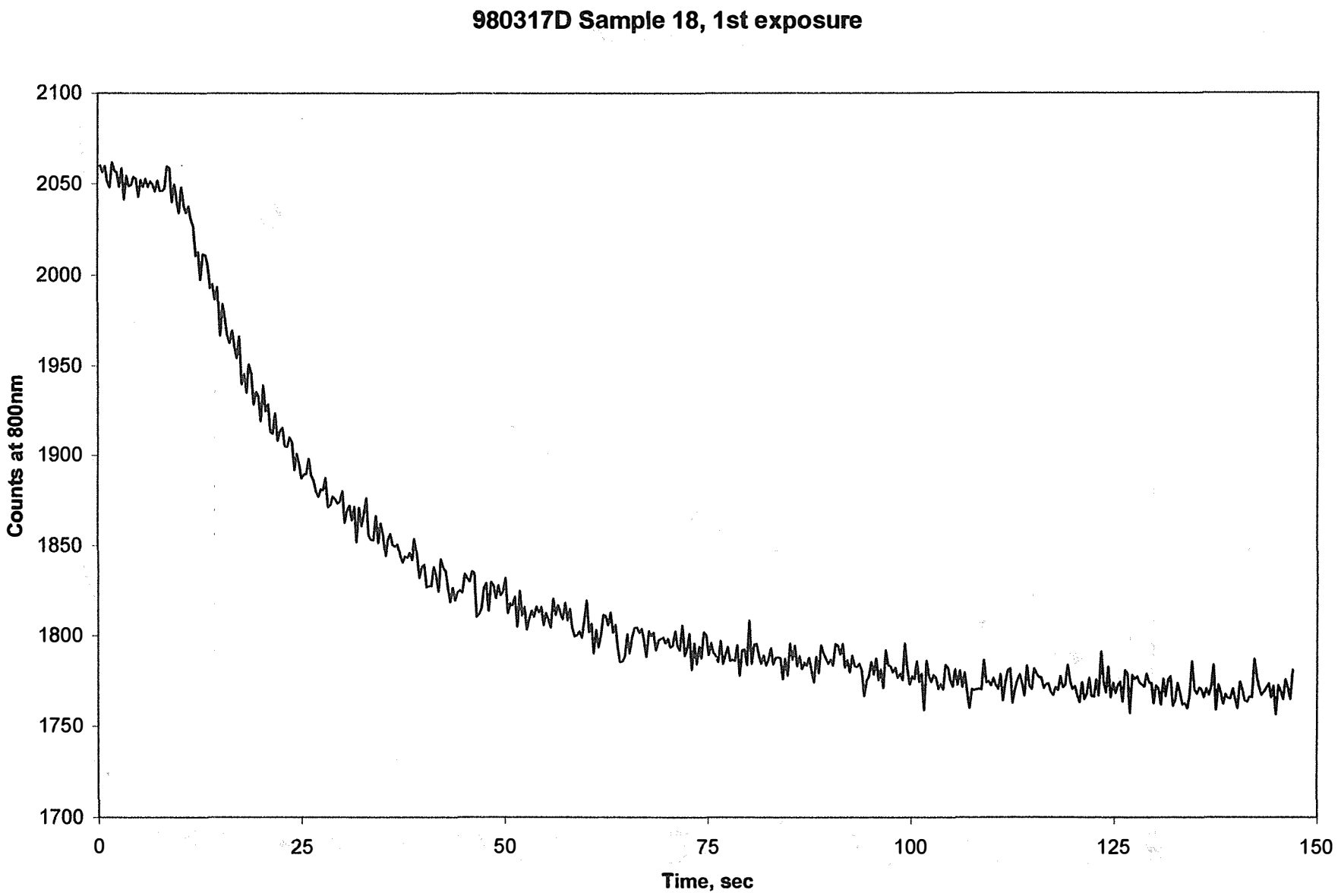
980317D Sample 18, 1st exposure
Counts at 800nm
2100
2050
2000
1950
1900
1850
1800
1750
1700
0
25
50
75
100
125
150
Time, sec

Figure 6

Degradation of Hydrogen Response

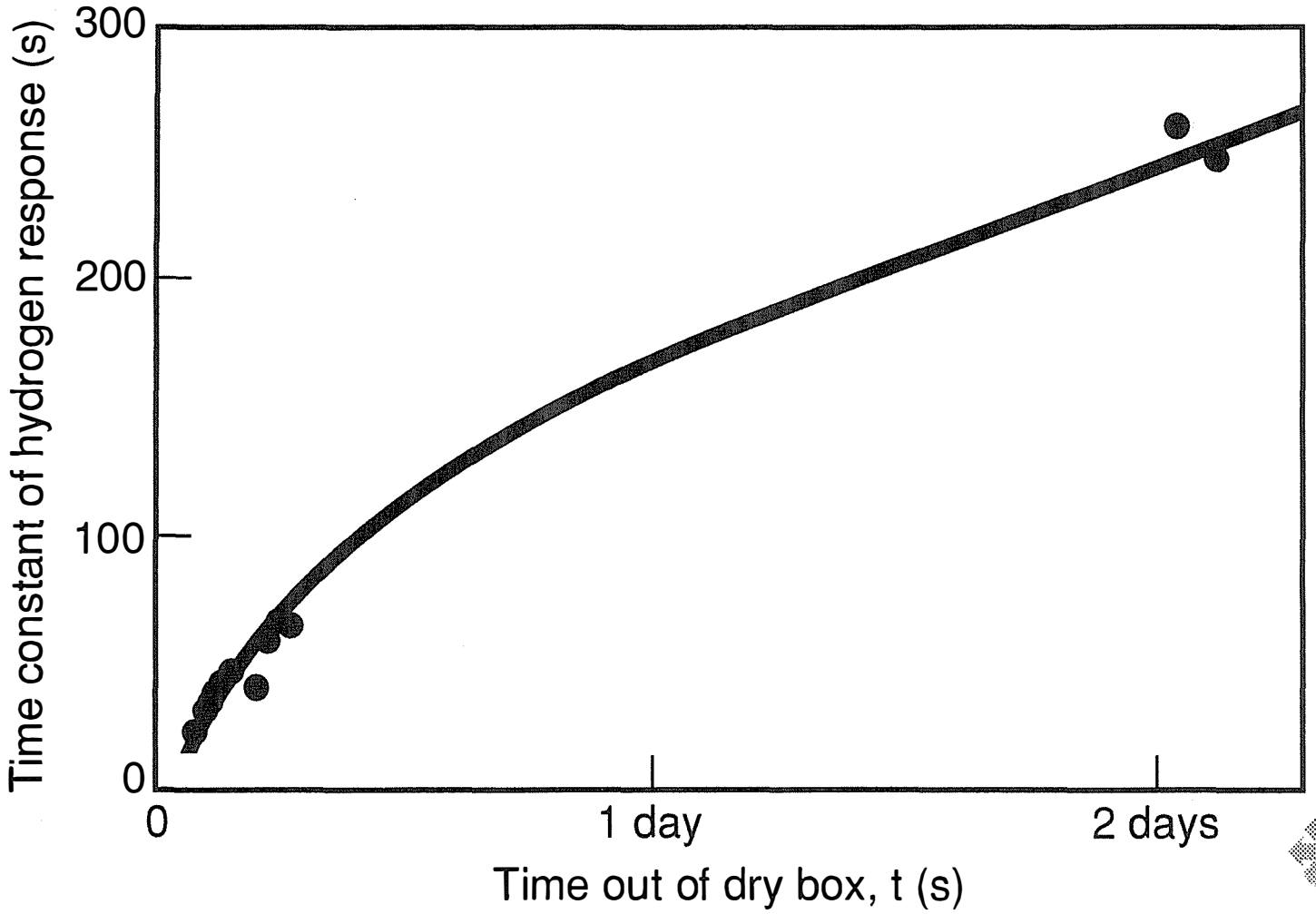

NREL

Z4-B322703

Figure 7

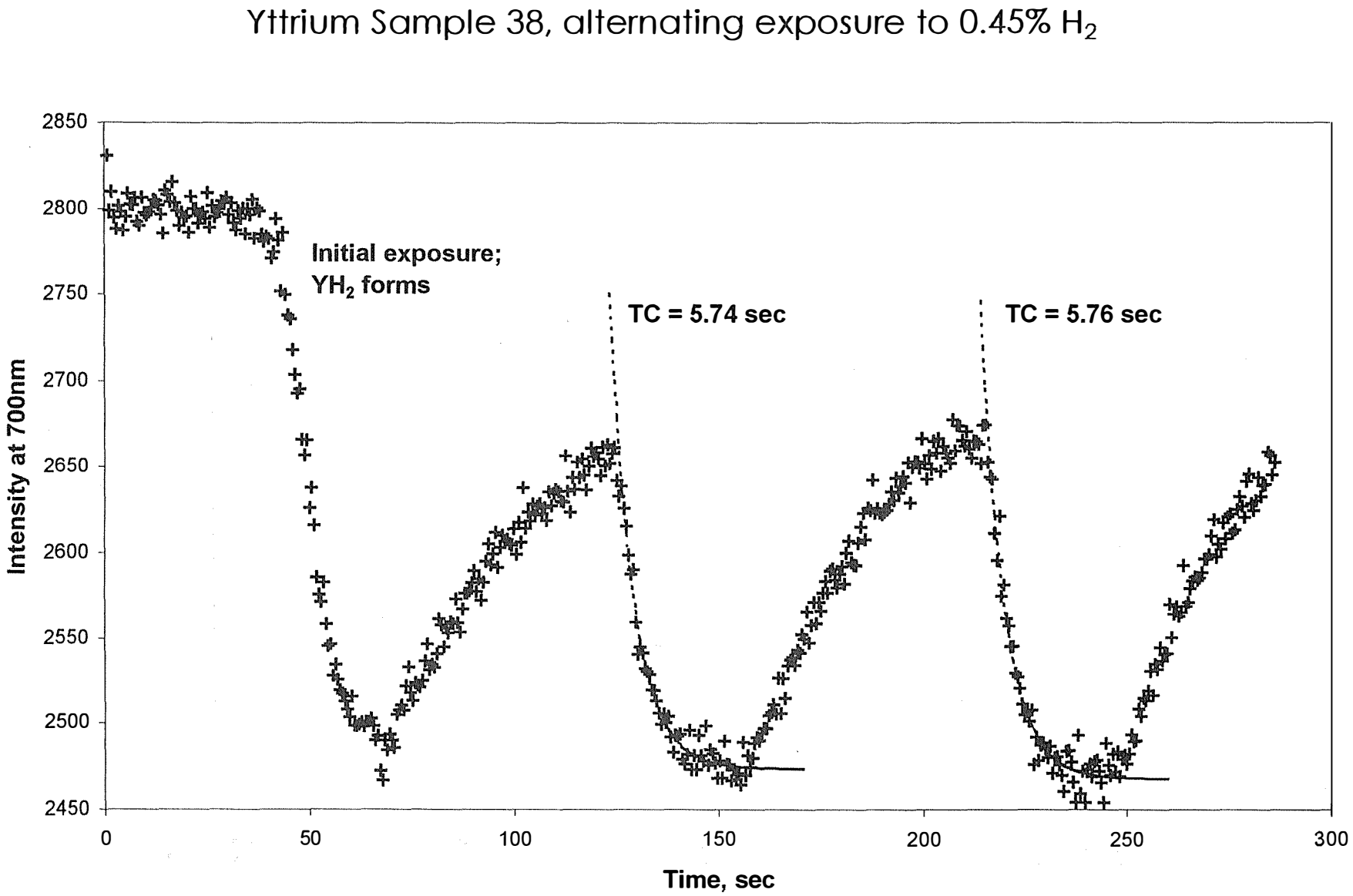
Yttrium Sample 38, alternating exposure to 0.45% H_2
Initial exposure;
YH_2 forms
TC = 5.74 sec
TC = 5.76 sec
Intensity at 700nm
Time, sec
2850
2800
2750
2700
2650
2600
2550
2500
2450
0
50
100
150
200
250
300

Figure 8

Portable Fiber-Optic Hydrogen Detector

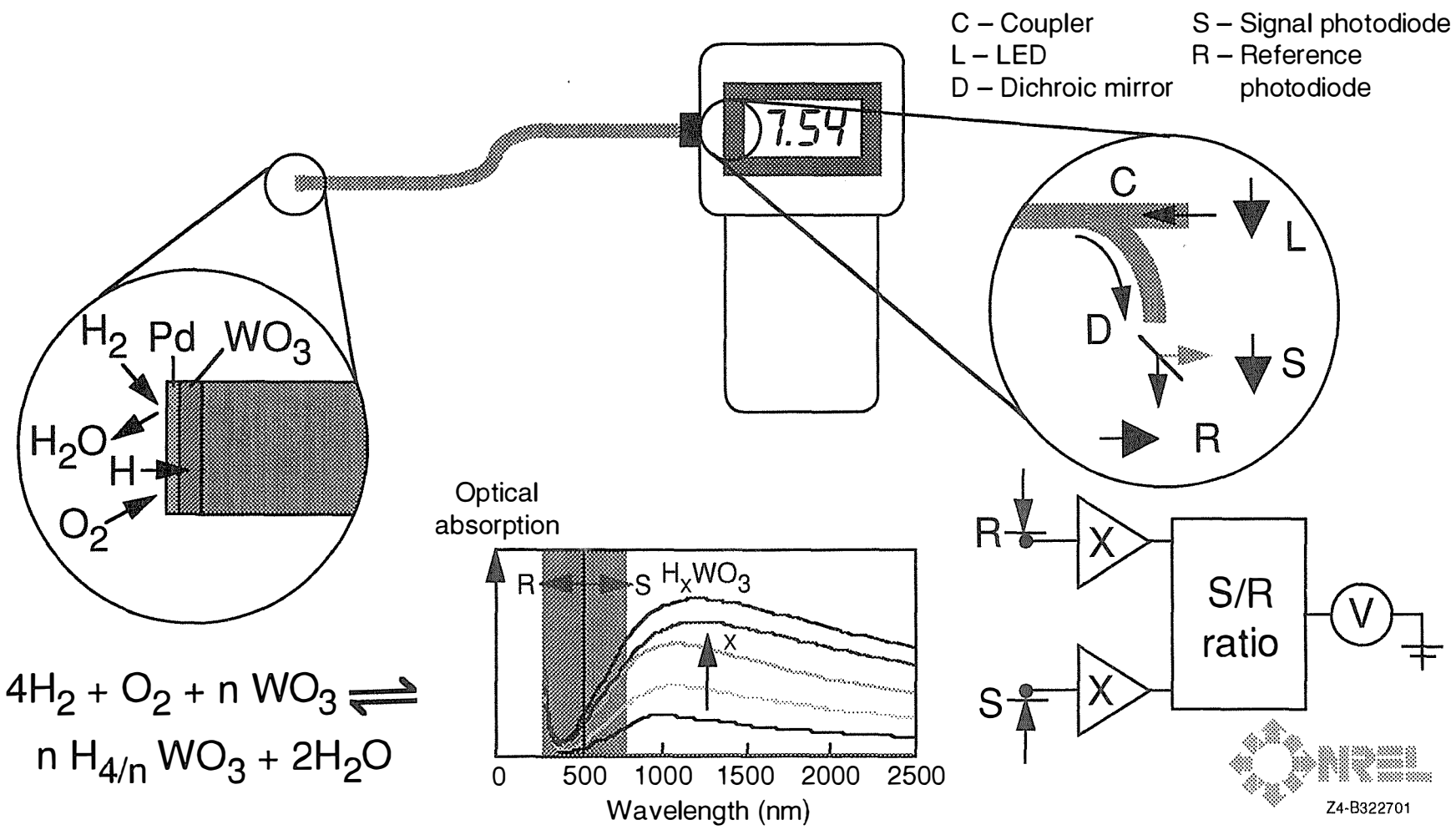

$$4H_2 + O_2 + n\,WO_3 \rightleftharpoons n\,H_{4/n}\,WO_3 + 2H_2O$$

Figure 9

Attenuation Due to F-O Bending

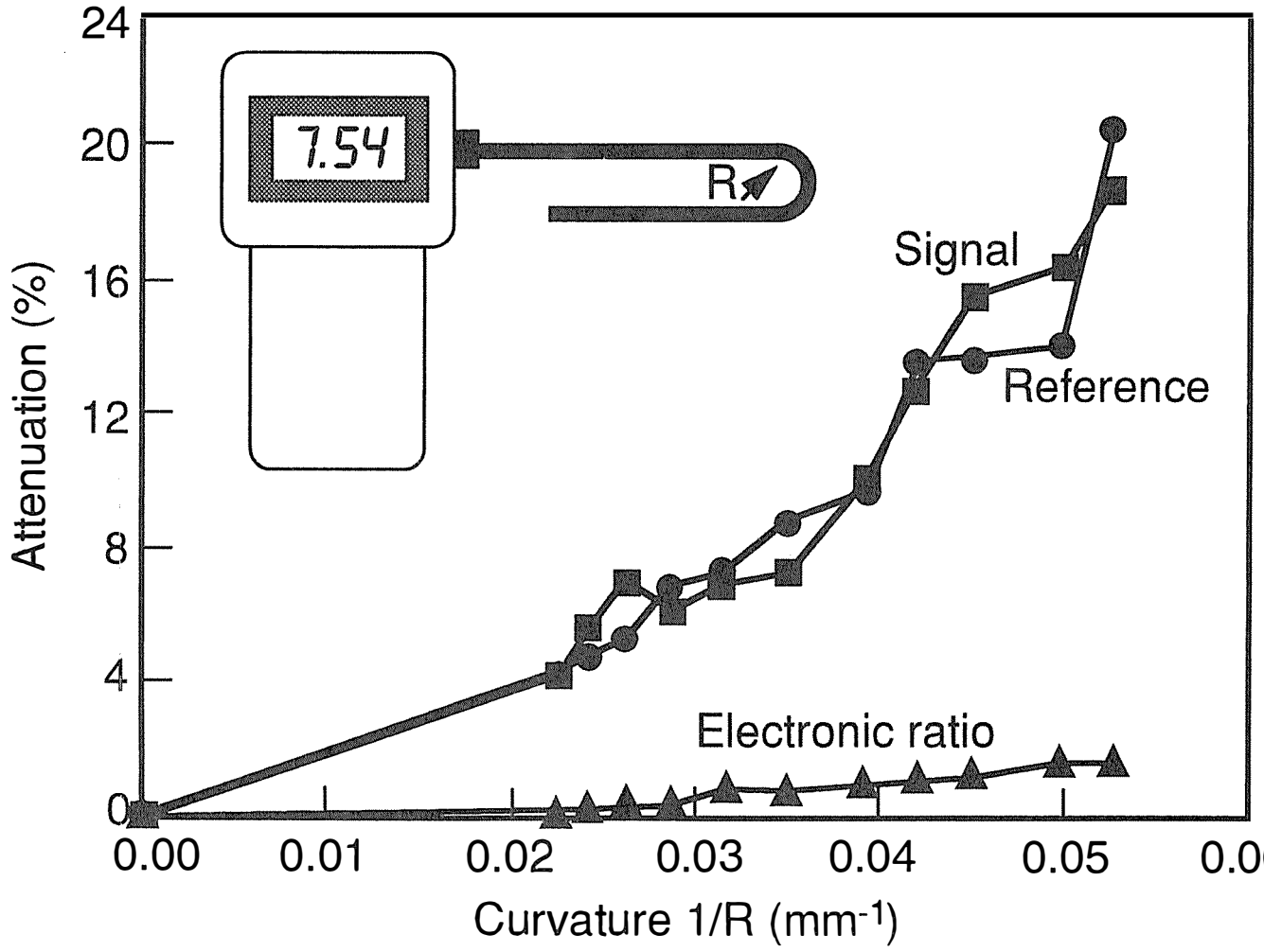

NREL

Z4-B322702

Figure 10

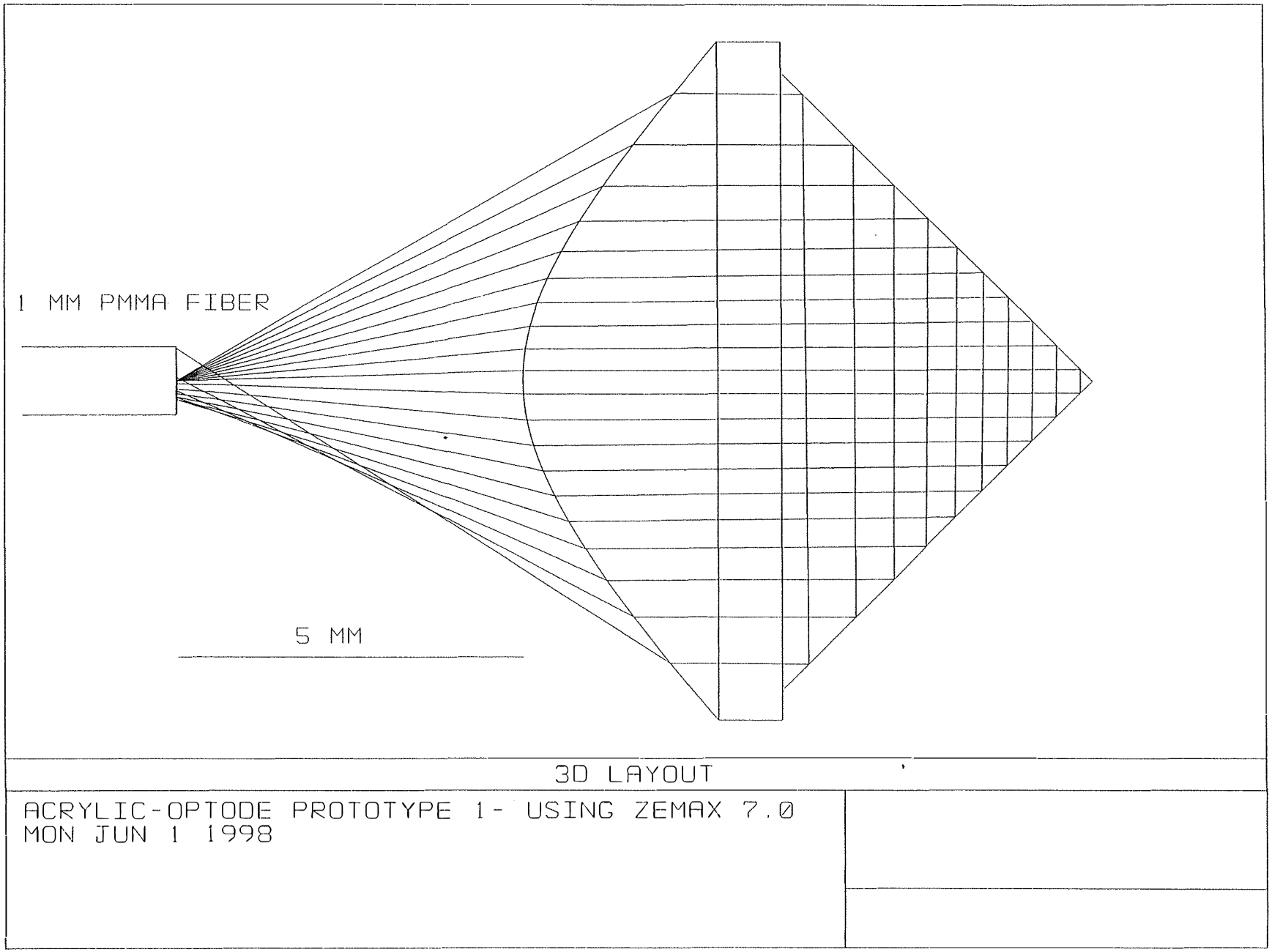
1 MM PMMA FIBER
5 MM
3D LAYOUT
ACRYLIC-OPTODE PROTOTYPE 1- USING ZEMAX 7.0
MON JUN 1 1998

Figure 11

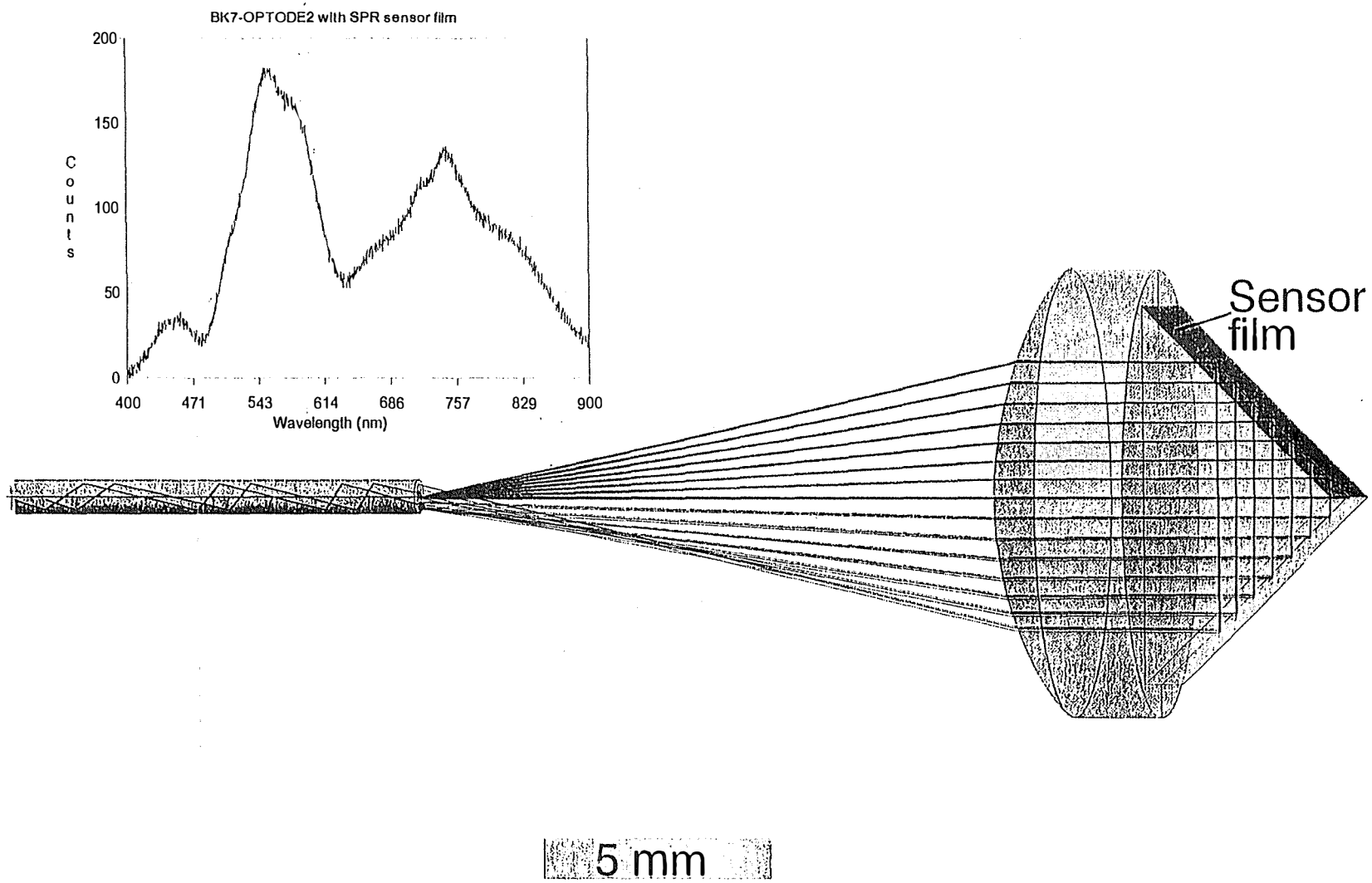
BK7-OPTODE2 with SPR sensor film
200
150
100
50
0
Counts
400
471
543
614
686
757
829
900
Wavelength (nm)
Sensor film
5 mm

Figure 12

LOW-COST HYDROGEN SENSORS: TECHNOLOGY MATURATION PROGRESS

B. S. Hoffheins, J. E. Rogers, R. J. Lauf, D. P. Haberman,* and C. M. Egert

Oak Ridge National Laboratory
P.O. Box 2008
Oak Ridge, Tennessee 37831-6004

*DCH Technology, Inc.,
14241 Ventura Blvd., Suite 208
Sherman Oaks, California 91423

Abstract

We are developing a low-cost, solid-state hydrogen sensor to support the long-term goals of the Department of Energy (DOE) Hydrogen Program to encourage acceptance and commercialization of renewable energy-based technologies. Development of efficient production, storage, and utilization technologies brings with it the need to detect and pinpoint hydrogen leaks to protect people and equipment. The solid-state hydrogen sensor, developed at Oak Ridge National Laboratory (ORNL), is potentially well suited to meet cost and performance objectives for many of these applications. Under a cooperative research and development Agreement and license agreement, we are teaming with a private company, DCH Technology, Inc., to develop the sensor for specific market applications related to the use of hydrogen as an energy vector. This report describes our current efforts to optimize materials and sensor performance to reach the goals of low-cost fabrication and suitability for relevant application areas.

Introduction

The development and availability of low-cost hydrogen detectors will help speed the market acceptance of hydrogen as a safe and reliable energy vector. There are also many applications for low-cost hydrogen sensors in today's industrial and utility environments. Other sensor requirements include ruggedness, ease of deployment, and adaptability to many detector and alarm configurations. Many commercially available sensors designed for hydrogen detection are thought to be too expensive, and often they are not particularly selective for hydrogen gas, especially in the presence of other fuel vapors or automotive exhaust. Development of sensors that are hydrogen selective has been a more recent activity (Butler 1984, Benson et al. 1997, Hughes et al. 1992, Lauf et al. 1995, Lechuga et al. 1991), although few are available.

Workers at Oak Ridge National Laboratory (ORNL) demonstrated monolithic, resistive sensors that are inherently robust, selective to hydrogen, and easy to manufacture (Hoffheins and Lauf 1995). The sensor design, to the largest extent possible, uses traditional materials and fabrication methods because of obvious cost and reliability advantages. The ORNL sensor is composed of three electronic compositions that are separately screen-printed and fired onto an alumina substrate that measures $2.5 \times 2.5 \times 0.06$ cm (Figure 1). Two of the compositions are standard electronic pastes, supplied by

DuPont Electronic Materials. Of those, one is a conductor and the other is a resistor encapsulant. The third composition is primarily composed of palladium metal, the key sensor component. Palladium easily forms a solid-state solution with hydrogen. DuPont developed this composition primarily for our application but is now a commercially available DuPont product (Felten 1994). In general, thick-film electronic materials are developed for use in reliable, high-temperature hybrid circuits and have an inherent ruggedness in challenging environmental conditions.

The sensing mechanism of the ORNL sensor relies on the reversible absorption of atomic hydrogen into and out of palladium metal, in proportion to the ambient partial pressure of hydrogen gas. The relationship of hydrogen and palladium is well known and characterized (Lewis 1967). Changes in hydrogen concentration in the palladium matrix lead to corresponding changes in the electrical resistance of the palladium, which can be easily measured. The sensor consists of four palladium resistors (or legs) that are arranged in a Wheatstone bridge configuration. Figure 1 depicts the sensor and its schematic representation. Two of the legs serve as reference resistors and are passivated with a thick-film resistor encapsulant to prevent entrance of hydrogen into the underlying palladium layer; thus, changes in the resistance of the palladium caused by temperature variation are compensated.

The sensor has been tested under a wide variety of conditions (Hoffheins et al. 1997). The technology was patented and licensed to DCH Technology, Inc., for the field of use encompassing hydrogen production, storage, and application as an energy vector. We continue to develop and refine design concepts and materials formulations.

Approach

During the previous year of this project, we prepared an assessment of sensor performance under various conditions of temperature and humidity for a range of hydrogen concentrations. The sensor performed successfully between a selected temperature range of 20 to 200°C and from 0 to 100% relative humidity. We began to study and analyze sensors that have failed under extreme conditions to better understand material limitations and possible approaches for improving the lifetime and stability. Preliminary results from tests of possible interference gases such as methane and propane were encouraging. During performance evaluations, we identified specific areas for improvement. These include stability of the materials over time, sensitivity and response to hydrogen, power consumption, and sensor packaging. Sensor material optimization is focused primarily on the palladium layer; however, the effectiveness of the passivation layer is also of interest. At the same time, we are exploring optimized materials and sensor layout designs to increase sensitivity and reduce power consumption over that of existing prototypes. This requires an iterative approach and close collaboration with our cooperative research and development agreement (CRADA) partner and thick-film materials suppliers.

Experimental

Sensor performance testing

In previous tests, a 9-V dc input voltage was used for the sensor excitation. We have also demonstrated sensor performance powered by a 9-V dc battery. Many commercial electronic interface products offer a 5-V dc supply for sensors and transducers. We tested the sensor at the lower voltage at various temperatures to compare the performance. A variety of sensor designs were tested to evaluate and compare sensor sensitivity and response time at three different temperatures (20, 40, and 60°C) and two input voltages (5-V dc and 9-V dc). The test configuration is shown in Figure 2.

The sensor was placed in a small test chamber inside a Tenny Junior Furnace (Model TJR). A thermocouple, attached to the back of the sensor substrate, continually measured sensor temperature. For all sensors tested, input power (HP 6205 dual dc power supply) was supplied across the passive legs of the sensor and output voltage was measured across the active legs. The gas flow to the sensor test chamber was controlled by two mass flow controllers (SEC-7330), one for air and one for 2% H_2 in dry air. Data acquisition and gas flow control was performed using a Dell laptop computer interfaced with a National Instruments DAQPad-MIO-16X2-50 (16-bit acquisition and control for the parallel port). National Instrument's LabView software was programmed to set test controls and acquire data. Temperature set points for the Tenny furnace were set manually using a Watlow Series 942 1/4 DIN ramping control.

The furnace temperature was initially set to 20°C with a sensor input voltage of 5-V dc. The test began by exposing sensors to 2% H_2 test gas for 3 minutes. The test gas was then turned off, and the test chamber was purged with air for 3 minutes. Readings were acquired every second and plotted (time in seconds vs. sensor output in volts).The test continued to alternate between 2% H_2 and air until a steady-state sensor response was observed. The same alternating 2 to 0% H_2 exposure cycles were performed at 40 and 60°C. The input voltage was then changed to 9-V dc and the same series of tests were performed.

Materials Optimization

Palladium composition modifications

During previous studies we noted that after many cycles of high hydrogen concentration cycling (10 to 30% H_2 in air), the palladium metallization swelled, cracked, and broke free from the underlying substrate. This volumetric expansion of the palladium matrix from hydrogen absorption has been noted (Lewis 1967) and some sensing approaches rely on this phenomenon. DuPont Electronics Materials formulated a new composition having a larger palladium particle size intended for better hydrogen cycling performance and improved fabrication results (Version 2). Both the original palladium composition and this new composition have a printed resistance that is too low for battery operation. A thick-film dielectric material (DuPont 5704) was mixed with the Version 2 DuPont palladium composition (4 parts palladium to 1 part dielectric by volume) to increase the printed electrical resistance and improve the adhesion of the layer to the alumina

substrate. The dielectric material has a much higher percentage of glass particles, which decreases the conductivity of the palladium and at the same time adheres more strongly to the substrate.

Sensor design modifications

Another way to increase resistance of the printed palladium layer is to alter the geometry. The original sensor design used a serpentine pattern with a line width of 10 mil (250 μm). New sensors were fabricated using a line width of 5 mil (120 μm), which should at least double the printed resistance of the sensor. The Version 2 DuPont palladium composition was used for the serpentine pattern. The as-fired resistors (5 mil) measured 250 ohms, compared with 40 ohms for the 10-mil resistors. The dramatic increase in resistance was a consequence of reducing the thickness as well as the line width of the pattern.

Protective coating for palladium layer

Previous test results pointed to a slowing of sensor response over time. We suspect this is caused by adhesion of water vapor, oxygen, and other species that form a temporary barrier to hydrogen gas. Hydrogen-permeable protective coatings for the palladium layer were suggested to improve response time reliability. Among the candidates are SiO_2, Teflon™, thick-film dielectrics, acrylic, and silicone rubber. Teflon™ has been used in other hydrogen sensor work (Benson 1998). Thick-film dielectrics would be inherently compatible with existing sensor fabrication techniques. Silicone rubbers have very high permeabilities for H_2, approaching those for palladium. We are evaluating several of these materials.

A number of sensors were sputtered with SiO_2. Sputtered composition was maintained close to stoichiometric proportions, although it was not measured. This material was chosen because it exhibits a somewhat greater H_2 permeability compared with other ceramic materials, especially in thin layers. In addition, it is a mature and available process. SiO_2 coatings are widely applied for their optical properties, electrical insulation, and resistance to physical and chemical attack. Its columnar microstructure, a consequence of sputtering, should enhance H_2 permeability. The coating thickness is in the range of 100 to 150 nm. Testing has begun, but results are not yet available.

Results and Discussion

Sensor operation

Sensor operation was evaluated at two input levels. Figure 3 shows the responses of one sensor to 2% H_2 (in air) cycles at 5-V dc and at 9-V dc for three temperatures. The H_2 gas cycle was 3 minutes (seconds 1 through 180 along the x axis of the chart). An air cycle followed (seconds 181 through 345 along the x axis). At 20°C, the sensor responses are similar, suggesting no significant difference in performance because of the excitation voltage. The time to reach 90% of full response is on the order of 1 minute. At the higher temperatures, the response is faster, about 30 seconds, and more level but the magnitude of the response is significantly diminished. Recovery times in air follow a similar pattern. It is known that as temperature increases palladium's solubility for hydrogen decreases.

For sensor applications that experience wide shifts in temperatures, temperature measurement may be incorporated in the sensor design and signal-conditioning electronics. In general, these results are preliminary and the data do not indicate that overall performance or sensitivity is limited.

Materials optimization

Palladium composition modifications

Thick-film materials, in general, are designed to be stable over time. Our thick-film application is somewhat unusual in that we are requiring the palladium composition to be "active" rather than "passive" to respond accordingly to changes in the ambient partial pressure of hydrogen. The material structure must accommodate rapid shifts in hydrogen absorption and desorption without becoming brittle. The electrical resistance of the fired pattern must be high enough to be easily measured and to prolong battery life. The material must also adhere well and reliably. These requirements, though not necessarily in conflict with each other, necessitate an iterative approach to arrive at the final design for the palladium composition.

Planned tasks include the following. (1) Modify the Version 2 DuPont composition with materials that increase the electrical resistance and possibly alter the fired structure to favor repeated reversible hydrogen absorption. (2) Reformulate the palladium compositions through the addition of alloying elements to reduce or eliminate phase changes and minimize volume expansion. This approach has been used successfully for a sensor developed at Sandia National Laboratories (Hughes et al. 1992). (3) Optimize the glass content required for adequate adhesion to the substrate. The glass also acts as an insulator and can increase the electrical resistance of the fired pattern. (4) Study palladium particle size and the effects of printing and firing on mechanical and absorption properties. We will also evaluate optimum printing geometries for measurement and power conservation. We have begun working in a number of these areas.

Sensors were fabricated with the Version 2 DuPont palladium plus DuPont 5704 dielectric compositions described earlier. One sensor (DT052) was cycled through many exposures to hydrogen from 0 to 4% in air. When compared with an unexposed sensor, DT053, from the same fabrication series, the metallization looks intact and similar in uniformity (Figure 4). Each of these sensors was scratched with a small, wooden dowel to test the brittleness and adhesion of the palladium metallization. There were no discernible differences between the sensors. The palladium layer for each was solid and held firmly to the substrate.

Sensors printed with the unmodified Version 2 DuPont using the narrower pattern were also tested. At 4% hydrogen in air, the sensors quickly peeled away from the substrate. Using different sensors, better results were obtained for tests with 2% hydrogen in air.

A comparison of three sensors with different palladium compositions is shown in Figure 5. Sensor DT052 shows the best sensitivity overall with a 150-mV output at 2% H_2. Sensor K0136 with Version 1 DuPont composition and Sensor DT227 with Version 2 DuPont composition exhibit similar sensitivity although the hydrogen exposure time for DT227 was 180 seconds instead of the 600 seconds used for the other two tests. Further tests of the modified composition used for DT052 will be required to verify the promising results of improved sensitivity and durability. A summary of results for the palladium compositions is shown in Table 1. Note that the modified composition called DT "C" also shows an improvement in power consumption over Version 1 (KS series). It is evident that reducing the line width will improve power consumption of the sensor. A next step will be to fabricate sensors with the modified palladium and use the finer line width pattern.

Table 1. Comparison of palladium metallizations

Sensor series	KS	DT 1xx	DT 2xx	DT "C"
Sensor paste	DuPont, Ver. 1	DuPont, Ver. 2	DuPont, Ver. 2	80 vol% DuPont, Ver. 2 20 vol% DuPont 5704
Line width (mil)	10	10	5	10
Power consumption (mW)	400	600	100	250
Sensitivity at 2% H_2/air (mV)	100	Not tested	100	50-160
Durability (4% H_2 cycling)	Yes	Not tested	No	Yes

Sensor design and packaging

As we continue materials optimization, we will also be involved with DCH Technology to refine sensor layout and packaging design. A new sensor layout was designed to reduce the size of the sensor. The sensor patterns are printed on both sides of a square alumina substrate measuring $1.3 \times 1.3 \times 0.06$ cm. This size is convenient for conventional and prototype sensor packages (Figure 6). The small size demands that the sensor patterns are narrower, which also reduces power consumption.

Thick-film designs are relatively simple to lay out and fabricate. In addition, small fabrication batches are economical. Many sensors can be printed and fired on a single substrate and then separated for individual packaging (Figure 7). (Our facility has the capability of screen-printing up to 3×3-in. substrates, but commercial manufacturers can produce circuits on much larger substrates.) Our goal is to complete as many of the fabrication steps as possible on large, unbroken substrates so that a high level of uniformity is maintained. This will also control fabrication costs by limiting the number of different process steps.

CRADA Partner Activities

DCH Technology has been conducting an economic evaluation to prepare the sensor for market acceptance in the emerging hydrogen energy based industries. The following activities describe recent efforts.

A market survey of acceptable cost/price thresholds in both hydrogen safety and process monitoring applications was completed. A product price strategy has been created for the new generation hydrogen sensors, and this provides a baseline for design and fabrication costs.

A continuing activity is the establishment of a working relationship with the insurance industry to ensure acceptance of new technology into the existing Standard Industrial Categories (SIC). This includes the creation of a joint venture on insurance for hydrogen project protection called the Renewable Energy Group.

The case for hydrogen sensors was presented to the DOE Hydrogen Source Book task force and the International Organization for Standardization Working Group No. 7. New generation sensors have been included in the dialog with the National Fire Protection Association update to standards. This is a continuing activity.

A series of agreements is now in place for beta testing of new generation hydrogen sensors into application areas most appropriate to the sensor attributes. Product development is under way that includes packaging, controls, interfaces, and integration into larger-scale systems. Staff from DCH and ORNL will be working more closely to tailor sensor design and performance to specific applications. Strategic marketing activities, including a prototype demonstration at the 1998 National Hydrogen Association meeting, have been accomplished and will continue in the future.

Future Work

Our plans are to continue materials and performance optimization for challenging target applications (high-temperature, humidity, and corrosive environments). We will evaluate sensor design and size along with various packaging and communication schemes for optimal acceptance by end users.

Conclusions

Our continuing evaluation of sensor performance points to the need to better understand the dynamics of the sensor's palladium metallization. We are planning to use infrared imaging technology to evaluate surface heating from catalytic effects. Other results include a need to further understand the effects of possible interferences such as combustible gases and automotive exhaust.

We continue testing to evaluate sensor material stability and durability. We have successfully tested a modified sensor metallization for repeated hydrogen cycling at low concentrations. We are working to optimize this composition regarding sensitivity and lower power consumption.

We continue to evaluate the interfering effects of adsorbed water and oxygen on sensor response. We are coating sensors with materials that block molecules and atoms larger than hydrogen gas.

A modified design for the sensor metallization was completed and is under evaluation. Preliminary results indicate that sensitivity is maintained and that power consumption is lower by a factor of four.

We demonstrated the current sensor prototypes at the 1998 National Hydrogen Association meeting. We showed that the sensor is easily compatible with commercial data acquisition hardware and software and ultimately with "smart sensor" plug and play concepts proposed in the IEEE 1451 standard.

Acknowledgments

ORNL is managed by Lockheed Martin Energy Research Corp. for the U.S. Department of Energy under contract No. DE-AC05-84OR22464. The authors would like to thank the following ORNL staff: Mr. Richard E. Hutchens for assembling and designing test stands and test fixtures and for photographic assistance; Mr. Timothy E. McKnight for design of the computer control and data acquisition system; Mr. Boyd Evans for photography; and Ms. R. Elaine Cooper for sensor fabrication. This work was funded by the U.S. Department of Energy Hydrogen Program.

References

Benson, D.K, et al. 1997. "Design and Development of a Low-Cost Fiber-Optic Hydrogen Detector," *Proceedings of the 1997 U.S. DOE Hydrogen Program Review,* NREL/CP-430-23722, Golden, Colo. National Renewable Energy Laboratory.

Benson, D. K. March 1998, personal communication.

Butler, A. 1984. "Optical Fiber Hydrogen Sensor." *Appl. Phys. Lett.,* **45** 1007–9.

Felten, J. J. 1994. "Palladium Thick Film Conductor," U.S. Patent No. 5,338,708.

Hoffheins, B. S., and R. J. Lauf. 1995. "Thick Film Hydrogen Sensor." U.S. Patent No. 5,451,920.

Hoffheins, B.S., et al., 1997. "Evaluation of a Prototype Hydrogen Sensor for Use in Safety Applications," *Energy and Fuels*, (in publication).

Hughes, R.C., et al. 1992. *Wide Range H_2 Sensor Using Catalytic Alloys*, SAND--92-2382C, Albuquerque, N.M. Sandia National Laboratories.

Lauf, R.J., et al. 1994. "Thin-Film Hydrogen Sensor." U.S. Patent 5,367,283.

Lechuga, L.M., et al. 1991. "Hydrogen Sensor Based on a Pt/GaAs Schottky Diode." *Sens. Actuators B* **4**, 515–18.

Lewis, A. 1967. *The Palladium Hydrogen System*, Academic Press, New York.

Figure Captions

Figure 1. Prototype hydrogen sensor, 1.5X actual size (left) and schematic representation (right).

Figure 2. Configuration for sensor testing.

Figure 3. Sensor response to 2% H_2/air for indicated input voltage and temperature.

Figure 4. Comparison of palladium metallizations for sensors DT052 (left) and DT053 (right) (magnification: 100X).

Figure 5. Comparison of sensor performance for three palladium compositions (2% H_2/air, 5-V sensor input).

Figure 6. Sensor packaging scenarios compatible with 1.3 X 1.3 cm sensor size.

Figure 7. The ORNL sensor can be mass-produced on large substrates and then be broken apart for individual packaging.

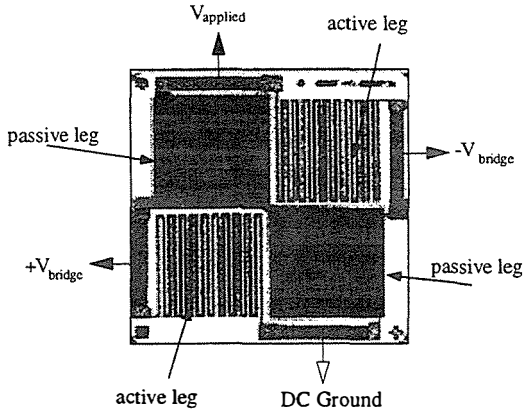
$V_{applied}$
active leg
passive leg
$-V_{bridge}$
$+V_{bridge}$
passive leg
active leg
DC Ground

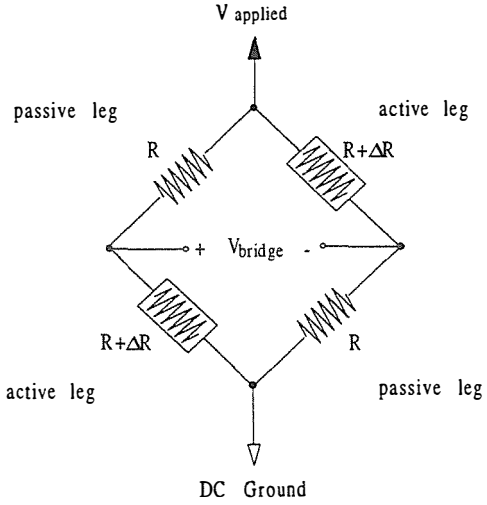
V applied
passive leg
active leg
R
R+ΔR
+ Vbridge -
R+ΔR
R
active leg
passive leg
DC Ground

Figure 1

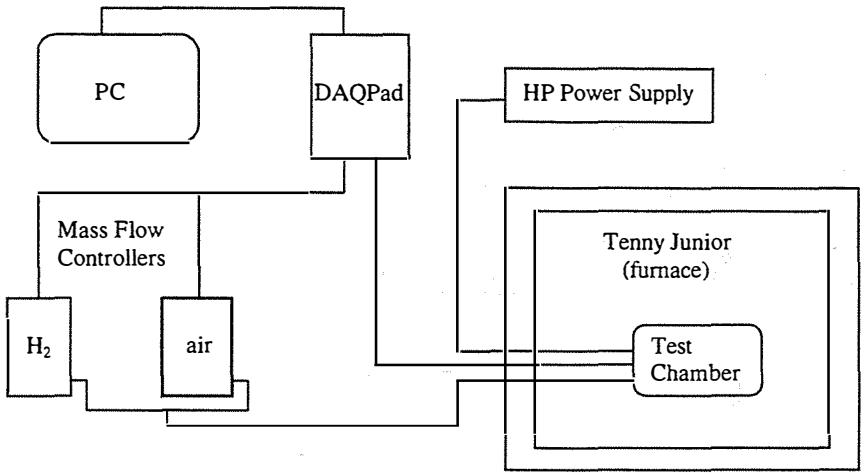
PC
DAQPad
HP Power Supply
Mass Flow
Controllers
Tenny Junior
(furnace)
H_2
air
Test
Chamber

Figure 2.

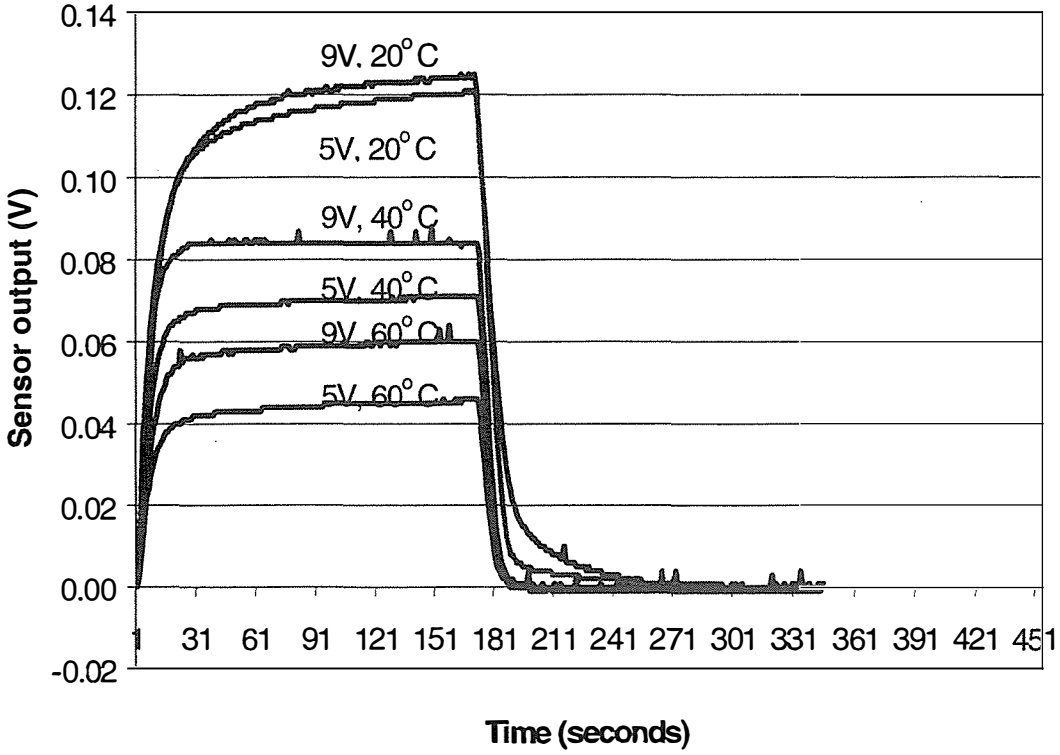
0.14
0.12
0.10
0.08
0.06
0.04
0.02
0.00
-0.02
Sensor output (V)
9V, 20° C
5V, 20° C
9V, 40° C
5V, 40° C
9V, 60° C
5V, 60° C
1 31 61 91 121 151 181 211 241 271 301 331 361 391 421 451
Time (seconds)

Figure 3

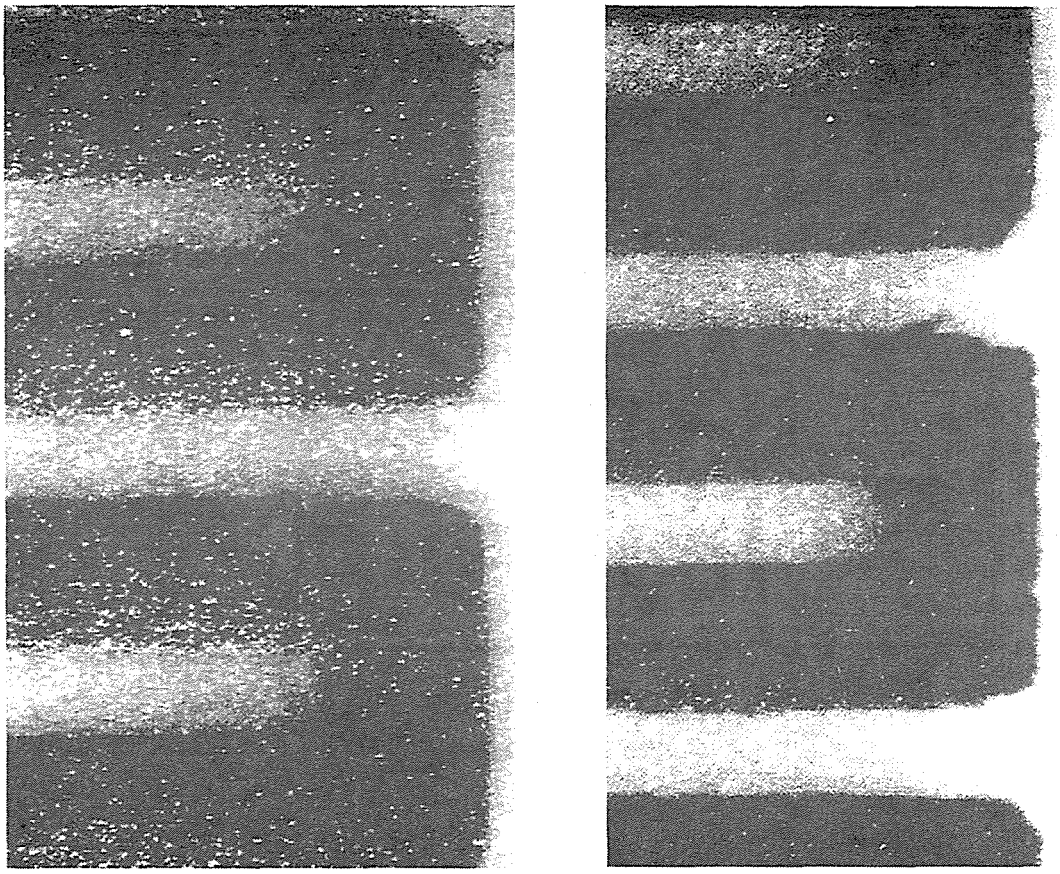

Figure 4.

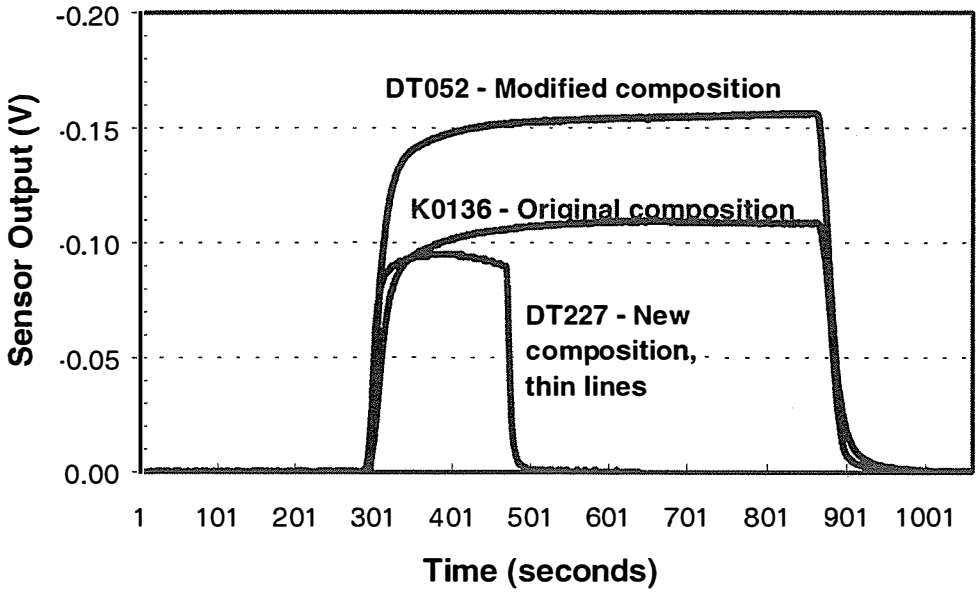
-0.20
-0.15
-0.10
-0.05
0.00
Sensor Output (V)
DT052 - Modified composition
K0136 - Original composition
DT227 - New composition, thin lines
1
101
201
301
401
501
601
701
801
901
1001
Time (seconds)

Figure 5.

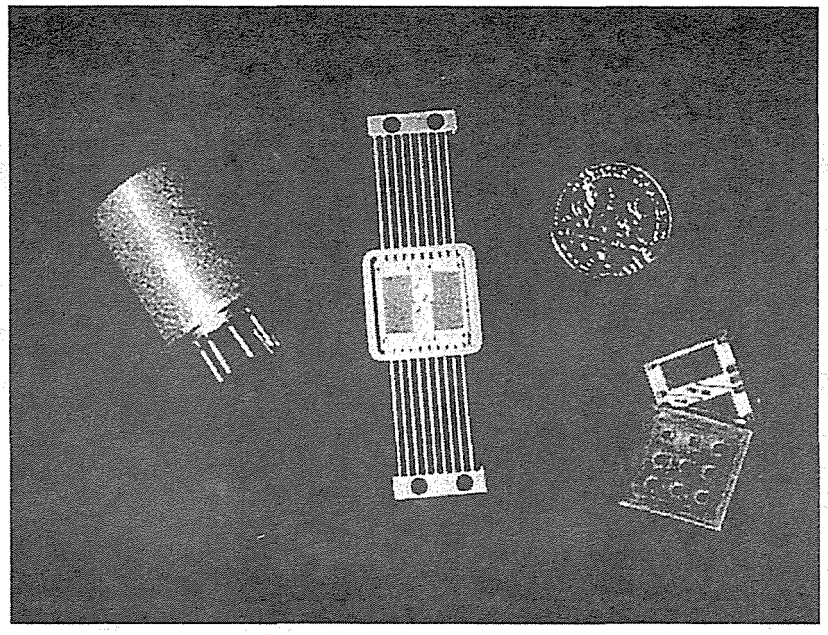

Figure 6.

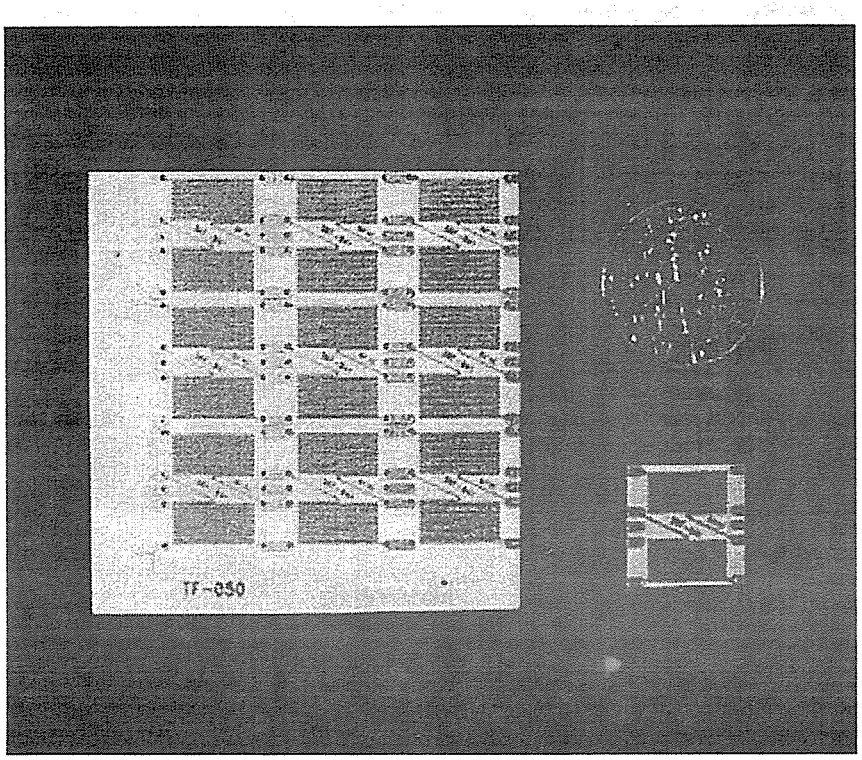

Figure 7.

PHOTOELECTROCHEMICAL HYDROGEN PRODUCTION

Richard Rocheleau, Anupam Misra, Eric Miller
Hawaii Natural Energy Institute
School of Ocean and Earth Science and Technology
University of Hawaii at Manoa
Honolulu, HI 96822, USA

Abstract

A significant component of the U.S. DOE Hydrogen Program is the development of a practical technology for the direct production of hydrogen using a renewable source of energy. High efficiency photoelectrochemical systems to produce hydrogen directly from water using sunlight as the energy source represent one of the technologies identified by DOE to meet this mission. Reactor modeling and experiments conducted at UH provide strong evidence that direct solar-to-hydrogen conversion efficiency greater than 10% can be expected using photoelectrodes fabricated from low-cost, multijunction (MJ) amorphous silicon solar cells. Solar-to-hydrogen conversion efficiencies as high as 7.8% have been achieved using a 10.3% efficient MJ amorphous silicon solar cell. Higher efficiency can be expected with the use of higher efficiency solar cells, further improvement of the thin film oxidation and reduction catalysts, and optimization of the solar cell for hydrogen production rather than electricity production. Hydrogen and oxygen catalysts developed under this project are very stable, exhibiting no measurable degradation in 1N KOH after over 13,000 hours of operation. Additional research is needed to fully optimize the transparent, conducting coatings which will be needed for large area integrated arrays. To date, the best protection has been afforded by wide bandgap amorphous silicon carbide films.

Introduction

One of most ambitious goals of the US Department of Energy's Hydrogen Program is the large-scale production of hydrogen utilizing a renewable energy source to split water. High efficiency photoelectrochemical systems to produce hydrogen directly from water using sunlight as the energy source is one of the technologies identified by DOE to meet this mission. In order to meet DOE goals, such a system must be low cost, must operate at solar-to-chemical conversion efficiencies greater than 10% and must have long operating lifetimes. Although numerous approaches involving a variety of semiconductors have been explored since the early 1980's, progress has been slow, limited by the high voltage required to dissociate water and corrosiveness of the aqueous electrolytes. Modeling and proof-of-concept experiments conducted at UH provide strong evidence that future direct solar-to-hydrogen conversion efficiency greater than 10% can be expected with photoelectrodes fabricated from low-cost, multijunction (MJ) amorphous silicon solar cells. Based on the very thin semiconductor layers involved and on compatibility with high-throughput manufacturing processes, these systems have the potential for very low cost.

In the past, our effort was mostly focused on demonstrating the feasibility of the photoelectrochemical approach, and on improving photoelectrode efficiency by optimizing the hydrogen and oxygen catalysts. To date, solar-to-hydrogen efficiencies as high as 7.8% have been achieved using a 10.3% efficient MJ solar cell (Rocheleau et al., 1998). The relative electrochemical efficiency, the ratio of the energy content of hydrogen produced (LHV) to the maximum electrical output of the solar cells, is approximately 75% - 80% in outdoor testing for both MJ amorphous silicon on glass (from Solarex Inc.) and on stainless steel (from Energy Conversion Devices Inc.). Higher efficiency can be expected with the use of higher efficiency solar cells (13% is the current world record efficiency for stabilized amorphous silicon), further reduction in the anodic and cathodic overpotentials, and optimization of the solar cell for hydrogen production rather than electricity production. After successful demonstration of proof of concept, we are now focusing on more important issues - stability of the photoelectrode in aqueous electrolyte and development of a photoelectrode configuration amenable to scale-up.

While specialized laboratory cells using separate anodes and cathodes have been used for efficiency testing, conceptual designs of PEC reactors indicate that these configurations will not be appropriate for large integrated systems. The current research is focused on the development of transparent, conductive coatings which effectively protect the underlying semiconductor structures without causing loss of light transmission or adding significant resistive losses. To date, the best results have been obtained with wide bandgap amorphous silicon carbide films. Although these films do cause a modest increase in series resistance, this material is very transparent and in tests to date, has been very stable even in strong alkaline electrolyte.

In this report we describe progress in several parallel efforts including reactor modeling and design, catalysts development, protective film development, and outdoor testing of photoelectrochemical system.

Scope/Technical Approach

Our approach, as it has been in the past, is to compare alternate materials and system configurations using reactor modeling, and to identify and address the critical materials and photoelectrode-operation issues through extensive experiments in materials synthesis and in photoelectrode fabrication and testing. We have developed quantitative models for the photoelectrochemical production of hydrogen by combining detailed models of the performance of multijunction amorphous silicon solar cells with standard kinetic expressions describing the electrochemical reactions. We've continued our development of state-of-the-art thin film catalysts and made significant advances in the development of transparent protective thin films. Preliminary conceptual reactor designs, prepared in collaboration with NREL, indicate several important advantages of using the solar cell configurations traditionally fabricated onto metal substrates. Therefore, while continuing our strategy of working closely with the solar cell manufacturers, we are shifting our focus from the glass superstrate cells produced by Solarex to the metal substrate cells produced by Energy Conversion Devices for compatibility with the proposed conceptual designs. Use of the ECD type devices in a practical system requires development of very high quality protective films, a key focus of the current work.

Results

Loss Analysis

In 1991 we conducted a systematic analysis of semiconductor materials and photoelectrode designs (Rocheleau and Miller, 1997) to compare the potential hydrogen production rates of different semiconductor materials and in various single and multijunction configurations. This study showed that series-connected multijunction (MJ) devices could be designed to operate at voltages optimized for direct water splitting while still using a large fraction of the available solar spectrum resulting in significantly higher efficiencies than conventional single junction (single photon) systems. The multijunction approach also eliminates the need for direct contact between the semiconductor and electrolyte allowing the use of protective films to prevent corrosion. Of the photovoltaic technologies which are sufficiently developed to be considered for hydrogen production (namely, Group III-V crystalline cells and amorphous silicon) the high quality III-V materials were clearly shown to have the potential for higher solar-to-hydrogen conversion efficiencies. However, their high-cost makes them impractical for commercial PEC systems.

Surprisingly, the solar-to hydrogen conversion efficiencies predicted for the much lower cost multijunction amorphous silicon ranged up to 50% of those calculated for the best Group III-V heterojunctions. Based on the scale of manufacture under development for amorphous silicon, and on the related cost reductions predicted by the PV industry for a-Si thin-film technologies, the UH program has focused on MJ amorphous silicon devices in the development of high efficiency photoelectrodes. Figure 1 illustrates the modeling of multijunction amorphous silicon photoelectrodes as a solar cell structure series-connected with an electrochemical load. This analysis includes the current-dependent overpotentials

due to charge transfer kinetics at the electrode surfaces in addition to resistances for the potential drop due to ion transport through the electrolyte. Details of the a-Si solar cell modeling as well as assumptions used in the analysis of the electrochemical kinetics have been described elsewhere (Rocheleau and Vierthaler,1994; Rocheleau,Tun and Hegedus, 1997; Miller, 1996). The predicted hydrogen-production rate based on an integration of actual data into the photoelectrode model is shown in Figure 2, where the JV curve of a triple junction Solarex solar cell (10.3% stabilized) is superimposed with a measured electrochemical operating curve. As described later, the indicated 7.8% solar-to hydrogen efficiency of this system has been verified in experimental results. Small area amorphous silicon solar cells with 13%-stabilized efficiency have been developed (Yang, et al., 1997). Although solar cells of this efficiency level have not yet been made available for testing, use of this quality device in a hydrogen production system using the thin film catalysts developed at UH would be expected to yield solar-to-hydrogen efficiencies greater than 10%.

Reactor Design

Figure 3 shows a conceptualized picture of a photoelectrochemical reactor for hydrogen production utilizing multijunction (MJ) amorphous silicon photoelectrodes. This reactor is based on designs developed in collaboration with NREL, Energetics, and Distributed Utility Associates during the fall of 1997. Figure 4, shows a conceptualized cross section of the active MJ photoelectrode element. The active cell may be configured for light through the p-layer (pinpinpin-as shown), or in the alternate configuration for light through the n-layer (nipnipnip). Photogenerated electrons drift, under the influence of the internal fields, toward the n-layer while the holes drift toward the p-layer for collection. A key difference of this photoelectrochemical configuration, compared with the solid-state solar cell configuration is absence of the lateral current collection required in solar cells. We believe that significant cost advantage of the integrated photoelectrochemical system over conventional PV-electrolysis (i.e., solid-state solar cells driving electrolyzers) can be realized since the integrated system can take advantage of the simpler processing and reduced materials constraints allowed when current is transferred directly through, rather than collected laterally in the transparent contact.

The photoelectrode structure (Figure 4) consists of a MJ amorphous silicon solar cell deposited directly onto a supporting substrate. This substrate may be conductive such as the stainless steel used in the ECD cell configuration, or it may be a nonconductive material. If the latter is used, additional processing is necessary to provide a conductive path between the backside of the cell and the back-side catalyst. In the configuration shown, the contact/membrane is assumed to be conductive, the solar cell is grown nipnipnip so that light is incident on the p-layer, the catalyst on the back side drives the hydrogen reaction (e.g. CoMo or similar material) and the front p-side includes a transparent protective coating, and a low overpotential oxygen evolution catalysts (e.g. Fe:NiOx). In this configuration, the backside hydrogen electrode is not required to be transparent and is not in direct contact with the semiconductor and thus is easily processed. In the case of ECD cells on stainless steel substrates, we have successfully demonstrated the performance of this element of the system using sputter deposited CoMo.

Since ions involved in the electrochemical reactions are not transported through the solar cell, a path for ionic continuity must be provided. Figure 4 depicts a configuration in which the substrate is physically attached to an ionic transport membrane to provide electrical continuity around the cell. However, if a suitable ionic conducting material can be developed, the back contact and solar cell could be deposited directly on the membrane, simplifying fabrication of the system. These design/synthesis issues are to be addressed next year. For the configuration shown, stability of the hydrogen electrode is determined by the hydrogen catalyst. Per the results discussed in the next section, stable, high activity thin film hydrogen catalysts have already been developed at UH. Stability at the front (p) interface is more complicated, requiring a thin layer which fully protects the underlying semiconductor while retaining its transparency and conductivity, and is compatible with the catalyst. While progress has been made this year, we feel this is the critical problem to be solved if a practical low-cost PEC system is to be developed. Progress to date is described later in this report.

Elements of the reactor system include arrays of photoelectrode modules, separation systems to remove hydrogen and oxygen from the electrolyte, storage tanks and fluid pumps etc. It is envisioned that the PEC reactor will operate at modest solar concentration, 5 to 10 suns, taking advantage of the fact that carrier transport directly through the transparent window (vs. the lateral current collection) reduces series resistance. Properly designed, the cylindrical reactor body itself could provide some or all of the concentration. The reactor is easily expandable by adding additional arrays of photoelectrodes. It is desirable to allow the photoelectrode to be changed out to accommodate replacements should failure occur or new photoelectrodes with better performance be discovered. Since only water is consumed in the reaction, makeup is simple and could be accomplished using simple gravity feed.

Catalyst Development

The University of Hawaii has made considerable progress in the development of stable high performance catalysts for hydrogen-producing planar photoelectrodes. Reactively-sputtered layers of Fe:NiOx with high activity for oxygen evolution have been demonstrated and reported in detail elsewhere (Miller and Rocheleau, 1997; Miller and Rocheleau, 1997). Although under certain processing conditions good transparency is maintained in these oxide films, this has come at the expense of reduced activity. Additional improvements to optimize both transparency and OER activity are desired. UH has also demonstrated reactively-sputtered films of cobalt/molybdenum with excellent stability and high hydrogen evolution activity. Since these thin film catalysts are in direct contact with the electrolyte, stability under normal operating conditions is essential.

Long term stability testing of both oxygen and hydrogen catalysts was conducted by mounting samples of Fe:NiOx (oxygen catalyst) and CoMo (hydrogen catalyst) on a specially designed Plexiglas PEC cell using Teflon gaskets. The stability test consists of monitoring electrode potentials at constant current density of 20 mA/cm^2 in 1 N KOH made from ACS grade KOH and commercially available drinking water. Use of low grade chemical and water was required

to keep the cost of electrolyte low, however use of dirty electrolyte requires very stable oxygen and hydrogen catalysts to be developed and utilized. Figure 5(a) shows the total cell potential (V_{cell}) and the anodic ($Fe:NiO_x$) half cell potential for the 13,600 hour test at a continuous current of 20 mA/cm^2. Although there is some variation in both the total and half cell potentials during the testing, there is no consistent trend toward higher potential, i.e. degraded electrodes for either. The constant anodic half cell potential is indicative of a stable Fe:NiOx OER catalyst. The constant difference between the total cell and half cell potentials is indicative of stable CoMo HER catalyst. The high total cell potential includes a significant IR drop through the electrolyte due to the large anode/cathode separation in this particular test cell, however, the catalytic activity of the OER and HER are similar to our best materials previously reported.

Figure 5(b) shows the anodic half cell (vs SCE) and total cell current-potential (JV) sweeps at the start of and following 13600 hrs at a constant current density of 20 mA/cm^2. Consistent with the results in Figure 5(a) the oxygen catalyst (nickel iron oxide) shows very stable performance. The total cell potential actually shows some improvement indicating improvement in the CoMo. The additional experiments evaluating properties of electrolyte at various times during test indicate that the improvement of CoMo is due to the hydrogen reduction and is not related to the change in electrolyte properties. Molybdenum is known to oxidize readily during deposition and during stand alone periods. A constant hydrogen evolution on CoMo catalyst seems to remove oxygen and improve the catalytic action. The hydrogen catalyst was found to recover from damage from the oxidation during a 5 day stand alone non-operational period. Data indicate that for commercial system, one would either need cathodic protection or artificial light during night hours. The long term testing of these two electrodes is continuing.

Previously, we have improved the performance of the oxygen catalysts by introducing transition metals into the sputtered NiOx films. Similar experiments were conducted during this phase of the project in an effort to further reduce the overpotentials associated with the hydrogen evolution reaction. The replacement of Co by Ni was found to reduce the overpotential in 1N KOH by approximately 50 mV as shown in Figure 6. The improvement in the NiMo during the first 1500 seconds of operation is believed to be due to removal of surface oxide under the reducing conditions found at the anode. Experiments are underway to further optimize the hydrogen catalyst and to characterize the surface reaction.

Protective Coatings

Protective coatings for the surface of the photoelectrode exposed to electrolyte and through which the light passes (top p-layer in the configuration shown in Figure 4) must be transparent, corrosion resistant and pinhole free, and electrically conducting. A literature search of potential materials meeting these requirements included zinc oxide (ZnOx), indium tin oxide (ITO), tin oxide (SnOx), doped and undoped amorphous silicon carbide (a-SiC:H), and diamond and diamond-like carbon (DLC) films. All of these films are transparent and can be doped to become conducting. The choice of suitable protective film is then mainly

dependent on its chemical inertness, ease of processing and physical protection for the underlying semiconductor layers (e.g. ability to deposit pinhole free). ZnOx films are reported to be unstable in 1 N KOH and so were not included in the corrosion testing. The literature indicates that SnOx films are more stable than either the ITO or ZnOx films. Commercial samples of SnOx were obtained and tested in our electrochemical cells. These films dissolved in 1 N KOH within a day. Since alloying or the addition of dopants can play an important role in determining the electrochemical behaviors of a protective film, it still may be possible to develop a stable SnOx film in the future by adjusting the film composition. ITO films of variable resistivities are currently being deposited using the same sputtering system used for catalyst deposition. Testing of the electrochemical/corrosion characteristics is planned but has not yet started.

The best results to date have been obtained using amorphous silicon carbide films deposited using plasma enhanced chemical vapor deposition, a process which has been described in some detail in previous reports (Rocheleau, Miller and Misra, 1997). It was previously reported that a-SiC:H films deposited under conditions of high hydrogen dilution were physically harder and were more resistive to corrosion than films deposited from undiluted mixtures of silane and methane.

Figure 7 shows the anodic polarization curve for a bare nickel substrate and for four Ni substrates coated with a-SiC:H. The polarization curves were obtained by sweeping from the corrosion potential into the anodic region in 1N KOH. Data were taken at an interval of 0.01 V although, for clarity, data are shown only every 0.20 volts. The a-SiC:H was deposited at silane to methane ratios ranging from(4:6 to 1:9). At a deposition pressure of 0.5 torr, the bandgap of the a-SiC:H films increased from 2.0 to 2.25 eV as the methane fraction in the feedgas increased from 60% to 90%. The bandgap was further increased, to 2.72 eV, when the film was grown from the gas with the 1:9 silane to methane ratio at a reduced pressure of 0.133 torr. We speculate that the increase in bandgap is the direct result of greater C incorporation into the films. Confirming measurements will be conducted. As the bandgap increased, the films became significantly more transparent in the visible spectrum. Figure 7 shows that as the bandgap is increased, the silicon carbide films also become more corrosion resistant. Since the underlying nickel substrate is more noble than a-SiC:H in KOH solution, the anodic polarization below 0.1 Vsce represents the characteristic behavior of the a-SiC:H films in KOH electrolyte. With the increase in the methane concentration and bandgap, the samples show systematic decrease in the corrosion current density and become more noble. The increase in the current density at about 0.5 Vsce is due to oxygen evolution from the samples.

Figure 8 shows the electrochemical behavior of a Ni substrate coated with the intrinsic 2.25eV a-SiC:H film held at constant current density of 20mA/cm^2 in 1 N KOH. Any dissolution of the films resulting in exposure of the underlying Ni should be accompanied by a decrease in the potential (Vsce approaching substrate potential). None was observed. Visual inspection of the film after 120 hours of corrosion testing (Figure 9a) showed no evidence of dissolution or thinning of the film. The intrinsic a-SiC:H is extremely stable in the 1N KOH.

While the transparency and corrosion resistance of the a-SiC:H films increases as the bandgap increases (e.g. with greater carbon incorporation) the resistivity of the film, hence the series resistance loss in photoelectrodes using these protective films increases. A select number of films were produced with boron doping to see if resistance could be reduced while maintaining transparency and chemical stability. Figure 10 shows the anodic polarization curve of a boron doped film with an optical bandgap of 2.0 eV. Although showing a higher corrosion current and being less noble than the very high bandgap intrinsic film shown for comparison in Figure 10, comparison to Figure 7 shows the boron doped films to be as or slightly more corrosion resistant than intrinsic films of comparable bandgap. The long term stability of the p type a-SiC:H:B films under anodic bias in 1 N KOH is shown in Figure 11. After 20 hours the half cell potential approached the substrate potential indicating dissolution of the film. This was confirmed by visual inspection (Figure 9b). Additional experiments will be conducted to simultaneously optimize the chemical resistance and electrical properties of the film.

To date, all electrochemical testing has been conducted in 1N KOH which was selected due to the low overpotential and good stability of the catalysts in KOH. Since the reactivity of the protective film will change with electrolyte, additional improvements in the performance of the films may result by changing the composition of the electrolyte. Development of a more neutral, less corrosive electrolyte which maintains the low overpotential of the sputter deposited catalysts is a suggested area of research for next year.

Our research plan calls for the installation of an ASTEX reactor to allow the evaluation of diamond-like carbon films. Funds from other sources have been obtained to assist in the installation of this equipment and laboratory space has been acquired. Progress in this area will be reported later.

Bilayer structures including protective a-SiC:H and Fe:NiOx catalyst films were also fabricated and characterized. Corrosion testing of these bilayers was again conducted at constant current of 20 mA/cm^2 in 1 N KOH. Figure 12 shows the bias required to maintain constant current on a Ni/i-SiC:H/Fe:NiOx multilayered sample over the 140 hour test. The initial potential is slightly higher than that of Fe:NiOx on Ni due the to series resistance introduced by the intrinsic a-SiC:H. Although both films used in this structure are stable by themselves (e.g. on Ni) the half cell potential of the bilayer gradually increases during the 140 hour test. Examination of the electrolyte and films showed that this rise was caused by poor adhesion of the oxygen catalyst (Fe:NiOx) to the amorphous silicon film, causing a decrease in the area of the catalytic film. Additional experiments are planned to improve bonding between these materials.

Similar testing was conducted using boron doped films, i.e. Ni/p-SiC:H:B/Fe:NiOx. In contrast to the bilayer with the intrinsic film, the boron doped p-type SiC film is not stable in KOH. Stability of this structure thus depends on the ability of the Fe:NiOx to protect the underlying films. The initial potential is very close to that of Fe:NiOx alone, as expected for the more conductive boron doped silicon film. However, as shown in Figure 13, there again is a gradual increase in the potential, this time, toward the potential of the Ni substrate indicating corrosion of the a-SiC:H:B film. The corrosion of this film is

presumably caused by pinholes in Fe:NiOx film and/or poor adhesion of Fe:NiOx to the a-SiC. Figure 14 shows the photograph of the two bilayers after corrosion testing. Adhesion of the FeNiOx was a problem in both cases. We plan on exploring remedies to this problem in the future with systematic test runs and optimization of the deposition process.

Outdoor Testing

Previously we have reported an outdoor solar-to-hydrogen conversion efficiency of 7.8% using photoelectrodes fabricated from glass/CTO/pin-pin-pin triple junction a-Si solar cell provided by Solarex Inc. The experimental efficiency was consistent with those predictions from the load line analysis. The hydrogen production efficiency of photoelectrodes was 7.8%, which was about 77% of the efficiency of the triple junction cell (Rocheleau et al., 1998).

Triple junction a-Si solar cells on stainless steel substrates are available from ECD Inc. in the configuration ss/nip-nip-nip/CTO. As already discussed, this configuration offers potential design advantages and is expected to be more applicable for commercial reactors. Outdoor testing of photoelectrochemical cells constructed from these solar cells was conducted using same setup as described in previous reports (Rocheleau, Miller and Misra, 1997). Figure 15 shows the JV behavior of the triple junction solar cell available to us at the time of this test. Insolation was monitored using a standard crystalline silicon cell (pn junction) mounted onto the reactor in the same plane as the photoelectrode. A maximum solar cell efficiency of 8.7% was measured for the batch of cells cut from a sheet from their pilot scale reactor.

Figure 16 shows the result of a one hour outdoor test performed between 1:00 PM and 2:00 PM on a clear day. The photoelectrode configuration was CoMo catalyst deposited directly on the stainless steel substrate with an nip-nip-nip solar cell coated with ITO. Electrical leads were attached to the ITO and to a separate Fe:NiOx/Ni anode. The line shows the insolation on the cell measured with our secondary standard, the crystalline cell. The symbols (cross: left ordinate) show the current passing between the anodic and cathodic surfaces of the photoelectrode. The middle inset of figure 15 shows the net solar-to-hydrogen conversion efficiency of the photoelectrode as a function of time, approximately 6.6%. The ratio of the hydrogen conversion efficiency to solar cell efficiency is approximately 78% as shown in the inset at top of Figure 16. This is consistent with the electrochemical efficiency obtained with the Solarex cell in the earlier testing.

Summary and Plans

Direct solar-to-hydrogen conversion efficiency of photoelectrodes fabricated from low cost triple junction amorphous silicon solar cells has been shown to be about 78% that of solar cell efficiency. Results from outdoor tests on commercially available multijuction cells in two different configurations are consistent with each other and also with the loss analysis

model capable of predicting PEC efficiency. Thin film oxygen and hydrogen catalyst films have been shown to be very stable over 13,000 hours in strong alkaline electrolyte. Further improvement in the solar-to-hydrogen efficiency are expected with higher efficiency solar cells, better catalysts, and use of MJ cells optimized for hydrogen production. With proof of concept efficiency experiments completed, we are now focusing on long term stability issue of the system which, we believe, is the most critical materials issue remaining to be solved. Substantial progress has been made in the development of stable, protective a-SiC:H films. Intrinsic films show no degradation in 1N KOH. However, further optimization of transparency and electrical properties are needed. In order to fabricate a highly stable photoelectrode, we plan to continue our research into the development of stable conducting transparent protective films and to expand the effort to include the development of less corrosive electrolytes. We will continue to explore multilayer structures to take advantage of the best features of each material.

Increased attention to the development of conceptual and engineering designs of photoelectrochemical systems is needed to insure that the materials problems identified for research are relevant to the eventual production of commercial systems.

Acknowledgments

We wish to thank the US Department of Energy for support of this work under Grant DE-FG04-94AL85804. We also wish to Solarex Inc. and Energy Conversion Devices for amorphous silicon samples. We also wish to thank Maggie Mann of NREL and Phil DiPietro of Energetics for their useful discussions and input in the development of conceptual designs for large scale systems.

References

Miller, E. L., and R. E. Rocheleau. 1997. "Electrochemical Behavior of Reactively Sputtered Iron-doped Nickel Oxide" J. Electrochem. Soc. 144(9):3072-3077.

Miller, E. L., and R. E. Rocheleau. 1997. "Electrochemical and Electrochromic Behavior of Reactively Sputtered Nickel Oxide" J. Electrochem. Soc. 144(6):1995-2003.

Miller, E. L., 1996. "A Study of the Electrochemical Behavior and Optical Properties of Reactively-sputtered Nickel Oxide and Nickel-Iron Oxide" University of Hawaii PH.D. Dissertation.

Rocheleau, R. E., and Miller, E. L. 1997. "Photoelectrochemical Production of Hydrogen: Engineering Loss Analysis" Int. J. Hydrogen Energy. 22(8):771-782.

Rocheleau, R. E., Miller, E. L., and A. Misra. 1997. " Photoelectrochemical Hydrogen Production" *Proceedings of the 1996 U.S. DOE Hydrogen Program Review,* 345-358. Miami FL. U.S. Department of Energy.

Rocheleau, R. E., Miller, E. L., and A. Misra. 1998. "High-Efficiency Photoelectrochemical Hydrogen Production using Multijunction Amorphous Silicon Photoelectrodes" Energy and Fuels. 12: 3-10.

Rocheleau, R. E., Tun, M., and S. S. Hegedus. 1997. "Analysis and Optimization of High Efficiency Multijunction a-Si:H Solar Cells" *Proceedings of the 26th IEEE Photovoltaic Specialists Conference*, 703-706. Anaheim CA: IEEE.

Rocheleau, R.E., and Vierthaler, M. 1994. "Optimization of Multijunction a-Si:H Solar Cells Using an Integrated Optical/Electrical Model." *Proceedings of the 21st World Conference on Photovoltaic Energy Conversion* , 567-570. Honolulu HI: IEEE.

Yang, J., Banerjee, A., Glatfelter, T., Sugiyama, S., and S. Guha. 1997. "Recent Progress in Amorphous silicon Alloy Leading to 13% Stable Cell Efficiency" *Proceedings of the 26th IEEE Photovoltaic Specialists Conference*, 703-706. Anaheim CA: IEEE.

FIGURE CAPTIONS

Figure 1: Analytical model for photo-electrolysis based on a solid-state photogenerator (shown for a triple-junction device) driving an electrochemical load.

Figure 2: Load line analysis showing the operating point of a photoelectrochemical cell as the intersection of the JV curve of the photocell and the load curve of the electrochemical components.

Figure 3: Conceptual design of photoelectrochemical reactor for hydrogen production.

Figure 4: Cross section of multijunction photoelectrode for direct water splitting.

Figure 5: Long term stability test results for sputtered Fe:NiOx and CoMo catalyst films at constant current of 20 mA/cm^2 in 1N KOH.

Figure 6. Electrochemical behavior of sputter deposited CoMo and NiMo thin films at constant current of 20 mA/cm^2 in 1N KOH.

Figure 7. Anodic polarization scans of a-SiC:H films deposited on Ni substrate in 1N KOH.

Figure 8. Electrochemical behavior of a-SiC:H on Ni under anodic bias in 1N KOH.

Figure 9: Photographs of a-SiC:H, boron doped a-SiC:H and SnO think films after exposure to 1N KOH.

Figure 10. Comparison of the anodic corrosion of boron doped and intrinsic a-SiC:H films on Ni in 1N KOH.

Figure 11. Electrochemical behavior of boron doped a-SiC:H on Ni under anodic bias at constant current density in 1N KOH.

Figure 12. Electrochemical behavior of Fe:NiOx/intrinic a-SiC:H bilayers on Ni under anodic bias 1N KOH.

Figure 13. Electrochemical behavior of Fe:NiOx/boron doped a-SiC:H bilayers on Ni under anodic bias 1N KOH.

Figure 14. Photographs of bilayer films (catalyst/amorphous silicon carbide) showing poor adhesion of Fe:NiOx to amorphous silicon film.

Figure 15. JV behavior of ECD solar cell used to fabricate CoMo/ss/nip-nip-nip-Fe:NiOx photoelectrode.

Figure 16. Photoelectrode current density (x's) and solar-to-hydrogen conversion efficiency (middle inset), and electrochemical efficiency (top inset) during a one hour outdoor test on a clear afternoon (measured insolation shown by line in lower plot).

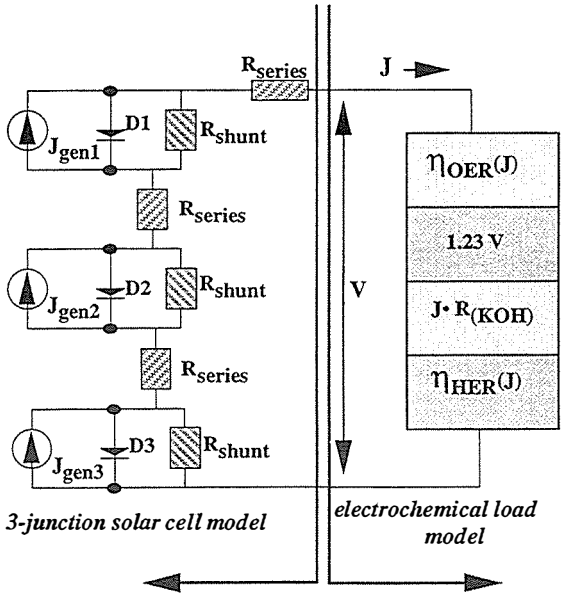
R_series
J
D1
R_shunt
J_gen1
R_series
D2
R_shunt
J_gen2
V
R_series
D3
R_shunt
J_gen3
η_OER(J)
1.23 V
J• R_(KOH)
η_HER(J)
3-junction solar cell model
electrochemical load model

Figure 1

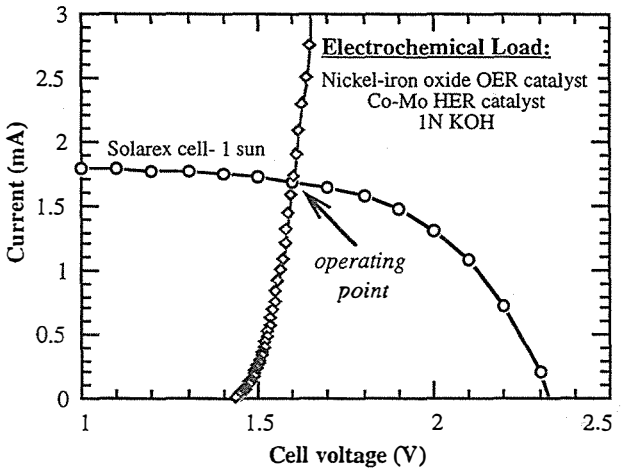
Electrochemical Load:
Nickel-iron oxide OER catalyst
Co-Mo HER catalyst
1N KOH
Solarex cell- 1 sun
operating point
Current (mA)
Cell voltage (V)
3
2.5
2
1.5
1
0.5
0
1
1.5
2
2.5

Figure 2

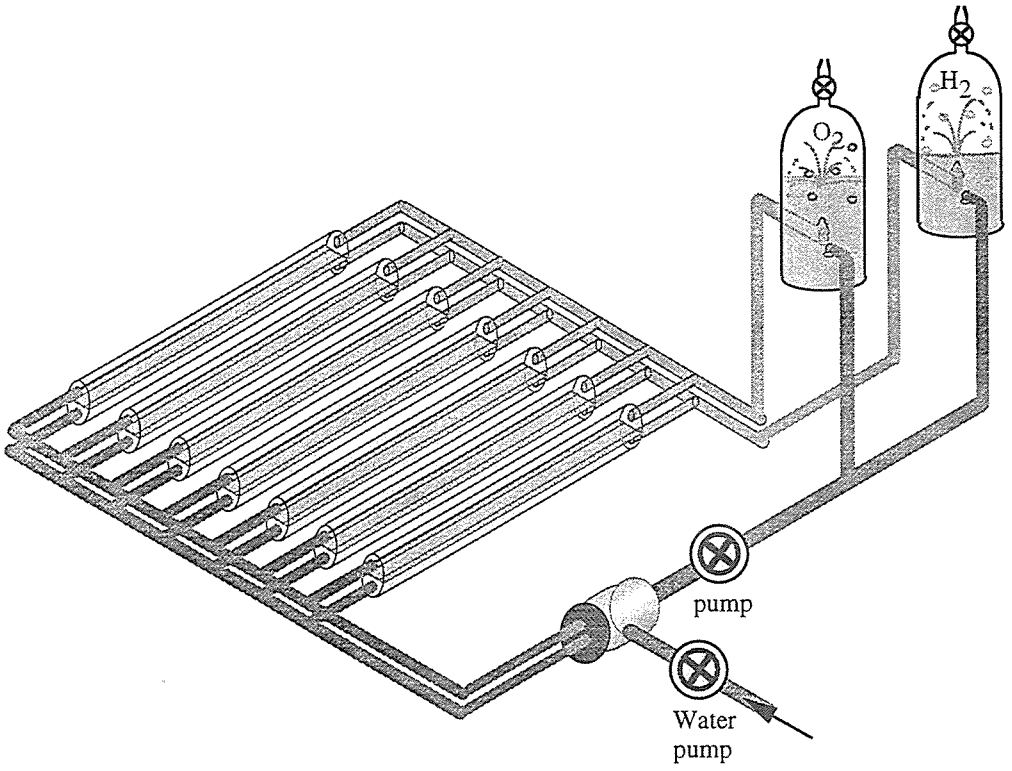

Figure 3

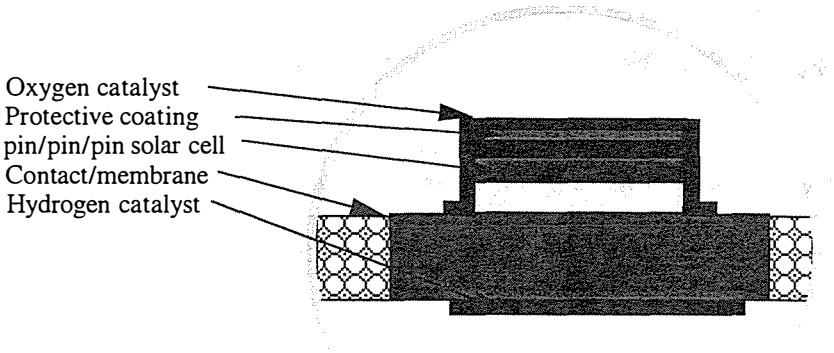
Oxygen catalyst
Protective coating
pin/pin/pin solar cell
Contact/membrane
Hydrogen catalyst

Figure 4

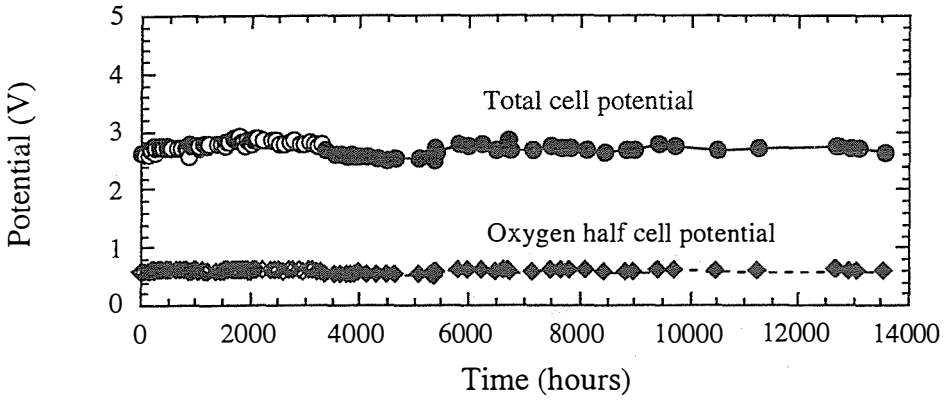
Potential (V)
Total cell potential
Oxygen half cell potential
Time (hours)

(a)

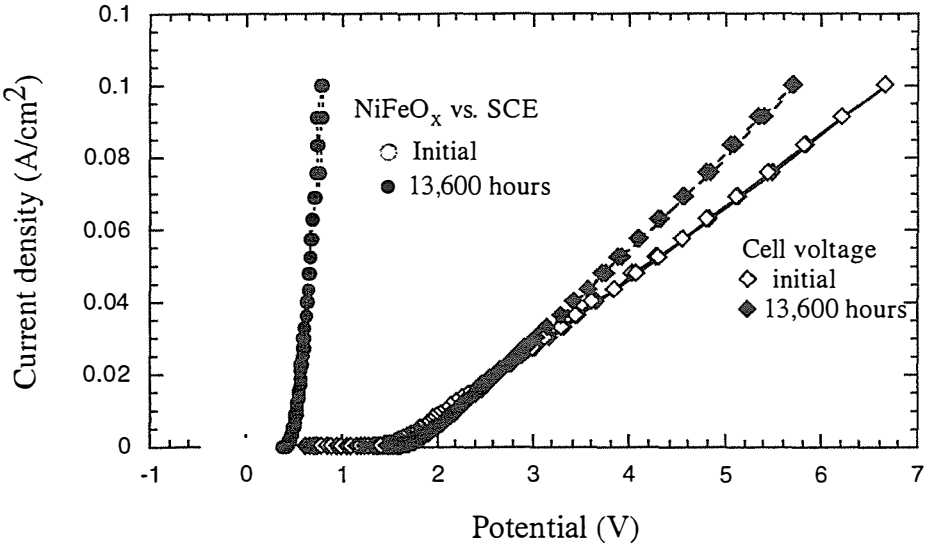
Current density (A/cm2)
NiFeOx vs. SCE
Initial
13,600 hours
Cell voltage
initial
13,600 hours
Potential (V)

(b)

Figure 5

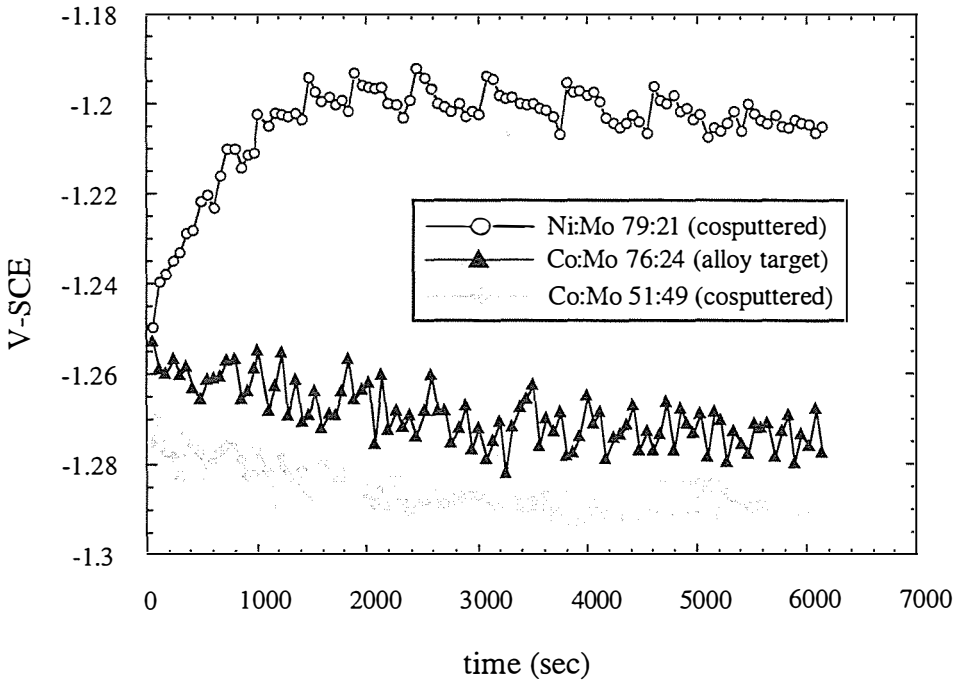
-1.18
-1.2
-1.22
-1.24
-1.26
-1.28
-1.3
V-SCE
0
1000
2000
3000
4000
5000
6000
7000
time (sec)
Ni:Mo 79:21 (cosputtered)
Co:Mo 76:24 (alloy target)
Co:Mo 51:49 (cosputtered)

Figure 6

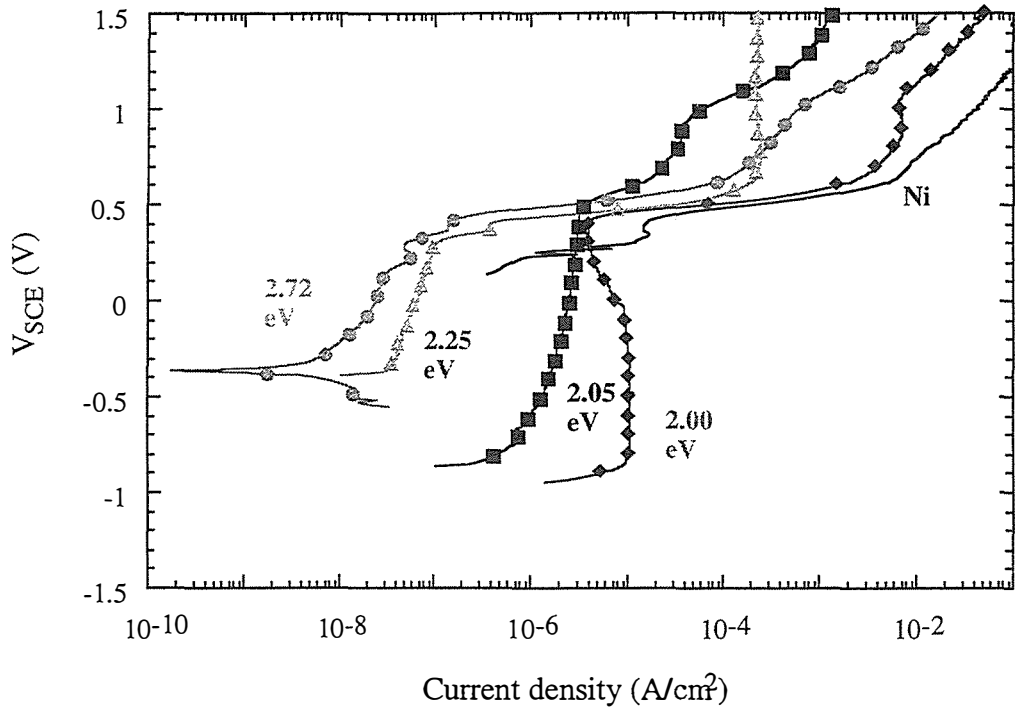
1.5
1
0.5
0
-0.5
-1
-1.5
V_{SCE} (V)
10-10
10-8
10-6
10-4
10-2
Current density (A/cm2)
2.72 eV
2.25 eV
2.05 eV
2.00 eV
Ni

Figure 7

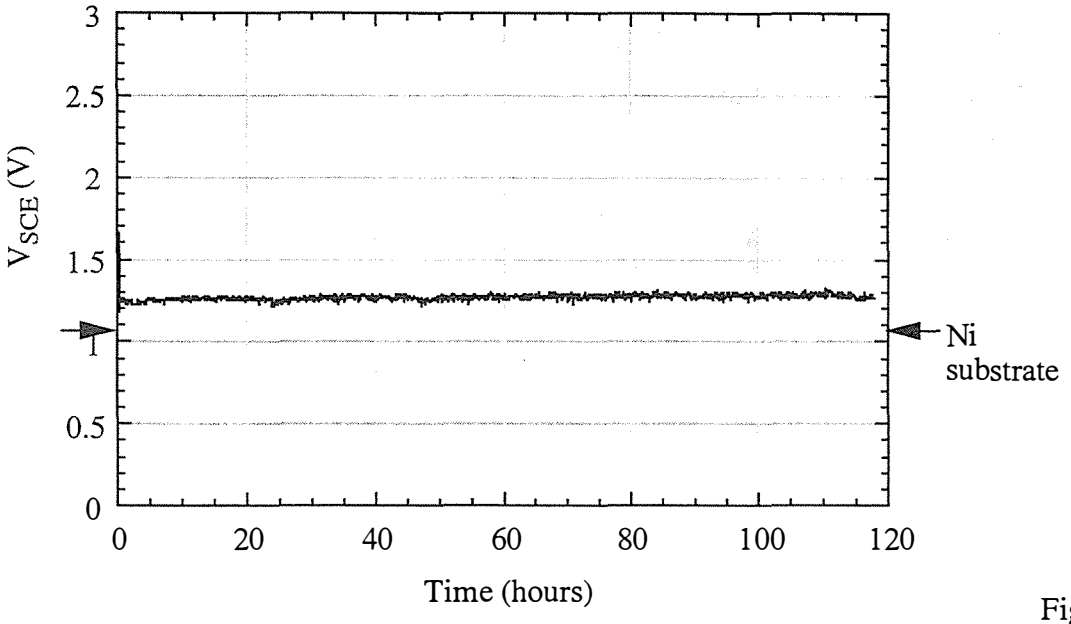
3
2.5
2
1.5
1
0.5
0
V_{SCE} (V)
0
20
40
60
80
100
120
Time (hours)
Ni
substrate

Figure 8

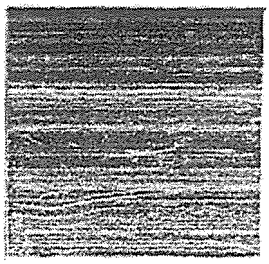

Intrinsic a-SiC:H
(5 days)

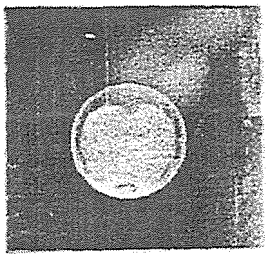

P-type a-SiC:H:B
(2 days)

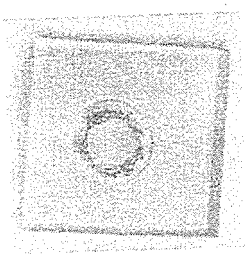

Conducting SnO
(1 day)

Figure 9

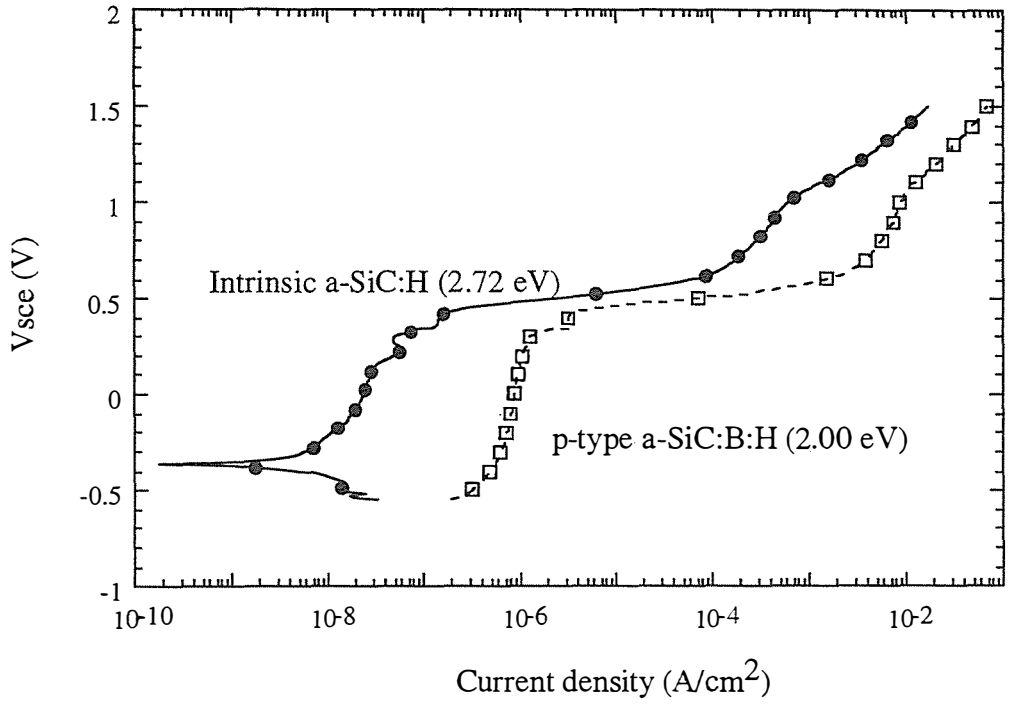
2
1.5
1
0.5
0
-0.5
-1
Vsce (V)
Intrinsic a-SiC:H (2.72 eV)
p-type a-SiC:B:H (2.00 eV)
10-10
10-8
10-6
10-4
10-2
Current density (A/cm2)

Figure 10

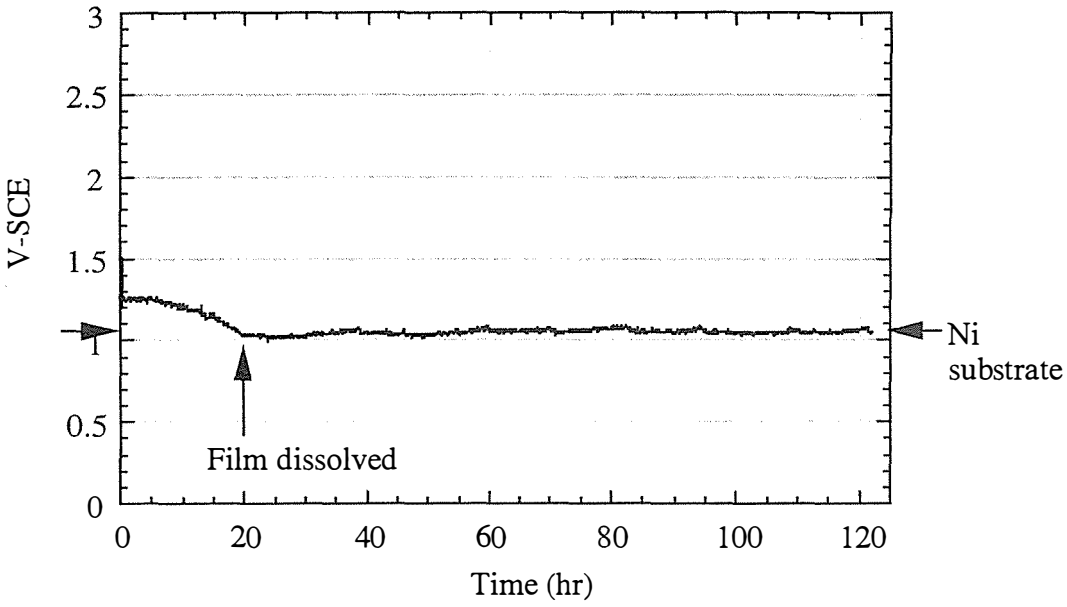
3
2.5
2
1.5
1
0.5
0
V-SCE
0
20
40
60
80
100
120
Time (hr)
Film dissolved
Ni
substrate

Figure 11

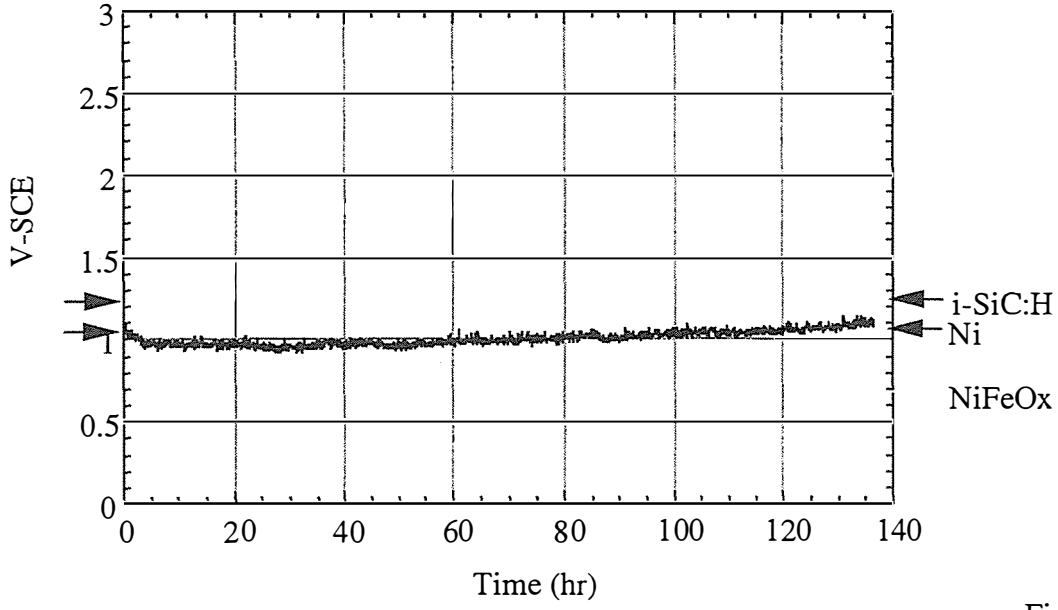
3
2.5
2
1.5
1
0.5
0
V-SCE
0
20
40
60
80
100
120
140
Time (hr)
i-SiC:H
Ni
NiFeOx

Figure 12

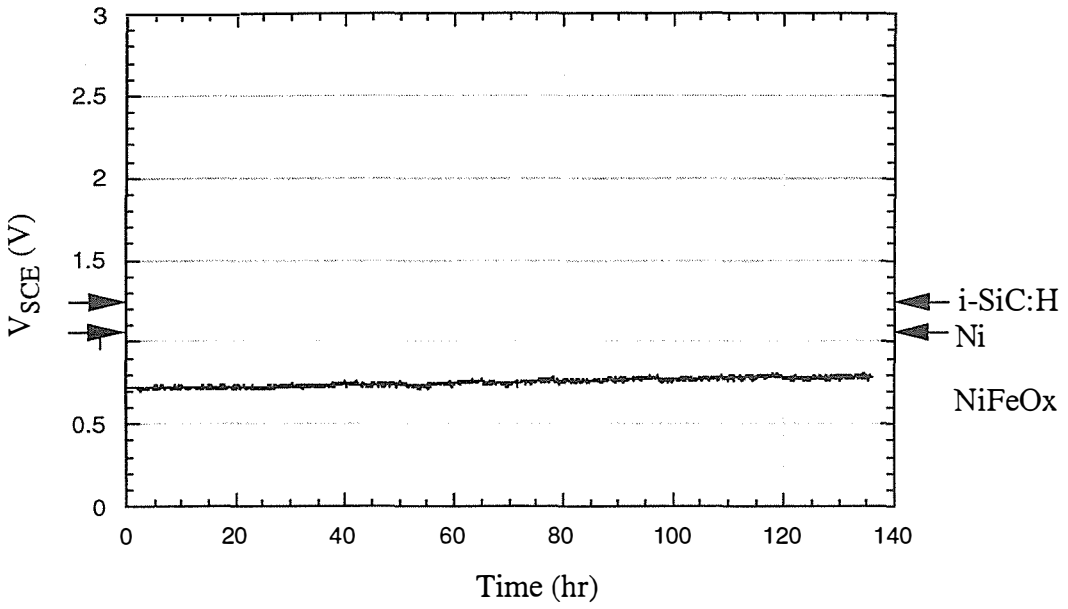
3
2.5
2
1.5
0.5
0
V_{SCE} (V)
0
20
40
60
80
100
120
140
Time (hr)
i-SiC:H
Ni
NiFeOx

Figure 13

Ni/i-SiC:H/NiFeOx

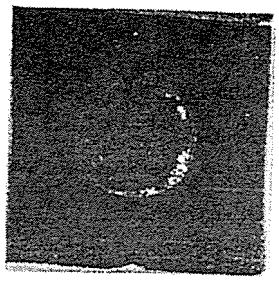

Ni/p-SiC:H:B/NiFeOx

Figure 14

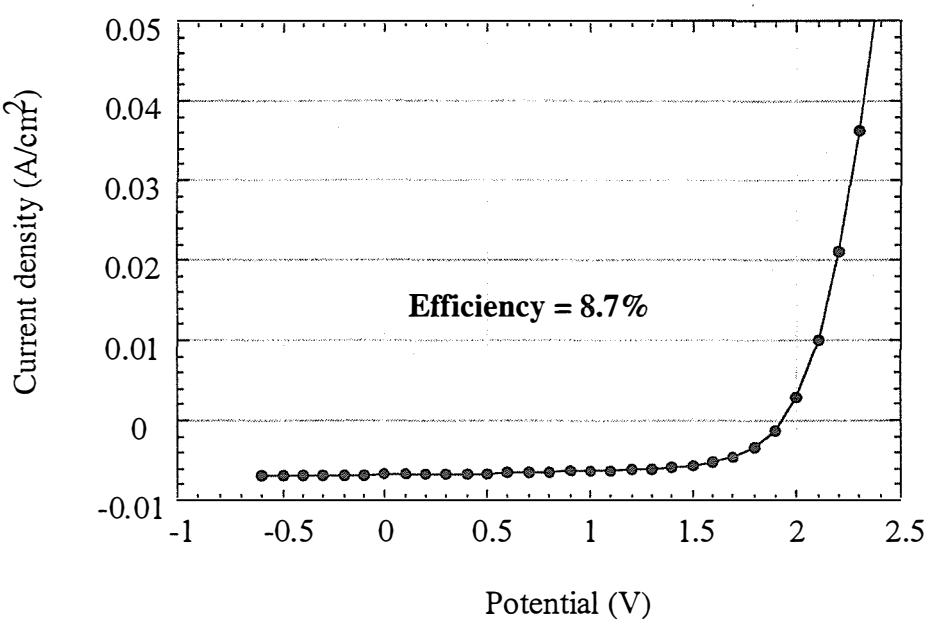
0.05
0.04
0.03
0.02
0.01
0
-0.01
Current density (A/cm2)
Efficiency = 8.7%
-1
-0.5
0
0.5
1
1.5
2
2.5
Potential (V)

Figure 15

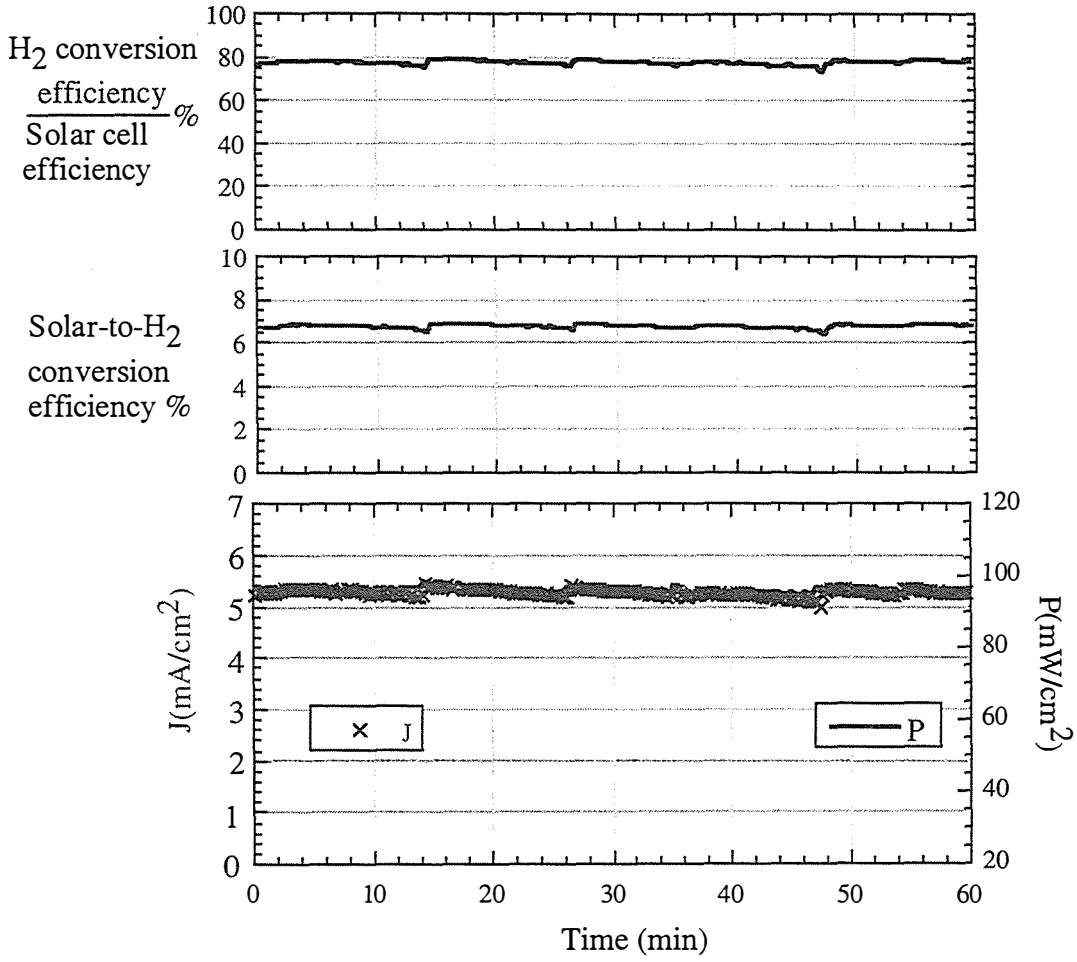
H2 conversion efficiency / Solar cell efficiency %
Solar-to-H2 conversion efficiency %
J(mA/cm2)
P(mW/cm2)
× J
P
Time (min)

Figure 16

PHOTOELECTROCHEMICAL BASED DIRECT CONVERSION SYSTEMS FOR HYDROGEN PRODUCTION

Oscar Khaselev, Ashish Bansal, Shyam Kocha, and John A. Turner
National Renewable Energy Laboratory
Golden, CO 80401-3393

Abstract

With an eye towards developing a photoelectrochemical system for hydrogen production using sunlight as the only energy input, two types of systems were studied, both involving multijunction devices. One set of cells consisted of a-Si triple junctions and the other a $GaInP_2$/GaAs tandem cell combination. Additional investigations were carried out on semiconductor surface modifications to move semiconductor band edges to more favorable energetic positions.

Introduction

An ideal renewable direct hydrogen production system would consist of an efficient light harvesting system and a highly catalytic water electrolysis system as a single monolithic device. This direct conversion system would decompose water directly upon illumination. For a one-step process to be viable, the light harvesting system must generate sufficient voltage to effect the decomposition of water, and the system also must be stable in an aqueous environment. Splitting water into hydrogen and oxygen requires a thermodynamic potential of 1.23 eV at 25 °C. Typical values of the overvoltage for the cathode and anode reactions are 100 mV and 250 mV respectively. An equivalent potential then, of at least 1.6 V is required for a water splitting system.

An illuminated semiconductor immersed in aqueous solution exemplifies such a direct conversion system. These systems have been the focus of a number of researchers for over 20 years. For a single gap semiconductor based direct conversion water splitting system, the fundamental requirement of at least 1.6 V implies a minimum bandgap of 1.8 electron volts. Surface catalysts would also be required in order to bring the overvoltage for the oxygen and hydrogen evolution reactions down to an acceptable level. An additional requirement is that the semiconductor band edges span both redox potentials of the hydrogen and oxygen evolution reactions.

The goal of this research is to develop a stable semiconductor based system that will split water directly. We are focusing our study of these systems in three basic areas: materials research, surface stability and catalysts. NREL's Photovoltaic and Basic Sciences Divisions provide a state of the art resource for new solid state materials that could be used in a direct conversion system. From a study of their materials, we have focused on gallium indium phosphide, $GaInP_2$, as an ideal material for our initial studies. Because its bandgap of 1.83 is ideal for photoelectrolysis, it is a promising semiconducting material for water splitting as a single bap material, and as a test system for our novel multi-junction designs. In general, we believe that semiconducting materials that have indium as a constituent have a greater opportunity for long-term stability in an aqueous environment. In aqueous solution, indium can form a conductive oxide layer that stabilizes the interface. If the surface of the semiconductor becomes damaged, indium ions, under the proper conditions, will form an oxide, ameliorating the surface. This self-healing of the interface will greatly increase the long-term stability of the system. Our work on $GaInP_2$ then is focused on its use as a direct conversion photoelectrochemical water-splitting system

Our past work on single crystal $GaInP_2$ has shown that while its bandgap is sufficient, its bandedges are from 100 to 400 mV more negative than would be ideal. For this material, our approach has been to study the feasibility of inducing changes in the surface to obtain a more energetically favorable situation, as well as engineering solid state designs to integrate a bias voltage to effect the water decomposition reaction. Additional studies include passivating and stabilizing the semiconductor surface, and colloidal platinum catalysts.

A possible low cost direct conversion system for water splitting is one based on amorphous silicon (α-Si). Amorphorous silicon multijunction devices consist of multiple layers of a-Si cells. These multi-layer cells provide higher efficiency than single junction cells and reduce the amount of photodegradation that is common to all a-Si devices. The combination of lower system

cost and higher efficiency, represent an important area of research for hydrogen production systems. Further, manufacturing capability for α-Si systems is high, with current production capability of these type of devices at over 10 megawatts per year in the US alone. Our approach here is to work with an industrial collaborator to develop optimized α-Si systems designed specifically for water splitting.

Our discussion this year then will focus on a novel multi-junction concept to split H_2O, HBr and HI, corrosion of $GaInP_2$, surface modification studies, and α-Si multi-junction systems.

Discussion

Technical Approach and Results

Corrosion of III-V Materials

The results of our work with $GaInP_2$ showed that it susceptible to photo-induced corrosion, which can suppress constructive photo-driven redox processes after several hours of irradiation. Identification of solution compositions and additives that stabilize the semiconductor/electrolyte interface will be critical if a stable PEC-based, water-splitting system is to be developed. We have studied the stability of the p-$GaInP_2$ electrode in aqueous electrolytes of different pHs. To find the optimum operating conditions for the p-$GaInP_2$ photocathode, the electrochemical behavior of p-$GaInP_2$ was studied in 10 **M** KOH, 3 **M** H_2SO_4, and a phosphate buffer of pH=7. Of particular interest is the electrochemical behavior of the illuminated electrode under both open-circuit conditions and cathodic polarization where hydrogen evolution would occur.

Our results show that upon illumination, anodic processes increase. The effect of light on the anodic current density is greatest in 10 **M** KOH, less pronounced in neutral solution, and only slight in 3 **M** H_2SO_4. It should be noted, that under illumination the electronic transition of promoting an electron from the valance band to the conduction band is a bond-breaking transformation in these materials. The electron is promoted from a bonding orbital to an anti-bonding orbital. This bond breaking under illumination increases the susceptibility of the surface to corrosion, giving rise to an increase in the anodic current.

A potentiodynamic test in 3 **M** H_2SO_4 (Figure 1) showed the onset of the anodic current at ~-0.05 V, which is a much more positive potential than in 10 **M** KOH. The electrode was passive up to 0.25 V when anodic current density began rapidly increasing with potential. Upon illumination, the cathodic current density was almost constant with potential, indicating a light-limited photocurrent. Unlike what was observed in 10 **M** KOH, the onset of the anodic current was seen at ~0.180 V, which represents a shift to a more positive potential as compared to the dark. The anodic current densities were only slightly higher than those in the dark, but much lower than the anodic current densities observed for p-$GaInP_2$ in 10 **M** KOH solution.

The cathodic current density transients in 3 **M** H_2SO_4 are shown in Figure 2. At -0.15 V the transient showed a relatively low initial value of 20 mA/cm^2, which rapidly decayed with time. At -0.8 V, the initial cathodic current density was ~110 mA/cm^2 and remained almost constant throughout the experiment. A similar current-density transient was observed for a bias of -2.0 V. The current density of 120 mA/cm^2 observed in this experiment was almost the same as that observed in 10 **M** KOH at the same potential. This indicates the value of the light-limited saturated photocurrent density under the illumination intensity that was used.

In summary, this semiconductor is susceptible to corrosion in the dark in all investigated solutions. Upon illumination, anodic processes grow. Potentiodynamic tests revealed the onset of the anodic current at -1.55 V, -1 V, and -0.05 V in 10 M KOH, 3 M H_2SO_4, and a pH=7 phosphate buffer, respectively. In 10 M KOH, under cathodic polarization, the p-$GaInP_2$ electrode showed a photo-limited current density, however, the current slowly decreased with time due to precipitation of indium-enriched oxide. In neutral solution, the p-$GaInP_2$ is covered by a semi-insulating oxide film, and the observed cathodic photocurrent densities were much lower than those in 10 M KOH and 3 M H_2SO_4. For the p-$GaInP_2$ electrode in 3 M H_2SO_4, the anodic process can be inhibited under relatively low cathodic potentials, giving rise to a stabilized electrode and a stable photocurrent for hydrogen evolution. Our conclusion is that 3 M H_2SO_4 is the solution of choice for photoelectrolysis using p-$GaInP_2$ semiconductor electrodes.

Water Splitting using III-V Tandem Cells Configuration

The first successful direct electrolysis device based on a novel integrated monolithic PEC/PV device showed outstanding hydrogen production efficiency. The basic structure of the device is shown in figure 3. This device is patterned after the well known $GaInP_2$/GaAs p/n,p/n tandem cell device grown at NREL. The solid state tandem cell consists of a gallium arsenide (GaAs) bottom cell connected to a gallium indium phosphide ($GaInP_2$) top cell via a tunnel diode interconnect. Our device differs from the standard solid state tandem cell in that a PEC Schottky type junction has replaced the top p/n junction. This device then is a PEC Schottky barrier device, voltage biased with an integrated PV device. The top junction bandgap of the $GaInP_2$ at 1.83 volts is designed to absorb the visible portion of the solar spectrum and the bottom GaAs junction (bandgap of 1.42 eV) absorbs the near infrared portion of the spectrum transmitted through the top junction. Operationally, under illumination, electrons flow towards the surface and holes towards the back ohmic contact.

For this device configuration to work properly, the GaAs cell must provide sufficient voltage to overcome the bandedge mismatch between the $GaInP_2$ and the water redox reactions and also provide additional voltage to overcome any overvoltage losses from the hydrogen and oxygen evolution reactions.

A photocurrent voltage curve for the mixed PEC/PV device is given in figure 4. Note that the onset of hydrogen occurs before short circuit, indicating a spontaneous water splitting reaction . The efficiency (η) for hydrogen production is calculated using the equation η=(power out)/(power in). The input power is the incident light intensity of 100 mW/cm^2. For the output power, assuming 100% photocurrent electrolysis efficiency, the hydrogen production photocurrent of 11.2 mA/cm^2 is multiplied by 1.23 volts, the ideal fuel cell limit at 25 C. The hydrogen production efficiency calculated by this method is 13.7%.

Photoelectrolysis of HBr and HI Utilizing the Monolithic Combined PV/Photoelectrochemical Device.

We have also used this PV/PEC device to demonstrate the photoelectrolysis of HBr and HI. As expected, this system splits these acids directly upon illumination, using light as the only energy input. In addition, in contrast to water splitting, the device can simultaneously produce electrical energy. In this case, the device not only can produce chemicals, but also electrical energy. The HBr cell operating at zero bias and a light intensity of 380 mW/cm^2 showed a photocurrent

density of 37 mA/cm^2 corresponding to 8.1% light to chemical conversion efficiency. The HI cell operating at zero bias and a light intensity of 106 mW/cm^2 showed a photocurrent density of 8.5 mA/cm^2 corresponding to a 2.6% light to chemical conversion efficiency.

Surface Modification Studies

The suppression of corrosion and the control of the energetics is of paramount importance for the development of a viable photoelectrochemical water splitting system. Based on our results on the corrosion of $GaInP_2$, we have initiated work towards the prevention/suppression of photo-corrosion and photooxidation of this material. We are studying three parallel approaches, each involving semiconductor surface modification. These three approaches are: 1) adsorption of alkanethiols, 2) alkylation and 3) adsorption of transition metal ions. The adsorption of two transition metal ions, iron and vanadium, showed shifts in the energetics of the photocurrent onset of $GaInP_2$. The shift of the photocurrent for iron is shown in figure 5.

Amorphous Silicon Systems

There are two main technological problems that must be solved before an α-Si based system could operate as a photoelectrolysis device: 1) its bandgap is insufficient to effect the decomposition of water and 2) α-Si is not stable in contact with aqueous electrolytes, it decomposes within a few minutes. The first issue is easily addressed because current state-of-the art α-Si triple junction devices can have voltages greater than 1.8 volts (even up to 2.3v), which is sufficient for water splitting. Stabilized efficiency for these systems can be greater than 10%.

For this work we are partnering with Energy Conversion Devices to grow samples specifically for water splitting. For these samples, two areas of research were of interest to us: 1) a device structures that pushed electrons toward the semiconductor/electrolyte interface and 2) protective coatings for the surface that offered minimum light absorption, but stability at high and low pH. The reason we want electrons to be driven toward the semiconductor electrolyte interface is because we want hydrogen to be evolved from the illuminated surface. Of the two reactions involved in water splitting (hydrogen evolution and oxygen evolution), hydrogen evolution is the easiest, requiring the least amount a catalyst and it has the lowest overvoltage. We also expect that it will be easier to protect a surface under reducing conditions than under oxidizing conditions.

Growing a-Si multijunctions specifically for this purpose, involves growing the a-Si layers in reverse order than what is usually done for the solid state device. Instead of growing the layers in the order n-i-p, they need to be grown in the order p-i-n. We have contracted with ECD to grow this new design.

The results of our latest samples from the subcontract is shown in figure 6. Note that the efficiency for water splitting is rather low, and the curve shows that there is a good deal of series resistance with in the cell. Also, this samples did not have the a-SiC surface protective layer, so some of the resistance could be due to a surface oxide layer being formed. However, we are very encouraged with this result. ECD has raised the efficiency of this reverse design from around 4% to over 9% in less than a year (with very little funding). The PV efficiency is approaching that of the standard PV cells and this should translate to better photoelectrolysis efficiency. We expect a much improvement in this system in the coming year.

Plans for Future Work:

In general, our future work will involve: the identification of new materials and the growth of promising multi-junction systems including designing unique multi-junction systems focused specifically on water splitting; establishment of cooperative efforts to obtain samples or development of in-house growth capabilities; and lifetime testing and efficiency measurements for working systems. Since we have had good success with the III-V PV/PEC system, we intend to increase our efforts with our industrial collaborators to optimize the α-Si multi-junction systems for water splitting. We would like to bring the α-Si multi-junction systems up to the same level of excellence.

The subject of the interaction of colloidal catalysts with the various tandem cell surfaces is also a very important area for future work. More specifically, we will focus on continued investigation of the III-V material system concentrating on tailoring the tandem cell structure specifically for an aqueous environment and the energetics of the water splitting reaction. We will be evaluating various surface treatments to enhance stability and energetics. The semiconductor corrosion mechanisms will also be a point of study.

Major Barriers

In general, the major problems that must be addressed in order to produce a viable system are: stability of the semiconductor/electrolyte interface, and system energetics. Materials and catalysts must be found that protect the semiconductor surface, but allow electrons to pass through unimpeded. While we lack full understanding of the fundamental characteristics of the semiconductor/electrolyte interface, considerable progress has been made. For the a-Si multi-junction cells the design of the water-splitting cells must be optimized for maximum efficiency. For the III-V systems, to maximize their efficiency, materials and designs must be identified for lower voltage, higher current applications. Promising new systems currently under development may directly address this issue.

Figure Captions

Figure 1. Potentiodynamic curves for p-$GaInP_2$ in 3 **M** H_2SO_4. The E^0 for hydrogen evolution is indicated by the dashed line.

Figure 2. Cathodic photocurrent density transients for p-$GaInP_2$ in 3 **M** H_2SO_4.

Figure 3 Schematic of monolithic PEC/PV device

Figure 4. Current voltage characteristics for p-$GaInP_2$(Pt)/TJ/GaAs electrode in 3 **M** H_2SO_4 under white light illumination.

Figure 5. Current voltage characteristics for p-$GaInP_2$ electrode in 3 **M** H_2SO_4 under white light illumination with and without iron.

Figure 6. Current voltage curve for a-Si triple cell electrode in 3 **M** H_2SO_4 under white light illumination.

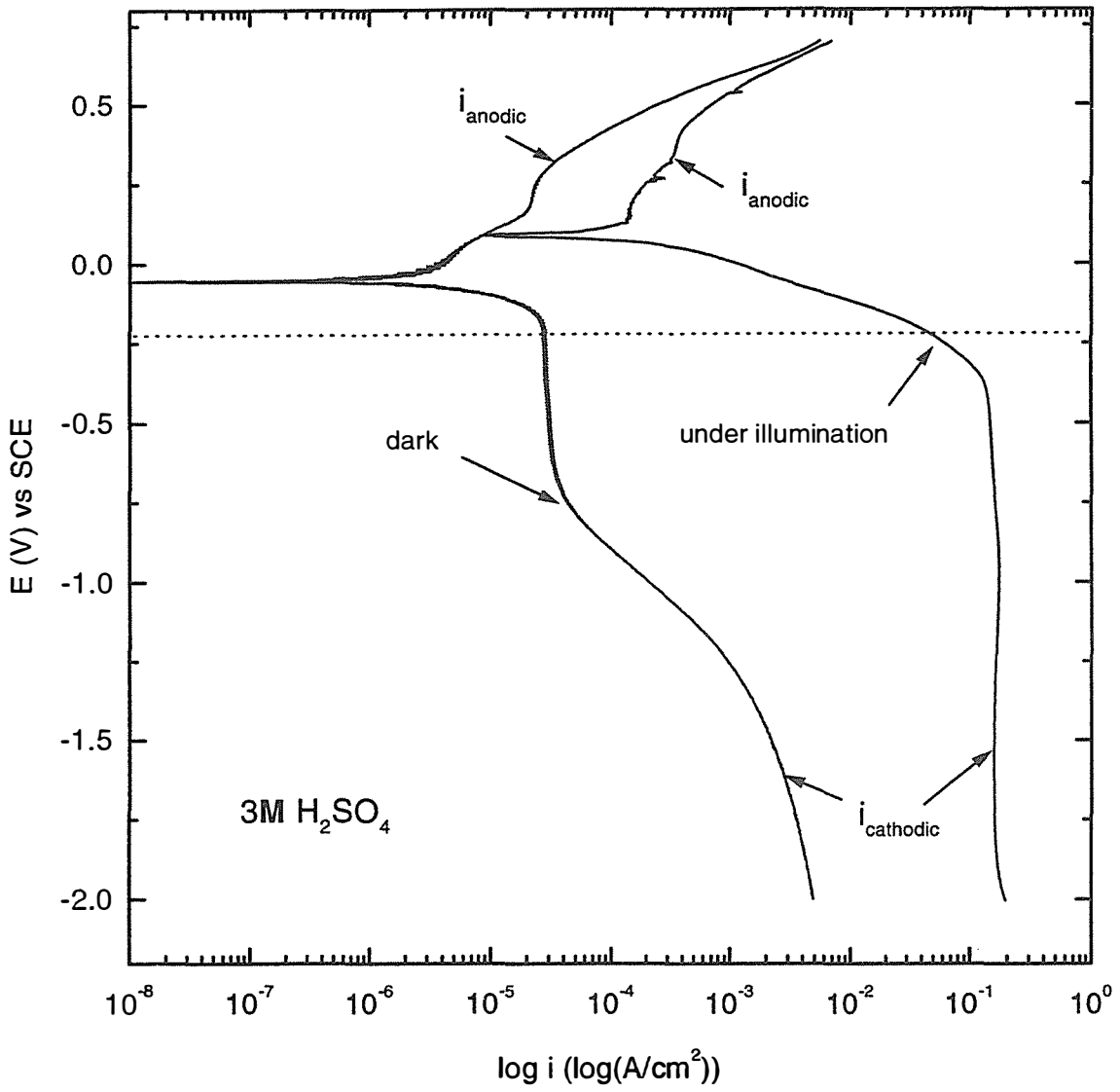
0.5
0.0
-0.5
-1.0
-1.5
-2.0
E (V) vs SCE
i_{anodic}
i_{anodic}
dark
under illumination
3M H_2SO_4
$i_{cathodic}$
10^{-8}
10^{-7}
10^{-6}
10^{-5}
10^{-4}
10^{-3}
10^{-2}
10^{-1}
10^{0}
log i (log(A/cm^2))

Figure 1

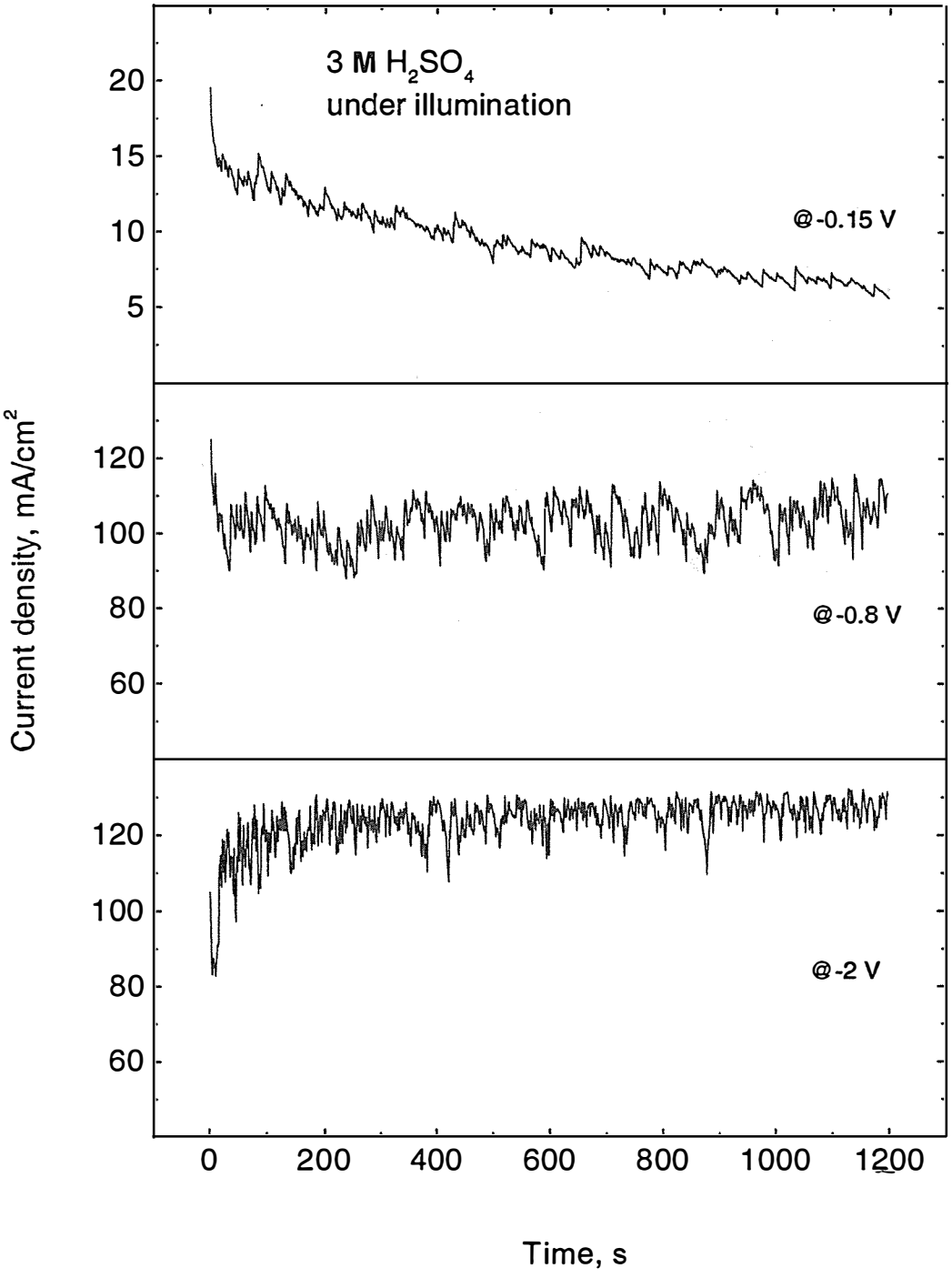
3 M H_2SO_4
under illumination
@-0.15 V
@-0.8 V
@-2 V
Current density, mA/cm^2
Time, s
20
15
10
5
120
100
80
60
120
100
80
60
0
200
400
600
800
1000
1200

Figure 2

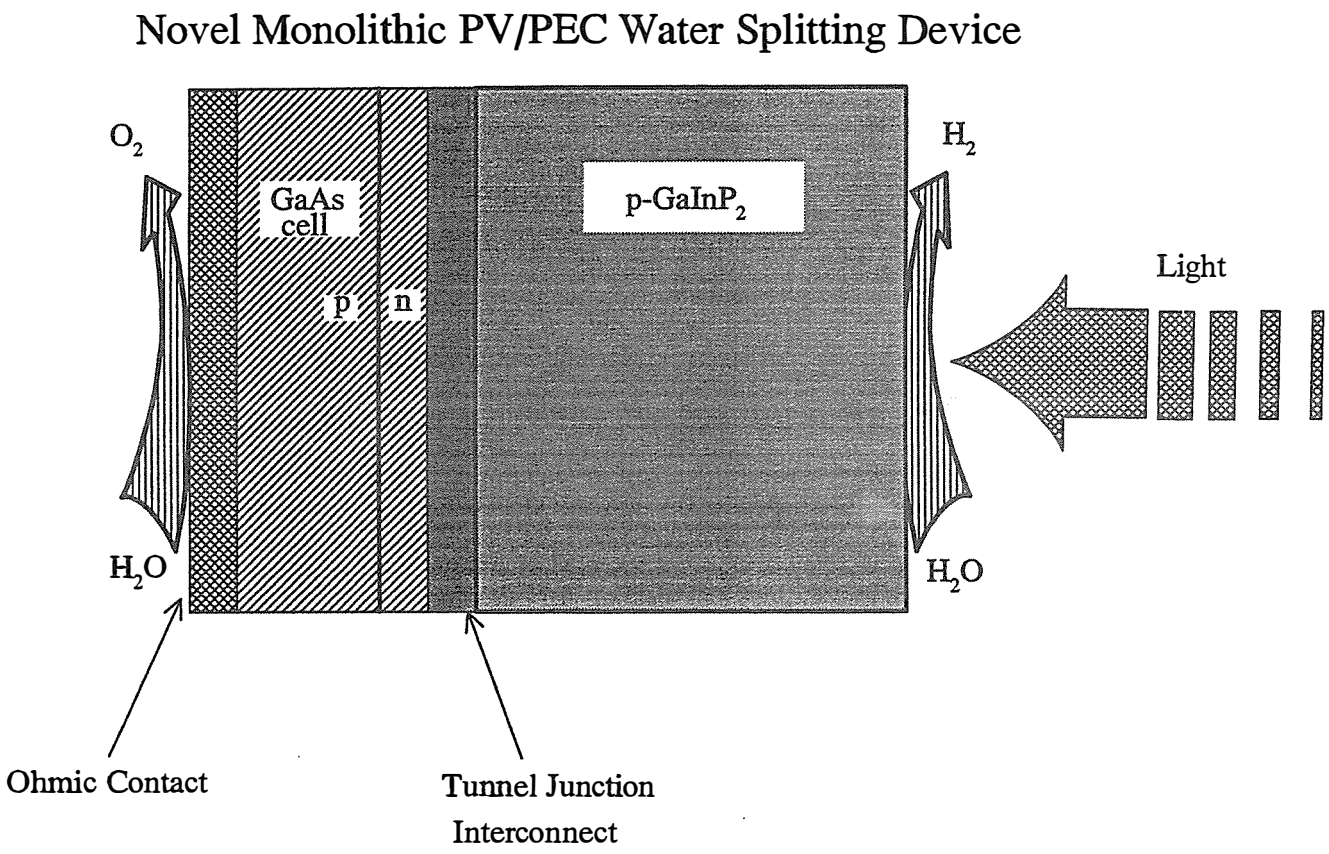
Novel Monolithic PV/PEC Water Splitting Device
O_2
H_2
GaAs cell
p
n
p-GaInP$_2$
Light
H_2O
H_2O
Ohmic Contact
Tunnel Junction
Interconnect

Figure 3

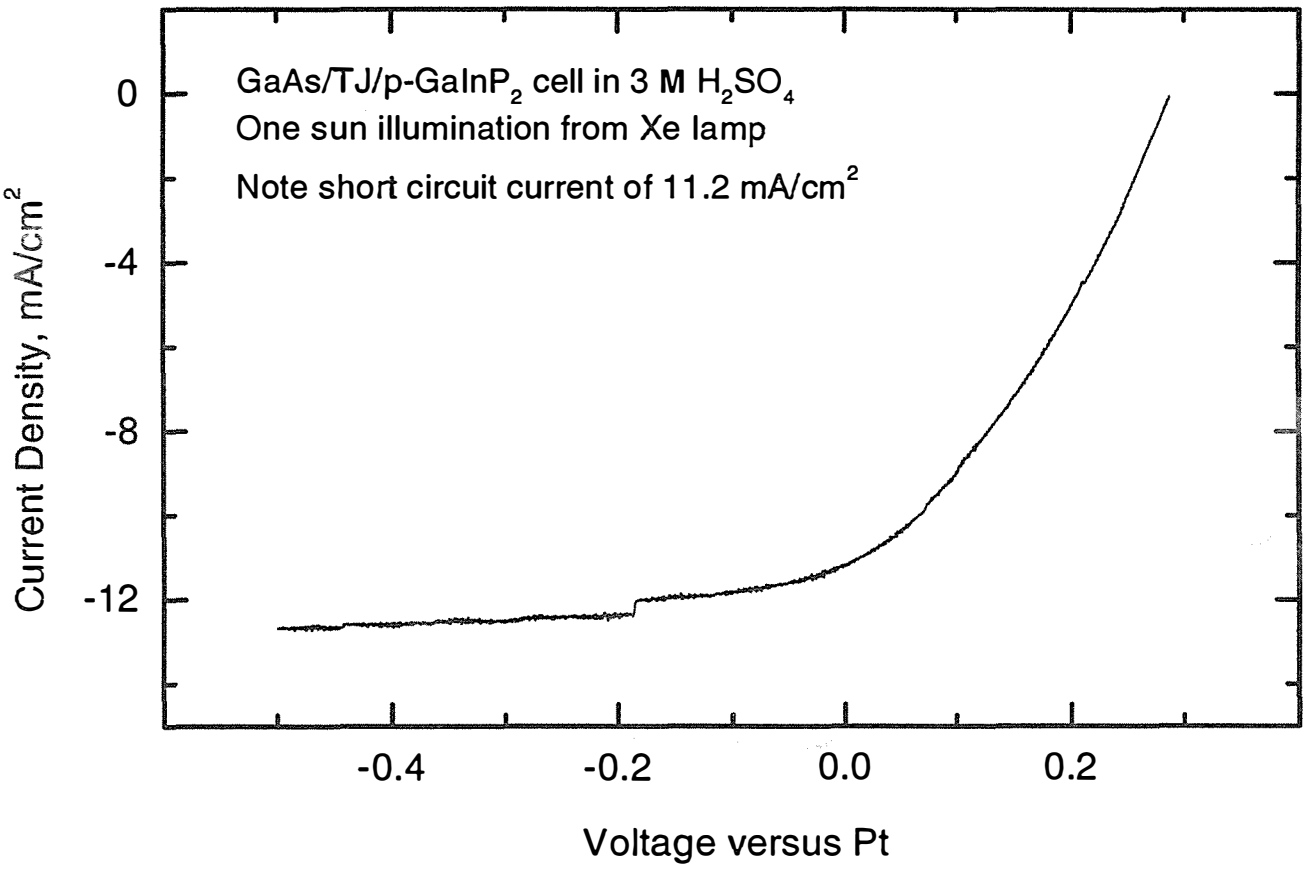
GaAs/TJ/p-GaInP2 cell in 3 M H2SO4
One sun illumination from Xe lamp
Note short circuit current of 11.2 mA/cm2
Current Density, mA/cm2
0
-4
-8
-12
-0.4
-0.2
0.0
0.2
Voltage versus Pt

Figure 4

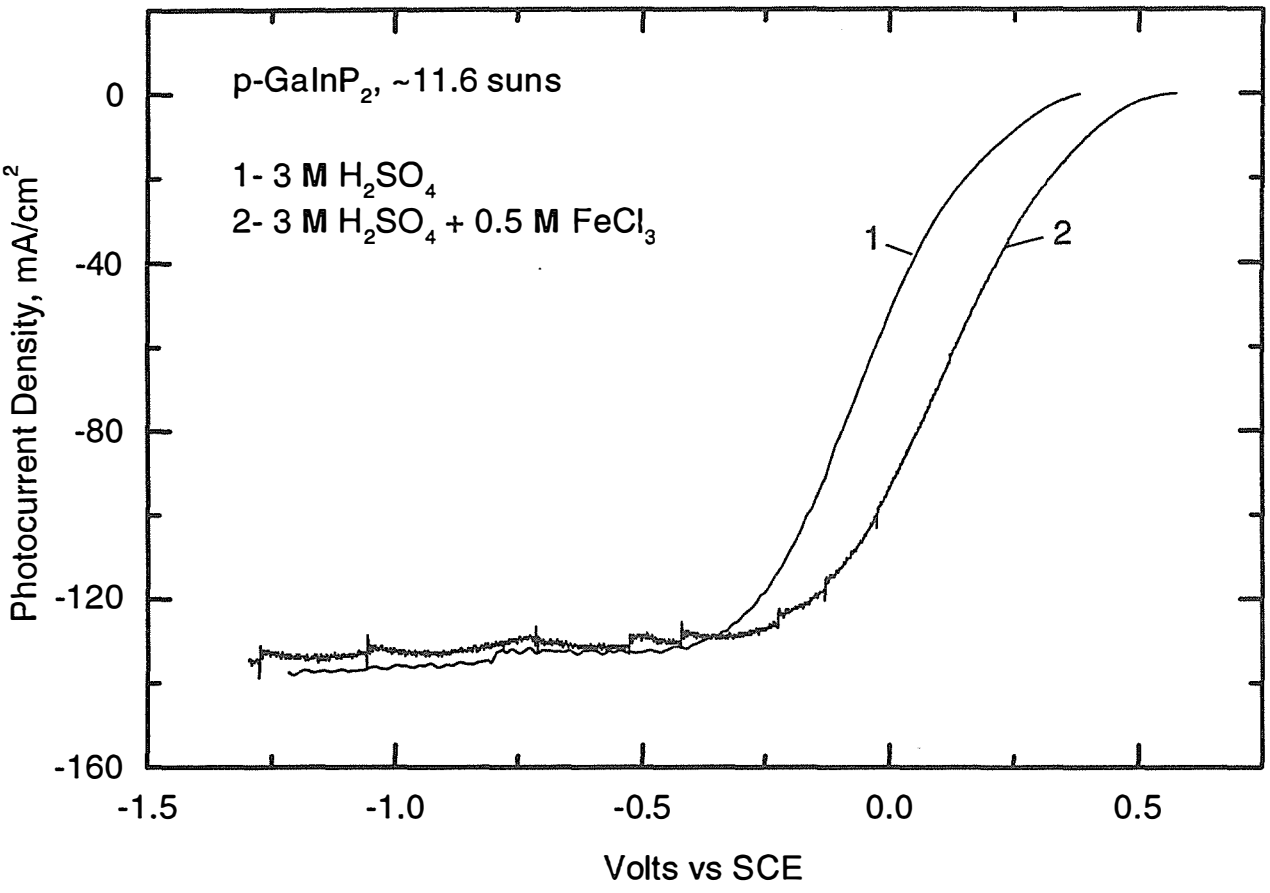
p-GaInP2, ~11.6 suns
1- 3 M H2SO4
2- 3 M H2SO4 + 0.5 M FeCl3
1
2
0
-40
-80
-120
-160
-1.5
-1.0
-0.5
0.0
0.5
Photocurrent Density, mA/cm2
Volts vs SCE

Figure 5

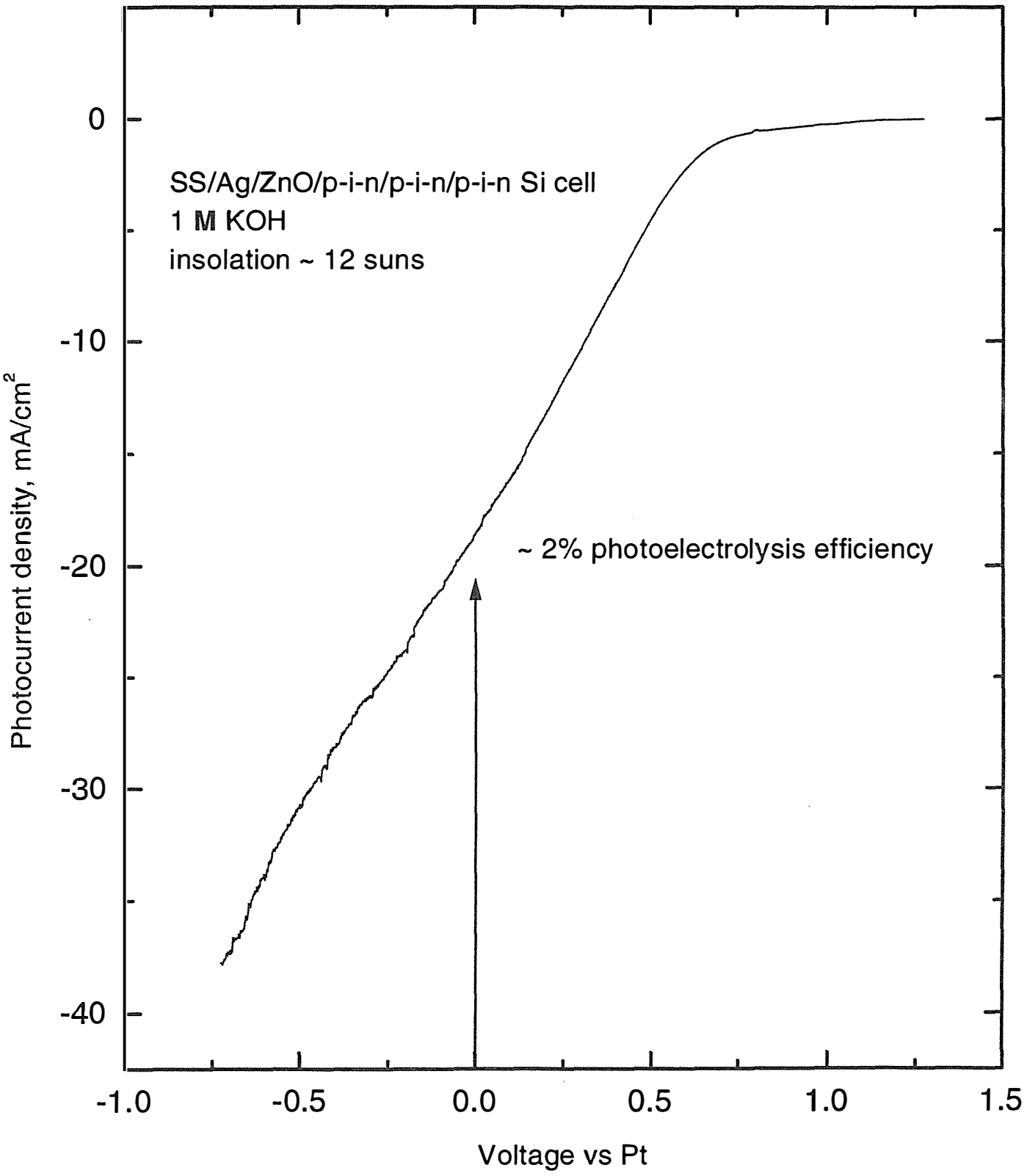
SS/Ag/ZnO/p-i-n/p-i-n/p-i-n Si cell
1 M KOH
insolation ~ 12 suns
~ 2% photoelectrolysis efficiency
Photocurrent density, mA/cm2
0
-10
-20
-30
-40
-1.0
-0.5
0.0
0.5
1.0
1.5
Voltage vs Pt

Figure 6

DEVELOPMENT OF HIGH PERFORMANCE PROTON-CONDUCTING SOLID ELECTROLYTES

Clovis A. Linkous
Robert W. Kopitzke
Florida Solar Energy Center
1679 Clearlake Road
Cocoa, FL 32922-5703

Abstract

This work seeks to improve the efficiency of fuel cell and electrolyzer operation by developing solid electrolytes that will function at higher temperatures. Two objectives were pursued: 1) determine the mechanism of hydrolytic decomposition of aromatic sulfonic acid ionomers, with the intent of identifying structural weaknesses that can be avoided in future materials; and 2) identify new directions in solid electrolyte development. After evaluating a number of aromatic sulfonates, it became apparent that no common mechanism was going to be found; instead, each polymer had its own sequence of degradation steps, involving some combination of de-sulfonation and/or chain scission. For electrochemical cell operation at temperatures > 200° C, it will be necessary to develop solid electrolytes that do not require sulfonic acids and do not require water to maintain its conductivity mechanism.

Background

Water electrolysis offers a means of making H_2 without consumption of hydrocarbon or biomass resources. Fuel cells offer a means of efficiently generating electricity from that hydrogen.

These devices have been found to operate more efficiently at higher temperature. The fundamental reason is that, like any other chemical process, the activation barriers associated with the electrode surface reactions are more easily surmounted at higher temperature. This makes for a faster rate of reaction, or higher current density, at the same overpotential. A further advantage for fuel cells is that if the cell operates at higher temperature than the boiling point of water, the electrolyte will spontaneously reject the product water resulting from the electrochemical reaction of H_2 and O_2, simplifying water management. An additional advantage for electrolyzers is that open circuit voltage, or the minimum thermodynamic voltage to drive the reaction, drops as temperature increases.

Solid electrolytes allow cell construction with much closer tolerances, especially with regard to the gap between anode and cathode. This reduces ohmic losses in the cell and alleviates containment problems. While hydroxide and lattice oxide conductors are known, most solid electrolytes employed in electrolytic H_2 technology are proton-conductors. The most common proton-conducting solid electrolytes are perfluoroalkyl sulfonic acid polymers, such as Nafion®.

It would be desirable to exploit both the ideas of solid polymer electrolytes and high temperature operation. However, most proton exchange membrane (PEM) devices operate at 80° C. At higher temperature, water management problems hurt performance, and ultimately the increasing applied pressure causes degradation of the membrane at ~150° C. We conducted a considerable effort at attempting to raise the decomposition temperature of the PEM polymer electrolyte. Toward this end, several aromatic sulfonic acid polymers were synthesized and characterized (Linkous 1997). These were polyetheretherketone (PEEK), polyethersulfone (PES), poly(phenylquinoxaline (PPQ), and poly(benzimidazole), PBI. Their base structures, along with that of Nafion, are shown in Figure 1.

Thermohydrolytic analysis on the polymers was performed and compared to conventional dry thermogravimetry. The susceptibility of theses polymers toward hydrolytic attack was certainly greater than for autoxidation (dry air combustion), especially for PPQ (Kopitzke 1998). The results of the hydrolytic degradation indicated that our aromatic PEM sulfonates could approach, but not exceed, the thermohydrolytic resilience demonstrated by Nafion. The remaining question to answer was, what is the hydrolytic degradation mechanism of aromatic sulfonic acids? Is there some weak link in the chain that can be removed in subsequent structures? Much of the work this year was directed at answering that question.

Results and Discussion

The original thermohydrolytic steam degradation studies involved 24 hr trials at saturating steam pressure in a batch reactor. Sometimes the extent of polymer degradation was very great, exceeding 30-40% of the original sample weight, representing a plethora of chemical reactions. In the present work, the idea was to just reach the onset of degradation, so as to identify the most vulnerable moiety to hydrolytic attack. Consequently, the present steam trials were run under a continuous flow of Ar carrier gas that went through a water bath before contacting the polymer, ensuring a 0.5 atm of steam pressure regardless of oven temperature. It was intended to hold oven temperature at a level corresponding to just a few percent weight loss, but that was difficult

to control. Essentially, oven temperature was held at a value that resulted in some measurable level of weight loss over a few hours' time.

The effluent passed through a series of traps to condense the steam effluent and any volatile decomposition products. Acidity (pH), infrared spectroscopy, and gas chromatography/mass spectrometry were used to analyze the decomposition products. Results are shown in Table 1. Both sulfonated and plain aromatic polymer samples were examined. Nafion was included as a comparison. Percents in parentheses after the compound names refer to degree of sulfonation, i.e., one sulfonic acid group per repeating monomer unit is 100%.

Table 1. Hydrolytic Degradation Results for Aromatic Sulfonic Acid Polymers

Material	Temperature (° C)	% Weight Loss	Decomposition Products
Nafion	300	22.1	acid + "PTFE-like"
S-PEEK	350	26.1	acid + organics[1]
PEEK	350	0.40	none
PEEK	400	3.0	mild acid + organics[2]
S-PPQ (132%)	300	11.8	acid
S-PPQ (75%)	350	8.2	acid
S-PPQ (50%)	400	9.4	acid + organics[3]
S-PBI (100%)	300	17.1	acid + organics[3]

[1] 4-phenoxyphenol and 1,4-diphenoxybenzene
[2] phenol and 4-phenoxyphenol
[3] under analysis

The Nafion did not change its appearance to any extent, but a white ring formed at the reaction tube exit that was at least partially fluoroalkyl in nature. Sulfonation substantially weakened PEEK, as the underivatized material was quite resistant to attack. The predominate S-PEEK decomposition products were 4-phenoxyphenol and 1,4-diphenoxybenzene, suggesting that attack at the carbonyl linkage was most likely. Effluent from steam treatment of S-PPQ produced an acidic solution that tested positive for sulfate, but no indication of organic decomposition was evident, implying a clean de-sulfonation. While polyimides were examined early on, it was found that they could only be sulfonated as a Li salt; attempts to make the sulfonic acid via ion exchange failed, ostensibly because of hydrolytic attack on the imide linkage. Since this occurred at room temperature, there was no reason to treat them to conditions shown in Table 1 above. The PBI was susceptible to attack under comparatively mild conditions; product analysis is in progress.

Considerations in Higher Temperature Proton Conductors

There are many attributes that a solid electrolyte should possess. Among these are:

- facile H^+-conduction (> 10^{-2} S/cm)
- electrically nonconductive
- resists chemical attack in oxidizing (O_2) atmospheres
- resists chemical attack in reducing (H_2) atmospheres
- dimensionally stable
- gas impermeable
- water insoluble
- reasonable cost

The need to go to higher temperature operation puts additional requisites on the system. A recurring problem is that waters of hydration or other means of association are lost, and with them the proton conductivity. The overwhelming majority of proton conductors contain some measure of water. Invariably, the water plays a major role in the proton-conducting mechanism. This was understood by Grotthus who early on defined a "bucket brigade" mechanism for proton transfer, as opposed to a conventional " vehicle" mechanism [Kreuer 1982]. The various solid oxide conductors, such as $H_3Mo_{12}PO_{40}\bullet 29H_2O$, $Zr(HPO_4)_2\bullet H_2O$, $H_3O^+\beta"Al_2O_3$, and $HUO_2PO_4\bullet 4H_2O$, all seem to lose their water between 100-200° C, with accompanying loss of conductivity. The Grotthus mechanism is apparently vital for good H^+ conductivity, but water is typically bonded so weakly that it cannot remain in the bulk of the electrolyte at high temperature.

Our criteria for making new higher temperature proton conductors are:

- maintain Grotthus proton transport mechanism
- avoid water as fundamental player in proton transport
- utilize tunnel or open planar structure.
- line conduction channels with strongly bonded basic species (-OH, -NH_2, -SH, etc.)
- possibly include acid and base functionalities

Conclusion

All sulfonic acid polymers are limited by the saturated steam requirement for maintaining good proton conductivity. As temperature rises, the absolute saturating steam pressure reaches a point where desulfonation is favored. Nevertheless, the various polymers each have their own peculiar hydrolytic decomposition characteristics. For S-PEEK, desulfonation appears to catalyze chain scission, thereby coupling the two reactions. For S-PPQ, clean desulfonation can occur, leaving the polymer chain intact. To increase operating temperature over 150-200° C, sulfonic acids will have to be set aside in favor of materials that do not contain water or otherwise require it to facilitate proton conduction.

Acknowledgements

The authors would like to thank Dr. Rich Leipfried from Victrex, Inc., Dr. Raj Savarian from Amoco Performance Products, Dr. Mike Sansone and Richard Tucker from Hoechst-Celanese,

Dr. Paul Hergenrother from NASA-Langley, and Dr. Robert Kovar from Foster-Miller for their support and encouragement. Financial support from the Department of Energy, Office of Solar Thermal, Biomass Power, and Hydrogen Technologies is gratefully acknowledged.

References

Kreuer, K.D., Rabenau, A., and Weppner, W. 1982. *Angew. Chem., Int. Ed. Engl.*, 21:208.

Kopitzke, R.W., Linkous, C.A., and Nelson, G.L. 1998. "Sulfonation of a Poly (phenylquinoxaline) Film." *J. Polymer Sci. A: Polymer Chem.*, 36:1197-1199.

Linkous, C.A. and Kopitzke, R.W. 1997. "Development of Solid Electrolytes for Water Electrolysis at Higher Temperature." In *Proceedings of the 1997 U.S. DOE Hydrogen Program Review.*

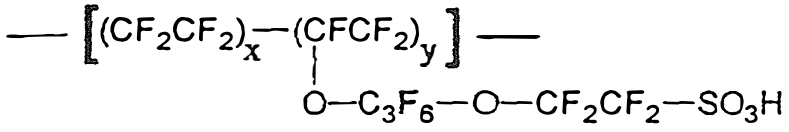

Nafion (TM)

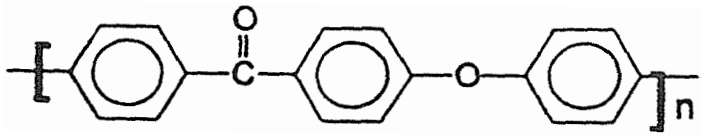

Polyetheretherketone (PEEK)

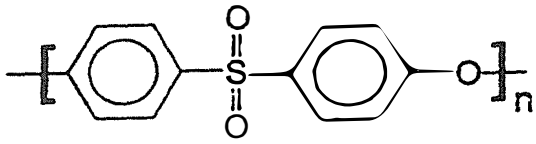

Polyethersulfone (PES)

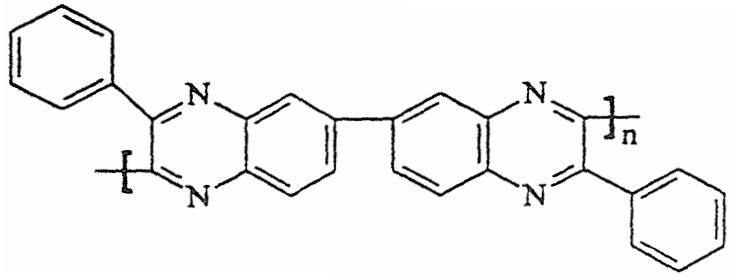

Polyphenylquinoxaline (PPQ)

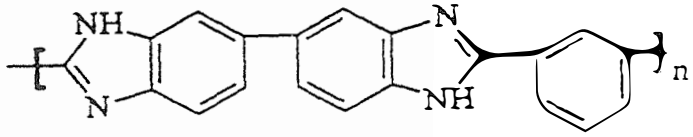

Polybenzimidazole (PBI)

Figure 1. Structures of Nafion® vs. Aromatic Sulfonic Acid Polymers.

A POLYMER ELECTROLYTE FUEL CELL STACK FOR STATIONARY POWER GENERATION FROM HYDROGEN FUEL

Mahlon S. Wilson, Steffen Møller-Holst, Daniel M. Webb,
Christine Zawodzinski and Shimshon Gottesfeld
Materials Science and Technology Division, MS D429
Los Alamos National Laboratory, Los Alamos, NM 87545

Abstract

Our objective is to develop and demonstrate a 4 kW, hydrogen-fueled polymer electrolyte fuel cell (PEFC) stack, based on non-machined stainless steel hardware and on membrane/electrode assemblies (MEAs) of low catalyst loadings. The stack is designed to operate at ambient pressure on the air-side and can accommodate operation at higher fuel pressures, if so required. This is to be accomplished by working jointly with a fuel cell stack manufacturer, based on a CRADA. The performance goals are 57% energy conversion efficiency hydrogen-to-electricity (DC) at a power density of 0.9 kW/liter for stack operating at ambient inlet pressures. The cost goal is $600/kW, based on present materials costs.

Technical Goals

Our main Tasks for FY-98 are centered on the fabrication of a 4 kW stainless steel ambient pressure Sstack. The first step in this effort is work with a single cell of the new, ambient pressure 300 cm^2 design, followed by the demonstration of a short, 3-5 cell stainless steel ambient pressure stack, demonstration of a 4 kW stack, and bench testing of a system which would include complete air and water management for the 4 kW stack, targeting parasitic power levels lower than 10%.

Major Barriers to Meeting Technical Goals

An important barrier to implementation of low cost, non-machined metal hardware technology in PEFC stacks, is the potential susceptibility of the metal or alloy selected to corrosion or to surface passivation under some combination of conditions likely to occur, for a given stack design, on either cathode or anode sides. Effective water management needs to be achieved, particularly at ambient pressure. While we have previously demonstrated relatively high performance ambient pressure 8 and 12 cell stacks with 100 cm^2 active areas and machined graphite hardware, the new, larger (300 cm^2 active area) metal hardware substantially alters many subtle factors that influence cell performance. To a large extent, the system needs to be re-optimized. Development of novel stack technology requires solving a variety of engineering issues such as effective component design, stack sealing, and (lab-scale) fabrication of a significant number of stack components. We were initially delayed when critical components were delivered months after originally scheduled. Unfortunately, these components were not to specifications and were not uniformly consistent. A considerable amount of further effort has been expended in designing around and/or accommodating the deficiencies of these critical components.

Approach/Background

The approach of this project is to integrate recent PEFC technology developments at LANL with stack development activities in industry, in order to fabricate and demonstrate a manufacturable, low-cost/high-performance hydrogen/air fuel cell stack operating at

ambient inlet pressures for generation of electric power from hydrogen. The stack is to be based on MEAs (patents issued) and non-machined stainless steel hardware (patent allowed for the pressurized embodiment), developed at LANL. A co-operative research and development agreement (CRADA) between LANL and an industrial partner includes tasks ranging from the exchange, testing and optimization of membrane-electrode assemblies of larger areas, through development and demonstration of manufacturable flow-fields, electrode backing and bipolar plate components, to testing of stacks at the 3-5 cell level and finally, stack demonstration at the 4-5 kW level.

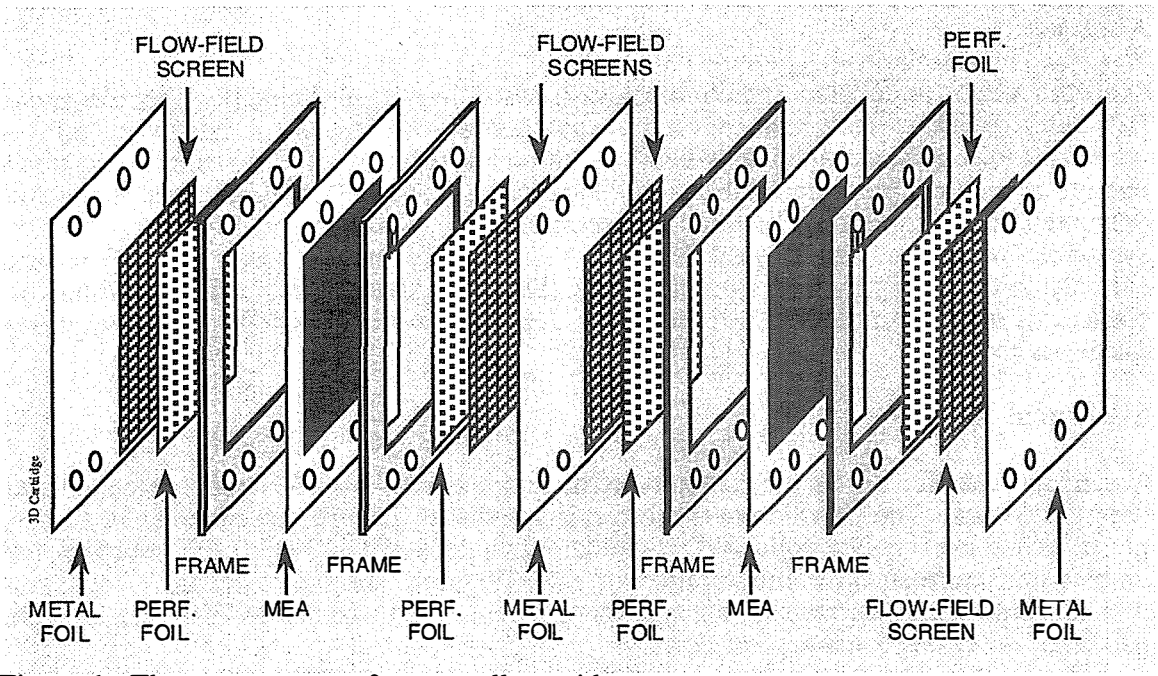

Figure 1. The components of a two-cell cartridge.

Past Results

Past results were oriented around a stack designed for pressurized operation utilizing low-cost 316 stainless steel wire screens and foils as gas flow-fields/bipolar plates. A 100 cm^2 single cell was operated for 2000 hours of continuous testing using such 316 stainless steel screen/foil hardware. There was no significant drop in cell performance. Specifically, no rise was recorded in the high frequency resistance after 2000 hours of continuous operation. Tests with similar stainless steel hardware were repeated by industry under ambient pressure conditions. We developed a two-cell "cartridge" configuration, the components of which are shown in Figure 1. Relatively coarse wire screens are used as the flow-fields and, in a new development, thin perforated foils are used instead of the original fine screens to prevent the membrane electrode assembly from impalement by the flow-field screen. Thin metal foils function as the gas-tight separators between the flow-field elements and plastic frames provide sealing surfaces and manifolding for the reactant supply to the individual flow-fields through channels formed in the corners. The "corner-to-corner" flow that was thus attained provided effective reactant distribution, as indicated by the good performances attained with only two times stoichiometric air-flow.

Figure 2 provides a possible explanation of the success of the corner-to-corner flow configuration. Since reactant flow can not proceed in a diagonal direction between neighboring "elements" of the square weave wire screen, it must still assume a staircase path to proceed directly form one opposing corner to the other. The effective length of this

staircase path is the same as straight down and straight across or of any progressive path. Consequently, the flow distribution to all areas is relatively uniform.

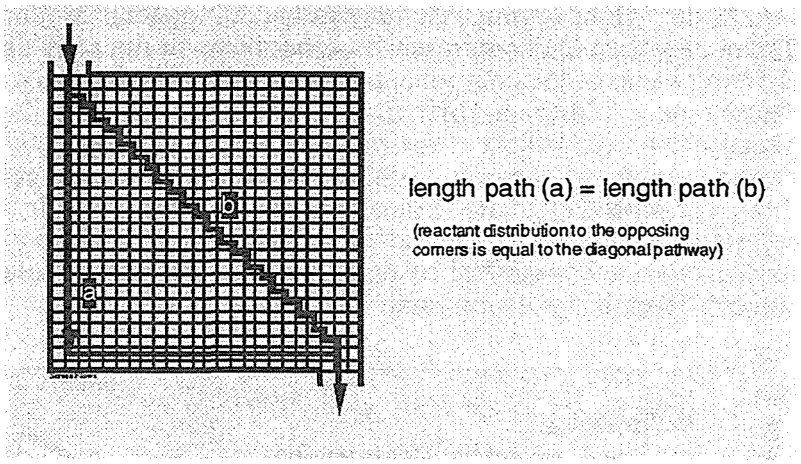

Figure 2. The corner-to-corner reactant flow scheme.

One of the developments not reported last year was the replacement of the fine screen used to protect the MEA from the flow-field screen with a fine perforated foil. One of the difficulties with the fine screen shown in Figure 3 was that water tended to collect within the grids unless the screens were rendered hydrophobic by heat-treatment with PTFE, and then it was necessary to abrade the sides placed against the carbon-cloth backings of the MEAs for conductivity. Despite all this, some stability problems still occurred. Our solution was to replace the fine screens with thin perforated foils that were about 50% open area with 1 mm diameter staggered perforations. Under compression, the relatively soft carbon cloth backing deformed somewhat into the openings in the foil and were immediately adjacent to but still protected from the flow-field screen. As such, no "cells" were available for water entrapment and stability was attained without requiring any treatments. The perforated foils in this case are prepared by photolithography techniques utilizing acid-etching so large scale production can possibly be competitive with standard mechanical perforation plus final shaping.

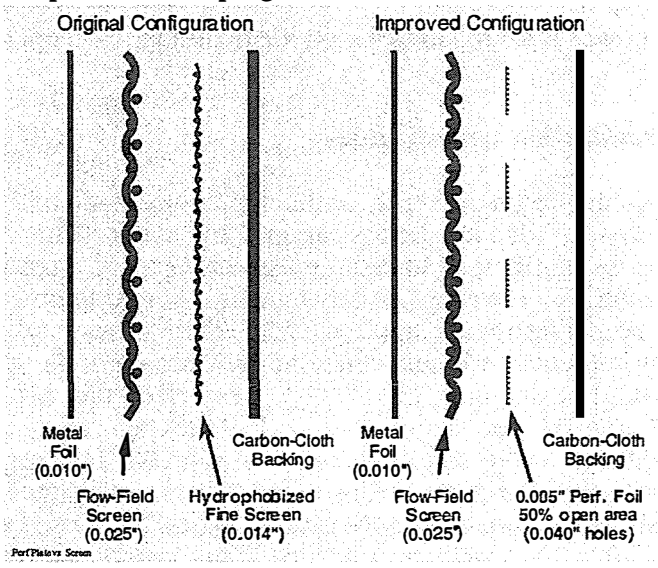

Figure 3. Comparison of cell configurations using either treated fine screens or fine perforated foils.

Several four cell stacks were assembled using the perforated foils and two 2-cell cartridges sandwiched around a cooling plate. Some difficulties were encountered first with shearing of the membranes in the MEAs during assembly as the components around the periphery settled at a different rate than the compressible components in the active area. This was solved by overlapping some of the components in a manner that protected the vulnerable region of the membrane. Additional difficulties were obtained using the water-cooled cooling plate because the cells adjacent the plate dropped in performance significantly whenever the cooling pump switched on. Similar difficulties have been reported in other stack designs, but were probably greatly exacerbated with our thin foil/low thermal mass design. Four-cell stacks that provided individual cell performances close to single cells or double cell cartridges were accomplished by carefully moderating the coolant supply such that the temperature differentials were minimal.

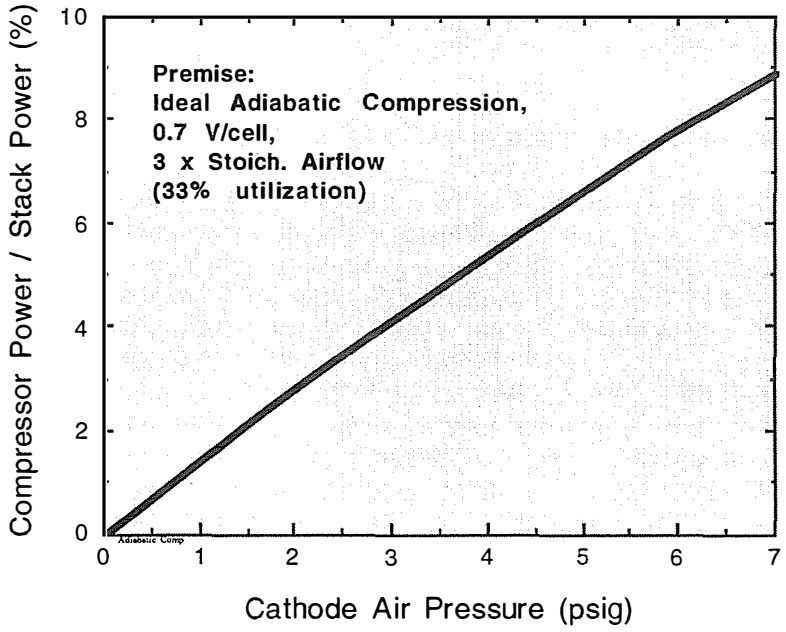

Figure 4. Parasitic power requirements for an ideal adiabatic compressor as a function of air-side pressure.

Current Year Accomplishments/Status

Efforts this year have been redirected to an ambient pressure stack and the cell size has been scaled up to active area of 300 cm^2 for the target 4 kW stack. This redirection originally resulted from a programmatic need to coordinate testing with a mobile system requiring ambient pressure operation, however, the advantages inherent to ambient air operation are also beneficial for some stationary applications. The primary advantage is the lower parasitic power requirements with near-ambient pressure cathode operation compared to pressurized operation. For example, the 30 psig pressurized fuel cell system operating on hydrogen demonstrated by one major fuel cell developer requires about 20% of the electrical power produced to operate the system auxiliaries. The largest power loss is the air compressor even though the system runs at an efficient two times stoichiometric flow. The situation would be even worse except that an expander is used on the air effluent to recover as much of the PV work as possible. This compressor/expander package is becoming a major technical and cost challenge in fuel cell system design. Neither turbine nor positive displacement (e.g. rotary scroll) compressor/expander systems promise to be

particularly efficient (ca. 50% each step) or inexpensive. Thus, substantial complexity, cost and power savings can conceivably be realized by operating at ambient pressure on the air side. Others, such as the Shatz Energy Research Center and International Fuel Cells have developed near ambient pressure systems, and we are correspondingly developing non-machined fuel cell hardware based on 316 stainless steel as before, but now the flow-field design must be amenable to ambient pressure operation. As such, we have needed to evolve our earlier pressurized foil and screen design such that the reactant pressure drop on the air side is extremely low. We are targeting pressure drops of about 1" H_2O or less (there are about 28" H_2O per psi). The desire for such low pressure drops can be understood by considering Figure 4. This figure depicts the ideal adiabatic power requirements as a percentage of total stack power to compress air at three times stoichiometric flow to the corresponding pressures of the abscissa. If, for example, a pressure of only two psig was required to push the appropriate amount of air through a fuel cell stack and water-recovery condenser, then about 3% of the stack power would ideally be required for the 2 psig compression. In reality, a bladed compressor would be only about 50% efficient, so already 6% of the stack power is required just for a seemingly modest amount of pressure. Hence, we are attempting to keep the total pressure required below about 3" H_2O.

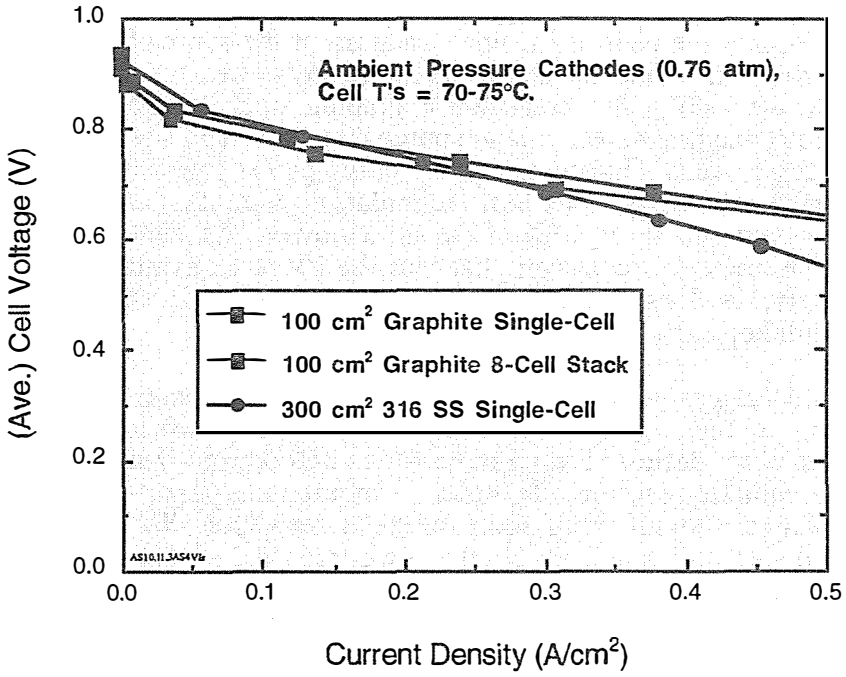

Figure 5. Polarization curves comparing the ambient pressure performance of the new 300 cm^2 metal hardware design to smaller, optimized graphite cells and stacks.

In addition to very low pressure drops, the new metal hardware configuration provides a pitch per unit cell of just 2.2 mm (including cooling). With a current density of 0.3 A/cm^2 at 0.7V (57% energy conversion efficiency hydrogen-to-electricity (DC)), the "active" volumetric power density approaches 1 kW/liter, which compares favorably with pressurized systems. Figure 5 depicts a polarization curve for a 300 cm^2 metal hardware single cell of the new design compared to results we obtained previously with a 100 cm^2 active area ambient pressure system that used relatively thick graphite plates. As can be observed, we nearly replicate the performance of the smaller cells/stack at 0.7 V although the larger cells drop off more quickly which may reflect less uniform reactant distribution in

a relatively non-optimized configuration. Note that these curves are at an ambient pressure of 0.76 atm because our laboratory is at an altitude of 7300 ft (2250 m). Between the water vapor pressure and the diminished total pressure, operation at sea level would increase the oxygen partial pressure in the plenum about 60%, so considerably higher performances may be attained under conditions that are, in most cases, more relevant.

We have had some difficulties identifying blowers that provide sufficient pressures and flowrates at reasonable power levels. Most of the low flowrate commercial DC blowers are inadequate because they are invariably designed with forward swept blades for maximum airflow at zero pressure head and so are particularly inefficient at even the modest 2" H_2O pressure. As a compromise, we are using a somewhat oversized backward swept controllable AC blower, that is still sufficiently efficient (at 2" H_2O and about 20 cfm for the 4 kW stack) that the parasitic power requirement should be comfortably less than 2% of the stack power.

Currently, the other significant parasitic power draws are for a hydrogen recirculation system and for the fan for the air effluent condenser. The former is required because in a dead-ended hydrogen feed stack the hydrogen feed tends to become humidified within the cell but condensate is left behind in the flow-field as the hydrogen reacts away. If the condensate collection is excessive, it blocks hydrogen access and cell performance suffers. One approach, employed in the hydrogen fueled Ballard bus, is to use a venturi ejector on the hydrogen supply line to instill a small vacuum at the stack effluent such that some circulation is achieved. While this doesn't consume any power, it is difficult and expensive to implement on the 4 kW scale. In the 400 W graphite stack depicted in Figure 5, we were able to use a small diaphragm recirculation pump that consumed less than 2 W (or less than 0.5% of the stack power). Unfortunately, the pump power requirement does not scale to the 4 kW level as efficiently. The best recirculation pump that we have thus far found would require about 100 W or 2.5% of the stack power. As such, we are working on a simple hydrogen recirculation system that uses the PV work available in the pressurized hydrogen supply, as does Ballard, to instill recirculation in the stack. The power requirements will hopefully be less than several watts.

The other significant power draw is the fan for the water condenser. An ambient pressure system running at, for example, 70° C and several times stoichiometric airflow, will operate in a net water deficit because more water will be removed as vapor than will be formed in the cathode reaction. In order to maintain a positive water balance, it is necessary to recover a significant fraction of the water vapor. We initially experimented with a modified automobile radiator but the power required for the cooling fan was on the order of 3% of the total power and the pressure drop through the radiator for the cathode effluent was uncomfortably high. One of the reasons for the high fan power requirement was that an inordinate amount of cooling air was required to achieve the required cooling. A conventional radiator essentially consists of primary flow tubes with numerous cooling strips or fins in order to increase the heat transfer surface area several fold. Unfortunately, the operating temperature of the fuel cell condenser may only be 60° C whereas an internal combustion engine radiator operates at a significantly higher temperature. As such, the fin efficiencies are particularly poor with the modest temperature differentials and the available surface area is not effectively utilized. Correspondingly, we have assembled a lightweight, low-pressure drop condenser that maximizes the surface area of the flow channels. While we have not yet fully characterized the heat transfer coefficients, etc., it appears that we should be able to need only about 1.5% of the power to run the cooling fan.

Taking all of the above into account, the parasitic power levels for this evolving nominal 4 kW system are favorably projected to be:

Blower:	< 2 %
New H_2 recirculation system:	< 0.1 %
Water pump	< 0.1 %
Fan for new condenser design	1.5 %
Total Parasitic Power Loss	**< 3.7 %**

The electronics for monitoring and controlling such a system are not included but the power consumption of the microprocessors and digital interface electronics are nearly negligible compared to the other factors. Motor controller inefficiencies are already included in the blower value and the others may be simple off-on systems. In any case, the ability to operate with less than 5% parasitic power losses may make such systems competitive with more sophisticated efforts, notwithstanding the cost and complexity advantages. For example, a pressurized system with 20% parasitic power losses would need to operate at 0.83 V/cell in order to provide the same overall efficiency as the ambient pressure system with 5% parasitic power losses operating at 0.70 V/cell. In this comparison, equivalent current densities provide equivalent net power densities. As such, the pressurized system would also need to achieve 300 mA/cm^2 at 0.83 V to match the ambient pressure power density at 0.7 V. Even with pressurization, it would be difficult to achieve the 300 mA/cm^2 at 0.83 V with low platinum catalyst loadings. In order to improve the kinetics sufficiently to attain this performance, it would probably be necessary to increase the catalyst loadings by a factor of 5 to 10, which would incur a significant cost penalty.

In stationary power applications, the condenser (and fan) could conceivably be eliminated if a water supply is available at the site. This roughly 1.5% increase in efficiency would require the supply and demineralization of about 12 gallons per day of water for a 4 kW system. This trade-off may be attractive for a number of situations. Another practical consideration of stationary power applications is that the preferred fuel will eventually most likely be natural gas. Depending on the fuel processor design approach, a pressurized anode (e.g., 30 psig) may be advantageous in some cases. The general scheme that we are adopting is amenable to operation with a pressurized anode and an ambient pressure cathode. Such a combination may provide the most efficient package overall.

We are continuing investigating corrosion in cells using 316 SS components. Most of our previous testing was performed on single cells or using immersion cells. While the single cell results that we reported were very encouraging, one of the difficulties with multiple cell stacks is that higher (than single cell) voltages may occur due to shunt currents in the manifold region. Testing of the effluent water from the 4-cell pressurized screen/foil stacks on the 100 h time scale indicated that the levels of Mn, Ni, Cr, Mo and Mg were all significantly below 1 ppm and, while greater, Fe was also still below 1 ppm. Thus, it appears that any dissolution processes were relatively minor and no visible corrosion was apparent after disassembly. We have heard from others that they have experienced corrosion difficulties using 316 SS although the liquid effluents from their stacks were indicated to have pH's significantly lower than the 6 to 7 that we typically observe. Last year, we investigated corrosion rates in aggressive immersion testing using pH 2 solutions at 80°C as well as micromolar amounts of chloride ions (which are known to exacerbate corrosion). Substantial metal ion contents were observed for the hydrogen sparged solutions (e.g., up to 70 ppm for Fe), much less so for the air-sparged (all metal ions less than 1 ppm), and a chloride ion effect was not evident. Given that difficulties were apparent at pH's of two, this year we extended the immersion testing to cover pH's of 2, 3, 4, 5 and DI water, as well as longer immersion times (500 vs. 250 h), and more samples for better statistics. The solutions were analyzed for metal ion contents using ICP-MS or ICP-ES. They were also weighed before and after. While not particularly accurate because

of the small changes involved, the gravimetric results yielded corrosion rates less than 0.34 μm/yr for all samples.

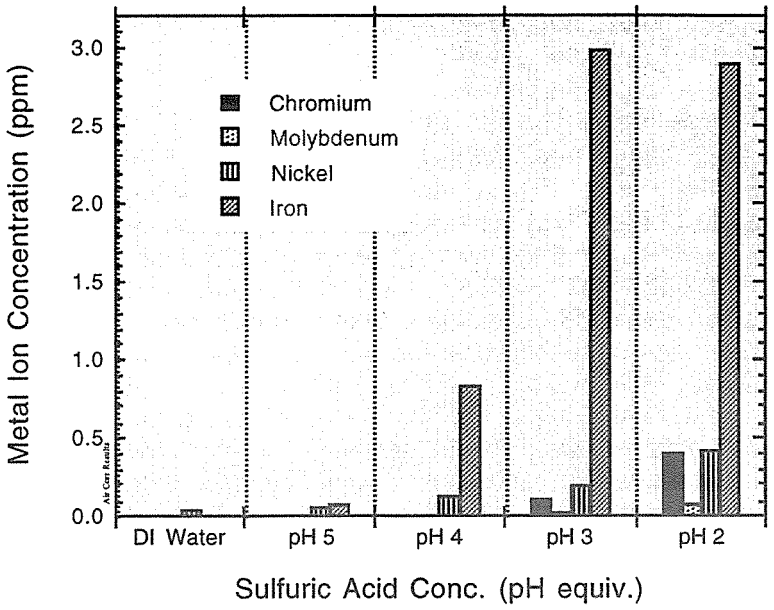

Figure 6. Metal ion contents as a function of solution acidity of the air sparged immersion solutions containing 316 SS samples.

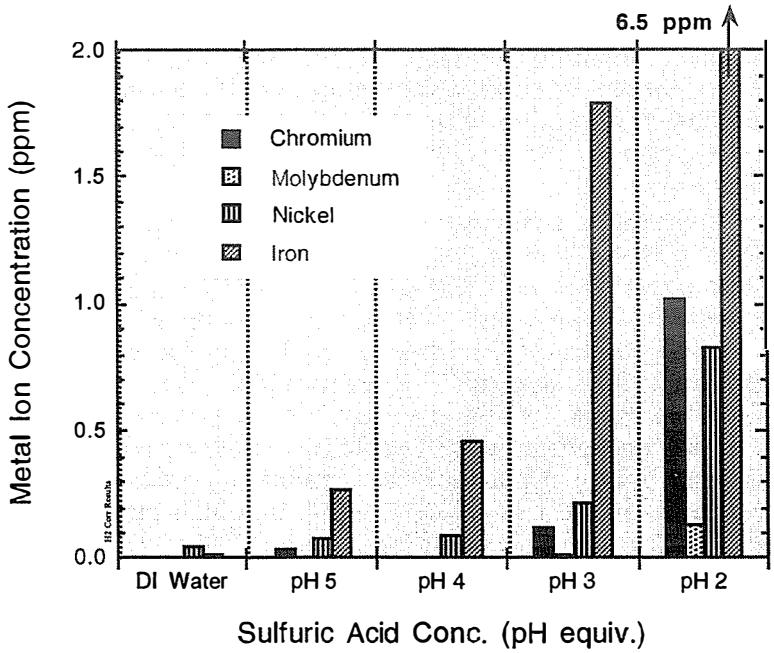

Figure 7. Metal ion contents as a function of solution acidity of the hydrogen sparged immersion solutions containing 316 SS samples.

Figure 6 depicts the average metal ion contents of the air-sparged samples and Figure 7 summarizes the results for the hydrogen sparged experiments. In both cases, the metal ion contents are near or below detection levels in DI water (pH 6 - 7) and gradually escalate

with acidity until the concentrations are several orders of magnitude higher in some cases. As before, most ion contents in the hydrogen sparged solutions are higher, which might be expected from the reduction and dissolution of the passivation layer. In general, it is clear that if abnormal liquid water acidities within the cell can be avoided there is a good possibility that long term stability can be achieved.

One of the hazards of dissolution is that the metal ions may, in some manner, make it to the ionomeric membrane and tie up functional sites effectively increasing the ionic resistivity and cell resistance. It was also considered that, in some designs, the metal hardware may be in direct contact with the membrane, which may facilitate the dissolution and uptake of metal ions. As such, in an experiment, 316 SS screen hardware was placed in direct contact with an uncatalyzed Nafion 112 membrane and the "cell" was operated at 80°C under heavily humidified H_2 and air with an imposed "open circuit" voltage of 0.94 V for 120 h. Afterwards, the hardware showed no visible signs of corrosion, however, the membrane was indeed discolored. Analysis of the membrane by EDAX could only detect Cu above the 304 SS background of the SEM instrument. More sensitive analysis with XRF did detect minute traces of stainless steel components such as Fe, Ni, Cr and Mn but other elements such as Cu, Zn and Ca were observed. No molybdenum (Mo), which differentiates 316 from 304 SS, was detected. If no 316 SS dissolution actually occurred, possible sources of the 304-type metal ions could conceivably have been the 304 SS humidifier system in the test station. The Cu and Zn may have come from aluminum alloy in the endplate manifold region, and Ca may come from non-ionic colloidal oxides not removed by the deionization system. Si from colloidal silicates and Al from the endplates may have been present but below the detection threshold of the XRF. In any case, the total ionic concentrations are quite small and it does not appear that the 316 SS was unduly affected by direct contact with the membrane. In retrospect, a possible weakness with this experiment was that no current was passing through the membrane in the simulated open circuit conditions, and contaminant ion inclusion has been demonstrated to be a function of current in some industrial membrane electrochemical reactors.

The effluent pH's from the above cell were about 6 from both sides. Metal against the membrane did not prompt low effluent pH's although a possible mechanism is not clear anyway. It is still somewhat of a mystery to us why the low pH effluents observed by others may occur. Possibilities are contaminants from the particular fabrication processes employed or from the materials used themselves or the reactants or water supply. Cell reversals or shunt currents may result in unusual chemistries, although again, it is not clear what mechanisms could conceivably result in acidic ionic species.

The general conclusion from the additional corrosion testing this year is that there still does not appear to be any readily evident difficulties with the use of untreated or uncoated 316 stainless steel for the fuel cell hardware, at least on the single-cell or short-stack level. The primary challenge then, will be to minimize or eliminate shunt currents in large stacks. We have naturally attempted to design our components to alleviate such occurrences, but have not yet had the opportunity to evaluate their performance under such conditions.

Economic Evaluation

Compared with present day PEFC stack technologies, the metal flow-fields demonstrated provide very low costs. The most recent configuration could conceivably cost $2-3/kW, vs. $100/kW projected for machined graphite flow fields. This brings the total cost of fuel cell materials down to practically the cost of the MEA, which today is about $300/kW at 60% energy conversion efficiency. A present day overall cost estimate of $600/kW would

be quite acceptable, considering a stationary power generation market entry cost target of around $2000/kW (per J. Ogden & co-workers and an A.D. Little Report).

Plans for Future Work

Milestone 1: Complete fabrication of 4 kW stack based on stainless steel hardware and operating at ambient air pressure -- July 15, 1998.
Milestone 2: Demonstrate stack system bench operation at parasitic power loss < 10% -- Sept. 30, 1998.

Publications

1. Simon Cleghorn, Xiaoming Ren, Thomas Springer, Mahlon Wilson, Christine Zawodzinski, Thomas Zawodzinski and Shimshon Gottesfeld, "PEM Fuel Cells For Transportation And Stationary Power Generation Applications," *Int. J. Hydrogen Energy,* **22**, 1137-1144 (1997).

2. Christine Zawodzinski, Mahlon S. Wilson and Shimshon Gottesfeld, "Corrosion Testing of Stainless Steel Fuel Cell Hardware," paper submitted to The 1998 Fuel Cell Seminar, Palm Springs, CA.

3. Christine Zawodzinski, Mahlon S. Wilson and Shimshon Gottesfeld, "Metal Screen and Foil Hardware for Polymer Electrolyte Fuel Cells," abstract submitted to the Fall 1998 ECS Meeting, Boston, MA

REGENERATIVE FUEL CELL SYSTEMS R&D

Fred Mitlitsky, Blake Myers, and Andrew H. Weisberg
Lawrence Livermore National Laboratory
7000 East Avenue, L-174, Livermore, CA 94551-0808

Abstract

Regenerative fuel cell (RFC) systems produce power and electrolytically regenerate their reactants using stacks of electrochemical cells. Energy storage systems with extremely high specific energy (>400 Wh/kg) have been designed that use lightweight pressure vessels to contain the gases generated by reversible (unitized) regenerative fuel cells (URFCs). Progress is reported on the development, integration, and operation of rechargeable energy storage systems with such high specific energy. Lightweight pressure vessels that enable high specific energies have been designed with performance factors (burst pressure * internal volume / tank weight) >50 km (2.0 million inches), and a vessel with performance factor of 40 km (1.6 million inches) was fabricated. New generations of both advanced and industry-supplied hydrogen tankage are under development. A primary fuel cell test rig with a single cell (46 cm^2 active area) has been modified and operated reversibly as a URFC (for up to 2010 cycles on a single cell). This URFC uses bifunctional electrodes (oxidation and reduction electrodes reverse roles when switching from charge to discharge, as with a rechargeable battery) and cathode feed electrolysis (water is fed from the hydrogen side of the cell). Recent modifications also enable anode feed electrolysis (water is fed from the oxygen side of the cell). Hydrogen/halogen URFCs, capable of higher round-trip efficiency than hydrogen/oxygen URFCs, have been considered, and will be significantly heavier. Progress is reported on higher performance hydrogen/oxygen URFC operation with reduced catalyst loading.

Introduction

The LLNL effort to develop electrochemical energy storage systems occupies a crucial regime in the hydrogen technologies' adoption process, between pure research/conceptual feasibility and near-term demonstrations of commercial systems. This effort leaves as many component innovations as possible to others, and seeks to integrate the best systems from the highest performance, readily procurable components. The integration research and component testing being undertaken has already uncovered many operational and design issues that might hinder the adoption of breakthrough technologies being funded by the DOE and NASA. A focus on delivering energy storage to the most weight-sensitive applications (aircraft and spacecraft) ensures that key technologies will be properly implemented and combined to perform in real, upcoming vehicle tests.

The two key technologies that LLNL is aggressively implementing are proton exchange membrane (PEM) -based RFCs and high-performance tankage for storing compressed hydrogen and oxygen gases. Tankage built from available technologies must be lightweight and must cope with volume penalties, gas permeation, and moisture handling to adequately furnish the breakthrough levels of specific energy that RFC systems offer. Such multidisciplinary specifications have yet to be combined in the form of a commercial product. Were it not for LLNL's role as integrator leading industry, and as technical monitor promoting relevant specifications from within DOE-funded demonstration efforts in industry, such functional combinations of component performances would be years rather than months away. In particular, the DOE PRDA funded at Thiokol is on track to deliver vehicle-compatible hydrogen test tanks to support the Ford P2000 demonstration vehicle early next year. The supervision of and close interaction with this industrial demonstration project is one important example of the real effort DOE is sponsoring at LLNL to bridge research into demonstrations.

Another DOE-funded industrial demonstration effort, with Proton Energy Systems as prime contractor, has recently been funded to introduce PEM-based energy storage into electrical utility applications. Besides monitoring this field demonstration, LLNL will be directly supporting Proton Energy Systems's technology development by testing electrolyzer and URFC cell stacks. In the cases of Proton Energy Systems, Thiokol, and Hamilton Standard (which currently offers the most advanced electrochemical components) LLNL has achieved close cooperation with industrial partners who hold the intellectual property. With these partners, LLNL is jointly developing systems relevant to a wide spectrum of applications, as depicted in Figure 1. These systems include high altitude long endurance (HALE) solar rechargeable aircraft (SRA), zero emission vehicles (ZEVs), hybrid energy storage/propulsion systems for spacecraft, energy storage for remote (off-grid) power sources, and peak shaving for on-grid applications (Carter 1998, de Groot 1997, Mitlitsky 1998, Mitlitsky 1996-a, Mitlitsky 1996-b, Mitlitsky 1996-c, Mitlitsky 1996-d, Mitlitsky 1994, Mitlitsky 1993). Figure 2 illustrates the original application for this set of innovations: solar powered aircraft. This aircraft (Pathfinder) set the altitude record (71,500 ft) for all propeller-driven aircraft on July 7, 1997 (Mitlitsky 1998, NASA 1997).

Energy Storage Systems

Requirements for RFC energy storage systems are similar across a wide range of applications. Although stationary applications generally are not mass sensitive, they join a cluster of mobile, vehicular, and transportable applications that might advantageously store and retrieve energy with RFC systems. Those applications that are most mass sensitive are most likely to find RFC

systems an enabling technology. The LLNL RFC Systems effort is pursuing the most mass sensitive applications where their advantage will be clearest compared to secondary batteries. LLNL has also considered RFC systems that use hydrogen/air or hydrogen/halogen chemistries instead of hydrogen/oxygen. Both of these alternatives may emerge as advantageous in some stationary applications, as discussed in the **RFC Systems** section herein.

The energy storage requirements of a solar rechargeable aircraft (SRA) prompted LLNL to commission a study of secondary batteries (Arthur D. Little 1993). Although its predictions for lithium/ion and nickel metal hydride ($NiMH_X$) batteries have recently been adjusted upward, the basic result still holds in favor of RFC systems. Table 1 compares Specific Energy, a fundamental performance measure of any energy storage technique, and distinguishes between theoretical and packaged performance for various battery chemistries.

Table 1: Specific Energies for URFC and Rechargeable Batteries

Battery System	Theoretical Specific Energy [Wh/kg]	Packaged Specific Energy [Wh/kg]	Comments
H_2/O_2 URFC	3660	400-1000	URFC with lightweight pressure vessels
Li-SPE/MO_x	735	220	Novel packaging for unmanned system
Ag/Zn	450	200	Excess Zn required, low charge rate
Li/$LiCoO_2$	735	150	Poor cycle life, high capacity fade
Li/$AlFeS_2$	515	150	≥400°C thermal management
Na/S	1180	150	~350°C thermal management
Li/TiS_2	470	130	~50% DOD for high cycle life (900 cycles)
Li/ion	700	100 (135)[a]	Projection revised November 1996
Ni/Zn	305	90	Excess Zn required, low specific energy
Ni/MH_x	470	70 (85)[a]	Projection revised November 1996
Ni/H_2	470	60	Low specific energy
Ni/Cd	240	60	Low specific energy
Pb/acid	170	50	Low specific energy

Survey by A.D. Little, Inc., July 1993 for LLNL, excluding URFCs

[a] Projections revised in November 1996 (private communications, Brian Barnett)

Figure 3 sketches the distinction between total reactant mass that could theoretically store a chemistry-limited specific energy, and packaged performance of a battery technology. Due to reaction kinetics, not all reactants are accessible, so that batteries introduce depth of discharge limitations which fuel cells can ignore. Because fuel cell systems store their reactants outside the electrochemically active cell stack, their specific energy is limited by the mass of the reactant

containers. Such containers do not need to satisfy the complex requirements of battery packaging, but they must be sufficiently chemically inert and impermeable.

LLNL is developing containers suitable for storing gaseous hydrogen and oxygen in the most mass sensitive applications. These containers are pressure vessels derived from aerospace pressure vessel technology. The earliest example of actual, hydrogen impermeable tankage suitable for vehicular energy storage applications is likely to be produced by Thiokol later this year, acting in close collaboration with LLNL under a DOE PRDA. Figure 4 illustrates Thiokol's conformable two cell tank configuration now being adapted from compressed natural gas (CNG) to hydrogen service. Figure 5 illustrates a more advanced configuration of conformable tank, employing three cell tanks that provides the best fit for Ford's P2000 demonstration vehicle.

Much of the complexity of battery technology is dispensed with in RFC systems, where a Proton Exchange Membrane (PEM) cell stack can convert energy between electrical and chemical forms without having to store energetic chemicals as part of the electrode package. LLNL has chosen to explore the Unitized Regenerative Fuel Cell (URFC), since detailed mass projections showed energy storage system mass will be significantly reduced by using the same cell stack to convert energy in both directions. Slight efficiency compromises could accompany the choice of a particular set of catalysts (on oxygen and hydrogen sides of a PEM cell membrane) that must serve both electrolysis and fuel cell operating modes. To date, no such performance compromises have been observed, while characterization of unidirectional cell stacks, especially pure electrolyzers, is soon to begin at LLNL in parallel with URFC testing. The sequence of electrochemical progress at LLNL, including recent groundbreaking results, will be presented after progress is reported in the various other components and operation of RFC Systems.

Tankage

Tankage mass puts a ceiling on RFC energy storage density. Even if the cell stack and ancillaries weigh nothing, system specific energy will be diluted by the mass required to contain reactants. Because cryogenic storage, especially of hydrogen, is such a challenging frontier in itself, a different DOE funded effort is underway at LLNL to explore its expected characteristics (Aceves 1998). The significant amount of thermal energy that must be transferred to employ cryogenic hydrogen suggests that cryogenic energy storage media will first find application in primary power plants. Thus this system integration effort is pursuing the most mass effective storage of gaseous hydrogen and oxygen.

The need for advanced development of compressed hydrogen tankage technology becomes apparent when the specifications commensurate with energy storage applications are combined. Aerospace tankage technology can take advantage of the best composite materials to contain the gas pressure, but relies on liners for permeation control that are massive, ill-conceived, and pose additional mass penalties for cycle life. Other forms of tankage simply do not compete strongly with the best composites, as shown in Figure 6. That figure compares a performance factor that is proportional to contained gas mass over tank mass independent of tank scale. (In ideal gases the performance factor sizes tank mass independent of operating pressure as well.) Detailed point designs showed the advantages of developing a tank liner technology that could contain the

most reactant (esp. hydrogen) for a given tank mass, and the advantages of a thin liner technology appear in the rightmost bar of Figure 6.

Figure 7 shows LLNL's previous development of thin liner technology under the DOE/Ford program. These vessels use lightweight bladder liners that act as inflatable mandrels for composite overwrap and provide the permeation barrier for gas storage.(Mitlitsky 1998, Mitlitsky 1996-a, Mitlitsky 1996-c, Souers 1986). Bladders are fabricated using materials which are compatible with humidified, electrolyzed gases, and are designed to be compatible with elevated temperatures that occur during fast fills or epoxy curing cycles. The cylindrical tank geometry is important not just for aircraft energy storage, wherein LLNL has been funded by NASA to develop runway-replaceable tank liners, but also to evaluate the potential of structural tankage. Effective specific energies for storage systems that also perform structural functions can be boosted several-fold above the predicted URFC system performance in Table 1.

Several thermal issues must be considered to design pressure vessels capable of fast filling with hydrogen. Gas compression during pressure vessel filling results in gas heating which can result in underfilling and/or overpressurization. The temperature rise associated with filling a pressure vessel is related to the pressure ratio, fill rate, properties of the gas, thermal mass of the vessel and plumbing, and heat transfer coefficients. Large pressure ratios, rapid fill rates, hydrogen gas, and lightweight pressure vessels with poor heat transfer coefficient can result in large temperature rises. Neglecting heat transfer and the thermal mass of the vessel and plumbing, a study (Daney 1995) shows that for an infinite pressure ratio of an ideal gas, the temperature ratio for a fast fill is equal to the ratio of specific heats (which is 1.41 for hydrogen). By this criterion, a vessel with 300 K (27 °C = 81 °F) initial gas temperature would achieve a final gas temperature of up to 420 K (147 °C = 297 °F). Such worst case temperature rise would result in filling the tank to only 71.4% of rated capacity at the maximum operating pressure. The final gas temperature peaks can be worsened by high ambient temperature or gas lines that are already warm.

Temperature rise (underfilling) for natural gas vessels is less than for hydrogen due to lower ratio of specific heats (~1.32). Even so, by the criterion above a fast fill from 300 K would yield a temperature of 396 K (253 °F). A typical temperature rise to ~140 °F (333 K), from an initial temperature of 70 °F, for fast fills of compressed natural gas (CNG) into a vessel with an adiabatic inner wall has been reported (Kountz 1994). One of the main reasons for the discrepancy is the due to the heat capacity of the pressure vessel (Mitlitsky 1998).

In order to package gaseous hydrogen into an automobile without enormous changes in vehicle layout, a different approach to tankage makes sense for volume-constrained systems. The LLNL effort is employing DOE funds in a high leverage opportunity to innovate this regime. The tankage technology closest to delivering hydrogen pressure vessels suitable for many mobile applications, including hydrogen-powered passenger vehicles, should soon exist through a development program underway at Thiokol. Thiokol is the most capable of the aerospace tankage suppliers, and has won the DOE PRDA to develop commercial hydrogen pressure vessel technology. LLNL serves as technical monitor in this development effort, and has intervened repeatedly to insure that Thiokol's developments are most likely to satisfy the true requirements of a hydrogen economy.

The hydrogen gas storage technology Thiokol is developing is most relevant to passenger vehicles, and is unlikely to do better than other aerospace tankage approaches at the most mass sensitive applications LLNL is pursuing. Thiokol anticipates its extraordinary expertise will allow it to withstand cheaper competitors because their development will produce non-axisymmetric pressure vessels it calls Conformable Tanks. Enroute to these unprecedented geometries, Thiokol has expended internal funds developing subscale prototypes that are conventional domed cylinders. LLNL tankage developments which should substantially improve the mass performance of high pressure hydrogen tanks can take advantage of the tooling and winding already developed at Thiokol. This existing capability enables LLNL to effectively pursue a new generation of thin tank liners, this iteration using rotational molding to avoid the problematic transition between a thin sidewall and a thick end dome.

Figure 8 provides a high-level roadmap of the advanced tankage developments underway at LLNL. Figure 9 shows earlier work on structural performance of cylindrical tanks suitable for thin bladder liners. Development of radical tankage is proceeding along this branch, and three others shown in Figure 8. Two other approaches with potentially higher payoff are receiving preliminary attention, besides the removable, cylindrical bladders and the rotationally molded liners. Linerless approaches offer potentially maximal weight savings, at the expense of a total change from the epoxy matrix formulations familiar to composite fabricators. Blow molding is a likely follow on process that can produce much thinner liners at minimal expense, however production volumes must grow several orders of magnitude to justify costly tooling and materials development. These later options are being pursued at a low level. Both main lines of advances in tankage, as well as an LLNL capability to test commercial hydrogen tanks, call for the creation of a new experimental facility at LLNL. Figure 10 is a picture of the explosion-proof room in that facility required to safely test unproven approaches to hydrogen tankage.

Thiokol Collaboration

Tankage development can only proceed so far before strenuous testing is required to prove new concepts. Figure 11 graphically illustrates the rigors of getting actual tanks to live up to predicted performance. The photogenic wreckage documents the first successful test, where burst pressures fell within 5% of Thiokol's prediction. Using Thiokol IR&D funds to reduce risks on the DOE PRDA, this subscale test program went through several rounds of alarming failures before this success, the previous failure mode damaged the test apparatus by spitting out its inadequately anchored boss. Technical risks continue to be run as various fiber and winding process variables remain to be reduced to predictability by the procedure illustrated in Figure 12.

LLNL has been steadily contributing expertise to the ongoing design and debugging of Thiokol's tankage developments under the DOE PRDA, while Thiokol has operated essentially without feedback in the part of their design that relies on their unique expertise. Figure 13 shows the completed fruit of Thiokol's non-axisymmetric design capability. This liner contour is compatible with an optimized design for the shape of composite wrapped layers that form a conformable tank's complicated end dome. Figure 14 shows Thiokol's' finite element analysis that projects stresses in their end dome design, and outlines their approach to verifying the design code's prediction.

Much of the close collaboration between LLNL and the DOE tankage PRDA contractors, including Aero Tec Laboratories (ATL) and Thiokol, anticipates the difficult qualification of a liner suitable for resisting hydrogen permeability, matching the process requirements of subsequent composite overwrap, and capable of a high-cycle-life interface with the tanks boss/end detail. Although Thiokol is contributing most of the design, and considerable intellectual property, to the boss, all three organizations have learned the necessity of close communication on liner design. The difficulties of liner material selection were initially underestimated by all the available experts. A screening process is currently underway which should select a liner material suitable to proceed into rotational molding. This screening process relies on a testing contractor, Southern Research Institute (SRI), that has a long history for furnishing test results to Thiokol's specifications. Figure 15 summarizes Thiokol's approach to down-selecting the liner material based on SRI's hydrogen permeation measurements.

The LLNL effort to develop the next generation of advanced hydrogen tankage was able to take advantage of existing SRI capability and further a broader understanding of hydrogen permeability. AlthoughThiokol is internally funding a new facility at SRI capable of permeation testing at high pressure with hydrogen, SRI offered to employ its 200 psi permeation test capability under direct contract to LLNL during the short interval before the Thiokolwork commenced. LLNL took advantage of this interval to procure ASTM-traceable calibrationfor all subsequent measurements, to confirm previous measurements made at LLNL on LLNL-developed liners, and to further study hydrogen permeation through thin films. Figure 16 shows the 200 psi permeation test rig at SRI that performed LLNL's measurements.

The graph in Figure 17 not only confirms the hydrogen permeability (of P-03 liner material developed at LLNL) using a different technique, it extends the earlier LLNL results to a range of pressures, temperatures, and specimens. Although the high pressure rig at SRI will be required to confirm a material's acceptability as a thick liner for high pressure tankage, further LLNL experiments on the low pressure rig at SRI will support the development of advanced liners.

RFC Systems

Although tank masses dominate the specific energy performance of RFC systems, many other components and operations must be integrated to deliver functional energy storage systems. This integration research has been a continual learning process, with the past year's progress built on a foundation of developments already proven and listed in Figure 18. Figure 19 brings this list of accomplishments up to date.

URFCs should be capable of higher specific energy and less complexity(due toreduced parts count) compared with RFCs using separate (dedicated)fuel cell and electrolyzer stacks. However, there is an erroneous presumption that URFCs are not capable of high cycle life, due to the lack of well publicized data showing tests lasting more than ~25 cycles. Results from tests reported recently (Mitlitsky 1998) are an existence proof that URFC cells can be cycled repeatedly (>2000 cycles) without significant degradation (less than a few percent). These tests are also an existence proof that bifunctional catalysts can operate reversibly without significant degradation.

Even though bifunctional catalysts will not be simultaneously optimized for both oxidation and reduction reactions, URFC systems will not necessarily be less efficient than RFC systems using dedicated stacks. Although it is true that bifunctional catalysts may have slightly reduced performance in either the oxidation or reduction reaction (depending on catalyst composition, which may be optimized for a given system application), this will result in a modest round-trip efficiency decrease per unit of active area for the URFC stack, and not necessarily an efficiency decrease for the entire URFC system. It should be realized that the efficiency of a dedicated fuel cell (FC) during the charge cycle is zero, and likewise, the efficiency of a dedicated electrolyzer (EC) during the discharge cycle is also zero. Therefore, it is more reasonable to compare the efficiency of RFC systems which use similar active areas. By this criterion, the active area for the URFC stack is equivalent to the sum of the active areas for the dedicated FC and EC stacks combined. In such a comparison, a given power setting (either input or output) will result in less power per unit active area for the URFC by virtue of the larger active area utilized in each mode of operation. The operational current densities in the URFC will be below the corresponding current densities in the dedicated FC/EC stacks, resulting in an improved voltage efficiency for the URFC system. This efficiency improvement may even overwhelm the efficiency reduction caused by using compromise catalysts (Mitlitsky 1998).

URFCs may have other system advantages over dedicated FC/EC stacks in cases where ambient temperatures are prone to be below freezing conditions and where the typical system operation cycle requires near-continuous operation of either charge or discharge without long periods of system idling. In such cases, URFC stacks will stay warm by virtue of their continuous operation, whereas dedicated FC/EC stacks will require additional insulation and/or parasitic power to maintain the non-operating stack at required temperatures.

The electrochemical reactions for FC and EC operations for hydrogen/oxygen based systems are depicted in Figure 20. The URFC can be designed for electrolysis with water fed from either the anode (oxygen side) or the cathode (hydrogen side). For cathode feed electrolysis, a single phase separator is used in the hydrogen/water recirculation loop. Water must then diffuse through the cell to the oxygen side in order to be split. This necessary flow is decreased by an opposing flow of water caused by proton pumping, whereby each proton migrating through the membrane toward the cathode must be accompanied by at least four water molecules (Appleby 1986). This creates a situation where cell drying at the anode may result, especially at high current densities. Anode feed electrolysis provides excess water at the anode, avoiding the drying (at high current densities) that may be caused by proton pumping. For anode feed, phase separators are required in both the anode/water and the cathode/water recirculation loops, which add complexity and weight to the system (Mitlitsky 1998).

Other URFC chemistries are possible, such as hydrogen/halogen (Beaufrere 1977, McElroy 1979, McElroy 1977). These are of interest because they are capable of higher round-trip electrical efficiencies. Since they may be more than an order of magnitude heavier for comparable energy content, they are not of interest for mobile applications, but are considered for stationary applications. Since halogens and their acids are corrosive and toxic, safety considerations may limit the use of hydrogen/halogen URFCs to specific niches where the improved efficiency is an overriding consideration. Efficiency of hydrogen/halogen URFC systems is a function of acid concentration and current density (McElroy 1979). Unlike for water cycle URFCs,

hydrogen/halogen stacks can be nearly 100% efficient, if operation is restricted to very low current densities, where FC and EC polarization curves approach one another. Greater than 90% electric-to-electric (ETE) voltage efficiency was achieved at low current density (108 mA/cm^2) in the 1970s (McElroy 1979). It was estimated that system-level parasitics would reduce the actual round-trip energy storage efficiency by ~10% due to pumping power, current inefficiencies, and power conditioning inefficiencies (Mitlitsky 1998).

Electric utilities are interested in peak shaving energy storage systems to maximize utilization of existing base load electric generators and to postpone the installation of new generating equipment. Lead acid batteries are a preferred utility energy storage technology. Unlike the lead acid battery, RFCs uncouple power and energy ratings. This allows the RFC to accommodate weekly and even seasonal cycles. The H_2/bromine URFC has been demonstrated in single cells for up to 4000 hours with 80% round-trip energy storage efficiency, and showed stable cyclic performance in the early 1980's for a Boeing MX missile program (Nutall 1982). Scale up of cells to >0.23 m^2 (2.5 ft^2) and minimization of corrosion currents have yet to be demonstrated.

Less conventional stationary applications currently use lead acid batteries to store electric energy for remote off-grid applications. Primary electricity for these applications can come from solar, wind, or diesel generators. Up to ~3 days of energy capacity are typically stored in the lead acid systems. H_2/O_2 or H_2/air URFC systems will have longer life, could have lower life cycle cost, as well as allowing weekly and seasonal energy storage capabilities. The selection of H_2/O_2 versus H_2/air URFCs depends on a number of considerations. URFC systems based on H_2/O_2 have higher performance per unit area of membrane, do not need oxidant compressors, can operate completely closed cycle with little maintenance, are capable of slightly higher efficiency, but require ~50% more tankage to store oxygen. H_2/O_2 systems are generally preferred in cases where the compressed oxygen storage does not pose a significant safety hazard (Mitlitsky 1998).

Daytime shortages of electrical power (brown-outs or black-outs) are becoming more frequent in industrial countries. Total energy supplies are adequate on average, but daytime peaks cannot be sustained. A small H_2/air URFC could provide the utility customer with energy during peak power periods. With sufficient numbers of individual home owner units in place, this significant pressure on electric utilities would be reduced. Hydrogen/halogen URFC systems with an attractive mix of high efficiency and low capital cost for utility load leveling are being investigated enroute to a demonstration facility.

URFC systems with lightweight pressure vessels have been designed for automobiles and are expected to be cost competitive with primary FC powered vehicles that operate on hydrogen/air with capacitors or batteries for power peaking and regenerative braking (Mitlitsky 1994). URFC powered vehicles can be safely and rapidly (< 5 minutes) refueled from high pressure hydrogen sources, when available, to achieve driving ranges in excess of 360 miles (600 km). The employment of URFCs would save the consumer the entire capital cost of a home hydrogen generation unit. That consumer would now be able to electrically recharge at any available electrical source, instead of being tethered to a single home electrolysis unit. URFC-powered automobiles would still be able to rapidly refuel by direct hydrogen transfer when a hydrogen infrastructure becomes available.

Ancillaries

The URFC test facility at LLNL has been described elsewhere (Mitlitsky 1998). A primary fuel cell test rig from Hamilton Standard with a single cell (46 cm^2 active area) was modified for use as a URFC test rig. Hydrogen and oxygen are supplied by source bottles, or by recycle bottles that can be filled by electrolysis. This rig has undergone nearly continuous upgrading. In the core of that rig is a single cell 'stack' which Hamilton Standard used for internal development in the early 1980s. Figure 21 is a photograph of the central cabinet within this rig. Nearly triple the original fluidic component count has been added to this rig to allow testing of URFCs. Figure 22 is a fluid schematic indicating the current flow capabilities and features of this rig. The wealth of unusual components indicates how many operating characteristics and design issues have already been encountered. The last ~25% in fluidic component count was added to the rig, producing the symmetric section with identical hydrogen and oxygen phase separators, to enable testing of anode feed electrolysis.

The current LLNL test rig has been upgraded to a space and modification limit. Not only is expansion space missing within its equipment case and hood, the density of its current components poses major risks to its test capability if the improvements necessary to test higher power levels are attempted. Therefore the existing rig's test capability will be left intact to study the electrochemical components discussed below, and a second generation of rig hardware has commenced construction. This new generation is intended to operate in the new facility, under much larger hoods with the capacity to test multi-kilowatt components. Figure 23 shows the first use of next-generation valves, which are being tested in two critical locations on the existing test rig. It was desirable to introduce these valves as the final modification to the existing rig's plumbing because their high pressure ratings (for blocking flow) in both directions have proved to be important in these two locations, minimizing the amount of water that is released into gas plumbing as a result of shifting into electrolysis modes. Considerable progress in LLNL capabilities and understanding accompanied these rig upgrades, as well as a protracted period of debugging that suggested many ways to improve a second generation rig.

The list in Figure 19 summarizes the accomplishments that have already occurred in FY98. This list collects the many facets of progress being made at LLNL toward deploying and understanding RFC energy storage systems. It includes the development of appropriate tankage, the ability to properly specify PEM stacks, and the development of many unique ancillary components. Except for the ongoing electrochemical investigations being performed with the existing rig, the next stage in many of these facets awaits a new facility. Figure 24 shows the new facility at LLNL prior to occupancy. The radiation-hardened room with two steels doors is ideal for the explosion-proof tank testing mentioned above. The entire facility has yet to be connected to a ductwork, blower, and stack system of sufficient capacity to safely exhaust the worst-case hydrogen release, but it is anticipated on-line and safety-approved later this year.

URFC Experiments and Results

Experiments with the LLNL URFC test rig were limited within a parameter space of "safe" testing that could be performed while unattended. The maximum allowable working pressure

(MAWP) of the hydrogen side of the system is 80 psig (0.653 MPa), and the MAWP for the oxygen side is 160 psig (1.20 MPa). For safety reasons, the oxygen pressure was required to be slightly higher (consistently) than the hydrogen pressure. Maximum operating temperature of ~90 °C is limited by some of the solenoid valves in the system. The H_2 and O_2 gas flows in the test rig are plumbed for flow through (rather than dead-ended) FC operation. High flow rates can cause some gas to flow past the membrane and electrode assembly (M&E) without reacting. Flow and pressure settings in the test rig were initially somewhat variable due to lack of feedback control. Data logging accuracy can be improved by measuring under conditions of high gas flow, in order to make measurements insensitive to slight flow variations.

When switching from electrolyzer to fuel cell mode, short drying cycles may be required to remove the small amount of water that has been trapped in the "dead space" of the cell after water supply has been turned off. For cells requiring very rapid switching times, this dead space should be minimized to reduce drying time. For the cell configuration being tested (which was a designed initially for dedicated fuel cell operation and converted to a URFC without considering this design parameter), it was determined that 2.0-2.5 minutes at 240 ASF (250 mA/cm^2) were required for drying. Drying time can be reduced under the current configuration by increasing current density. By increasing the drying current density to >1000 ASF (>1.08 A/cm^2), drying time was reduced to 25-30 seconds. Using this rapid drying technique, round-trip cycle times of <1 minute were demonstrated on URFCs at current densities in excess of 1000 ASF (1.08 A/cm^2) in both fuel cell and cathode feed electrolysis modes. The drying procedure has also been accomplished in ~15 seconds using a current density of 1.5 A/cm^2. It is expected that redesign of the cell, catalyst, and drying procedure could reduce this drying time to a fraction of a second.

The method of cycle testing URFC cells at LLNL was described recently (Mitlitsky 1998). Cycle testing of a single cell URFC was started in November 1996 at LLNL. The test results for a single cell cycled 2010 times are presented in Figure 25 at four different current densities for both fuel cell (FC) and electrolyzer (EC) modes (eight curves total). This experiment accurately measured the cell voltage under repeatable conditions to determine the extent of cell degradation. Zero degradation would be reflected in horizontal curves (no change in voltage as a function of cycle life). If there was significant degradation due to cycling, the FC curves would display larger negative slopes and the EC curves would display larger positive slopes. The curves in Figure 25 show negligible degradation in both FC and EC performance, over a range of current densities; and are a higher fidelity and greater range of data compared to the earlier work at General Electric (Chludzinski 1973).

Another URFC membrane and electrode assembly (M&E) was installed and tested (cell #9734A). This cell had an internal resistance of 6.3 milliohm/46 cm^2 active area at 297 K, a value much closer to the expected value for a good cell. Internal resistance was measured to be 3.8 milliohm at 188 °F inlet temperature (360 K). A polarization curve for this cell is shown in Figure 26 at conditions which are very close to the highest temperatures and pressures allowable for the test rig in its present configuration. This figure proves that URFC cells can be cycled at >1000 ASF (>1.08 A/cm^2) in both fuel cell and cathode feed electrolyzer modes using Nafion 117 membrane. This figure shows that cathode feed electrolysis may take place at relatively high current densities, despite the concern that cathode feed designs may be prone to membrane dry-out. Figure 26 also shows polarization curves for cell #LLNL01 that were cycle tested as

described above, in order to emphasize the performance improvement achieved in the cell design of cell #9734A (Mitlitsky 1998).

These results are an important milestone and a significant improvement over what has previously been demonstrated. Both of the cells (#9734A and #LLNL01) tested used Nafion 117 membrane and Hamilton Standard's E-5 catalyst, which is a proprietary mixture of platinum, platinum group metals, and their oxides. Catalyst loading was 4 mg/cm^2 per electrode in both cells. The reduced internal resistance of cell #9734A and its corresponding performance improvement is attributed to the use of a new porous plate.

LLNL recently starting testing URFC cells using Nafion 105 membrane and reduced catalyst loading. Cell #9804A uses Nafion 105, Hamilton Standard's E-5 catalyst, and catalyst loading of 1 mg/cm^2 per electrode. Figure 27 shows the high performance polarization curve data taken on this cell at the same conditions that cell #9734A was measured under in Figure 26. Data from cell #9734A is replotted on the same curve as Cell #9804A in Figure 27 to highlight the performance improvement of cell #9804A. This figure shows that fuel cell operation on URFCs is feasible at current densities >2000 ASF (2.15 A/cm^2). Cathode feed electrolysis data was limited to 1200 ASF due to cell dryout. Anode feed electrolysis data was taken at current densities >2000 ASF (2.15 A/cm^2), but has not yet been approved for publication.

Figure 27 shows that reduced catalyst loading operation of PEM electrolyzers and URFCs is feasible, and shows that consumer markets that may require reduced catalyst loading to achieve inexpensive unit costs at high volume may be filled by PEM electrolyzers and URFCs. Experiments are continuing to reduce catalyst loading even further.

Acknowledgments

This work was performed under the auspices of the U.S. Department of Energy by Lawrence Livermore National Laboratory under Contract W-7405-Eng-48. This work was funded in part by: Ballistic Missile Defense Organization, Ford Motor Company, LLNL Laboratory Discretionary Research Funds, NASA, and U.S. Department of Energy. This work was performed in conjunction with various organizations, including: Aero Tec Laboratories (Ramsey, NJ), AeroVironment (Monrovia, CA), Brigham Young University (Provo, UT), Composite Solutions (Salt Lake City, UT), Directed Technologies Inc. (Arlington, VA), EDO Fiber Science Division (Salt Lake City, UT), Proton Energy Systems (Rocky Hill, CT), Thiokol Corporation (Brigham City, UT), and United Technologies, Hamilton Standard Division (Windsor Locks, CT). Figure 28 combines the logos of several of LLNL's industrial partners.

References

Aceves, S., (in these proceedings), 1998.

Appleby, A.J. and E.B. Yeager, *Energy*, 1986, *11*, 137.

Arthur D. Little, Inc., "Multi-fuel reformers for fuel cells used in transportation: Assessment of hydrogen storage technologies," Report Number DOE/CE/50343-1, March 1994.

Beaufrere, A., R.S. Yeo, S. Srinivasan, J. McElroy, and G. Hart, *12th IECEC*, 1977, 959-963.

Carter II, P.H., F. Mitlitsky, A.H. Weisberg, J.C. Whitehead, and R.W. Humble, "Design trade space for a Mars ascent vehicle for a Mars sample return mission," IAA Conference on Low-Cost Planetary Missions, Pasadena, CA, April 27-May 1 (1998), UCRL-JC-130277.

Chludzinski, P.J., I.F. Danzig, A.P. Fickett, and D.W. Craft, General Electric Company Technical Report AFAPL-TR-73-34, June 1973.

Daney, D.E., F.J. Edeskuty, M.A. Daugherty, F.C. Prenger, and D.D. Hill, *Cryogenic Engineering Conference*, July 17-21, 1995.

de Groot, W.A., L.A. Arrington, J.F. McElroy, F. Mitlitsky, A.H. Weisberg, P.H. Carter II, B. Myers, and B.D. Reed, "Electrolysis propulsion for spacecraft applications," AIAA 97-2948, 33rd AIAA/ASME/SAE/ASEE Joint Propulsion Conference, July 7-9 (1997).

Jasionowski, W., K.J. Kountz, and C.F. Blazek, Gas Research Institute Report #GRI-92/0350, July 1992.

Kountz, K.J., *Proc. 207th ACS-Division of Fuel Chemistry*, March 13-17, 1994.

McElroy, J. and G.G. Patwa, *Proc. 72nd AICHE*, Nov. 25-29, 1979.

McElroy, J., *Proc. DOE Chemical Energy Storage and Hydrogen Energy Systems Contract Review*, JPL Publication 78-1, November 16-17, 1977, 27-33.

Mitlitsky, F., A.H. Weisberg, and B. Myers, "Regenerative fuel cell systems," *Energy & Fuels*, 12 (1), 56 -71, January 12 (1998), UCRL-JC-128267 Rev 1, http://pubs.acs.org/isubscribe/journals/enfuem/jtext.cgi?enfuem/12/i01/html/ef970151w.html

Mitlitsky, F., B. Myers, and A.H. Weisberg, "Lightweight pressure vessels and unitized regenerative fuel cells," *1996 Fuel Cell Seminar*, Orlando, FL, November 17-20 (1996-a), UCRL-JC-125220 (paper) and UCRL-MI-125220 (viewgraphs).

Mitlitsky, F., W.A. de Groot, L. Butler, and J.F. McElroy, "Integrated modular propulsion and regenerative electro-energy storage system (IMPRESS) for small satellites," *AIAA Small Satellite Conference*, September 16-20 (1996-b), UCRL-JC-125242.

Mitlitsky, F. and B. Myers, "Development of an advanced, composite, lightweight, high pressure storage tank for on-board storage of compressed hydrogen," *Fuel Cells for Transportation TOPTEC: Addressing the Fuel Infrastructure Issue,* Alexandria, VA, April 1-2 (1996-c), UCRL-MI-123802.

Mitlitsky, F., "Rechargeable solar powered aircraft using regenerative fuel cells," *High Altitude Long Endurance (HALE) Roundtable Meeting, European Space Research and Technology Centre (ESTEC)*, invited presentation, Noordwijk, The Netherlands, January 17 (1996-d), UCRL-MI-122808.

Mitlitsky, F, N.J. Colella, and B. Myers, *1994 Fuel Cell Seminar*, 1994, 624-627, UCRL-JC-117130.

Mitlitsky, F, N.J. Colella, B. Myers, and C.J. Anderson, *28th IECEC,* 1993, *1*, 1.1255-1.1262, UCRL-JC-113485.

NASA Headquarters Press Release 97-153, July 14, 1997, http://www.dfrc.nasa.gov/PAO/PressReleases/1997/97-153.html .

Nutall, L. J., "Development progress on solid polymer electrolyte fuel cells with various reactant sources," General Electric, Electrochemical Energy Conversion Programs, Report, 1982.

Souers, P.C., *Hydrogen Properties for Fusion Energy*, University of California Press: Berkeley, CA, 1986, pp 370-373.

Figure Titles

Figure 1: URFCs with Lightweight Structure/Tankage Applications
Figure 2: Solar Powered Aircraft Sets New Record (71,500 ft on 7/7/97)
Figure 3: Theoretical and Packaged Specific Energies
Figure 4: Thiokol's Conformable Tankage – Two Cell Prototype
Figure 5: Thiokol's Three Cell Configuration for Ford P2000
Figure 6: Performance Factor (P_bV/W) for High Cycle Life Cylinders
Figure 7: High Performance Factor Bladder-Lined Tanks Fabricated
Figure 8: Roadmap for LLNL Tankage Development
Figure 9: Hybrid Structural Tanks Load Tested to Failure in Bending
Figure 10: Explosion-Mitigation Room in New Facility
Figure 11: Thiokol IR&D-Funded Subscale Testing
Figure 12: Thiokol Co-Funded Internal Research
Figure 13: Finite Element Solid Model of Conformable Liner
Figure 14: Structural Verification of Solid Model
Figure 15: Full-Scale Liner Development at Thiokol
Figure 16: Southern Research Institute (SRI) Permeability Test Rig
Figure 17: SRI Confirms & Extends H_2 Permeance of LLNL's Laminate
Figure 18: Past Results of RFC Project at LLNL
Figure 19: Current Year Accomplishments / Status
Figure 20: URFC Electrochemical Operating Modes
Figure 21: URFC Test Rig at LLNL Demonstrated >2000 Cycles
Figure 22: Current LLNL Test Rig Schematic
Figure 23: Progress In PEM Ancillary Components Extends Functionality
Figure 24: New Facility for URFC and Tankage Development
Figure 25: URFC Cycle Test Demonstrated Negligible Degradation
Figure 26: URFC Performance Improvement Reported in Energy & Fuels
Figure 27: Higher Performance URFC Using Reduced Catalyst Loading
Figure 28: Logos of LLNL's Industrial Partners

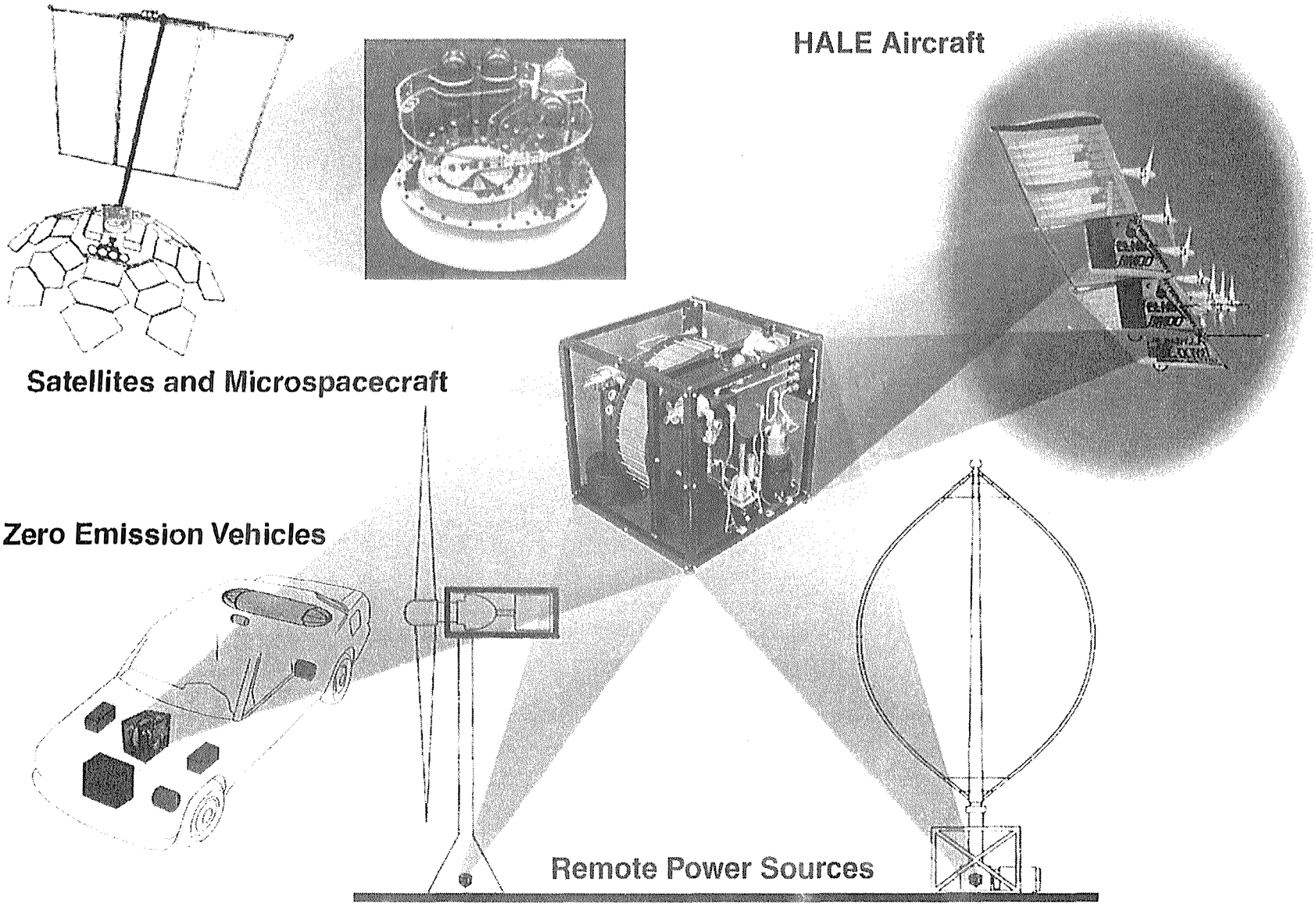
HALE Aircraft
Satellites and Microspacecraft
Zero Emission Vehicles
Remote Power Sources

Figure 1

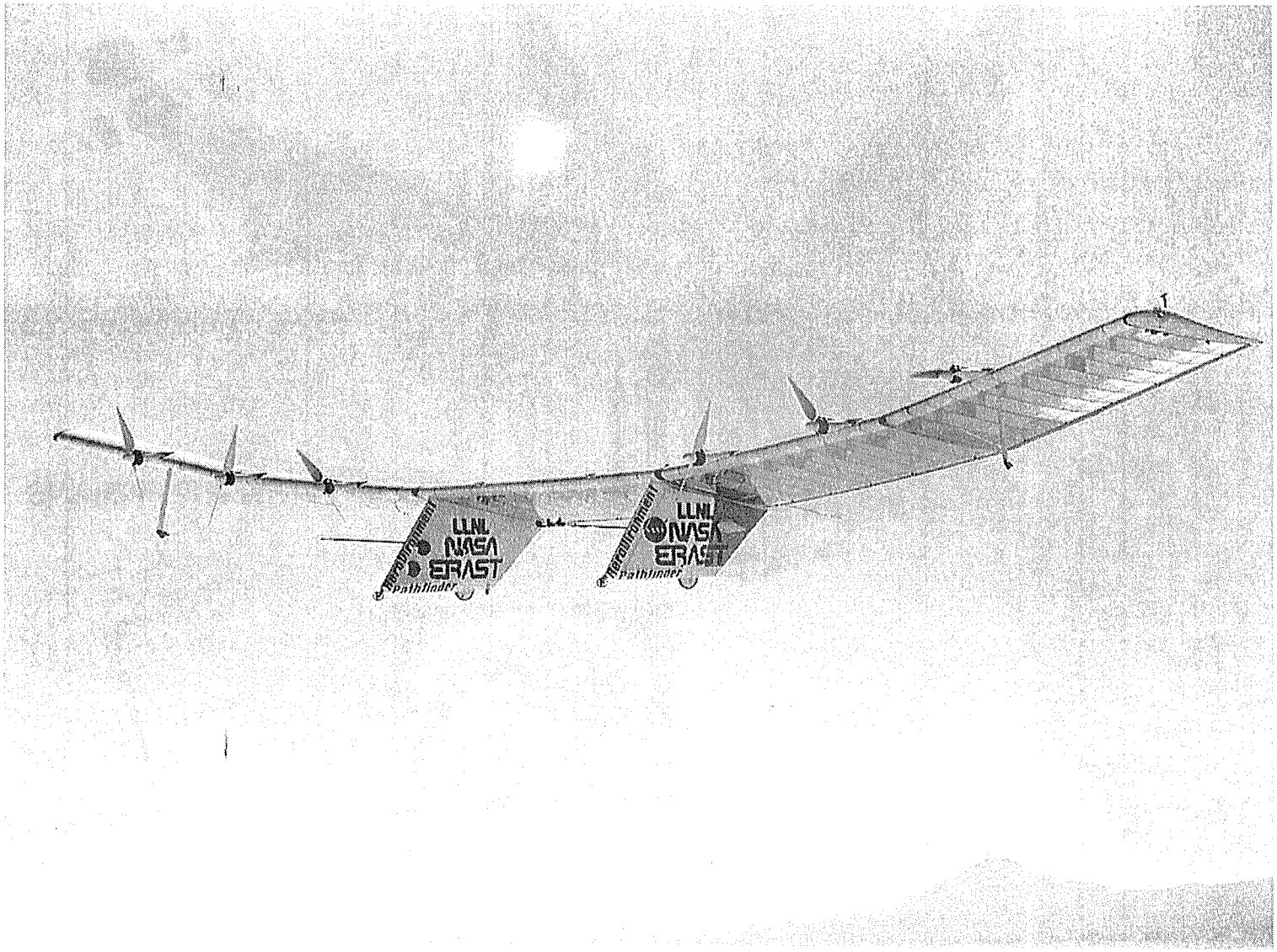

Dryden Flight Research Center EC95 43261-1 Photo 9/11/95 9:29AM
Pathfinder taking off from Edwards, CA: On way to setting new solar-powered altitude record. Photo by T. Landis

Figure 2

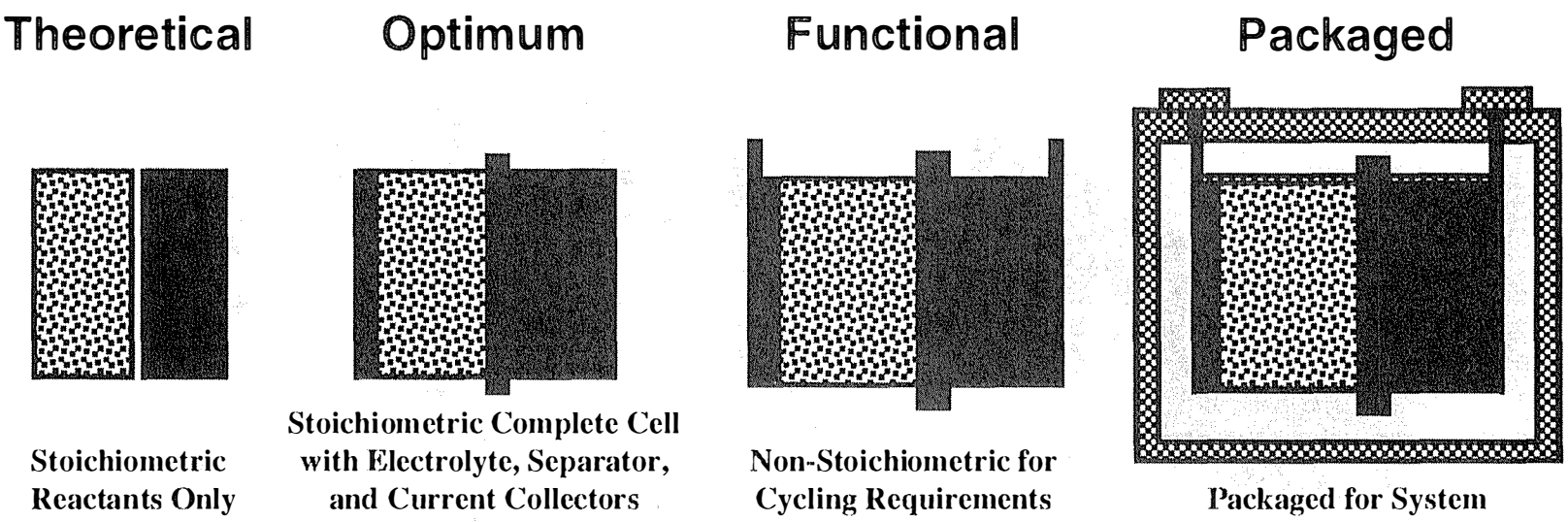

- Theoretical specific energy uses the weight of stoichiometric reactants only
- Stoichiometric complete cell adds weight of electrolyte, separator, and current collector required to draw current from the cell
- Functional cell adds weight of non-stoichiometric reactants to achieve required cycle life
- Packaged cell adds weight of packaging required for safe containment, shipping, handling, and extended life

Figure 3

THIOKOL
AEROSPACE & INDUSTRIAL TECHNOLOGIES

Figure 4

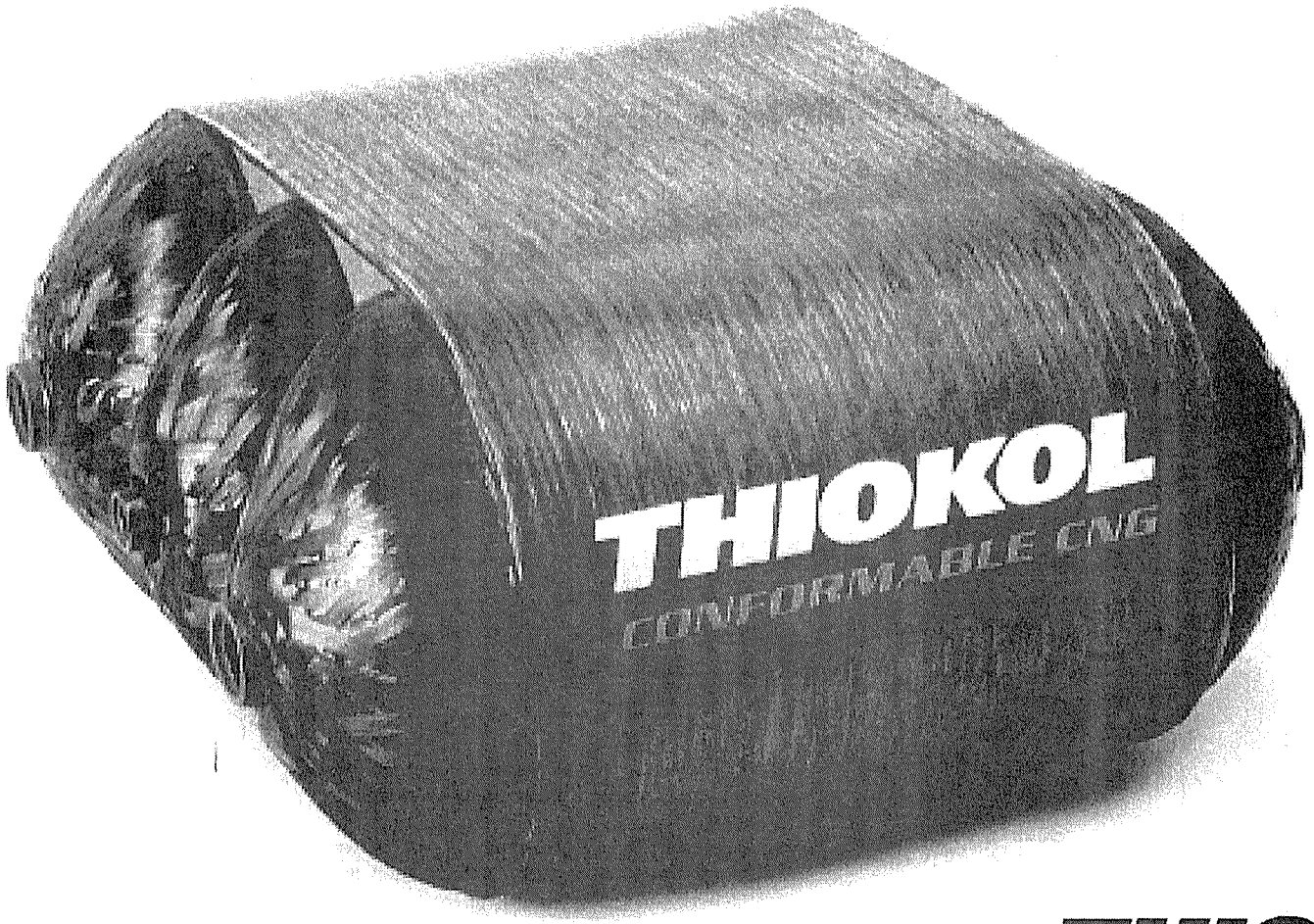

THIOKOL
AEROSPACE & INDUSTRIAL TECHNOLOGIES

Figure 5

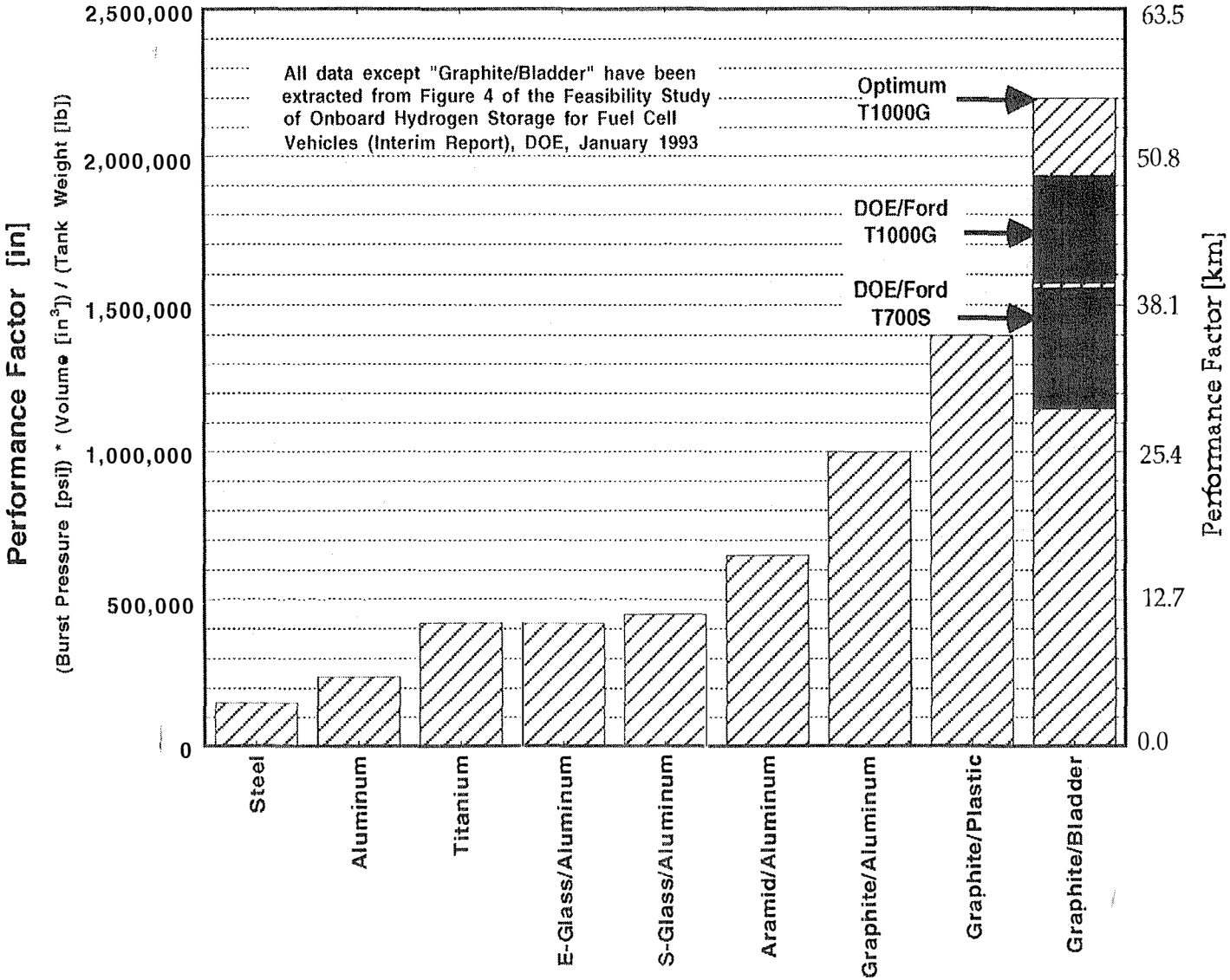
Performance Factor [in]
(Burst Pressure [psi] * (Volume [in3]) / (Tank Weight [lb])
2,500,000
2,000,000
1,500,000
1,000,000
500,000
0
All data except "Graphite/Bladder" have been extracted from Figure 4 of the Feasibility Study of Onboard Hydrogen Storage for Fuel Cell Vehicles (Interim Report), DOE, January 1993
Optimum T1000G
DOE/Ford T1000G
DOE/Ford T700S
63.5
50.8
38.1
25.4
12.7
0.0
Performance Factor [km]
Steel
Aluminum
Titanium
E-Glass/Aluminum
S-Glass/Aluminum
Aramid/Aluminum
Graphite/Aluminum
Graphite/Plastic
Graphite/Bladder

Figure 6

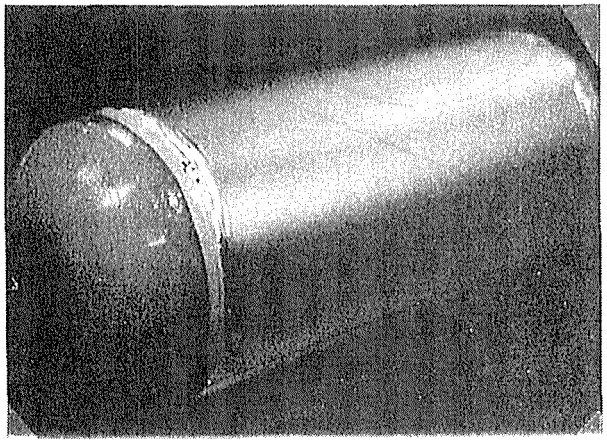

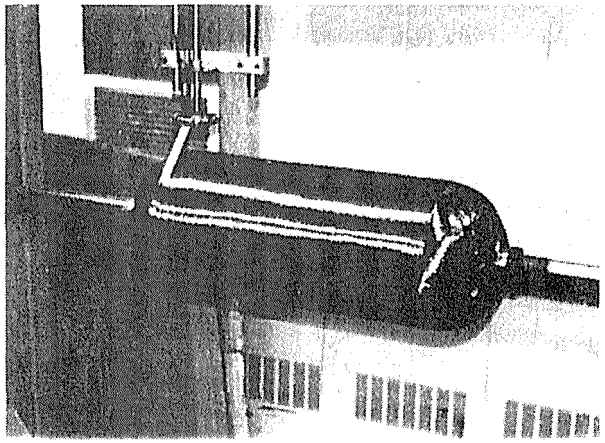

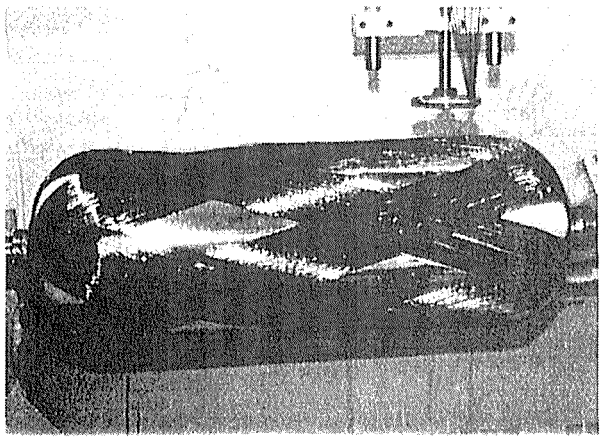

- LLNL bladders fabricated with metallized polymers
- Bladders used as inflatable integral mandrel
- Prototype tanks fabricated with composite overwrap
- PbV/W ~40 km (1.6 million inches) for 0.056 m^3 prototype
- PbV/W ~50 km (2.0 million inches) for some designs

Figure 7

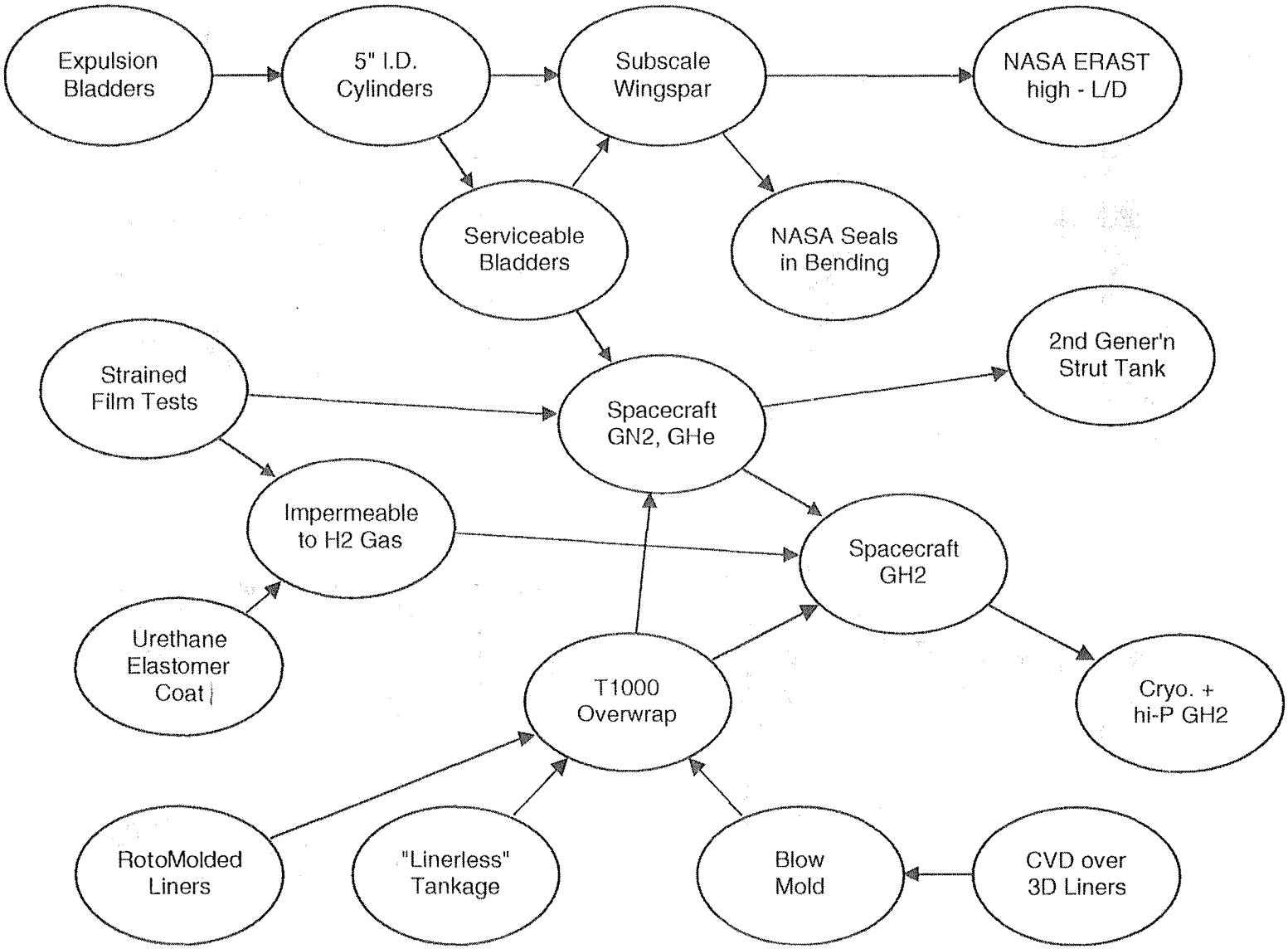
Expulsion Bladders
5" I.D. Cylinders
Subscale Wingspar
NASA ERAST high - L/D
Serviceable Bladders
NASA Seals in Bending
Strained Film Tests
Spacecraft GN2, GHe
2nd Gener'n Strut Tank
Impermeable to H2 Gas
Spacecraft GH2
Urethane Elastomer Coat
T1000 Overwrap
Cryo. + hi-P GH2
RotoMolded Liners
"Linerless" Tankage
Blow Mold
CVD over 3D Liners

Figure 8

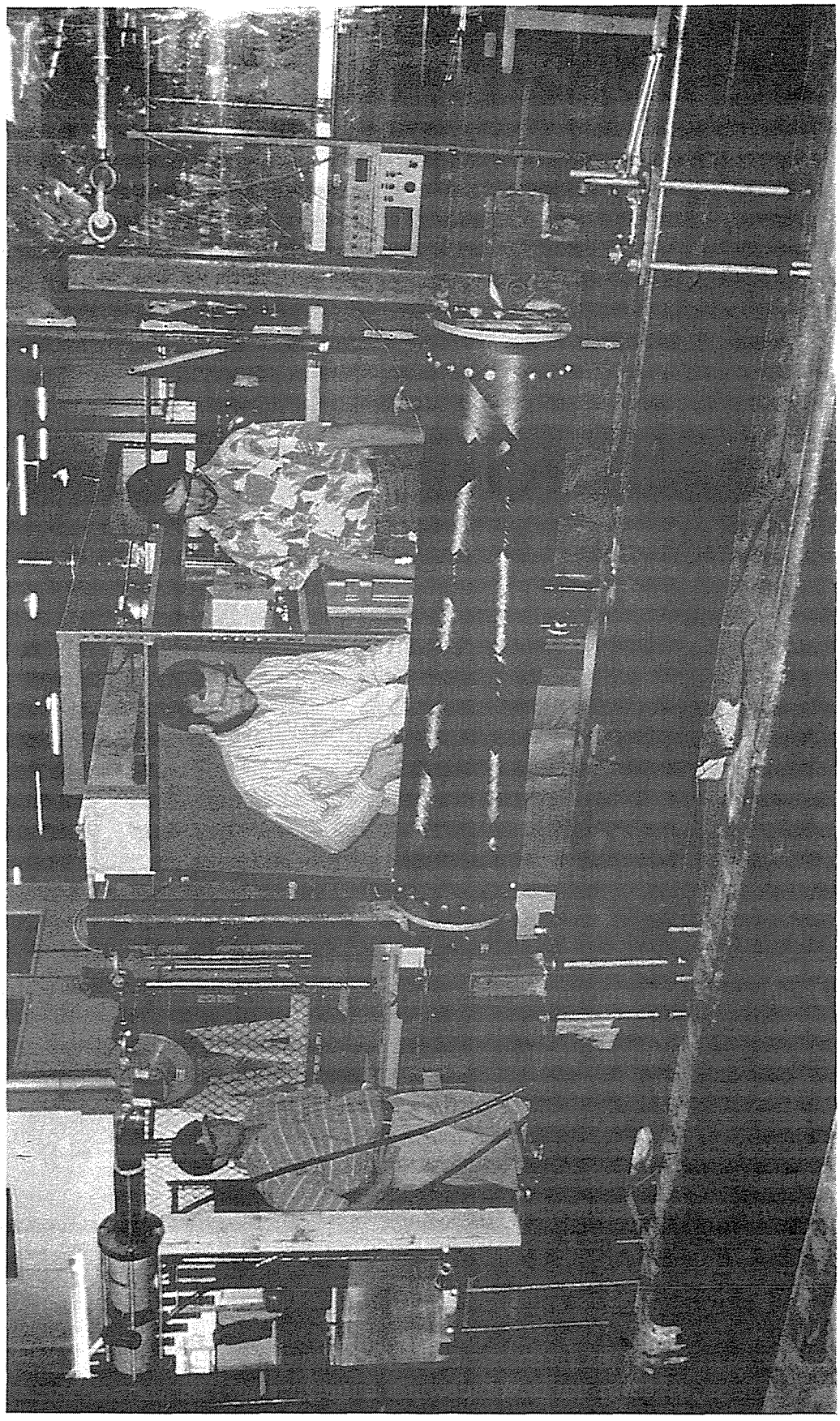

Figure 9

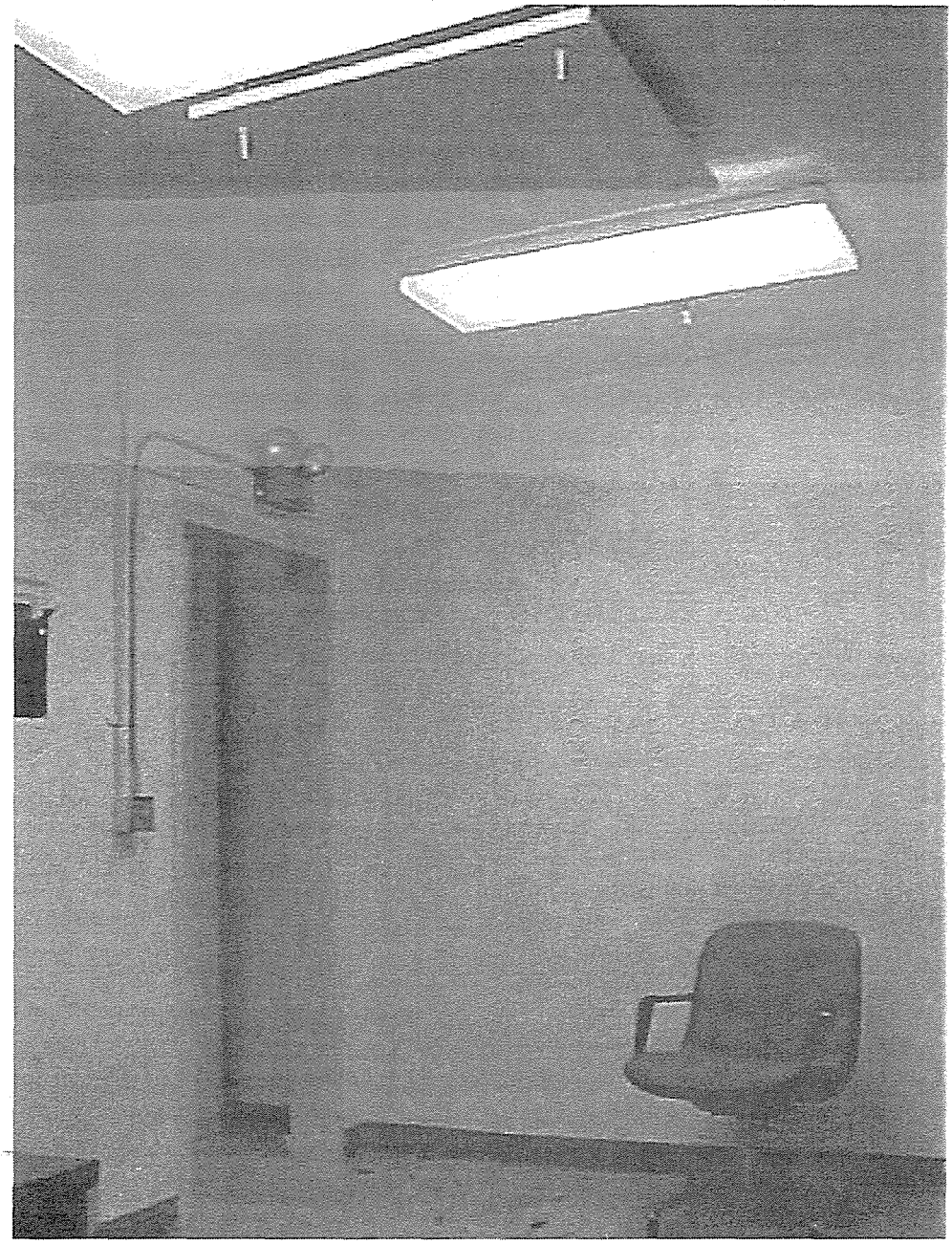

Figure 10

THIOKOL
AEROSPACE & INDUSTRIAL TECHNOLOGIES

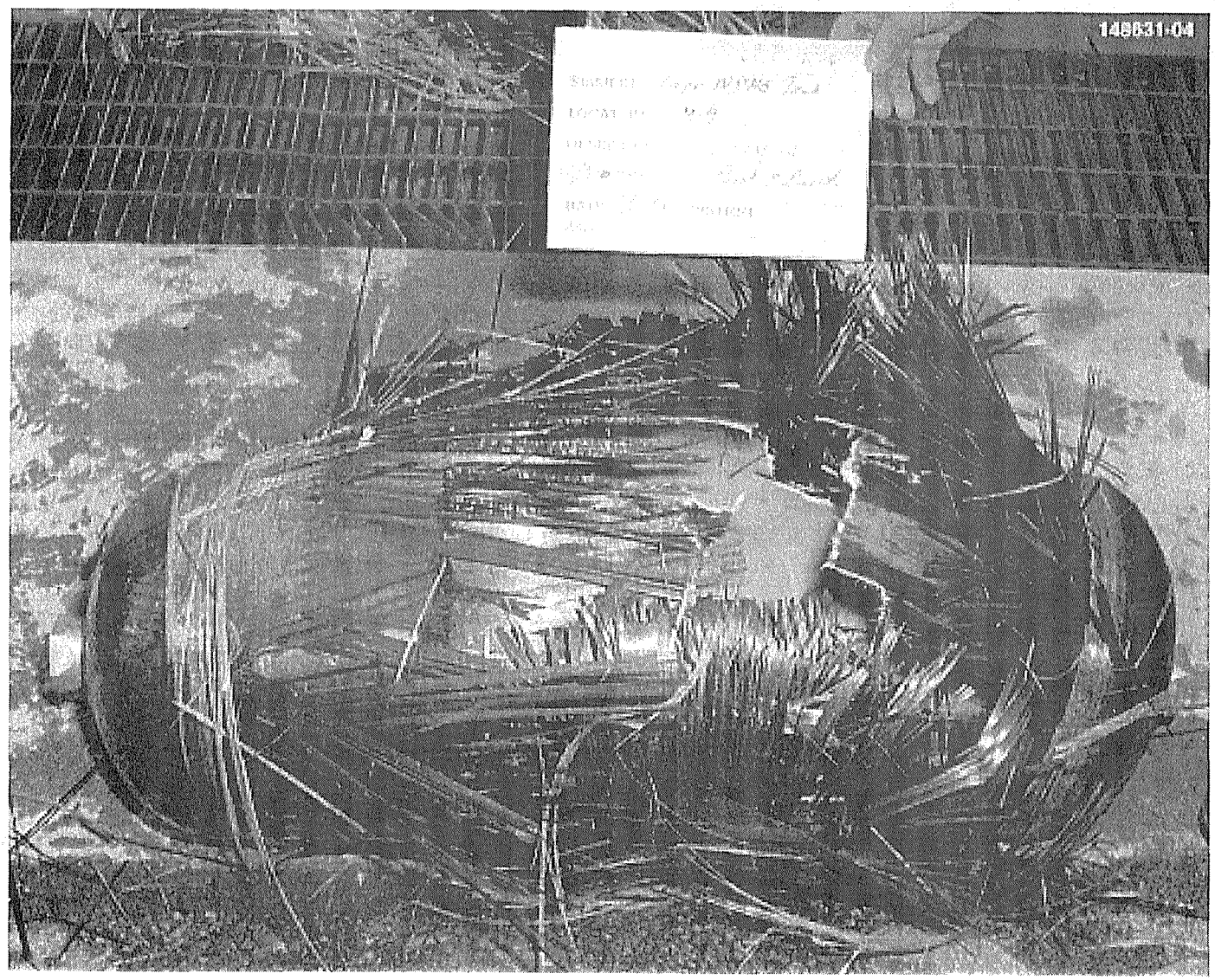

Figure 11

- **Critical technical issues confronting plastic-lined tanks are being identified and addressed**
  - **Cylindrical tanks are being used as a low-cost testbed prior to transition to conformable tanks**
    - » Filament winding on plastic cylindrical liners to establish process parameters
    - » Design optimization
    - » Risk-reduction testing in progress - hydroburst, drop, cycling
  - **Liner/polar boss interface seal issues are being addressed with ambient, hot, and cold cycling of an analog test fixture**
    - » Seal design configuration
    - » Materials selection

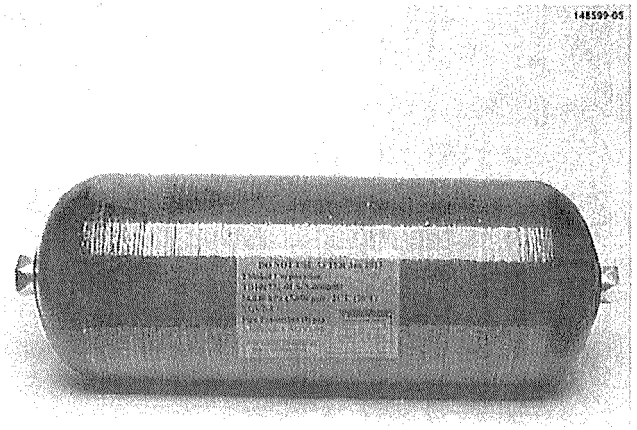

Plastic-Lined Cylindrical Tank . . .

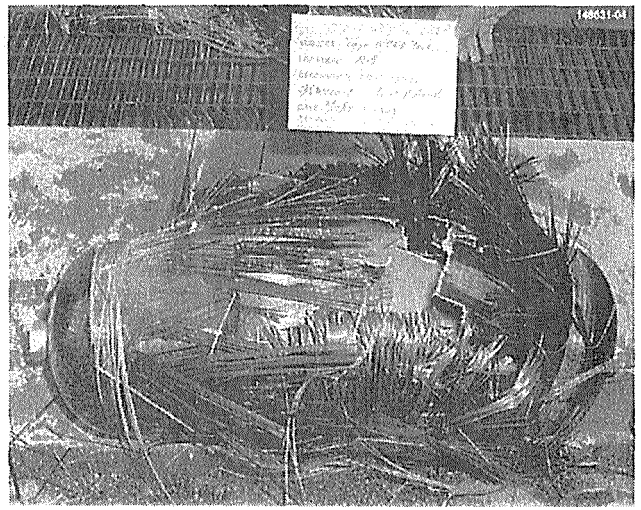

Following Hydroburst Testing

THIOKOL

AEROSPACE & INDUSTRIAL TECHNOLOGIES

Figure 12

THIOKOL
AEROSPACE & INDUSTRIAL TECHNOLOGIES

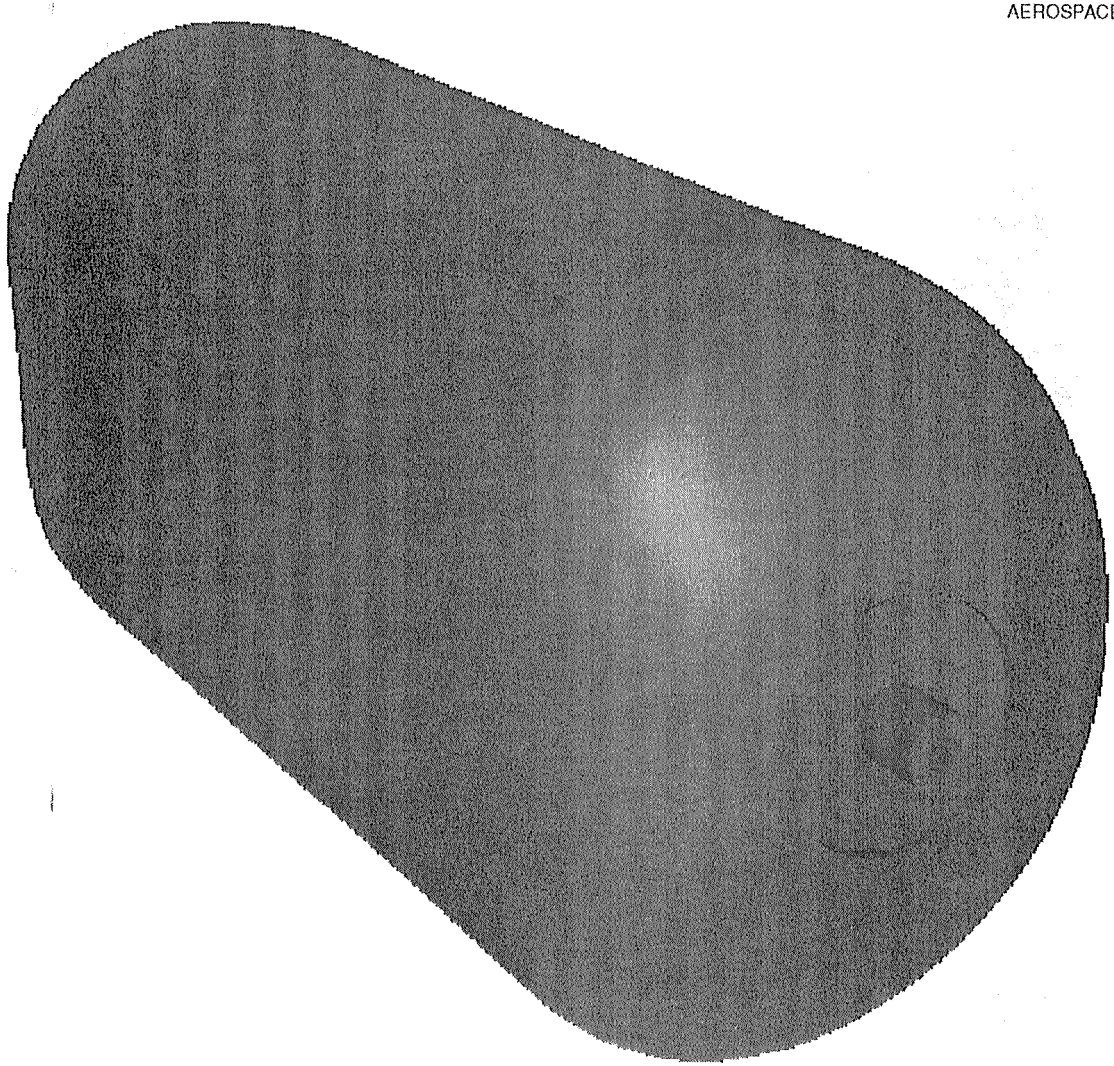

Figure 13

- Purpose - to demonstrate 11,250 psi burst pressure (5,000 psi service pressure x 2.25 safety factor) in a conformable tank
- Structural design and analysis are in progress
- Subscale tooling is available
  - Two cell configuration
  - 10.5 in. x 15.5 in. x 19 in.
- Carbon fiber composite filament to be wound on sand washout mandrels with elastomeric liner
- Hydroburst testing planned to verify structural capabilities

THIOKOL
AEROSPACE & INDUSTRIAL TECHNOLOGIES

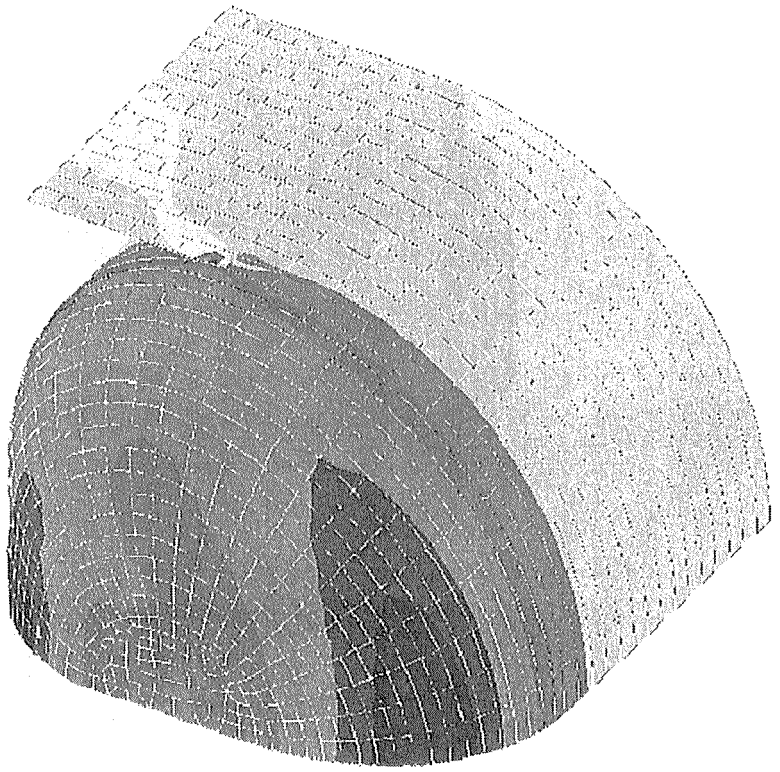

Finite element model of Prototype Tank

Figure 14

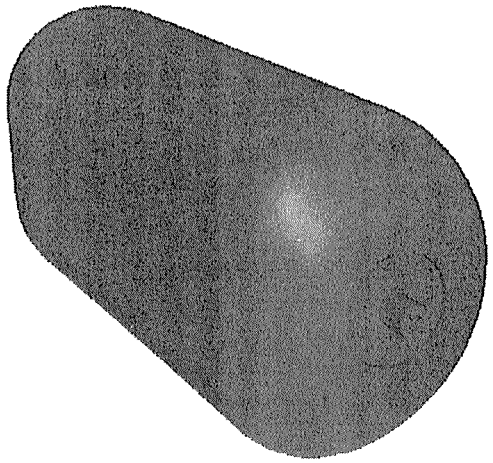

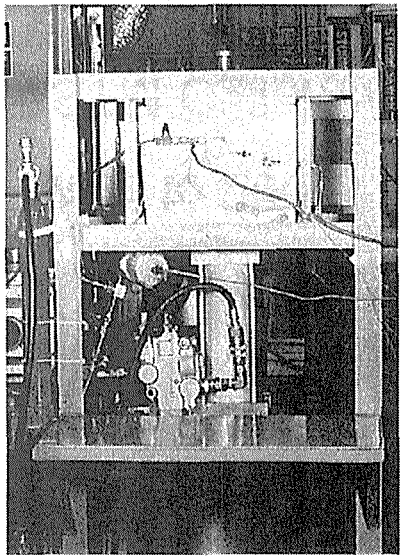

- Liner design drawings completed at Thiokol and sent to Aero Tec Laboratories for mold fabrication
- Preliminary screening of liner materials complete for rotomolding
  - High-density polyethylenes
  - Nylon 6, Nylon 11
    PEEK
  - PVDF
- Permeation test facility developed at Southern Research, Inc. for further material down-select
  - High pressure permeation testing
  - Ability to test samples under biaxial strain

THIOKOL

Figure 15

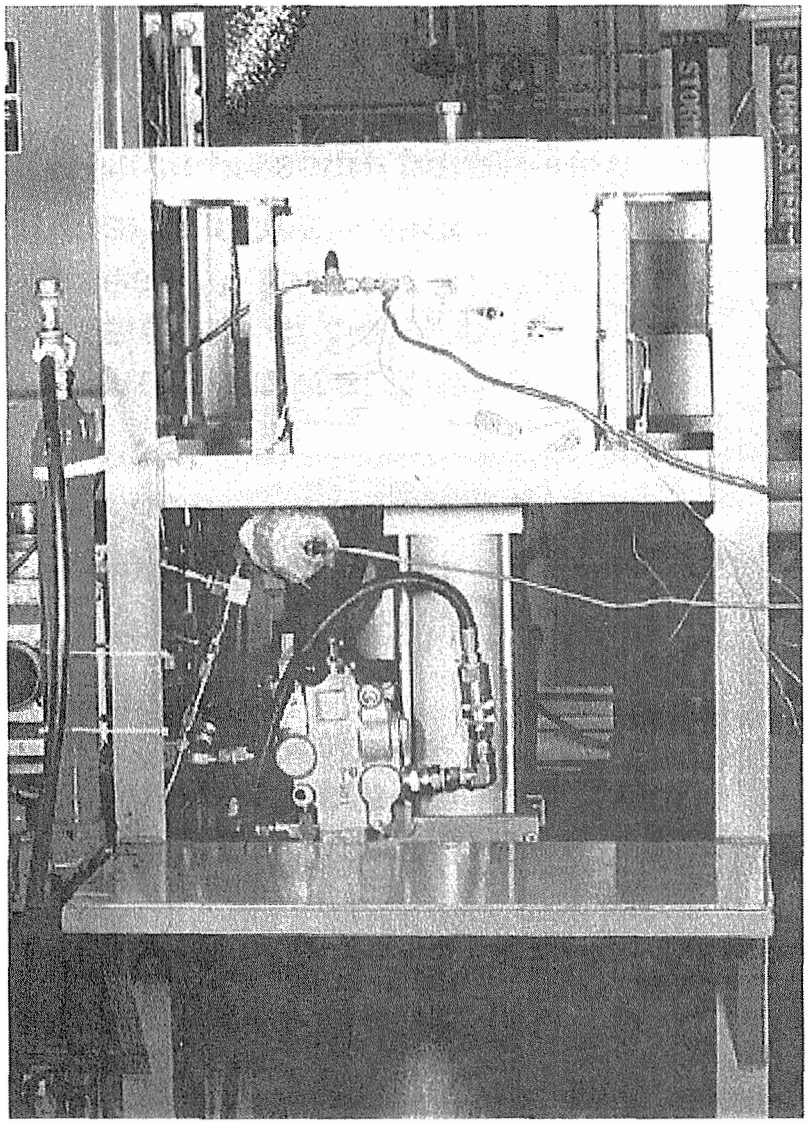

- Existing Test Rig at SRI
- Permeance to 200 psi
- Gases, Liquids to 200 C
- Recently ASTM Calibrated
- Now producing H2 data

- Next-generation rig at SRI
- Built, Now being qualified
- Permeance to 5000 psi
- First-ever test at 1% strain
- Thiokol IR&D, DoE PRDA

Figure 16

Permeance of P-03/Graphite to Hydrogen Gas (EAA/PET/Ag/EAA laminate)

SOUTHERN RESEARCH INSTITUTE

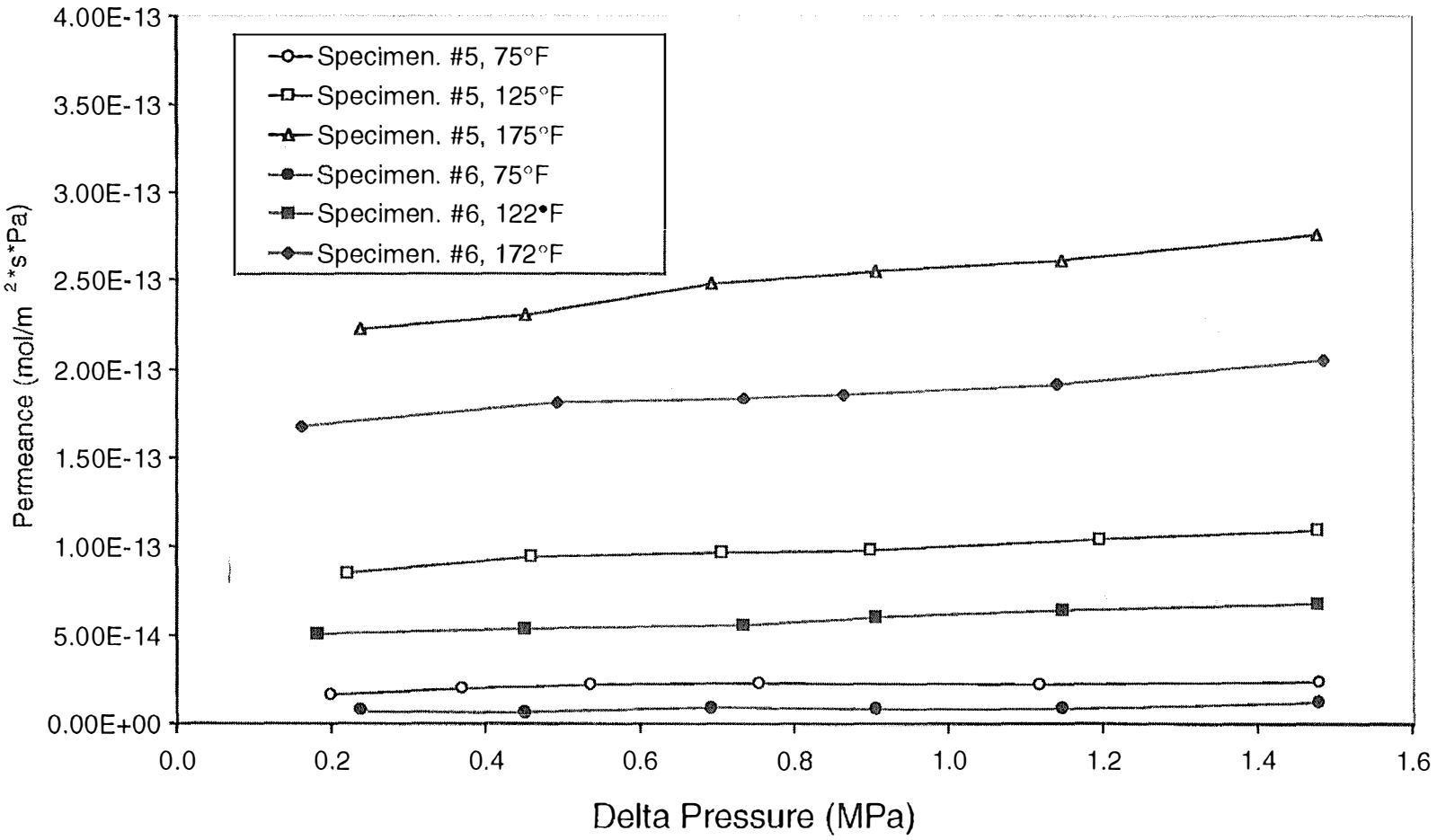

Figure 17

- Energy storage systems designed for aircraft and automotive applications with >400 Wh/kg packaged specific energy
- Primary fuel cell test rig converted into unique test capability
- URFC cell tested using H_2/O_2 for more than 2000 cycles between fuel cell and cathode feed electrolysis modes demonstrated less than a few percent cyclic degradation over a range of current densities
- Operation at >1000 ASF (>1.1 A/cm^2) for URFC in both fuel cell and cathode feed electrolysis modes
- Thin tank liners (bladders) fabricated with low-permeability laminates, seamed to thick end domes with bosses molded in place
- Thin bladders used as inflatable mandrels to fabricate composite tanks
- Prototype composite tanks with estimated performance factors of 1.6 million inches (40 km) have >10% hydrogen storage mass fraction at 300 K
- Composite tanks designed with performance factors of 2.0 million inches (50 km) have >12.5% hydrogen storage mass fraction at 300 K

Figure 18

- URFC operated in fuel cell mode at 0.6 V to >1000 ASF (>1.1 A/cm^2)
- URFC test rig upgraded to accomodate anode feed electrolysis in addition to cathode feed electrolysis and fuel cell modes
- Rapid cycling (<1 minute cycle between electrolysis and fuel cell) demonstrated, enabling rapid response energy storage applications
- Agreements in place to test Hamilton Standard and Proton Energy Systems proprietary hardware on loan to LLNL -- preserving ownership
- Investigation of high performance membranes initiated with partners
- Investigation of reduced catalyst loading for URFC operation underway
- New facility capable of wider range of electrochemical, pressure, and contained mass testing is being prepared at LLNL (uncleared white area)
- Close collaboration and monitoring of Thiokol under DOE tankage PRDA
- Actively interfacing design between Thiokol & DOE/Ford demonstrations
- New generation of liner development with Aero Tec Laboratories, Inc.

Figure 19

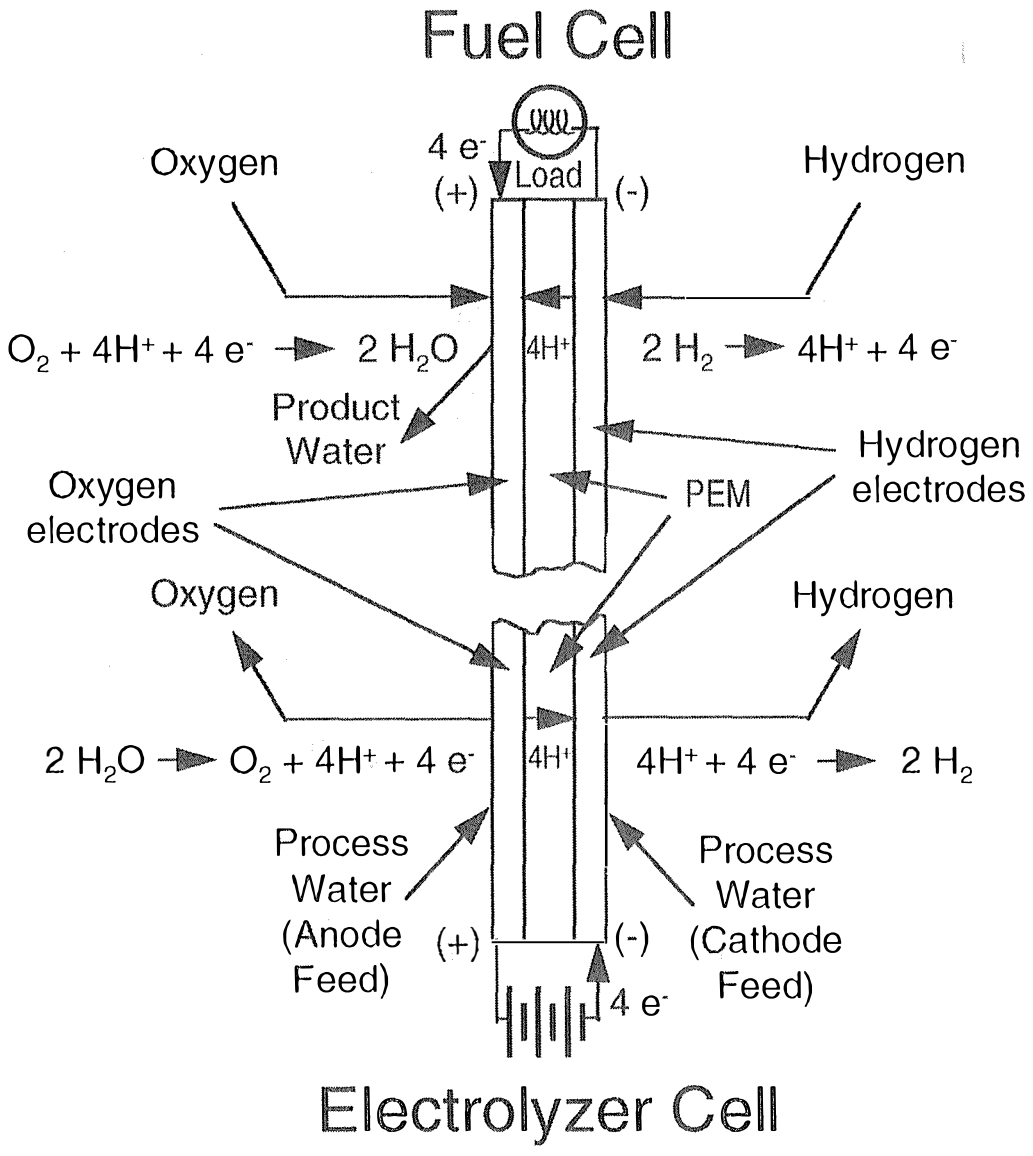
Fuel Cell
Oxygen
4 e-
(+)
Load
(-)
Hydrogen
O2 + 4H+ + 4 e- → 2 H2O
4H+
2 H2 → 4H+ + 4 e-
Product
Water
Hydrogen
electrodes
Oxygen
electrodes
PEM
Oxygen
Hydrogen
2 H2O → O2 + 4H+ + 4 e-
4H+
4H+ + 4 e- → 2 H2
Process
Water
(Anode
Feed)
Process
Water
(Cathode
Feed)
(+)
(-)
4 e-
Electrolyzer Cell

Figure 20

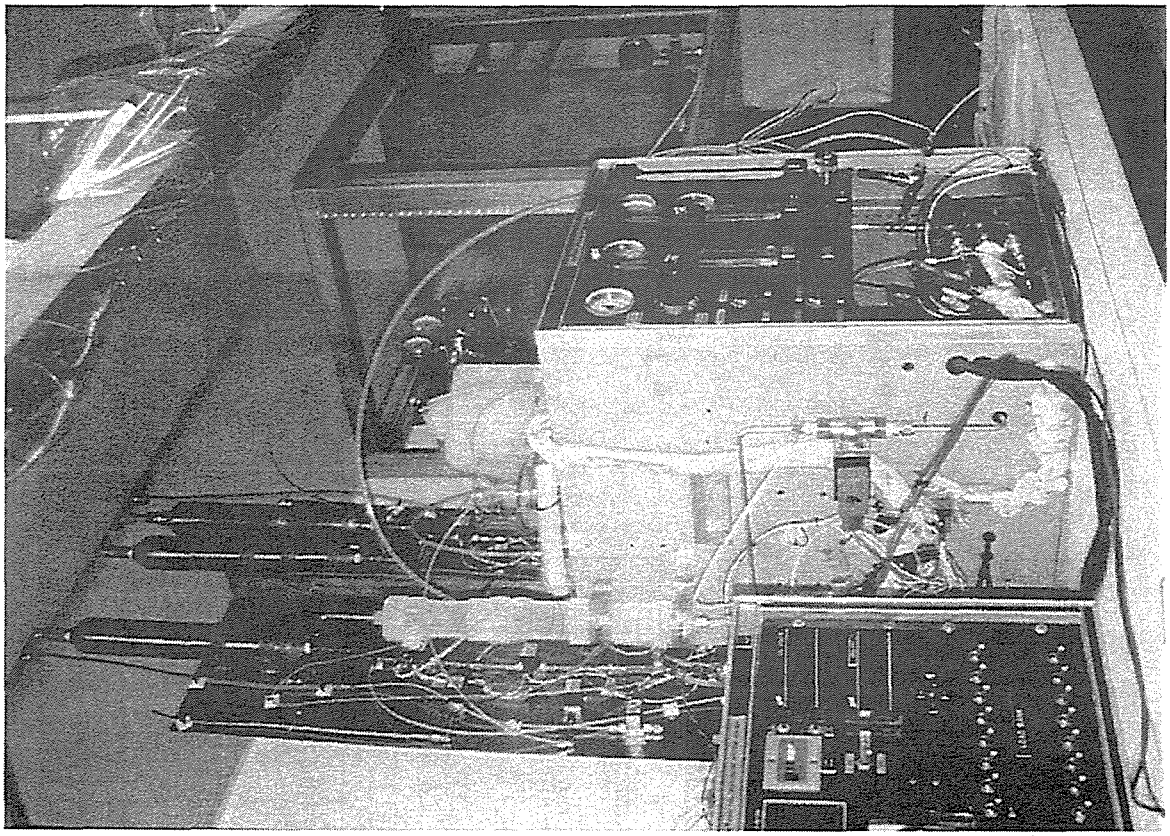

Figure 21

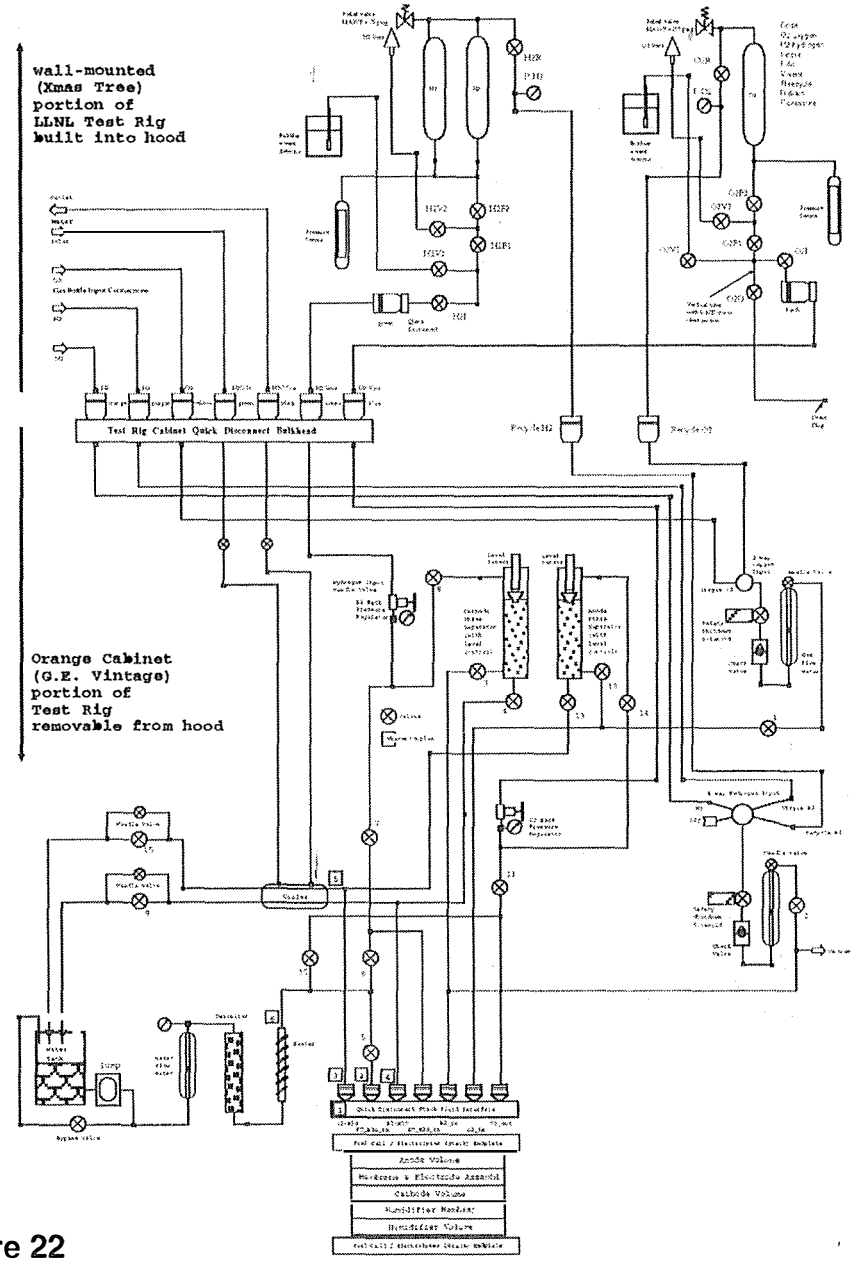

- Able to test cells, stacks, M&E assemblies
- Now able to test both cathode feed and anode feed electrolysis
- Prepared and certified to test with recycled gases (fuel cell operation consuming products of prior electrolysis)
- Allows safe, unattended operation including data logging and multi-mode cycling
- Unique capability to test PEM energy storage systems

Figure 22

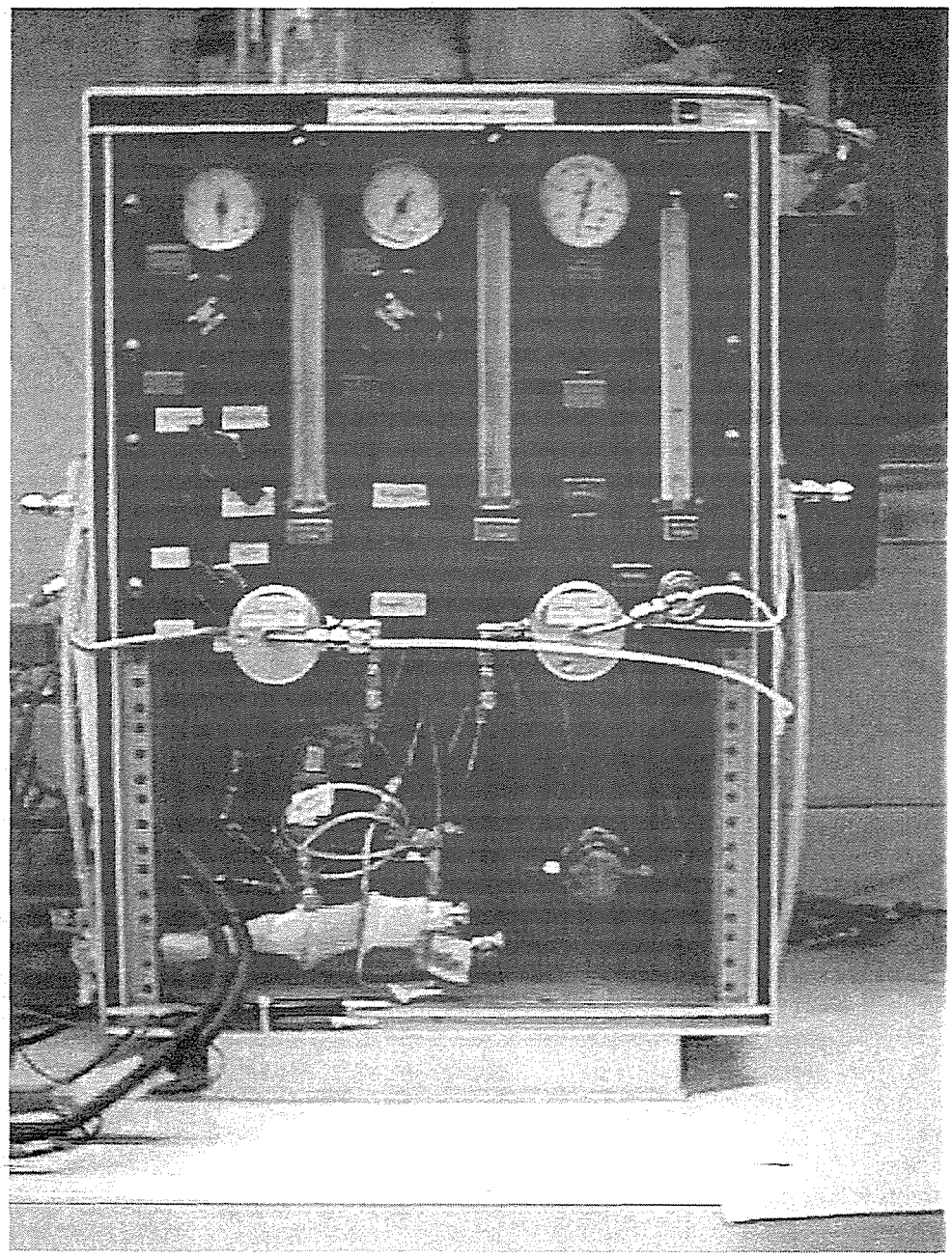

Figure 23

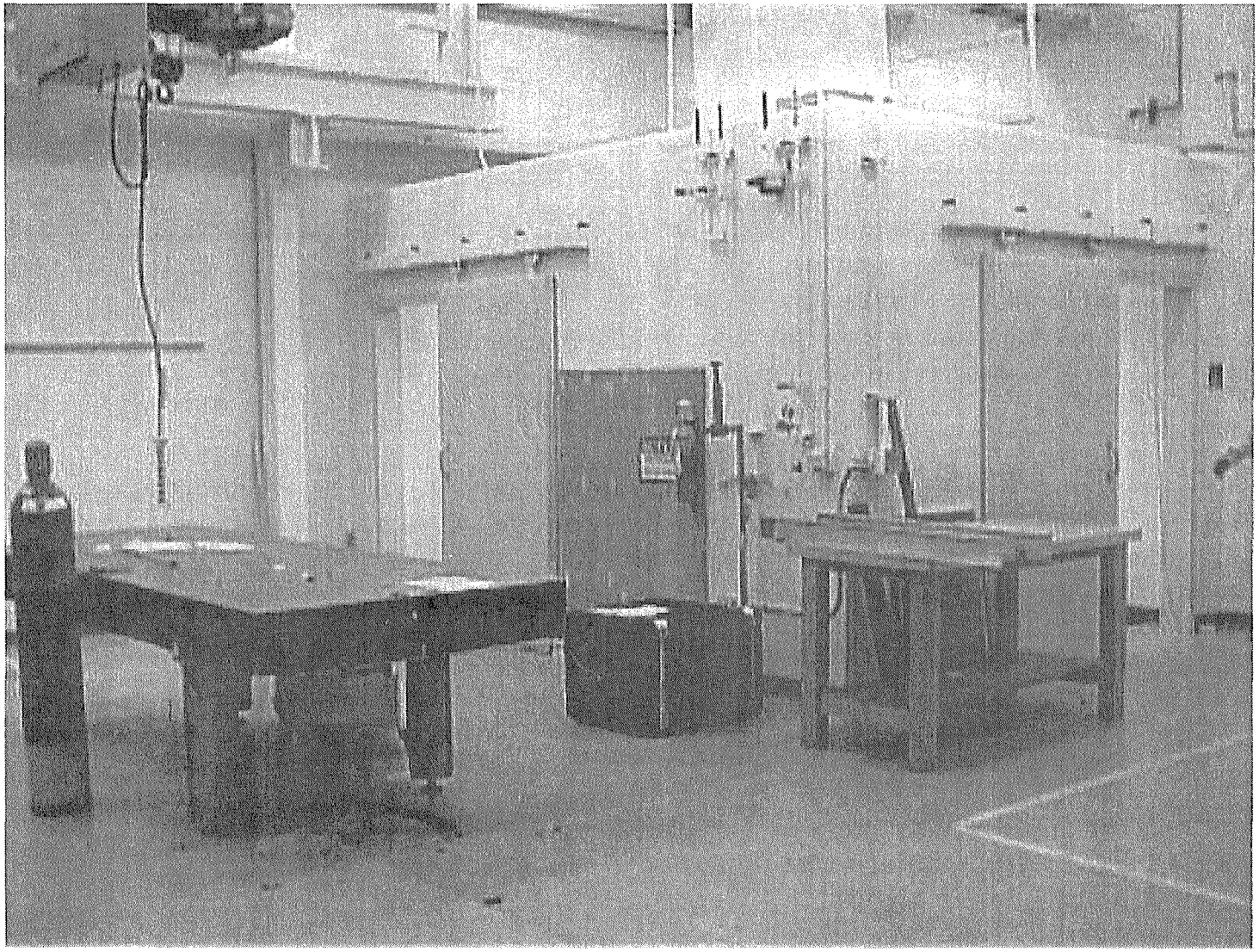

228

Figure 24

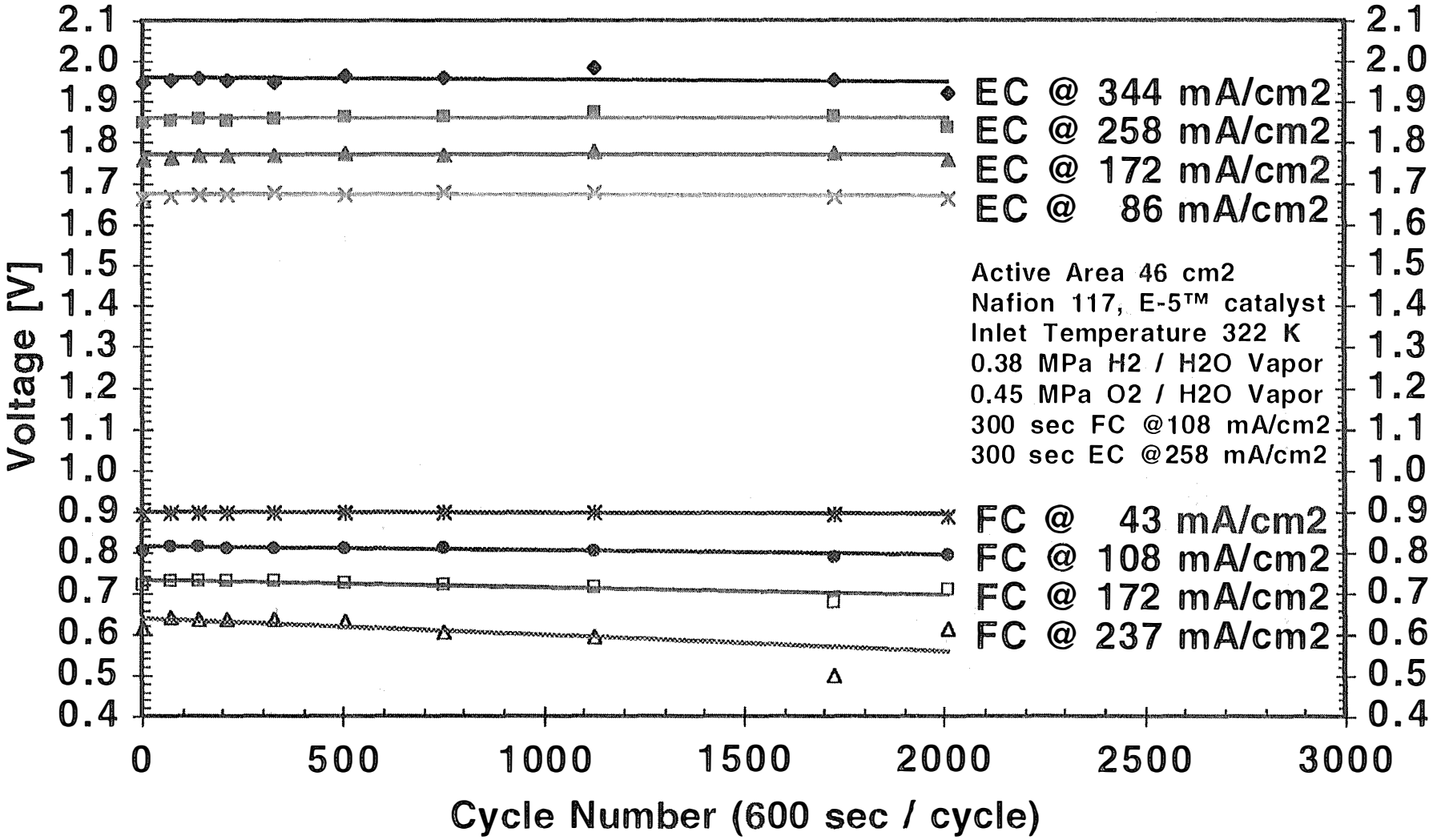
Voltage [V]
Cycle Number (600 sec / cycle)
EC @ 344 mA/cm2
EC @ 258 mA/cm2
EC @ 172 mA/cm2
EC @ 86 mA/cm2
Active Area 46 cm2
Nafion 117, E-5™ catalyst
Inlet Temperature 322 K
0.38 MPa H2 / H2O Vapor
0.45 MPa O2 / H2O Vapor
300 sec FC @108 mA/cm2
300 sec EC @258 mA/cm2
FC @ 43 mA/cm2
FC @ 108 mA/cm2
FC @ 172 mA/cm2
FC @ 237 mA/cm2

Figure 25

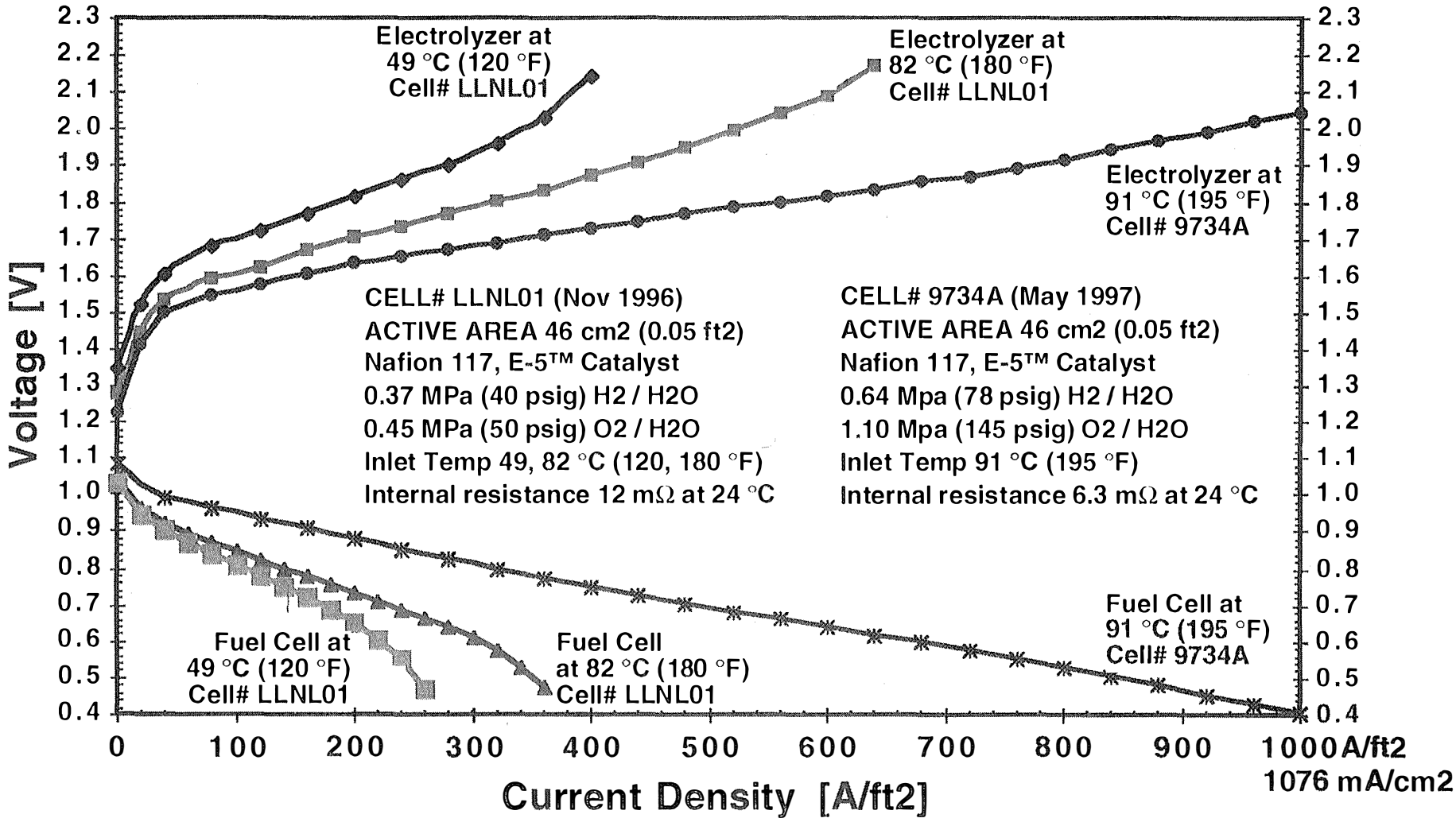
Electrolyzer at
49 °C (120 °F)
Cell# LLNL01
Electrolyzer at
82 °C (180 °F)
Cell# LLNL01
Electrolyzer at
91 °C (195 °F)
Cell# 9734A
CELL# LLNL01 (Nov 1996)
ACTIVE AREA 46 cm2 (0.05 ft2)
Nafion 117, E-5™ Catalyst
0.37 MPa (40 psig) H2 / H2O
0.45 MPa (50 psig) O2 / H2O
Inlet Temp 49, 82 °C (120, 180 °F)
Internal resistance 12 mΩ at 24 °C
CELL# 9734A (May 1997)
ACTIVE AREA 46 cm2 (0.05 ft2)
Nafion 117, E-5™ Catalyst
0.64 Mpa (78 psig) H2 / H2O
1.10 Mpa (145 psig) O2 / H2O
Inlet Temp 91 °C (195 °F)
Internal resistance 6.3 mΩ at 24 °C
Fuel Cell at
49 °C (120 °F)
Cell# LLNL01
Fuel Cell
at 82 °C (180 °F)
Cell# LLNL01
Fuel Cell at
91 °C (195 °F)
Cell# 9734A
Voltage [V]
2.3
2.2
2.1
2.0
1.9
1.8
1.7
1.6
1.5
1.4
1.3
1.2
1.1
1.0
0.9
0.8
0.7
0.6
0.5
0.4
0
100
200
300
400
500
600
700
800
900
1000A/ft2
1076 mA/cm2
Current Density [A/ft2]

Figure 26

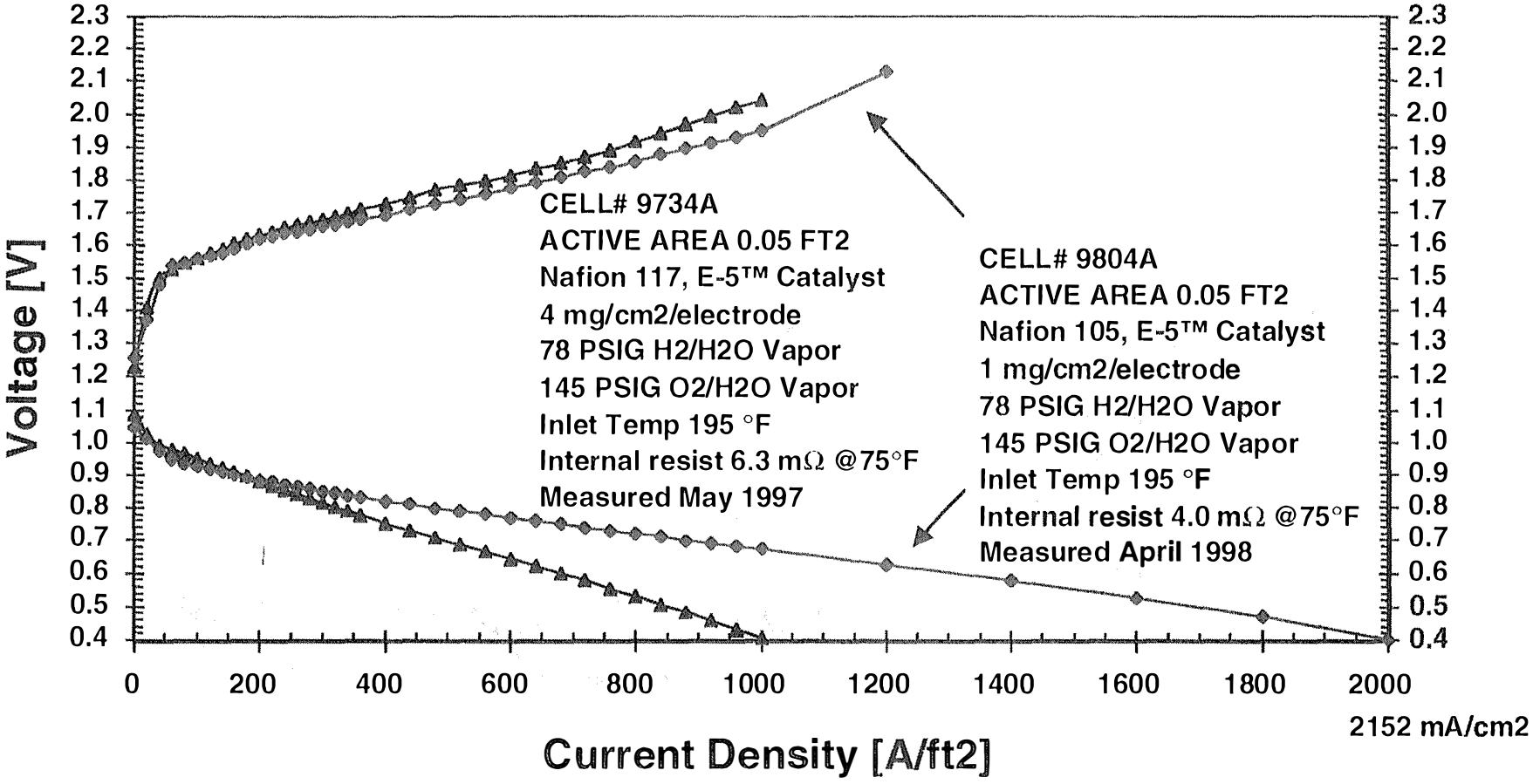
Voltage [V]
2.3
2.2
2.1
2.0
1.9
1.8
1.7
1.6
1.5
1.4
1.3
1.2
1.1
1.0
0.9
0.8
0.7
0.6
0.5
0.4
0
200
400
600
800
1000
1200
1400
1600
1800
2000
2152 mA/cm2
Current Density [A/ft2]
CELL# 9734A
ACTIVE AREA 0.05 FT2
Nafion 117, E-5™ Catalyst
4 mg/cm2/electrode
78 PSIG H2/H2O Vapor
145 PSIG O2/H2O Vapor
Inlet Temp 195 °F
Internal resist 6.3 mΩ @75°F
Measured May 1997
CELL# 9804A
ACTIVE AREA 0.05 FT2
Nafion 105, E-5™ Catalyst
1 mg/cm2/electrode
78 PSIG H2/H2O Vapor
145 PSIG O2/H2O Vapor
Inlet Temp 195 °F
Internal resist 4.0 mΩ @75°F
Measured April 1998

Figure 27

THIOKOL

AEROSPACE & INDUSTRIAL TECHNOLOGIES

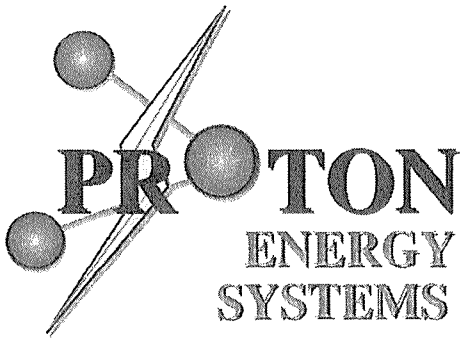

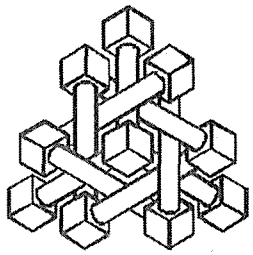

SOUTHERN RESEARCH
INSTITUTE

ATK®
SPACE TANKAGE
AERO TEC LABORATORIES INC.

Figure 28

INTEGRATED ANALYSIS OF HYDROGEN PASSENGER VEHICLE TRANSPORTATION PATHWAYS

C. E. (Sandy) Thomas
Brian D. James
Franklin D. Lomax, Jr. and
Ira F. Kuhn, Jr.
Directed Technologies, Inc.
4001 North Fairfax Drive, Suite 775
Arlington, Virginia 22203

Abstract

Hydrogen-powered fuel cell vehicles will reduce local air pollution, greenhouse gas emissions and oil imports. Other alternative vehicles such as gasoline- or methanol-powered fuel cell vehicles, natural gas vehicles and various hybrid electric vehicles with internal combustion engines may also provide significant environmental and national security advantages. This report summarizes a two-year project to compare the direct hydrogen fuel cell vehicle with other alternatives in terms of estimated cost and estimated societal benefits, all relative to a conventional gasoline-powered internal combustion engine vehicle.

The cost estimates used in this study involve ground-up, detailed analysis of the major components of a fuel cell vehicle system, assuming mass production in automotive quantities. We have also estimated the cost of both gasoline and methanol onboard fuel processors, as well as the cost of stationary hydrogen fueling system components including steam methane reformers, electrolyzers, compressors and stationary storage systems. Sixteen different vehicle types are compared with respect to mass production cost, local air pollution and greenhouse gas emissions.

Introduction

Hydrogen could become an important energy carrier in the 21st century, supplementing electricity as a non-polluting method of delivering energy. Hydrogen would be particularly beneficial in the transportation sector, since hydrogen can be stored onboard a moving vehicle more readily than electricity. Zero emission electric or hydrogen vehicles would help to clean the air we breathe and reduce our dependence on foreign oil. Battery-powered electrical vehicles might also benefit society, but even EVs with advanced batteries would have limited range, high cost, and possibly limited battery life and long recharging times. If customers do not accept these limitations of battery-powered EVs, then market penetration would be restricted, and air pollution and oil independence gains would be marginal, too.

Hydrogen-powered fuel cell vehicles (FCVs), however, have the potential to provide the same range, acceleration, refueling time and other creature comforts associated with modern internal combustion engine vehicles (ICEVs). In the long run, FCVs could cost less to manufacture than the mechanically complex ICEVs they would replace, and maintenance and operating costs of a FCV would most certainly be less than those of conventional gasoline-powered ICE vehicle. With more potential driver appeal, FCVs have a greater chance than battery powered electric vehicles (BPEVs) of succeeding in the marketplace, and thereby to make a significant contribution to cleaner air and reduced oil imports.

Despite the existence of effective onboard hydrogen storage options (James 1996) and economic hydrogen supply options (Thomas 1997, Thomas 1998a), some decision makers in both industry and government are still skeptical of direct hydrogen FCVs. We therefore need to compare the alternatives to the direct hydrogen FCV. The two primary alternative vehicle classes are FCVs with onboard fuel processors to convert liquid fuels to hydrogen, and hybrid electric vehicles using low power internal combustion engines (ICEs) or other thermal engines operating at a fixed or limited range of speeds and power levels. This report analyzes the cost and societal benefits of 14 different vehicles:

1. Fuel Cell Vehicles (FCV)
   - -Direct hydrogen FCV
   - -Methanol FCV (probable and best case)
   - -Gasoline FCV (probable and best case)

2. Natural gas Vehicles
   - -Pure natural gas
   - -Hydrogen/Natural gas mixtures

3. Hybrid Electric Vehicles (HEV) with Internal Combustion Engines (Nine Combinations)
   - -Hydrogen, natural gas and diesel fuel
   - -Thermostat series, load-following series, and parallel HEV.

For each vehicle type, we analyzed four attributes:

* Vehicle cost in automotive-scale mass production
* Local emissions (VOCs, CO, NOx and PM)
* Greenhouse gas (GHG) emissions
* Oil imports

The last three attributes all depend on fuel economy. Fuel economy in turn depends on vehicle weight, so vehicle weight and fuel economy on various driving schedules were estimated for all 14 vehicle types.

Vehicle Descriptions

All vehicles are based on the Ford AIV (aluminum intensive vehicle) Sable, with a curb weight of 1,168 kg, compared to about 1,490 kg for the standard Sable. All other features of the vehicle such as aerodynamic drag (0.33), cross sectional area (2.13 m^2) and tire rolling resistance (0.0092) are maintained at the same level as the production Ford Taurus. The resulting fuel economies calculated below are therefore lower than would be expected if future vehicles incorporate some of the improved body characteristics being developed under the U.S. Partnership for a New Generation of Vehicles (PNGV) program. However, all types of vehicles would achieve higher fuel economy with improved body characteristics, so the relative comparisons shown here should be applicable to a PNGV type future vehicle.

Direct Hydrogen Fuel Cell Vehicle

The direct hydrogen fuel cell vehicle in this analysis has an onboard 5,000 psi compressed gas tank to provide hydrogen for the proton exchange membrane (PEM) fuel cell system. The ICE, 4-speed automatic transmission, exhaust system including catalytic converter, starter motor, alternator and other ICE related components are removed from the AIV Sable glider, replaced by the PEM fuel cell system, peak power battery bank, inverter, traction motor, motor controller and single speed transmission.

Methanol Fuel Cell Vehicle

To eliminate the need for onboard hydrogen storage, several companies have built or are proposing to use methanol-powered fuel cell vehicles. Daimler-Benz has demonstrated an A-Car FCV (Necar-3) that has an onboard methanol steam reformer to extract hydrogen to power the fuel cell. While new infrastructure would be required to supply large quantities of methanol FCVs, there are at least some methanol pumps available and consumers are more used to liquid than gaseous fuels.

However, developing a low-cost, low weight, efficient and time responsive methanol reformer and

gas cleanup system to remove all but traces of carbon monoxide from the hydrogen stream is a significant challenge. Methanol does have the advantage of being the most easily reformed liquid fuel with only one carbon atom (CH_3OH) and hence no carbon-carbon bonds. Methanol can be reformed at 250 to 300°C, compared to 850 to 900°C typical of steam methane reformers or even higher for gasoline partial oxidation reformers.

Gasoline Fuel Cell Vehicle

The primary focus of the U.S. Department of Energy's fuel cell vehicle program is currently the development of onboard multi-fuel partial oxidation (POX) reformers to allow the use of existing fuel infrastructure, including gasoline. This approach eliminates the need for a totally new fuel infrastructure[1], but places the greatest burden on the vehicle itself. Reforming gasoline or other fuels such as diesel fuel, natural gas or ethanol is much more difficult than reforming methanol, generally requiring much higher temperatures in the 800 to 1000°C with somewhat lower efficiency.

A partial oxidation system is very effective at reforming virtually any type of hydrocarbon fuel. Table 1 lists the output characteristics from a Texaco industrial POX system using pure oxygen, illustrating that even oil bottoms or asphalt can be converted to a stream of over 90% hydrogen and carbon monoxide. The CO can then be converted to more hydrogen by the water-gas shift reaction:

$$CO + H_2O = CO_2 + H_2$$

A gasoline POX system with existing gas cleanup technology would produce lower hydrogen content than a methanol processor, with as little as 30 to 40% hydrogen, compared to 75% hydrogen from a steam methanol processor. A partial oxidation system, as the name implies, adds some oxygen directly into the reactor. Industrial POX systems usually include an air separation plant to provide pure oxygen, but this would not be economic for a mobile reformer. Rather, air is added which introduces 3.76 moles of nitrogen for each mole of oxygen. Nitrogen is the primary diluent in the POX reformate, along with the carbon dioxide that is also present in methanol reformate. These diluents affect the ability of the hydrogen to reach the electrochemically active catalyst sites on the anode, reducing peak fuel cell power. The peak power of an older technology Ballard fuel cell system was reduced by 26% operating on 35% hydrogen content. It is not clear whether this drop in peak power with dilute hydrogen mixtures can be reduced with new fuel cell designs.

---

[1]While the primary intent is to use gasoline fuel, in all likelihood a new grade of gasoline would be required for onboard reformer systems. A fuel cell grade gasoline would probably require much lower (near zero?) sulfur content than existing grades, effectively requiring a separate set of gasoline tanks, pumps, tanker trucks, etc., and modified refinery equipment. Thus there will probably be some required infrastructure investment even if onboard POX processors are developed.

Table 1. Output Gas Composition (mol %) from Texaco Partial Oxidation Reactor with Pure Oxygen

	Natural Gas	Naphtha	Fuel Oil	Vacuum Residual	Oil Bottoms	Asphalt
Hydrogen	61.1	51.2	45.9	44.2	41.4	42.1
Carbon Monoxide	35.0	45.3	48.5	48.3	51.2	49.3
Carbon Dioxide	2.6	2.7	4.6	5.2	5.3	6.5
Methane	0.3	0.7	0.2	0.6	0.3	0.4
Nitrogen + Argon	1.0	0.1	0.7	0.2	0.4	0.4
Hydrogen Sulfide	-	-	0.1	1.4	1.3	1.2
Efficiency (HHV - %)	83.8	82.7	83.1	84.1	82	81.9

Hybrid Electric Vehicles

We have analyzed three different ICE hybrid electric vehicles, each with three different fuels or a combination of nine different HEVs. Each HEV is described briefly below. Energy flow diagrams are provided for each HEV type in Figures 1 through 3, assuming constant vehicle weight. In reality each HEV will have different total vehicle weights, so these three figures illustrate the effects of the hybrid driving mode on fuel economy independent of weight changes.

Thermostat Mode Series Hybrid Electric Vehicle

An electric motor supplies all mechanical power to the wheels. The ICE plus generator are used to provide electrical energy to the motor and to recharge the batteries. The ICE is turned on at a fixed power level when the battery state of charge (SOC) reaches a pre-set minimum (40%), and turned off when the SOC exceeds a maximum (60%). Since the ICE in turned off when the battery is within the set SOC levels, the battery bank must have enough power to provide the peak required acceleration for the vehicle. The weight and cost of this peak power battery reduces the performance of the thermostat series HEV.

Load-Following Series Hybrid Electric Vehicle

The ICE is turned on when the vehicle power demand (road power plus accessory power assumed to be 500 watts) exceeds a threshold, and turned off whenever the vehicle stops, the battery SOC exceeds a maximum set point, or the power demand falls below a lower threshold. Both upper and lower power thresholds vary according to pre-programmed algorithms as a function of battery SOC to maintain the battery SOC within a narrow range. The ICE output power varies over a limited range to optimize system efficiency by minimizing the energy passing into and out of the battery. That

is, the computer algorithms keep the ICE operating as long as possible. The ICE is only turned off when its efficiency falls below the battery round trip efficiency. The load-following series HEV can have a smaller peak power battery, since the engine is turned on whenever the driver demands peak power.

Parallel Hybrid Electric Vehicle

The ICE and a supplemental traction motor are both mechanically coupled to the transmission through appropriate gear sets. A computer algorithm determines when to turn the ICE on, what power level to produce, and when to turn the ICE off. Since the ICE is now mechanically coupled to the road (unlike the two series hybrids describe above), the one-speed transmission used in FCVs and series HEVs must be replaced with a 4-speed automatic transmission. This increases weight and cost and reduces engine efficiency, since the ICE must now operate over a wider range of output powers away from its "sweet spot" of maximum efficiency. However, the parallel mode does eliminate the need for the generator that is required for a series hybrid, and some of the ICE energy passes directly from the engine to the transmission without the efficiency losses associated with the generator, rectifier, inverter and AC induction motor used in the series HEVs.

Vehicle Weight Estimates

The detailed weight estimates are shown for the fuel cell vehicles below. For details on weight estimate of the other vehicles, refer to (Thomas 1998b).

Direct Hydrogen Fuel Cell Vehicle Weight Estimate

The weight of the fuel cell vehicle power train is summarized in Table 2 to illustrate the method used to calculate all vehicle weights. We have assumed a net fuel cell system specific power of 500 watt/kg, which is also the DOE goal for mobile fuel cell systems for 2004 (DOE 1998, p. 3-40). The specific power of the electric motor, inverter and controller is assumed to be just over 1 kW/kg, near the DOE goal of 1.2 kW/kg for the total motor/electronics package -- 1.6 kW/kg for the motor and 5 kW/kg for the inverter/controller by 2004 (DOE 1998, p. 3-68). The battery specific power (560 watts/kg) is based on demonstrated performance of the Bolder thin plate, high peak power lead acid battery at 50% state of charge (SOC)[2]. Specific power is even greater at higher SOC, but we assume here that the battery is normally maintained near 50% SOC to accommodate regenerative braking energy on long hill descents. The DOE goal for a power-assist battery subsystem for a hybrid vehicle

[2]Battery sizing is normally determined by specific energy, not specific power, since energy storage is critical for EVs to attain adequate range. The peak power battery for a FCV is only needed for brief accelerations which might last for 10 to 20 seconds, requiring very little energy. Indeed the Bolder battery technology provides much more energy storage capability than is needed for the FCV. Sizing is therefore determined exclusively by specific power.

is 800 Watts/kg (DOE 1998, p. 3-56). We have added a 10% margin to the peak power of both the motor and the battery system.

Table 2. Estimated Weight of a 5-Passenger Direct Hydrogen Fuel Cell Vehicle

	Peak Power Required (kW)	Specific Power (kW/kg)	Total Weight (kg)
Fuel Cell System	38.1	.5	76.2
H_2 Storage Tank			34.9
Hydrogen			4.7
Electric Motor/Inverter/Controller	82	1.09	75.2
Peak Power Batteries	40.3	.56	71.9
Battery Controller			9.0
Gear Box			27.0
Radiator & Coolant			14.0
Cables & Misc.			21.0
Total Fuel Cell-Unique Components			334
Glider[3]			821
Curb Weight			1,155
Test Weight			1,291

The FCV net test weight is estimated at 1,291 kg, which is almost the same weight as the AIV Sable with an internal combustion engine drivetrain at 1,304 kg. In other words, the fuel cell power train weight is projected to be very close to that of the current ICEV drivetrain weight, with room for net improvements if electric motors and particularly their controllers can be manufactured with less mass. On the other hand, the specific power of conventional ICE power trains will undoubtedly improve, although the current PNGV front-runner, the direct injection diesel, will need major weight reductions just to reach the specific power of spark ignition engines assumed in this ICEV comparison.

[3]"Glider" weight here means vehicle curb weight minus the ICE power train, 4-speed automatic transmission, gasoline fuel tank and exhaust system -- all components not used in the fuel cell vehicle.

Methanol Fuel Cell Vehicle Weight Estimates

Estimating the weight of a methanol FCV is complicated due to the closed-loop nature of an onboard reformer/fuel cell system. In a direct hydrogen fuel cell, virtually all of the hydrogen can be consumed in the anode of the fuel cell. In principle the fuel cell can be operated "dead-ended," with no exhaust from the anode chamber. In practice, though, a small portion of the fuel cell anode gas is recirculated to the anode input to help manage water vapor and to prevent buildup of other trace gases.

The output gas stream from a methanol reformer is not pure hydrogen with current technology.[4] The methanol reformate from a steam reformer is typically 75% hydrogen with most of the rest CO_2 (all CO down to 10 to 50 ppm must be removed in a special gas cleanup step, currently using a preferential oxidation (PROX) step.) If methanol is processed with a partial oxidation (POX) system, hydrogen content will be even lower due to nitrogen dilution. As a result, the anode chamber of the fuel cell stack must have significant exhaust gas to remove the CO_2. By definition, then, some hydrogen must also exit the system; otherwise the last section of the fuel cell near the exit would have zero hydrogen partial pressure and would not produce any electricity. Typically 10 to 20% of the hydrogen passes through the anode of the fuel cell unreacted. To avoid a safety hazard and to limit excessive efficiency losses, this unused hydrogen must be burned, and the heat utilized in some manner such as to raise steam for the reformer.

Existing fuel cell systems also experience a drop in peak power operating on 75% hydrogen compared to pure hydrogen. The peak power of an early generation of the Ballard fuel cell system dropped 10 to 12% operating on simulated methanol reformate (See Appendix B, section 2 of Thomas-1998b for details). Since the fuel cell peak power must be sized to provide the necessary vehicle hill climbing capability, the fuel cell suitable for a FCV with an onboard reformer must be larger to make up for this lost peak power capability, thereby increasing vehicle weight and cost. In addition. all other components of the vehicle must be increased in size to maintain a given vehicle performance. That is, the vehicle power to weight ratio must be kept constant. Adding any weight to the vehicle technically requires a resizing of all power train components. But this added weight in turn requires small increments in all other components -- the weight compounding effect.

This weight compounding effect is discussed in detail in Appendix B-2 of (Thomas-1998b) for the methanol FCV. Given the uncertainty regarding the performance and characteristics of onboard reformers, we have estimated a "probable" and "best case" set of parameters for all onboard fuel processors. For the methanol FCV, we are projecting a total vehicle weight increase of 100 to 123

---

[4]Several companies are working on thin metal membranes to separate out pure hydrogen from the methanol reformate. If these efforts are successful, then the fuel cell would operate on pure hydrogen, but the exhaust from the membrane separation system would contain some hydrogen, reducing system efficiency to the degree that not all of the hydrogen exiting the membrane could be used to raise steam for the reformer.

kg -- 1390 to 1414 kg test weight compared to 1291 kg for the direct hydrogen FCV. The actual methanol reformer weight is only 46 to 60 kg (best case/probable case), or 49.5 to 65.7 kg after weight compounding (The reformer size itself must grow to accommodate the higher vehicle weight.) The final vehicle weight increment is about twice the initial estimate for extra reformer weight, due to larger fuel cell systems, and slightly larger battery banks, motors and controllers. Only 15% of this weight compounding is due to structural weight to hold the extra components. The estimated weights for the key power train components are summarized in Table 3 for the direct hydrogen FCV and the two methanol FCV cases.

Table 3. Methanol Fuel Cell Vehicle Weight Estimates after Weight Compounding (kg)

	Direct Hydrogen Fuel Cell Vehicle	Methanol Fuel Cell Vehicle	
		Best Case	Probable Case
Fuel Weight	4.71	41.4	41.4
Fuel Tank Weight	34.9	14	14
Reformer System	0	49.0	64.8
Peak Power Battery	71.9	77.1	78.4
Fuel Cell System	76.2	89.0	91.9
Motor/Controller	75.3	79.9	81.0
Glider[5], Gear Box, Radiator, Cables & Misc.	892	904	905
Curb Weight	1,155	1,254	1,277
Test Weight	1,291	1,390	1,414

The initial 46 to 60 kg reformer weight estimates could be much too low. DTI has analyzed a stationary steam methane reformer in some detail. We estimate that a stationary reformer with a 66-kW peak hydrogen capacity (48 kg/day) would weigh over 310 kg. The reformer would provide enough hydrogen to generate 33 kW of electrical energy -- almost enough for one FCV.[6] While we have not yet conducted a thorough analysis of onboard methanol steam reformers, achieving 46 to

[5]"Glider" here refers to all vehicle weight except the power train -- those components that are common to both fuel cell vehicles.

[6]This one 66-kW stationary reformer could produce enough hydrogen to support an average of 96 FCVs, graphically illustrating the economic advantage of placing the fuel processor on the curb: a processor barely large enough to support one FCV placed onboard that vehicle can provide hydrogen for almost 100 FCVs.

60 kg steam reformer weights will be a significant challenge.

Gasoline Fuel Cell Vehicle Weight Estimates

As a result of lower fuel cell peak power due to the low hydrogen content in a gasoline POX reformate (typically 35%), the gasoline FCV will require a larger fuel cell system to provide the necessary vehicle hill climbing capability. The extra weight of the larger fuel cell combined with the added weight of the processor itself also requires slightly larger battery capacity and motor power, as summarized in Table 4. As with the methanol FCV, the weights for the fuel processors are very optimistic. DTI has completed a very thorough design and costing exercise for onboard POX systems for the U.S. Department of Energy. We estimate that the POX reformer alone would weigh 100 kg. However, Arthur D. Little, Inc., the company developing the POX system for DOE, has estimated that a fully functioning POX system including gas cleanup would weigh only 87 kg. The DOE has set a specific power target of 1 kW/kg for the POX processor system, which would amount to 55 kg for a 55-kW system. We have used this 55 kg initial processor weight estimate for the best case, even though we have seen no credible design that could be built with this low weight. We have assumed the DTI calculated weight for the POX system (100 kg) as the probable case POX processor total weight.

Table 4. Gasoline Fuel Cell Vehicle Weight Estimates after Weight Compounding (kg)

	Direct Hydrogen Fuel Cell Vehicle	Gasoline Fuel Cell Vehicle	
		Best Case	Probable Case
Fuel Weight	4.71	22.7	22.7
Fuel Tank Weight	34.9	14	14
Reformer System	0	58.5	112.1
Peak Power Battery	71.9	77.0	81.6
Fuel Cell System	69.3	97.7	115.5
Motor/Controller	75.3	79.8	83.9
Glider, Gear Box, Radiator, Cables & Misc.	899	901	909
Curb Weight	1,155	1,251	1,339
Test Weight	1,291	1,387	1,475

Hybrid Electric Vehicle Weight Estimates

Weight estimates for the diesel hybrid electric vehicles are summarized in Table 5. Weights are similar for other HEVs. Representative weights are summarized in Table 6. For details of the other

vehicles, see (Thomas-1998b).

Table 5. Diesel Hybrid Vehicle Weight Estimates after Weight Compounding (kg)

	Thermostat Series Hybrid		Load-Following Series Hybrid		Parallel Hybrid	
	Peak Power (kW)	Weight (kg)	Peak Power (kW)	Weight (kg)	Peak Power (kW)	Weight (kg)
Fuel		20.9		19.1		15.0
Fuel Tank		14		14		14
Peak Power Battery	94.5	163.9	38.1	68.3	35.5	63.9
Motor/Inverter/Controller	94.5	84.4	86.7	78.7	35.5	41.1
Internal Combustion Engine	46.3	115	43.2	108.5	33.5	85.1
Generator + Rectifier & Controls	46.3	40	43.2	37.8	0	0
Glider, Gear Box, Radiator, Cables & Misc.		918		899		890
Curb Weight		1,357		1,225		1,109
Test Weight		1,493		1,361		1,245

Vehicle Fuel Economy Estimates

Three of the four major vehicle attributes analyzed here (local air pollution, greenhouse gas emissions and oil imports -- all except cost) depend on the net vehicle fuel economy. We have developed a vehicle driving simulation computer spreadsheet program to estimate the fuel economy of various alternative fueled vehicles.

Table 6. Weight Estimates for Alternatively Fueled Vehicles (kg)
[AIV Sable Test Weight = 1,304 kg]

	Direct H_2 FCV	Methanol FCV[7] (Probable)	Gasoline FCV (Probable)	FC Range Extender	H2 Parallel Hybrid[8]	NG Parallel Hybrid	Diesel Parallel Hybrid
Fuel	4.71	41.4	22.7	6.71	5.92	14.8	15
Fuel Tank	34.9	14.0	14.0	49.7	45.8	15.7	14.0
Fuel Cell System	76.2	91.9	115.5	36.0			
Fuel Processor		64.8	112.1				
ICE					71.9	71.0	98.2
Motor/Controller	75.3	81.0	83.9	100.0	41.2	40.6	41.1
Battery	71.9	78.4	81.6	497.0	64.0	62.6	63.9
Transmission	27.0	27.0	27.0	27.0	44.0	44.0	44.0
Glider[9]	865.0	878.5	882.2	973.6	838.2	834.3	832.8
Curb Weight	1,155	1,277	1,339	1,690	1,111	1,083	1,109
Test Weight	1,291	1,413	1,475	1,826	1,247	1,219	1,245

The estimated fuel economy[10] for three classes of vehicles are summarized in Figure 4:

---

[7]Both methanol and gasoline FCV's include a "best case" estimate in addition to the "probable" case shown here.

[8]Two types of series hybrid vehicles are also analyzed for each of the three fuels in the main report (Thomas 1998b).

[9]"Glider" includes all components of the AIV Sable common to the ICEV and the alternative vehicle, including extra structure to carry additional weight of the alternative vehicles.

[10]All fuel economies are expressed in miles per gallon of gasoline equivalent -- for fuels other than gasoline, this measure represents the fuel energy consumed per mile on a lower heating value basis. Assuming that gasoline has a lower heating value of 0.115 MBTU/gallon, then 30 mpg-equivalent is equal to fuel consumption at the rate of 260.9 miles/MBTU. Natural gas with a lower heating value of 913 BTU/SCF would then have a fuel economy of 0.238 miles/SCF of natural gas consumed.

conventional internal combustion engine vehicles (ICEVs), fuel cell vehicles (FCVs) and hybrid electric vehicles (HEVs). Each vehicle group is represented by three fuels: for ICEVs, gasoline, natural gas and hythane[11] -- in this case a 30% mixture of hydrogen in natural gas. We assume here that all ICEVs have the same fuel economy of 30 mpg-equivalent in the 2000 time period. For the fuel cell vehicles, the fuels are hydrogen, gasoline and methanol. For the hybrid vehicles, the fuels are natural gas, hydrogen and diesel fuel.

Two sets of data are shown for the methanol- and gasoline-powered fuel cell vehicles: a probable case (lower fuel economy), and a best case, assuming a more optimistic outcome for several onboard fuel processor parameters as described in Sections 2.2 and 2.3 of (Thomas-1998b).

For all fuels, the thermostat mode series hybrid produces the lowest fuel economy, the load-following series hybrid slightly higher fuel economy, and the parallel hybrid the highest fuel economy.

Many analysts estimate the fuel economy of vehicles on the Federal Urban Driving Schedule (FUDS) and the Federal Highway Driving Schedule. However, these driving schedules are notoriously anemic. For example, the average speed on the highway schedule is 48.6 mph, and the maximum speed in 60 mph, which does not represent modern highway driving. To better reflect actual driving conditions, we have multiplied all speeds in the federal schedules by a factor of 1.25, as suggested by Harold Haskens of the Ford Motor Company. The fuel economy shown in Figure 4 is the combination of 55% urban and 45% highway driving, each with the 1.25 times accelerated speeds. For details of the vehicle and fuel economy calculations, see (Thomas 1998b.)

As shown in Figure 4, the direct hydrogen FCV has the highest estimated fuel economy at 66 mpg-equivalent, or a factor of 2.2 times greater than the conventional gasoline ICEV. However, this ratio would be larger for the slower federal driving schedules used by some analysts, as shown in Table 7. On the FUDS, the FCV would have over three times the fuel economy of a conventional car, or a factor of 2.6 on the EPA combined schedule. The FCV advantage drops on the more realistic 1.25 times accelerated schedule because fuel cell efficiency decreases almost monotonicly with increasing power level above a low power threshold, whereas the ICE engine map has maximum efficiency at an intermediate power level -- the ICE efficiency will improve with higher acceleration over low power portions of the driving cycle.

[11]"Hythane," a mixture of natural gas and hydrogen, is a registered trademark of Hydrogen Components, Inc. of Littleton, Colorado.

Table 7. Fuel Economy of Fuel Cell Vehicle Compared to Conventional ICEV (mpg-equivalent)

	Standard Federal Schedules			1.25 Times Accelerated Schedules		
	Urban	Highway	Combined (55/45)	Urban	Highway	Combined (55/45)
FCV	79.7	85.4	82.3	68.6	62.7	66.0
(FCV without Regen Braking)	(71.6)	(83.2)	(76.8)	(60.4)	(61.2)	(60.8)
ICEV	25.5	38.5	31.4	26.4	34.4	30.0
Ratio FCV/ICEV	3.13	2.22	2.62	2.60	1.82	2.20

Returning to Figure 4, the two liquid-fueled FCVs have lower fuel economy than the direct hydrogen FCV, due to a combination of added vehicle weight, the inefficiency of the onboard fuel processor, and the reduced efficiency of the fuel cell operating on reformate. We estimate a modest drop in fuel economy for methanol FCVs compared to direct hydrogen FCVs, and a significant decrease for gasoline FCVs. In fact, the "probable" case of the gasoline FCV has slightly lower fuel economy than the gasoline ICEV, which would mean no reduction in oil imports. However, the best case gasoline-FCV estimate would increase ICEV fuel economy by 40%. This large spread in estimates reflects our degree of uncertainty regarding the performance of onboard POX fuel processors and gas cleanup devices.

For the hybrid ICEs, we assume spark ignition engine efficiencies of 38% for natural gas, 40% for hydrogen, and 43% for the diesel fuel compression ignition, direct injection (CIDI) engine. The series hybrid vehicles all have fuel economies comparable to the methanol FCV and the best case gasoline FCV. But the parallel hybrids have better fuel economy than liquid-fueled FCVs, with the diesel parallel hybrid fuel economy (58 mpg-equivalent) approaching that of the direct hydrogen FCV at 66 mpg-equivalent.

Comparison of Fuel Economy Estimates

Fuel economy estimates in the literature vary widely, particularly for hybrid vehicles. While our analysis projects substantially higher fuel economy for parallel hybrids than for series hybrids, some analysts have concluded that series hybrids would be more efficient. This diversity may simply reflect the wide range of operating strategies possible for hybrid vehicles. In this section we compare our fuel economy results with two recent analyses from the literature.

Wipke et al.(1997) from the National Renewable Energy Laboratory have recently analyzed the fuel economies of various vehicles. We ran the DTI vehicle simulation code, matching the specified NREL vehicle parameters including drag coefficient, cross sectional area (C_dA product of 1.6 m^2), rolling resistance (0.006), regenerative braking availability (70%), vehicle test weight (variable from

1,162 kg for a CIDI ICEV to 1,536 for the FCV[12]), and accessory load (700 watts). Other parameters were not specified in the NREL article, such as transmission efficiency map, motor efficiency map, generator and power electronics efficiencies, and battery efficiency. We assumed 96% one-way battery efficiency for this comparison only, which is higher than our battery standard efficiency of 80% charge efficiency and 89% discharge efficiency used in all other estimates in this report.

We have compared the NREL and DTI fuel economy estimates in Figure 5 for various diesel CIDI engines and for the FCV. Fuel economy is shown for the standard EPA cycles (no 1.25 factor acceleration). The DTI fuel economy estimates are consistently lower for the conventional ICEV, the series hybrid and the FCV. This is probably due to lower DTI efficiency estimates for the motor, generator, power electronics and transmission. However, our results for the parallel hybrid are comparable, indicating a relatively higher fuel economy, suggesting that our parallel hybrid control strategy may be more efficient that the strategy chosen by NREL.

We have also compared our fuel economy results (Figure 6) with those from Aceves and Smith (1997) at the Lawrence Livermore National Laboratory. Again we have matched the input parameters stated by LLNL, including a 96% one-way energy storage system efficiency to simulate their proposed flywheel storage system. In this case we match reasonably closely for the hydrogen spark ignition ICEV, assuming 36% peak efficiency. But our two analyses arrive at opposite conclusions regarding the efficiency of series vs. parallel hybrids -- LLNL shows a 15% drop from series to parallel (62.5 to 52.9 mpg-equivalent), while DTI projects a 21% improvement in fuel economy (55.6 to 67.6 mpg-equivalent) on the combined driving schedules. The lower series hybrid fuel economy is probably due to lower assumed motor/generator/ power electronic efficiencies that are not specified in the LLNL report. But the large relative improvement in fuel economy for the parallel hybrid must be the result of a more aggressive control strategy, as described in Section 4.1.3 of (Thomas 1998b).

Vehicle Emissions

Given the vehicle fuel economies, we can estimate both global greenhouse gas emissions and local emissions of criteria pollutants.

Greenhouse Gas Emissions

We have estimated the total greenhouse gas (GHG) emissions for each vehicle type, including all emissions due to fuel extraction, refining and delivery, as well as fuel consumption on the vehicle.

---

[12]We estimate that the FCV weights will be comparable to those of current ICEVs; we ran this simulation with higher FCV weight only to compare DTI and NREL results.

Most GHG emission estimates are based primarily on the work of Mark Delucchi at the University of California at Davis (DeLuchi 1991, DeLuchi 1993, Delucchi 1996). In addition to CO_2 emissions, the primary greenhouse gas, we include emissions of five other GHGs (VOCs, CO, CH_4, N_2O, and NOx), with each converted to a CO_2-equivalent rating assuming a 100-year time horizon.

The GHG results are summarized in Figure 7. Starting at the bottom, the last three bars show a modest 19% reduction in GHGs with a conventional natural gas vehicle (NGV). Adding hydrogen to natural gas increases GHG emissions, since hydrogen produced from natural gas contains less energy than burning the natural gas directly in the car. Thus hythane (30% hydrogen) would only cut GHGs by 8% relative to gasoline ICEVs.

The middle bars of Figure 7 compare the fuel cell vehicles (FCVs). A direct hydrogen FCV would reduce GHGs by 41%. Methanol-FCVs would emit more GHGs than direct hydrogen, but still less than the NGV. The probable case gasoline -FCV would only reduce GHGs by 4%, although the best case gasoline-FCV could provide a 34% reduction, similar to the best case methanol-FCV.

The upper set of nine hybrid ICE vehicles illustrate that either natural gas or diesel parallel hybrid vehicles could produce greater GHG reductions than the direct hydrogen FCV, providing a 52% reduction compared to the gasoline ICEV[13]. Hydrogen hybrids fare worse, due to the extra natural gas consumed to produce the hydrogen and also the electrical power plant emissions necessary to run the steam reformer plant and to compress the hydrogen. We conclude that either natural gas or diesel parallel hybrid vehicles would provide the greatest reduction in GHG emissions.

The data in Figure 7 assume that all hydrogen is produced by steam reforming of natural gas, with the hydrogen compressed to 5,000 psig by electric motor-driven compressors. If, however, hydrogen were generated by electrolyzing water with grid electricity, then the picture changes dramatically for all hydrogen powered vehicles, as shown in Figure 8 (note the large scale change compared to the previous figure). The direct hydrogen FCV GHG emissions would surge from an estimated 245 g/mile for hydrogen derived from natural gas to 936 g/mile with electrolytic hydrogen, assuming the projected average U.S. utility generation mix for the post-2000 time period -- the FCV would increase GHGs by a factor of 2.3 compared to the gasoline ICEV with electrolytic hydrogen. A conventional ICEV powered with hythane would also increase GHGs by 33%, and the hydrogen hybrids would produce up to 3.8 times greater GHGs than conventional gasoline vehicles. From a strictly GHG perspective, then, electrolytic hydrogen is not a viable option for the transportation sector until such time as a significant fraction of the utility generation capacity has been converted

---

[13]To minimize GHG emissions, the hydrogen for a FCV could be compressed with a natural gas-driven ICE compressor instead of a motor using grid electricity generated with 70% coal as assumed here. We estimate that this natural gas-powered compressor would reduce the FCV GHG emissions from 245 to 234 g/mile, still above the 200 g/mile for the NG or diesel parallel hybrids.

to some combination of renewables and nuclear energy, or the hydrogen was produced by electrolysis from off-grid renewable sources.

Local Criteria Pollutant Emissions

One major motivation for developing alternatively fueled vehicles is to reduce local emissions of volatile organic compounds (VOCs)[14], carbon monoxide (CO) and oxides of nitrogen (NOx). VOCs and NOx combine in the presence of sunlight to form ozone, the primary summer smog irritant, while CO is the primary cold weather pollutant. Particulate matter (PM) emissions are also a health hazard, but most vehicular PM is produced by diesel fuel, although other tailpipe emissions including VOCs and NOx can also combine in the atmosphere to produce secondary particulates. Since diesel engines are now prevalent in Europe and are being considered as a hybrid vehicle option in the U.S., California is proposing to limit PM emissions in their new super ultra-low emissions vehicle (SULEV) standard to below 0.01 grams per mile.

All local emissions reported here are based on real world driving averaged over the life of the vehicle. These estimates are higher than the results published from laboratory tests of various vehicles, due to several factors. Actual vehicles are accelerated and driven faster than the standard federal test procedure (FTP)[15], resulting in "off-cycle" emissions. Some small fraction of actual vehicles have malfunctioning emission control devices, resulting in excessive emissions. Furthermore, laboratory tests are run on Federal "certified gasoline," which contains less than 100 ppm of sulfur, compared to 300 to 350 ppm average sulfur content for gasoline in the U.S.[16] Additional sulfur tends to degrade the performance of catalytic converters. As a result of all of these effects, actual emissions averaged over the life of the car may be five times the emissions measured in the laboratory. Therefore a vehicle may be "certified" to meet various standards such as the California ultra-low emission vehicle (ULEV) standard, while those same vehicles driven in the real world exceed those standards by a large factor. Hence the emissions reported here are larger than those found in some of the literature. All vehicles have been treated the same, however, so the relative emissions levels should be comparable to other evaluations.

---

[14]VOC's include a wide variety of hydrocarbons. Related terms for these HC emissions are non-methane hydrocarbons (NMHC), non-methane organic gases (NMOG), etc. We use the term VOC here, with the assumption that methane is excluded, since methane does not readily form ozone in the atmosphere.

[15]The FTP utilizes the rather anemic federal urban driving schedule, split into three "bags" or segments to catch the affects of cold start versus warm vehicle emissions.

[16]California has imposed stricter sulfur standards: 50 ppm average and 80 ppm maximum sulfur content.

Volatile Organic Compound Emissions

The estimated "real world" VOC emissions are summarized on a logarithmic scale in Figure 9 for the nine primary vehicles. The horizontal lines correspond to various emissions standards: the federal "Tier II" standard which begins in 2004, the California ULEV standard which started in 1994, the newly proposed California SULEV standard, and the old proposed (but now abandoned) equivalent zero emission vehicle (EZEV) standard. As in previous figures, two bars are shown for the liquid-fueled FCVs corresponding to the probable (higher emissions) and best cases, and three bars are shown for each hybrid fuel, corresponding to thermostat series hybrids (highest emissions), load-following series hybrids, and parallel hybrids (lowest emissions).

Although some NGVs have been certified as ULEVs, this analysis of real world emissions indicates that only hythane NGVs[17], direct hydrogen and methanol FCVs and hydrogen hybrids could meet the ULEV standard for VOCs. And only direct hydrogen FCVs and hydrogen hybrids would qualify for the SULEV VOC standard. The high gasoline-FCV VOCs are due primarily to evaporative emissions.[18] The small VOC emissions from the direct hydrogen FCV and the hydrogen hybrid are due primarily to emissions from the local steam methane reformer plant. While these are not strictly "tailpipe" emissions, they are released in the urban airshed, and could have the same effect on photochemical smog formation as tailpipe VOC emissions. We have not, however, included any upstream emissions from electrical generation plants, on the assumption that they would be located outside the urban airshed.

From a regulatory viewpoint, however, the direct hydrogen FCV would be the only vehicle considered here that would qualify as a zero emissions vehicle (ZEV), since it alone has no onboard tailpipe or evaporative emissions. Even if hydrogen hybrid vehicles did meet the proposed California SULEV standards, as currently written the SULEV certification could only be used to meet a maximum of 60% of each auto manufacturer's ZEV requirement. That is, beginning in 2004, each car company could supply up to 6% of its sales as SULEVs (60% of the 10% ZEV mandate), but the other 4% would still have to be true ZEVs -- battery EVs or direct hydrogen FCVs.

---

[17]The hythane ICE emissions shown here are based on lean burn operation. We are projecting higher emissions for stoichiometric operation, as described in Section 3.2 of (Thomas 1998b).

[18]Strictly speaking, the Tier II, ULEV and other standards are tailpipe emission standards. Evaporative emissions are covered by other testing requirements. However, we have included both tailpipe and evaporative VOC emissions here, since both contribute to photochemical ozone formation.

Carbon Monoxide Emissions

The corresponding CO emissions for these vehicles are shown in Figure 10. The federal Tier II and California ULEV levels are identical for CO (and for NOx). In this case all vehicles except the gasoline and natural gas ICEVs would meet the proposed SULEV standard for CO. By raising the CO standard compared to EZEV, the SULEV standard would allow both natural gas and diesel hybrids to qualify although, again, the certified emissions of these hybrids would likely have qualified under the more strict EZEV proposal, since the certified emissions are consistently lower than the real world emissions estimated in this report.

Nitrogen Oxide Emissions

NOx emissions are summarized in Figure 11. In this case the proposed SULEV standard is identical to the previous EZEV proposal. According to our analysis of real world NOx emissions, only the fuel cell vehicles would qualify. We estimate very high NOx emissions for the hybrid vehicles, based primarily on the nonlinear relationship between NOx and engine power level. Both VOCs and CO increase nearly linearly with engine output power. In this case it makes no difference if the engine supplies the necessary power in one high power surge (to charge batteries, for example) or whether the engine cycles over a range of power levels as in conventional ICEVs. NOx, emissions, on the other hand, depend strongly on ICE power level. Below a threshold power level, very little NOx is produced. Above this threshold, however, NOx emissions grow rapidly. In a hybrid mode, when the ICE is consistently operated at moderate to high power, NOx emissions are high. When the wheel load demand is low and NOx emissions would be negligible for a conventional car, the ICE is usually shut off in the hybrid mode. As a result, we are projecting increased NOx emissions for hybrid operation for both natural gas and diesel fuel. In essence, the nonlinear increase in NOx at higher average engine power is not offset by the higher fuel economy due to hybrid operation.[19]

Particulate Matter Emissions

Only the diesel hybrid vehicles would emit substantial particulate matter. The proposed SULEV standard is 0.01 g/mile. We are projecting in the range from 0.023 g/mile for the diesel parallel hybrid up to 0.032 g/mile of PM-10 for the thermostat mode series hybrid diesel vehicle, or two to three times the proposed standard. The EPA has also issued new regulations on particles smaller than 2.5 microns (PM-2.5), on the assumption that the smaller particles cause the most damage to human lungs. This new ruling could further jeopardize the introduction of diesel hybrids. Over 90% of diesel particulates have been measured at less than one micron in diameter (Walsh 1997).

---

[19]Jay Keller at Sandia National Laboratories (Livermore) estimates that NOx emissions can be reduced dramatically with the development and use of homogeneous charge, compression ignition engines. This development, if implemented in future parallel hybrid vehicles, would improve the emissions from diesel cycle engines, leaving only particulates to contend with.

Vehicle Cost Estimates

Clean vehicles will not reduce pollution if they are too costly for the consumer, as the makers of battery-powered electric vehicles are discovering. We have estimated the mass production cost of each of the alternatively fueled vehicles. We have used a combination of DTI mass production cost estimates for fuel cells, onboard processors, and compressed hydrogen storage tanks prepared under contract to the Ford Motor Company and the Department of Energy, along with DOE cost goals and other cost projections for electric vehicle components such as motors, controllers and batteries. In all cases we assume large automotive quantity production on the order of 300,000 vehicles.

The cost and power requirements for a direct hydrogen and a methanol FCV are summarized in Table 8 for a best case and a probable case methanol FCV. We estimate that the methanol FCV would most likely cost almost $900 more in mass production than the direct hydrogen FCV, but it could cost only $177 more in the best case analyzed here. We estimate that the gasoline FCV would cost between $900 (best case) and $3,000 more than a direct hydrogen FCV, as shown in Table 9. (See Appendix C of Thomas (1998b) for cost details of the other vehicles.)

Table 8. Power and Mass Production Cost Estimates for Methanol Fuel Cell Vehicles

		Direct Hydrogen FCV	Methanol FCV		Cost Differential	
			Best Case	Probable	Best Case	Probable
Vehicle Test Weight	kg	1,291	1,390	1,413		
Fuel Cell System	Power (kW)	38.1	44.4	45.9		
	Cost ($)	$1,911	$2,143	$2,370	$232	$459
Peak Power Battery ($15.7/kW + $100)	Power (kW)	40.3	43.2	43.9		
	Cost ($)	$728	$774	$785	$46	$57
Motor/Inverter/ Controller	Power (kW)	82	88.3	89.8		
	Cost ($)	$906	$945	$954	$39	$48
Fuel Tank		$760	$176	$176	($584)	($584)
Methanol Processor ($10/kW to $20/kW)	Power (kW)		44.4	45.9		
	Cost ($)		$444	$917	$444	$917
Gear Box		$200	$200	$200		
Controller & Misc.		$150	$150	$150	$0	$0
Total Drivetrain Costs		$4,655	$4,832	$5,552	$177	$897
Vehicle Cost		$20,179	$20,356	$21,076		

The increased mass production costs for all the alternative vehicles compared to a conventional gasoline ICEV are shown in Figure 12. The baseline AIV Sable price is assumed to be $18,000. The costs in Figure 12 represent the difference between the alternative fueled vehicle power train and the ICE powertrain it replaces. We currently estimate that the direct hydrogen FCV would cost about $2,200 more than a conventional car. Additional FCV cost savings are possible, but cannot be demonstrated at this time.

Table 9. Power and Mass Production Cost Estimates for Gasoline Fuel Cell Vehicles

		Direct Hydrogen FCV	Gasoline FCV		Cost Differential	
			Best Case	Probable	Best Case	Probable
Vehicle Test Weight	kg	1,291	1,387	1,475		
Fuel Cell System	Power (kW)	38.1	48.8	57.6		
	Cost ($)	$1,911	$2,371	$2,991	$460	$1,080
Peak Power Battery ($7.8/kg + $100)	Power (kW)	40.3	43.1	45.7		
	Cost ($)	$728	$772	$813	$44	$85
Motor/Inverter/ Controller ($12.7/kW)	Power (kW)	82	88.1	93.7		
	Cost ($)	$906	$945	$979	$39	$73
Fuel Tank ($133/kg)		$760	$176	$176	($584)	($584)
POX Processor ($20/kW to $40/kW)	Power (kW)		48.8	57.6		
	Cost ($)		$976	$2,305	$976	$2,305
Transmission		$200	$200	$200		
Controller & Misc.		$150	$150	$150	$0	$0
Power Train Costs		$4,655	$5,590	$7,614	$935	$2,959
Total Vehicle Costs		$20,179	$21,114	$23,138		

The hybrid vehicles fare surprisingly well in this analysis, considering that these hybrids have two separate power trains -- an ICE and an electric traction motor plus battery bank. While the hybrids have more drive train components, they are generally lower power and hence lower cost than the large ICE in a conventional vehicle. The thermostat series hybrids could cost $2,300 to $3,200 more than an ICEV. But the parallel hybrids could cost less than $1,370 more, with the natural gas parallel hybrid estimated at only $770 more -- the lowest cost HEV option and second only to the conventional NGV at an estimated $360 more than a gasoline vehicle in mass production. The cost accounting for the natural gas parallel hybrid and the direct hydrogen fuel cell vehicle is reconciled with the conventional ICEV in Table 10, to illustrate the cost differences between conventional, hybrid and fuel cell vehicles.

Table 10. Drivetrain Power and Mass Production Cost Comparison: Conventional Internal Combustion Engine Vehicle vs. Natural Gas Parallel Hybrid and Fuel Cell Vehicles

	Conventional ICEV		Natural Gas Parallel Hybrid		Direct Hydrogen Fuel Cell Vehicle	
	Power (kW)	Cost ($)	Power (kW)	Cost ($)	Power (kW)	Cost ($)
Fuel Cell System					38.1	1911
ICE & Ancillaries	100	1600	32.9	889		
Transmission[20]		700		700		200
Fuel Tank System		176	72.6 liters	334	4.71 kg	760
Motor/Controller		0	34.8	533	82	906
Battery System		0	34.8	642	40.3	728
Controller		0		150		150
Drivetrain Total Costs		2476		3,248		4,655
Additional Cost				772		2,179

For early market penetration, the initial vehicle costs for very low production volumes may also be important. GM, for example, has introduced its EV1 electric vehicle with production runs of a few hundred vehicles. As shown in Figure 13, the natural gas and hythane vehicles would have significant cost advantage over the other alternatives for such early market entry. The parallel hybrid vehicles might also have a significant cost advantage over fuel cell vehicles in low production volumes. The liquid-fueled FCVs would suffer a significant disadvantage over direct hydrogen FCVs in terms of initial vehicle cost. From a transportation system perspective, this increased cost for onboard liquid fuel reformers might equal or exceed the cost of providing stationary hydrogen fueling appliances for the direct hydrogen fuel cell vehicles.

Oil Import Reductions

Most of the vehicles considered here either use natural gas or derive their fuel from natural gas (hydrogen and methanol.) These vehicles will eliminate almost all demand for crude oil, except for lubrication, products derived from crude oil, and crude oil fuel used in vehicle manufacture or transportation of components. The diesel hybrid and gasoline-powered fuel cell vehicle are the only

[20] Conventional and parallel hybrid vehicles have 4-speed automatic transmissions; fuel cell vehicles and series hybrids have single speed gear boxes.

two that would use fuel derived from crude oil.

Each ICEV requires about 7.8 barrels of crude oil each year to supply gasoline to travel 12,000 miles at 30 mpg fuel economy. This assumes that one barrel of crude oil supplies about 1.22 barrels of gasoline, due to its lower density -- mass is conserved in the refinery, not volume. The gasoline-powered FCV would achieve from 29.1 (probable) to 42.1 mpg (best case), so the likely outcome would be no reduction in oil imports. For the best case gasoline FCV, oil consumption would be reduced from 7.8 barrels per year per vehicle to 5.6 barrels -- a 28% reduction at best.

The diesel hybrid would benefit due to diesel fuel's 11.7% higher energy content relative to gasoline and higher onboard fuel economy, but this is offset slightly by its higher density. Each barrel of crude oil produces about 1.09 barrels of diesel. For the diesel parallel hybrid at 57.6 mpg-equivalent fuel economy, the actual diesel consumption would be 64.3 miles per gallon of diesel fuel, and the crude oil consumption would be 4.1 barrels per year -- a 47% reduction compared to the conventional ICEV. Therefore the diesel parallel hybrid has almost twice the oil import reduction potential than even the best case gasoline FCV.

Conclusions

We conclude from this detailed analysis of alternative vehicles that there is no clear winner. The choice of optimum vehicle from a societal viewpoint depends on the weighting factors given to our three main objectives: reduced local air pollution, reduced greenhouse gases and reduced oil imports. To help assess and compare the relative merits of each vehicle, we have assigned a dollar cost to each vehicle pollutant, based on the lowest avoided cost reported in the literature for each pollutant, as summarized in Table 11.

Table 11. Annual Pollution Avoided Costs (U.S. $)

	(Tellus 1990)	Massachusetts (Edison Electric Institute 1994)	Nevada	New York (Mark 1996)	Used Here:
VOC	5,300	6,140	6,190	17,300	**5,300**
CO	870	1,010	1,040	2,100	**870**
NOx	6,500	7,540	7,650	14,400	**6,500**
PM-10	4,000	--	--	--	**4,000**
CO_2	22	26	25		**22**

Conclusions Based on Local Air Pollution

Using these cost estimates, we then plotted the incremental vehicle cost vs. the resulting total pollution cost for the local criteria pollutants in Figure 14. The ideal vehicle would be plotted in the lower left hand corner -- no increase in vehicle cost and zero pollution cost. The gasoline ICEV is plotted on the x-axis (no increased vehicle cost by definition) at $200/year annual pollutant cost.

Based solely on local air pollution, we arrive at these conclusions:

1. Hydrogen is the superior "clean fuel," providing the only true zero emission vehicle (zero tailpipe and zero evaporative emissions) with the full range capabilities of conventional vehicles.

2. The direct hydrogen FCV produces the least local air pollution (with the methanol FCV and the hydrogen hybrids as close seconds).

3. From a cost-effective viewpoint, however, a conventional natural gas vehicle provides a 65% reduction in estimated real-world ICEV emissions with a modest increase in vehicle cost.

4. Adding hydrogen to natural gas (hythane) is cost effective for reducing local emissions, substantially reducing criteria emissions with a small increment in cost.

5. The diesel hybrids are not cost effective from the local air quality viewpoint.

Conclusions Based on Greenhouse Gas Emissions

Next we generated a plot of incremental vehicle cost vs. greenhouse gas emissions instead of local criteria pollutants, as shown in Figure 15. The ideal vehicle would be located in the lower left-hand corner of Figure 15 -- low cost and low greenhouse gas emissions. The internal combustion engine vehicle (ICEV) is plotted on the x-axis (no cost increase) at 415 g/mile. The alternative vehicles all reduce greenhouse gases to some degree, but with increased vehicle cost. Natural gas parallel hybrid vehicles offer the greatest potential for reducing greenhouse gas emissions at low incremental production cost, followed by diesel parallel hybrids and direct hydrogen fuel cell vehicles (FCVs).

Based solely on the criterion of reducing greenhouse gas emissions, we conclude the following:

1. Natural gas is the preferred fuel, providing the lowest cost alternative vehicles in either conventional or hybrid mode.

2. The natural gas parallel hybrid vehicle provides the best combination of low additional vehicle cost and the lowest projected greenhouse gas emissions. Series hybrids are not as effective in all cases, adding cost and increasing greenhouse gas emissions relative to parallel hybrids.

3. Adding hydrogen to natural gas (hythane) is ***not*** an effective strategy for greenhouse gas reduction, since it adds cost and also increases greenhouse gases compared to neat natural gas.

4. Similarly, hydrogen hybrid vehicles are ***not*** an effective choice, since natural gas hybrids provide much lower greenhouse gas emissions at lower vehicle cost.

5. The direct hydrogen fuel cell vehicle (FCV) provides substantial greenhouse gas emission savings if the hydrogen is produced from natural gas, but is not as effective as either the natural gas or diesel parallel hybrid vehicles, both of which are projected to cost less and emit lower greenhouse gases.

6. Both methanol- and gasoline-powered FCVs are even less attractive, costing more and reducing greenhouse gases less than the direct hydrogen FCV. The most probable gasoline-FCV case would cost over $5,000 more than a conventional car and provide negligible greenhouse gas reductions compared to conventional gasoline ICEVs. The methanol FCV would most likely provide greater GHG reductions than the gasoline FCV at lower incremental cost.

7. Electrolysis of water to produce hydrogen is ***not*** a viable option from a greenhouse gas perspective, since the projected year 2000^{+} utility generator mix in the U.S. would more than double greenhouse gases (to 936 g/mile -- not shown in Figure 15 -- far off scale to the right) relative to conventional ICEVs, even when used in a direct hydrogen fuel cell vehicle.[21]

Conclusions Based on Local and Greenhouse Gas Emissions

The cost of greenhouse gas emissions is even harder to quantify, but some analysts have estimated a cost of $24/tonne of CO_2 (compared to much higher costs for VOCs - $5,840/tonne, CO - $960/tonne, NOx - $7,150/tonne, and PM-10 - $4,410/tonne.) The combined costs of GHGs and local emissions are plotted in Figure 16. The direct hydrogen fuel cell vehicle has the lowest total emission and GHG cost with these parameters. But natural gas and hydrogen parallel hybrids and hythane ICEVs have only moderately higher environmental costs at somewhat lower incremental vehicle costs.

---

[21]Hydrogen produced by electrolysis using intermittent renewable energy sources such as photovoltaics and wind would generate zero emissions and zero greenhouse gases in operation. However, until intermittent renewables achieve greater than 15% to 20% utility grid penetration, greenhouse gases would be reduced 1.8 times more by displacing grid electricity than by electrolyzing water to provide hydrogen for use in FCVs. When renewables supply 15% to 20% of the utility energy, then the grid could not absorb more renewable energy, and making hydrogen would be effective in reducing GHGs further. Since even the most optimistic renewable energy projections do not show renewables at 15% before 2020 to 2030, substantial use of renewable electrolytic hydrogen in the industrialized nations is probably two to three decades away.

Conclusions Based on Oil Import Costs

The societal costs of protecting our access to imported oil are even more subjective. However, all of the most promising fuel/vehicle combinations from the environmental viewpoint (Figure 16) derive their fuel from natural gas -- either natural gas itself or methanol or hydrogen derived from natural gas. Hence all of the front-runners from an environmental viewpoint would eliminate virtually all vehicle dependence on imported oil. Adding an oil import cost would merely shift the gasoline-FCV, ICEV and diesel hybrids to the right in Figure 16, farther out of contention, leaving the other vehicles unchanged.

For the two vehicles that rely on crude oil, the diesel parallel hybrid would cut crude oil consumption by 59%, while the gasoline-powered FCV would at best reduce oil consumption by 40%, and, in the probable case, would not reduce oil consumption at all.

Final Alternative Vehicle Conclusions

The key societal attributes of the major alternative vehicles[22] are summarized in Table 12. Each vehicle/fuel choice has at least one shaded box corresponding to an undesirable trait. There is no clear winner.

Both of the alternative vehicles that could utilize the existing gasoline or diesel fuel infrastructure have major hurdles to overcome:

The gasoline-powered FCV faces three major hurdles: the highest estimated vehicle incremental cost ($3,110 to $5,135) in mass production, the highest greenhouse gas emissions in the probable case (with the exception of electrolytic hydrogen in a FCV), and the likelihood of little or no reduction in oil imports. However, successful development of the gasoline-FCV could pave the way for FCVs with more environmentally friendly domestic fuels in the future. Hence development of the gasoline-FCV does have long term merit, if the cost and performance obstacles can be overcome so that market penetration could begin earlier than the other FCV options.

The diesel parallel hybrid has lower hurdles compared to the gasoline-FCV: lower but still substantial cost differential, one of the best greenhouse gas potentials (similar to the natural gas hybrid), and the diesel parallel hybrid would reduce oil imports by half. However, local emissions from the diesel hybrid could be a show-stopper, particularly if the new EPA regulations on smaller

---

[22] In addition to the nine vehicles reported here, we also evaluated two variations on the fuel cell vehicle: a fuel cell range extender (see Section 2.4 of Thomas 1998b) and a FCV with a regenerative fuel cell that could be used at night as an electrolyzer to refill the hydrogen tanks (see Section 2.5 of Thomas 1998b).

particulates (below 2.5 microns) go into full force in five years as planned.

Of those vehicle that require new fuel infrastructure, the natural gas parallel hybrid has the best short-term attributes: lowest greenhouse gas emissions, lowest incremental cost, and moderately low local emissions of criteria pollutants. On the negative side, the natural gas hybrid does not provide a pathway to a sustainable energy transportation option. Natural gas itself is not readily manufactured from biomass or other renewable resources (although it can be generated by anaerobic digestion of municipal solid waste or collected from landfills), and development of the hybrid vehicle could preclude or delay mass market development of the fuel cell system that has higher fuel economy and potentially lower life cycle costs than the ICE hybrid.

The methanol-powered fuel cell vehicle does provide a sustainable energy pathway: methanol itself can be readily manufactured from biomass or municipal solid waste, and the fuel cell vehicle could be powered by renewable hydrogen in the future. But in a sense the methanol FCV could be considered the worst of both worlds: it eventually requires added fuel production capacity and a new fueling infrastructure while still having very high vehicle incremental costs and moderately high greenhouse gas emissions for the probable case.

Finally, the direct hydrogen FCV provides zero tailpipe and evaporative emissions (the only ZEV considered here), with moderately good greenhouse gas reductions and moderate vehicle cost increase of $2,176 per vehicle. Hydrogen-powered FCVs face three perceived challenges, however: onboard hydrogen storage, the need for a new hydrogen fueling infrastructure, and the general public perception of an unsafe fuel. Directed Technologies, Inc. (DTI) and the Ford Motor Company, working under contract to the U.S. Department of Energy, have previously shown the efficacy of onboard hydrogen storage using 5,000 psia carbon fiber wrapped composite tanks or liquid hydrogen tanks (James-1996), and, working with the hydrogen merchant gas suppliers, we have also laid out an economically plausible approach to provide a cost-effective, dispersed supply of hydrogen to match an evolving fuel cell vehicle market(Thomas 1997, Thomas 1998a). By producing hydrogen on-site at the dispensing station, either by water electrolysis with low cost off-peak electricity or by small scale steam methane reforming of natural gas, hydrogen could be produced and sold at a price comparable to the cost of gasoline per mile driven. This on-site hydrogen generation approach effectively utilizes the existing electrical grid and the existing natural gas pipeline system, obviating the need for installing a national hydrogen pipeline or liquid hydrogen tanker truck fleet.

Table 12. Summary Vehicle Attribute Comparison Chart

		Incremental Vehicle Cost ($)	Greenhouse Gas Emissions (g/mile)	Local Pollution Costs ($/yr)	Oil Imports (Barrels/y)	New Fuel Infrastructure Required?
Direct Hydrogen Fuel Cell Vehicle	(H_2 from NG)	2,178	245	0	0	Yes
	(H_2 by electrolysis)	2,178	939	0	0	Yes
Range Extender FCV	(H_2 from NG)	2,273	313	0	0	Yes
Gasoline Fuel Cell Vehicle	Probable	6,135	398	27	7.9	No
	Best Case	3,110	275	19	5.6	No
Methanol Fuel Cell Vehicle	Probable	3,074	311	2	0	Yes
	Best Case	2,353	278	2	0	Yes
Parallel Hybrid Vehicles	Hydrogen	1,890	322	3	0	Yes
	Natural Gas	1,292	199	42	0	Yes
	Diesel Fuel	1,606	203	140	4.1	No
NGV		363	336	65	0	Yes
Hythane ICEV		467	381	7	0	Yes
Gasoline ICEV		0	415	200	7.8	No

Acknowledgements

We acknowledge the support of the U.S. Department of Energy through both the Hydrogen Program office for this systems analysis work, as well as the Office of Transportation Technologies for funding of the direct hydrogen fuel cell infrastructure work through the Ford Motor Company. We thank Jim Ohi and Cathy Gregoire-Padró, the NREL hydrogen technical managers and Sig Gronich, the DOE Hydrogen Team Leader, for many helpful discussions, along with Ron Sims, Jim Adams, Bob Mooradian and others from the Ford Motor Company, Bob Moore and Venki Raman (Air Products & Chemicals), Anne Kotar (BOC Gases), Matthew Fairlie (Electrolyser Corporation), Al Meyer and Paul Farris (IFC), Frank Lynch (Hydrogen Components, Inc.), Gene Berry, Salvador Aceves and Ray Smith (Lawrence Livermore National Laboratory), Nick Vanderborgh and Shimshon Gottesfeld (Los Alamos National Laboratory), Kirk Collier (NRG Technologies, Inc.), Geoff Wood (Oak Ridge National Laboratory), Joan Ogden and Margaret Steinbugler (Princeton), Tom Halvorson (Praxair), Jay Keller (Sandia National Laboratory) and Jason Mark (Union of Concerned Scientists).

References

Aceves, S.M. and J. Ray Smith. 1997. "Hybrid and Conventional Hydrogen Engine Vehicles that Meet EZEV Emissions," SAE paper 970290, *Electric and Hybrid Vehicle Design Studies*, SP-1243, p. 113.

DeLuchi, M. A. 1991. *Emissions of Greenhouse Gases from the Use of Transportation Fuels and Electricity*, Vol. 1, Main Text, Argonne National Laboratory Report ANL/ESD/TM-22, Vol. 1.

DeLuchi, M. A. 1993. *Emissions of Greenhouse Gases from the Use of Transportation Fuels and Electricity*, Vol. 2, Appendixes A-S, Argonne National Laboratory Report ANL/ESD/TM-22, Vol. 2.

Delucchi, M. A. 1996. *Summary of Results from the Revised Model of Emissions of Greenhouse Gases from the use of Transportation Fuels and Electricity*, Institute of Transportation Studies, University of California, Davis, California, November 1996.

DOE. 1998. *Office of Advanced Automotive Technologies R&D Plan: Energy-Efficient Vehicles for a Cleaner Environment*, U.S. Department of Energy, Office of Transportation Technologies, Energy Efficiency and Renewable Energy Report DOE/ORO/2065.

Edison Electric Institute 1994. *Environmental Externalities: an Issue Under Critical Review*, IRP Monograph Series No. 3, pp. 4-11.

James, B. D., G. N. Baum, F. D. Lomax, Jr., C. E. Thomas, and I. F. Kuhn, Jr.. 1996. *Comparison of Onboard Hydrogen Storage for Fuel Cell Vehicles,* Task 4.2 Final Report under Subcontract 47-2-R31148 from the Ford Motor Company under Prime Contract DE-AC02-94CE50389 with the U.S. Department of Energy.

Mark, J. 1996. *Zeroing Out Pollution: the Promise of Fuel Cell Vehicles*, Union of Concerned Scientists, Cambridge, Massachusetts pg. 54.

Tellus Institute. 1990. *Valuation of Environmental Externalities for Energy Planning and Operations, May 1990 Update*.

Thomas, C.E., B. D. James, I. F. Kuhn, Jr., F. D. Lomax, Jr., and G. N. Baum. 1997. *Hydrogen Infrastructure Study Summary*, Prepared for the Ford Motor Company by Directed Technologies, Inc., Arlington, Virginia.

Thomas, C.E., I. F. Kuhn, Jr., B. D. James, F. D. Lomax, Jr. and G. N. Baum. 1998a "Affordable Hydrogen Supply Pathways for Fuel Cell Vehicles," *Int. J. Hydrogen Energy,* Vol. 23, No. 6, pp. 507-516.

Thomas, C.E., B. D. James, F. D. Lomax, Jr., and I. F. Kuhn, Jr. 1998b. *Integrated Analysis of Hydrogen Passenger Vehicle Transportation Pathways*, draft final report prepared for the National Renewable Energy Laboratory under Subcontract No. AXE-6-16685-01.

Walsh, M. P. 1997. "Global Trends in Diesel Emissions Control - A 1997 Update," SAE paper 970179, in *Diesel Exhaust Aftertreatment - 1997, SP-1227*, p.1.

Wipke, K., M. Cuddy, and D. Rausen. 1997, "Using Systems Modeling to Facilitate the PNGV Technology Selection Process," Center for Transportation Technologies and Systems, National Renewable Energy Laboratory, presented at the *1997 Automotive Technology Development Customers' Coordination Meeting*, Dearborn, Michigan.

Figure 1 Series Hybrid ICE Vehicle Energy Flow Diagram (Thermostat Mode)

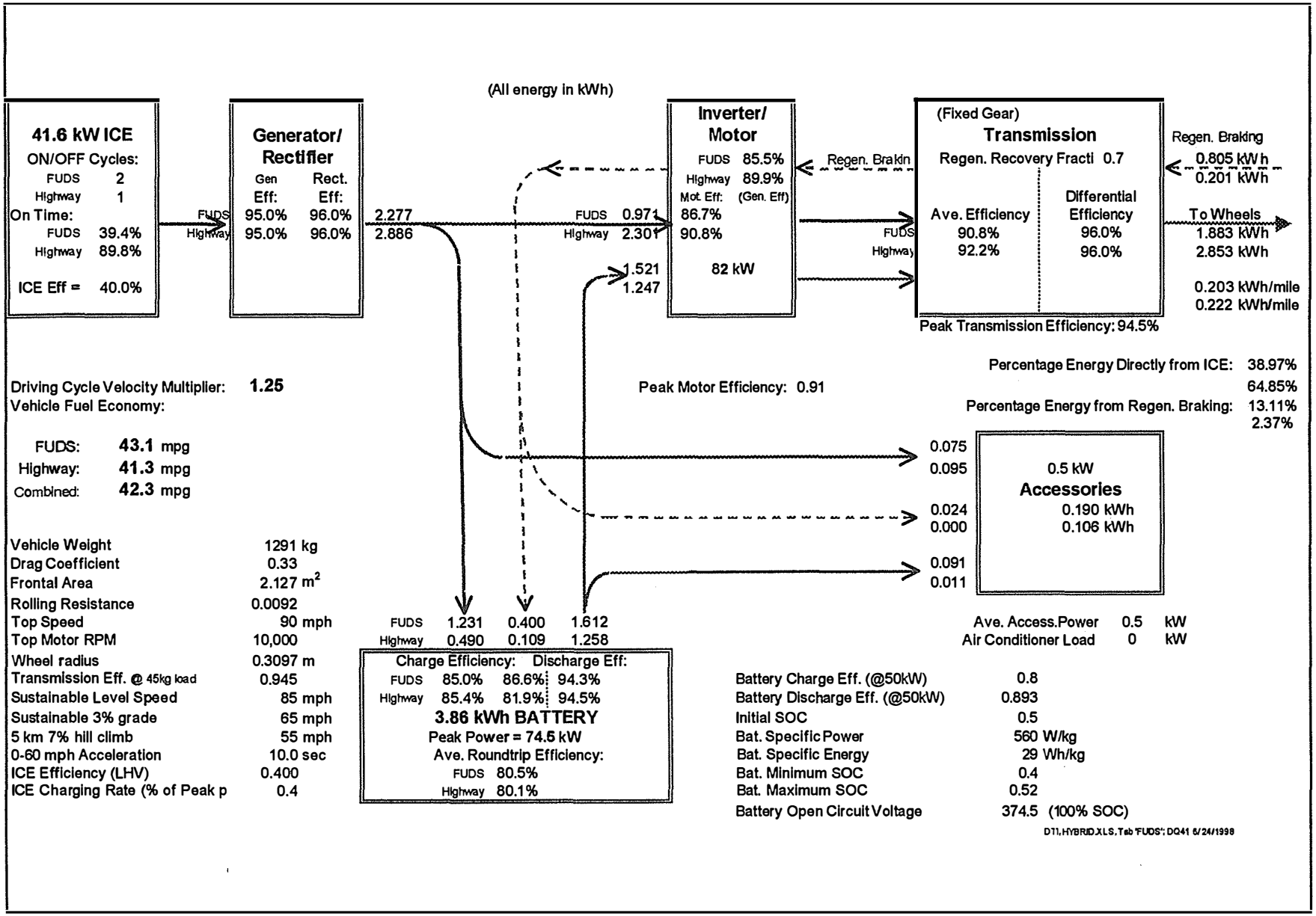

Figure 2 Series Hybrid ICE Vehicle Energy Flow Diagram (Load-Following Mode)

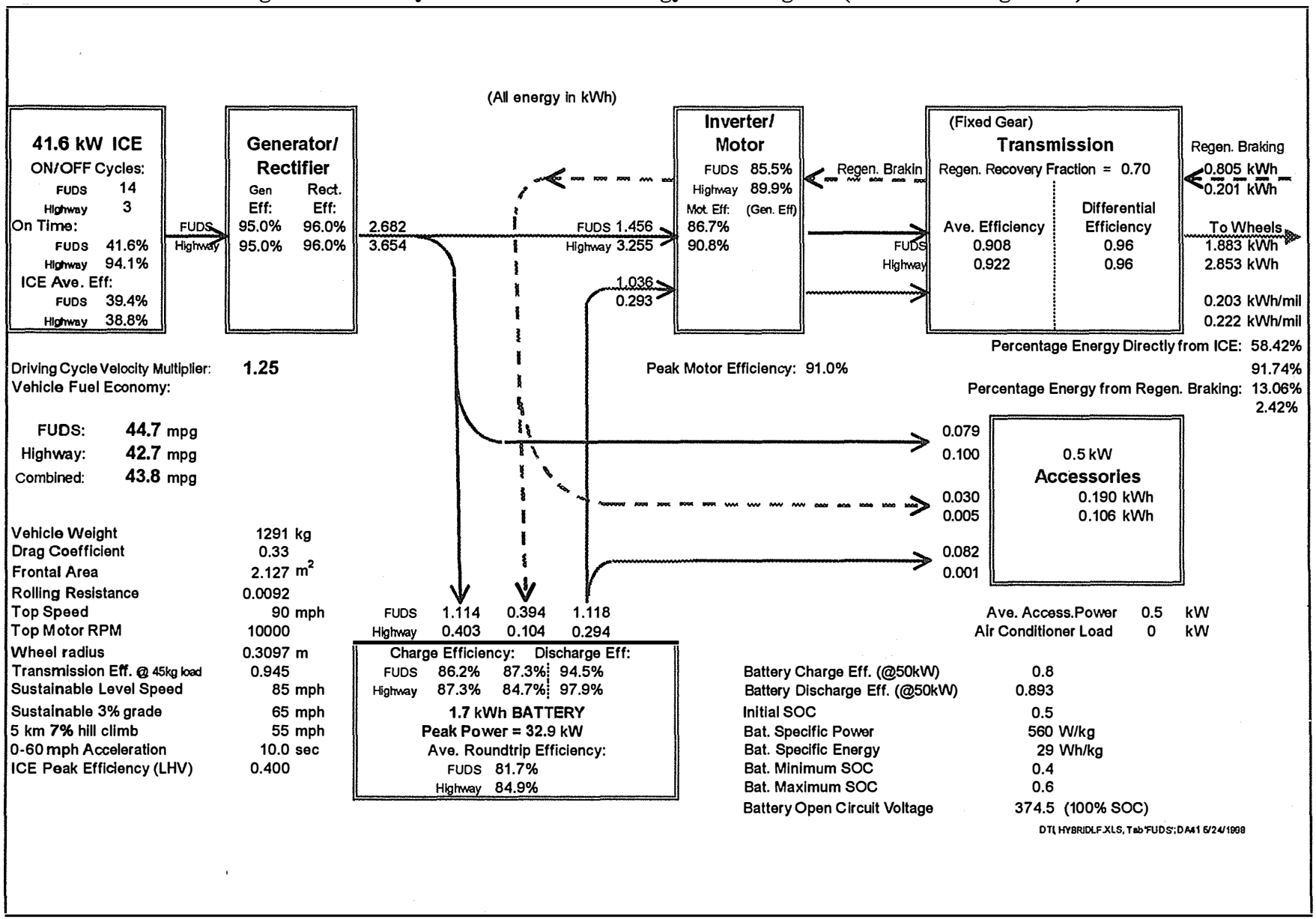

Figure 3. Parallel ICE Hybrid Vehicle Energy Flow Diagram

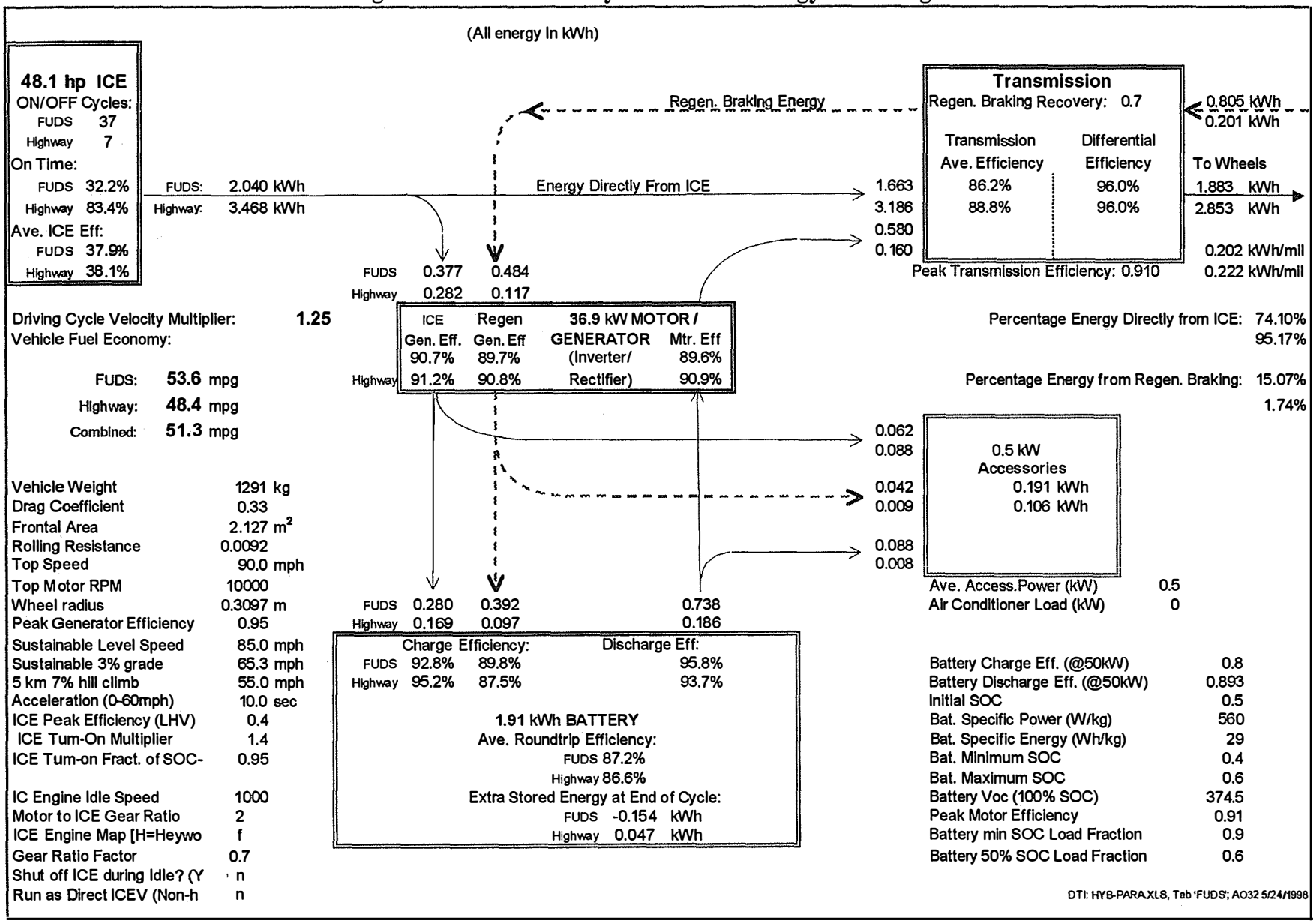

Figure 4. Estimated Fuel Economy for Conventional, Fuel Cell and Hybrid Vehicles

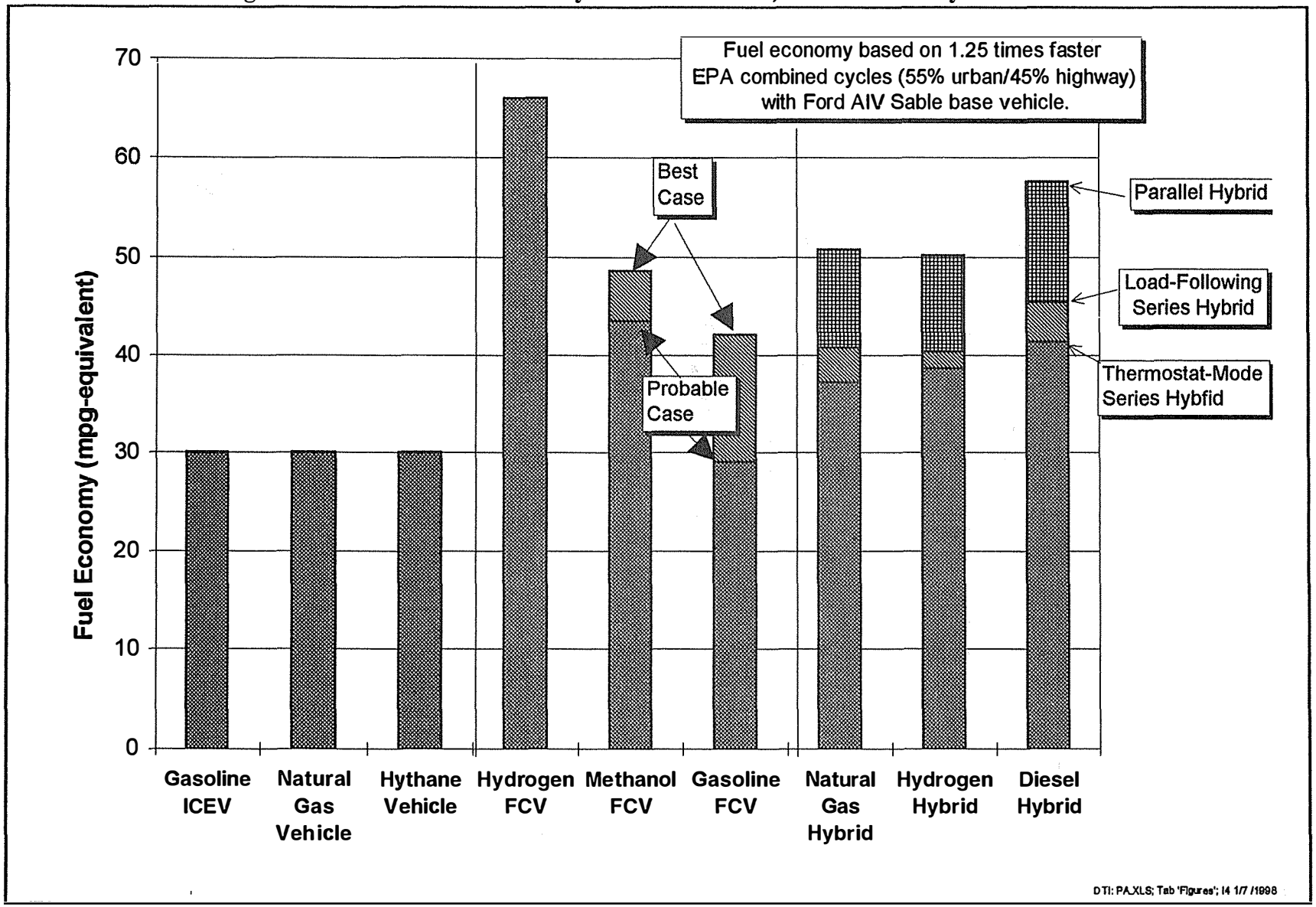

Figure 5. Comparison of NREL and DTI Fuel Economy Estimates

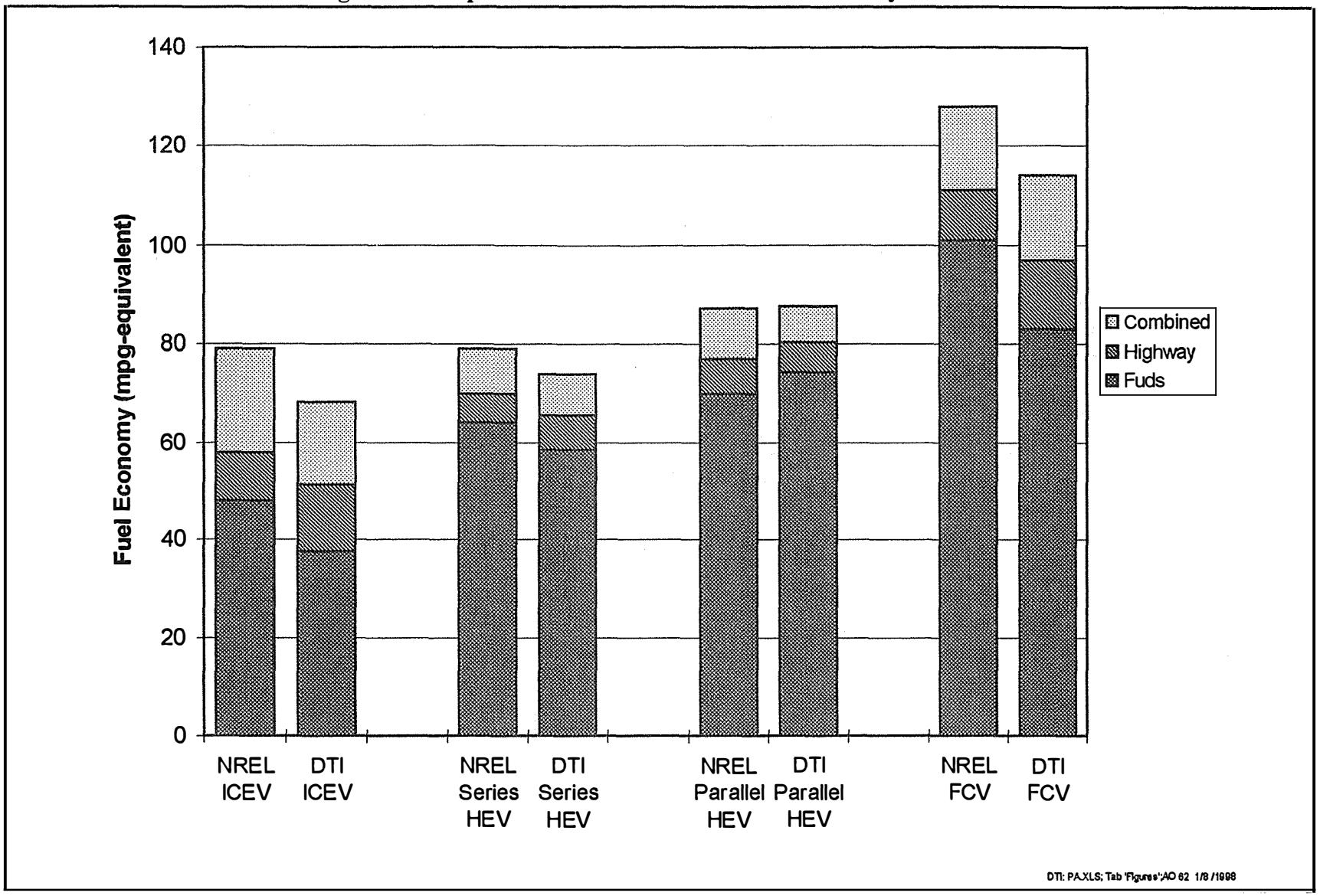

Figure 6. Fuel Economy Comparison Between LLNL and DTI ICEVs and Hybrid Vehicles

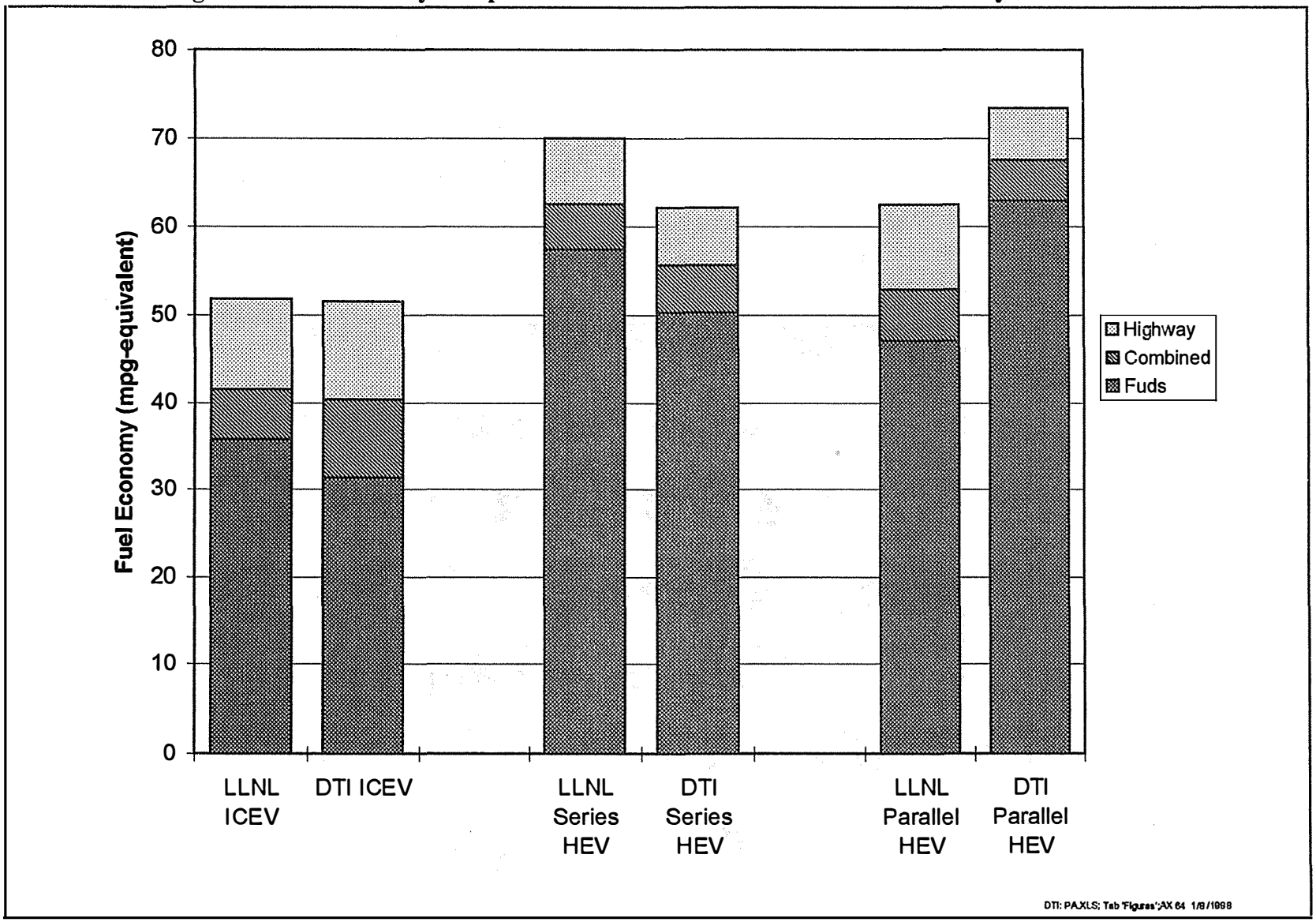

Figure 7. Vehicle Greenhouse Gas Emissions in 2000 (Hydrogen Produced by Steam Reforming of Natural Gas)

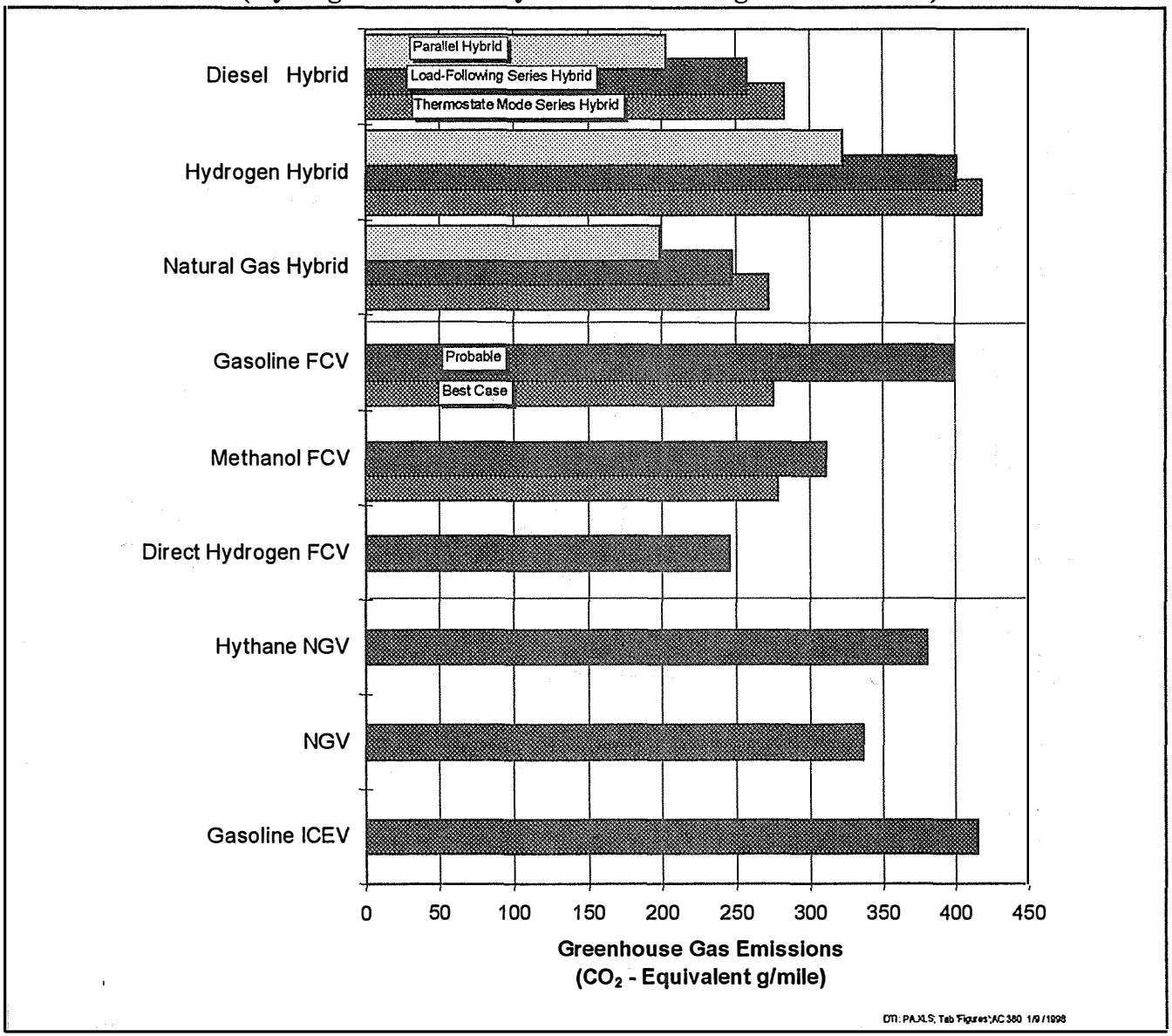

Figure 8. Vehicle Greenhouse Gas Emissions (Hydrogen Derived by Electrolysis with Grid Electricity)

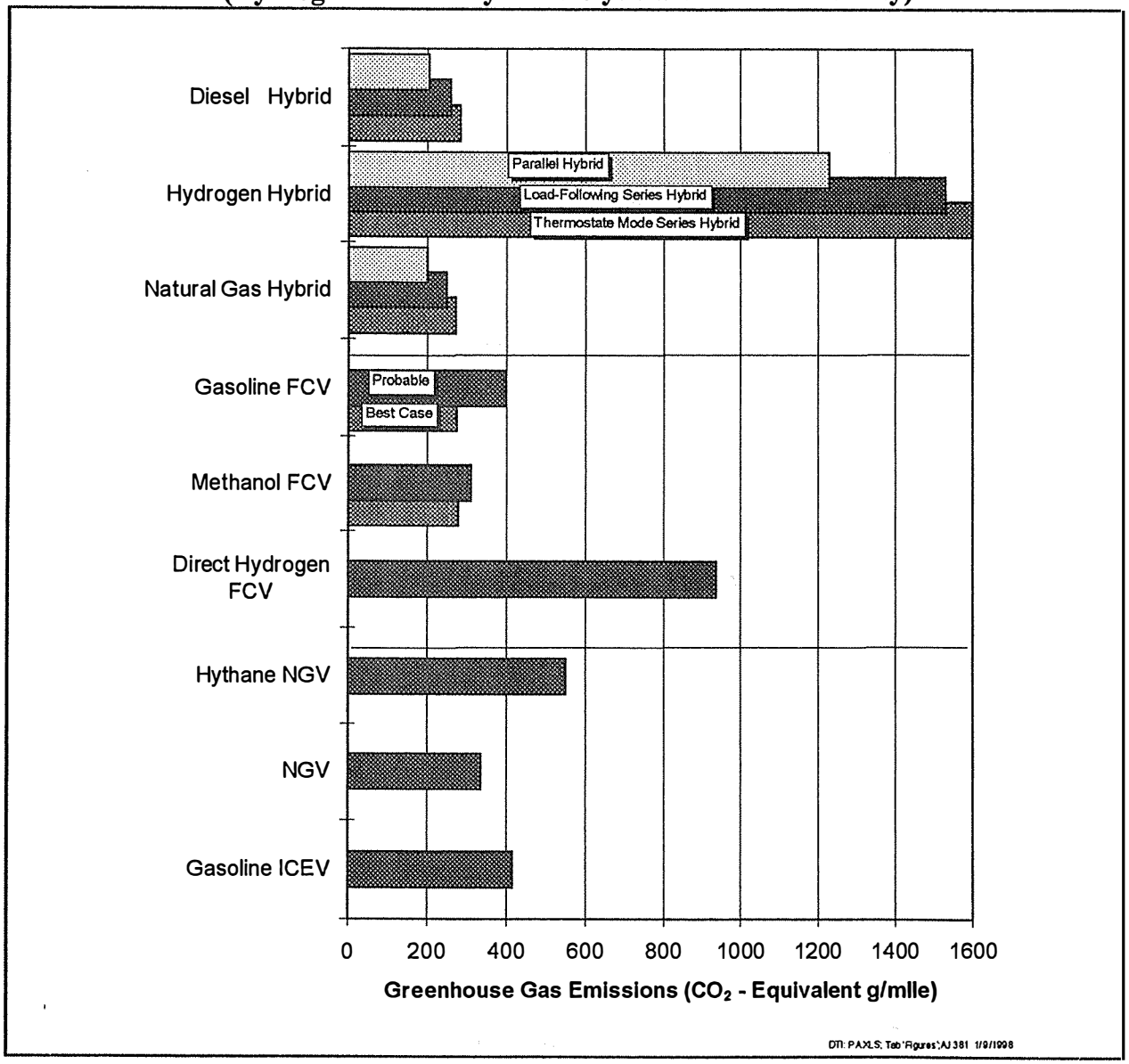

Figure 9. "Real World" Volatile Organic Compound Emissions in 2000

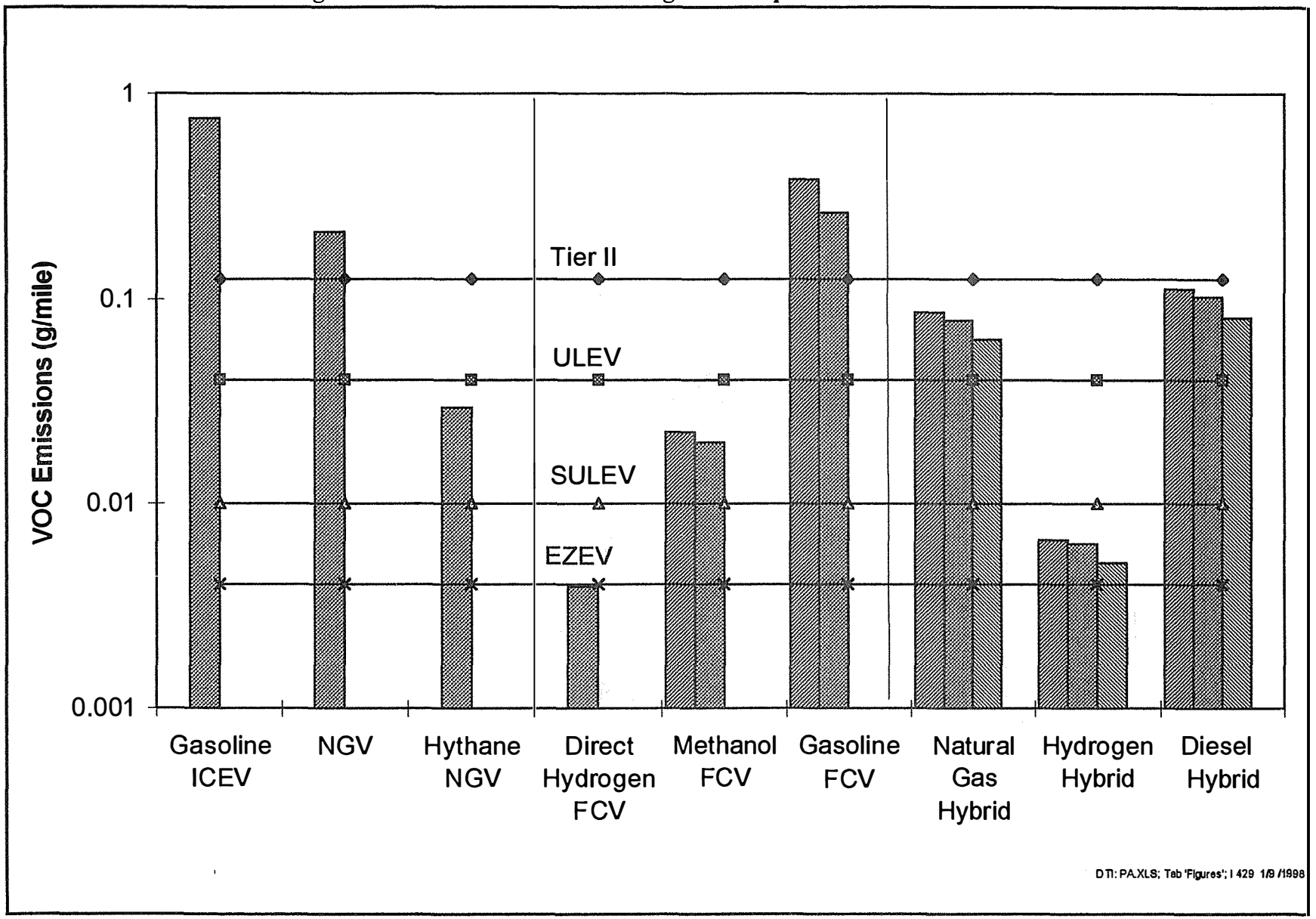

Figure 10. "Real World" Carbon Monoxide Emissions in 2000

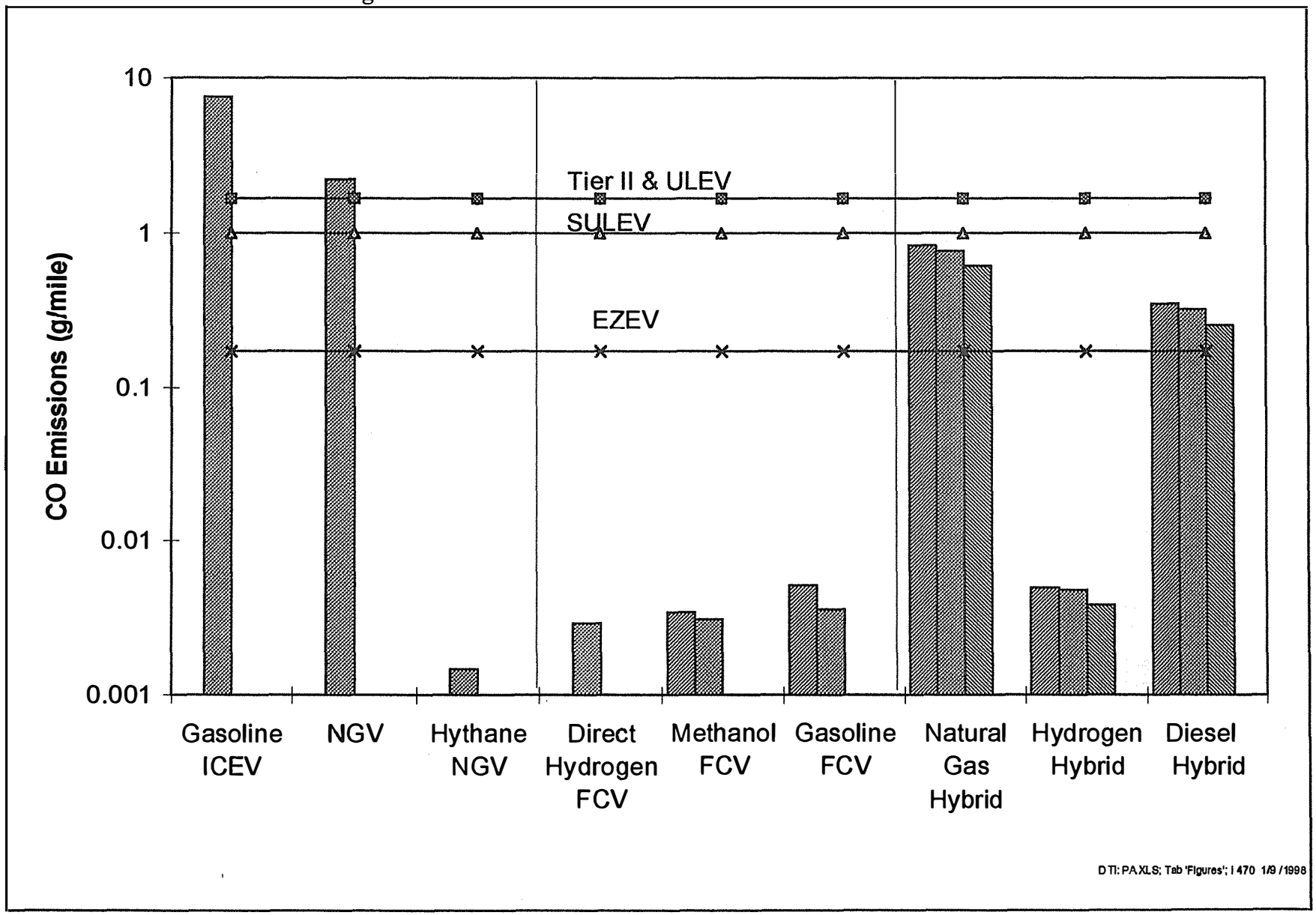

Figure 11. "Real World" Oxides of Nitrogen Emissions in 2000

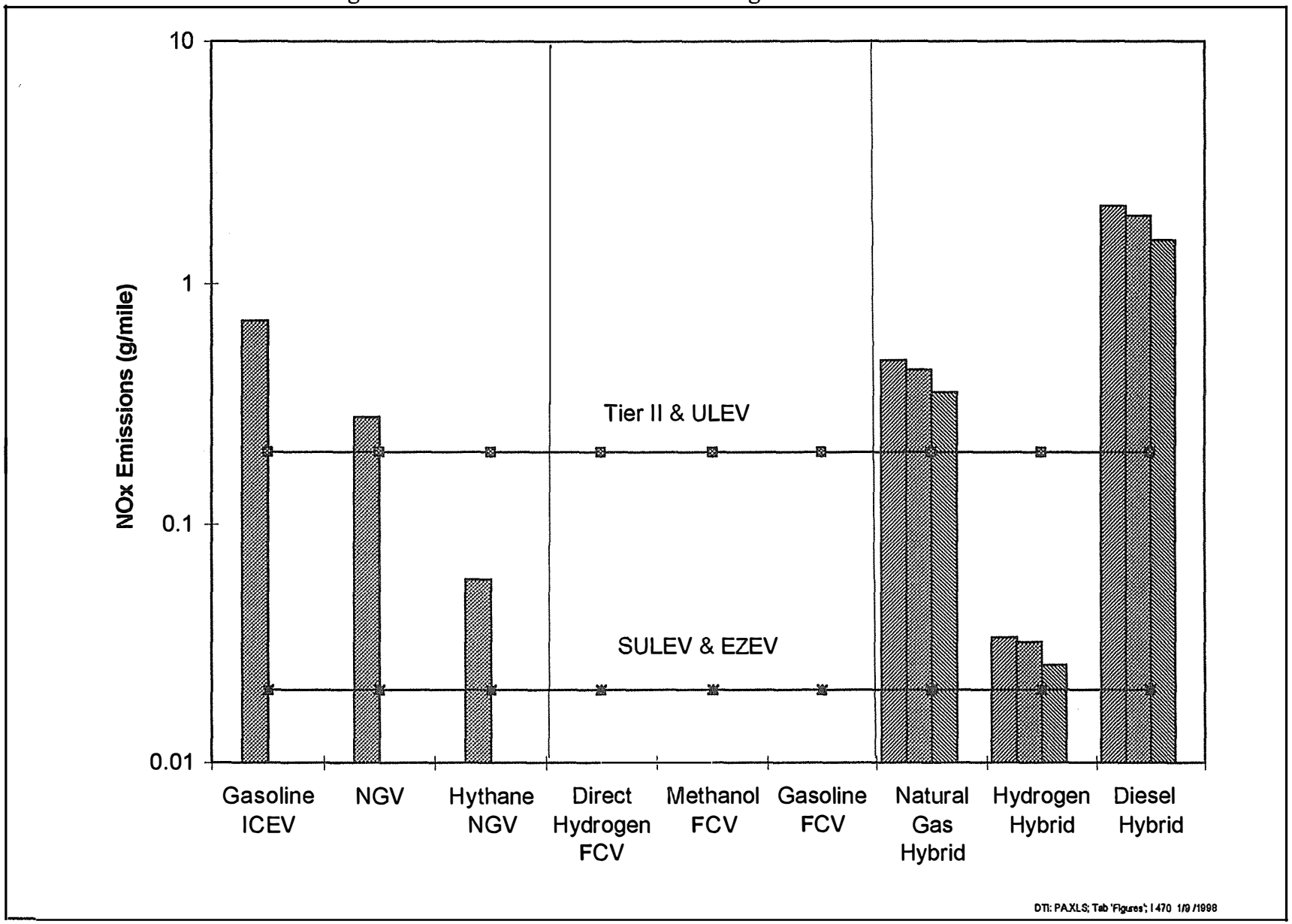

Figure 12. Incremental Mass Production Cost of Alternative Vehicles

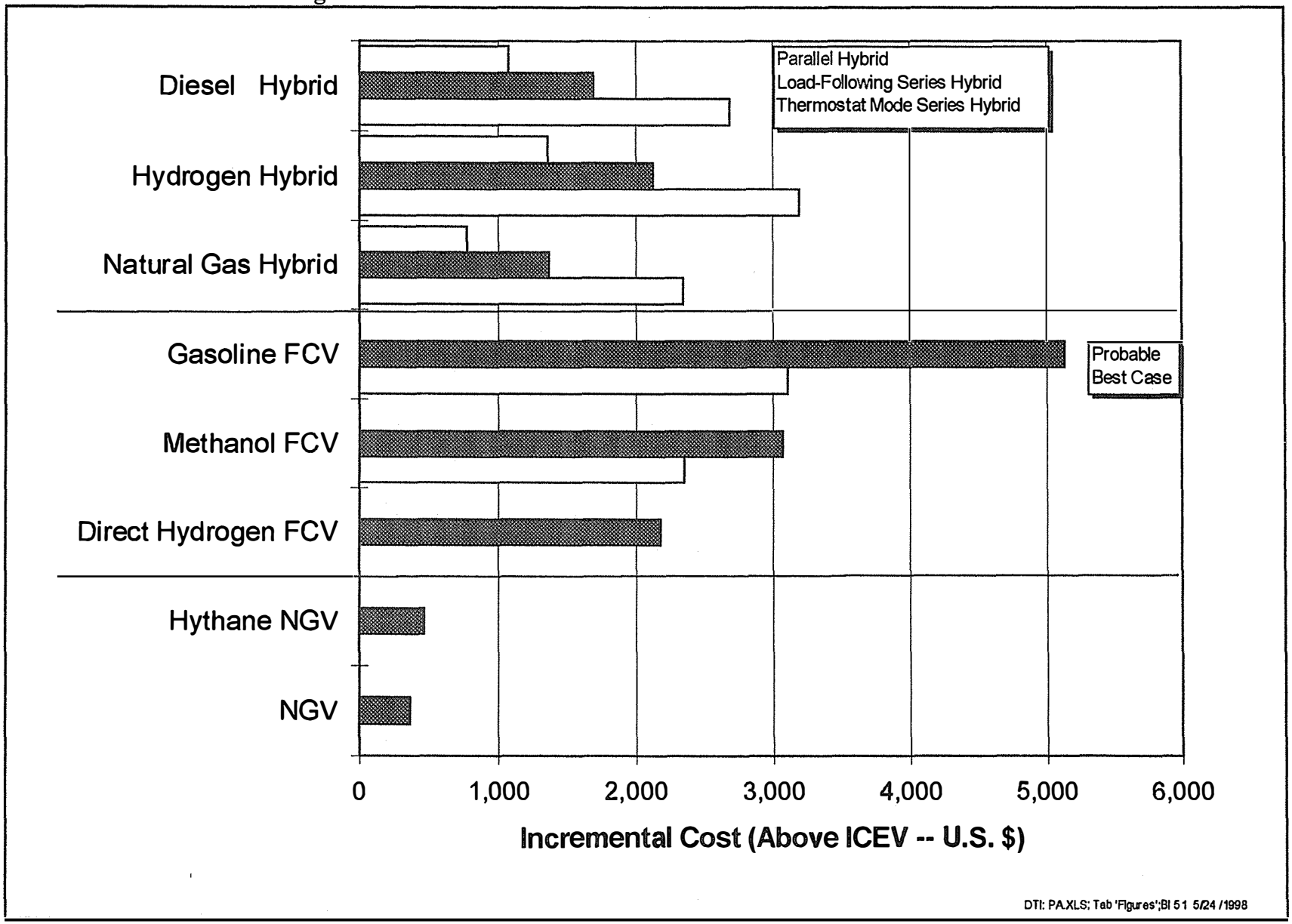

Figure 13. Initial Cost Differential Between Alternative and Conventional Vehicles

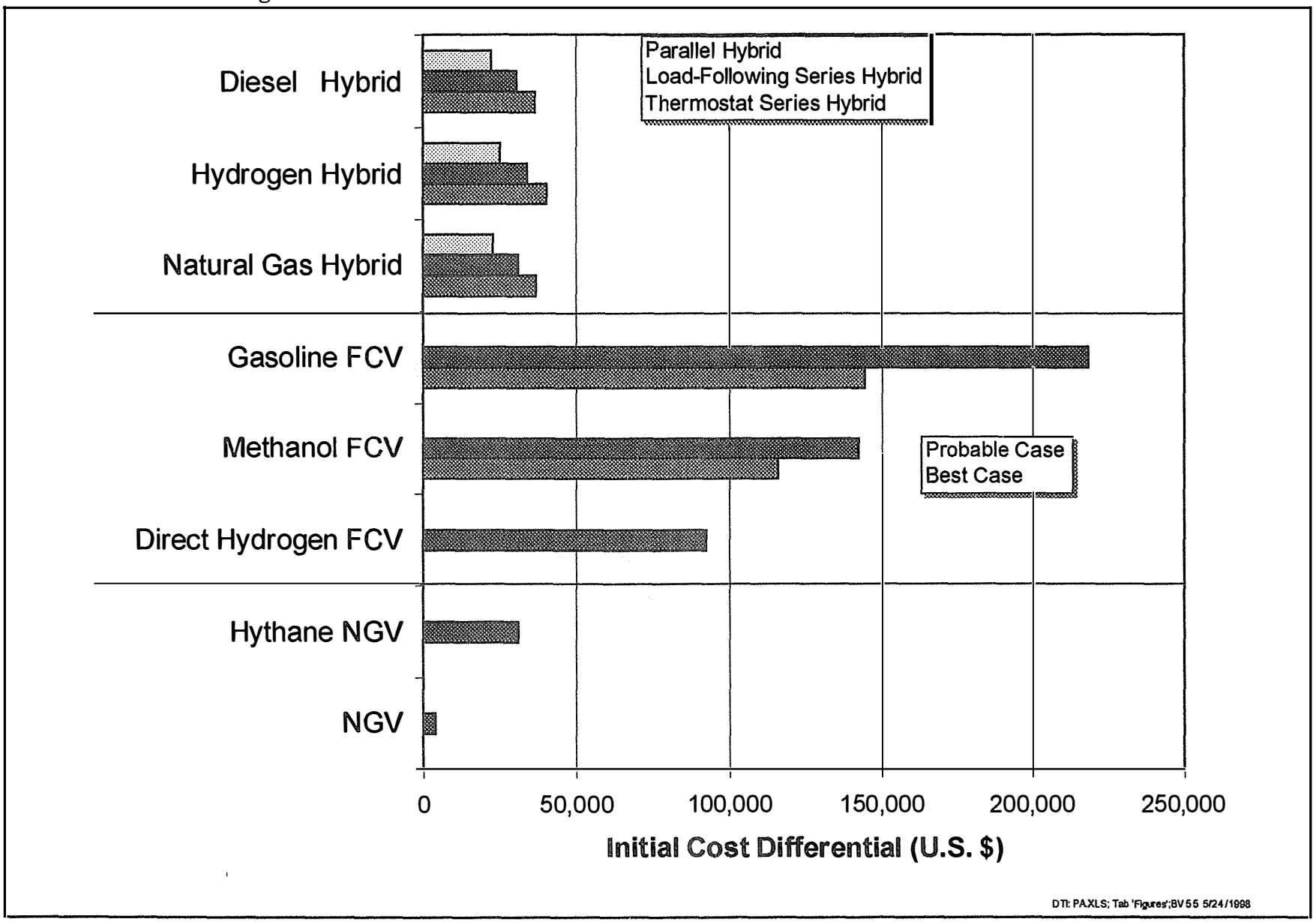

Figure 14. Incremental Mass Production Vehicle Cost vs. Annual Local Emissions Cost

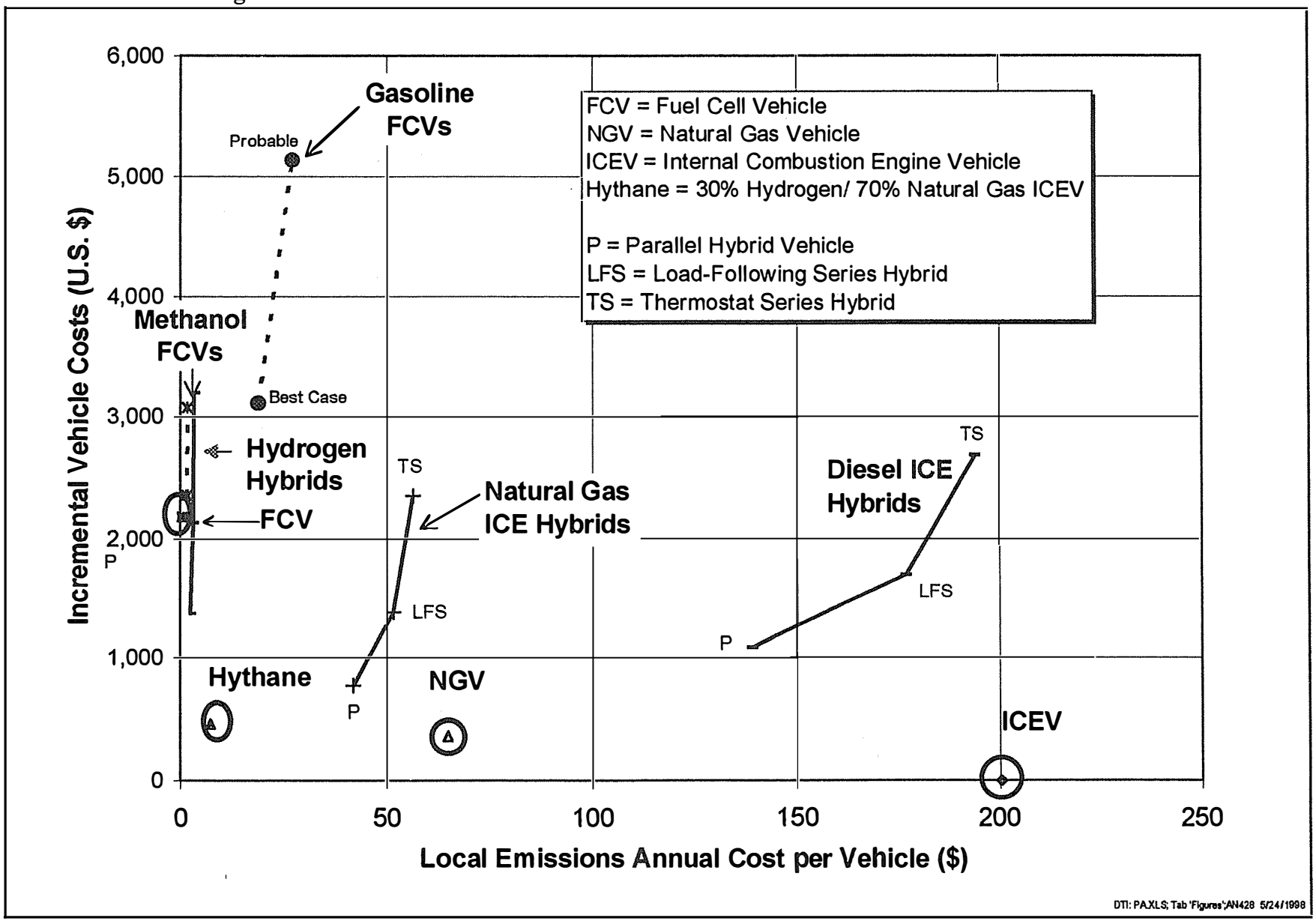

Figure 15. Incremental Mass Production Vehicle Cost vs. Greenhouse Gas Emissions

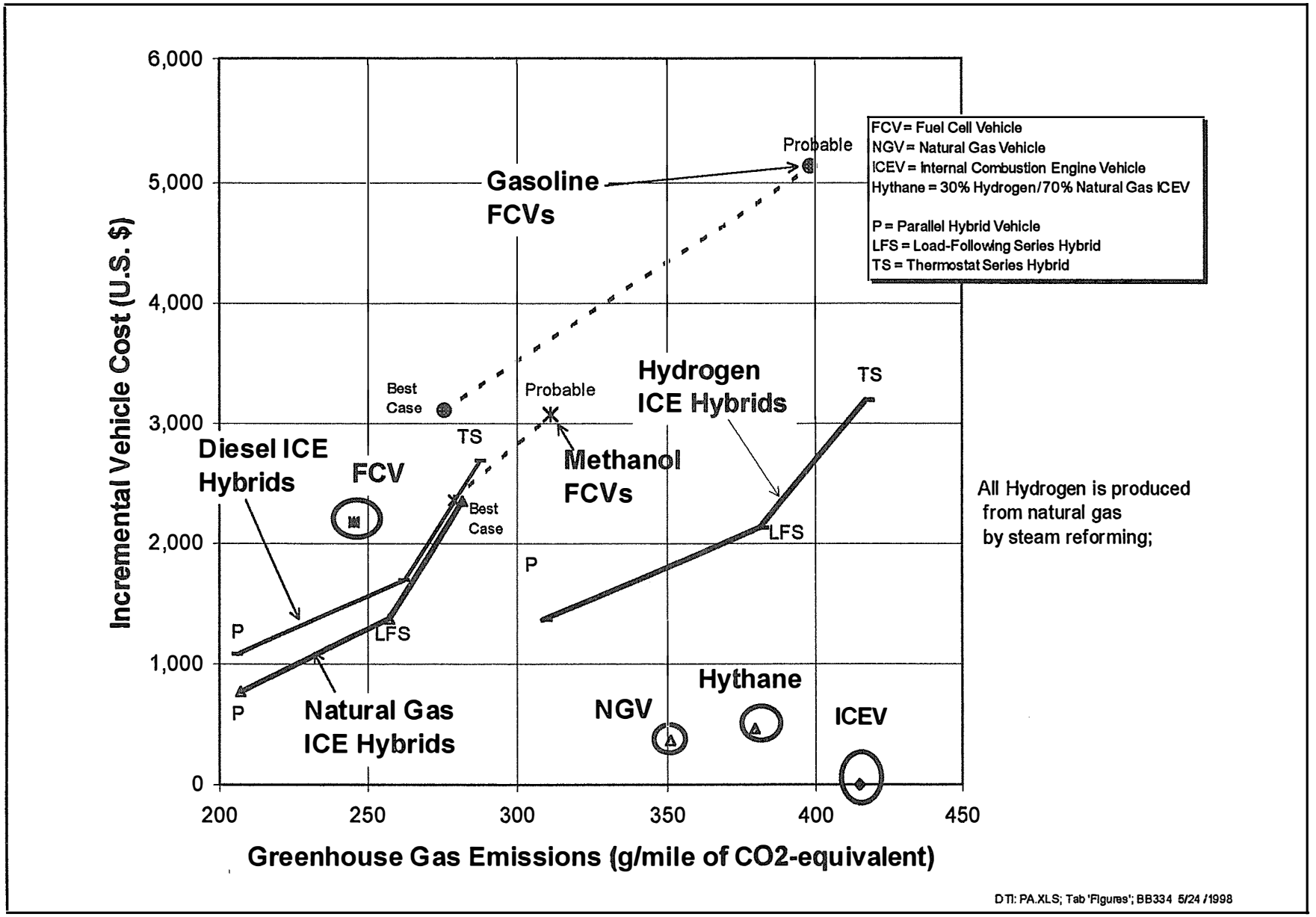

Figure 16. Incremental Mass Production Vehicle Cost vs. Combined Annual Local and Greenhouse Gas Emissions

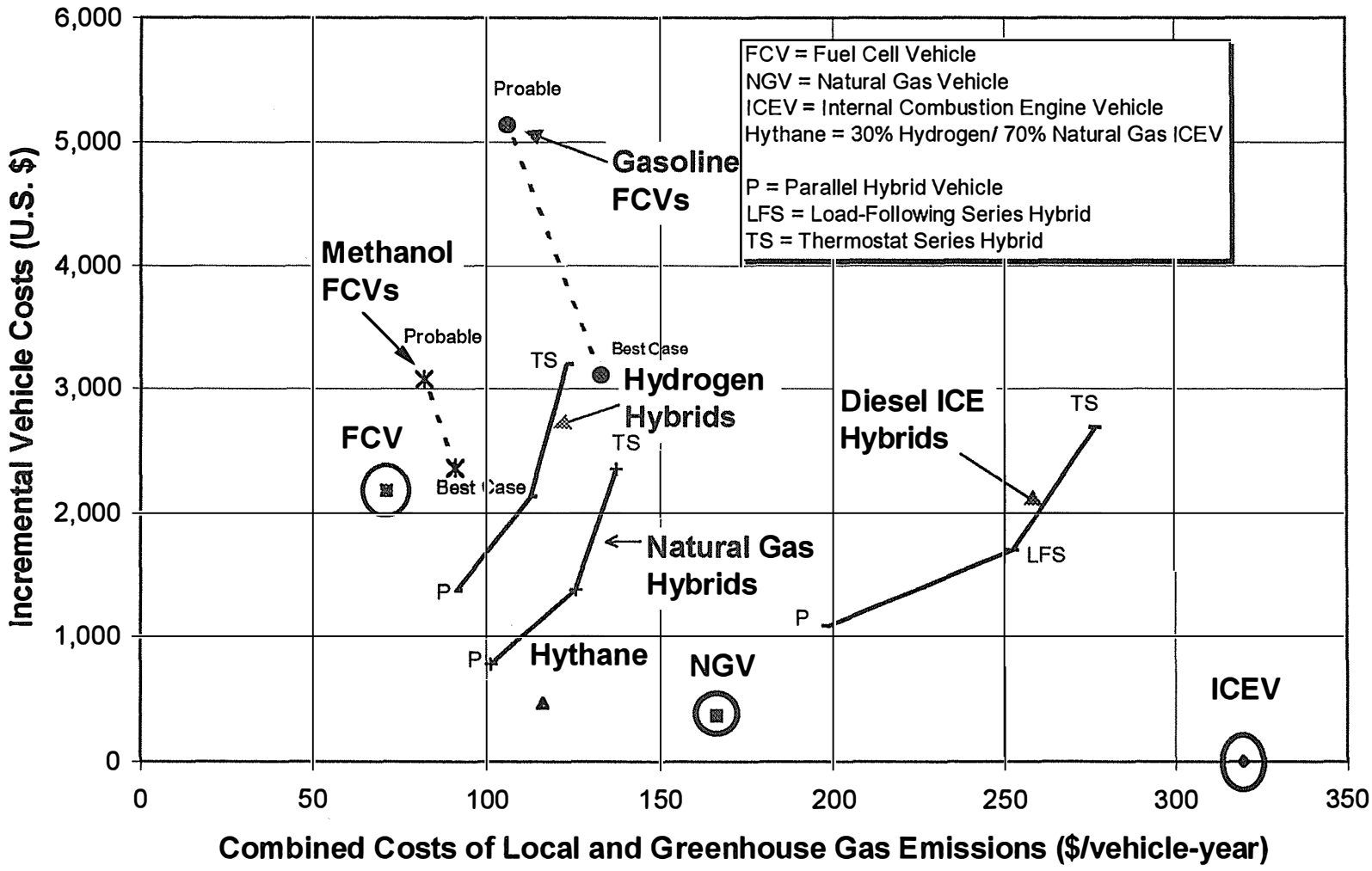

ECONOMIC AND TECHNICAL ANALYSIS OF DISTRIBUTED UTILITY BENEFITS FOR HYDROGEN REFUELING STATIONS

Joseph J. Iannucci
James M. Eyer
Susan A. Horgan
Distributed Utility Associates
Livermore, CA 94550
Susan M. Schoenung
Longitude 122 West, Inc.
Menlo Park, CA 94025

Abstract

This paper discusses the potential economic benefits of operating hydrogen refueling stations to supplying pressurized hydrogen for vehicles, and supplying distributed utility generation, transmission and distribution peaking needs to the utility.

The study determined under what circumstances using a hydrogen-fueled generator as a distributed utility generation source, co-located with the hydrogen refueling station components (electrolyzer and storage), would result in cost savings to the station owner, and hence lower hydrogen production costs.

Introduction and Background

Hydrogen refueling stations will represent a major capital investment in the hydrogen

transportation infrastructure of the future. As a way to offset some of those costs and expand hydrogen markets, it is possible that a second use (an additional benefit) can be found for some of the on-site components if employed as part of a modern distributed electric utility. By dispatching a fuel cell on-peak with hydrogen created off-peak, appreciable benefits may be gained for the local utility. As those utility benefits are realized and shared with the owner of the hydrogen refueling station, the hydrogen transportation scenario becomes more economical. This project required selection of an operational hydrogen transportation/refueling scenario, station redesign to accommodate generation of power, determination of relevant economic figures of merit, and construction of an economic model with which to compare the system options.

Objective

The objective of this analysis was to determine if, for a re-optimized system configuration, this dual-use concept provides superior economic value over separate refueling and distributed utility systems. US market estimates were also created.

Approach

The hydrogen refueling/distributed utility station consists of either a regenerative fuel cell, or a fuel cell and electrolyzer, or a hydrogen-fueled engine, plus an inverter, a converter, a hydrogen storage system, transportation hydrogen refueling station components capable of handling an appropriate number of vehicles per hour, and a control system to coordinate operations.

The refueling station is connected to a utility source of electricity to power the electrolyzer to produce hydrogen. The refueling of cars results in a time-varying electrical demand for power to the dispensing systems and energy from the hydrogen storage system.

The combined hydrogen refueling/distributed utility system is designed to add value to the simple hydrogen refueling station by dispatching a hydrogen-fueled generator (fuel cell or engine) to meet critical local and system electrical needs of the local utility.

Using a stochastic approach to the range of avoided costs in U.S. utilities, an estimate was made for the range of hydrogen cost reductions possible across the U.S. and their likelihood of occurrence. Sensitivity to the on- and off-peak costs of electricity was also analyzed.

Distributed Utility/Refueling Station Assumptions

Figure 1 shows the components of the distributed utility/refueling station system. In this figure, a regenerative (or reversible) fuel cell is shown as the generation system.

Technology Assumptions

In this study, we begin with Princeton University's onsite-electrolysis base case (Ogden, 1995). Within the boundaries of the Princeton University study, we selected cases that appeared to have the best potential for substantial distributed utility benefits. A few parameters were adjusted to allow for reverse power flow, to better define the electrical and mechanical interfaces, and to calculate energy and maximum electrolysis load costs for the station owner.

Figure 1. System Components

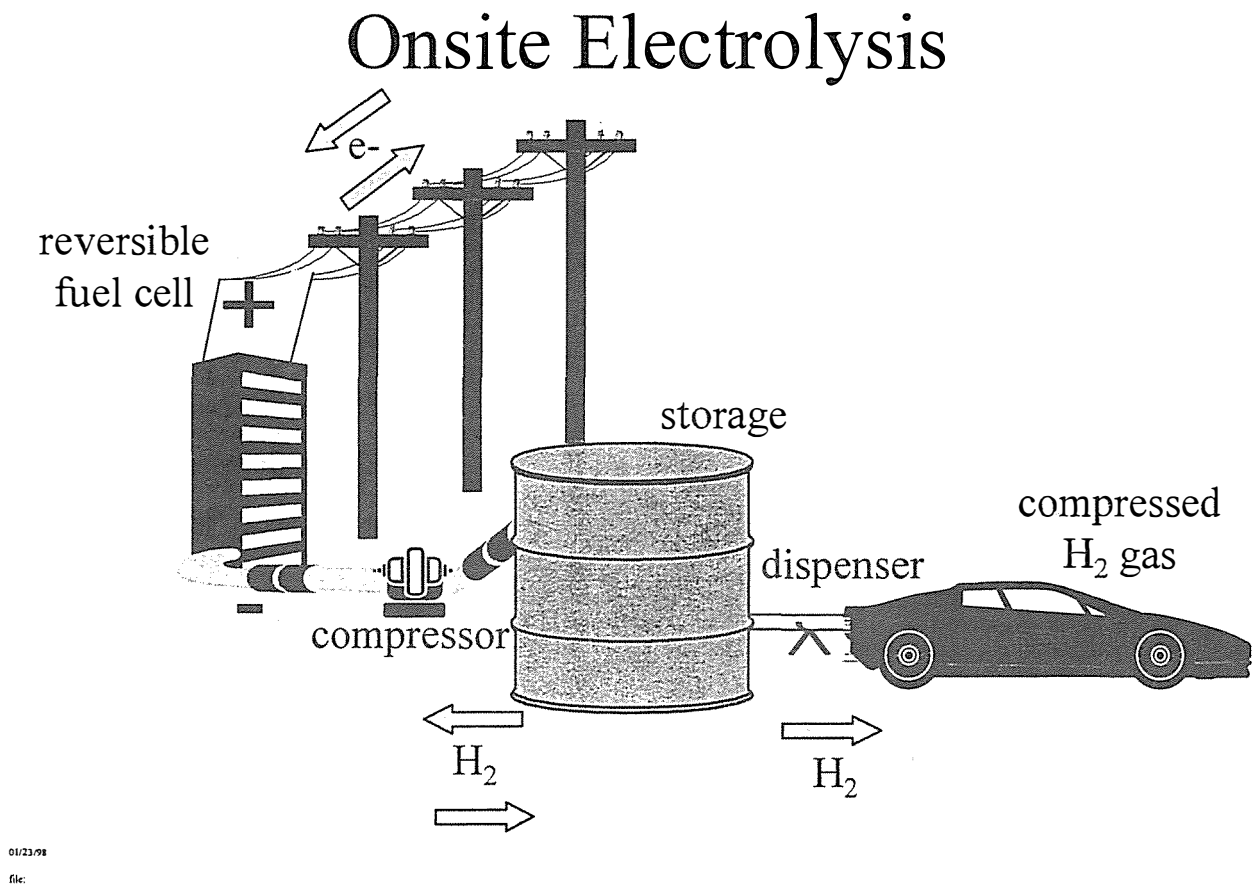

Our system consists of:

- Storage in pressurized cylinders; the pressure varies throughout the day from a minimum of 2000 psi to a maximum of 5000 psi.
- An advanced electrolysis process.
- Refueling station components, including a boost compressor that delivers hydrogen at 5000 psi.

We assume that hydrogen production occurs 100% off-peak, during the 18 hours from 6PM to 12PM.

For the combined station to provide electricity for distributed utility functions, we added the following to the Princeton design:

- additional electrolysis capability to create the H_2 needed for fuel cell operation; additional storage for this hydrogen, and
- generation capability, either as a separate fuel cell unit, or in the form of a regenerative fuel cell, or some combination of the two; or in the form of a hydrogen-fuel combustion engine. All of these options are examined.

Layout flow charts for the cases considered in this study are shown in Figure 2.

Figure 2. Component Layouts

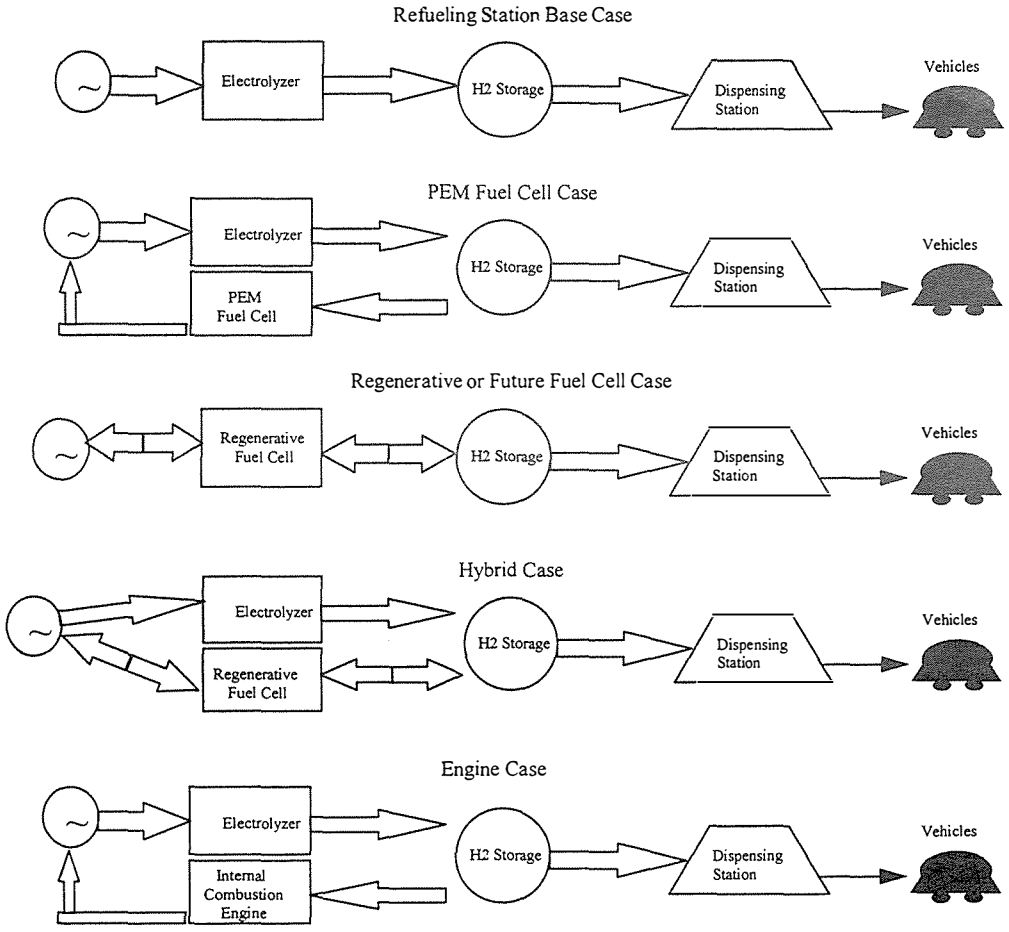

Analysis Assumptions

1. The number of vehicles served per day is either 200 or 400. In the Princeton studies, the number of vehicle ranges from 100 to 1000 per day (Ogden, et. al., 1995). The lower end of the Princeton University range was used to increase the potential benefits of the old dispatch. Above 400 cars/day, the utility would likely build a dedicated substation for the refueling station, making distributed utility and its value nearly irrelevant.
2. Refueling availability is undisturbed by the electrolysis or distributed utility function; i.e., the station is open 24 hours per day. We assumed station owners and clients would not adjust their lives or economics for the sake of distributed utility benefits increases, e.g. by stopping all refueling or boost compression during daily peak utility demand hours.
3. All hydrogen to meet the distributed utility function and refueling need is produced off-peak, during the 18 hours from 6 PM to 12 noon. This minimizes the cost of electricity use, minimizes electrolyzer sizes, and minimizes load factors.
4. Additional storage is the same type as the base case (pressurized cylinders) at the same $/scf.

5. Electricity generation (i.e. fuel cell dispatch) always occurs at the time of optimum utility benefit. The major analytical work of this project involves optimizing the benefit versus cost of adding more hydrogen and generation components for distributed utility operation.
6. This study's base case has a distributed utility operating 1 hr/day and approximately sized at the same size as the electrolyzer, i.e. 1.4 MW for 200 cars, and 2.8 MW for 400 cars.
7. The daily schedule of power flows and stored hydrogen energy is charging and discharging during peak and off-peak periods, with a regularly spaced traffic of cars throughout the day. If all the cars arrived during the peak period when the electrolyzer does not operate, the stored hydrogen would decrease to 40% full. This is the minimum needed to maintain 2000 psi in the storage cylinders.

Hydrogen System Cost and Performance Analysis

The components of the system are:

- electrolyzer
- storage cylinders
- storage compressors
- fuel cell or combustion engine plus power conditioning components
- station components, including boost compressor, dispensers, and fixed infrastructure

The assumed capital cost, operating cost, lifetime and efficiency of these components are listed in Table 1. For those components which are the same as the Princeton study, the cost assumptions are identical (Ogden, et. al., 1995).

Two types of PEM fuel cells were included in the analysis: a simple hydrogen-fueled PEM, and a regenerative PEM. The regenerative PEM includes the electrolyzer function when operated in reverse. This makes it more expensive because the catalyst loading must be higher to operate in the higher temperature electrolysis mode (Thomas, 1995). It is possible that future regenerative fuel cells may not need the additional catalyst (Mitlitsky, 1998) and could cost the same as a simple PEM.

An internal combustion engine was also considered for this application. Diesel engine manufacturers have indicated that hydrogen combustion could be accomplished with little modification and at reasonable capital cost (Keller, 1998 and NREL, 1997). Other operating costs, in addition to O&M, are labor costs of $131, 400/yr and electricity costs at 2¢/ kWh off-peak and 7¢/kWh on-peak. These are identical to the Princeton study assumptions. An identical capital charge rate of 15% is also assumed. This is consistent with private (rather than utility) ownership of the station.

Energy and Power Requirements

The energy required per day and the peak power to the system depend on:

- the number of vehicles served per day
- the number of dispensers operating at the station (assumed to be four)

Table 1. Technology Data

Component	Capital Cost	O&M Cost	Efficiency or Energy required	Lifetime
Advanced electrolyzer	300 $/kW H2 out	4% of cap cost/yr	η=0.8	20 yrs
Storage cylinders	1.1 $/scf	100 $/yr/cylinder		20 yrs
Storage compressor	2000 $/kW	$3000/yr/unit (2 units)	(.6225 kW/car × # cars/day × 18 hrs/day) +DU	10 yrs
PEM fuel cell	500 $/kW	4% of cap cost/yr	η=0.60	20 yrs
Regenerative fuel cell	1000 $/kW	4% of cap cost/yr	η=0.60 in gen mode	20 yrs
Future regenerative fuel cell	500 $/kW	4% of cap cost/yr	η=0.60 in gen mode	20 yrs
Internal combustion engine	350 $/kW	4$ of cap cost/ yr	η=0.40	20 yrs
Fixed components	$277,100 (= 4 dispensers + boost compressor)	4% of cap cost/yr	1.875 kWh/car × # cars/day	10 yrs

- the power level of the distributed resource (approximately same order of magnitude as electrolyzer, so as to not adversely affect distribution service rating)

The distributed utility rating of 1.4 MW equals the electrolyzer rating for the refueling function alone for 200 cars per day. The 2.8 MW rating corresponds to the 400 cars per day.

Capital Cost Trade Study

To obtain a set of capital costs for the Benefit/Cost study, a range of distributed utility types, sizes and operating times were considered for two service levels, 200 cars day and 400 cars/day.

Four relatively near-term fuel cell technologies (PEM, RFC, hybrid, and IC Engine) and one long-term future regenerative fuel cell option (future RFC) were compared to one another.

- The PEM design has separate electrolyzer and fuel cell components, the electrolyzer sized to meet the hydrogen supply needs and the fuel cell sized to provide the desired distributed utility output.
- The RFC design has a single electrolyzer/fuel cell unit, sized to meet the hydrogen supply needs; this makes the fuel cell capability oversized to provide the desired distributed utility output.

- The hybrid design has a small RFC sized to provide the desired distributed utility output and a small portion of the hydrogen supply needs, plus a separate electrolyzer component sized to meet the remainder of the hydrogen supply needs. This is a cost-efficient design since it uses the more expensive reversible component precisely for the distributed utility aspects only.
- The future RFC design has a single electrolyzer/fuel cell unit, sized to meet the hydrogen supply needs; this makes the fuel cell capability oversized to provide the desired distributed utility output.
- The engine system assumes mass produced diesel generator technology suitable for hydrogen combustion; the separate electrolyzer is sized to meet the hydrogen supply needs and the fuel cell sized to provide the desired distributed utility output.

Note that the electrolysis rating for the combined refueling/generation station will always be somewhat larger than for the refueling station because the electrolyzer must generate enough hydrogen for both the generation and refueling functions.

The least-cost approach, under most conditions and for the assumed costs, appears to be the future regenerative fuel cell. The lowest cost system does not necessarily yield the highest net benefits, however.

For the 200 cars and 400 cars 1 hr/day cases, Figure 3 shows the component costs for the

Figure 3. Capital Cost Components for all Technologies (Distributed Utility operates 1 hr per day)

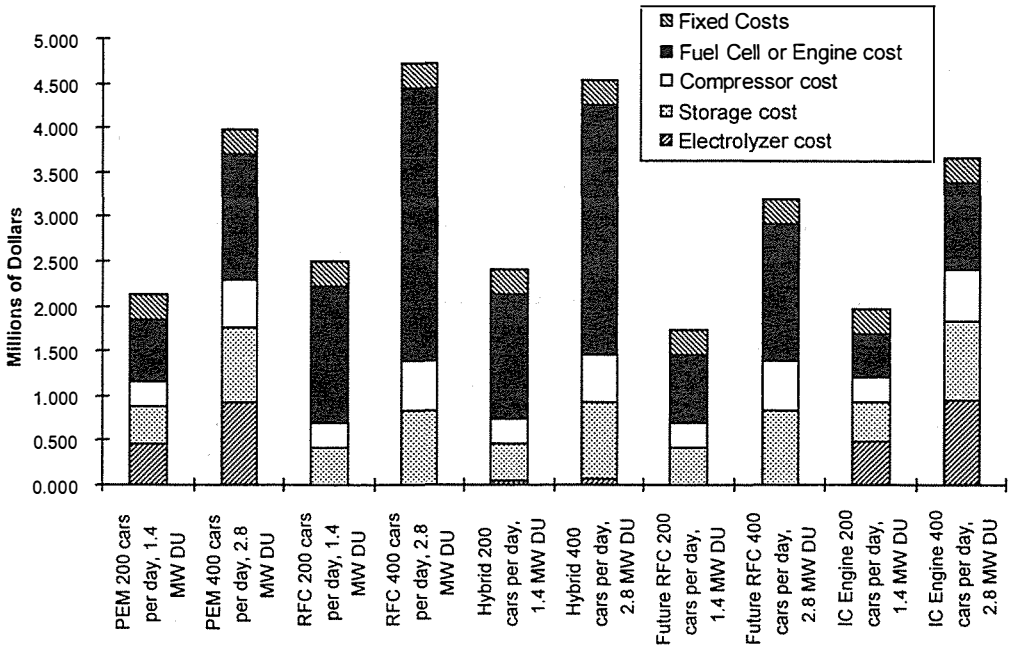

different technologies. Not unexpectedly, the generator (fuel cell or engine) cost is the largest single component. The fixed costs are the same for both 200 and 400 car cases because a 4-dispenser station is assumed for both.

Utility System Benefits

Economic Analysis Approach

The metric chosen for the economic optimization of the combined hydrogen refueling station/distributed utility plant is the delivered cost of hydrogen to the vehicles. If the distributed utility dispatch capability can more than pay for itself, the cost of delivered hydrogen should be reduced. The owner may choose to pass any savings along to the clients of the station, or may use them for higher profitability.

The station is considered to be owned by a private party, purchasing electricity from the local utility at prevailing rates. Most of the purchased electricity is used to power the electrolyzer (or equivalently the regenerative fuel cell), but additional power is needed for the storage compressor during electrolysis, for the boost compressor during fueling, and for other miscellaneous on-site loads.

In an effort to reduce his operating costs or increase the station's cash flow, the owner is considering dispatching an on-site fuel cell on demand for the utility. The owner is planning on receiving some or all of the benefits the utility gains by this dispatch. The fraction of the utility savings he receives is the subject of a negotiation with the local utility.

Operational Issues

Although each station's location and operation would be slightly different, we have assumed that the utility calls everyday in mid-afternoon to request dispatch of the fuel cell to meet system and transmission and distribution peaking needs. This is usually the peak of a utility's demand and costs and the most stressful time for the refueling station owner to dispatch the unit. We assume that the owner responds by dispatching the unit for the specified length of time as directed by the utility. An imperfect reliability is included in the economic analysis by decreasing the utility benefits by the presumed lack of availability of the fuel cell, 5%.

In addition, the full capacity of the distributed utility unit cannot be assured during the utility-requested dispatch time due to the need to continue serving calls and operating the boost compressor. Again the benefits of the generation, transmission and distribution capacities are reduced by the peak boost compressor demand. An alternative operational approach could have been to close the station during the utility's peak demand period, but this was rejected as being detrimental to station business. Note that the station owner does not operate the electrolyzer at all during the peak rate period of noon to six PM, to avoid high demand or energy charges.

We have also considered three durations of dispatch (one-half, one and two hours) which should cover most utility peak width situations. The half hour dispatch case is highly beneficial to a distributed utility owner since almost no fuel (in this case fairly expensive hydrogen) is needed to obtain the same capacity benefits as a longer dispatch period. The energy benefits are not very valuable for low-capacity-factor distributed utility units. The one hour dispatch is probably the

most important case since system and especially local peaks are not often very broad. Two hours every day is conservative. If weekend and off season dispatch could be avoided, it is possible that the economics could be improved marginally although the capital costs of the fuel cells, extra compressor and storage capacities remain sunk. The results of the modeling are independent of the actual time that the utility calls for load relief, but our assumption is that it comes at the most inopportune time in the mid-afternoon.

Economic Analysis with the Distributed Utility Units

Of course, the capital costs for cases with distributed utility components are higher than the base case due to the need for the fuel cell (in all cases except the future regenerative fuel cell) and for more hydrogen storage capacity in all cases. Additionally the need for more hydrogen for dispatch of the fuel cell means a larger compressor, more cushion hydrogen gas, and more electricity for the electrolyzer and storage compressor.

In the cases with distributed utility components included, the distributed utility benefits are subtracted from the annual system costs to yield a net annual cost including these benefits. Depending on the magnitude of the distributed utility benefits, they may or may not pay for the additional distributed utility dispatch hardware. This is the subject of this study.

Utility avoided costs consist of both central and distributed components, assuming utility type economics for their avoided costs. The central benefits included in this study are central capacity (the ability to avoid the purchase of additional peaking capacity) and energy (the ability to avoid fuel purchases). If a utility can dispatch a distributed generation plant it can benefit by this avoided or deferred investment in capacity. If the fuel is not paid for by the utility this is an added benefit. The magnitude of these benefits depends upon whether the utility currently needs more peaking capability and the type and cost of fuel, and the utility plantís heatrate on the margin. Central capacity benefits can be as low as zero or as high as 50 $/kW-yr; the units of $/kW-yr are used as a way to annualize the carrying cost of owning or contracting for peaking capacity; the same units are used for transmission and distribution avoided costs. The fuel used by the power plants on the margin can range up to five cents per kWh, but rarely would fall below three cents per kWh. This unit is converted to $/kW-yr by multiplying by the appropriate hours per year of distributed utility unit operation.

The distributed benefits included are the avoided transmission and distribution investments for wires and transformers by the local distribution company and the value of improved reliability to the local customers. Similar to the central capacity benefits, if local load can be served by local generation, wires investments can be reduced, saving the utility money. Transmission and distribution avoided costs (benefits are rarely zero since wires capacity expansions are never done without need being proven first) can be as high as 20 $/kW-yr. and 70 $/kW-yr., respectively. Improved customer reliability is not an immediate, direct bottom-line benefit to the utility, but is increasingly important to utilities as they strive for customer loyalty as deregulation unfolds. Reliability benefits can be as low as zero and can range up to many dollars per lost kWh. We have used 25 $/kW-yr.

If a distributed utility unit is perfectly dependable, all of these benefits (avoided costs) can theoretically be earned by the owner of the unit. The owner of the distributed utility unit of course must pay for the fuel used, the carrying costs of the capital and the O&M costs.

In order to evaluate a range of utility situations the generation, transmission and distribution, energy and reliability avoided costs were evaluated for bins each representing one fifth of the U.S. Thus the costs range from the lowest avoided costs in the U.S. up to the highest (best for distributed utility) 20% in the country. In this way the broad range of values in the U.S. could be examined without site-specific information.

The utility avoided costs are derived from many sources, such as EIA annual summaries of utility capital investments, FERC Form 1, GRI projections of future fuel costs, etc. All utility avoided costs are annualized assuming a typical amortization of 30 years for generation, transmission and distribution investments

Cost of Hydrogen Results

Overview

A wide range of technologies, sizes, dispatch durations and numbers of cars refueled per day were examined to determine the overall viability of using distributed utility dispatch at hydrogen refueling stations.

The majority of the analysis was done using nominal or median values for the distributed utility benefits which these hydrogen refueling station installations could earn; one sensitivity section examines a range of avoided costs and the impact of sharing the benefits between the utility and the station owner. Another sensitivity section considers the impact of changing on-peak and off-peak electricity costs from the original Princeton values.

Base Case Results

For the 200 car per day base case (refueling station only with no distributed resource), hydrogen could be delivered to the clients for 18.33 $/GJ. For the 400 car per day capability the costs dropped to 15.55 $/GJ. The capital cost of the larger capability station is only 79% more than the smaller version, and since the throughput is doubled the overall economics are approximately twenty percent superior. This substantial superiority of the higher capacity station is reflected in all of the results of the study, whether including distributed utility units or not. The improvement with number of cars served per day agrees with the Princeton Study.

These two base cases are used for comparison to the distributed utility economics to evaluate the relative value of adding dispatch capability.

Overview of Distributed Utility Results Using National Average Data

Technology Ranking

In a general sense the future RFC has the best (lowest) cost of hydrogen production followed by the engine, the PEM, the HYB and least desirable is the RFC. Using any of the near-term joint refueling/distributed utility designs to reduce the cost of hydrogen does not appear to be likely, but it is very close to making sense for the PEM.

The long-term future RFC design is ideal for distributed utility applications at refueling stations, handily beating the base case at both car handling sizes. The future RFC design, should it ever be realized, is ideal for such a refueling station application since the hardware is used nearly continuously, whether electrolyzing off-peak or discharging for an hour or so per day.

Figure 4. Cost of Hydrogen for 1 hr/day Distributed Utility Cases with Median Benefits

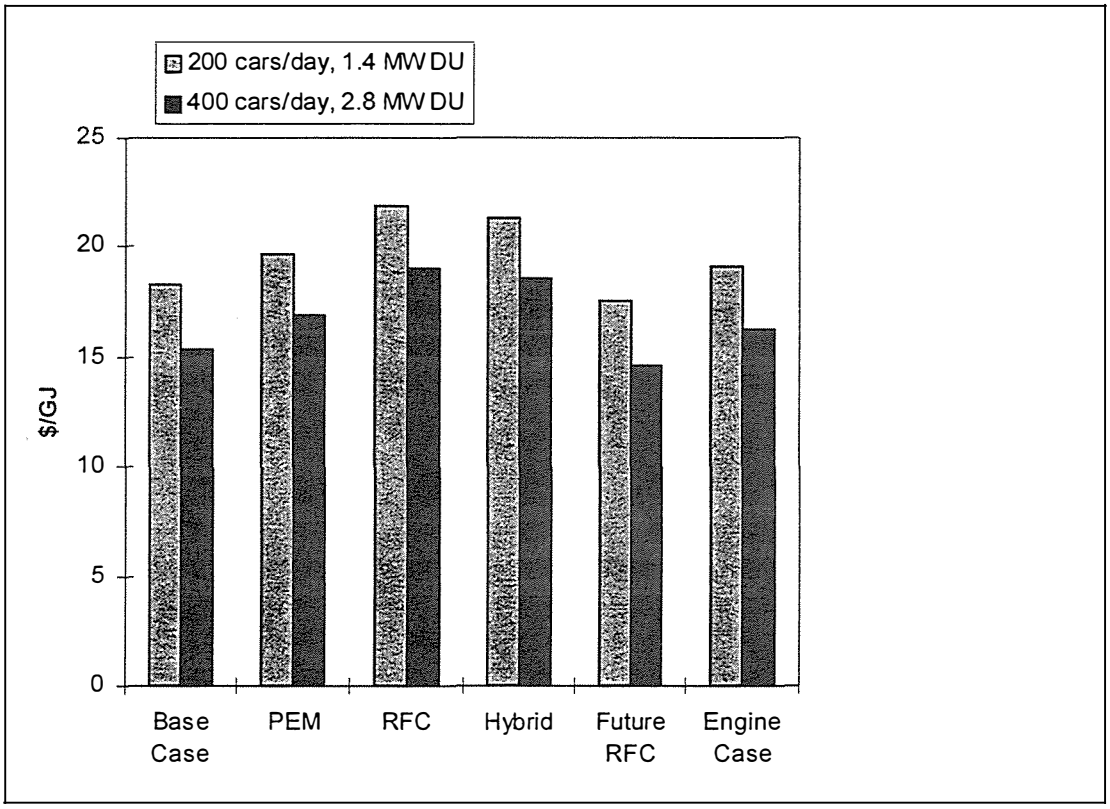

Sensitivity to the Dispatch Rating of the Distributed Utility Units

The rating of the distributed utility unit provides a much more interesting story. The PEM and HYB cases become less attractive as the distributed utility unit is dispatched at higher and higher power. Apparently as more power is demanded the additional capital costs for the fuel cell portions are not outweighed by the additional distributed utility benefits. Thus the economics are pushing the size toward zero fuel cell size.

However in the single component designs (RFC and future RFC) the fuel cell function is underutilized at low power, so that requesting that it operate at higher power levels reduces the net cost of hydrogen from the station. This is not an unlimited capability however since the electrolyzer side has capabilities at 1.6 MW and 3.2 MW for the 200 and 400 car per day respectively, only slightly higher than the dispatch rating maximum studied here. Thus the most reasonable size to consider for distributed utility applications of refueling stations for single

component designs is the electrolyzer forward rating, approximately the same as the high end of the dispatch size selected herein.

Sensitivity to Utility Benefits Using a Distribution of Avoided Costs

The near-term applications potential for distributed utility operation of fuel cells in conjunction with refueling stations looked near enough to economic viability that a closer look seemed reasonable. Perhaps the use of a national average for the utility benefits of distributed utility dispatch was hiding the application of these units in some fraction of the upper end of utility avoided costs.

We selected the PEM case for further in-depth analysis. We added two features to the analysis to provide more insight into the potential for this application:

- a distribution of utility avoided costs into five bins, and
- a parameter to show the amount of savings which a utility and a distributed utility owner might negotiate

The results for the five bins are shown in Figure 4 for both the 200 car/day case and the 400 car/day case.

Figure 5. Cost of Hydrogen vs. Hours/day of Operation 400 cars/day, PEM

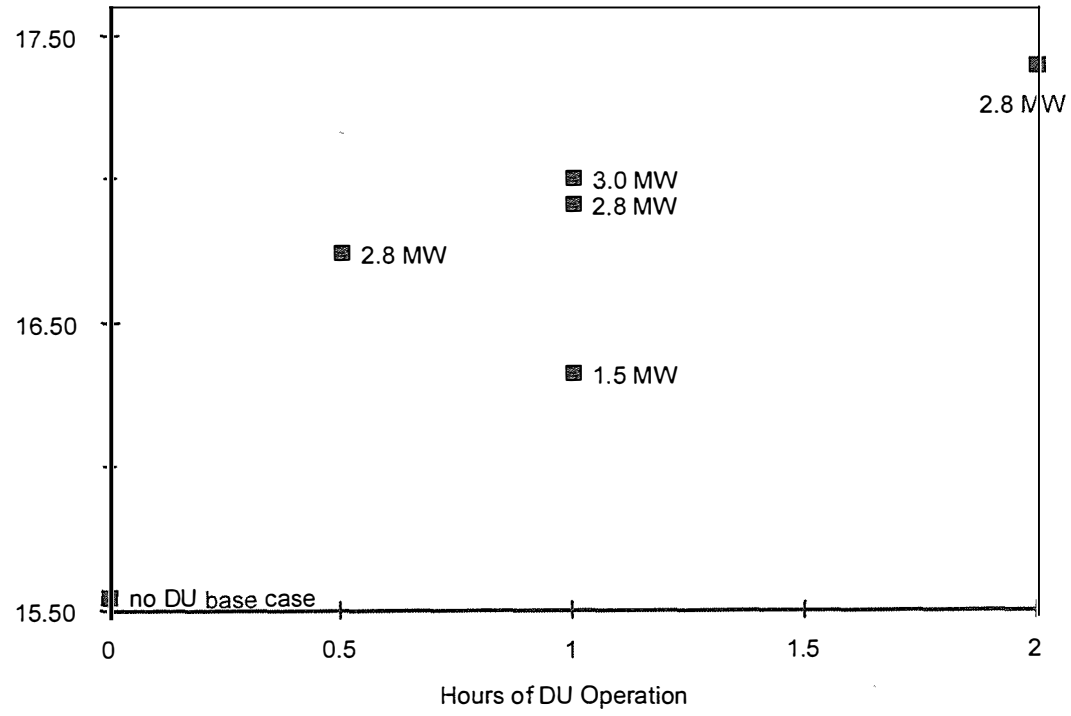

Figure 6. Cost of Hydrogen vs. Hours/day of Operation 400 cars/day, Future RFC

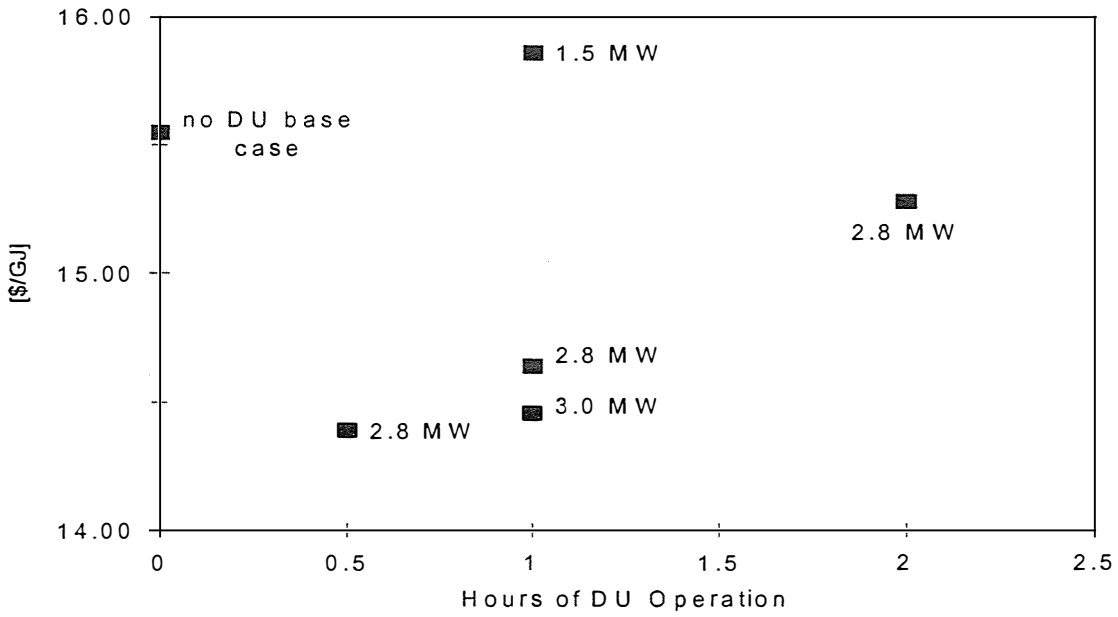

Figure 7. Cost of Hydrogen vs. Range of Utility Benefits for 1 hr/day, PEM, 400 cars/day

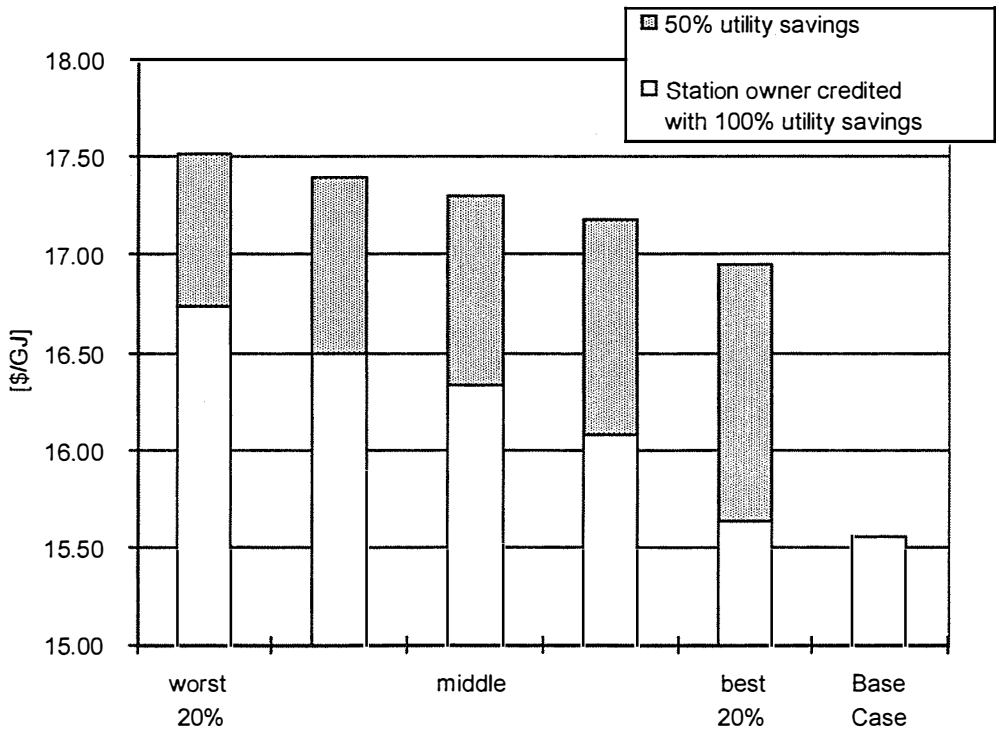

Studying the Sensitivity to Electricity Costs

The baseline electricity costs (2 cents per kWh off-peak and 7 cents per kWh on-peak), while consistent with the Princeton refueling station economics study, may not be representative of a large portion of the US. These original electricity costs are more representative of electricity production costs than the price a commercial customer would pay for electricity. Further, electricity costs have risen somewhat in the last few years in parts of the country and the relationship between peak and off-peak is not the same everywhere.

To study the sensitivity to this important variable in estimating the cost of electrolysis, we have used an alternative set of higher costs to purchase electricity:

- 4 cents per kWh off-peak and
- 8 cents per kWh on-peak.

The results are shown in Figure 8. Even though the hydrogen production costs rise by roughly one-third with more expensive electricity, the technology ranking results are not impacted to first order by the use of higher electricity costs, since the base case hydrogen costs also rise proportionately. Slight relative advantage will be found for the more efficient fuel cells compared to the less efficient hydrogen engine technology since the electricity to make the extra hydrogen for distributed utility dispatch has become more costly.

A more subtle issue is whether the electrolyzer should still operate eighteen hours per day if the off-peak costs average as high 4 cents per kWh.

Figure 9 shows the components of delivered hydrogen cost ($/GJ) for several cases at both the baseline and alternative (higher) electricity costs. The figure indicates that electricity and capital are the major cost elements. The final cost of hydrogen is very sensitive to off-peak electricity costs. The size of the DU benefits is also shown for these cases. These values are negative since they subtract from the cost components in computing the final cost of hydrogen.

Discussion

As utilities become more comfortable negotiating such shared distributed utility savings arrangements with owners of distributed utility plants, the near-term PEM or hydrogen engine technical options should be re-evaluated for economic viability.

For example, the top 20% bin of utility avoided costs still represents an average of almost 200,000 MW of installed capacity in the US; at the upper end of that bin can be large markets and profitable locations which could be quite viable if the utility is motivated to share the distributed benefits.

Even small reductions in some of the technology costs or improvements in performance could swing the equation in favor of PEM or hydrogen engine distributed utility units at refueling stations.

A decision to slow down or eliminate refueling during the utility peak hour (to eliminate the parasitic load of the boost pump), would have made the PEM or hydrogen engine attractive.

Figure 8. Cost of Hydrogen for 1 hr/day Distributed Utility Cases with Median Benefits (Baseline Electricity Costs: 2¢/kWh off-peak, 7¢/kWh on-peak; Alternative Electricity Costs: 4¢/kWh off-peak, 8¢/kWh on-peak)

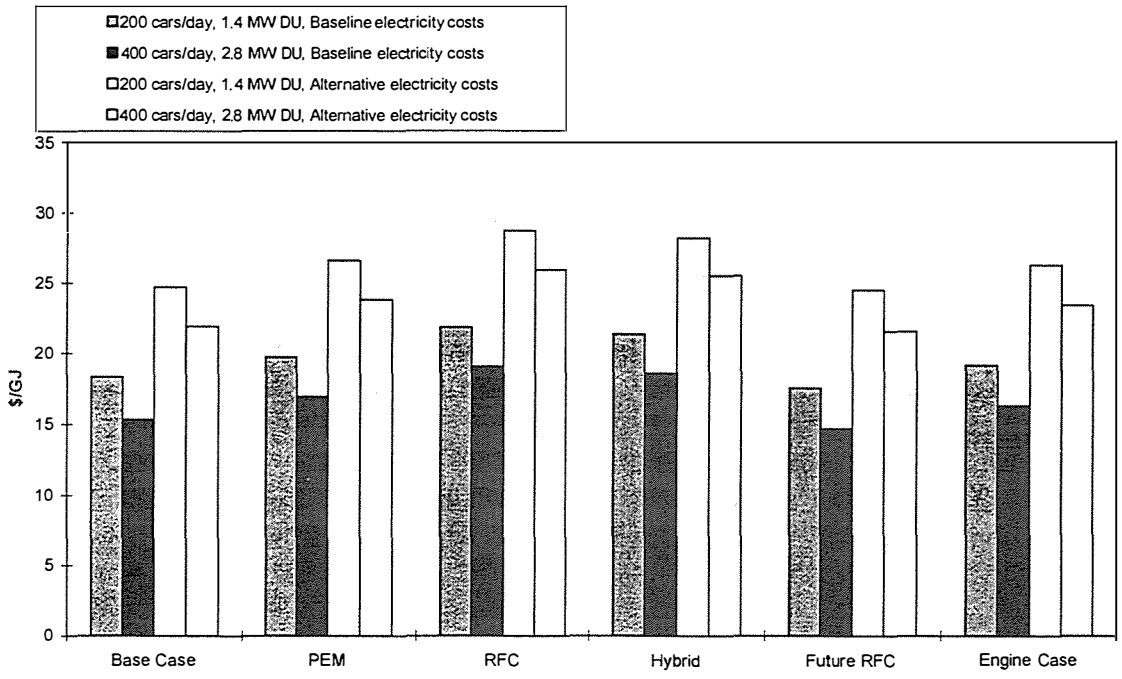

Alternatively, allowing the pressure in the cushion gas to drop below 40% of maximum (which would only occur if all 200 or 400 vehicles/day were fueled during the peak period with no electrolyzer operating) might have been cost effective. The lost distributed utility benefits would need to be traded off with an occasional excessive power drain to get storage pressure back within operating range once the utility's daily peak hour is over.

Another major factor which could make these hydrogen engine or PEM distributed utility units compellingly cost-effective would be even small incentives or green power credits for their operation. A one cent per kWh credit for hydrogen derived output would make DU at a refueling station much more attractive economically. Likewise, a strategy in which the DU plants are not scheduled for dispatch on weekends and during the off-peak season could provide some savings in electrolysis costs.

The hydrogen fueled engine results deserve discussion for two reasons: 1) the engine could be the nearest term technology option, and 2) its cost and performance assumptions depend on different factors than the other electric generation technologies. All of the generation technology

Figure 9. Components of Cost of Hydrogen for 1 hr/day Distributed Utility Cases with Median Benefits (Baseline Electricity Costs: 2¢/kWh off-peak, 7¢/kWh on-peak; Alternative Electricity Costs: 4¢/kWh off-peak, 8¢/kWh on-peak)

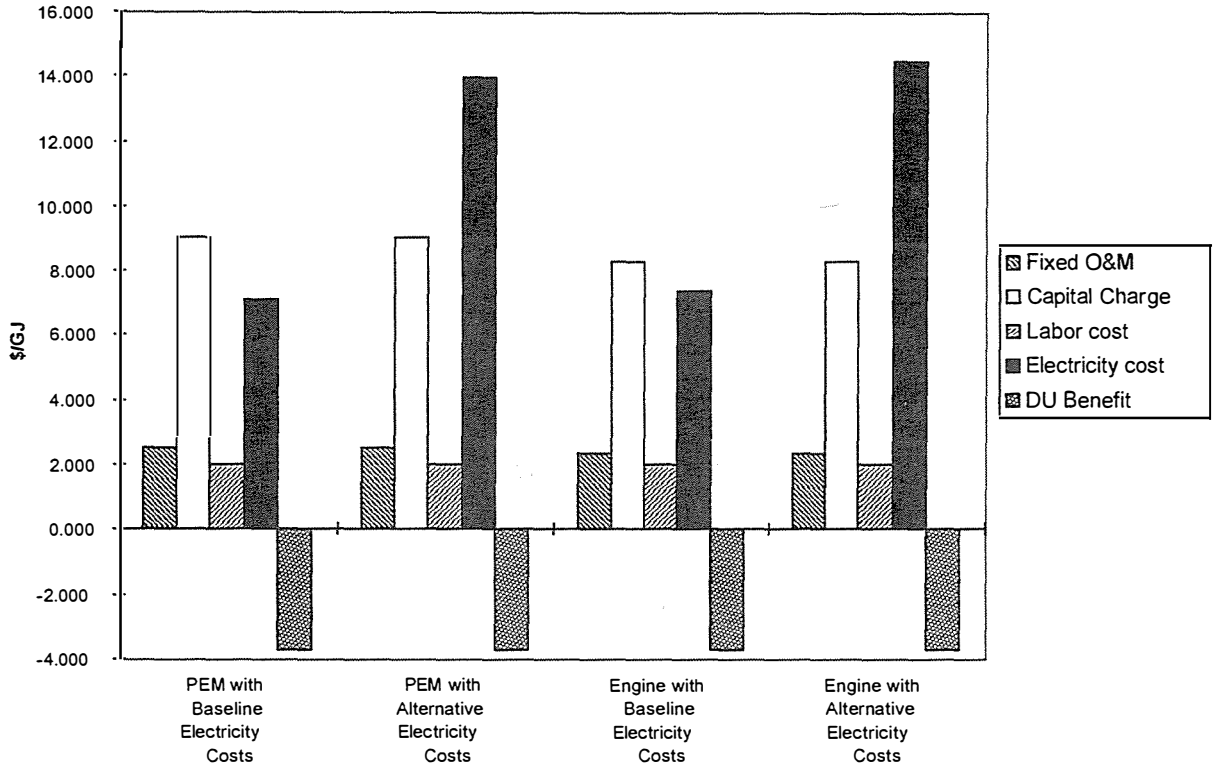

cost and performance estimates used in this study anticipate technical success and mass production levels (for utility or transportation applications). The hydrogen fueled engine costs may be the most sensitive to transportation market mass-production levels. The fuel cells may reach mass production via utility applications at prices higher than the transportation market sector can likely support. However the simplicity of the hydrogen engine approach may be very attractive to the transportation industry. The hydrogen engine distributed utility generator might have looked even more promising if the station had been designed to service vehicles with hydride storage or if hydride storage had been used for the bulk on-site storage.

The future RFC seems to be ideally suited to the distributed utility application at refueling stations. This technology should studied carefully and the economics reexamined as it comes closer to the marketplace.

Utilities should be alerted to the potential for use of hydrogen refueling technologies as assets in their electric systems. As utilities become more familiar with hydrogen as a fuel and with the distributed utility concept in general this option will gain in importance.

The higher electricity cost sensitivity suggests that there might be a preferred operational strategy. A more detailed analysis might consider dispatch of the electrolyzer against real time

of day rates, varying seasonally and daily; more detailed vehicle refueling patterns would need to be included also. The results of such a study might recommend using the electrolyzer only during super-off-peak times, perhaps less than twelve hours per day, when commercial rates can approach 2 cents per kWh. Of course, more electrolyzer capacity would be needed and its capacity factor would diminish, but this might be economically preferred. The analysis of all of these optimum electrolyzer dispatch options was beyond the scope of the study.

Acknowledgments

The authors would like to thank Dr. Joan Ogden of Princeton University for her helpful insights, input and review. Dr. Ogden gave generously of her time and expertise.

The authors appreciate the modeling and computational support of Mr. Peter Sigmund.

The authors also acknowledge useful conversations with Mr. Fred Mitilsky of Lawrence Livermore National Laboratory, Dr. Sandy Thomas of Directed Technologies, Inc., Dr. Jay Keller of Sandia National Laboratories, and Mr. Phil DiPietro of Energetics, Inc.

References

1. Joan M. Ogden, *Hydrogen Energy System Studies*, Monthly report to U. S. Department of Energy, Contract No. DE-FG36-95GO10061, December 1995.
2. J. M. Ogden, E. Dennis, M. Steinbugler, and J. W. Strohbehn, *Hydrogen Energy System Studies*, Final report to the U.S. Department of Energy, Contract No.XR-11265-2, January 18, 1995.
3. C. E. Thomas, *Integrated Analysis of Hydrogen Passenger Vehicle Transportation Pathways*, Activity report to the U.S. Department of Energy, Subcontract No. AXE-6-16685-01, November 6, 1997.
4. Private communication with Fred Mitlisky, Lawrence Livermore National Laboratory, February 1998.
5. Private communication with Jay Keller, Sandia National Laboratories, March 1998.
6. NREL Data Sheet: Engine Generator Sets, June 4, 1997.

HYDROGEN ENERGY SYSTEMS STUDIES

Joan M. Ogden
Margaret Steinbugler
Thomas Kreutz

Center for Energy and Environmental Studies
Princeton University
Princeton, NJ 08544

Abstract

In this progress report (covering the period May 1997-May 1998), we summarize results from ongoing technical and economic assessments of hydrogen energy systems. Generally, the goal of our research is to illuminate possible pathways leading from present hydrogen markets and technologies toward wide scale use of hydrogen as an energy carrier, highlighting important technologies for RD&D. This work is being carried out as part of the systems analysis activity of the US Department of Energy Hydrogen R&D Program.

Over the past year we worked on three projects.

From May 1997-November 1997, we completed an assessment of hydrogen as a fuel for fuel cell vehicles, as compared to methanol and gasoline. (This study began in July 1996 and finished in November 1997).

Two other studies were begun in November 1997 and are scheduled for completion in September 1998.

* We are carrying out an assessment of potential supplies and demands for hydrogen energy in the New York City/New Jersey area. The goal of this study is to provide useful data and suggest possible implementation strategies for the New York City/New Jersey area, as the Hydrogen Program plans demonstrations of hydrogen vehicles and refueling infrastructure.

* We are assessing the implications of CO_2 sequestration for hydrogen energy systems. The goals of this work are a) to understand the implications of CO_2 sequestration for hydrogen energy system design; b) to understand the conditions under which CO_2 sequestration might become economically viable; and c) to understand design issues for future low-CO_2 emitting hydrogen energy systems based on fossil fuels.

Introduction

Summary of Approach/Rationale

Since 1986, researchers at Princeton University's Center for Energy and Environmental Studies have carried out technical and economic assessments of hydrogen energy systems. Our approach has been to assess the entire hydrogen energy system from production through end-use from several perspectives (fuel producer, consumer, society) considering technical performance, economics (e.g. capital cost, delivered hydrogen cost, cost of energy services), infrastructure, environmental and resource issues. The goal of our work is to illuminate possible pathways leading from present hydrogen markets and technologies toward wide scale use of hydrogen as an energy carrier, highlighting important technologies for RD&D. This work has been part of the systems analysis activity of the DOE Hydrogen Program since 1991.

Past Results

In the late 1980s and early 1990s we focussed on the long term potential of hydrogen derived from renewables (solar, wind, biomass). These studies suggested that renewable hydrogen used in energy efficient end-use devices (e.g. fuel cells) could become economically competitive, beginning in the next century. More recently we have explored how a transition to large scale use of hydrogen energy might begin, starting with the use of hydrogen from natural gas.

Over the past few years our focus has been on strategies for producing, distributing and using hydrogen as a fuel for zero emission vehicles. We have looked in detail at various near term options available for providing hydrogen transportation fuel to vehicles (production of hydrogen from natural gas or off-peak power). We have also considered longer term options such as gasification of biomass or MSW and hydrogen from wind or solar. In FY '95 and FY '96 we assessed the potential impact of advances in small scale hydrogen production technologies (steam reforming of natural gas, electrolysis using off-peak power) on the cost of hydrogen transportation fuel. In particular, we assessed the possibilities for low cost, small scale hydrogen production from natural gas. During FY'96 (July 1995-July 1996), we completed a case study of developing a hydrogen refueling infrastructure in Southern California.

In FY'97 and FY'98 (July 1996-November 1997), we studied the prospects for using hydrogen as a fuel for fuel cell vehicles, compared to vehicles witrh onboard reformation of methanol or gasoline. Vehicle performance and cost and refueling infrastructure issues were considered.

In FY'98 (November 1997-present), two new projects were begun:

* an assessment of potential supplies and demands for hydrogen transportation fuel in the New York City/New Jersey area and

* an assessment of the implications of CO2 sequestration for the design of hydrogen energy systems.

Table 1 and the attached bibliography summarize Princeton CEES work related to hydrogen and fuel cells. Studies supported by the USDOE Hydrogen R&D Program are indicated with a star "*".

Table 1. Hydrogen and Fuel Cell Related Research at the Center for Energy and Environmental Studies, Princeton University, 1986-Present (* = USDOE Supported Research) -- see attached Bibliography

YEAR	TOPIC	INVESTIGATORS	REF.S
*1985-1991	Design and economics of solar PV/ electrolytic hydrogen systems	J. Ogden, R. Williams	[1-4]
*1991-1993	Renewable hydrogen energy systems studies	J.Ogden	[4-5]
*1991-present	Assessments of hydrogen fuel cell vehicles	M. Delucchi, M. Steinbugler, J. Ogden, T. Kreutz R. Williams, L. Iwan	[8-11,13-16, 24, 25, 31, 34]
1991-1993	Production of hydrogen and methanol from biomass	E.Larson, R. Katofsky, R. Williams	[6-8]
*1993-present	Production of hydrogen from municipal solid waste	E. Larson, J. Chen, E. Worrell, R. Williams	[14, 17, 29]
*1993-present	Role of natural gas in a transition to hydrogen	J. Ogden, J. Strohbehn, E.Dennis	[12,13,16]
*1993-present	Assessments of fuels for fuel cell vehicles	R. Williams, J. Ogden, E. Larson, R. Katofsky, J. Chen, M. Steinbugler	[14, 14a, 31]
*1993-1994	Assessment of using the existing natural gas transmission and distribution system w/H2	J. Ogden, J. Strohbehn	[12,16]
*1993-1994	Development of refueling infrastructure for hydrogen vehicles	J. Ogden, E. Dennis, K. Montemayor	[12,13,16, 30, 33]
*1993-1995	Assessment of PEM fuels cells for residential cogeneration	M. Steinbugler, J. Ogden, K. Kissock, R. Williams	[16]
*1994-1996	Assessment of small scale methane reformer technologies	J.Ogden	[22, 26]
*1995- present	Studies of CO2 sequestration	R. Williams, J. Ogden, R. Socolow	[28, 36, 37]
*1995-1996	Case study of developing refueling infrastructure for fuel cell vehicles in So. California	J. Ogden, A. Cox, J. White	[21,22,23,27, 30]
*1996-present	Comparison of hydrogen, methanol and gasoline as fuels for fuel cell vehicles	J. Ogden, T. Kreutz, M. Steinbugler	[24, 25, 31, 38]
*1996-present	Models of onboard fuel processors for fuel cell vehicles	T. Kreutz, J. Ogden, S. Kartha	[25, 31, 32]
*1997-present	Case study refueling infrastructure for H2 vehicles in the New York/New Jersey area	J. Ogden	

Notes for Table 1: Bibliography of Hydrogen and Fuel Cell Related Work at Princeton Center for Energy and Environmental Studies

1. J.M. Ogden and R.H. Williams, Solar Hydrogen : Moving Beyond Fossil Fuels, World Resources Institute, Washington DC, October 1989.

2. J.M. Ogden and R.H. Williams, "Electrolytic Hydrogen from Thin Film Solar Cells," International Journal of Hydrogen Energy, v. 15, 1990, p.155.

3. J.M. Ogden, "Cost and Performance Sensitivity Studies for Solar Photovoltaic/Electrolytic Hydrogen Systems," Solar Cells, v. 30, No. 1-4, May 1991, p. 515.

4 J.M. Ogden and J. Nitsch, "Solar Hydrogen," Chapter 22 in T. Johansson, H. Kelly, A.K.N. Reddy and R.H. Williams, Renewable Energy: Fuels and Electricity from Renewable Sources, Island Press, Washington, DC, 1993.

5. J.M. Ogden, Renewable Hydrogen Energy Systems Studies, final report for NREL Contract No. XR-2-11265-1, June 24, 1993.

6. E.D. Larson and R.E. Katofsky, "Production of Methanol and Hydrogen from Biomass," Princeton University, Center for Energy and Environmental Studies Report No. 271 July 1992.

7. Katofsky, R.E., "Production of Fluid Fuels from Biomass," Princeton University, Center for Energy and Environmental Studies Report No. 279, June 1993.

8. M.A. DeLuchi, E.D. Larson and R.H. Williams, "Hydrogen and Methanol from Biomass and its Use in Fuel Cell and Internal Combustion Engine Vehicles," Princeton University, Center for Energy and Environmental Studies Report No. 250, August 1991.

9. J.M. Ogden and M.A. DeLuchi, "Solar Hydrogen Transportation Fuels," Chapter 8, in D. Greene and D. Santini, eds., Proceedings of the Conference on Transportation and Global Climate Change, American Council for an Energy Efficient Economy, Washington, DC, 1993.

9a. Delucchi, M.A. 1992. "Hydrogen Fuel Cell Vehicles," UCD-ITS-RR-92-14, Institute of Transportation Studies, University of California, Davis.

10. M.A. DeLuchi and J.M. Ogden, "Solar Hydrogen Fuel Cell Vehicles," Transportation Research-A, Vol. 27A, No. 3, pp. 255-275.

11. J.M. Ogden, E.D. Larson and M.A. Delucchi, "An Assessment of Renewable Transportation Fuels and Technologies," report to the US Congress Office of Technology Assessment, May 27, 1994.

12. J.M. Ogden, J.W. Strohbehn and E. Dennis, “Hydrogen Energy Systems Studies,” Proceedings of the USDOE Hydrogen Program Review Meeting, April 19, 1994.

13. J.M. Ogden, E. Dennis and J.W. Strohbehn, “A Technical and Economic Assessment of the Role of Natural Gas in a Transition to Hydrogen Transportatio Fuel,” presented at the 10th World Hydrogen Energy Conference, Cocoa Beach, FL, June 21-24, 1994.

14. J.M. Ogden, E.D. Larson, R.H. Williams, R. Katofsky, J. Chen, and M. Steinbugler,"Fuels for Fuel Cell Vehicles," presented at the Vice President's Meeting on Fuel Cell Vehicles, Partnership for a New Generation of Vehicles, Washington DC, July 27, 1994.

14a. R.H. Williams, "Fuel Cells, Their Fuels and the US Automobile," First Annual World Car Conference," University of California at Riverside, Riverside, CA, June 20-24, 1993.

15. M. Steinbugler, and J.M. Ogden, "Design Considerations for Fuel Cell Vehicles," presented at the Fuel Cell Seminar, November 28-December 1, 1994.

16. J.M. Ogden, E. Dennis, M. Steinbugler, and J. Strohbehn, "Hydrogen Energy Systems Studies," Final Report to NREL for Contract No. XR-11265-2, January 18, 1995.

17. J.S. Chen, "The Production of Methanol and Hydrogen from Municipal Solid Waste," Princeton University, Center for Energy and Environmental Studies Report No. 289, March 1995.

18.J.M. Ogden, E. Dennis and K. Montemayor, "Development of Refueling Infrastructure for Hydrogen Vehicles," Proceedings of the 6th National Hydrogen Association Meeting, March 7-9, 1995.

19. J.M. Ogden, E.D. Larson and M.A. Delucchi, "Assessment of Renewable Transportation Fuels and Technologies," Proceedings of the American Solar Energy Society Meeting, Minneapolis, MN, July 17-20, 1995.

20. J.M. Ogden, "Refueling Infrastructure Needs for Fuel Cell Vehicles," presented at the Society of Automotive Engineers Topical Technical Conference on Fuel Cells for Transportation, Alexandria, VA April 1, 1996.

21. J.M. Ogden, "Options for Refueling Hydrogen Vehicles: A Southern California Case Study", presented at the 7th National Hydrogen Association Meeting, Alexandria, VA, April 3, 1996.

22. J.M. Ogden, T.G. Kreutz, M. Steinbugler, A Cox, J. White, "Hydrogen Energy Systems Studies," USDOE Hydrogen R&D Program Review Meeting, Miami, FL, April 29-May 2, 1996.

23. J.M. Ogden, "Development of Refueling Infrastructure for Hydrogen Vehicles," Proceedings of the 11th World Hydrogen Energy Conference, Stuttgart, Germany, June 2 23-28, 1996.

24. M. Steinbugler and J. Ogden, "Fuel Economy and Range Estimates for Fuel Cell Vehicles," '96 Fuel Cell Seminar, Orlando, FL, Nov 17-20, 1996.

25. T. Kreutz, M. Steinbugler and J. Ogden, "Onboard Fuel Reformers for Fuel Cell Vehicles: Equilibrium, Kinetic and System Modelling," 96 Fuel Cell Seminar, Orlando, FL, Nov 17-20, 1996.

26. J. Ogden, T Kreutz, S. Kartha and L. Iwan, " Assessment of Technologies for Producing Hydrogen from Natural Gas at Small Scale," Princeton University Center for Energy and Environmental Studies Draft Report, November 26, 1996.

27. J. Ogden, A Cox and J. White, " Case Study of Developing Hydrogen Refueling Infrastructure in Southern California," Princeton University Center for Energy and Environmental Studies Draft Report, December 9, 1996.

28. R. Williams, "Fuel Decarbonization for Fuel Cell Applications and Sequestration of the Separated CO2," Princeton Center for Energy and Environmental Studies Report No. 295, January 1996.

29. E. Larson, E. Worrell and J. Chen, "Clean Fuels from Municipal Solid Waste for Fuel Cell Buses in Metropolitan Areas," Resources, Conservation and Recycling, v. 17, p. 273-298, 1996.

30. J.M. Ogden, "Infrastructure for Hydrogen Fuel Cell Vehicles: A Southern California Case Study," Proceedings of the '97 World Car Conference, Riverside, CA, January 19-22, 1997.

31. J. Ogden, M. Steinbugler and T. Kreutz, "Hydrogen as a Fuel for Fuel Cell Vehicles," Proceedings of the 8th National Hydrogen Association Meeting, Alexandria, VA, March 11-13, 1997.

32. S. Kartha, S. Fischer and T. Kreutz, "Analysis of Onboard Fuel Procesing Designs for PEM Fuel Cell Vehicles," 96 Fuel Cell Seminar, Orlando, FL, Nov 17-20, 1996.

33. J.M. Ogden, M. Steinbugler, E. Dennis, S. Kartha, L. Iwan, A. Jones, J. Strohbehn, "Hydrogen Energy System Studies," Proceedings of the 1995 US DOE Hydrogen Program Review, vol. 1, April 18-21, 1995, Coral Gables, FL, NREL/CP-430-20036, United States Department of Energy, National Renewable Energy Laboratory, Golden, CO, September 1995.

34. M. Steinbugler, "How Far, How Fast, How Much Fuel: Evaluating Fuel Cell Vehicle Configurations," presented at the Commercializing Fuel Cell Vehicles

Conference, Intertech Conferences, Hyatt Regency O'Hare, Chicago, September 17-19, 1996.

35. J. Ogden, "Prospects for Non-carbon Fuels," presentation to the ASPEN Energy Forum, Aspen Institute, Aspen, CO, July 1997.

36. J. Ogden, "Hydrogen Systems and CO2 Sequestration," DOE Workshop on Fuels Decarbonization and CO2 Sequestration, July 28-30, 1997, Washington, DC.

37. J. Ogden, "Hydrogen Systems and CO2 Sequestration, '' 9th National Hydrogen Association Meeting, Arlington, VA, March 3-5, 1998.

38. J. Ogden, "Refueling Infrastructure," invited panel presentation to the SAE TOPTEC on Fuel Cell Vehicles, March 17-19, 1998, Cambridge, MA.

Table 2. Industrial, Government and Academic Contacts

INDUSTRY

Industrial Gas Suppliers
- Air Products and Chemicals, Praxair
- BOC Gases
- MG Gases

Reformer Manufacturers
- Howe-Baker Engineering
- Hydrochem
- Haldor-Topsoe
- KTI
  - Hydrogen Burner Technology

Electric and Gas Utilities
- Public Service Gas &Elec.,Jersey Central Power &Light, Atlantic Electric Company, Rockland Electric, New Jersey Natural Gas, South Jersey Gas, and Elizabethtown Gas, Consolidated Edison, New York Power Authority, Brooklyn Union Gas, Lilco

Fuel Cell Developers
- Ballard Power Systems
- International Fuel Cells
- Energy Partners
- H-Power

Oil Companies
- Exxon
- Mobil

Electrolysis Manufacturers
- Electrolyser, Inc.
- Teledyne

Automotive Companies
- Ford
- GM
- Chrysler
- Daimler-Benz
- Toyota
- Mazda

Engineering/Research Co.
- Directed Technologies, Inc.
- Arthur D. Little
- Xerox/Clean Air Now Project
- Gas Research Institute
- Glyn Short (consultant)

GOVERNMENT

National Laboratories
- National Renewable Energy Laboratory
- Lawrence Livermore National Laboratories
- Los Alamos National Laboratories
- Argonne National Laboratories
- Sandia National Laboratories
- Oak Ridge National Laboratories

US Department of Energy

South Coast Air Quality Management District

California Air Resources Board

Los Angeles Metropolitan Transit Authority

New Jersey Department of Environmental Protection

New Jersey Department of Transportation

New Jersey Board of Public Utilities, Energy Department

New Jersey Transit

NYSERDA

Northeast Alternative Vebicle Consortium

Federal Highway Administration

ACADEMIC INSTITUTIONS
- University of California at Davis
- University of California at Riverside
- University of Michigan
- TexasA&M
- Humboldt State University
- Georgetown University

Papers on our USDOE sponsored work on hydrogen infrastructure and fuel cell vehicle modeling have been presented to a variety of audiences including invited talks at the Society of Automotive Engineers Topical Technical Conferences on Fuel Cell Vehicles (in April 1996 and March 1998), the 11th World Hydrogen Energy Conference (June 1996), two National Hydrogen Association Meetings (March 1997 and March 1998), the '97 World Car Conference (January 1997), and the Aspen Energy Forum (July 1997). We have presented papers on our work on Hydrogen Energy Systems and CO_2 Sequestration at the DOE Workshop on Fuels Decarbonization and Carbon Sequestration (July 1997), the 9th National Hydrogen Association Meeting (March 1998), and the 12th World Hydrogen Energy Conference (June 1998).

Current Year Results

Overview

Over the past year we worked on three projects, which are described below.

From May 1997-November 1997, we completed an assessment of hydrogen as a fuel for fuel cell vehicles. (This study began in July 1996 and finished in November 1997).

Two other studies were begun in November 1997 and are scheduled for completion in September 1998:

* an assessment of potential supplies and demands for hydrogen energy in the New York City/New Jersey area,

* an assessment of the implications of CO_2 sequestration for the design of hydrogen energy systems.

Cost And Performance Benchmarks For Hydrogen As A Fuel For Fuel Cell Vehicles (July 1996-November 1997)

Since the last DOE Hydrogen Program Review Meeting in May 1997, we completed our technical and economic comparisons of hydrogen, methanol and gasoline as fuels for fuel cell vehicles. A detailed description of the methodology and preliminary results of these studies were reported in the Proceedings of the May 1997 Hydrogen Program Review Meeting (Ogden, Steinbugler, and Kreutz 1997). In this report we summarize the final results of this study.

All fuel cells currently being developed for near term use in vehicles require hydrogen as a fuel. Hydrogen can be stored directly or produced onboard the vehicle by reforming methanol, ethanol or hydrocarbon fuels derived from crude oil (e.g. gasoline, Diesel, middle distillates). The vehicle design is simpler with direct hydrogen storage, but requires developing a more complex refueling infrastructure. Figure 1 shows three alternative configurations for fuel cell vehicles using direct hydrogen storage, onboard steam reforming of methanol and onboard partial oxidation of gasoline.

In this study, we concentrated on a set of related tasks aimed at assessing the potential for using hydrogen directly as a fuel for fuel cell vehicles, as compared to onboard reforming of methanol and gasoline. This work builds on our earlier studies of hydrogen

infrastructure, and extends it to consider alternative fuel cell vehicle designs as well as the refueling system.

The following tasks were completed:

Task 1 . Evaluate the projected performance and cost characteristics of alternative fuel cell vehicles with:

* compressed gas hydrogen storage

* onboard reforming of methanol

* onboard partial oxidation of hydrocarbon fuels derived from crude oil

To estimate the performance of fuel cell vehicles, we employ fuel cell vehicle models developed at Princeton. We also draw on existing vehicle modelling work ongoing as part of the DOE/OTT (DOE/Office of Transportation Technologies) and PNGV (Partnership for a New Generation of Vehicles) programs on fuel cell vehicles, and related studies by other academic groups (UC Davis, U of Michigan, Georgetown U.). Although a considerable amount of modelling work has been done on hydrogen and methanol fuel cell vehicles, there is little published data on vehicles where hydrogen is produced onboard via partial oxidation of hydrocarbon fuels derived from crude oil. We have concentrated on understanding the issues for this alternative.

Task 2. Evaulate the refueling infrastructure requirements for each alternative. As part of this study we consider strategies for building a hydrogen infrastructure, e.g. examine how hydrogen might be introduced for centrally refueled buses and automotive fleets first, eventually moving to public use.

Task 3. Determine the delivered fuel cost for the various fuels including hydrogen from natural gas, coal, solar, wind, biomass or nuclear; methanol from natural gas, biomass or coal; and hydrocarbon fuels such as gasoline or Diesel from crude oil.

Task 4. Calculate the lifecycle cost of transportation for each alternative.

Task 5. Compare the design and economics of hydrogen refueling station options including using small scale onsite steam reforming of natural gas and methanol, POX processing of hydrocarbon fuels and electrolysis. The results of this task are a comparison of designs for hydrogen refueling stations, which might be appropriate for vehicle demonstrations. This builds on previous work at Princeton, as well as work published as part of the PNGV and DOE/OTT programs.

Summary of Results

Task 1: Evaluate the projected performance and cost characteristics of alternative fuel cell vehicles

* Equilibrium, kinetic and heat integrated system (ASPEN) models have been developed to estimate the performance of onboard steam reforming and POX fuel processors for fuel cell vehicles (Kreutz, Steinbugler and Ogden 1996, Ogden, Steinbugler and Kreutz 1997). These results have been incorporated into Princeton's fuel cell vehicle model (Steinbugler 1998, Ogden, Steinbugler and Kreutz 1997, Steinbugler and Ogden 1996, Steinbugler 1996), allowing us to

compare the vehicle performance, fuel economy, weight, and cost for various fuel storage choices and driving cycles. Each vehicle is designed to meet specified performance criteria. The model is described in detail in (Ogden, Steinbugler and Kreutz 1997).

* A range of technical and economic parameters were considered. (Our base case modeling assumptions are given in Table 3.) For the same vehicle performance, we find that hydrogen fuel cell vehicles are simpler in design, lighter weight, more energy efficient and lower cost than those with onboard fuel processors (Table 4).

* A fuel cell vehicle with onboard methanol steam reforming is 10% heavier than one with direct hydrogen storage. A gasoline/POX vehicle is about 20% heavier. The weight contributions of various components (fuel cell, fuel processor, fuel storage, peak battery, etc.) are shown in Figure 2.

* Vehicles with onboard steam reforming of methanol or partial oxidation of gasoline have roughly two thirds the fuel economy of direct hydrogen vehicles. The efficiency is lower because of the conversion losses in the fuel processor (losses in making hydrogen from another fuel), reduced fuel cell performance on reformate, added weight of fuel processor components, and effects of fuel processor response time.

* For mid-size automobiles with PNGV type characteristics (base vehicle weight of 800 kg -- e.g. weight without the power train and fuel storage, aerodynamic drag of 0.20, and rolling resistance of 0.007), fuel economies (on the combined FUDS/FHDS drving cycle) are projected to be about 106 mpeg for hydrogen fuel cell vehicles, 69 mpeg for fuel cell vehicles with onboard methanol steam reforming, and 71 mpeg for onboard gasoline partial oxidation.

* Based on projections for mass produced fuel cell vehicles developed as part of the PNGV program (see Table 5), methanol fuel cell automobiles are projected to cost about $500-600 more than comparable hydrogen fuel cell vehicles. Gasoline/POX fuel cell automobiles are projected to cost $800-1200 more than hydrogen fuel cell vehicles (Figure 3).

Task 2: Evaluate the refueling infrastructure requirements for each alternative

* The cost of developing hydrogen refueling infrastructure based on near term technologies was estimated for various scenarios. We consider the following hydrogen supply options (see Figure 4):

    * hydrogen produced from natural gas in a large, centralized steam reforming plant, and truck delivered as a liquid to refueling stations,

    * hydrogen produced in a large, centralized steam reforming plant, and delivered via small scale hydrogen gas pipeline to refueling stations,

    * hydrogen from chemical industry sources (e.g. excess capacity in ammonia plants, refineries which have recently upgraded their hydrogen production capacity, etc.), with pipeline delivery to a refuelingstation.

Table 3. Parameters Used in Fuel Cell Vehicle Modelling

Vehicle Parameters	
Glider Weight (= vehicle - power train)[a]	800 kg
Drag Coefficient[a]	0.20
Rolling Resistance[b]	0.007
Frontal Area[a]	2.0 m^2
Accessory Load[c]	0.4 kW
Structural Weight Compounding Factor[d]	15%
Fuel Cell System	
Operating pressure	3 atm
Cathode Stoichiometry	2
System weight (including air handling, thermal and water management)[e]	4.0 kg/kW
Fuel Processor Systems	
Methanol Steam Reformer	
Gross efficiency (HHV H2 consumed in fuel cell/HHV MeOH in)	62%
$V_{comp/exp}$	0.067 Volts
Hydrogen utilization[g]	80%
Voltage Penalty for reformate operation[h]	0.06 x current (amp/cm^2)
Weight of system[i]	32 kg+1.1 kg/kW
Response time	5 sec
Reformate Composition	70% H_2, 24% CO_2, 6% N_2
Gasoline POX	
Efficiency (HHV H2 consumed/HHV gasoline in)[j]	69.4%
Hydrogen utilization[g]	80%
Voltage Penalty for reformate operation[h]	0.128 x current (amp/cm^2)
Weight of system[i]	32 kg+1.1 kg/kW
Response time	1 sec
Reformate Composition	42% N_2, 38% H_2, 18% CO_2, 2% CH_4
Peak Power Battery	
Battery type	Spiral wound, thin film, lead-acid
System weight[k]	1.0 kg/kW
Maximum charge rate	30 amps
Nominal state of charge[k]	50%
Energy stored[k]	15 Wh/kg
Motor and Controller	
Overall efficiency[b]	77%
Overall weight[l]	2.0 kg/kW
Fuel Storage	
Hydrogen[d]	5000 psi compressed gas tank total weight 50 kg, 7.5% H2 by weight
Methanol, Gasoline	12 kg tank, 13 gallon capacity total weight 50 kg
Driving schedules	FUDS, FHDS
Regenerative braking recovered up to battery capabilities	

Notes for Table 3

a. Based on PNGV targets. (Source: CALSTART website. http://www.calstart.org/about/pngv/pngv_ta.html)

b. Energy and Environmental Analysis, "Analysis of Fuel Economy Boundary for 2010 and Comparison to Prototypes," p. 4-11, prepared for Martin Marietta Energy Systems, Contract No. 11X-SB0824, November 1990.

c. Ross, M. and W. Wu, "Fuel Economy Analysis for a Hybrid Concept Car Based on a Buffered Fuel-Engine Operating at a Single Point," SAE Paper No. 950958, presented at the SAE Interantional Exposition, Detroit, MI, Feb 27-March 2, 1995.

d. C.E. Thomas and R. Sims, "Overview of Onboard Liquid Fuel Storage and Reforming Systems," "Fueling Aspects of Hydrogen Fuel Cell Powered Vehicles," Society of Automotive Engineers, Proceedings, Fuel Cells for Transportation TOPTEC, April 1-2, 1996, Arlington, VA.

e. Based on a Ballard-type PEM fuel cell system with a stack power density of 1 kg/kW. Other weight is due to auxiliaries for heat and water management equipment and air compression.

f.Arthur D. Little 1994. "Multi-Fuel Reformers for Fuel Cells Used in Transportation, Multi-Fuel Reformers, Phase I Final Report," USDOE Office of Transportation Technologies, Contract No. DE-AC02-92-CE50343-2.

g. This estimate was verified with fuel cell developers.

h. The voltage penalty for operation on reformate is based on models by Shimson Gottesfeld at Los Alamos National Laboratory.

i. William Mitchell, Arthur D. Little, private communications, 1997.

j. Mitchell, W. April 2, 1996. "Development of a Partial Oxidation Reformer for Liquid Fuels," Society of Automotive Engineers, Proceedings, Fuel Cells for Transportation TOPTEC, Arlington, VA.

k. Keating, J., B. Schroeder and R. Nelson 1996. "Development of a Valve-Regulated, Lead/Acid Battery for Power-Assist Hybrid Electric Vehicle Use," Bolder Technologies Corporation, Wheat Ridge, CO.

l. Chang, L. "Recent Developments of Electric Vehicles and Their Propulsion Systems," Proceedings of the 28th Intersociety Engineering Conference, vol. 2, pp. 2.205-2.210, American Chemical Society, 1993.

Table 4.
Model Results:
Comparison of Alternative Fuel Cell Vehicle Designs

Fuel Storage/ H2 Generation System	Vehicle mass (kg)	Peak Power (kW) (FC/Battry)	FUDS mpeg	FHDS mpeg	Combined 55% FUDS 45% FHDS mpeg	range (mi)
Direct H2	1170	77.5 (34.4/43.1)	100	115	106	425
Methanol Steam Reformer	1287	83.7 (37.0/46.7)	62	79	69	460
Gasoline POX	1395	89.4 (39.4/50.0)	65	80	71	940

For the assumptions in Table 3.

Table 5. Cost Estimates for Mass Produced Fuel Cell Vehicle Components

Component	High estimate	Low estimate
Fuel cell system[a]	$100/kW	$50/kW
Fuel processor system [b]	$25/kW	$15/kW
Hydrogen storage cylinder rated at 5000 psia[c]	$1000	$500
Motor and controller[d]	$26/kW	$13/kW
Peak power battery[e]	$20/kW	$10/kW
Extra structural support	$1/kg	$1/kg
Cost of 12 kg gasoline or methanol tank	$100	$100

Notes for Table 5

a. Based on a range of estimates found in the literature. For example, GM/Allison projects a fuel cell "electrochemical engine" cost of $3899 for a 60 kW system including the fuel cell, fuel processor (methanol reformer), heat and water management. This is about $65/kW (at the rated power of 60 kW) or $46/kWpeak. About 45% of the cost per peak kW ($21/kW) is for the fuel cell stack, 28% ($13/kW) for the methanol reformer and the rest for auxiliaries. This cost assumes large scale mass production. (Allison Gas Turbine Division of General Motors December 16, 1992).

Mark Delucchi of Institute of Transportation Studies at UC Davis estimates a retail cost of $2954 for a mass produced 25 kW hydrogen/air PEM fuel cell system or about $120/kW. (The manufacturing cost is $59/kW, with a materials costs for the fuel cell stack plus auxiliaries estimated to be $41/kW, and the labor cost $18/kW.) (J. M. Ogden, E.D. Larson and M.A. Delucchi May 1994).

A study by Directed Technologies for the USDOE estimated a cost in mass production of $2712 for a hydrogen/air fuel cell plus auxiliaries with net output of 85 kW power (about $32/kW). Directed Technologies is now working with Ford Motor Company on fuel cell vehicles as part of the PNGV program. (Ref: B.D. James, G.N. Baum and I.F. Kuhn, Directed Technologies, Inc. "Technology Development Goals for Automotive Fuel Cell Power Systems," prepared for the Electrochemical Technology Division, Argonne National Laboratory, Contract No. W-31-109-Eng-28, February 1994.)

Chrysler estimates that even with current fuel cell manufacturing technology, mass produced costs would be $200/kW (Chris Boroni-Bird, private communications 1997).

b. W. Mitchell, J. Thijssen, J.M. Bentley, "Development of a Catalytic Partial Oxiidation Ethanol Reformer for Fuel Cell Applications," Society of Automotive Engineers, Paper No. 9527611, 1995.

c. C.E. Thomas and R. Sims, "Overview of Onboard Liquid Fuel Storage and Reforming Systems," "Fueling Aspects of Hydrogen Fuel Cell Powered Vehicles," Society of Automotive Engineers, Proceedings, Fuel Cells for Transportation TOPTEC, April 1-2, 1996, Arlington, VA.

d. Derived from estimates in B. James, G. Baum, I. Kuhn, "Development Goals for Automotive Fuel Cell Power Systems," ANL-94/44, August 1994.

e. Based on PNGV goals

  - * hydrogen produced at the refueling station via small scale steam reforming of natural gas, (in either a conventional steam reformer or an advanced steam reformer of the type developed as part of fuel cell cogeneration systems)

  - * hydrogen produced via small scale electrolysis at the refueling station.

* We find that the capital cost of hydrogen infrastructure would be about $400-800/car depending on the type of hydrogen supply. [Figure 5 and Tables 6a and 6b summarize the assumed infrastructure capital costs for two levels of infrastructure development: a) early development serving a total vehicle fleet of 17,800 fuel cell cars or 280 fuel cell buses, b) a large scale system serving 1.4 million fuel cell cars.]

* Options for methanol fuel delivery infrastructure are shown in Figure 7. Worldwide there is currently methanol production capacity of about 28 million metric tonnes per year (Table 7). If all the methanol were used for fuel cell cars, about 29 million vehicles could be fueled. Methanol production capacity is not fully utilized at present, suggesting that up to several million fuel cell vehicles could be served worldwide without building new production capacity. Initially, developing a methanol refueling infrastructure for vehicles should entail relatively modest costs per car. Retrofitting gasoline refueling stations and delivery trucks to handle methanol might cost only about $50/car, and the excess capacity in the existing industrial methanol supply system should be adequate to supply fuel to perhaps a few million fuel cell cars worldwide. Once fuel cell cars reached beyond this level, new methanol production capacity would be needed, which we estimate might cost $400-800/car (Tables 8 and 9, Figure 8). No extra costs are assumed for developing gasoline infrastructure.

* Defining "infrastructure" to mean all the equipment (both on and off the vehicle) required to bring hydrogen to the fuel cell, we find that the cost is comparable for hydrogen ($400-800/car for off-vehicle infrastructure), methanol ($500-600/car for onboard fuel processor, plus in the longer term $400-800/car for methanol production capacity) and gasoline POX fuel cell vehicles ($800-1200/car for onboard fuel processor). (See Figure 9.)

* It is likely that hydrogen fuel cells might be introduced first for transit buses, where centralized refueling is the norm, and the cost requirements are less stringent than for automobiles.

Task 3: Determine the delivered fuel cost

* Considering near term options, the delivered cost of hydrogen ftransportation fuel for Southern California conditions is found to be $14-40/GJ depending on the refueling station size and the technology. This is shown in Figure 6.

* The delivered costs of alternative transportation fuels for fuel cells (hydrogen, methanol and gasoline) are shown in Figure 10. We see that the delivered cost of hydrogen is higher on an energy basis than methanol or gasoline. However, because of the hydrogen fuel cell vehicle's higher fuel economy the fuel cost per km is about the same for hydrogen made from natural gas as for gasoline (Figure 11).

Table 6a. Capital Cost for Developing New Hydrogen Delivery and Refueling Station Infrastructure Serving a Total Fleet of 17,800 FCV Cars, Delivering 2 million scf H_2/day (assuming that existing production capacity is used)

	Centralized Production via Steam Reforming of Natural Gas w/LH2 Delivery	Centralized Production via Steam Reforming of Natural Gas w/Pipeline Delivery	Onsite Steam Reforming of Natural Gas: Convention Steam Methane Reformer	Onsite Steam Reforming of Natural Gas: Advanced Steam Methane Reformer	Onsite Advanced Electrolysis Using Off-Peak Power
Centralized Hydrogen Production	0 (assumed that existing capacity is used)	0 (assumed that existing capacity is used)			
Hydrogen Distribution	0 (assumed that existing trucks are used)	10 km pipeline = $6.2 million (at $1 million per mile)			
2 Refueling Stations each serving 654 cars/day	$1.4 million ($0.7 per station)	$3.4 million ($1.7 million per station)	$10.8 million ($5.4 million per station)	$6.8 million ($3.4 million per station)	$11.4 million ($5.7 million per station)
TOTAL	$1.4 million	$9.6 million	$10.8 million	$6.8 million	$11.4 million
infrastruct. cost per car	$79	$539	$607	$382	$640

Adapted from Ogden, Kreutz, Iwan and Kartha 1996.

Table 6b. Capital Cost for Developing New Hydrogen Production, Delivery and Refueling Station Infrastructure Serving a Total Fleet of 1.36 million Fuel Cell Cars, Delivering 153 million scf H_2/day

	Centralized Production via Steam Reforming of Natural Gas w/LH2 Delivery	Centralized Production via Steam Reforming of Natural Gas w/Pipeline Delivery	Onsite Steam Reforming of Natural Gas: Convention Steam Methane Reformer	Onsite Steam Reforming of Natural Gas: Advanced Steam Methane Reformer	Onsite Advanced Electrolysis Using Off-Peak Power
Centralized Hydrogen Production	$100 million for reformer + $ 200 million for liquefier + LH2 storage	$170 million for reformer + H_2 compressor			
Hydrogen Distribution	80 LH2 trucks each with a 3 tonne capacity, each making 2 local deliveries/day = $40 million	600 km pipeline = $380 million (at $1 million per mile)			
153 1 million scf H2/day Refueling Stations each serving 654 cars/day	$104 million ($0.7 million per station)	$260 million ($1.7 million per station)	$830 million ($5.4 million per station)	$516 million ($3.4 million per station)	$870 million $5.7 million per station)
TOTAL	$440 million	$810 million	$830 million	$516 million	$870 million
Infrastructur Cost per Car	$324	$596	$610	$379	$640

Adapted from Ogden, Kreutz, Iwan and Kartha 1996.

Table 7. Methanol Production Capacity 1995[a]

Region	1000 Metric Tonnes/y	EJ/yr (LHV)	Methanol FCV cars fueled (millions)[b]
North America	9550	0.19	9.8
Europe	7280	0.14	7.5
South America	3590	0.07	3.7
Far East and Asia	4680	0.09	4.8
Middle East and Africa	3460	0.07	3.6
WORLD	28,260	0.56	29.0

In 1995 total MeOH demand was 23.4 million metric tonnes or 83% of nameplate production capacity. This suggests that significant numbers (several million?) FCVs could be fueled without having to build new MeOH production capacity

a. CMAI 1995 World Methanol Analysis, p. 25.

b. It is assumed that methanol fuel cell cars have the fuel economy given in Table 4, and are driven 11,000 miles/year.

Table 8. Projected Capital Cost Of Methanol Refueling Infrastructure Development

Item	Cost
Convert Gasoline Refueling Station to Methanol	$5000- 45,000/station[a] (for a station dispensing 1100 gallons MeOH/d)
Methanol Delivery truck	No cost (use existing gasoline trucks)[a] $140,000 (per new 8500 gallon MeOH truck)[a]
Marine Terminal Bulk Storage Tank for Methanol (for a terminal with 1.3 million bbl storage = 20 days storage)	$2.50/bbl (convert gasoline storage)[a] $15/bbl (build new MeOH storage)[a]
Other terminal equipment	$1/bbl[a]
Methanol Overseas Shipping Costs	No capital cost - use existing tankers; trans cost=3-5 cents/gallon[b,c]
Methanol Production Plant (from NG)	$880-1540 million[c] (10,000 metric tonnes/day) $330-570 million[c] (2500 mt/d)

a. DOE/PE-0095P, "Assessment of Costs and Benefits of Flexible and Alternative Fuel Use in the US Transportation Sector," USDOE, Policy, Planning and Analysis, Washington, DC, August 1990. This assumes that the storage capacity holds 20 days worth of fuel.

b. M. Lawrence and J. Kapler, "Natural Gas, Methanol and CNG: Projected Supplies and Costs," presented to "Transportation Fuels in the 1990s and Beyond, A Conference of the Transportation Research Board, Monterey, CA, July 1988.

c. A. Krupnik, M. Walls, M. Tolman, "The Cost Effectiveness and Energy Security Benefits of Methanol Vehicles," Resources for the Future, Discussion Paper QE90-25, September 1990.

Table 9. Capital Cost Of Methanol Infrastructure Per Car

Item	Capital Cost	#Cars Served	Capital Cost per car ($/car)	Capital Cost per car (1995$/car)
Refueling station conversion (1100 gallons/d) (1990$)	$45,000	1244	36	42
Marine Terminal Conversion (1990$)	@$18.5/bbl storage capacity 6500 barrels (minumum)	2.4 cars/bbl of storage capacity 15,400 cars (minimum)	8	9
Tanker Shipping Capacity	No cost (minimum delivery about 3-6 million bbl)	4-16 million cars (if 10-20 deliv/yr)	0	0
New Production Capacity (1988$)	$880-1540 million (10,000 metric tonnes/day) $330-570 million (2500 mt/d)	3.8 million cars 0.94 million cars	230-400 350-600	290-500 440-750

Task 4: Calculate the lifecycle cost of transportation

* The total lifecycle cost of transportation (cents/km) of fuel cell vehicles (counting vehicle capital costs, O&M and fuel) is slightly lower for hydrogen fueled vehicles (assuming the hydrogen is derived from natural gas) than for fuel cell vehicles using methanol or gasoline. This is true because the hydrogen fuel cell vehicles are likely to cost less to buy, and have roughly 50% higher fuel economy than methanol or gasoline fuel cell vehicles. (See Figure 12)

Task 5: Compare the design and economics of hydrogen refueling station options

* As part of our studies, a series of conceptual designs for hydrogen refueling stations were developed. These are summarized in Table 10.

Summary

* Hydrogen is the prefered fuel for fuel cell vehicles, for reasons of vehicle design, cost and efficiency, as well as potential energy supply and environmental benefits. The cost of developing hydrogen refueling infrastructure is comparable to the total cost (on and off the vehicle) for methanol or gasoline fuel cell vehicles. Like CNG or methanol, hydrogen faces the issue of reaching beyond centrally refueled fleet markets. Valuable experience can be gained in the near term by building the refueling systems for centrally refueled hydrogen fuel cell vehicle demonstrations, and investing now in technologies which could play a role in a future hydrogen infrastructure.

Data Sources

To estimate the infrastructure requirements for various fuels, we have used data developed as part of earlier studies of hydrogen refueling systems as well as data published as part of the PNGV and DOE/OTT programs. The emphasis is on studying infrastructure issues in Southern California, a likely site for hydrogen vehicle and refueling infrastructure demonstrations.

The work also involves estimating the cost and performance of alternative fuel cell vehicles. These estimates draw in part on existing published studies of fuel cell vehicle designs by Ford, GM, Chrysler and other PNGV participants. We also use the results of fuel cell vehicle component models developed at Princeton and at DTI. A large number of industry, government and academic sources have provided the data needed for our fuel cell vehicle calculations.

Carrying out conceptual designs of hydrogen energy systems requires a large data base on the performance and cost of hydrogen production, distribution and end-use equipment. A partial list of industrial, government, and academic sources used in the work is contained in Table 2.

Methods Of Analysis

As discussed above, where necessary, engineering models of fuel cell vehicles, fuel processors, and refueling station equipment have been developed.

Table 10. Cost Comparison of Alternative Designs for Gaseous Hydrogen Vehicle Refueling Stations

REFUELING STATION TYPE	STATION CAPACITY SCF H2/DAY (Cars Fueled Per Day)		
	100,000 (80 cars/day)	366,000 (300 cars/day)	1,000,000 (800 cars/day)
1) LH2 Truck Delivery	175,000	307,000	680,000
2) Pipeline H2 Delivery	200,500	620,500	1,681,500
3) Onsite Reforming (Conventional SMR)	1,769,900	3,054,740	5,379,500
4) Onsite reforming (FC SMR)	626,300	1,369,740	3,378,500
5) Onsite Electrolysis from Off-Peak Power: Current Electrolysis Technology	860,500	3,042,500	8,2455,500
6) Onsite Electrolysis from Off-Peak Power: Advanced Electrolysis Technology	608,500	2,132,500	5,745,500

Sources: Ogden et.al 1995, Ogden et.al. 1996)

The levelized cost of hydrogen production, delivered hydrogen cost and lifecycle costs of transportation are estimated using standard microeconomic techniques.

Interaction With Other Groups/Technology Transfer

In this research Princeton has coordinated with Directed Technologies, Inc. (DTI), Lawrence Livermore National Laboratory (LLNL) and other members of the Hydrogen Program Analysis Team to discuss cost and performance issues for hydrogen as a fuel for fuel cell vehicles. It has been particularly useful to compare our results with those from a recent infrastructure study undertaken by DTI for Ford and the Office of Transportation Technology.

This work has also involved interaction with fuel cell manufacturers and with automotive companies (including Ford, Chrysler and GM and their subcontractors) which are considering or planning fuel cell vehicle demonstrations as part of the DOE/OTT and PNGV programs. We have also interacted with groups at Los Alamos National Laboratory, and Argonne National Laboratory who are studying fuel cell vehicle systems, as well as other academic groups (UC Davis, U of Michigan, Georgetown U), fuel providers (Exxon, Mobil, ARCO), and other companies such as Arthur D. Little (ADL). A partial list of groups who have assisted us with useful data and discussions is given in Table 2.

Preliminary Results: Assessment of Potential Supplies and Demands for Hydrogen Energy in The New York City/New Jersey Area (November 1997-present)

The New York City/New Jersey metropolitan area is a possible candidate for "Clean Cluster" type demonstrations of hydrogen energy technologies. Like California, New York City and New Jersey have severe urban air quality problems and are considering the use of zero and low emission vehicles. Unlike California, relatively little analysis has been done looking into the possibilities for hydrogen and fuel cell vehicles.

As part of this year's research, we are carrying out a preliminary study of potential hydrogen demands and supplies in the New York City/New Jersey area, similar to our earlier work in Southern California. This study builds on our previous work on hydrogen infrastructure, and on preliminary studies at CEES on the potential for hydrogen production from muncipal solid waste (Larson, Chen and Worrell 1996.).

In particular, we are addressing the following questions:

Task 1.1. What are potential demands for hydrogen for transportation markets in the New York City/New Jersey area. We consider centrally refueled applications such as urban buses, vans and fleet autos, as well as public automobiles.

Task. 1.2. What are potential demands for hydrogen for transportation markets in the New York City/New Jersey area. considering:

* truck delivered or pipeline delivered merchant hydrogen,

* hydrogen byproduct from chemical plants and refineries,

* onsite hydrogen production from steam reforming of natural gas at small scale,

* electrolytic hydrogen from off-peak power,

* hydrogen from gasification of municipal solid waste.

Task 1.3 What is the production cost and delivered cost of hydrogen transportation fuel from these various sources.

Preliminary Results

Task 1.1: What are potential demands for hydrogen for transportation markets in the New York City/New Jersey area.

* There is a strong impetus to develop low polluting vehicles in the New York City/New Jersey area, which may present opportunities for hydrogen and fuel cell vehicles. Both the New York City metropolitan area and the state of New Jersey are currently non-attainment areas for ozone, carbon monoxide and particulates. New York state has a zero emission vehicle mandate, similar to the California ZEV regulations, and in August 1997 passed legislation offering tax credits for the incremental cost of alternative fueled vehicles and refueling stations, including hydrogen. New York City has undertaken a variety of efforts to introduce alternative vehicles. New York is probably second only to California in its commitment to alternative vehicles. New Jersey has a smaller but active program in alternative fueled vehicles, and a growing awareness of fuel cells and hydrogen, encouraged by the presence of several fuel cell companies, hydrogen suppliers and large scale hydrogen users such as refineries based in the state. New Jersey recently decided to develop a state climate change action plan, and has endorsed a National LEV standard.

* If siginficant numbers of vehicles in New York City or New Jersey were converted to hydrogen, a large hydrogen demand would develop.

    o The current light duty vehicle population in New Jersey is about 5.7 vehicles (including 1.0 million light trucks). The average annual mileage is 10,330 miles/yr, and the average fuel economy is 20.3 mpg. Vehicle miles are projected to increase from their 1995 level of 187 million miles/day to 209 million miles/day in 2010. We assume that the average fuel economy of light duty vehicles can be increased by a factor of four over present levels through a combination of lighter weight, more streamlined design (which could improve fuel economy by perhaps a factor of 1.5) and adoption of fuel cells rather than ICEs (which would increase fuel econony by another factor of 2.5). In this case, we find that the statewide average fuel economy would be 80 mpg equivlent. The hydrogen needed would be about 1000 million scf/day to supply all NJ light duty vehicles in 2010.

    o There are about 5300 buses in New Jersey including commercial and public fleets. Virtually all the buses are centrally refueled. The total energy use by buses in New Jersey in 1990 was estimated to be 5.9 Trillion BTU/yr of Diesel. Assuming that a fuel cell bus would acheive a 50% higher fuel economy than a Diesel, the hydrogen needed to power New Jersey's fuel cell transit buses would be about 33 million H2/day.

- For New York City, the total vehicle miles are estimated to be 19 billion/year for light duty vehicles (or 52 million vehicle miles/day). The energy use is 127 million GJ/yr. Assuming that fuel cell vehicles could improve fuel economy from the current average of 20 mpg to 80 mpg, the corresponding hydrogen use for all NYC light duty vehicles would be about 250 million scf H2/day.

- New York City's 3600 public transit buses log a total of about 90 million bus-miles, requiring perhaps 15 million scf/day of hydrogen, if fuel cell buses were used.

Task 1.2: What are potential hydrogen supplies in the New York City/New Jersey area.

* There are a variety of potential near term hydrogen supplies in the New York City/New Jersey area, which could be used to provide hydrogen transportation fuel. These include truck delivered merchant hydrogen, byproduct hydrogen from refineries and chemical plants, onsite hydrogen production via small scale steam reforming of natural gas, onsite hydrogen production via small scale water electrolysis. In the longer term hydrogen might be produced from large scale steam reforming of natural gas with pipeline distribution or gasification of municipal solid waste.

* Industrial gas companies in the NYC/NJ area generally meet hydrogen demands in the range needed for refueling stations (0.1-2.0 million scf H2/day) via truck delivery of either liquid hydrogen or compressed hydrogen gas. The hydrogen is originally produced at distant Chloralkali plants, and trucked into the area, rather than at nearby large steam methane reformers dedicated to merchant hydrogen production (as in Southern California). There are currently no hydrogen pipelines operating in the New York City/New Jersey area, except perhaps within refineries. The primary industrial gas companies (Air Products and Chemicals, Praxair, BOC Gases, Air Liquide, MG Gases) all serve this area.

* Excess byproduct hydrogen may be available from refineries and chemical plants located in New Jersey. Several large chemical/refinery complexes are found in New Jersey located in: 1) the Newark area, 2) the Philadelphia/Camden area, 3) the area near the Delaware Memorial Bridge at the NJ/DE border, which has both refineries and a Chloralkali plant. Details are still being gathered, but it appears likely that some hydrogen may be available from such sources, totalling perhaps a few million scf/day, enough for a few hundred buses.

* There is a significant amount of off-peak power available in New Jersey (total generation capacity is approximately 18,000 MW, and in theory about one third to half this capacity could be available for off-peak power generation), but the price of off-peak power is presently high, on the order of 7-8 cents/kWh . This may make it difficult for onsite electrolysis to compete as a source of hydrogen. Many analysts believe that the price of off-peak power should eventually go down with deregulation and utility restructuring, although the ultimate price is difficult to predict.

* Onsite production of hydrogen from natural gas in small steam refomers is another possibility. However, the cost of natural gas is moderately high in the

region, as New York and New Jersey are at the "end of the pipeline" bringing gas from the Gulf states. Moreover, there is little excess capacity in the existing natural gas interstate pipelines serving the New Jersey area. In the winter, gas delivery is limited by long distance pipeline capacity (rather than local distribution pipelines). Increasing natural gas supplies to the region (for example, to produce enough hydrogen to meet the demands for a large fleet of vehicles) could be costly if it entailed building new interstate natural gas pipeline capacity. Supplying enough natural gas to make hydrogen for all light vehicles in New Jersey (assuming fuel cell vehicles are used) would increase the natural gas flow into the state by perhaps 25%.

* Gasification of municipal solid waste is an intriguing longer term possibility for hydrogen production in the New York City/New Jersey area. (A system for hydrogen production from MSW gasification has not been commercialized although the component technologies are available) This would also help solve the problem of waste disposal, a serious issue in a region where landfill space is virtually exhausted. Preliminary calculations show that if all the non-recycleable waste streams in New York City were used to make hydrogen for fuel cell vehicles about 44% of New York City's estimated 19 billion light duty vehicle miles could served by this resource alone. Equivalently all of transit buses in New York City could be served by about 16% of the MSW. A similar fraction of LDVs in New Jersey could be served if all New Jersey's municipal solid waste were gasified for hydrogen production. The economics of this approach depend upon the scale of the plant (nominally a MSW to hydrogen plant might produce 25 million scf H2/day, enough for a fleet of perhaps 250,000 fuel cell cars, although smaller plants may be possible), and the tipping fee.

* Because the New York City/New Jersey region has higher energy prices than many regions of the US (electricity prices are among the highest in the nation, and natural gas prices above average), onsite small scale hydrogen production may be more expensive than in regions with lower energy costs.

* Figures 11 and 12 summarize the potential hydrogen supplies and demands in New Jersey. In the near term, refinery excess hydrogen and hydrogen from natural gas would be sufficient to get started. In the longer term gasification of MSW may be an interesting option.

Task 1.3: What is the production cost and delivered cost of hydrogen transportation fuel from these various sources.

* The economics of the various hydrogen supply options will be estimated in future work.

Data Sources

Data on vehicle energy use and alternative vehicles were obtained from the New Jersey Board of Public Utilities Energy Department (NJBPU), the New Jersey Department of Environmental Protection (NJDEP), the New Jersey Department of Transportation (NJDOT), and the NJ Office of Sustainability, the New York Power Authority, NYSERDA, the Northeast Alternative Vehicle Consortium and the Northeast Sustainable Energy Association.

For current energy prices in the area, we have contacted or are contacting the individual electric and gas utilities in the area (Public Service Gas and Electric, GPU/Jersey Central Power &Light, Atlantic Electric Company, Rockland Electric, New Jersey Natural Gas, South Jersey Gas, and Elizabethtown Gas, Consolidated Edison, New York Power Authority, Brooklyn Union Gas, Lilco), and using data from annual reports of the NJBPU.

For an understanding of current merchant hydrogen infrastructure in the area, we contacted Air Products, Praxair, and BOC Gases.

For data on hydrogen production in refineries and other chemical plants (Chloralkali, etc.), we collected data from the industrial gas companies, as well as from oil companies (Mobil and Exxon).

For data on the availability and content of municipal solid waste as a feedstock for hydrogen production, we contacted the New Jersey DEP, the New York Power Authority and the NY Department of Sanitation.

For data on fleet vehicles, and vehicle populations we consulted studies by the NJDOT, the NJBPU, Oak Ridge National Laboratory, the American Automobile Manufacturers' Association, and the Federal Highway Administration.

For estimates of hydrogen production, distribution and refueling systems, we utilized data collected in earlier studies of hydrogen infrastructure.

Methods Of Analysis

Where necessary, engineering models of hydrogen production, distribution and refueling station equipment are being developed or adapted from our earlier work on hydrogen infrastructure.

The levelized cost of hydrogen production, delivered hydrogen cost and lifecycle costs of transportation are estimated using standard microeconomic techniques.

Interaction With Other Groups/Technology Transfer

Understanding the potential demand for hydrogen vehicles in New York City and New Jersey involved interactions with the state and local governmental groups involved in alternative vehicles and energy, and with local gas and electric utilities.

These include the New Jersey Board of Public Utilities Energy Department, the New Jersey Department of Environmental Protection (NJDEP), which is rapidly developing an interest in hydrogen and fuel cells, and the New Jersey Department of Transportation (NJDOT), which is currently sponsoring H-Power's development of small scale fuel cells as battery replacements for highway warning signs. Governor Whitman of New Jersey has issued an order to develop a statewide "Climate Change Action Plan".

We have had several meetings with New Jersey officials involved in assessing the potential of new technologies to reduce greenhouse gas emissions in New Jersey. One of the most active interchanges thusfar has been with the NJ Department of Environmental Protection. We have given a number of briefings to this group, and to others in the newly created NJ Office of Sustainability and in the New Jersey Science and Technology Group on fuel cell vehicles, hydrogen and CO_2 sequestration. There is a growing interest in hydrogen and

fuel cells in New Jersey, that may make it attractive as a potential site for hydrogen vehicle implementation.

Other valuable data were obtained from the New York Power Authority, NYSERDA and the Northeast Alternative Vehicle Consortium.

Preliminary Results: Implications Of CO_2 Sequestration For Hydrogen Energy Systems (November 1997-present)

Recently, it has been proposed that hydrogen could be produced at large scale via steam reforming of natural gas, or gasification of coal or biomass, with low cost separation of CO_2 and permanent sequestration underground, for example in depleted gas wells or in deep aquifers. The basic idea is sketched in Figure 15, showing hydrogen production from hydrocarbon feedstocks, with separation of CO_2 during the process. CO_2 is piped to a site for underground storage. The hydrogen is compressed and transmitted to distant users via high pressure hydrogen pipelines. A hydrogen energy system with sequestration would allow the continued large scale use of fossil fuel resources while greatly reducing CO_2 emissions into the atmosphere. The hydrogen would be separated out of hydrocarbon fuels and the CO_2 secured underground.

While CO_2 sequestration is an active research topic, under investigation by the USDOE (Socolow 1997) and internationally (Herzog 1997), there has been relatively little work done linking this idea to concepts of hydrogen energy systems. Indeed, CO_2 sequestration raises a host of interesting hydrogen systems questions, which we are addressing as part of our work for the Hydrogen R&D Program in FY'98. These include the following.

* What is the cost of hydrogen production with CO_2 sequestration compared to other hydrogen production methods? How does it compare to localized hydrogen production from natural gas and to fuel cycles with no net CO2 emissions (e.g. hydrogen from solar, wind or biomass)? How does the cost vary with demand? What are the potential impacts of new technologies for steam reforming and CO2 separation?

* When would it make sense to start sequestering CO2? In particular, at what scale of hydrogen production could you begin sequestering CO2? How large a demand must be in place before sequestering and long distance hydrogen transmission become attractive? Answering this question involves understanding the economies of scale of hydrogen production, CO2 separation and sequestration, and pipeline transmission.

* What are plausible scenarios for a transition toward a large scale hydrogen energy system with sequestration? Under what conditions will pipeline hydrogen (produced via large scale steam reforming and transmitted long distances via pipeline) compete with locally produced hydrogen (either at the city scale -- in a single city-sized refomer plant) or onsite (e.g. via small scale steam reforming at a hydrogen refueling station)?

To study these questions we are carrying out the following tasks:

Task 2.1: Understand scale economy issues for hydrogen energy systems with sequestration.

Task 2.1a. What are the scale economies of current and developing technologies for steam methane reforming and CO2 separation?

Task 2.1b. What are the scale economies of hydrogen pipeline transmission? Using pipeline transmission models developed at Princeton, we would estimate the cost of hydrogen pipeline transmission as a function of pipeline pressure, flow rate, and pipeline length.

Task 2.1c. What are the scale economies of pipeline transmission and sequestration of CO2? What determines the rate at which CO2 can be injected at the sequestration site?

Task 2.1d. How does the cost of hydrogen with sequestration vary with the energy demand and the distance of the hydrogen plant and sequestration site from the demand?

Task 2.1e. What is the cost of pipeline hydrogen with sequestration, compared to other hydrogen supply options (including "carbon-free" options such as renewable hydrogen), as a function of demand?

Task 2.2. Estimate the conditions under which pipeline hydrogen with sequestration will compete with other options. How large must the demand be? How close must the hydrogen production be to the demand? What are the potential impacts of new steam reforming technologies?

Task 2.3. Sketch possible scenarios for a transition toward a large scale hydrogen energy system employing CO2 sequestration.

Example: Understanding scale economy issues for natural gas-based hydrogen energy systems with CO_2 sequestration.

As an example, we consider a system with hydrogen production from natural gas and sequestration of CO_2. As shown in Figure 16 there are a number of options for delivering hydrogen to users, and for capturing CO_2. Key questions are

* "where do you make the hydrogen?" (hydrogen can be made at small scale at the user's site; at city scale with local distribution; or at large scale near the source of natural gas with long distance hydrogen pipeline transmission.)

and

* "where do you capture the CO_2?" (In theory CO_2 could be captured at small scale and collected, or captured at city scale and piped some distance to a sequestration site, or captured at a hydrogen production facility at the natural gas field and re-injected into gas wells).

The answers to these questions depend on scale economies in:

* hydrogen production,

* CO_2 separation,

* pipeline transmission of hydrogen, natural gas and CO_2,

* CO_2 injection at the sequestration site

To size the various components in the system, we first must understand the potential hydrogen demand and associated CO_2 production. Table 11 shows hydrogen flows needed to supply various end-use demands. Projected hydrogen demand varies over a wide range from 0.04 GJ/day for a single fuel cell car to 0.3 million GJ/day if all the cars in the Los Angeles Basin converted to hydrogen fuel cells to 3 million GJ/day to equal the energy in the current natural gas flow in the Southern Califormia Gas system.

The specific capital cost ($ per kW of hydrogen output) for various hydrogen production systems is shown as a function of plant size (in GJ/day) in Figure 17. Conventional steam methane reformer technology is shown, as well as advanced small scale reformers based on fuel cell reformer technology. Estimates for the mass produced capital cost of advanced small scale "fuel cell type" reformers are shown for various levels of cumulative production (1 unit up to 10,000 units), based on recent studies by Directed Technologies, Inc. (Thomas et.al. 1997). We see that the capital cost of small scale steam methane reformers could be significantly reduced with advanced technology.

However, the production cost of hydrogen would still be less for centralized production than for decentralized small scale production, because the feedstock cost will be less at a large central hydrogen plant. As shown in Figure 18, feedstock costs dominate the total cost of hydrogen production.

Of course, centrally produced hydrogen must be distributed to users, which adds distribution costs. The cost of small scale, local gaseous pipeline transmission is shown in Figure 19 as a function of pipeline length and number of fuel cell vehicles served. Costs are lowest for large flow rates and short pipelines (e.g. large, geographically concentrated hydrogen demands). The delivered cost of hydrogen transportation fuel is shown in Figure 20 including hydrogen production, local pipeline distribution (for centralized production) and refueling stations. We see that decentralized production with advanced reformers can compete with centralized pipeline production, because of pipeline distribution costs. As demand increases, the cost of pipeline transmission is reduced, and approaches that of decentralized production.

Let us now assume that we want to sequester CO_2. In this case centralized production will always be less costly because of the high cost of capturing and collecting CO_2 from many small dispersed sources. This is shown in Figure 21. But centralized production implies that a large demand has built up for hydrogen. Thus, sequestration may not be introduced until a large demand for hydrogen is in place.

Long distance pipeline transmission costs

Once hydrogen is produced and CO_2 separated, the CO_2 must be piped to a sequestration site. To understand the trade-offs in transmitting hydrogen and/or CO_2 long distances, we are developing engineering and economic models of pipeline transmission for hydrogen, methane and CO_2.

The cost of CO_2 transmission 250 km as a function of associated hydrogen production is shown in Table 12 and Figure 22. We see that for large scale energy systems, CO_2 pipeline costs add very little to the cost of producing hydrogen. At production scales of 0.2-8 million GJ of hydrogen/day, a CO_2 pipeline adds $0.27-0.04/GJ H2, as compared to hydrogen production costs of $5-8/GJ, depending on the production technology. (For reference, 0.2 million GJ H2/day would fuel half

Table 11. Hydrogen Demand: Scales Of Interest

DEMAND	H2 FLOW (GJ/day)
1 fuel cell car	0.038
1 fuel cell bus	2.7
10 fuel cell buses	27
100 fuel cell buses or 7000 fuel cell cars	270
1% of cars in LA Basin	3420
H2 Production at Large Refinery	36,200
10% of cars in LA Basin	34,200
100% of cars in LA Basin	342,000
Energy Flow = NG Flow in LA Basin	3,000,000

Table 12. Characteristics of 250 km CO_2 Pipelines

Pipeline Diameter (inches)	Flow Rate (million tonnes CO2/y)	Pipeline Capital Cost ($/m)	Trans Cost ($/tonne CO2)	Associated H2 Production (million GJ/d)	Added Cost to Hydrogen ($/GJ)
16	3	650	7.0	0.21	0.27
30	20	1300	2.1	1.4	0.08
40	35	1750	1.6	2.5	0.06
64	110	3300	1.0	7.7	0.04

Costs for CO_2 transmission include compression and pipeline capital and operating costs for a 250 km pipeline. The CO_2 is compressed to 110 bar for transmission as a supercritical fluid. The pressure at end of pipeline is 90 bar.

SOURCE: O. Skovholt, "CO2 Transportation System," Energy Conservation Management, Vol. 34, No. 9-11, pp. 1095-1103, (1993).

Associated hydrogen production is calculated assuming that hydrogen and CO_2 are produced by steam reforming natural gas. According to plant designs from Katofsky 1993, for each kg of hydrogen produced, 5.55 kg of CO_2 are recovered from the PSA. [39 kg of CO_2 are recovered from the PSA for each GJ of hydrogen produced (HHV basis).]

the cars in the Los Angeles Basin, if fuel cells were used, and 8 million GJ H2/day is twice the current total natural gas energy flow in Southern California.Gas Company's distribution system.)

More information on smaller CO_2 pipelines is needed to understand issues for smaller scale hydrogen production with CO_2 sequestration.

The cost of long distance pipeline transmission is shown for hydrogen and natural gas in Figures 23 and 24. Again, at large flow rates the cost contribution to the delivered fuel cost is small, perhaps 10-20% of the delivered hydrogen cost. Methane transmission is roughly 1/3 to 1/2 as costly as hydrogen transmission, for the same energy flow rate.

How do scale economies influence the design of energy systems with CO_2 sequestration?: preliminary insights

To justify putting a centralized hydrogen production plant and local hydrogen distribution pipeline system in place, a large, geographically concentrated hydrogen demand is needed. If you don't want to collect CO_2, and natural gas is plentiful, you may choose to make hydrogen onsite in advanced small scale reformers. If CO_2 sequestration is desired, the economics will always favor centralized hydrogen production, because of the high cost of separating and collecting CO_2 at small scale. The level of hydrogen demand required to implement a hydrogen energy system with CO_2 sequestration is probably something like 10-100% of cars in Los Angeles.

Large CO_2 flows are needed to make long distance transmission attractive. The associated hydrogen production is equal to that in 1 to 10 large refineries (in terms of chemical markets) or enough hydrogen about 10-100% of the cars in the Los Angeles Basin (in terms of energy markets).

Introduction of CO_2 sequestration requires a large hydrogen demand If PEM fuel cells are successfully commercialized for vehicles or combined heat and power, this could provide impetus toward such a market (Williams 1997). In the nearer term (before the build-up of large hydrogen energy markets), one could look for large scale point sources of CO_2 associated with hydrogen production from fossil fuels, which are currently vented, but could be captured at small additional cost and sequestered. Some possibilities are steam methane reformers in oil refineries ("reduced CO_2" gasoline?) or in ammonia manufacture. These may be about the right scale to consider CO_2 sequestration.

Summary of results to date

* Engineering/economic models are being developed of pipeline transmission for hydrogen, methane and CO_2, and hydrogen production with alternative methods of CO_2 separation.

* There are strong scale economies in gaseous pipeline transmission, hydrogen production, CO_2 separation and CO_2 injection which influence the design of a hydrogen energy system with CO_2 sequestration.

* If gases are piped long distances, a large flow rate is required to assure low transmission costs. Because of CO_2 pipeline scale economies, a large flow of CO_2 would be needed to reach low transmission costs, unless sequestration could be done near the site of hydrogen production. Large CO_2 flows imply a large geographically concentrated demand for the co-produced hydrogen would be required, before CO_2 sequestration could be done at low cost. The required

hydrogen energy demand would be equivalent to the fuel required for 10%-100% of the cars in the LA Basin (assuming hydrogen fuel cell cars were used), assuming the CO_2 must be piped 300-1000 km to a sequestration site.

* At large flows, the cost of hydrogen pipeline transmission is small, less than 10% (20%) of the cost of hydrogen production over a distance of 300 km (1000 km). The added cost of long distance CO2 transmission is less than 5% of the hydrogen production cost for very large flow rates (e.g. for an energy system which could serve half the cars in LA).

* It is not economically or technically attractive to collect CO_2 from many small dispersed sources. CO_2 sequestration favors large, centralized hydrogen production with local hydrogen pipeline distribution to users.

* Because of advances in small scale methane reformer technologies, it is likely that onsite production of hydrogen from natural gas (for example at refueling stations) will be economically preferable to centralized production with local hydrogen pipeline distribution until a large demand for hydrogen has developed. Once a large hydrogen demand is in place, pipeline distribution may become competitive.

* Initially, demand for hydrogen energy would probably be met by onsite production from natural gas. Once a large demand was present, CO_2 sequestration could be considered. When CO_2 sequestration was implented, a switch to centralized production with local hydrogen distribution would also take place.

* In the near term, large scale industrial production of hydrogen via steam methane reforming (e.g. in oil refineries or chemical plants) might produce enough byproduct CO_2, for CO_2 sequestration to be considered, if a sequestration site is near enough.

Data Sources

Data on CO_2 separation operations during hydrogen production were obtained via discussions with hydrogen producers and industrial gas companies.

Data on various aspects of CO_2 sequestration were also gathered at the USDOE workshop on Fuels Decarbonization and Carbon Sequestration held in Washington DC in July 1997.

Data on hydrogen pipeline systems were available from our earlier studies for the hydrogen program. Data on CO2 pipelines were obtained from the literature and from discussions with researchers at Argonne National Laboratory.

Methods Of Analysis

Engineering models of hydrogen production, CO_2 separation, hydrogen and CO_2 pipeline transmission and hydrogen refueling station equipment are being developed.

The levelized cost of hydrogen production, delivered hydrogen cost and lifecycle costs of transportation are estimated using standard microeconomic techniques.

Interaction With Other Groups/Technology Transfer

We have interacted with other researchers at MIT, Argonne National Laboratory, Air Products and Chemicals, and Mobil and benefitted from discussions with analysts at the USDOE, Directed Technologies Inc. and Energetics.

Plans for Future Work (beyond September 1998)

Assessment Of Hydrogen-Fueled Proton Exchange Membrane Fuel Cells For Distributed Generation And Cogeneration

Motivation And Background

Proton exchange membrane fuel cells (PEMFCs) are highly efficient power generators, achieving up to 50-60% conversion efficiency, even at very small sizes (down to the household level -- 3-5 kW). PEMFCs have zero pollutant emissions when fueled directly with hydrogen, and near zero emissions when coupled to reformers. These attributes make them potentially attractive for a variety of applications including electric vehicles and distributed generation and cogeneration of heat and power in buildings.

Over the past few years, there have been intense efforts worldwide to develop low-cost PEMFC systems. While the the primary focus has been on vehicle applications, an equally important application may be combined heat and power generation in commercial and residential buildings. The development of inexpensive PEMFC power systems for automotive applications may have powerful implications for the parallel development of analogous systems for residential-scale generation of distributed electric power and heat.

There are several reasons why PEMFCs might become competitive for buildings applications before they appear in vehicles:

1) The cost barrier is lower for PEMFC cogeneration systems than for automotive applications. To compete with internal combustion engines in automobiles, PEMFCs must achieve stringent cost goals of perhaps $50/kW. Recent studies indicate that significant cogeneration markets in commercial buildings could open for PEMFC stack costs of perhaps $300-500/kW (corresponding to complete system costs of $1000-1500/kW) (Arthur D. Little 1995). Residential markets might open at stack costs of $200-400/kW (O'Sullivan 1998).

2) The technical challenges are in many respects less severe for stationary power generation than for vehicles. (Start-up behavior and transient operation is likely to be less of a problem for power generation than for vehicles which are characterized by rapidly varying loads; heat and water management issues should be much easier; weight and volume constraints are less stringent; peak power devices will not be needed; control systems should be simpler; robustness and resistance to mechanical shocks during driving will not be an issue.) In one respect, technical requirements are more demanding for cogeneration applications: a longer operating lifetime (50,000-100,000 hours) would be needed for a stationary power system as compared to perhaps 5000 hours for vehicles.

Recently several initiatives have been launched to develop cogeneration systems based on PEM fuel cells. In 1997, GPU International (an international energy company) and Ballard Power Systems (a world leader in fuel cells) established a new company, Ballard

Generation Systems, to commercialize proton exchange membrane fuel cells for stationary power applications. Ballard's initial focus is on systems in the 250 kW range, a size appropriate for commercial buildings, where the economics of cogeneration can be favorable because of high electricity charges and significant heat loads.

If PEMFCs reach the cost goals set by the PNGV program for automotive fuel cells of $50/kW (PNGV 1997), it is likely that they would become competitive not only in commercial building markets, but for residential heat and power production, as well. In the past year two other companies, Plug Power (Chen 1998) and American Power in collaboration with EPRI (EPRI 1997) have begun development of small scale (e.g. 3-5 kWe) natural gas fueled PEM cogeneration systems, a size suitable for residential applications.

Much of the published work on residential scale PEMFC cogeneration systems has reported progress in building working prototypes which couple small scale methane reformers to PEM fuel cells (Ernst 1997, EPRI 1997). Relatively little analytical work has been done to identify promising PEMFC system configurations for residential cogeneration applications.

The potential role of hydrogen-fueled PEMFCs in future residential cogeneration markets has not been examined. As with vehicle applications, there is likely to be a trade-off between the fuel cell's superior efficiency, better performance, lower system cost and zero emissions on pure hydrogen, versus the convenience of using an existing fuel infrastructure (e.g. using a natural gas reformer close coupled to the fuel cell to provide hydrogen). As with vehicles, it is interesting to ask where the hydrogen should be made for PEMFC residential heat and power production (at the city, neighborhood, or household level).

Proposed Work:

Researchers at Princeton Center for Energy and Environmental Studies will carry out a series of detailed technical and economic assessments with the goal of understanding the prospects for hydrogen fueled PEM fuel cell cogeneration technology for residential applications. We concentrate on hydrogen derived from natural gas, a primary energy source which is widely available today, and is likely to give the lowest hydrogen cost in the near term.

We compare three types of PEM fuel cell cogeneration systems which could provide heat and power to residential users (see Figure 25).

Case 1) a centralized "neighborhood" scale (200-1000 kW) natural gas reformer/PEM fuel cell system which distributes heat (via district heating) and electricity (via wire) to 40-200 residential users. .

Case 2) a centralized "neighborhood" scale natural gas reformer, which produces hydrogen or a hydrogen rich gas for distribution to users. Each house has a small hydrogen fueled (5 kWe) PEM fuel cell providing electricity and heat.

Case 3) individual natural gas reformers coupled to 5 kW PEM fuel cells at each house.

For each case energy storage (in the form of hydrogen storage, hot water storage or electric batteries) could be used to meet time varying energy demands. Connections to the electric

utility system could be made at the household or neighborhood level, allowing dispatch of power.

In the proposed work, engineering and economic models of PEM fuel cell based cogeneration systems will be developed. The potential advantages and disadvantages of each configuration will be investigated in terms of overall energy efficiency, performance, economics (capital cost, delivered cost of electricity and heat), and greenhouse gas emissions. PEMFC cogeneration systems will be compared to other alternatives for production of residential heat and power.

Several tasks are proposed:

Task 1. Develop engineering models of various types of PEM fuel cell cogeneration systems capable of supplying residential heat and power (see Cases 1-3 above). Our existing data base on performance and cost of system components such as PEMFC stacks, small natural gas reformers and power electronics will be updated and extended to include small systems (3-5 kW). Where appropriate engineering models of components such as fuel cell stacks and reformers will be developed, drawing on related work we have done as part of our PEMFC vehicle modeling research. Heat-integrated PEMFC cogeneration system models will be developed using ASPEN software to model steady state performance.

Task 2 Develop component sizing algorithms for various types of PEMFC cogeneration systems, based on the demand profile, energy prices and component performance. We will use typical US residential building heat and electricity demands, and a range of energy prices. Several questions will be addressed. How well can each system match building (or neighborhood) energy demands? How does the level of demand aggregation (neighborhood vs. single house) effect the sizing of the equipment and the need for energy storage? What are the most desirable utility connection strategies?

Task 3 Investigate design trade-offs. What type of reformer technology is prefered? How do scale economies in reformer technologies, energy storage and power conditioning equipment effect the economics of combined heat and power generation? What are the effects of fuel cell operating pressure and temperature on the system design? What are the heat integration opportunities on each system's performance and cost? (For example, in cases 1 and 3 the fuel cell anode exhaust can be utilized to provide heat for the steam reforming reaction to produce hydrogen more efficiently, in case 2, it can be used for extra heating.)

Task 4. Discuss the costs and trade-offs involved in distributing different forms of energy to houses (case 1: electricity and hot water, case 2: hydrogen rich gas, case 3: natural gas).

Task 5. Estimate the cost of electricity and heat from PEM fuel cells, as compared to other technologies available for cogeneration and distributed generation.

Task 6. Estimate the potential greenhouse gas emissions reductions possible with residential PEMFC fuel cells as compared to competing technologies.

Task 7. Discuss the role of distributed benefits and emissions benefits in the economic competitiveness of fuel cells. Discuss the required component cost and performance goals for small scale PEMFC cogeneration systems to compete

economically with alternatives. (This task will be performed in coordination with researchers at Distributed Utilities Associates.)

Acknowledgments

The systems studies reported here were performed with support from U.S. Department of Energy Hydrogen R&D Program, under contract No. DE-FG36-95G010061.

For useful conversations, the author would like to thank Jeff Bentley (Arthur D. Little), Adam Cox (Princeton University), Paul Farris (IFC), Shimson Gottesfeld (Los Alamos National Laboratory), Brian James (Directed Technologies, Inc.), Joe Iannucci (Distributed Utilities Associates), Sivan Kartha (Princeton University), Ryan Katofsky (Arthur D. Little), Michael Kerr (Praxair), Ira Kuhn (Directed Technologies, Inc.), Paul Kydd (BOC), Christian Lenci (Praxair), Frank Lomax (Directed Technologies, Inc.), Robert Miller (Air Products and Chemicals, Inc.), William Mitchell (Arthur D. Little), David Moard (Hydrogen Burner Technology), Robert Moore (Air Products and Chemicals, Inc.), David Nahmias (National Hydrogen Association), Venki Raman (Air Products and Chemicals, Inc.), Robert Socolow (Princeton University), Sandy Thomas (Directed Technologies, Inc.), Jason White (Princeton University) and Robert Williams (Princeton University).

References

Allison Gas Turbine Division of General Motors December 16, 1992. Final Report DOE/CH/10435-01, "Research and Development of Proton Exchange Membrane (PEM) Fuel Cell System for Transportation Applications," prepared for the US Department of Energy Office of Transportation Technologies.

Arthur D. Little 1994. "Multi-Fuel Reformers for Fuel Cells Used in Transportation, Assessment of Hydrogen Storage Technologies, Phase I Final Report," USDOE Office of Transportation Technologies, Contract No. DE-AC02-92-CE50343-1.

Arthur D. Little 1994. "Multi-Fuel Reformers for Fuel Cells Used in Transportation, Multi-Fuel Reformers, Phase I Final Report," USDOE Office of Transportation Technologies, Contract No. DE-AC02-92-CE50343-2.

Arthur D, Little, "Fuel Cells for Building Cogeneration Applications - Cost/Performance Requirements and Markets," Final Report, to the Building Equipment Division, Office of Building Technologies, U.S. Department of Energy, Contract No. DE-AC01-89-CE23821, January 1995.

Chang, L. 1993. "Recent Developments of Electric Vehicles and Their Propulsion Systems," Proceedings of the 28th Intersociety Engineering Conference, vol. 2, pp. 2.205-2.210, American Chemical Society.

Chen, J., Plug Power, personal communication, February 26, 1998.

Delucchi, M.A. 1992. "Hydrogen Fuel Cell Vehicles," UCD-ITS-RR-92-14, Institute of Transportation Studies, University of California, Davis.

Dennis, E.B. May 1994. "Design and Feasibility of a Gaseous Hydrogen Refueling Station Based on Small Scale Steam Reforming of Natural Gas," Princeton University senior thesis, Department of Chemical Engineering.

Ernst, W. D., "Plug Power Fuel Cell Development Program", Proceedings of the Annual Automotive Technology Development Customer's Coordination Meeting, DOE-OTT, Dearborn, MI, October 27-30, 1997.

EPRI, "American Power Corp and EPRI Form Collaborative Alliance to Field Test Fuel Cells for Powering Homes and Businesses", Electric Power Research Institute press release, December 3, 1997.

Farris, Paul 1996. International Fuel Cells, private communications.

Halvorson, T., R. Victor and P.J. Farris , January 19-22, 1997."Onsite Hydrogen Generator for Vehicle Refueling Application," to appear in Proceedings of the '97 World Car Conference, Riverside, CA.

Herzog, H.J., ed., 1997. "Carbon Dioxide Removal," Proceedings of the Third International Conference on Carbon Dioxide Removal, Cambridge, MA, 9-11 September 1996, Energy Conversion and Management, Vol. 38, Suppl., 689 pp.

Iwan, L. C., Ballard Power Systems, personal communication, March 5, 1998.

James, B., G. Baum and I. Kuhn August 1994. "Technology Development Goals for Automotive Fuel Cell Power Systems," Argonne National Laboratory Report No. ANL-94/44.

Juergens, C. and R.F. Nelson 1995. "A New High-Rate, Fast-Charge, Lead/Acid Battery," Journal of Power Sources, Vol. 53, pp. 201-205.

Keating, J., B. Schroeder and R. Nelson 1996. "Development of a Valve-Regulated, Lead/Acid Battery for Power-Assist Hybrid Electric Vehicle Use," Bolder Technologies Corporation, Wheat Ridge, CO.

Kreutz, T., M. Steinbugler and J. Ogden Nov 17-20, 1996. "Onboard Fuel Reformers for Fuel Cell Vehicles: Equilibrium, Kinetic and System Modelling," Abstracts '96 Fuel Cell Seminar, Orlando, FL.

Kartha, S., S. Fischer and T. Kreutz Nov 17-20, 1996. "Analysis of Onboard Fuel Processing Designs for Fuel Cell Vehicles," 96 Fuel Cell Seminar, Orlando, FL.

E. Larson, E. Worrell and J. Chen, "Clean Fuels from Municipal Solid Waste for Fuel Cell Buses in Metropolitan Areas," Resources, Conservation and Recycling, v. 17, p. 273-298, 1996.

Mitchell, W., J. Thijssen, J.M. Bentley 1995. "Development of a Catalytic Partial Oxiidation Ethanol Reformer for Fuel Cell Applications," Society of Automotive Engineers, Paper No. 9527611.

Mitchell, W. April 2, 1996. "Development of a Partial Oxidation Reformer for Liquid Fuels," Society of Automotive Engineers, Proceedings, Fuel Cells for Transportation TOPTEC, Arlington, VA.

Ogden, J.M., E.D. Larson and M.A. Delucchi May 27, 1994. "An Assessment of Renewable Transportation Fuels and Technologies," report to the US Congress Office of Technology Assessment.

Ogden, J.M., E. Dennis, M. Steinbugler and J. Strohbehn Jan. 18, 1995. "Hydrogen Energy Systems Studies," final report to USDOE for Contract No. XR-11265-2.

Ogden, J.M., E. Dennis and K. Montemayor March 1995. "Development of Refueling Infrastructure for Hydrogen Vehicles," Proceedings of the 6th National Hydrogen Association Meeting, p. 237.

Ogden, J., T. Kreutz, S. Kartha and L. Iwan November 26, 1996. " Assessment of Technologies for Producing Hydrogen from Natural Gas at Small Scale," Princeton University Center for Energy and Environmental Studies Draft Report.

Ogden, J.M. January 19-22, 1997. "Infrastructure for Hydrogen Fuel Cell Vehicles: A Southern California Case Study," to appear in Proceedings of the '97 World Car Conference, Riverside, CA.

Ogden, J.M., A Cox and J. White December 9, 1996." Case Study of Developing Hydrogen Refueling Infrastructure in Southern California," Princeton University Center for Energy and Environmental Studies Draft Report.

J. Ogden, M. Steinbugler and T. Kreutz, "Hydrogen as a Fuel for Fuel Cell Vehicles," Proceedings of the 8th National Hydrogen Association Meeting, Alexandria, VA, March 11-13, 1997.

O'Sullivan, J., Electric Power Research Institute, personal communication, January 19, 1998.

Plichta, E.J. and G. W. Au June 1995. "High Power Evaluation of Thin Metal Foil Lead-Acid Cells," Report No. ARL-TR-431, Army Research Laboratory.

PNGV, "Review of the Research Program of the Partnership for a New Generation of Vehicles, Third Report", National Research Council, National Academy Press, Washington, D. C., 1997.

Ross, M. and W. Wu Feb 27-March 2, 1995. "Fuel Economy Analysis for a Hybrid Concept Car Based on a Buffered Fuel-Engine Operating at a Single Point," SAE Paper No. 950958, presented at the SAE Interantional Exposition, Detroit, MI.

Socolow, R.H., ed., "Fuels Decarbonization and Carbon Sequestration: Report of a Workshop," Princeton University Center for Energy and Environmental Studies Report No. 301, September 1997.

Steinbugler, M. September 17-19, 1996. "How Far, How Fast, How Much Fuel: Evaluating Fuel Cell Vehicle Configurations," presented at the Commercializing Fuel Cell Vehicles Conference, Intertech Conferences, Hyatt Regency O'Hare, Chicago.

Steinbugler , M. and J. Ogden Nov 17-20, 1996. "Fuel Economy and Range Estimates for Fuel Cell Vehicles," '96 Fuel Cell Seminar, Orlando, FL.

Steinbugler, M. 1997. "Modelling of PEM Fuel Cell Vehicles," Ph.D. Thesis (manuscript in preparation), Princeton University Center for Energy and Environmental Studies.

Thomas, C.E. and R. Sims April 1-2, 1996. "Overview of Onboard Liquid Fuel Storage and Reforming Systems," "Fueling Aspects of Hydrogen Fuel Cell Powered Vehicles," Society of Automotive Engineers, Proceedings, Fuel Cells for Transportation TOPTEC, Arlington, VA.

Thomas, C.E. January 19-22, 1997. "Affordable Hydrogen Supply Pathways for Fuel Cell Vehicles," presented at the '97 World Car Conference, Riverside, CA.

Figures

Figure 23,24 . Cost of long distance pipeline transmission for natural gas and hydrogen vs. energy flow rate and pipeline length.

Figure 25. Possible configurations for PEM fuel cell cogeneration in buildings

Figure 1: Possible Fuel Cell Vehicle Configurations

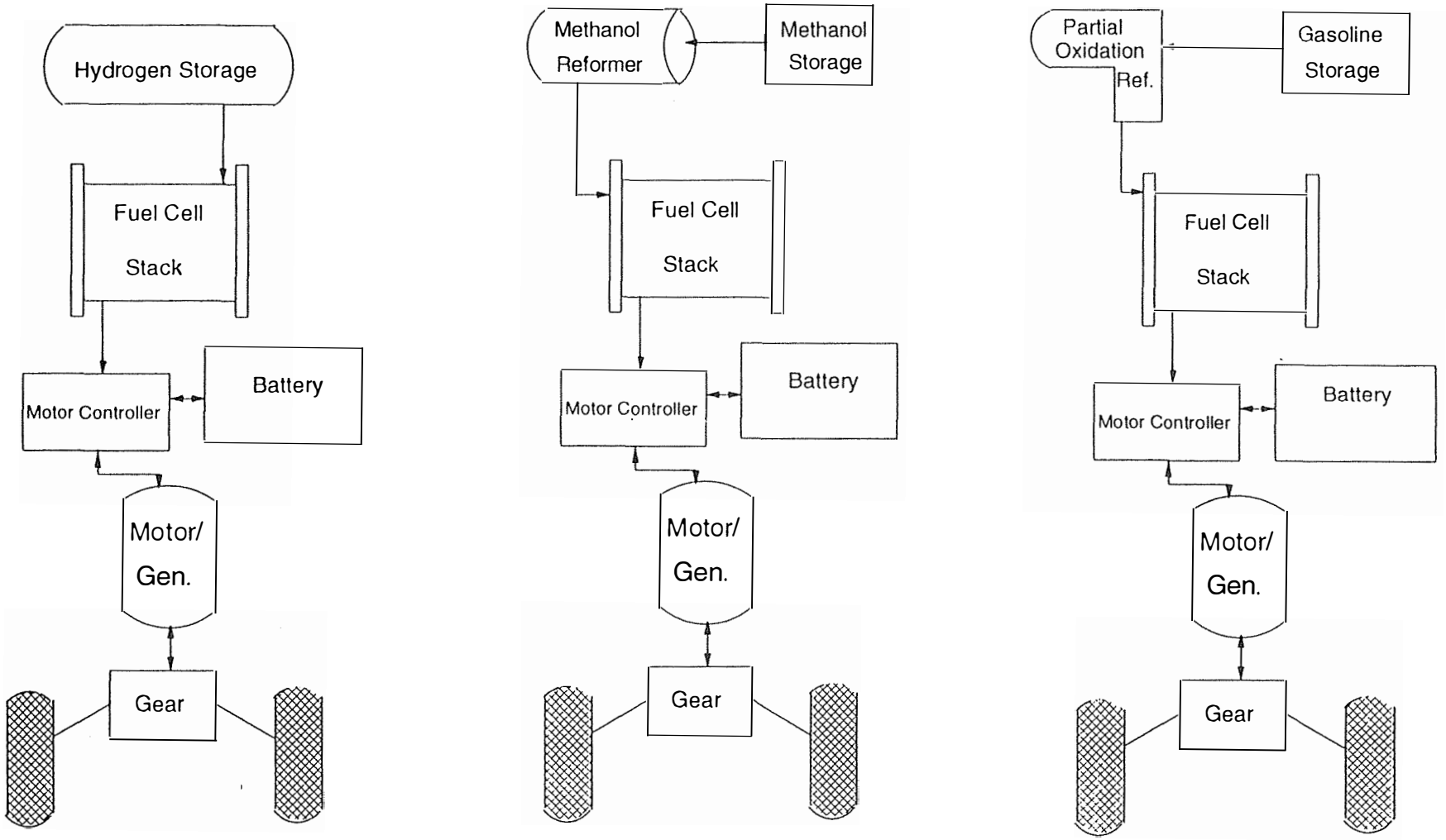

Figure 2. Contributions to Vehicle Weight

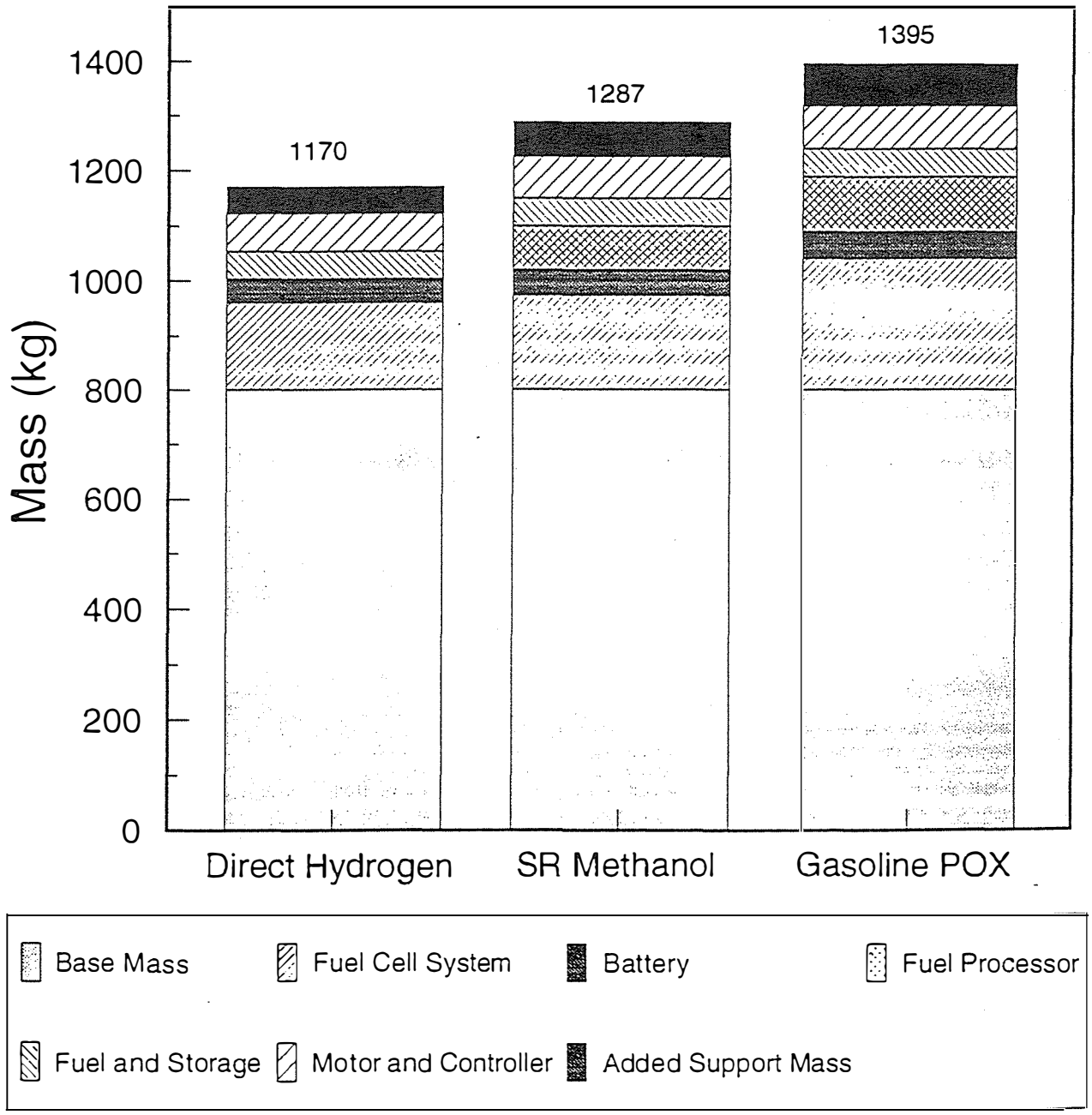

Figure 3. Capital Cost of Fuel Cell Vehicle Drive Train and Fuel Storage Components ($)

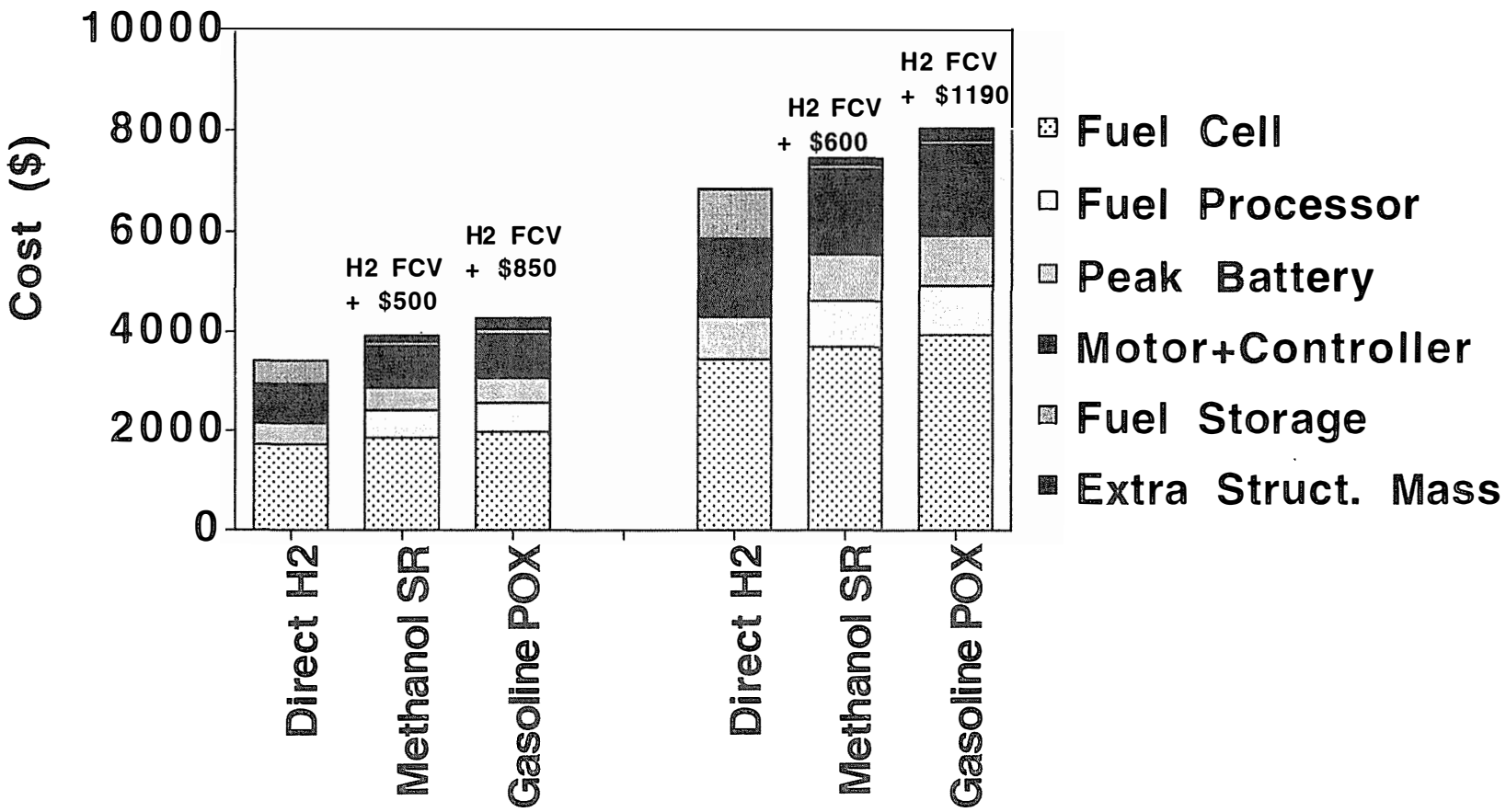

Fuel Cell = $50/kW
Fuel Processor=$15/kW
Peak Battery = $10/kW
H2 Cylinder = $500
Motor+Controller=$13/kW

Fuel Cell = $100/kW
Fuel Processor = $25/kW
Peak Battery = $20/kW
H2 Cylinder = $1000
Motor+Controller=$26/kW

Gasoline or Methanol Tank = $100
Extra Structural Mass = $1/kg

Figure 4. Near Term Gaseous H2 Supply Options

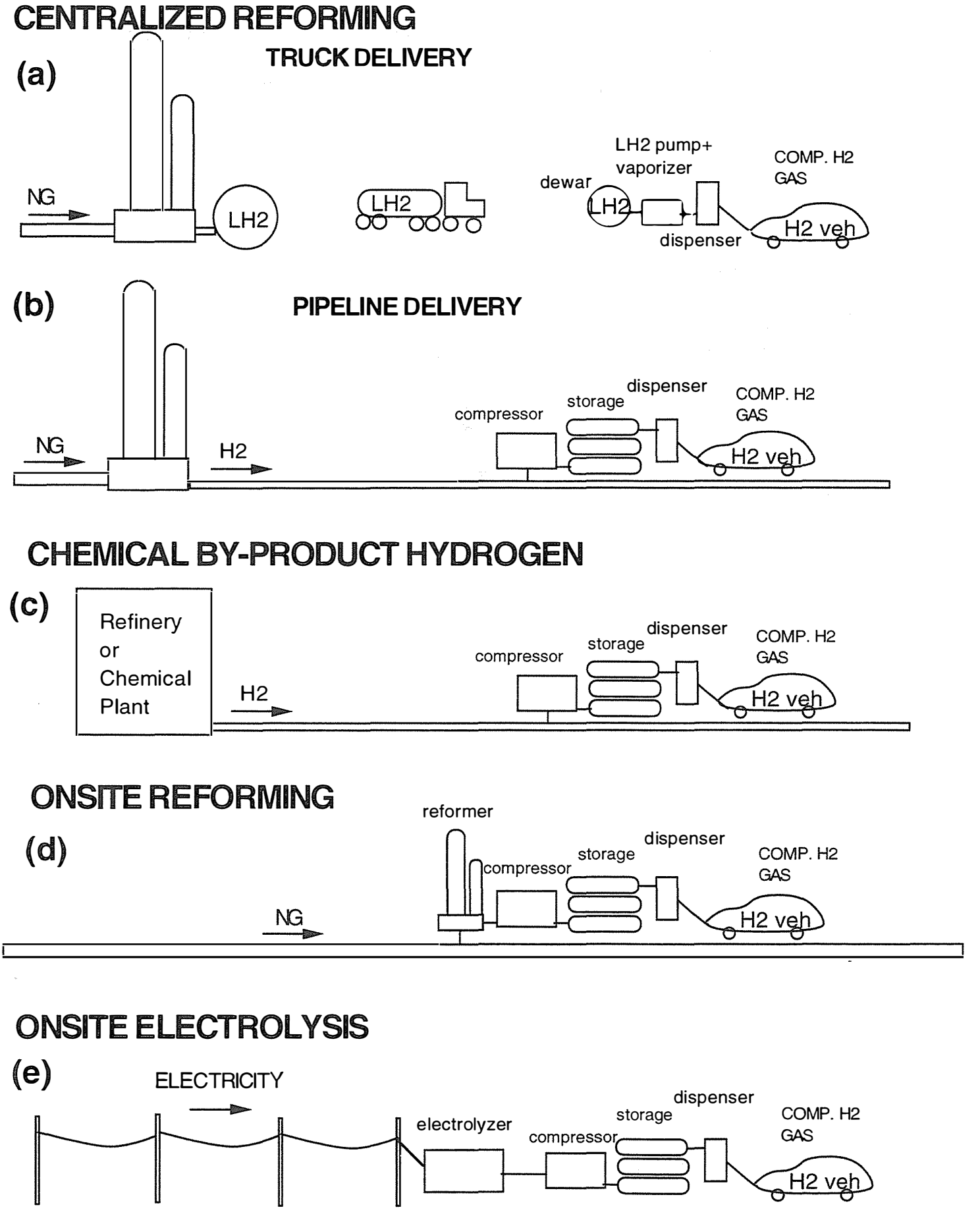

Figure 5. Capital Cost of H2 Refueling Infrastructure ($/car)

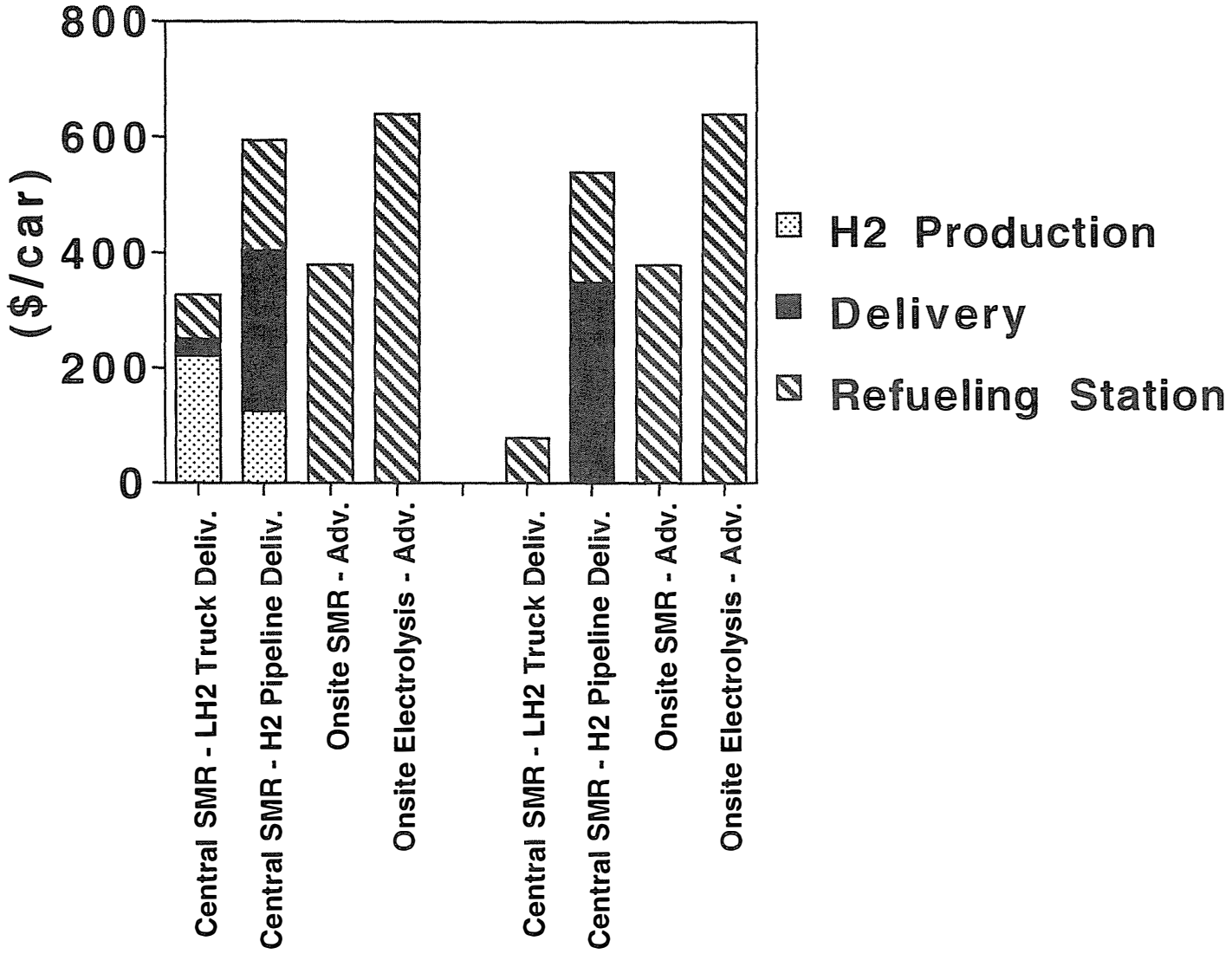

For a refueling system serving a fleet of 1.36 million H2 FCVs. Centralized options have new H2 production capacity

For a refueling system serving a fleet of 17,800 H2 FCV cars. Centralized options use existing H2 production capacity

Figure 6. Delivered Cost of Hydrogen Transportation Fuel ($/GJ)

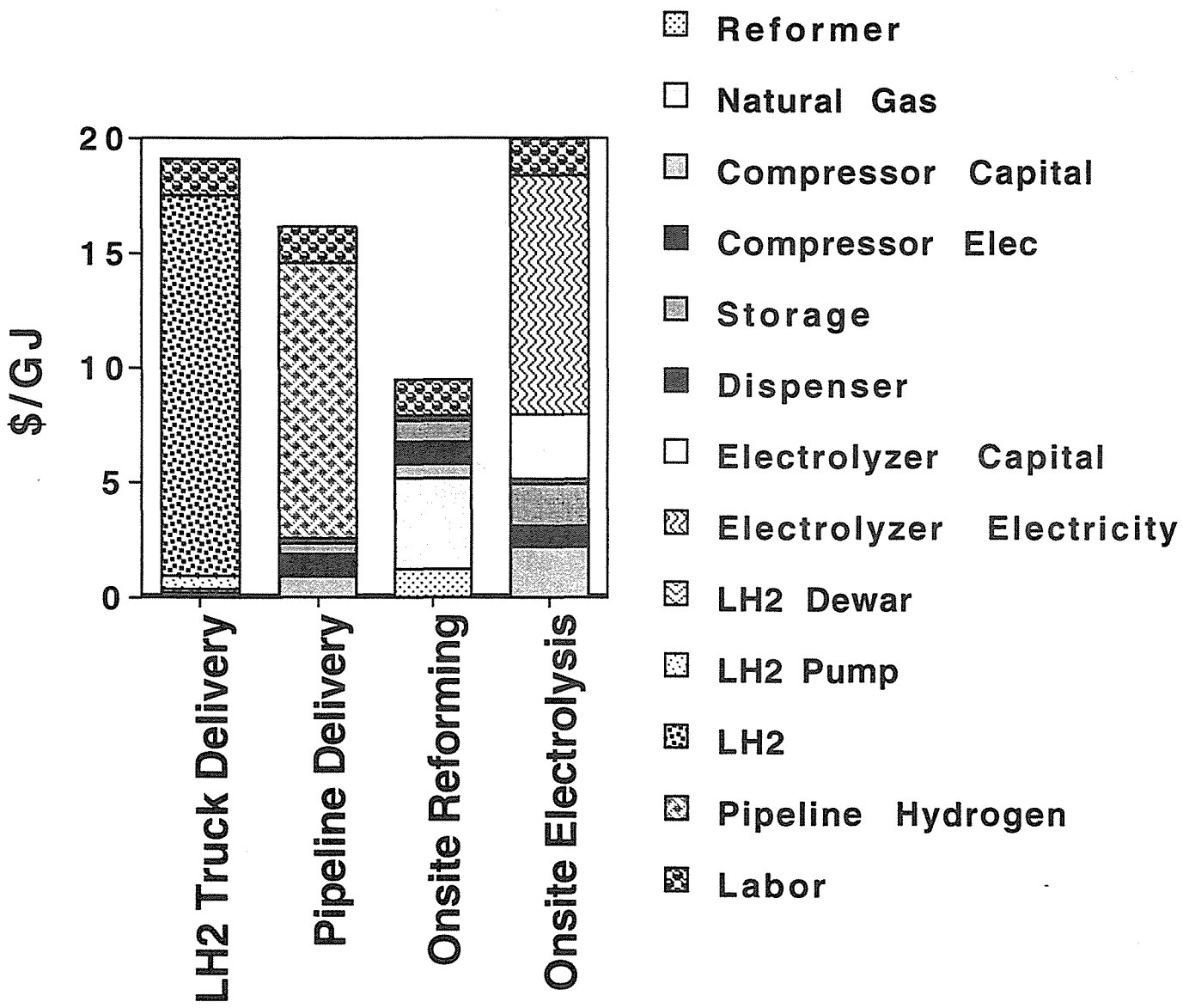

Figure 7. Methanol Supply Options

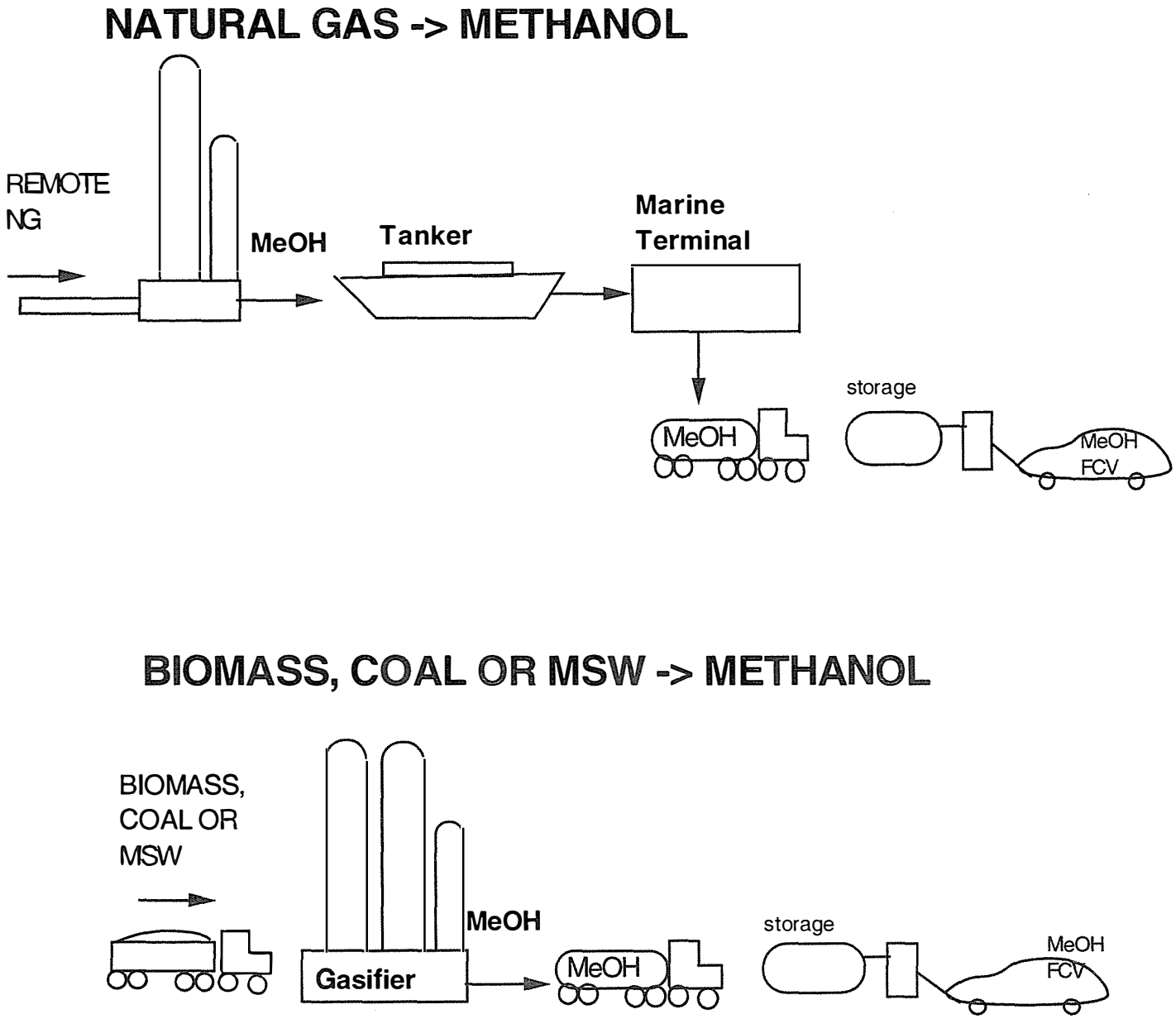

Figure 8. Capital Cost of Methanol Fuel Cell Vehicle Refueling Infrastructure ($/car)

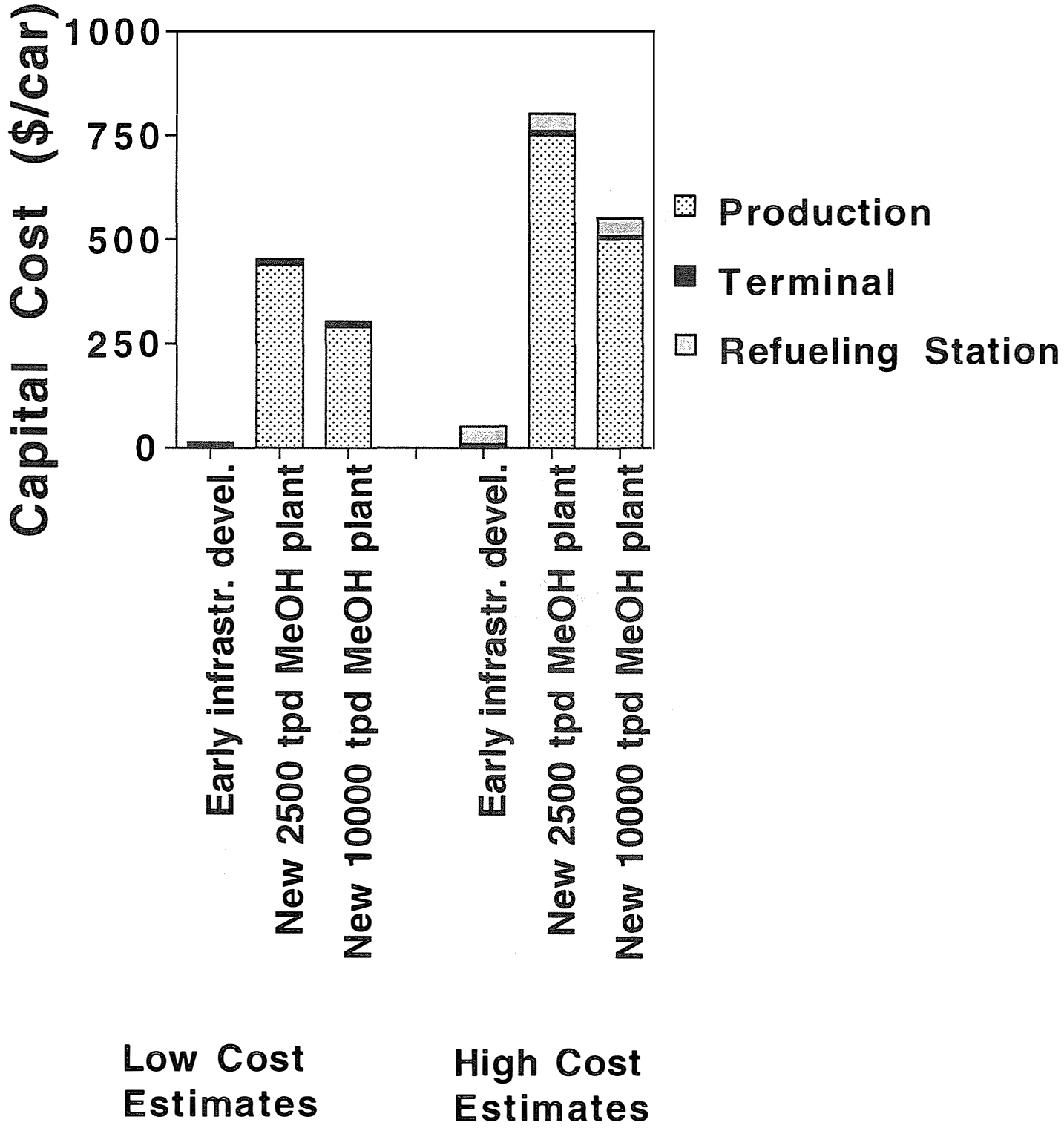

Figure 9. Comparison of Incremental Costs for Vehicles (Compared to H2 Fuel Cell Vehicle) and Refueling Infrastructure (Compared to Gasoline) ($/car)

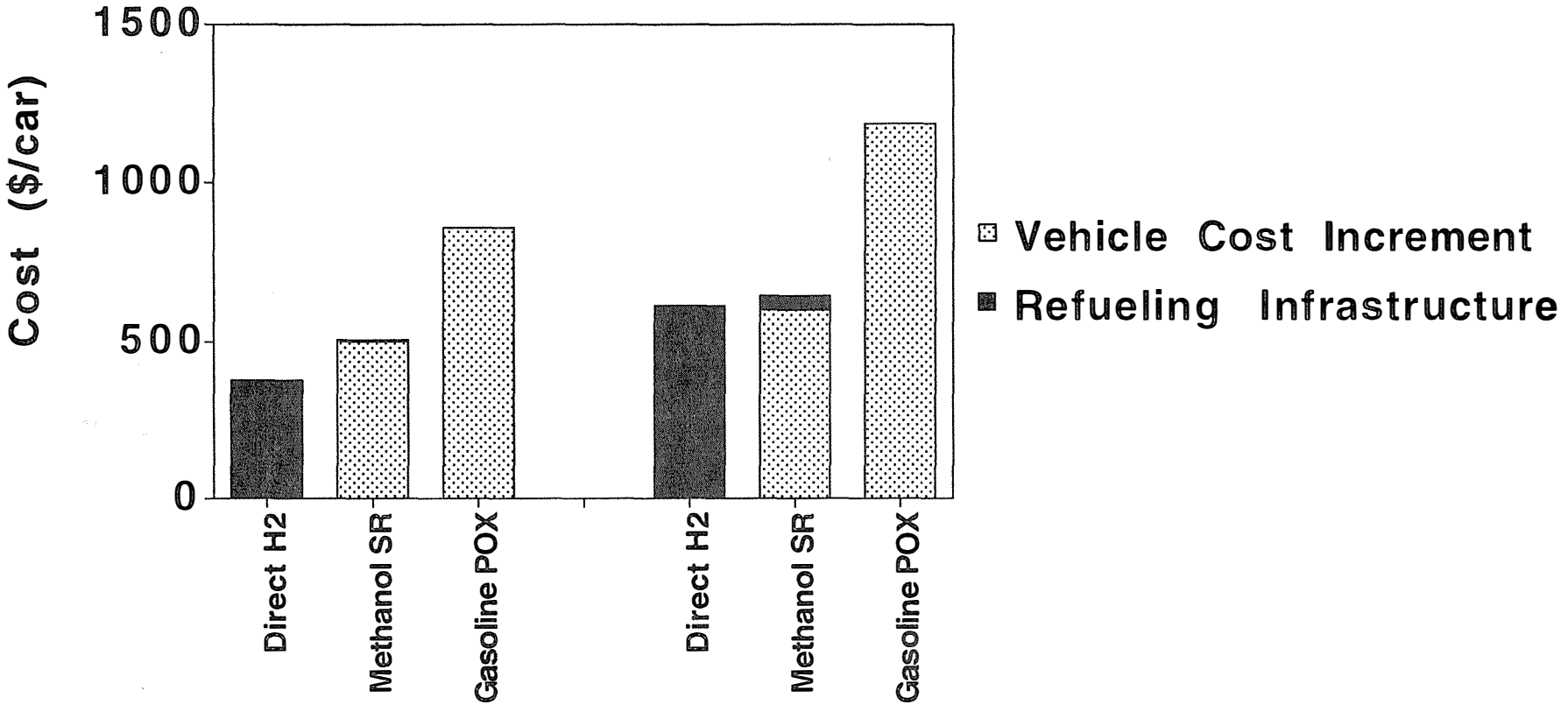

Fuel Cell = $50/kW
Fuel Processor = $15/kW
Peak Battery = $10/kW
H2 Cylinder = $500
Motor+Controller=$13/kW
H2 Infrastructure = $380/car
MeOH Infrastructure=$5/car

Fuel Cell = $100/kW
Fuel Processor = $25/kW
Peak Battery = $20/kW
H2 Cylinder = $1000
Motor+Controller=$26/kW
H2 Infrastructure= $610/car
MeOH Infrastructure=$42/car

Gasoline or Methanol Tank = $100
Extra Structural Mass = $1/kg

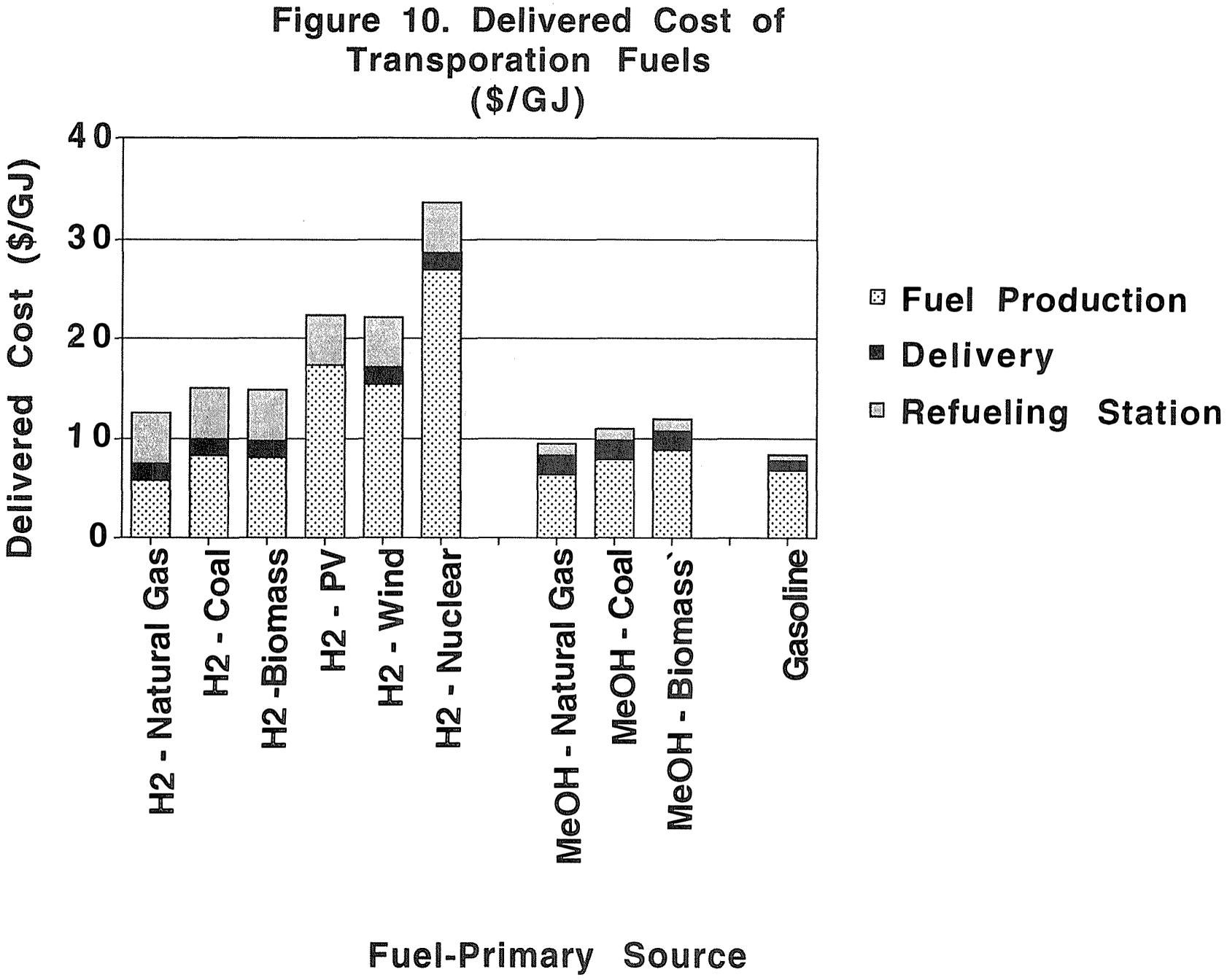
Figure 10. Delivered Cost of Transporation Fuels ($/GJ)
Delivered Cost ($/GJ)
40
30
20
10
0
H2 - Natural Gas
H2 - Coal
H2 -Biomass
H2 - PV
H2 - Wind
H2 - Nuclear
MeOH - Natural Gas
MeOH - Coal
MeOH - Biomass`
Gasoline
Fuel Production
Delivery
Refueling Station
Fuel-Primary Source

Figure 11. Fuel Cost Contribution to Fuel Cell Vehicle Lifecycle Cost ($/km)

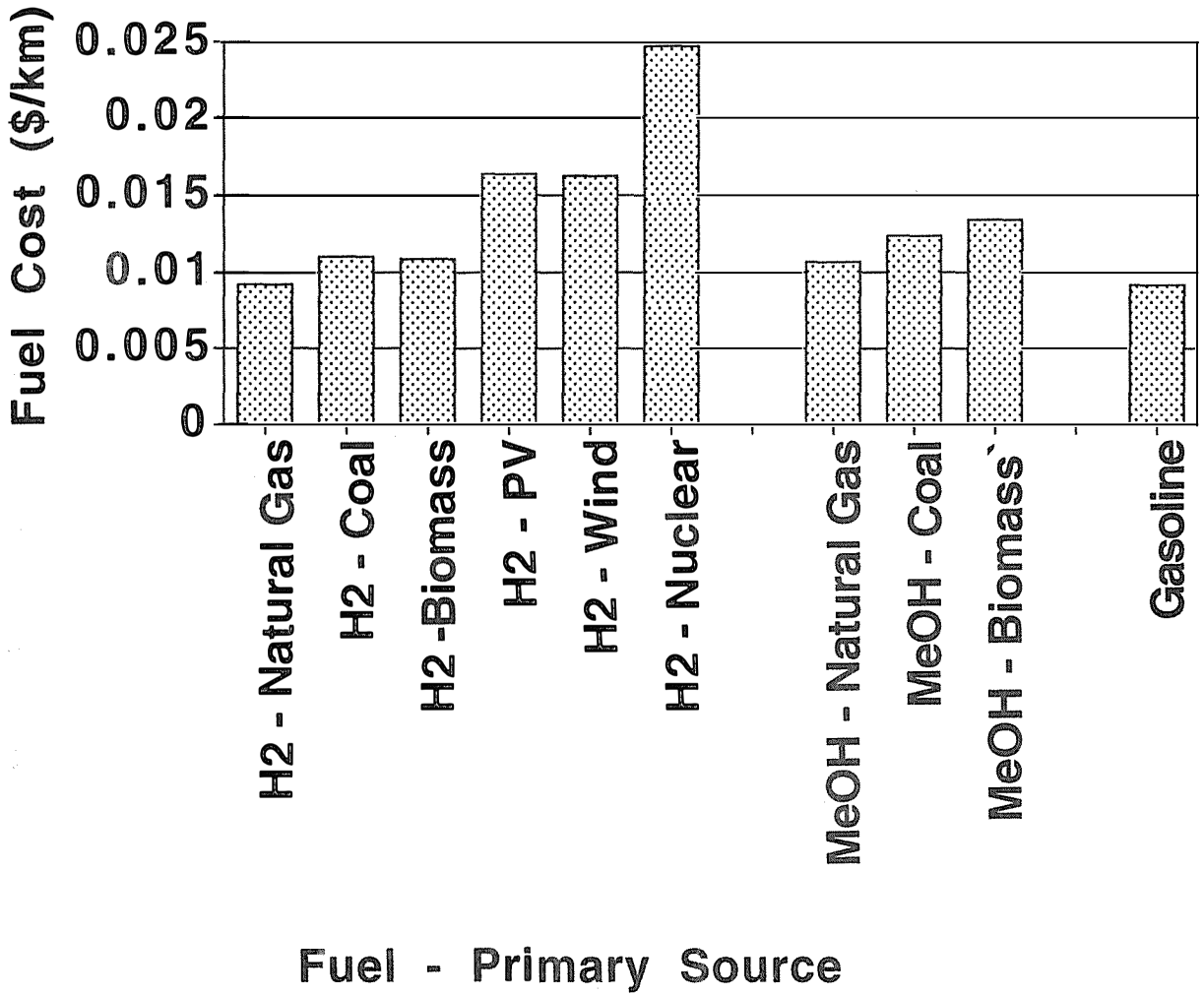

Figure 12. Lifecycle Cost of Transportation for Alternative Fuel Cell Vehicles and Primary Fuel Sources

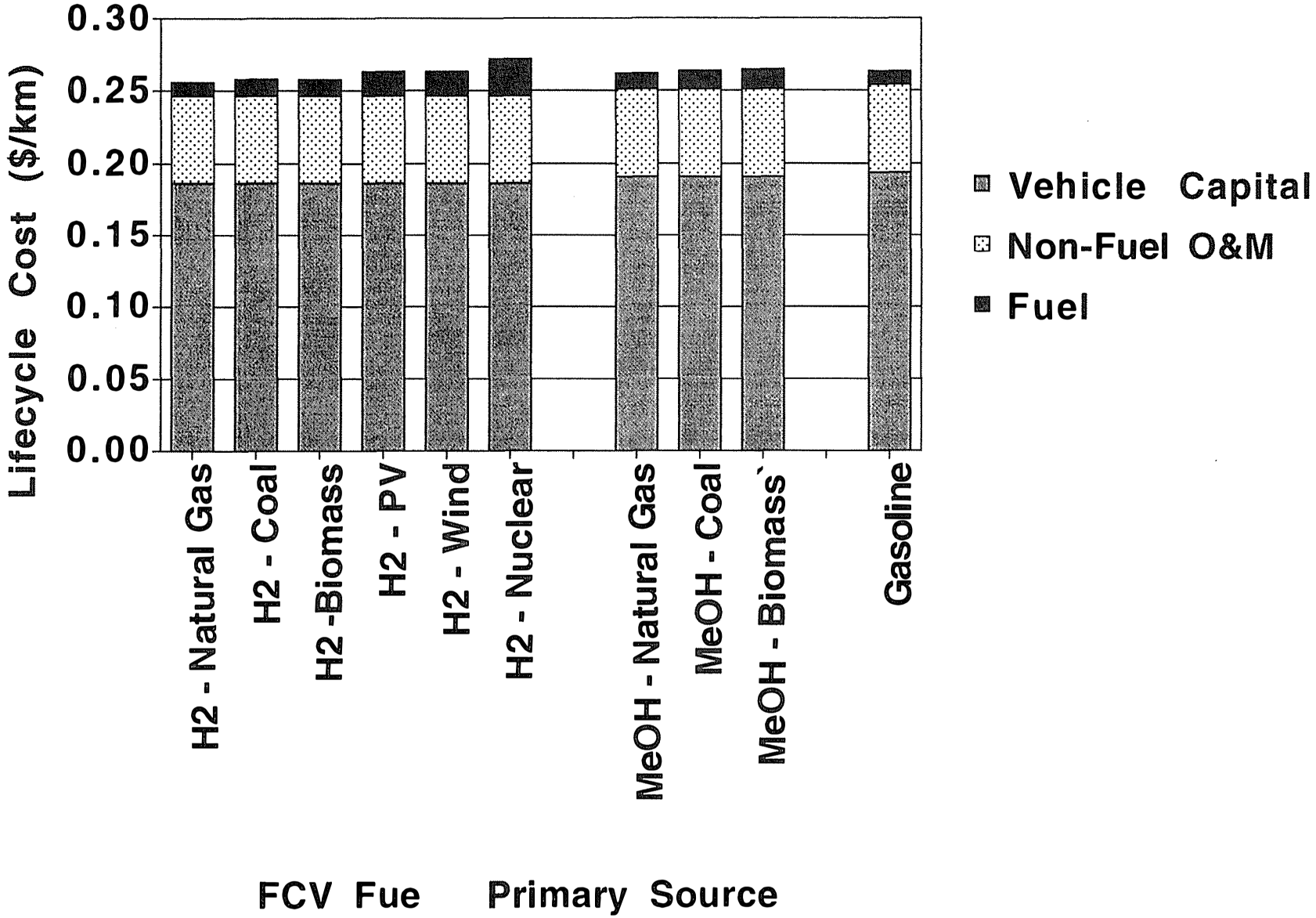

Figure 13. Potential Near Term Hydrogen Supplies and Demands in New Jersey
Million scf H2/day
25
20
15
10
5
0
Supply
Demand
Refinery Excess
H2 from NG (0.5% of 1997 NG use)
H2 from 10% off-peak power
H2 from MSW (from pop.100,000 city)
1 bus garage (200 buses)
NJ Transit system (1900 buses)
10% of fleet LDVs
2% of cars

Figure 14. Potential Long Term Hydrogen Supplies and Demands in New Jersey

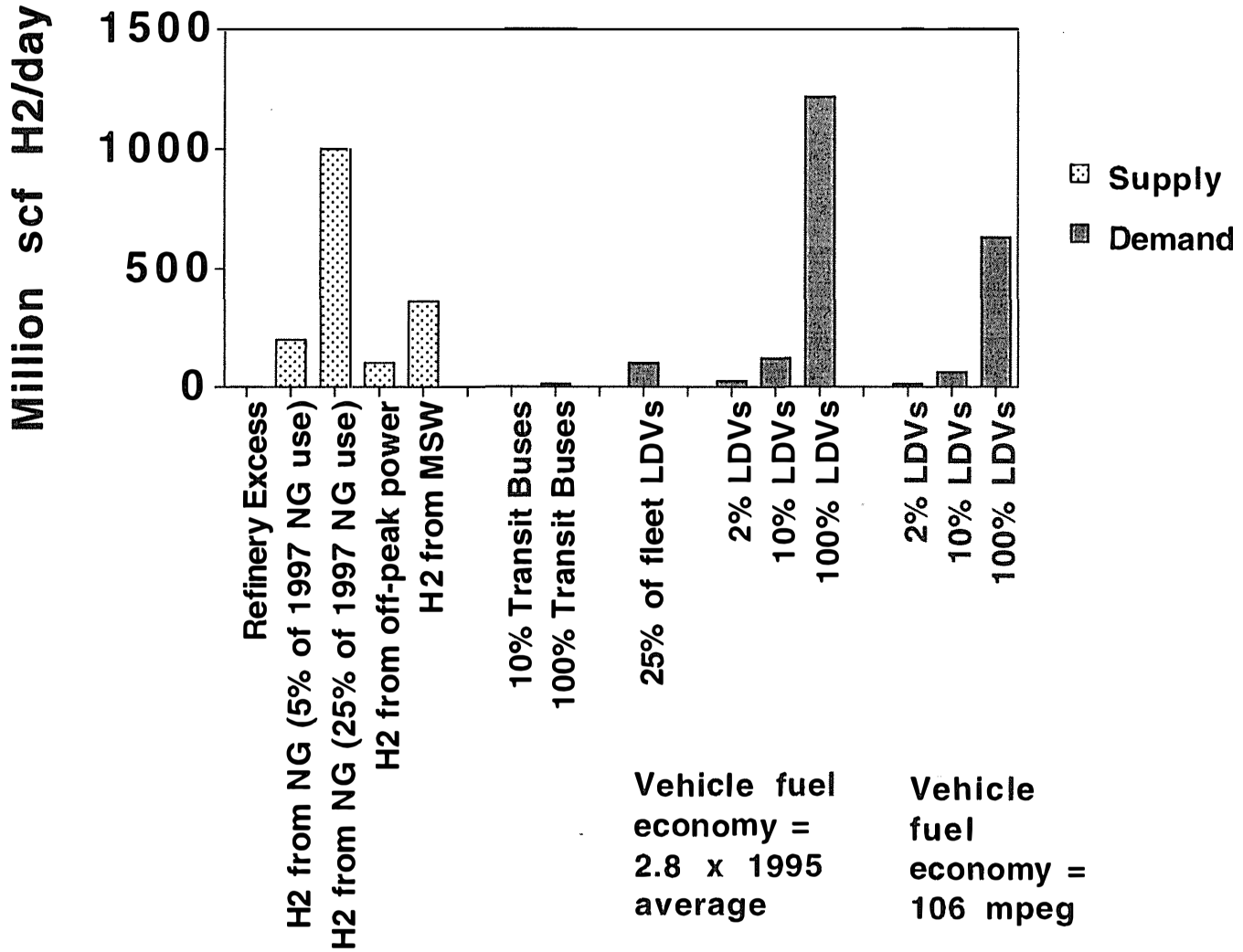

Figure. 15. Hydrogen Production from Hydrocarbons w/CO2 Sequestration

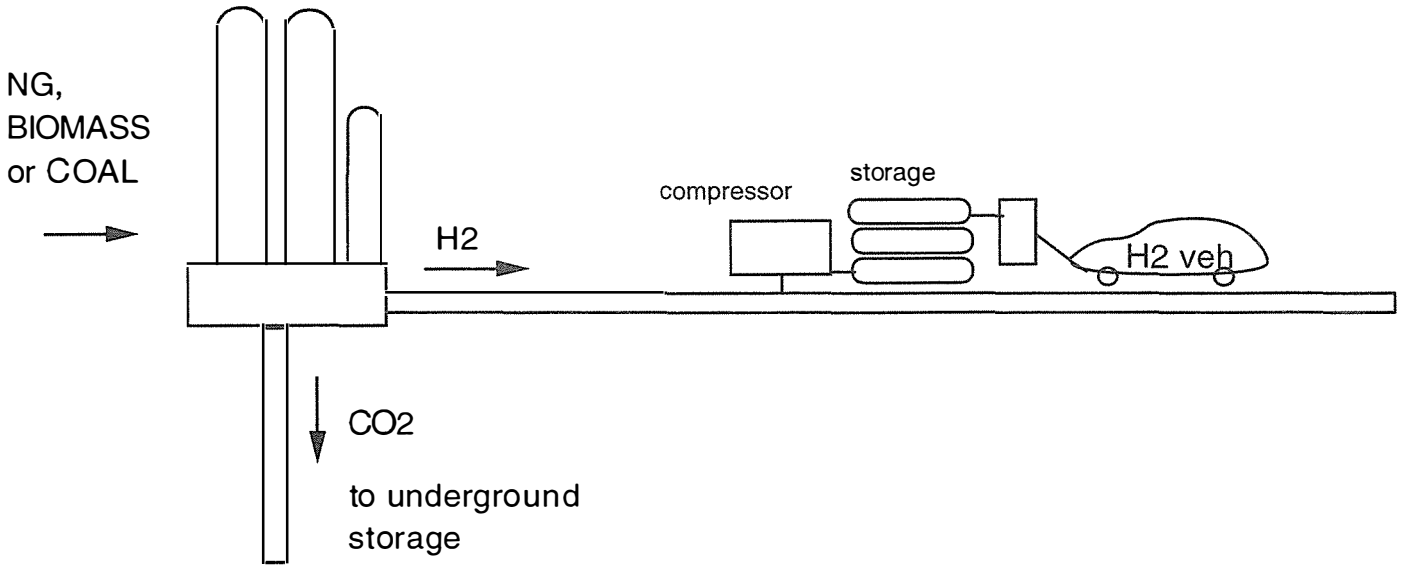

Figure 16. Example: H2 from Natural Gas

QUESTIONS:
Where do you make hydrogen?

When does it make sense to sequester CO2?

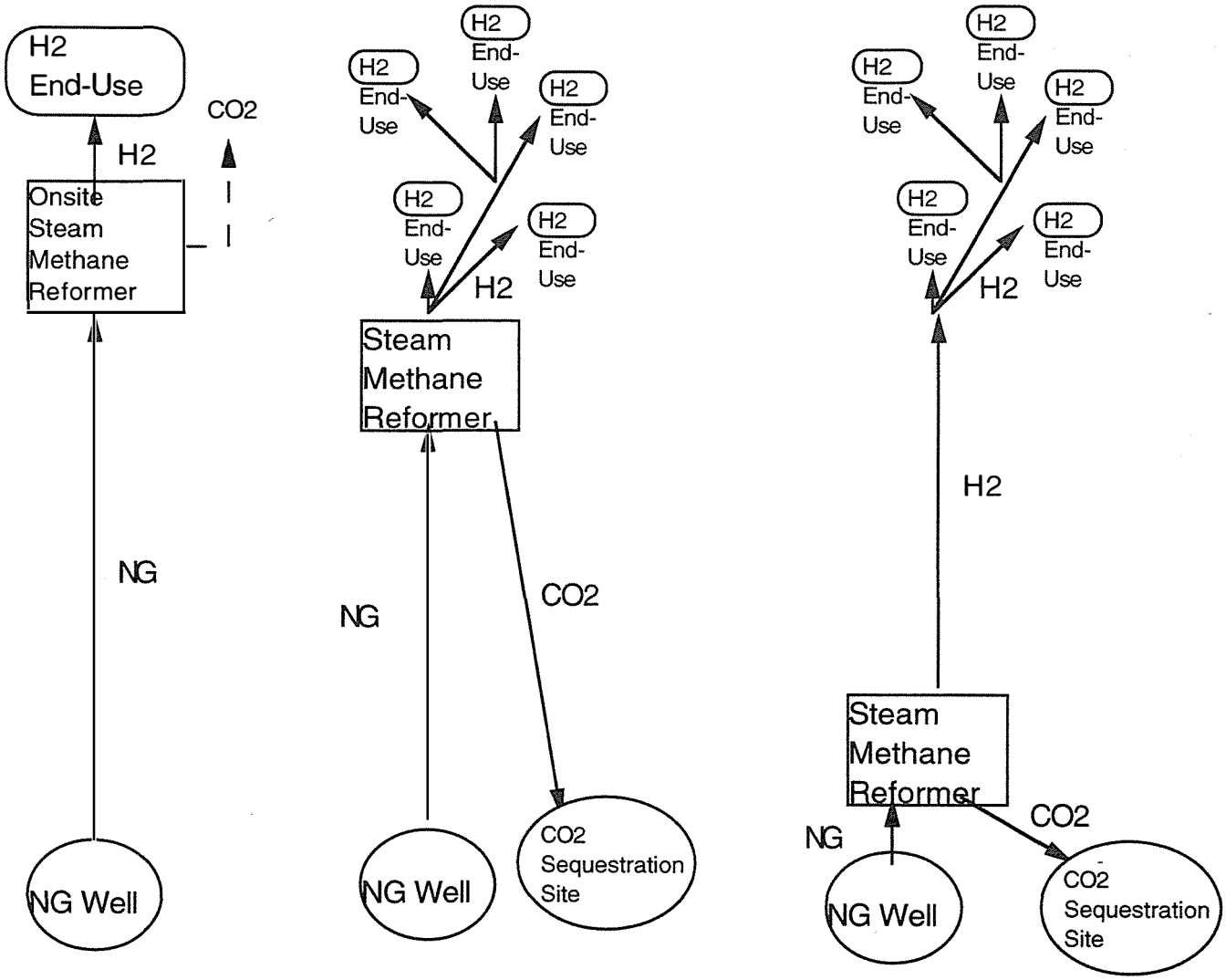

Figure 17. Capital Cost of Steam Methane Reformers vs. H2 Output Capacity

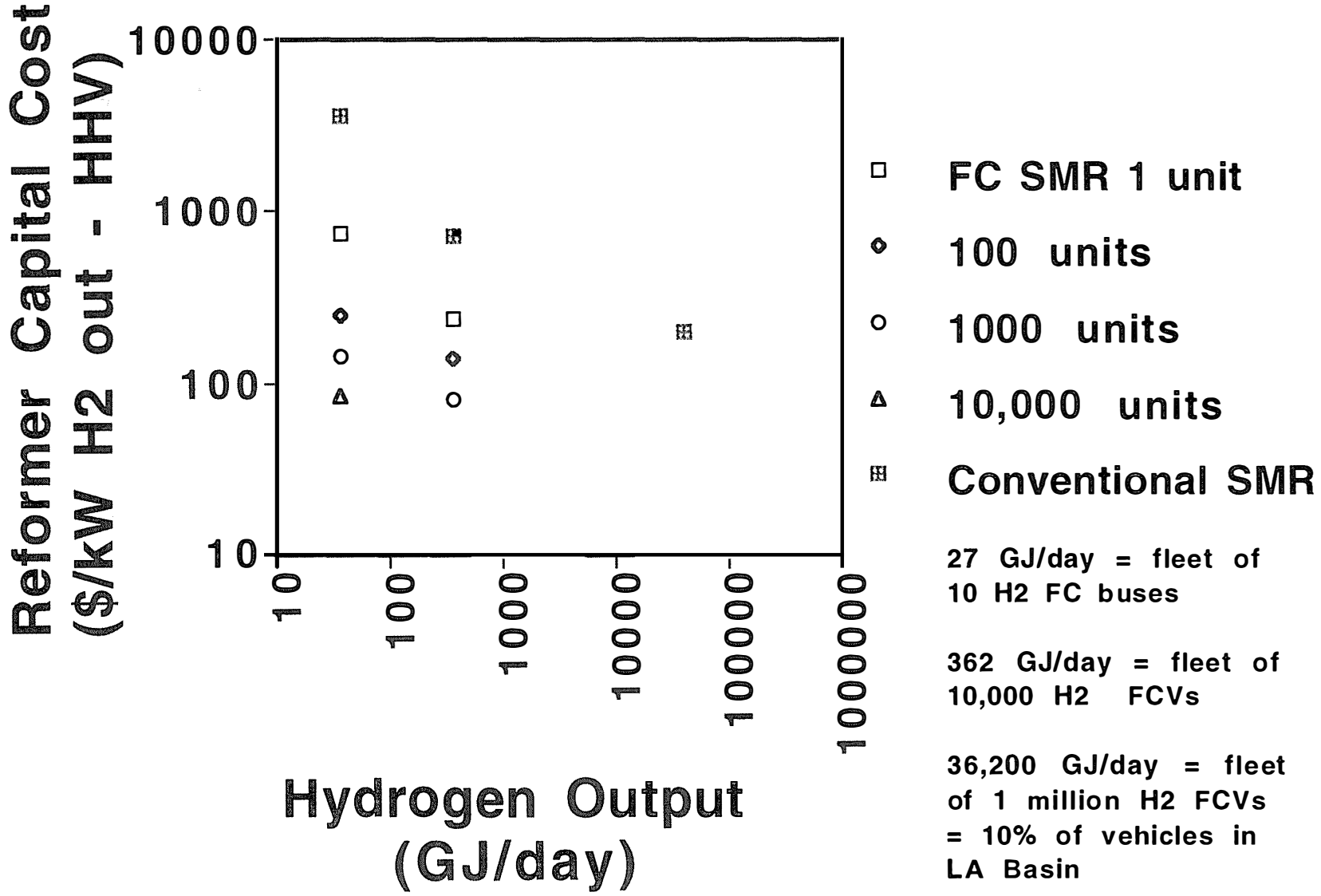

Figure 18. Hydrogen Production Cost in Small vs. Large Steam Methane Reformers ($/GJ)

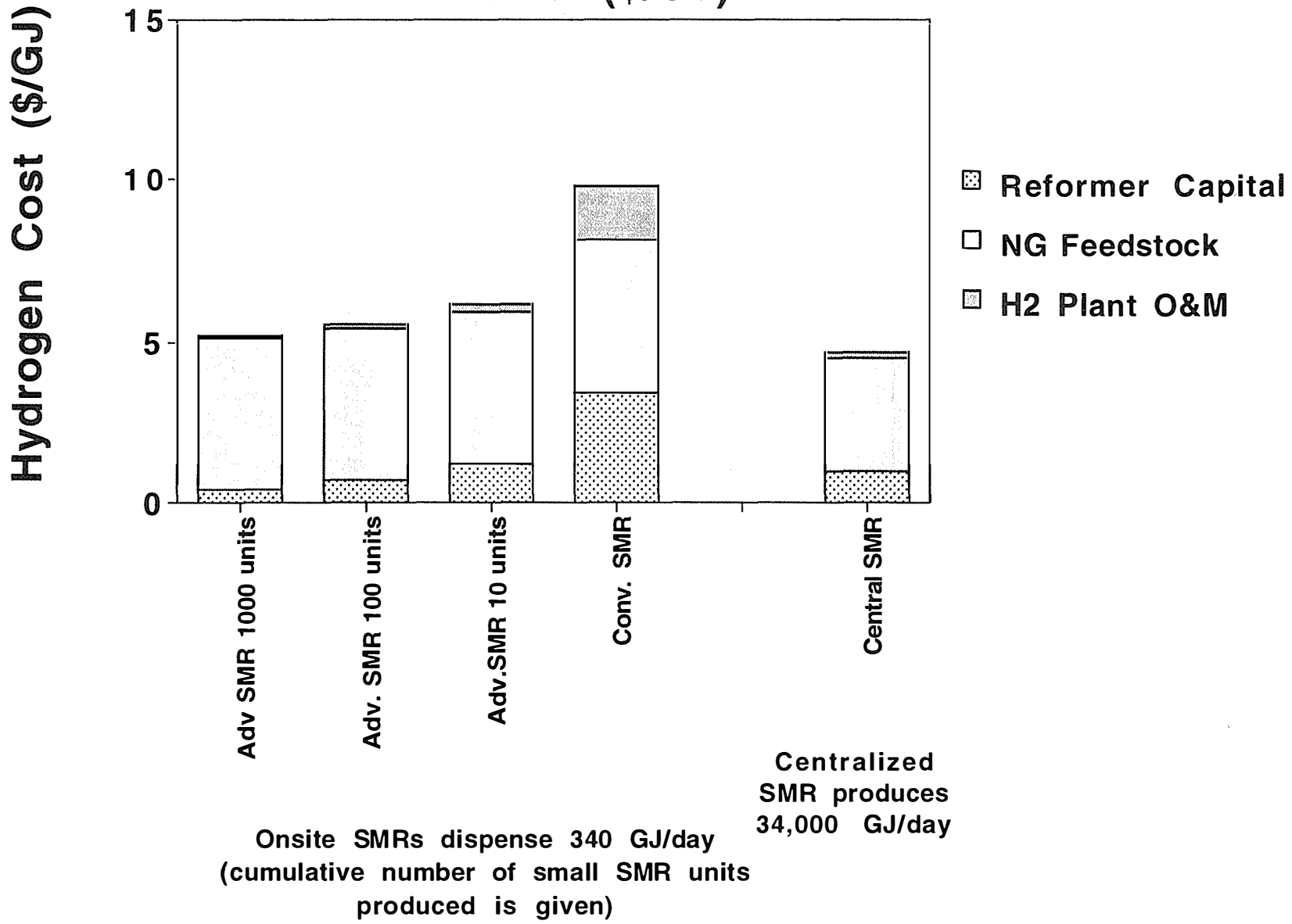

Figure 19. Cost of Hydrogen Pipeline Transmission vs. Pipeline Length and Vehicles Served

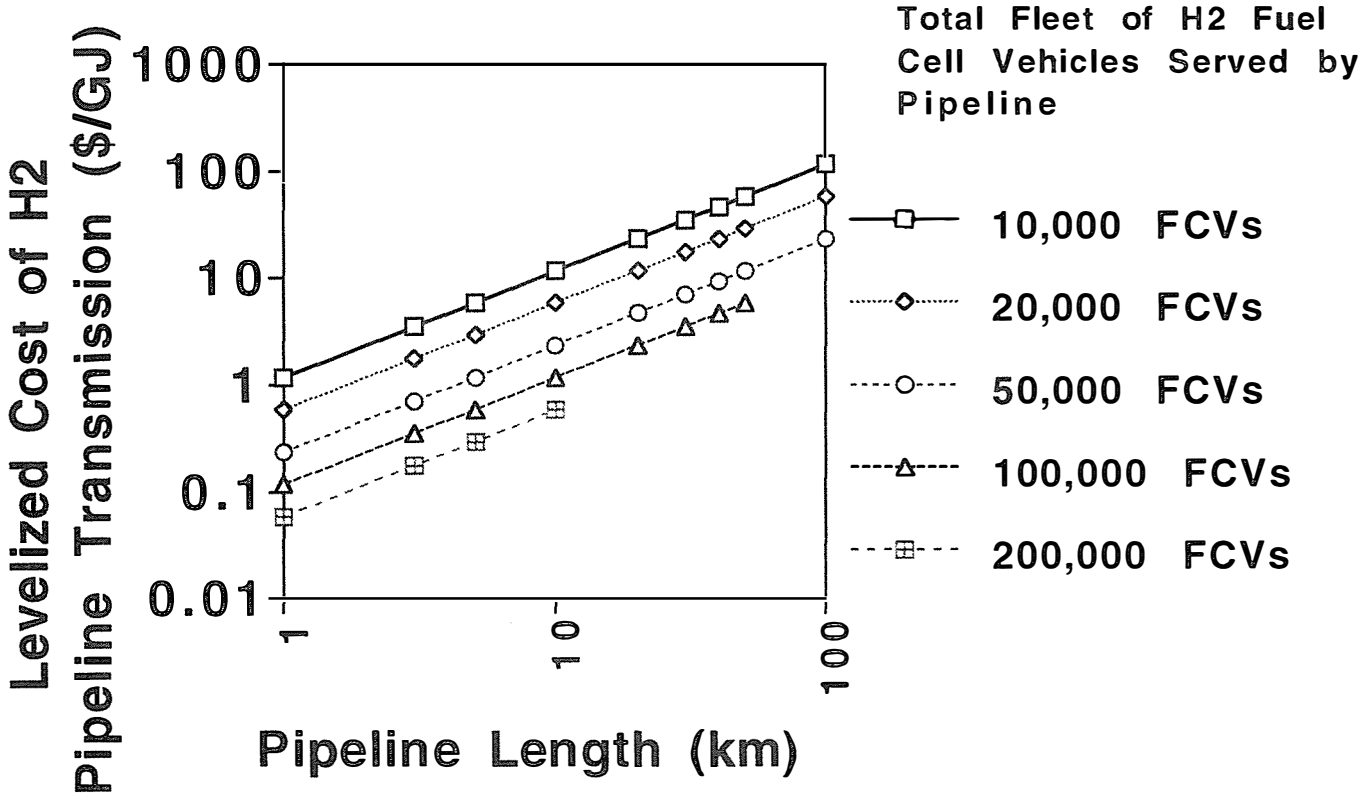

3" Hydrogen Pipeline
Rated up to 1000 psi

Pipeline cost =
$1 million/mile

Inlet Pressure = 1000 psia
Outlet Pressure > 200 psia

Figure 20. Delivered Cost of Hydrogen Transportation Fuel: Onsite vs. Centralized Production in SMRs

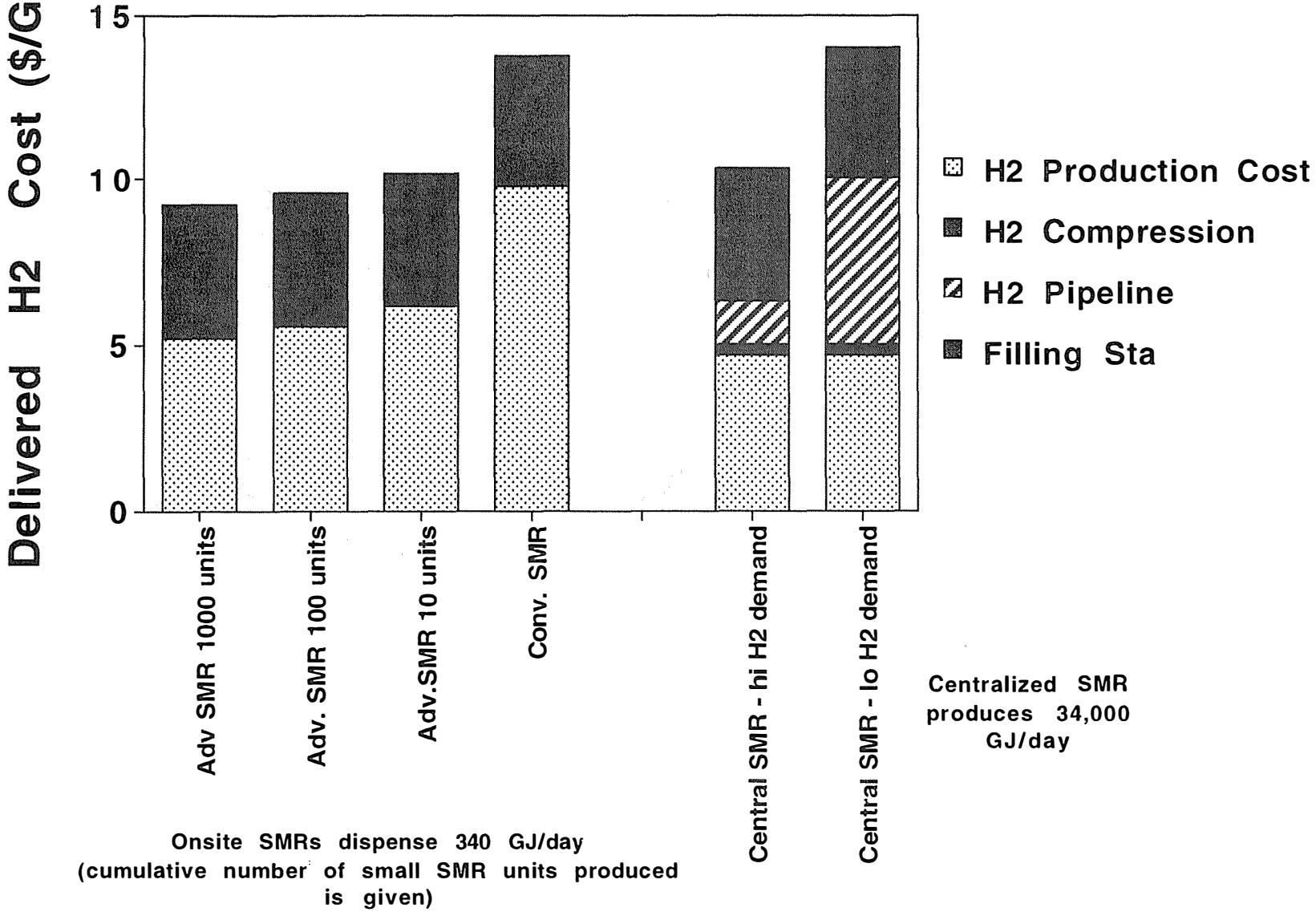

Figure 21. Delivered H2 Cost with CO2 Separation and Collection Central vs. Onsite SMR

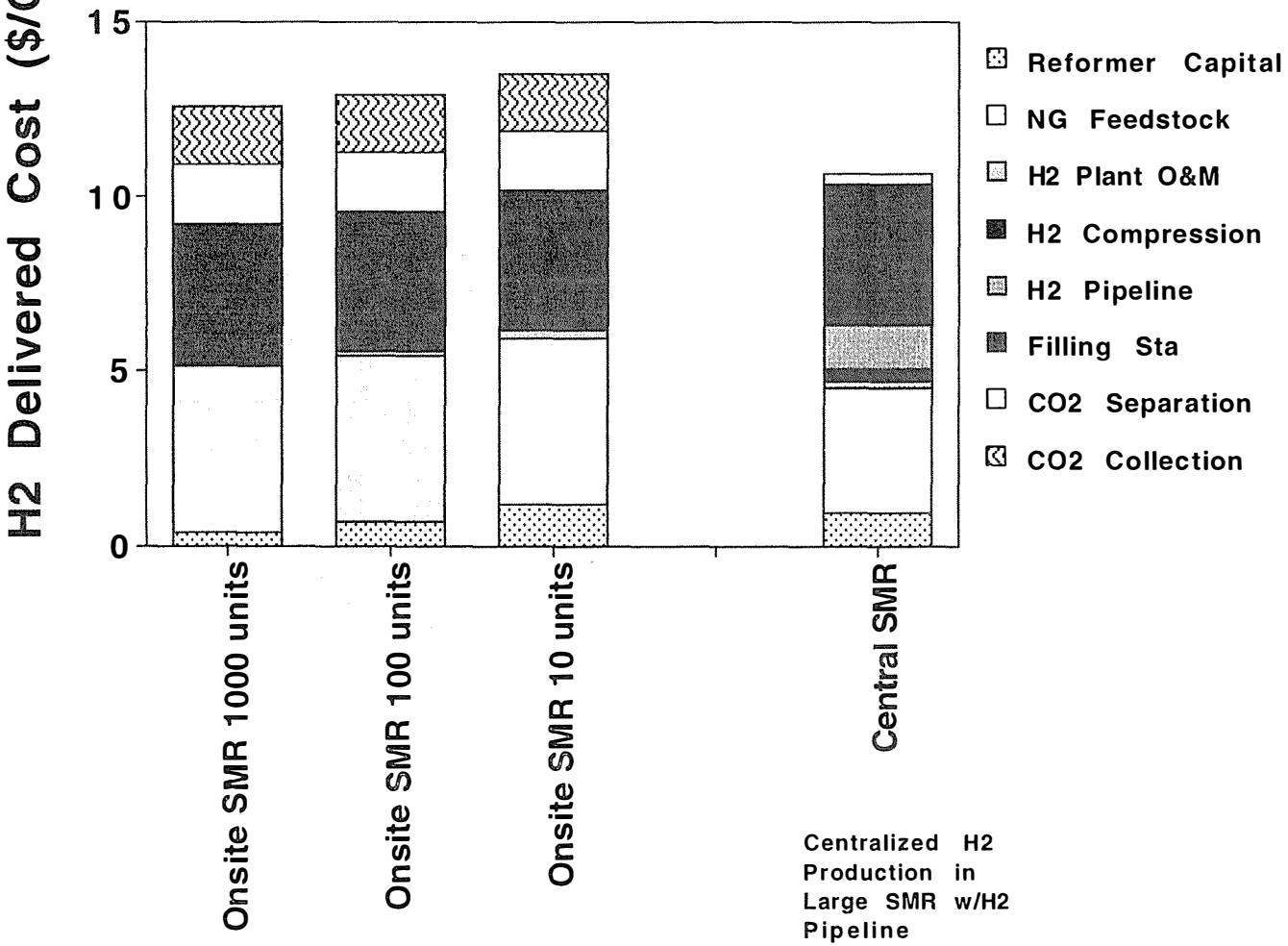

Onsite H2 Production in Mass Produced SMRs w/ CO2 local pipeline collection

NG Cost = $4/MBTU

Centralized H2 Production in Large SMR w/H2 Pipeline Distribution and CO2 Sep. at H2 Plant

NG Cost = $3/MBTU

Figure 22. Cost of CO2 Pipeline Transmission 250 km: Added Cost to H2 ($/GJ)

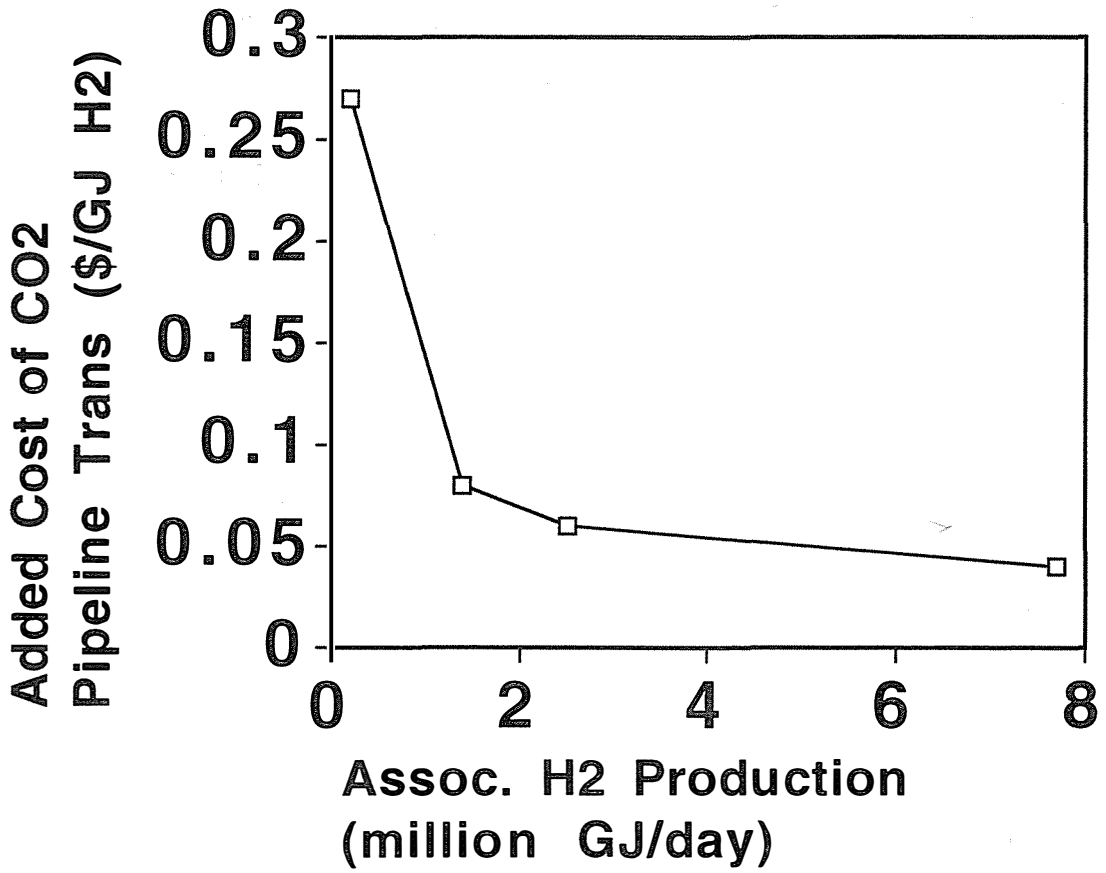

27 GJ/day = fleet of 10 H2 FC buses

362 GJ/day = fleet of 10,000 H2 FCVs

36,200 GJ/day = fleet of 1 million H2 FCVs = 10% of vehicles in LA Basin

Figure 23. Levelized Cost of Transmission for 300 km Hydrogen and Natural Gas Pipelines

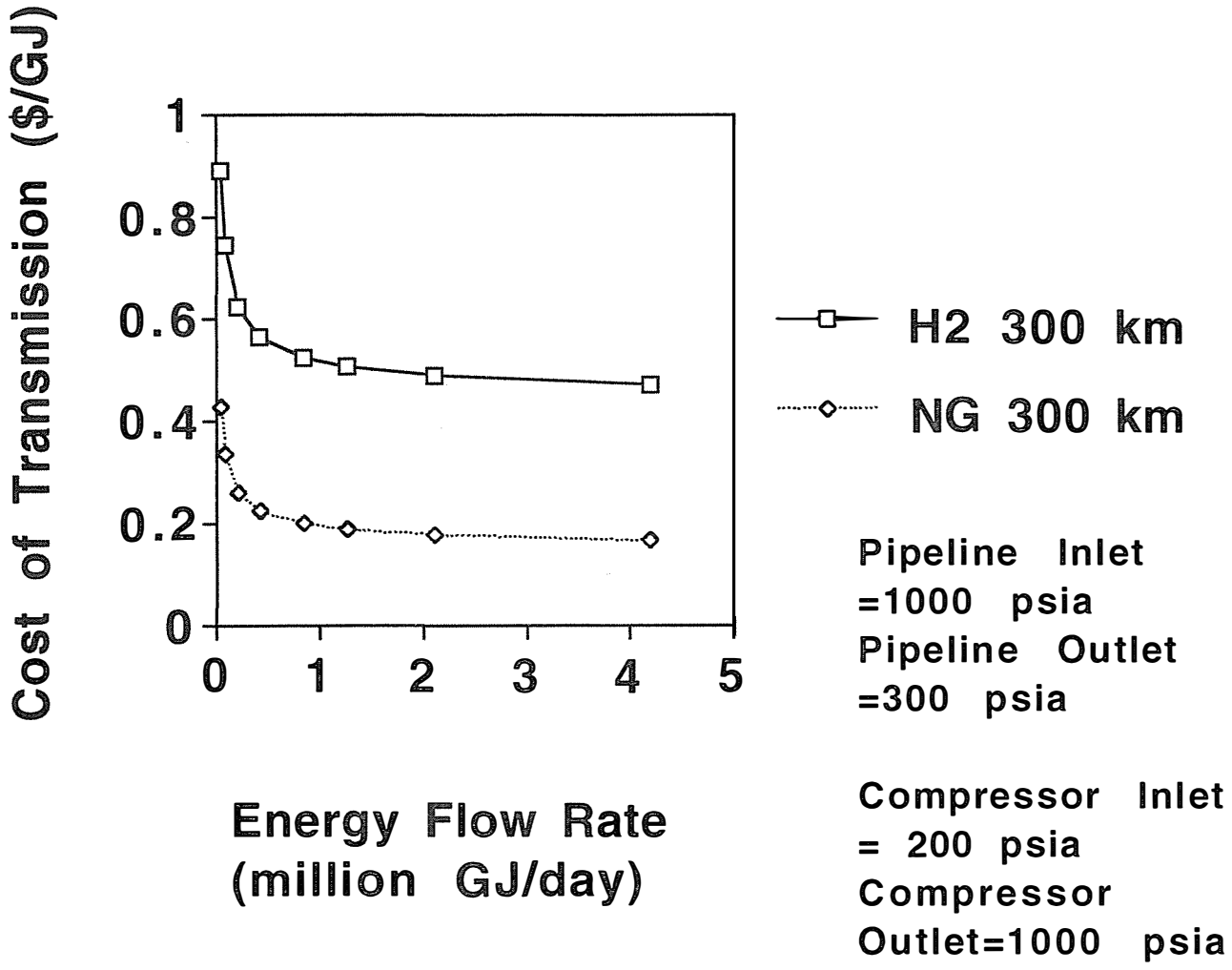

Figure 24. Levelized Cost of Transmission for 1000 km Hydrogen and Natural Gas Pipelines

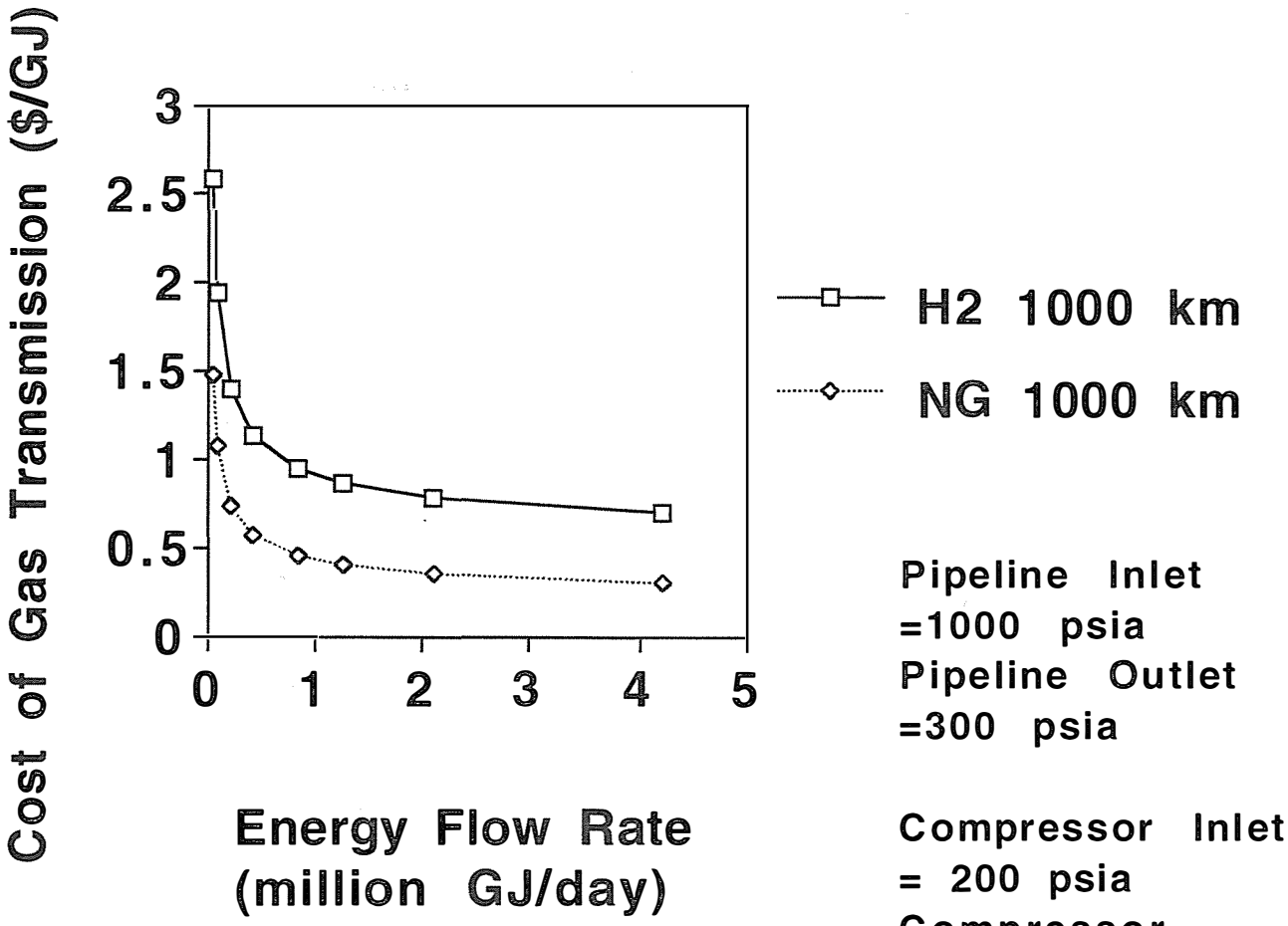

Figure. 25. Configurations for PEM Fuel Cell Cogeneration for Residential Users

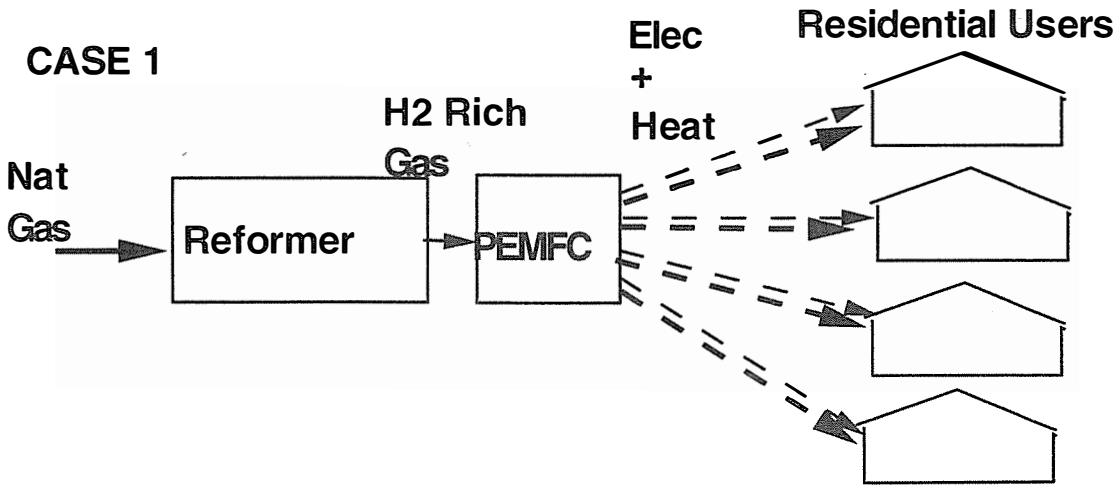

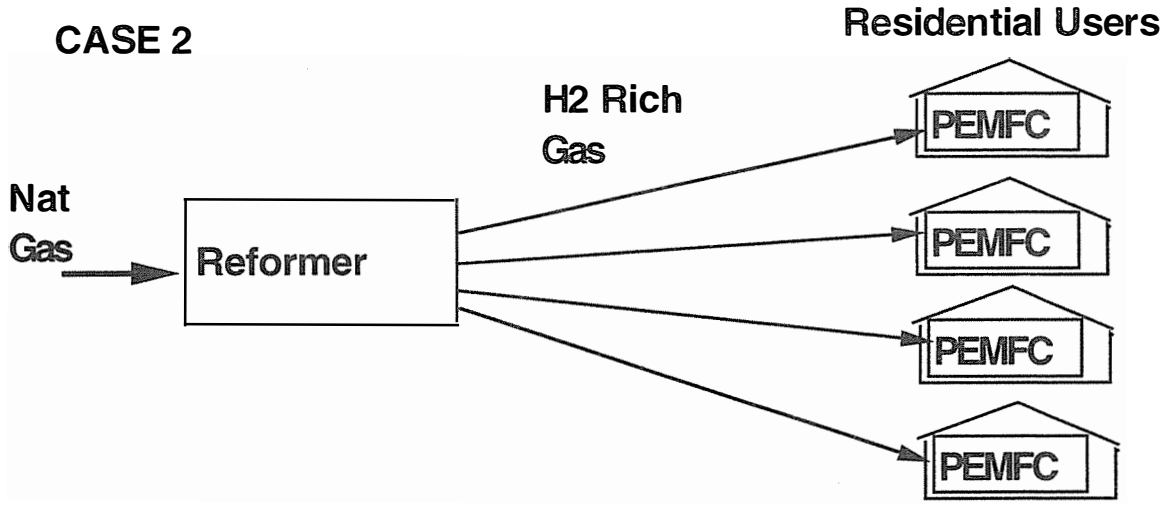

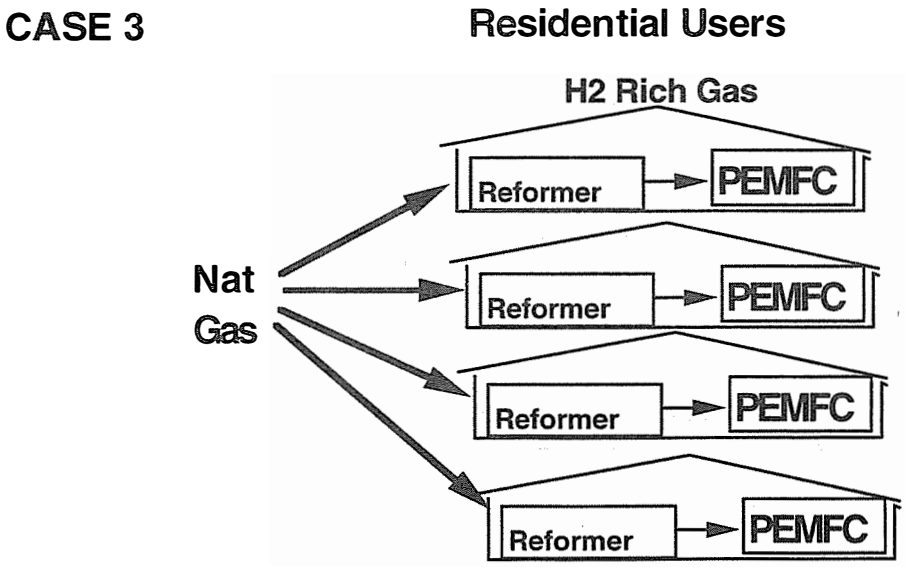

TECHNOECONOMIC ANALYSIS OF DIFFERENT OPTIONS FOR THE PRODUCTION OF HYDROGEN FROM SUNLIGHT, WIND, AND BIOMASS

M.K. Mann, P.L. Spath, W.A. Amos
National Renewable Energy Laboratory
Golden, CO 80401

Abstract

To determine their technical and economic viability and to provide insight into where each technology is in its development cycle, different options to produce hydrogen from sunlight, wind, and biomass were studied. Additionally, costs for storing and transporting hydrogen were determined for different hydrogen quantities and storage times.

The analysis of hydrogen from sunlight examined the selling price of hydrogen from two technologies: direct photoelectrochemical (PEC) conversion of sunlight and photovoltaic (PV)-generated electricity production followed by electrolysis. The wind analysis was based on wind-generated electricity production followed by electrolysis. In addition to the base case analyses, which assume that hydrogen is the sole product, three alternative scenarios explore the economic impact of integrating the PV- and wind-based systems with the electric utility grid. Results show that PEC hydrogen production has the potential to be economically feasible. Additionally, the economics of the PV and wind electrolysis systems are improved by interaction with the grid.

The analysis of hydrogen from biomass focused on three gasification technologies. The systems are: low pressure, indirectly-heated gasification followed by steam reforming; high pressure, oxygen-blown gasification followed by steam reforming; and pyrolysis followed by partial oxidation. For each of the systems studied, the downstream process steps include shift conversion followed by hydrogen purification. Only the low pressure system produces hydrogen within the range of the current industry selling prices (typically $0.7 - $2/kg, or $5-14/GJ on a HHV basis). A sensitivity analysis showed that, for the other two systems, in order to bring the hydrogen selling price down to $2/kg, negative-priced feedstocks would be required.

Summary

Renewable resources, such as solar, wind, and biomass are excellent feedstocks for hydrogen because of their inherently clean nature and sustainability. Technical and economic feasibility analyses were conducted on processes to produce hydrogen from sunlight, wind, and biomass. The degree to which a process can be said to have economic potential is measured by comparing the calculated hydrogen selling price to the current market value of hydrogen. Currently, this range is approximately $0.7 to $2/kg ($5/GJ to $14/GJ, HHV basis).

An important option for the production of hydrogen from renewables is from water by conversion of solar and wind energy. A study was made of the relative economic viability of three technologies: direct photoelectrochemical (PEC) conversion of sunlight, photovoltaic (PV)-generated electricity production followed by electrolysis, and wind-generated electricity production followed by electrolysis. PEC is an alternative to PV/electrolysis systems, combining a semiconductor and an electrocatalyst into a single monolithic device. The base case designs emphasize hydrogen as the only product, derived solely from renewable sources acting independently of the electric grid. However, to identify opportunities to improve the viability of PV- and wind-derived hydrogen, three alternative scenarios were also studied. The first of these explores making an electricity coproduct that can be sold at peak prices to an unspecified customer over the grid. Scenario 2 examines the use of electricity from both the renewable and the grid to produce only hydrogen. Scenario 3 looks at the situation of producing hydrogen at locations remote from where the renewables generate the electricity. Results show that PEC hydrogen has the potential to be economically competitive, and can produce hydrogen at prices below what the PV/electrolysis system can produce if it is not coupled with the utility grid. The selling price of hydrogen from PEC is projected to be $17.2/kg ($121/GJ) in the near term, and $4.7/kg ($33.1/GJ) in the mid- to long-term (~2010). The selling price of hydrogen from stand-alone PV/electrolysis systems was calculated to be $17.6/kg to $7.5/kg ($124/GJ to $52.8/GJ) in the years 2000 and 2010, respectively. Hydrogen from stand-alone wind/electrolysis plants can sell for $7.1/kg and $4.0/kg ($50/GJ and $28.2/GJ) in the same years. Integration with the grid was found to generally improve the economics of the PV and wind systems. The gate-price of hydrogen from PV/electrolysis plants operating in conjunction with the utility grid may be as low as $7.4/kg and $4.5/kg ($52.1/GJ and $31.7/GJ) in 2000 and 2010, respectively. The grid reduces gate prices from wind/electrolysis plants to $3.9/kg and $3.0/kg ($27.5/GJ and $21.1/GJ) in these years.

Biomass, such as agricultural waste, forest residue, urban wood waste, and trees and grasses, can be converted to hydrogen through both biological and thermochemical processes. To compare the economic potential of different thermochemical routes, three gasification systems were compared. The systems are: low pressure, indirectly-heated gasification followed by steam reforming; high pressure, oxygen-blown gasification followed by steam reforming; and pyrolysis followed by partial oxidation. For each system, the downstream process steps include shift conversion followed by hydrogen purification. Each system was modeled in ASPEN Plus©, and the resulting material and energy balances were used to determine the size and cost of each major piece of equipment. Discounted cash flow rate of return analyses were used to calculate the selling price of hydrogen from the systems for three biomass feed rates: 1,500, 1,000, and 300 bone dry Mg/day. A series of sensitivity analyses were conducted to determine the conditions under which each process is most feasible and to guide experimental efforts toward the areas that could result in the largest cost reductions.

The calculated selling price of hydrogen from these biomass conversion systems at a feed rate of 1,000 Mg/day ranged from $0.7/kg to $3.3/kg ($5/GJ to $23/GJ) for a dry feedstock cost of $0/Mg to $46/Mg. The low pressure system was found to have the most economic potential, producing hydrogen that can be sold for less than $2/kg ($14/GJ) for reasonable feedstock prices. Negative feedstock prices are required by the high pressure gasification and the partial oxidation systems for the hydrogen to be within the range of market values.

In addition to the technoeconomic analyses of hydrogen production processes, a detailed assessment of the costs of storing and transporting hydrogen was performed so that future analyses can be reported in terms of the delivered cost of hydrogen versus the gate price. This will provide a means for identifying markets for novel hydrogen production technologies. The storage options that were considered are liquid hydrogen, compressed gas, metal hydride, and underground storage. The modes of transportation examined are liquid hydrogen delivery by truck, rail and barge, gaseous hydrogen delivery by truck, rail, and pipeline, and metal hydride delivery by truck and rail.

Approach and Rationale

Technoeconomic analyses are performed for the U.S. Department of Energy's Hydrogen Program to advance the development of new technologies and to streamline the portfolio of projects being researched. The primary purpose of this work is to identify those areas of research in which improvements will result in the largest reductions in process costs. This helps to define research goals and moves novel technologies more quickly to commercialization. Additionally, results from these analyses provide information to DOE on the long-term technical and economic feasibility of ongoing and proposed research projects.

The determination of whether a system is economically feasible is made by comparing the calculated hydrogen selling price to the current market value of hydrogen. In today's hydrogen market, depending on the size of the production facility and the amount purchased by the end user, hydrogen is typically valued at between $0.7 - $2/kg, or $5-14/GJ on a HHV basis. Large steam methane reforming plants, which generate the majority of hydrogen on the market today, produce hydrogen at the low end of this range. It should be noted that the market size for hydrogen at the higher end of this price range is small, and large contributions to the hydrogen supply will come only at prices competitive with steam methane reforming.

The method of economic analysis used for determining the economic potential of the solar, wind, and biomass processes is discounted cash flow rate of return, which calculates the necessary selling price of hydrogen when the internal rate of return (IRR) is specified. The IRR is the minimum acceptable rate for an investor to finance a project. Therefore, the perceived risk of the project can be incorporated into the IRR. Because processes to produce hydrogen from renewables currently carry higher risks than conventional hydrogen-generating processes, the IRR specified in these analyses is 15% after tax. The rate for conventional processes is generally between 9% and 12%, depending on the economy and company practices. For a 37% tax rate, a 15% after-tax IRR corresponds to a pre-tax IRR of 20. Other major assumptions for the economic analysis are: equity financing for a 20 year plant life including two years of construction time, 90% on-stream factor except where noted in the PV and wind study, working capital of 18% of installed capital, a tax rate of 37%, and ten year straight-line depreciation. All equipment costs were adjusted to 1995 dollars.

Analysis of the Production of Hydrogen from Sunlight and Wind

An important option for the production of hydrogen from renewables is from water by conversion of solar and wind energy. A study was made of the relative economic viability of three technologies: direct photoelectrochemical (PEC) conversion of sunlight, photovoltaic (PV)-generated electricity production followed by electrolysis, and wind-generated electricity production followed by electrolysis. The base case analysis projected the selling price of hydrogen from these systems, assuming that they are operated independently of the electric grid. On the other hand, the ability to sell valuable electric energy and purchase inexpensive electric energy via the grid may be one of the more viable options for the commercialization of renewables-based hydrogen production. To examine this option, alternative scenarios in which the PV- and wind-based systems interact with the grid were also studied.

Photoelectrochemical Hydrogen Production

Photoelectrochemical (PEC) water splitting represents an alternative to PV/electrolysis systems, combining a semiconductor and an electrocatalyst into a single monolithic device. Researchers on this task are working to develop a stable, cost effective, semiconductor-based system that will collect solar energy and electrolyze water in one step to produce hydrogen, with sunlight as the only energy input. This system eliminates the need for an electrolyzer and additionally reduces semiconductor processing because surface contacts, interconnects, and wiring are no longer necessary. Two configurations are being studied: single gap systems and multijunction systems. The theoretical lower heating value efficiency of dual junction systems is 32% while single bandgap systems have an upper limit on the order of 24%. Practical systems could achieve 20% and 10% efficiencies for multijunction and single bandgap systems, respectively. More information on this research can be found in Kocha *et al* (1996), Kocha *et al* (1997), and Rocheleau *et al* (1996).

Work at the National Renewable Energy Laboratory and the University of Hawaii on PEC conversion systems involves three basic areas of research: semiconducting materials, surface modification, and catalysts. Work thus far has identified gallium indium phosphide ($GaInP_2$) as a promising semiconductor. $GaInP_2$ /gallium arsenide (GaAs) has been identified as a promising tandem cell system; additionally, amorphous silicon/amorphous silicon carbide (a-Si/a-SiC) appear to be promising thin-film systems. Initial work has shown that the $GaInP_2$/GaAs system will split water with very high efficiencies (12% thus far), and is relatively stable in aqueous environments. The a-Si/a-SiC system has also shown some promise, and the a-SiC has been shown to protect a-Si-based multijunction systems from surface oxidation, further enhancing the viability of using this low cost cell. Efficiencies on the order of 7% have been realized in laboratory tests on these cells.

A preliminary analysis determined the contribution of the semiconductor cell to the cost of hydrogen and the minimum photoconversion efficiency necessary for the system to have economic potential (Mann *et al* (1996). Results found that the more expensive tandem cells will not produce hydrogen economically, despite their higher efficiencies. Amorphous silicon thin films, however, have the potential to be viable systems. This previous analysis was not detailed enough to determine if the systems will be economic, but was able to contend that further analysis and research were warranted.

Although hydrogen production via photoelectrolysis will only have the potential to be economical with lower cost cells, reasons exist for continued work on the more expensive materials. Given that the tandem cells have the appropriate bandgap and stability for water splitting, research on these cells is vital to understanding the basic science behind PEC water splitting. Issues such as spectral response, current matching, surface catalyst preparation and application, corrosion control and measurement, efficiency determination, cell and system design, and gas collection techniques, can all be studied with this system while less expensive systems are being developed.

To expand the previous analysis and further determine the situations in which this technology will be viable, a detailed analysis of the costs of photoelectrochemical hydrogen production has been conducted. Table 1 gives the main assumptions not given in the Approach and Rationale section above. Photocatalyst cost is based on projected costs for a-Si PV cells, discounted to reflect the fact that some processing costs such as interconnects and wiring will not be required. This information is based on data in the Photovoltaics section of the Renewable Energy Technology Characterizations (EPRI, 1997) and from personal correspondence with scientists in the National Center for Photovoltaics at NREL. The photocatalyst is immersed in a weak solution ($< 3M$) of H_2SO_4, (NaOH solution could also be used) with its edges surrounded by a Nafion© (DuPont) type membrane that allows the transfer of ions between the anodic and cathodic parts of the cell. The membrane area is assumed to be equal to the photocatalyst area. This assembly is contained in an extruded plastic housing, which is shaped to concentrate the sunlight by a factor of five when filled with the acid solution. Higher concentrations produced with fresnel lenses and mirrors were found to be uneconomic given the

relatively low cost of the photocatalyst. Since the hydrogen and oxygen are evolved on different sides of the membrane, there isn't a requirement to separate them later. It is assumed that 39.89 kWh of energy are needed to split one kg of water at 1.5 V.

Table 1: Major Assumptions for the Economic Analysis of PEC Hydrogen Production

	Near term (~2000)	Mid-term (~2010)	Long term (~2020)
Photocatalyst efficiency (sunlight to hydrogen, LHV)	7.5%	9%	14%
Photocatalyst cost ($/m^2)	125	100	70
Membrane cost ($/m^2) [5]	475	225	50
Solar insolation = 5.74 kWh/m^2/day (Carrissa Plains, CA)			
Hydrogen production rate = 500,000 kg/year			

Designing the housing unit has proved to be a difficult issue for this technology. The material must have the following characteristics:

- Able to resist attack from the electrolyte solution
- Stable in an aqueous environment
- Transparent
- UV stable
- Able to withstand the range of operating temperatures
- Low hydrogen permeability
- Low cost

The hydrogen permeabilities of different plastics were calculated and found to range from approximately zero for glass, to 24% of the produced hydrogen for some polycarbonates. Some materials, including some other polycarbonate formulations, were found to have permeabilities lower that 0.6%. Polycarbonate was chosen for this design, and a vendor quote was obtained. Because of cost issues, it may be most feasible to apply a small layer of impermeable material to the inside of a cheaper plastic.

The results of the analysis, including the hydrogen selling and production costs, are shown in Table 2. These results highlight the parts of the system that contribute significant cost to the overall selling price of the product hydrogen. Although photocatalyst efficiency improvements play a large role in reducing the future selling price of the product, other equipment costs are sufficiently high as to temper the overall decrease. The dramatic reduction in the price of the membrane is due in large part to projected increased demand as PEM fuel cells are mass-produced. Other materials may work equally well and should be investigated, as the PEC system will certainly be less feasible if DuPont is unable to reduce the price of their membrane as much as they project. The cost of the unit supports, obtained from a PV manufacturer in the U.S., is not expected to decline because it is largely a function of the cost of steel. Therefore, as the overall system becomes cheaper, its share of the total cost increases. One of the biggest surprises of these results is the impact of the housing unit on the total cost. Further designs and materials should be investigated.

Table 2: Results of the Economic Analysis of the PEC System

	Current	Near-term (~2000)	Mid/Long term (~2010)
Total land required (ha)	16.9	14.1	9.1
Capital cost (millions of $)	36.0	21.0	9.4
Photocatalyst (% of total capital)	11%	11%	11%
Membrane (% of total capital)	37%	25%	8%
Unit supports (% of total capital)	17%	24%	34%
PEC housing (% of total capital)	19%	20%	23%
H_2 selling price ($/GJ) (given a 15% IRR)	120.9	71.4	33.1
H2 production cost ($/GJ) (given a 0% IRR)	31.9	20.5	10.3

Hydrogen from PV and Wind

Four options for the production of hydrogen from PV and wind systems were studied. The base case system involves direct coupling of the electrolyzer to the renewable. This system acts independently of the grid and produces only hydrogen. Three alternative scenarios were examined to explore the possibility of improving the project economics. The scenarios are structured to provide the framework for evaluation of the trade-offs between: 1) the high value/selling price of on-peak electricity from the grid, 2) the relatively low purchase price for non-peak electricity from the grid, 3) electrolyzer variable operating cost, and 4) amortization of the electrolyzer cost over more units of hydrogen produced.

In the first alternative scenario, hydrogen and electricity production are coupled to produce the lowest cost hydrogen possible. During periods of peak electricity demand, the electricity will be sent to the grid for sale to a customer or to a central pool. Hydrogen production occurs when the renewable is operating and a high selling price for the electricity cannot be obtained. The renewables are assumed to receive a capacity credit, prorated to reflect the fact that they are generating intermittently. This scenario reduces the total annual amount of electric energy available for hydrogen production by about 11% for PV and 9% for wind.

Scenario 2 involves producing hydrogen from the renewably-produced electricity, plus grid electricity purchased during periods of off-peak demand. The goal of this option, like that for Scenario 1, is to minimize the production cost of hydrogen. The electrolyzer size was based on the maximum output of the renewable, sized at 10 MW. Scenario 2 is divided into two parts. In the first case, Scenario 2a, energy is purchased from the grid during all hours (on-peak and off-peak) to augment renewable electricity production, such that the electrolyzer operates at 90% of its baseload capacity. Plant outages are assumed to occur uniformly throughout the hours of operation. In Scenario 2b, only less expensive non-peak electricity is purchased. Thus, the electrolyzer operates during on-peak hours when the renewable is producing, and during all non-peak hours. Using the electrolyzer over more hours than in Scenario 1 allows the owner to amortize capital equipment cost over a greater amount of product hydrogen.

In Scenario 3, electricity production is physically decoupled from the hydrogen production operation. Energy from the wind and PV systems is sent to the grid and to the electrolyzers operating elsewhere. This situation may be more realistic than the others because the times that the electrolyzer operates will not necessarily

coincide with hydrogen demand. Additionally, producing the hydrogen where it is needed mitigates the need for many storage and distribution costs. In Scenario 3a, energy generated by the PV and wind systems during on-peak hours is sold to the grid and all renewable energy produced during non-peak hours is sent over the grid to the hydrogen production site. Associated charges and resistive losses are included in the cost analysis. Scenario 3b involves selling all electricity generated by the renewables to the grid and purchasing only non-peak grid electricity to produce hydrogen. Note that in both of these cases, additional electric energy is purchased from the grid only during non-peak hours when the renewable is not producing. Further, it is assumed that operation of the electrolyzer only during non-peak hours allows the hydrogen producer to avoid demand charges. The renewable is also given a partial capacity credit.

All of the scenarios examined are based on the renewables having 10 MW nameplate capacities. The study was conducted for systems installed in the near term (~2000) and the mid-term (~2010) to show how costs will decline as the technologies mature. Table 3 shows the major assumptions for the PV and wind analyses.

Table 3: Assumptions for the PV and Wind Analyses

Date of plant installation	Year 2000	Year 2010
Efficiency of 2MW alkaline electrolyzer	82%	87%
Capital cost of 2MW alkaline electrolyzer	$600/kW	$300/kW
Operating costs for electrolyzer	3% of capital charges	2% of capital charges
Capital cost of wind plants, including necessary power conditioning units	$900/kW	$700/kW
Operating costs of wind plant, variable and fixed	$0.008/kWh, $0.0005/kWh	$0.005/kWh, $0.0005/kWh
Wind plant capacity factor	35%	40%
Capital cost of PV plant, including necessary power conditioning units	$3,133/kW	$1,662/kW
Operating costs of PV plant, variable and fixed	$0.008/kWh, $0.0003/kWh	$0.008/kWh, $0.0003/kWh
PV plant capacity factor	28%	30%
Wheeling charges	$1/kW-mo fixed, ½ ¢/kWh variable	
Capacity credit (applied for number of hours that electricity is sold)	PV: 85% of $4/kW-mo Wind: 40% of $4/kW-mo	

Electricity prices were provided by Distributed Utility Associates, obtained from a variety of proprietary sources and professional judgement. The price of fuel for electric generation is expected to remain fairly constant and stable throughout the study period of 2000 to 2010. Electricity prices in the U.S., however, are forecast to drop during this time, with prices stabilizing beyond the year 2012. These conditions are driven by several key factors: 1) increasing competition putting downward pressure on electricity costs and on prices as deregulation takes hold, 2) the existing overcapacity of inexpensive generation capacity in many regions, and 3) the apparent stability of natural gas and coal supplies and markets. An important unknown in this forecast is the cost, if any, associated with mandated air emission reductions. Electric energy bought by

customers (hydrogen producers in this case) is purchased at the retail price. Retail and wholesale prices depend on the time of day and season; however, to simplify the data analysis for this study, average electric prices for each cost period (shown in Table 4) were assumed.

Table 4: Electricity Price/Cost Assumptions

Cost period	Hours per year	Electricity cost/price
On-peak	650	purchase cost: 10¢/kWh - 18¢/kWh, averaging 14¢/kWh selling price: 3.5¢/kWh - 6¢/kWh, averaging 5¢/kWh
Off-peak	4,966	purchase cost: 4¢/kWh - 7¢/kWh, averaging 6¢/kWh selling price: 2.5¢/kWh - 3.5¢/kWh, averaging 3¢/kWh
Super off-peak	3,144	purchase cost: 3¢/kWh - 6¢/kWh, averaging 5¢/kWh selling price: 1.8¢/kWh - 2.2¢/kWh, averaging 2¢/kWh

Note: Electricity selling prices do not include the capacity credit applied (see Table 3)

Figures 1 and 2 show the selling price of hydrogen from the PV and wind-based systems for the years 2000 and 2010, respectively. Overall, process economics for hydrogen from PV and wind can greatly be improved by integration with the electric utility grid. Differences in results between the PV and wind systems can best be understood by noting that the hours of operation of PV coincide with on-peak electricity usage better than wind. Thus, in Scenario 1, the PV system is selling most of the electricity it makes to the grid, causing a substantial reduction in the electrolyzer on-stream factor. This more than outweighs the benefit of being able to sell high-priced electricity during peak hours. The wind system doesn't suffer this disadvantage because it's able to use the electrolyzer during the night as long as the wind is blowing. On the other hand, however, the economics of the PV system are more distinctly enhanced by the other scenarios because it has greater opportunities to sell higher priced electricity to the grid than the wind system. Additionally, when electricity is purchased, PV buys more during super-off peak periods than wind.

Analysis of the Production of Hydrogen from Biomass

Three gasification systems to convert biomass to hydrogen were comparatively studied. The gasifier systems examined were the Battelle Columbus Laboratory/Future Energy Resources Corporation (BCL/FERCO) indirectly-heated gasifier, the Institute of Gas Technology (IGT) direct-fired gasifier, and the Texaco partial oxidation reactor. Basic block flow diagrams of these options plus the process steps necessary for hydrogen production are shown in Figure 3. The high temperature and low temperature shift reactors convert the majority of the CO (and H_2O) into CO_2 and (H_2) through the water-gas shift reaction. Because this reaction is exothermic, it is beneficial to operate these reactors at temperatures lower than that of the reformer. A pressure swing adsorption (PSA) unit is used to separate the product hydrogen from the rest of the shift reactor product stream, which mainly contains H_2, CO_2, and unreacted CO, CH_4, and other hydrocarbons. Before this stream can be purified in a PSA unit, it must contain at least 70 mol% hydrogen. Purifying streams more dilute than this decreases the purity and recovery of the hydrogen. Therefore, part of the PSA product stream is recycled back into the PSA feed. The recovery of hydrogen in the PSA is 85% when purifying a 70 mol% H_2 stream.

All of the systems studied were integrated such that available heat could dry the biomass and generate any necessary process steam, as well as produce a substantial amount of export steam. The assumption that the steam will be able to be sold is probably valid for the medium and large plants as they will most likely be

located in more industrialized centers to take advantage of other infrastructure. However, it may be difficult to sell the steam produced by the small plant, as this size represents small refueling stations located near the demand for hydrogen.

The BCL/FERCO Low Pressure, Indirectly-heated Gasifier

The first option examined is based on a low pressure, indirectly heated gasifier, like that developed at Battelle Columbus Laboratories (BCL) specifically for biomass gasification. Future Energy Resources Corporation (FERCO) now owns the rights to this technology and is participating in its demonstration at the existing McNeil power plant in Burlington Vermont. This system is called indirectly heated because the heat necessary for the endothermic gasification reactions is supplied by sand circulating between the char combustor and the gasification vessel. The ASPEN Plus© simulation of this plant was made from test data from the Battelle Columbus Laboratory 9 Mg/day test facility.

After clean-up, the syngas, containing primarily CO, H_2, CH_4, CO_2, and some higher hydrocarbons, is cooled to 91°C (195°F) so that it can be compressed to the pressure required for the PSA system plus the expected pressure losses in the reactors. During this cooling, the water and higher hydrocarbons (tars) remaining in the syngas will most likely condense. Following compression to 3.5 MPa, the syngas is steam reformed to produce H_2 and CO_2 in a process based on that used for natural gas reforming. The primary reformer, a reactor similar to a process furnace with catalyst-filled tubes, converts the methane and higher hydrocarbons to CO and H_2, and performs a significant portion of the water-gas shift reaction to convert CO and water to H_2 and CO_2. The remaining CO is consumed via this reaction in the subsequent high temperature and low temperature shift reactors.

The reforming reactions typically take place at temperatures between 800°C and 850°C in the primary reformer. The heat necessary for these reactions is supplied by combusting the PSA offgas, which consists of unrecovered H_2, CH_4, CO, and inerts, outside of the reactor tubes through which the reactants and products are flowing. The tubes are filled with a commercial nickel-based catalyst. According to results from operating plants, the primary reformer was simulated as an equilibrium reactor with an 11 °C approach temperature. Practically all of the tar and C_2H_x species are consumed, 60 mol% of the CH_4 is converted, and there is a 22 mol% net conversion of CO.

The cost of the gasification train was estimated in a previous study (Craig and Mann, 1996), as well as by several consulting firms working for BCL (see Mann, 1995). These costs were scaled to the appropriate plant size for this study using a 0.7 scale factor. The cost of the primary reformer was based on a furnace reactor, taken from three literature and software sources.

The Institute of Gas Technology Direct-fired Gasifier

The Institute for Gas Technology (IGT) gasifier is a direct-fired high pressure gasifier, developed specifically for biomass power generation. The major system components for this analysis included wood handling and drying, followed by gasification for which an air separation unit is required, reforming, shift conversion, and hydrogen purification. Because the gasifier operates at a high pressure, 2 MPa, only a small amount of compression is needed to obtain the required steam reforming pressure of 3.5 MPa. A large amount of heat integration was required because of the wood drying and steam production requirements for the gasifier, reformer, and shift reactors. The reformer and shift reactors are of the same design as those used for the BCL analysis which is described in the above text. The gasifier was modeled in ASPEN Plus© using run data from the IGT 9 Mg/day test facility. The cost of the IGT gasifier was scaled from literature data and previous studies (Craig and Mann, 1996; Stone & Webster, Weyerhaeuser, Amoco, and Carolina Power & Light, 1995; Wright and Feinberg,1993).

The Texaco Partial Oxidation / Gasifier Reactor

The Texaco gasifier is a high temperature, high pressure entrained flow partial oxidation reactor. Both gasification and reforming reactions take place in this vessel. Thus, this is the only system examined that does not require a separate catalytic steam reforming step. Unlike the other two gasifiers studied in this analysis, the feedstock to the Texaco gasifier was biomass-derived pyrolysis oil. A liquid feedstock is preferred because it will be easier to feed to the high pressure gasifier than solid biomass. The Texaco gasifier has not yet been tested with pyrolysis oil (or biomass). Therefore, in order to estimate the synthesis gas yield, the gasifier was modeled in ASPEN Plus© using coal data (Pietruszkiewicz *et al*, 1988). An approach to equilibrium (ATE) was determined and the simulation was run using the following empirical formula for pyrolysis oil: $CH_{1.33}O_{0.53}$ (55 wt% C, 6 wt% H, 39 wt% O). The same steam requirement, temperature, pressure, and heat loss as the coal system were used. The oxygen required was varied until the heat loss from the gasifier equaled that derived from the coal data.

For this particular analysis, it was assumed that the pyrolysis oil will be shipped from several remote locations to the hydrogen production facility. Many small pyrolysis plants can be built to meet the oil feed requirements of the hydrogen production facility, allowing these plants to be constructed in areas where biomass residues are available, and thus at lower prices.

Because the Texaco gasifier operates at such high temperatures, two system designs were examined to determine which would be the most economical in regards to hydrogen production. In the first analysis, sensible heat was recovered for steam production by radiant and convective heat exchangers from the hot gas stream exiting the gasifier. This option is often considered economical for electricity production because the steam is used to produce power via a steam turbine. In the second analysis, the hot gas was cooled directly at the exit of the gasifier by a water quench. This option does not require the additional heat exchange equipment that is required in the first option, but because the water is put directly into the gas stream, heat recovery will be minimal.

Literature data along with information from Texaco were used to determine the cost of the Texaco gasifier and the oxygen plant while the heat exchangers, pumps, reactors, and PSA were costed individually (Pietruszkiewicz *et al*, 1988; Geosits *et al*, 1994; Matchak *et al*, 1984; Shemo, 1980; Simbeck *et al*, 1983; Winter, 1997). The operating costs for these processes include the wood or oil feedstock, electricity for operating pumps and compressors, water for cooling and steam generation, and labor. Operating costs were also obtained for the air separation unit and the PSA unit.

Results of the Biomass Analyses

Table 5 is a summary of the hydrogen production rates for each system for each of the three feed rates studied. The IGT system produces 5.6% more hydrogen than the BCL system and 12.5% more than the Texaco system.

Table 5: Hydrogen Production Rates

	H_2 produced (kg/day)		
Biomass feed rate (bone dry Mg/day)	BCL	IGT	Texaco
300	21,044	22,232	19,767
1,000	70,148	74,106	65,891
1,500	105,222	111,159	98,836

Table 6 shows the total capital investment (TCI) for each system for each of the three feed rates studied. The factors required to determine TCI based on the total delivered equipment costs were taken from Peters and Timmerhaus (1991), which gives a factor of 3.15. Note that for the Texaco system, the capital cost of the pyrolysis plant are included in the cost of the oil feedstock for the hydrogen production plant, making the capital cost of the Texaco quench system appear to be significantly less than that of the IGT system.

Table 6: Total Capital Investment Costs

	Total Installed Capital Investment (million U.S. $)			
Biomass feed rate (bone dry Mg/day)	BCL	IGT	Texaco - quench case	Texaco - high temp cooling case
300	40.7	75.4	56.8	83.0
1,000	105.0	175.6	127.6	207.0
1,500	144.5	234.3	168.8	282.8

The highest capital cost items for the BCL/FERCO system are the compressors. The compressor used to move the offgas from the PSA to the primary reformer furnace counts for 23% of the total installed capital equipment cost. The compressor that increases the pressure of the syngas prior to the reformer makes up approximately 17%. The primary reformer is the next most expensive item at 13%. The gasifier train is relatively inexpensive since it operates at low pressures and temperatures lower than the other systems.

For the Texaco system, the air separation unit, followed by the gasifier and water quench, make up the majority of the capital cost at 33% and 30% of the total, respectively. For the IGT analysis, the largest capital costs come from the air separation unit and gasifier at 24% and 23% of the total, respectively.

In the case of the Texaco-based system, the equipment costs of the high temperature gas cooling case were compared with those of the direct quench case. The former case was found to be much cheaper. The main difference is the gasifier and cooling equipment costs: $37.8 million for the gasifier plus high temperature cooling versus $12.7 million for the gasifier plus quench. The high temperature gas cooling case was found to be uneconomical for hydrogen production compared to the quench case. This is due to the fact that the installed capital cost is $25 million more than the quench case for the same hydrogen production rate, along with the fact that much of the steam produced from cooling the synthesis gas is required by the process and cannot be used to produce export power.

The stoichiometric efficiency (defined in Mann, 1995) and the energy conversion efficiency were calculated for each process. The stoichiometric efficiency is defined as the actual amount of hydrogen produced from the process divided by the maximum theoretical yield of hydrogen from the wood. The following equation shows the stoichiometry for converting bone dry wood to hydrogen.

$$CH_{1.47}O_{0.67} + 1.33H_2O \Rightarrow CO_2 + 2.07H_2$$

The energy conversion efficiency is defined as the energy out of the process divided by the energy into the process. In each process, excess heat is used to produce steam at two pressures: 690 kPa (100 psig) and 3,450 kPa (500 psig). The steam is exported and a by-product credit is taken for steam generation. The following equation shows how the energy conversion efficiency was calculated for these processes.

$$\frac{(H_2)(HHV_{H2}) + (STM_{ex})(\triangle H_{sh})}{(Feed)(HHV_{feed}) + \bar{e}}$$

H_2 = hydrogen produced (kg)
HHV_{H2} = higher heating value of hydrogen (GJ/kg)
STM_{ex} = steam produced which is sold (kg)
$\triangle H_{sh}$ = enthalpy difference between incoming water and steam produced which is sold (GJ)
Feed = wood feed rate (kg)
HHV_{feed} = higher heating value of the wood (GJ/kg)
$\bar{e}$ = imported electricity (GJ equivalents)

The efficiencies calculated for the three gasifier systems are shown in Table 7. The stoichiometric efficiency of the IGT process is slightly higher than the BCL and Texaco processes; however, the BCL system has the highest energy conversion efficiency.

Table 7· Process Efficiencies

	BCL	IGT	Texaco - quench case	Texaco - high temp cooling case
Stoichiometric efficiency	40.7%	43.0%	38.2%	38.2%
Energy conversion efficiency	79.2%	57.8%	76.4%	67.2%

Sensitivity Analyses on the Biomass Systems

Biomass costs were varied to reflect the range of possibilities for residues and those from dedicated biomass supply systems. Figures 4 and 5 show the hydrogen selling price in $/GJ for biomass feedstock costs of $0/dry Mg to $46/dry Mg for the 1,000 dry Mg/day and 300 dry Mg/day plant size, respectively. The lower end of this range represents residues that will be available in small quantities to the pyrolysis-based options and small gasification-based plants. The higher end represents a projected cost for biomass from dedicated feedstock supply systems (i.e., energy crops). Note that it's unlikely that residues will be available in sufficient quantities for the large plant.

Figure 6 shows the sensitivity of hydrogen selling price to capital cost at the 1,000 Mg/day feed rate. The total capital investment determined for each system's base case is shown inside the shaded boxes in bold-face type. The value in the shaded oval represents the necessary reduction in the capital for the hydrogen selling price to be $14.2/GJ, the high end of current market hydrogen costs. Additionally, the installed capital was varied by +/- 30%; the resulting hydrogen selling price are shown as the end-points of the shaded boxes for each case. With this reduction in capital, the BCL/FERCO gasifier is the only system that can produce hydrogen within the range of current market prices.

Determination of the Costs of Hydrogen Storage and Transportation

An analysis was performed to estimate the costs associated with storing and transporting hydrogen. These costs can be added to hydrogen production costs, like those determined for the solar, wind, and biomass processes, to determine the total delivered cost of hydrogen. Storage methods analyzed include compressed gas, liquid hydrogen, metal hydride, and underground storage. Major capital and operating costs were considered over a range of production rates and storage times. For the transport of hydrogen, compressed gas, liquid hydrogen, metal hydride, and pipeline delivery were considered. Modes of transportation included truck and rail transport for the compressed gas and metal hydride. For liquid hydrogen, ship or barge delivery was investigated as an option in addition to truck and rail transport. Transportation costs were estimated for a range

of production rates and delivery distances. For more information on the assumptions and data sources used to determine costs summarized here, consult Amos (1998).

Storage of Hydrogen

Figure 7 shows the effect of storage time and hydrogen flowrate on cost for four methods of hydrogen storage. Underground storage was found to be the cheapest method of storage at all production rates and storage times because of the low capital cost of the cavern. Most of the cost of underground storage is associated with the electricity requirements to compress the gas, which is independent of storage volume. This means the cost of underground storage is very insensitive to changes in production rate or storage time. An important consideration with underground storage, however, is the value of the hydrogen remaining in the cavern. Once a site is identified, the cost of not being able to use or sell this hydrogen should be added to the total storage costs.

It was assumed that the metal hydride storage provided no economy of scale, so its hydrogen storage costs are independent of flowrate. Therefore, it cannot compete with the other storage options at long storage times or high hydrogen flows. Because the alloy capital cost is a major portion of the total hydride storage cost, there is very little change in hydride storage costs with higher heating costs. Metal hydride storage, however, does compete with liquid hydrogen and compressed gas storage at low flowrates and short storage times.

Liquid hydrogen storage is not economical at low production rates because of the high capital cost of the liquefier. Even at higher production rates, compressed gas is more economical for short storage periods. However, as the storage time increases, liquid hydrogen has an advantage over compressed gas because the capital cost of a liquid hydrogen dewar is less than that of a compressed gas pressure vessel. Because of the low cost of the dewar, liquid hydrogen storage costs are relatively insensitive to storage time. At high production rates, economy of scale factors reduce the storage costs until they are eventually limited by the electricity costs associated with liquefaction. It was found in the analysis that boil-off rate is not a major cost factor until the storage time was longer than a week; for short-term storage, some cost savings may be possible by using cheaper insulation.

Compressed gas storage competes with liquid hydrogen and metal hydride storage for small quantities of hydrogen and low production rates. At low production rates, the capital cost of the pressure vessel is large, but at higher production rates, the storage cost is eventually limited by the compressor electricity cost because of an economy of scale effect. As storage time increases, the capital cost of the pressure vessel drives up the storage cost.

One option for compressed gas storage is to increase the operating pressure of the system. While this increases the cost of the pressure vessel and compressor, the reduction in tank size can result in overall savings. For short storage periods with compressed gas, an optimum occurs where the reduction in tank capital costs is balanced against the increased compressor and compressor electricity costs. At longer storage times, the capital cost reduction becomes the important factor, so the optimum occurs at the maximum operating pressure which minimizes the tank size and cost.

Transportation of Hydrogen

Figure 8 shows the effect of storage time and flowrate on the most important options for the transportation of hydrogen. Liquid hydrogen transport by truck is the cheapest alternative, except for large quantities of hydrogen, when pipeline delivery becomes competitive. At longer distances, the capital cost of the extra pipeline requires more hydrogen flow before it will compete with liquid hydrogen delivery. Because installation costs dominate the total cost of hydrogen transport by pipeline, sharing a larger pipeline between

several suppliers and users would reduce these costs; this is what is currently done along the Gulf Coast and around the Great Lakes. It's important to note that very little energy is required to move hydrogen through a pipeline. Bringing the hydrogen up to pressure would require a great deal more energy than is shown; such power requirements were incorporated into the previously described storage costs.

In all cases, except pipeline delivery, there is a minimum transport cost associated with each delivery method for a given distance. This point is reached when the production rate is high enough that the truck or rail car is being fully utilized 100% of the time. As an example, consider the case of a small hydrogen plant that doubles it's production rate and instead of making one trip per day with a liquid hydrogen truck, it makes two trips per day. The total capital cost remains the same, the cost of one truck, but this cost is now spread out over twice as much hydrogen. If a truck is already fully utilized, however, any increase in production will require purchasing another truck and produces no reduction in transport costs. The lowest capacity methods bottom-out first for any given distance as production rate increases.

As expected, the truck transport costs increases with distance because of the higher labor and fuel costs. Capital costs also increase with distance. For short distances, one truck can make multiple trips each day, but as the distance increases, more trucks are needed because more time is spent in transit--there is less chance to use the same truck for multiple trips. Compressed gas transport is affected the most because that method requires the most trips, but for all methods, labor costs quickly start to dominate for distances over about 160 km (100 miles). Compressed gas delivery costs also see the largest affect from fuel price for the same reason.

For small production rates, liquid hydrogen transport costs are high because the truck is not fully utilized and it may only make a few trips per week. At these low flows, the truck capital cost contribution is the largest cost, but the costs are also less sensitive to distance since there are far fewer trips compared to situations at larger production rates. At all flowrates, as distance increases, liquid hydrogen delivery charges become dominated by the labor costs. However, with liquid hydrogen, the effect is small compared to compressed gas because the driver is carrying more hydrogen per trip; one hydrogen tanker can carry over twenty times the amount of hydrogen as a tube trailer.

At medium production rates of 450 kg/hr (1,000 lb/hr) and 160 km (100 mile) delivery distances, liquid hydrogen tucking was the cheapest means of transport, but metal hydride also competes because of its high storage density. For comparison showing the effect of capacity, at the above production rate and delivery distance, you would need 15 tube trailers making sixty trips per day (four trips per truck), 6 hydride trucks making 24 trips per day (4 trips per truck) or one liquid hydrogen truck making three trips per day.

In comparing transportation costs, it's interesting to note differences in capital expenditures. For transporting the same amount of hydrogen the same distance in the above example, the price of one liquid hydrogen tanker with cab is $500,000; the price of 15 tube trailers with cabs is about $3.75 million, and the price of six metal hydride transports is $6.9 million.

Combined Storage and Transportation Costs

When considering the delivered cost of hydrogen, it is important to understand that there are three factors to consider: production rate, delivery distance and storage time. In some cases, these factors are dependant upon each other. For example, storage time may depend on delivery distance. If a small hydrogen plant is producing one truck of hydrogen every four days, it might need three days of storage if the truck is making a delivery far away and the truck is on the road the whole time. On the other hand, if the delivery distance is ten miles, the most that would be needed is one day, since the truck would only be gone from the site a short time. This becomes more of an issue with rail cars, which may be gone for an long as three days for a short

delivery distance. (One day in transit to the customer, one day to unload and switch and a third day to bring it back.)

Different transport and delivery options can also be mixed. For example, metal hydride delivery would be compatible with compressed gas, underground or even liquid hydrogen storage. (Although it does not make sense to evaporate liquid hydrogen for transport, it is theoretically possible.) Pipeline transport without any storage may also be an option.

Figures 9 and 10 give combined storage and transportation costs for two distances (160 km and 1,600 km) for a production rate of 500 kg/hr and a storage time of one day. This production rate may describe the situation for future renewable and small-scale generation. When both the storage and delivery costs are added, the benefit of liquid hydrogen becomes apparent. For a delivery distance of 160 km (100 mile), liquid hydrogen is only slightly cheaper than metal hydride transport. At a longer distance of 1,600 km (1,000 miles), however, liquid hydrogen is four times cheaper than metal hydride storage and seven times cheaper than compressed gas.

Conclusions

Hydrogen production by direct conversion of sunlight by photoelectrochemical devices has the potential to be economically feasible. If research goals on efficiency and stability can be met, the selling price of the product hydrogen will be less than that projected for direct PV/electrolysis systems. Interacting with the grid such that higher value electricity can be sold and lower priced electricity bought, while maximizing electrolyzer use, makes a significant impact on the economics of producing hydrogen by PV/electrolysis. Such coupling also makes wind-based systems more economical, although to a lesser extent. The optimal scenario studied involves electrolysis with only renewable electricity and less expensive non-peak electricity. However, the delivered cost of hydrogen will be cheapest from the decoupled scenarios (Scenarios 3a and 3b) since it is produced at its point of use.

In the analysis of biomass to hydrogen, the BCL/FERCO gasifier produces the cheapest hydrogen. For the 1,000 dry Mg/day plant size, the required hydrogen selling price for the three systems examined ranges from $5/GJ to $23/GJ for a feedstock cost of $0/Mg to $46/Mg. Of the different options studied, only the BCL system produces hydrogen for prices that can compete within the current range of industry selling prices for end-of-pipe hydrogen. For the IGT and Texaco systems, a feedstock sensitivity analysis showed that in order to bring the hydrogen selling price down to $14/GJ, negative-priced feedstocks would be required.

An assessment of the costs to store and transport hydrogen shows that at moderate production rates and short distances, gas storage and metal hydride transport is cheapest. At longer distances, liquid storage and liquid transport is the preferred combination.

Acknowledgments

Our thanks to the following researchers and analysts for providing information for analyses described in this paper: Dr. John Turner, Dr. John Thornton, Dr. Jerry Olson, and Mr. Richard Mitchell, Dr. Richard Rocheleau, Mr. Phillip DiPietro, Mr. Joseph Iannucci, Mr. James Eyer, Dr. Henrik Wallman. Additionally, our thanks to the Department of Energy for funding this work and to Catherine Gregoire Padró for providing valuable guidance.

References

Amos, W. (1998). *Costs of Storing and Transporting Hydrogen.* National Renewable Energy Laboratory Report no. NREL/TP-570-25106. Golden, CO: NREL.

Craig, K.R.; Mann, M.K. (October 1996). *Cost and Performance Analysis of Biomass-Based Integrated Gasification Combined Cycle (BIGCC) Power Systems.* National Renewable Energy Laboratory Report no. NREL/TP-430-21657. Golden, CO: NREL.

EPRI. (1997). *Renewable Energy Technology Characterizations.* Electric Power Research Institute. Report no. TR-109496. Palo Alto, California.

Geosits, R.; Wen, H.; Mohammad-Zadeh, Y.; Blamire, D.; Granatstein, D. (September 1994). *IGCC Integration Assessment.* Canadian Electrical Association. Montreal, Canada. Report number CEA-9139-G-941.

Kocha, S.; Peterson, M.; Arent, D.; Scott, H.; Frank, A.; Turner, J. (1996). Photoelectrochemical Based Direct Conversion Systems for Hydrogen Production. Proceedings of the 1996 U.S. DOE Hydrogen Program Review. Volume 1. National Renewable Energy Laboratory Report no. NREL/CP-430-21968. Golden, CO. pp. 333-344.

Kocha, S.; Gao, X.; Frank, A.; Turner, J. (1997). Photoelectrochemical Based Direct Conversion Systems for Hydrogen Production. Proceedings of the 1997 U.S. DOE Hydrogen Program Review. National Renewable Energy Laboratory Report no. NREL/CP-430-23722. Golden, CO. pp. 117-126.

Mann, M.K. (August 1995). *Technical and Economic Assessment of Producing Hydrogen by Reforming Syngas from the Battelle Indirectly Heated Biomass Gasifier.* National Renewable Energy Laboratory Report no. NREL/TP-431-8143. Golden, CO: NREL.

Mann, M.; Spath, P.; Kadam, K. (1996). Technoeconomic Analysis of Renewable Hydrogen Production, Storage, and Detection Systems. Proceedings of the 1996 U.S. DOE Hydrogen Program Review. Volume 1. National Renewable Energy Laboratory Report no. NREL/CP-430-21968. Golden, CO.

Matchak, T.; Rao, A.; Ramanathan, V.; Sander, M. (April 1984). *Cost and Performance for Commercial Applications of Texaco-Based Gasification-Combined-Cycle Plants.* Volume 1: Summary and Discussion of Results and Volume 2: Design Details. Prepared by Flour Engineers, Inc. for EPRI. Final Report number AP-3486.

Olivia, J; Shemo, S. (June 1980). *Texaco-Based Gasification-Combined-Cycle System Performance Studies.* Prepared by General Electric Company for EPRI. Final Report number AP-1429.

Peters, M.; Timmerhaus, K. (1991). *Plant Design and Economics for Chemical Engineers.* McGraw Hill, Inc. New York, New York.

Pietruszkiewicz, J.; Milkavich, R.; Booras, G.; Thomas, G.; Doss, H. (September 1988). *An Evaluation of Integrated-Gasification-Combined-Cycle and Pulverized-Coal-Fired Steam Plants.* Volume 1: Base Case Studies. Prepared by Bechtel Group, Inc. for EPRI. Final Report number AP-5950.

Quah, M. (1998). Presentation to the Hydrogen Technical Advisory Committee, Arlington, VA. March 2, 1998.

Rocheleau, R.; Miller, E.; Misra, A. (1996). Photoelectrochemical Hydrogen Production. Proceedings of the 1996 U.S. DOE Hydrogen Program Review. Volume 1. National Renewable Energy Laboratory Report no. NREL/CP-430-21968. Golden, CO. pp. 345-352.

Simbeck, D.; Dickenson, R.; Oliver, E. (June 1983). *Coal Gasification Systems: A Guide to Status, Application, and Economics.* Prepared by Bechtel Synthetic Fuels Associates, Inc. for EPRI. Final Report number AP-3109.

Stone & Webster, Weyerhaeuser, Amoco, and Carolina Power & Light. (June 1995). *New Bern Biomass to Energy Project Phase 1 Feasibility Study.* Response to NREL Contract No. LOI No. RCA-3-13326.

Winter, J. (1997). Personal correspondence. Technologist for Texaco at the Montebello Technology Center. Montebello, CA.

Wright, J.; Feinberg, D. (October 1993) *A Comparison of the Production of Methanol and Ethanol from Biomass.*

Figure 1: The Projected Selling Price of Hydrogen from Sunlight and Wind in 2000

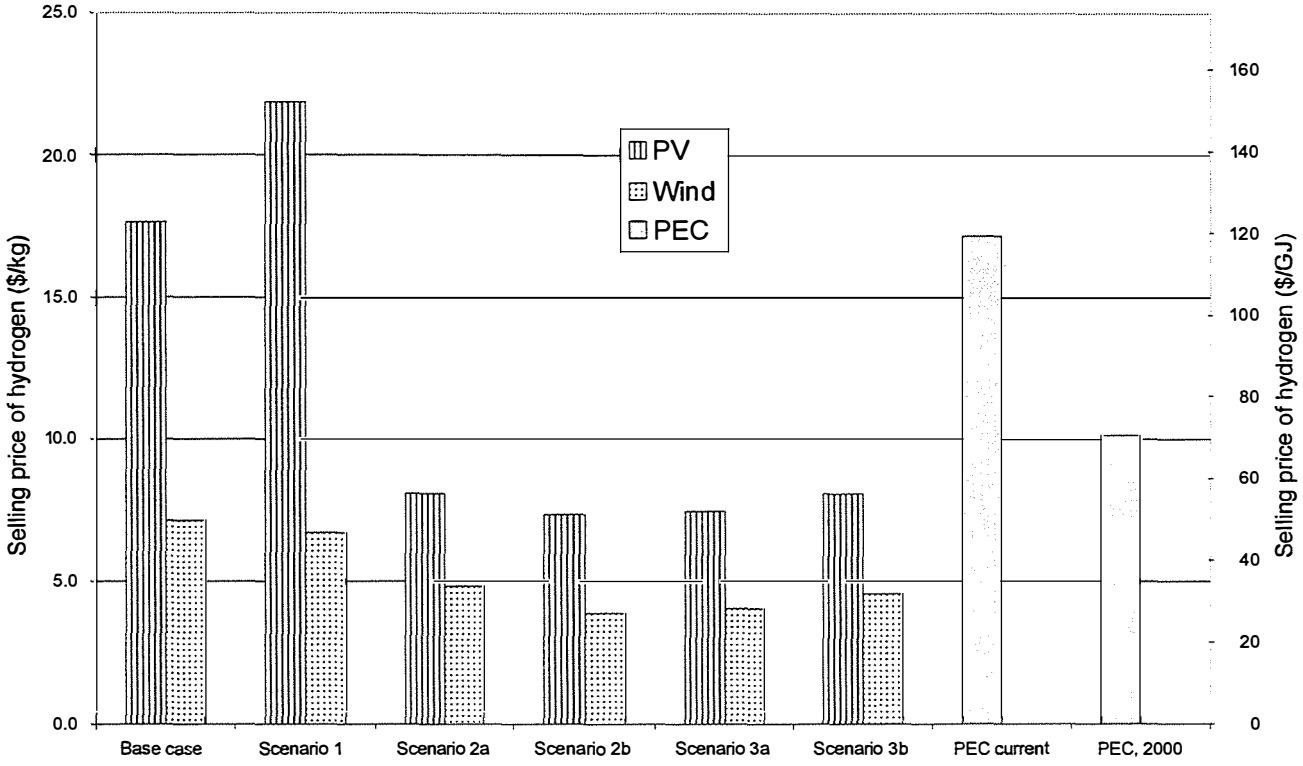

Figure 2: The Projected Selling Price of Hydrogen from Sunlight and Wind in 2010

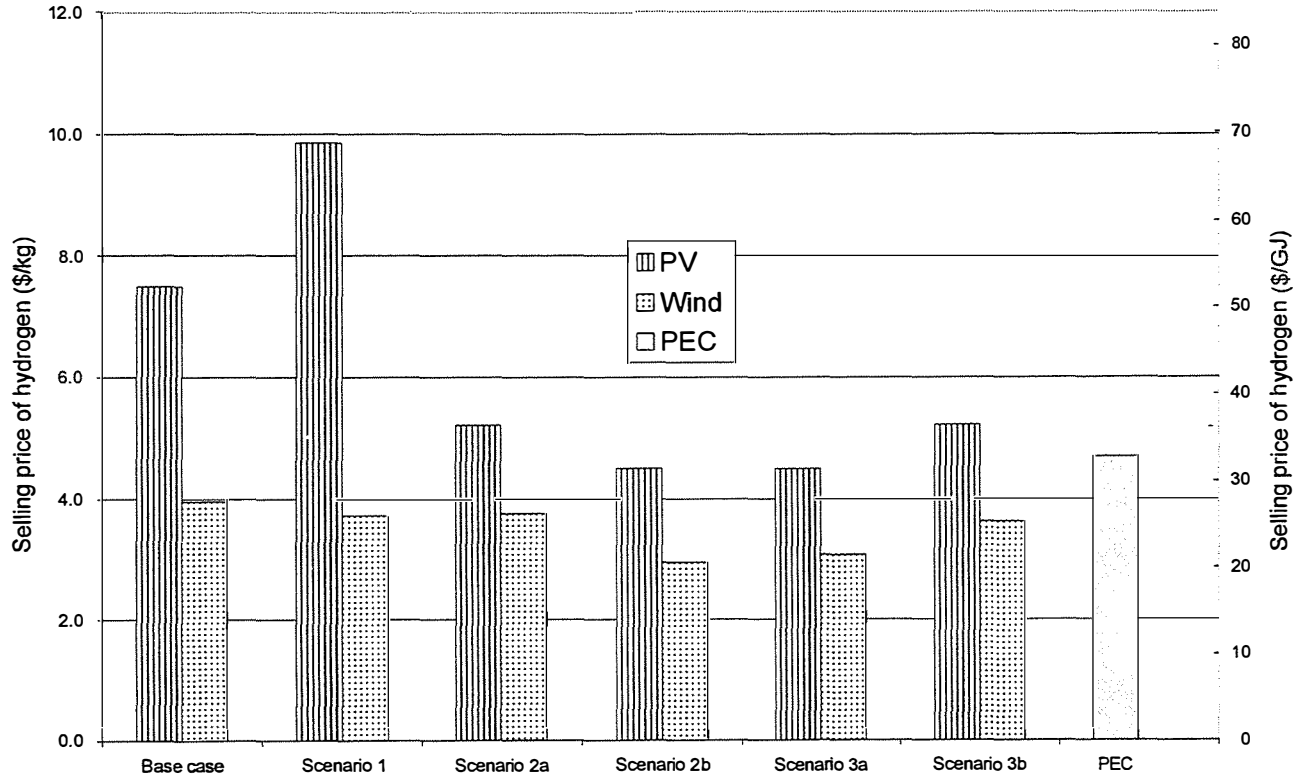

Figure 3: Major Thermochemical Options For The Conversion Of Biomass Into Hydrogen

Gasification in the BCL/FERCO Gasifier Followed by Steam Reforming

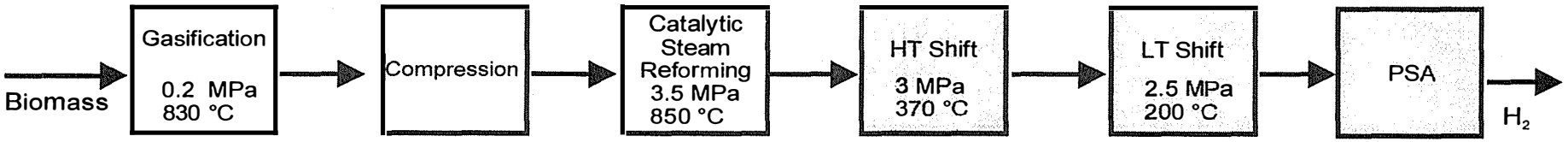

Gasification in the IGT Gasifier Followed by Steam Reforming

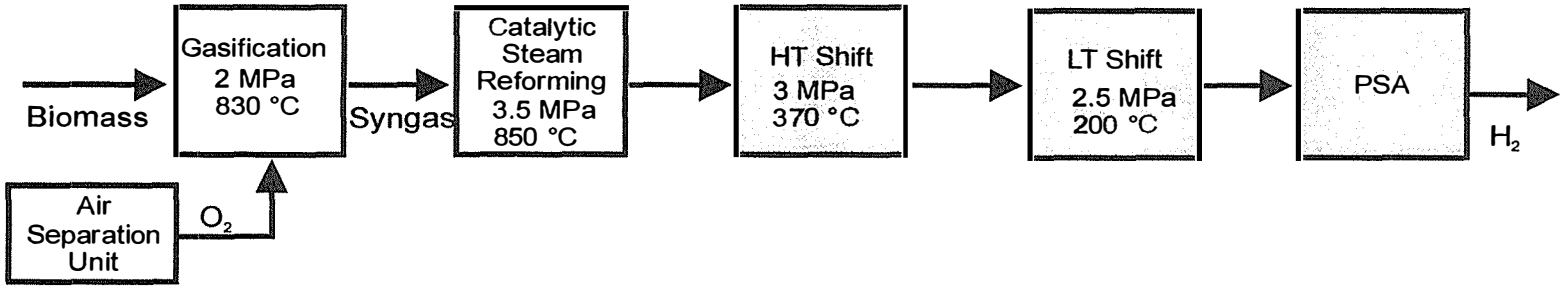

Pyrolysis Followed by Partial Oxidation in the Texaco Gasifier

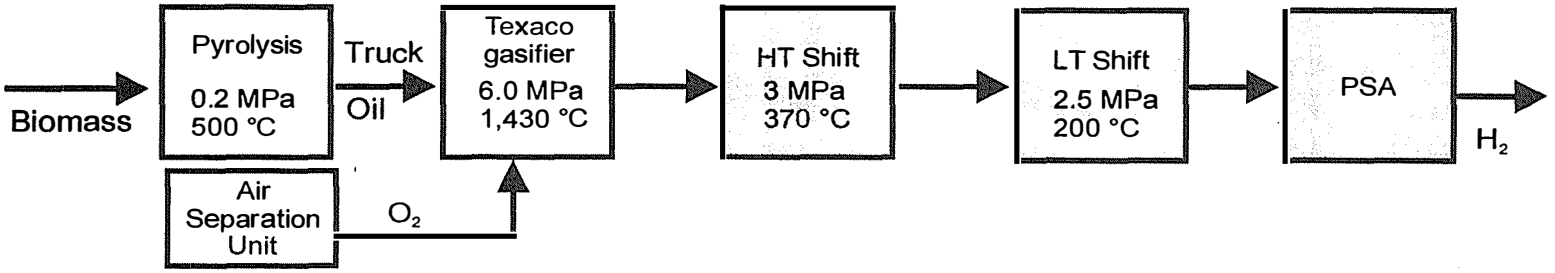

Shaded boxes represent process steps that are common to all systems

Figure 4: The Selling Price of Hydrogen from Biomass at 300 Mg/day

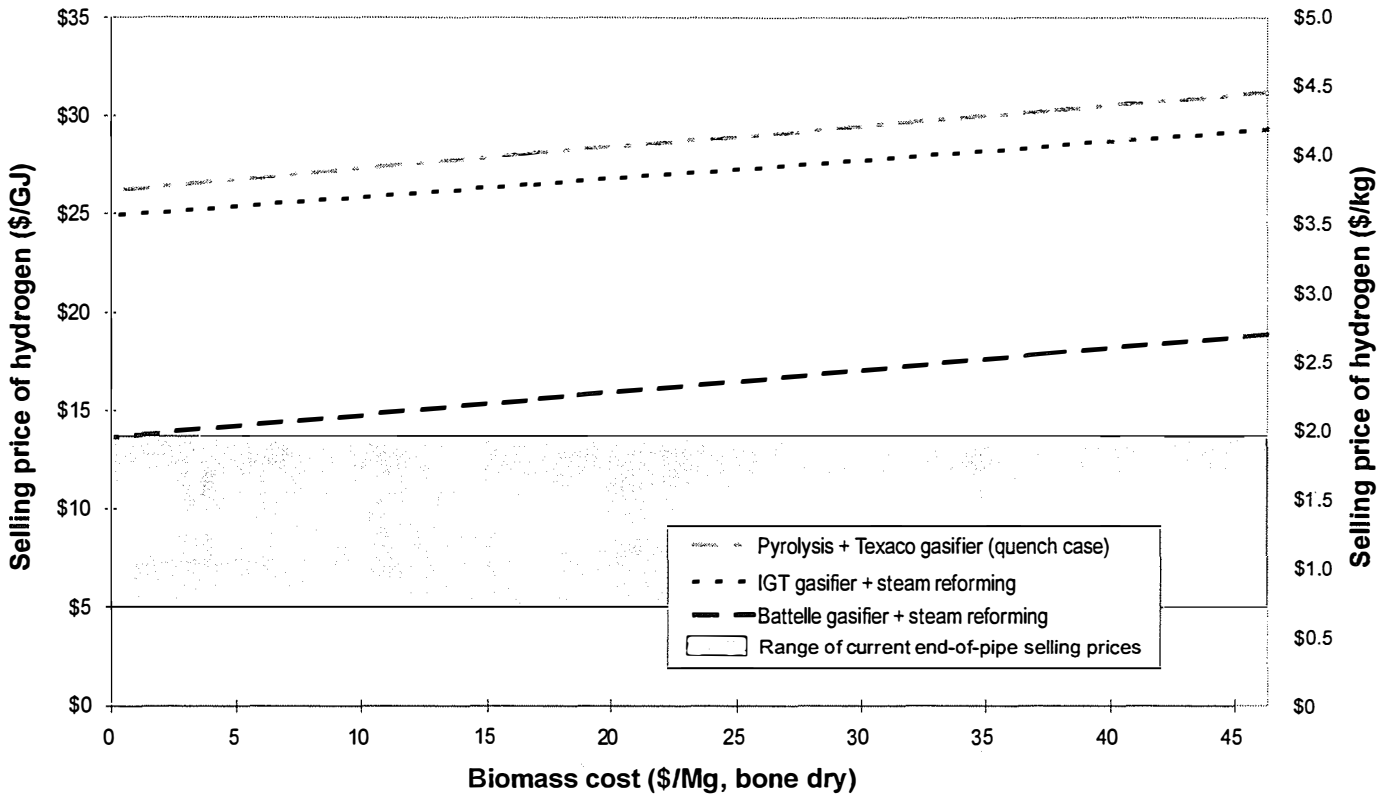

Figure 5: The Selling Price of Hydrogen from Biomass at 1,000 Mg/day

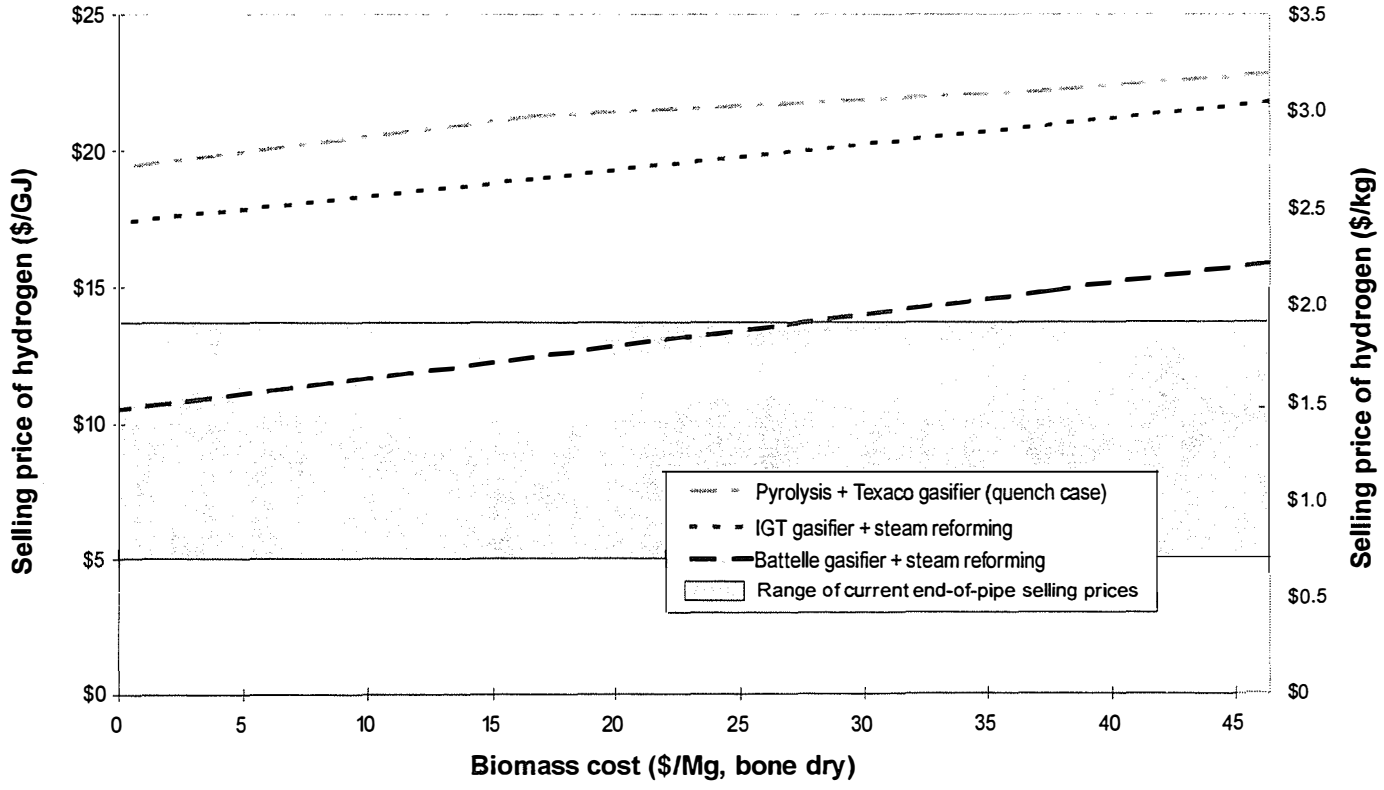

Figure 6: Hydrogen from Biomass: Sensitivity of Hydrogen Selling Price to Capital Cost (1,000 Mg/day plant size, wood feed = $46/dry Mg)

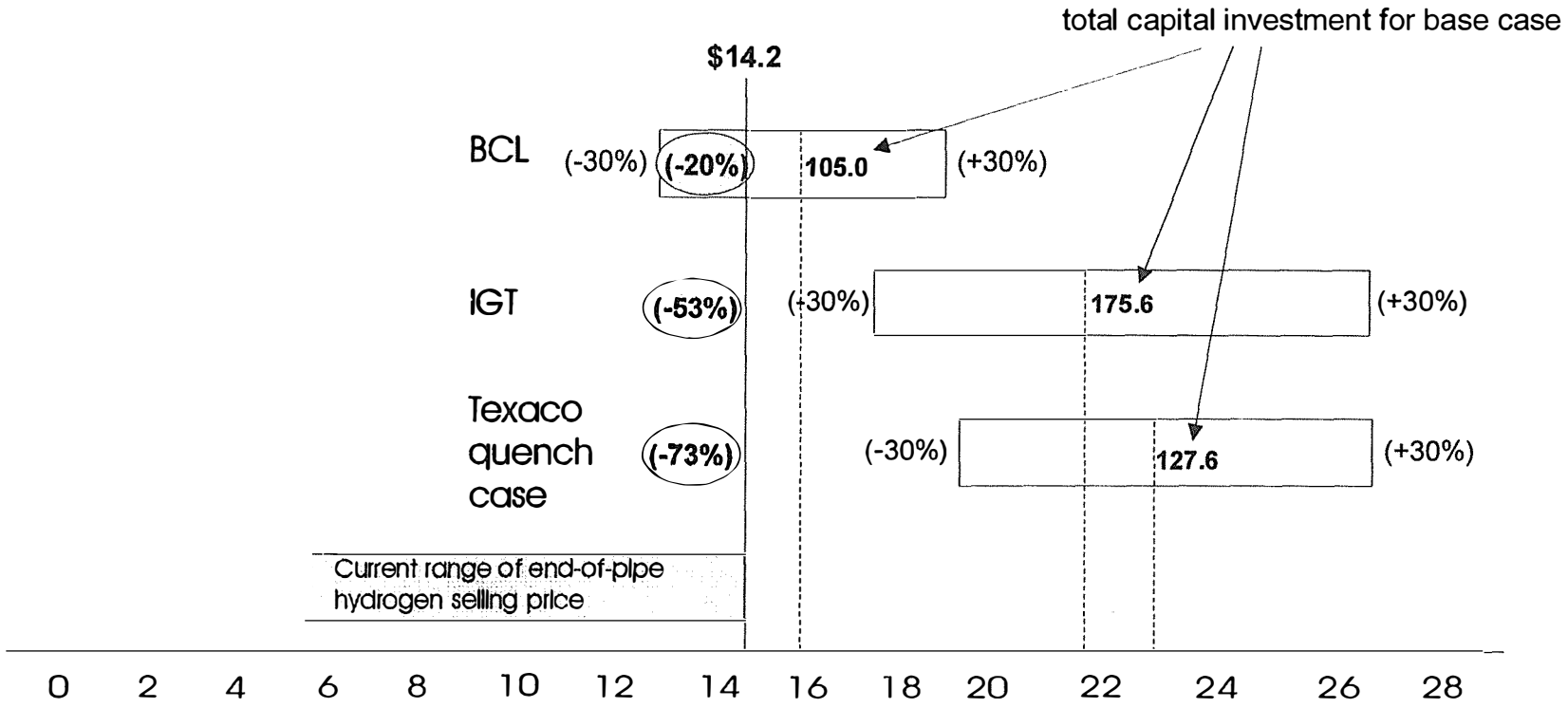

base case result indicated with dashed line

Figure 7: Primary Methods of Hydrogen Storage

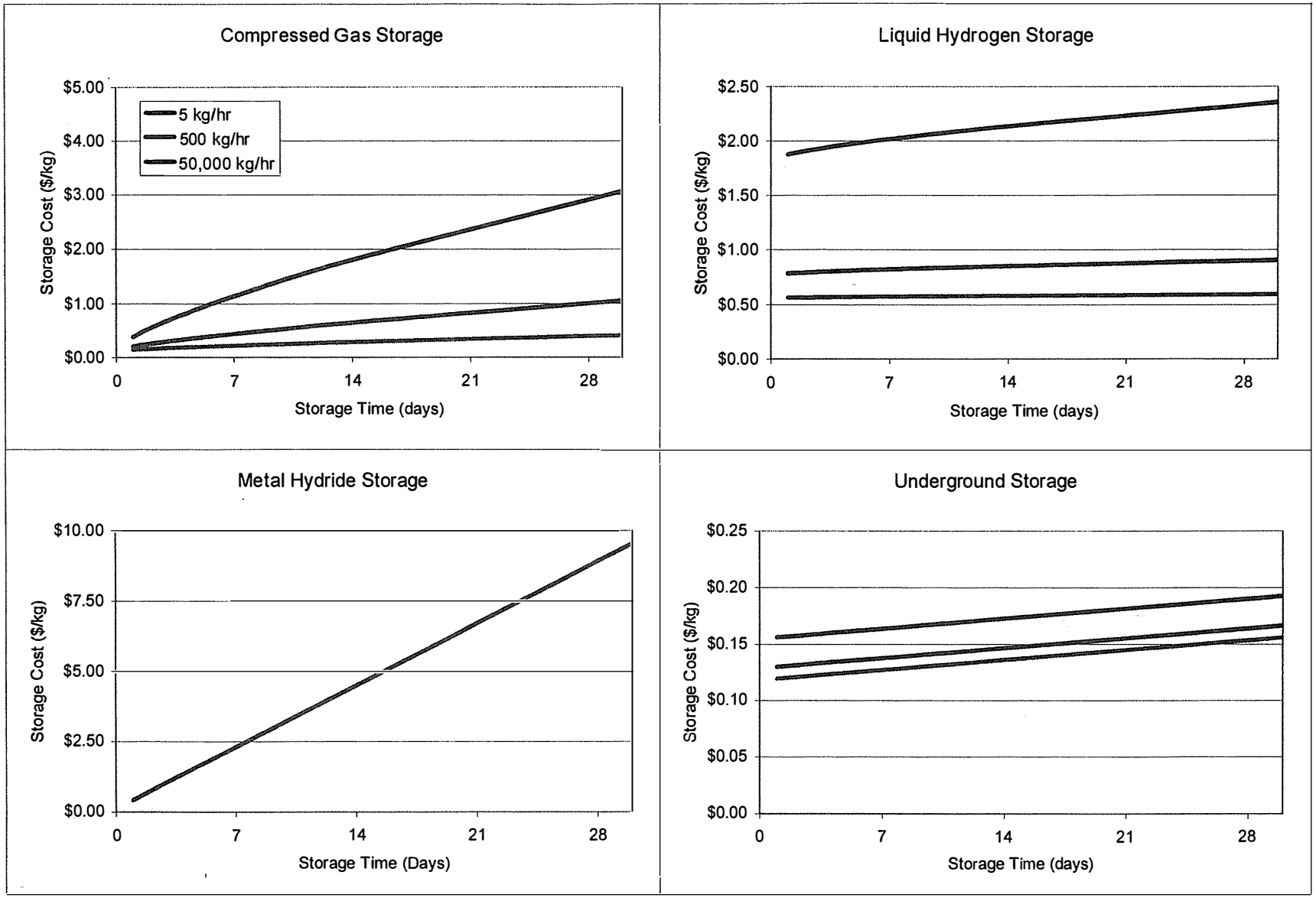

Figure 8: Primary Methods of Hydrogen Transportation

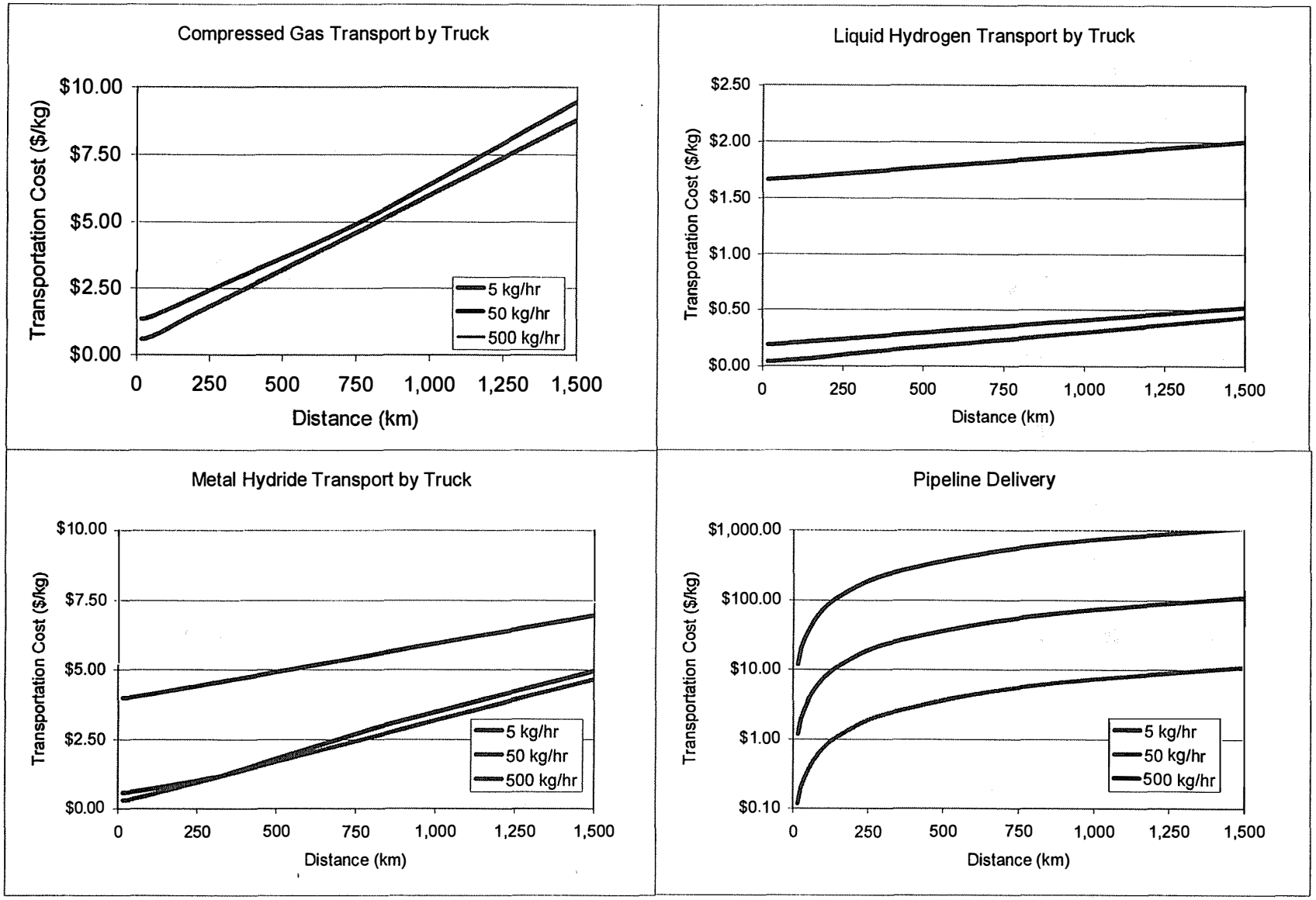

Figure 9: Combined Storage & Transportation Cost
(500 kg/hr, 160 km, 1 day of storage)

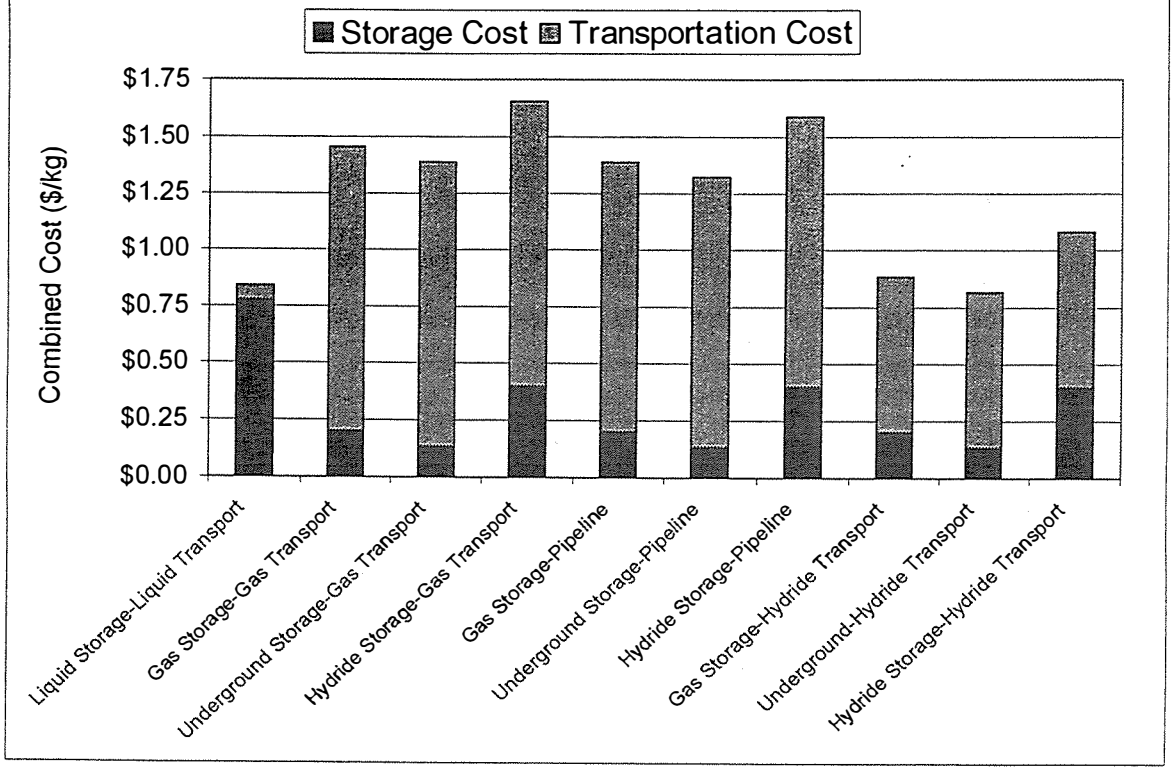

Figure 10: Combined Storage & Transportation Costs
(500 kg/hr, 1,600 km, 1 day of storage)

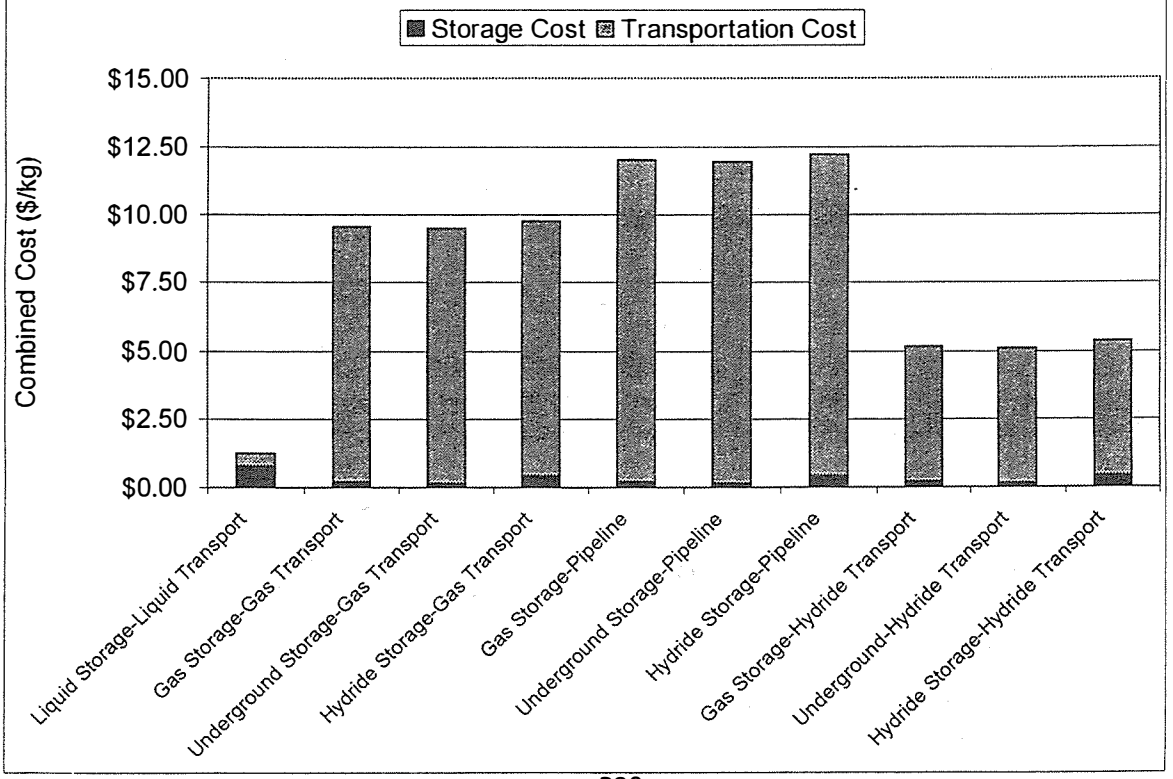

Technical and Systems Evaluations

Edward G. Skolnik and J. Philip DiPietro
Energetics, Inc.
501 School Street SW
Washington DC 20024

Abstract

During FY 1998 Energetics performed a variety of technology-based evaluations for the Hydrogen Program. Three evaluations are summarized below: hydrogen bromine-based electricity storage, carbon-based hydrogen storage, and hydrogen-fueled buses.

Hydrogen Bromine-based Electricity Storage

The hydrogen bromine electrochemical cycle, shown in reaction {1} below, has been previously recommended as a means of storing electricity because, unlike the water cycle, it is highly reversible with demonstrated electric-to-electric efficiencies of 80% or higher (Fritts and Savinell 1983, Balko and McElroy 1980). The HBr-based electricity storage system is best suited for 6-10 hour peak shaving applications and is envisioned as a part of a distributed generation system.

$$H_2 + Br_2 \text{ <-----> } 2\,HBr \qquad \{1\}$$

Figure 1 is a schematic of the proposed HBr-based electricity storage system. The heart of the system is the reversible PEM cell, which can be operated in either electrolysis or galvanic mode. Because the HBr reaction is highly reversible, the electrode catalysts for electrolysis and galvanic operation are not highly specialized, making it less challenging to fabricate a reversible cell that is efficient in both directions.

The process operation is as follows. HBr is electrolyzed during periods of low electricity demand, forming bromine liquid and hydrogen gas which are stored. Hydrogen gas and bromine are recombined in the cell during peak demand hours to produce electricity. A power electronics component rectifies/inverts electricity in and out of the electrochemical cell and manages the

voltage difference between the stack and the load.

This HBr technology is being developed by SRT Group and National Power, who have developed solar-based HBr energy systems and sodium bromide electrochemical energy storage systems, respectively. The hydrogen bromine electricity storage is in the pre-commercial stage and faces the following technical challenges:

> Previous laboratory scale demonstrations of HBr cell efficiencies were conducted at low current density (i.e., less than 200 Amps/ft^2). High efficiency must be demonstrated at a current density above 500 Amps/ft^2.
>
> Because hydrobromic acid is electrically conductive, shunt currents limit the number of cells that can be stacked in a bipolar configuration. Modular stack output potential is limited to 10-20 volts. Such low voltage will create high resistive losses and increase the cost of power electronics equipment, which is generally current-limited. Several stacks could be externally wired in series, but this increases the cost of the system as well. An optimal system that considers stack voltage limitation must be developed.
>
> The field life of the membrane electrode assemblies (MEAs) must be demonstrated. Because of the toxicity of the reactants, changing out the MEAs could be expensive compared to a water system. We project that an MEA life of 5-7 years is required for an economic system.
>
> The cost of the hydrogen compressor is based on the assumption that the gas outlet pressure from the PEM stack is 1,000 psi. In theory, a high hydrogen gas outlet pressure is achievable at low cost by pressuring the water inlet. If only a 200 psi outlet pressure is achievable, the cost of the hydrogen compressor would double.

Table 1 shows a capital cost estimate for a 300 kW 8 hour HBr-based electricity storage system. The estimate is based on a 72% AC/AC round-trip efficiency, a reversible PEM stack cost of 350 $/kW, and a power electronics cost of roughly 175 $/kW. All these estimates were provided by SRT Group and National Power and inherently rely on the resolution of the above technical issues.

A financial analysis of the system was conducted based on a hypothetical commercial or industrial facility that faces a time-of-use electric rate structure and buys an HBr system to reduce its electric bill. The HBr system would be operated 8 hours per day, 250 days per year. A pro forma cash flow analysis model was used to determine the energy rate for peak electricity required to yield a 15% after-tax internal rate of return based on an off-peak electric rate of 2 cent/kWh and a demand charge of 8 $/kW/month (financial analysis assumptions include 20 year system life, 50% debt/equity, 7.5% interest on debt, 10 year ACRS depreciation schedule and 28% marginal tax rate). The base case peak electricity cost is 7.9 cents/kWh. Figure 2 shows that the required cost of peak electricity varies between 6 and 12 cents/kWh based on changes in several key assumptions.

Table 1. Capital Cost Estimate for a 300 kW, 8 hour Hydrogen Bromine-based Electricity Storage System

Component	Cost
PEM stack (300 kW, 350 $/kW)	105,000
Power electronics (inverter 125 $/kW, rectifier 50 $/kW)	55,000
Hydrogen Compressor (10 kW, 12.6 kg H_2 per hr)	26,300
Hydrogen gas storage (84 kg, 400 $/kg)	33,800
Acid storage tank (Kynar, 10.7 m^3, 6,000 $/$m^3$ installed)	64,000
Piping and controls	30,000
Assembly and installation	30,000
Total capital cost	**$ 344,100**
Size of equipment based on a 72% round trip efficiency	

As a comparison, a diesel generator (12 kWh/gallon efficiency, 1 $/gallon fuel cost, 1 cent/kWh O&M) operated 8 hrs/day 250 days per year requires an electricity rate of 5.4 cents/kWh to yield a 15% IRR. On the other hand, the 1996 average rate for electricity for industrial customers in New England was 7.92 cents/kWh (both peak and off-peak, *Electric Power Annual* 1996 Volume II, 1997). Our assessment is that the HBr-based electricity storage system has the potential to be commercially viable if the developers achieve their cost and efficiency goals.

A proposed area of future work is to evaluate the HBr system as an addition to wind/diesel hybrid systems in remote applications. The HBr system would manage the interface among the wind turbine generators, the diesel generators, and the load. It would enable the diesel generators to run at a more level rate increasing the fuel efficiency and extending their useful life. Lead acid batteries have been proposed to serve the same function. The HBr system offers the benefit that longer duration storage is less costly. A deeper storage system can capture a significant amount of excess turbine energy and allow a higher capacity wind turbine system for a given size load.

Carbon-based Hydrogen Storage

Carbon-based storage systems use carbon-based structures as a matrix for reversibly binding hydrogen either chemically or physically, providing a hydrogen energy storage medium. Carbon is an attractive material for such a storage system in that it is relatively light and relatively inexpensive. These are two qualities of great importance toward a goal of being able to provide a cost-effective, efficient, on-board storage system for hydrogen. Figure 3 compares the gravimetric and volumetric loading potential of hydrogen in carbon structures with other standard and state-of-the-art hydrogen storage technologies. While some of these other

technologies are close to or at the DOE goal for gravimetric loading, most are well short of the volumetric goal. In addition, some storage systems (liquid hydrogen, for instance) involve an energy-intensive production process. This section compares three somewhat different technologies that rely on carbon to store hydrogen. Each is represented by a project that is currently being supported by the U.S. Department of Energy.

1. Carbon Nanotube Materials for Hydrogen Storage – National Renewable Energy Laboratory
2. Hydrogen Storage in Carbon Nanofibers – Northeastern University
3. Thermal Management Technology for Hydrogen Storage – Oak Ridge National Laboratory

Nanotubes are rolled planar structures in tubular form having nanometer-sized diameters, and lengths that are orders of magnitude (micron range) greater than the diameters. The end caps are fullerene-like structures that must be chemically or mechanically removed prior to hydrogen being able to be sorbed into the capillary. Nanofibers have similar dimensions to nanotubes, but are not hollow. Instead, they are stacked plates of graphitic carbon. The hydrogen selectively fits into the spaces between the plates and is adsorbed onto the planar surfaces. The Oak Ridge project uses C_{60} fullerene cage structures as a means to store hydrogen physically, chemically or both. Table 2 provides some comparative production and utilization parameters for the three carbon structures.

Table 2. Comparison of Technologies Using Carbon Structures for Hydrogen Storage

Project	Production Method	Projected weight % Hydrogen	Postulated Sorption Mechanism	Hydrogenation/ Dehydrogenation Temp	Hydrogenation/ Dehydrogenation Pressure
Nanotubes/ NREL	Arc-Discharge or Laser Vaporization	5-10	Adsorption on inner walls of nanotubes	Room Temp.	Currently 15 psi; (projected to be up to a few hundred psi to fill long tubes)
Nanofibers/ Northeastern	Vaporization and Catalytic Condensation	10-75	Several layers of hydrogen selectively condensed between graphite platelets	Near Room Temp. (possibility of needing additional heat to speed sorption process)	About 1500 psi; pressure to release hydrogen
Fullerenes/ ORNL and MER	Arc-furnace	6-8	Physical sorption and/or chemical reaction	200-400°C (lower w/ catalyst)	500 –4000 psi (lower w/ catalyst)

Carbon Nanotubes, NREL

The NREL project has several years of DOE research behind it, as opposed to the other two relatively newer projects. The project has focused on developing methods to produce nanotubes in quantity and on being able to fill the tubes with hydrogen. As a result, NREL pursued various modifications of arc-furnace and laser vaporization nanotube production methods. To date, the arc-furnace method has produced very low yields of nanotubes (less than 0.1 percent). The nanotubes that were present, however, were able to adsorb up to 10 weight percent hydrogen. The laser vaporization method has produced high yields of nanotubes (60-100 percent). These

tubes, however, are capped with difficult to remove fullerene-structured ends. (The arc-furnace nanotube ends are much less stable). In addition the laser nanotubes have a very high aspect ratio. These two properties are barriers to hydrogen adsorption. The NREL research team is currently focusing on the nanotubes made by laser vaporization, investigating methods that will cut (and in the same process, decap) the tubes.

Nanotubes hold promise for uniformity and reproducibility. Choosing one of the modes of nanotube production appears to produce bundles of nanotubes at a uniform diameter, and these nanotubes will be aligned parallel to one another due to Vander Waal's forces. This leads to an opportunity for easy packing of nanotube bundles into tanks.

Of the three projects discussed here, the NREL project appears to hold out the promise for the operation which is closest to ambient pressure and temperature conditions.

Fullerene Option, ORNL & MER

The fullerene project at ORNL and MER relies on preparation of so-called "bucky balls," caged structures having a basic formulation of C_{60} or higher, and physically or chemically incorporating hydrogen within the structure. The researchers have demonstrated hydrogenated fullerenes as a bulk powder, pelletized, and deposited in a thin film on aluminum foil. Stable three and four percent by weight hydrogen content has been shown.

If we assume that chemically each carbon, being bonded to three other carbons, can bond with one hydrogen forming $C_{60}H_{60}$, such a system would have a hydrogen weight percent of 7.7, effectively putting an upper limit on the maximum potential hydrogen loading.

An interesting argument can be developed if we look at some of the data coming out of this research project. The ORNL and MER researchers (Wang et al 1996) state that if one looks at the removal rate of hydrogen from the hydrogenated fullerene, where no catalyst is being used, it can be found to obey the expression:

$$\text{Rate} = A\,(C/C_{max})\,e^{-E/\kappa T} \qquad \{2\}$$

where C is the hydrogen concentration in the fullerene and C_{max} is its maximum concentration, A is the Arrhenius pre-exponential factor, E is the activation energy, κ is the molecular gas constant, and T is temperature. Since the rate of a chemical reaction, (dr/dt), is a function of the reactant concentrations and a rate constant, the rate of a reaction

$$aA + bB + \ldots nN \;\text{----->}\; \text{Products} \qquad \{3\}$$

can be expressed as:

$$(dr/dt) = \text{Rate} = k\,[C_A]^a[C_B]^b \ldots [C_N]^n \qquad \{4\}$$

where k is the rate constant and C represents the concentration of the species in question.

The Arrhenius expression for the rate constant, k, can be expressed as a function of temperature by:

$$k = A\, e^{-E/\kappa T} \qquad \{5\}$$

Therefore, the expression for the dehydrogenation process in {2} can also be expressed as:

$$\text{Rate} = k\,(C/C_{max}) \qquad \{6\}$$

This is the form of a first-order reaction, dependent only on the concentration of C, in this case, the concentration of hydrogen. This would indicate that since the reaction rate is not dependent on the rate of concentration of the fullerene hydrogenate, that the fullerene hydrogenate is not a chemical species, but that the hydrogen is physically held within the fullerene structure. At least, it indicates that the rate-determining step is the physical removal of hydrogen from the matrix. This means that the theoretical chemical limit to the degree of hydrogenation may not be the actual limit. It also adds some additional interest to this topic in that there is a possibility that both physical and chemical hydrogen take-up is possible, adding to the potential for hydrogen loading.

Indeed, in some of their later work, the researchers have shown that when a catalyst is used in the fullerene system, it appears that a second rate constant comes into effect (Murphy et al 1997). This may indicate that under these conditions a chemical component has been added to the hydrogen sorption mechanism.

Analysis of the fullerene project is not yet completed, and a visit is planned to MER during this fiscal year.

Carbon Nanofibers, Northeastern University

The Northeastern project is the most controversial of the three. The researchers have presented data indicating that they have attained up to 75 percent hydrogen by weight in a carbon nanofiber matrix. Their initial theoretical data indicated that the graphitic plates that make up the nanofiber are planar on a molecular level, and that hydrogen could adsorb on to these planar surfaces in a complete monolayer. Based on the sizes and packing structure of graphite platelets and hydrogen molecules, this would allow 6.9 liters of hydrogen (STP) to adsorb onto each gram of graphite. This is equal to:

(6.9 liters) x (2 g H_2/ 22.4 liters @STP) = 0.62 g H_2, and

0.62 g H_2 on 1 g carbon = 0.62/(0.62 +1) = 38.1 percent by weight hydrogen.

This is a very lofty claim. However, this number still assumes a perfect monolayer of hydrogen

on a perfect planar graphite surface, at the molecular level. One might surmise that a perfect monolayer is unlikely and that the actual amount of coverage of the graphite platelet might be much lower. The researchers, however, claimed that in actuality, the hydrogen take-up was much greater than the monolayer amount, and that in fact, hydrogen was condensing in amounts equivalent to several layers of thickness in between the graphite platelets. Numbers as high as 37 STP liters per gram of carbon (nearly 77 percent hydrogen by weight) were reported informally, and numbers as high as 67 percent hydrogen by weight are reported in the peer-reviewed literature (Chambers et al 1998). Data curves provided by the researchers indicated that exposing the fibers to hydrogen in a closed system at high pressure and room temperature resulted in a pressure drop equivalent to the hydrogen take-up levels claimed, and that exposure to non-nanofiber carbon structures or other materials resulted in little or no pressure drop. The multilayer coverage was attributed to delocalized B electrons associated with the graphite matrix.

The claims here are very great. So are the potential rewards. Inexpensive, safe, on-board storage is important to the use of hydrogen in transportation. If the nanofiber data is indeed accurate, it projects a driving range of up to several thousand miles on a tank of hydrogen (at 10 liters of hydrogen per gram of carbon, a tank 10 gallons in volume would contain enough hydrogen for over 2000 miles of driving).

None of the three carbon-based hydrogen storage projects are close to providing an on-board storage system today, but each has potential. The NREL project will, either by cutting the laser-generated nanotubes or increasing the yield of furnace-generated nanotubes, provide the system that will be able to cycle hydrogen most efficiently, being the closest to ambient conditions (See the Table 2) for temperature and pressure. The fullerene project has demonstrated stable hydrogen containing species with several percent hydrogen present. The fullerenes also require high temperature and pressure conditions to both store and desorb hydrogen. In this way, they are similar to hydrides. The major effort is to catalytically reduce the temperature and pressure requirements. The nanofibers require the most pressurization, and may require some heat to speed the process, but the claimed hydrogen take-up far exceeds all others. The nanotube project is badly in need of independent experimental verification.

Hydrogen-fueled Buses

Table 3 shows significant recent industrial activity aimed at developing hybrid electric power systems for vehicles. A hybrid electric vehicle (HEV) offers improved fuel efficiency, reduced pollutant emissions, and reduced wear and tear on the mechanical components over vehicles powered by a conventional internal combustion engine (ICE). For transit bus applications, hybrid electric vehiles offer adequate range where all-electric vehicles fall short. Most commercial efforts are focused on diesel, gasoline, or natural gas-fueled systems. Energetics has analyzed the feasibility of using hydrogen fuel for hybrid electric power systems and the incremental cost compared to diesel, gasoline, or natural gas-fueled systems. The objective of the analysis is to build on the Hydrogen Program's experience with the Savannah River Bus and explore the impact of more advanced hydrogen storage and hydrogen-fueled electricity generation components. A full report will be published later this year. The analysis and preliminary results are summarized below.

Table 3. Hybrid Electric Vehicle Development Activities

Market	Company /Model	Fuel and power system	Status
Passenger Vehicle	Toyota Prius	Gasoline ICE HEV	Began sales in Japan Dec 10, 1997, has delivered 700 and has 3700 on back order. Monthly production of this car has gone from 1000 to 2000 per month to meet demand. The car travels 66 miles per gallon
	GM Modified EV1	Diesel ICE, Natural gas ICE, and PEM HEV	Experimenting with hybrid electric power systems in the EV1 platform
	Chrysler Intrepid ESX	Diesel ICE HEV	Built a series hybrid electric four door car in 1996, working on a parallel hybrid electric.
	Mitsubishi Space Wagon/ Chariot	Diesel ICE HEV	Mitsubishi is expected to introduce these two cars over the next two years. They have also developed an all-electric Miata.
Transit & School Bus	Bluebird Bus	Diesel, natural gas and H2 ICE HEV	Involved in the hydrogen bus project. Have experimented with natural gas and diesel hybrid electric systems as range extenders for their electric school bus.
	Lockheed-Orion	Natural Gas ICE HEV	Recently won a competitive award to supply 4 diesel hybrid electric buses to New Jersey Transit and 10 diesel hybrid electric buses to New York Transit Authority. Units will be delivered in 1998. Future plans will depend on the performance of these units in the field.
	APS Systems	Prpoane ICE HEV	Plan to put one prototype bus into service in Calfornia in 1998. Nickel cadmium batteries, propane rotary engine.
	Advanced Vehicle Systems	Natural Gas ICE HEV	Built two natural gas hybrid electric buses to be used in Chattanooga, Tennessee.
Military	TDM	Diesel ICE HEV	Won an award to build 10-15 hybrid electric service vehilcles for the US Army.
	Unique mobility HE hummer	Diesel ICE HEV	Developed a hybrid electric hummer for the U.S. Army. Offers improved performance over conventionally-powered hummer. Also, can run in "Stealth mode," running only on the electric motor.

Table 4 shows the curb weights of several diesel, natural gas, and hydrogen-fueled transit buses. Notice that the curb weight of the diesel hybrid electric vehicle is 4,430 pounds higher than the conventional diesel ICE, mostly due to the weight of the batteries. The gross vehicle weight for a diesel hybrid is increased to 38,000 pounds giving a net reduction in people-carrying capacity of 1,430 pounds, or nearly 20%. The natural gas and hydrogen options are heavier still because of the increase in on-board fuel storage and ICE weight compared to diesel. This incremental weight directly displaces people-carrying capacity because the two-axle bus gross vehicle weight is limited to 38,000 pounds by the weight-bearing capacity of the roads.

The data in Table 4 indicate that reductions in the weights of the batteries and power systems are important to developing hybrid electric buses. In reduced range applications or smaller size transit buses the weight limitations may not be as severe.

Table 4. Weights of Conventional and HEV buses

	Diesel		Natural Gas	Hydrogen	
Bus Component	ICE	Hybrid	Hybrid	Pressure Vessel	Mg Hydride
Batteries	0	4,000	4,000	4,000	4,000
Fuel Storage[1]	200	130	170	650	1,900
ICE[2]	2,000	1,400	2,100	2,800	2,800
Motor/ Generator[3]	0	600	600	600	600
Balance	24,800	25,300	25,300	25,300	25,300
Vehicle Curb Weight	27,000	31,430	32,170	33,350	34,600
Gross vehicle weight limitation	36,000	38,000	38,000	38,000	38,000
Passenger weight capacity	**8,000**	**6,570**	**5,830**	**4,650**	**3,400**

[1] Based on a 200 mile range
[2] Diesel engine weight based on 275 hp Navistar Engine; 30% power reduction for HEV; multipliers of 1.5 and 2.0 used for natural gas and hydrogen ICE's respectively
[3] Estimates of advanced systems from Solectria and Fisher Electric Technology

A transit bus will be driven anywhere from 20,000 to 40,000 miles per year, and fuel cost is an important part of the overall bus cost. Figure 4 shows the fuel cost for diesel, natural gas, and hydrogen buses over a range of hydrogen fuel costs. A first-of-a-kind natural gas reformer sized to fuel 40 buses could deliver compressed hydrogen at a cost of 5 $/kg (Thomas, C.E., et al, 1997). Clearly, low-cost hydrogen is needed to enable commercialization of hydrogen fueled buses.

The success of the hybrid electric platform hinges largely on the development of a peaking battery. If an acceptable peaking battery is developed and the hybrid electric platform proves commercially viable, on-board natural gas combustion is a strong

competitor to hydrogen. Diesel emits relatively large amounts of nitrous oxides and particulate matter and not readily comparable to hydrogen. Natural gas exhibits full life-cycle pollutant and greenhouse gas emissions comparable to hydrogen. It is less expensive than hydrogen on a delivered-energy basis, and the efficiency differential between a hydrogen-fed PEM fuel cell and a natural gas ICE are reduced in a hybrid electric platform. (This is driven by the fact that the level operation of the ICE in a hybrid electric platform greatly increases its efficiency, and the parallel hybrid, a new development in hybrid electric vehicles that offers increased fuel efficiency, is not amenable to a fuel cell. A parallel hybrid is a hybrid of a hybrid in which mechanical torque from the ICE can be transferred directly to the wheels when it is optimal to do so. Since a fuel cell does not generate torque, it cannot utilize a parallel hybrid configuration.)

The question then is how can a hydrogen bus be differentiated from a natural gas bus to become preferable? One possible differentiating characteristic is carbon dioxide emissions and global climate change. Because a vehicle with on-board hydrogen storage is carbon-free, it is potentially carbon dioxide emission-free. However, the development of renewable-based hydrogen production technologies and/or carbon dioxide sequestration systems are required to realize zero full life-cycle carbon dioxide emissions. Another potential motivation characteristic is robustness of pollutant emissions. Natural gas ICE systems rely on tailpipe clean-up to achieve low emissions and the performance of the clean-up device may degrade over time and during transient conditions.

Advanced hydrogen storage options being developed by the Hydrogen Program can also differentiate hydrogen from natural gas. These are low-pressure systems that do not require a high-pressure gas compressor and have markedly different vehicle safety characteristics. Hydride and fullerene near- to mid-term options require heat at 120 to 250 °C to release hydrogen and so require an on-board heat balance. This is difficult to achieve with a PEM fuel cell that rejects heat at 60-80 °C. Internal combustion engines operate at 300-400 °C and are a better heat match with advanced hydrogen storage options.

Energetics hopes to pursue a more rigorous analysis of the on-board heat balance issue associated with advanced hydrogen storage options, and assess design tradeoffs among parasitic fuel loss, heat exchanger size, and power system efficiency and operating temperature.

Acknowledgments

Harley Heaton and Robin Parker aided us in our assessment of the HBr-based electricity storage and hydrogen production system. Michael Heben, Nellie Rodrigez, and Fang Chen aided us in our study of carbon-based hydrogen storage systems. Salvador Aceves, Jay Keller, George Thomas, and Sandy Thomas aided us in our assessment of carbon-based hydrogen storage systems. Our analyses are greatly improved due to the benefit of their expertise.

References

Balko, E.N. and McElroy, J.F 1980. "High Energy Density Hydrogen-halogen Fuel Cells for Advanced Military Applications." presented at the *29th Power Sources Conference.* Atlantic City, NJ

Chambers, A. C. Park, R.T.K. Baker and N.M. Rodriguez. *J Phys Chem B*, 1998, in press.

Electric Power Annual 1996 Volume II. 1997. DOE/EIA-0348(96)/2 Table 7. Energy Information Administration

Fritts, S.D. and R.F. Savinell. 1983. "Simulation of a Rechargeable Hydrogen-Bromine SPE Fuel Cell." *AIChE Symposium Series, Electrochemical Applications*, No. 254. Vol. 83

Murphy, R.W., J.C. Wang, F.C. Chen, R.O. Loufty, and X. Lu. 1997. "Thermal Management for Fullerene Based Hydrogen Storage." In *Proceedings of the 1997 U.S. DOE Hydrogen Program Review*, 315-331. Herndon, VA, National Renewable Energy Laboratory.

Thomas, C.E. 1997. *Hydrogen Infrastructure Study prepared for the Ford Motor Company*, Arlington, VA: Directed Technologies, Inc. Page 15, Praxair unit

Wang, J.C., F.C. Chen and R.W. Murphy 1996. . "Thermal Management Technology for Hydrogen Storage: Fullerene Option." In *Proceedings of the 1996 U.S. DOE Hydrogen Program Review*, 819-829. Miami, FL, National Renewable Energy Laboratory.

Figure 1. Schematic of the HBr-based Electricity Storage System

Figure 2. Financial Analysis of a 300 kW, 8 hour HBr-based electricity storage system

Figure 3. Weight and Volume Density of Hydrogen Storage Technologies

Figure 4. Fuel Cost for Transit Buses

Figure 1. Schematic of the HBr-based Electricity Storage System

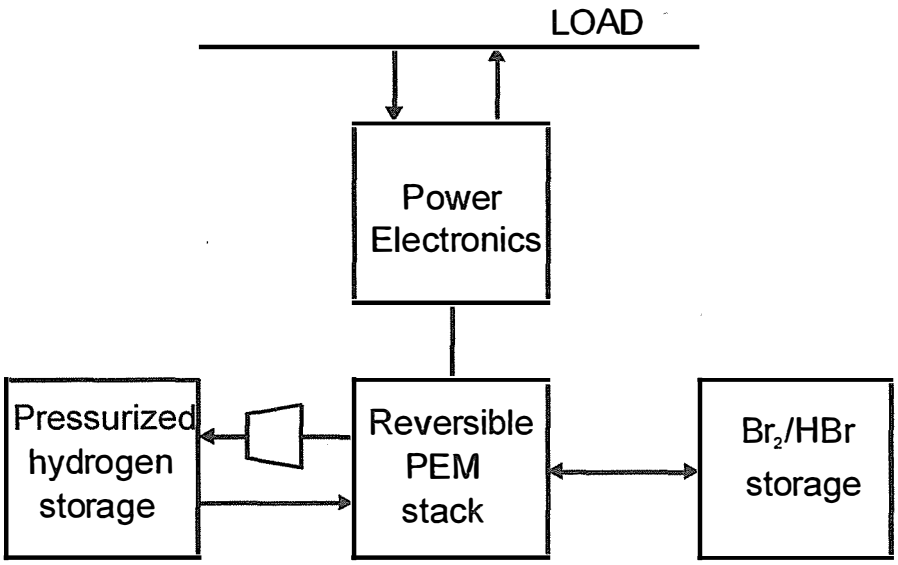

Figure 2. Financial Analysis of a 300 kW, 8 hour HBr-based Electricity Storage System

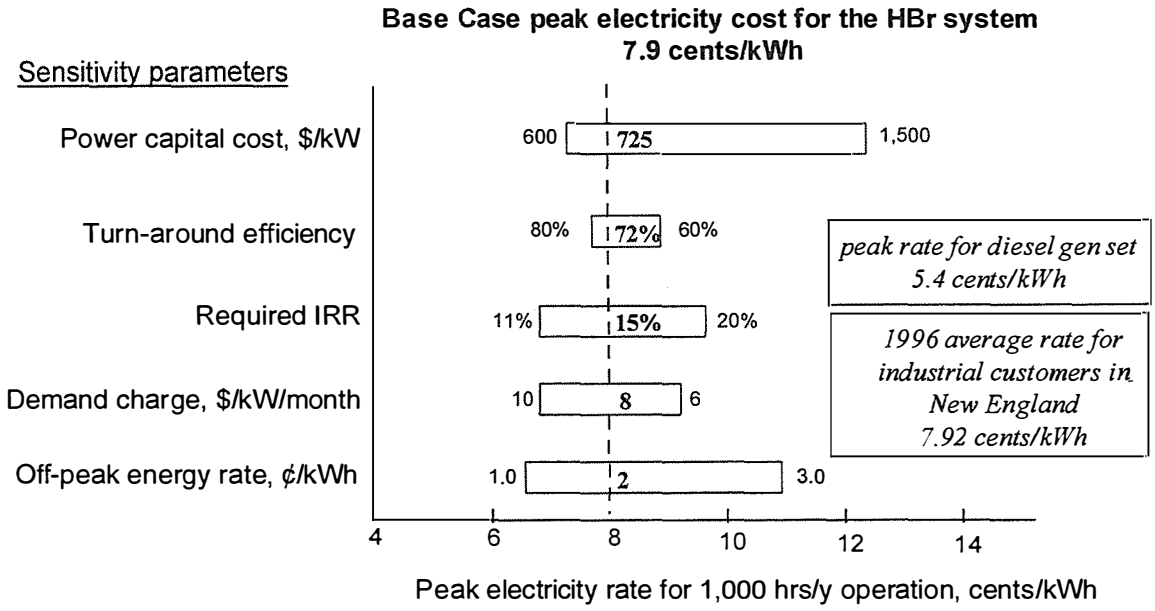

Figure 3 Weight and Volume Density of Hydrogen Storage Technologies

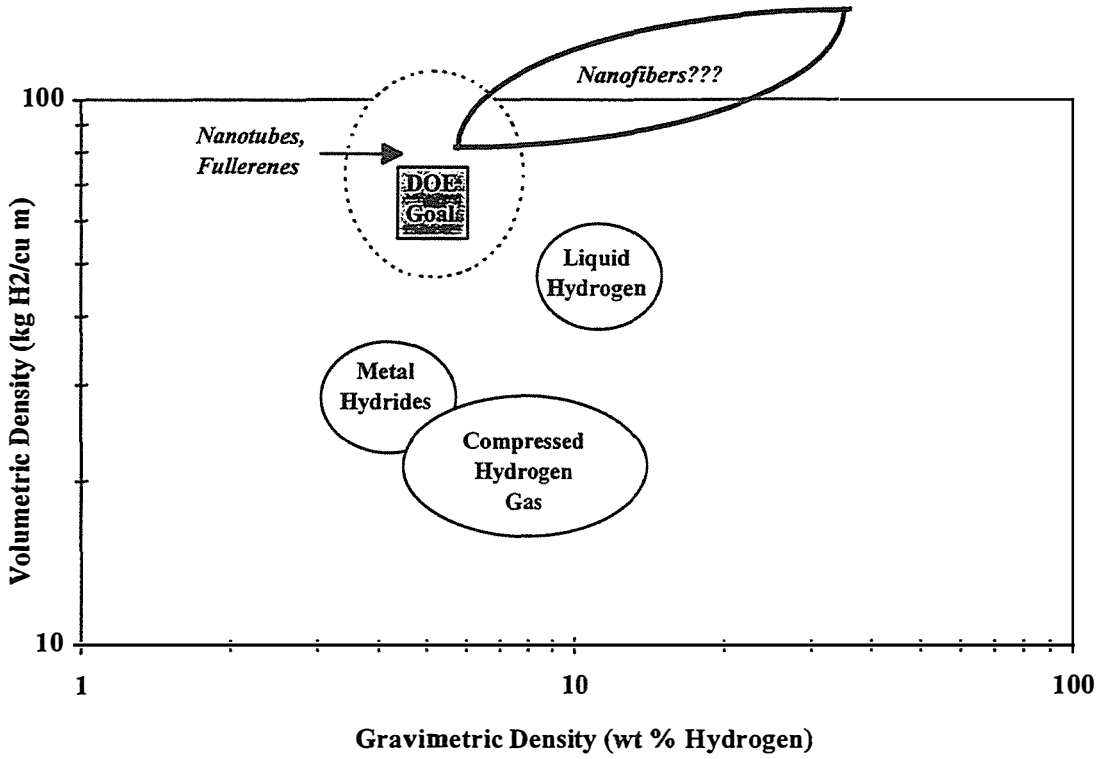

Figure 4. Fuel Cost for Transit Buses

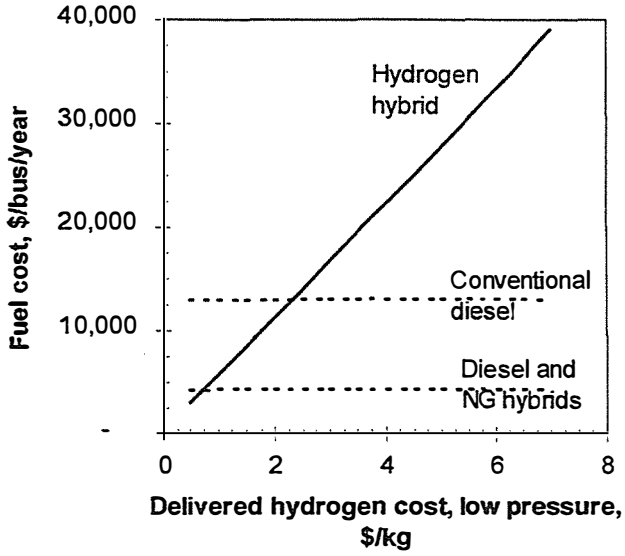

Based on 40,000 miles per year, diesel cost 1 $/gallon,
NG cost 2 cents/kWh, conventional diesel eff 3 mpg

Coupling Hydrogen Fuel and Carbonless Utilities

Gene D. Berry
Energy Analysis, Policy, and Planning
Energy Program, Lawrence Livermore National Laboratory
Livermore, CA 94550

Executive Summary

A number of previous analyses have focused on comparisons of single hydrogen vehicles to petroleum and alternative fuel vehicles or of stationary hydrogen storage for utility or local power applications. LLNL's approach is to compare combined transportation/utility storage *systems* using hydrogen and fossil fuels. Computer models have been constructed to test the hypothesis that combining carbonless electricity sources and vehicles fueled by electrolytic hydrogen can reduce carbon emissions more cost effectively than either approach alone. Three scenarios have been developed and compared using computer simulations, hourly utility demand data, representative data for solar and wind energy sites, and the latest available EIA projections for transportation and energy demand in the U.S. in 2020. Cost projections were based on estimates from GRI, EIA, and a recent DOE/EPRI report on renewable energy technologies. Hydrogen technology costs were drawn from recent or ongoing analyses by Princeton University (Ogden 1995) and Directed Technologies Inc. (DTI) (Thomas 1998)for the Hydrogen Program.

The key question guiding this analysis was:

What can be gained by combining hydrogen fuel production and renewable electricity?

Bounding scenarios were chosen to analyze three "carbon conscious" options for the U.S. transportation fuel and electricity supply system beyond 2020:

Reference Case:	petroleum transportation & natural gas electric sector
Benchmark Case:	petroleum transportation & carbonless electric sector
Target Case:	hydrogen transportation & carbonless electric sector

A large number of assumptions were necessary to construct these scenarios, but preliminary model results indicate that if wind and solar electricity were massively deployed to replace fossil electric generation in 2020, and costs approached today's levels, a carbon tax of $86 billion/yr (applied over 0.49 GtC/yr or $175/tonneC) would be needed for solar and wind electricity to compare favorably to efficient combined cycle natural gas electric plants.

This picture becomes more favorable if electrolytically fueled hydrogen vehicles are also deployed. Coupling a hydrogen transportation sector to augmented solar and wind electricity sources improved flexiblity and utilization of renewables in a carbonless electricity system, reducing 75% more carbon emissions (0.86 GtC/yr) for only 10% greater system cost. The addition of hydrogen transportation fuel demand reduced carbon emissions further while lowering likely carbon tax rates ($/tonneC). Given future long-term petroleum fuel prices of $1.50-2.00/gal, carbon taxes of only $80-150/tonneC would be needed for solar and wind dominated carbonless electricity systems, combined with hydrogen production for vehicles, to compete with natural gas electric generation and petroleum vehicles.

Introduction

Conventional wisdom (e.g. Winter, 1988, Ogden 1989) has rationalized the pursuit of hydrogen energy systems as a solution to problems stemming from the use of fossil fuels: energy security, pollution, and greenhouse gas emissions. But advanced energy technologies using natural gas can be quite cost-effective albeit partial, solutions to these energy and environmental challenges. Cost-effective fossil energy technologies may seriously undercut the conventional rationale for widespread adoption of hydrogen energy systems.

The most notable example is probably natural gas vehicles which, while similar to hydrogen vehicles are likely to be more cost-effective at reducing air pollution, greenhouse gases, and oil imports. It is likely more cost-effective to begin reducing utility emissions through efficiency improvements, fuel switching to natural gas, and/or directly using relatively small amounts of solar and wind electricity (without energy storage), before producing hydrogen for transportation fuel or electricity load leveling (Thomas 1998).

It appears a strengthened rationale for hydrogen energy development can be constructed based on the need for deep greenhouse gas reductions - if significant synergies can be found between carbonless utilities and transportation coupled by hydrogen fuel (Berry 1996).

The largest benefit unique to hydrogen energy technology is the capacity for deep reductions in greenhouse gas emissions. The two largest greenhouse gas sources, utility electric generation and transportation fuel emissions, can be eliminated if electrolytic hydrogen and carbonless electric generation are sufficiently inexpensive. This analysis tests the hypothesis that carbon emission reductions can be more cost-effectively achieved if electrolytic hydrogen fuel production and electricity generation are closely coupled (see Figure 1). Our approach is to simulate transportation and utility sectors under a variety of cost, technology, and operational scenarios. The objective of this analysis is to determine the prerequisite economic and hydrogen technology developments for which this hypothesis can be relevant, and to identify corresponding hydrogen production, storage and utilization technology benchmarks.

Approach, Methodology, and Model Description

Approach: Aggressive Fossil, Renewable, and Hydrogen Scenarios

Three scenarios were constructed and used in our computer models of utility and transportation sectors, a reference, benchmark, and target case. These three scenarios were chosen as aggressive, mature, boundary cases. These scenarios test the widest range of possibilities that were most interesting, while maintaining a balanced basis for comparison, and keeping the analysis as simple as possible. If the results of these scenarios are sufficiently compelling then future analyses can explore more complex, detailed and perhaps more realistic transition scenarios. The year 2020 was chosen as the time period to analyze because of available EIA projections. 2020 also likely represents the fastest technically possible (and therefore most aggressive) transition to carbonless energy systems. It was felt that aggressive scenarios should be analyzed, since the a hydrogen transition will not be attractive unless technology development (.e.g. advanced electrolysis, low cost renewables, energy storage etc.) is successful. The fossil reference case used for coomparison was also aggressive for balance.

Each scenario had costs lower than today's energy systems. Aggressive technical and economic assumptions used in the benchmark renewable and target hydrogen scenarios included: high efficiency electrolysis, low cost renewable electricity and hydrogen storage, perfect demand and supply forecasting, etc. But the reference fossil energy case was equally aggressive, PNGV light-duty vehicle fleets are assumed, as well as very efficient use of natural gas to produce electricity. In line with EIA projections, no new capacity is assumed, in any scenario, for conventional carbonless electricity sources, such as nuclear or hydroelectric.

Methodology: Only the detail necessary to capture supply and demand patterns

Our computer models used only as much data as necessary to establish the rough magnitude of the benefits gained by coupling hydrogen fuel production with carbonless electrical sources. Real electricity demand and wind and solar supply data for an entire year, at hourly resolution, was necessary. Data representative of both a summer peaking (e.g. California) and winter peaking (e.g. Washington state) utility were gathered. Wind and solar data from "second tier" sites was chosen to approximate PV, solar thermal, and wind electricity sources based mostly in the West, Southwest, and Midwest. (Iannucci 1998) Detailed time zone and regional effects were neglected for simplicity. Transportation fuel use patterns were based on 12 hour resolution DOT data for passenger vehicles (Klinger 1984), and monthly EIA data for commercial vehicles (EIA 1998).

Model construction was kept as simple as possible. National aggregates for transportation and electricity demand were used. Single reservoirs of electricity and hydrogen production and storage capacity, scaled to the entire U.S., were used to represent thousands of solar thermal and wind farms, liquefaction facilities, and hydrogen filling stations used by millions of vehicles. Lumped national average costs for electricity transmission and distribution were used. Utility energy storage, when necessary was presumed to employ hydrogen storage and fuel cells. Decentralization of photovoltaics and hydrogen infrastructure was assumed to circumvent the complex issues of additional electricity transmission and distribution needs.

Financial calculations were kept as simple as possible. Operating costs were neglected where they were less than the resolution of capital cost or fuel estimates (typically ~10%). Capital investments were discounted at 6% over a cost-weighted average of ~25 years. Electricity prices reflected electricity transmission, distribution, conventional generation, and in the target scenario prorated electric and hydrogen generation and storage investments.

Model Description: Scenario simulation and optimization

LLNL used two computer modeling approaches in this analysis: simulation and multiperiod (e.g. 8760 hours) equilibrium optimization. Simulation provides faster but simpler results. Any given simulation model run simply provides the energy and economic performance of a given energy system configuration and operational rules. An optimization model run is slower and more complex, but can, in principle, determine the lowest cost configuration of technologies and operation of those technologies to meet given electricity and hydrogen demand time series. To date LLNL's network optimization code "METAnet" (Lamont 1994) is still being fine tuned for operational optimization of hydrogen electricity systems (A model schematic and typical optimization results are shown in figures 2-3). Optimal renewable energy system configuratios based on preliminary METAnet results appear capable of achieving costs 10-20% lower than simulation models, which may somewhat understate the attractiveness of intermittent electricity, and especially hydrogen fuel production, relative to conventional fossil fuel scenarios. Further development and analysis is needed. Consequently, the results generated from simulation models are used here.

The graphical interface simulation model software used for this study, STELLA, is commercially available (High Performance Systems Inc. of Hanover, NH). Visualization, conceptualization, and interconnection of technical, economic, or market variables is exceptionally easy. The value of each factor and its relationship to other factors are easily modified, allowing exploration of strategic parameter spaces such as production and storage scale, efficiency, discount rate, equipment lifetimes, fuel efficiency, and demand patterns. The model therefore allows dynamic analysis, and data can be easily updated.

Annual electricity flows from various sources (nuclear, hydroelectric, wind, solar thermal, and photovoltaic) to the electric grid and/or, stored as hydrogen (liquid, compressed, onboard, stationary etc.), and ultimately to transportation use in light-duty vehicles and commercial trucks, aircraft, and trains were modeled on an hour by hour basis. Supply and storage

Input Assumptions and Simulation Results

Preparation for a model run requires specification of equipment capacities, conversion efficiencies, and fuel use corresponding to a desired scenario. After each model run these paramaters were varied to explore the sensitivities of results to individual parameters and to achieve lower projected costs, more efficient operation etc. The final parameters chosen for each scenario and output results are given in Table 1. The data are discussed below.

Electricity Supply and Demand Assumptions

Solar and wind electricity generation patterns were based on annual data gathered at sites in California and Wyoming. as well as utility demand patterns from utilities in the Southwest and Northwest, provided by Distributed Utility Associates (DUA). These data were scaled up to meet the end-use electricity and hydrogen production needs based in EIA's reference case forecast for 2020. For example U.S. electric generation capacity is projected by EIA to be 993 GW in 2020 (up from ~700 GW today) (EIA 1998). This was rounded to 1 TW for simplicity and became thse scaling factor for both northern and southern utility demand pattern data from DUA. In the final results, southern utility demand data were used after model results were not strongly affected by which electricity demand pattern was used. Nuclear and hydroelectric capacity were taken from EIA data representing ~5% and ~10% of U.S. electric generating capacity in 2020 respectively.

During the simulation, in periods of insufficient renewable electricity, (windless nights, cloudy days etc.) electricity from fuel cells was produced using hydrogen in compressed (if available) or liquid stationary storage. In periods of excess electricity availability hydrogen was produced and stored.

Cost projections for renewable electric capacity were gathered by DUA using *Renewable Energy Technology Characterizations*(a joint project of EPRI and DOE). Natural gas fired electricity projections are from GRI. Transmission and generation electric costs were estimated by DUA, and scaled to meet a 1 TW peak demand (including coincident loads) (Iannucci 1998).

Hydrogen Transportation Fuel Demand and Use Assumptions

Transportation demand was modeled differently for different vehicle classes. Light-duty vehicle travel patterns (for days, nights, weekdays, and weekends) were taken from the 1983 Nationwide Personal Transportation Study (NPTS) completed for the National Highway Traffic Safety Administration (Klinger 1984). These patterns were then scaled to 12,000 miles/yr for a projected 270 million light-duty vehicles in 2020., equalliing the 3.24 trillion vmt projected y EIA for 2020. Drawing from the 1983 NPTS data, it was assumed that 15% (1800 miles/yr for an average driver)of vmt was due to long trips (<75 miles) and would require liquid hydrogen. PNGV fuel economy (~80 mpeg) was assumed for hydrogen vehicles.

Commercial vehicle fuel demand was approximated using monthly energy demand patterns from 1995-1997 for diesel (trucks and trains), and jet fuel (aircraft) using EIA data, and aggregate projections of fuel demand in 2020. Trucks and trains were are powered by compressed hydrogen, with the same fuel economy projected by EIA for diesel fueled vehicles.. Aircraft were fueled by liquid hydrogen, a 10% higher fuel economy than EIA projections due to hydrogen's low mass.

Hydrogen refueling patterns were identical to fuel use patterns (so that vehicles were essentially always full) except for light-duty vehicles which refueled less when station supplies were low for a few days, presuming a high fuel price sensitivity for drivers. Onboard hydrogen storage equipment costs for passenger vehicles and commercial trucks were included in the model.

Scenario Assumptions

Reference Scenario (natural gas electricity and petroleum transportation)

The reference scenario was the simplest because no intermittent resources were used. It was designed to be a strong competitor to carbonless electricity and hydrogen scenarios. In the reference scenario all transportation needs are met by petroleum. Light-duty transportation fleet efficiency has increased to PNGV levels (80 mpg or roughly 3 times greater than EIA projections for 2020). Petroleum demand for trucks, trains, and aircraft were taken directly from EIA projections. All electricity demand was met by natural gas combined cycle plants with an average 57% efficiency. Natural gas prices in 2020 were $3.05/GJ as per EIA projections. A key optimistic assumption was that greenhouse gas emissions from natural gas (methane)leakage would be negligible (methane is believed to be 10-20 times more potent than carbon dioxide as a greenhouse gas). In our aggressive reference scenario passenger vehicle efficiency and the efficient use of natural gas by utilities combine to reduce carbon emissions from transportation and utilities to only 870 mmtC/yr, compared to 1400 mmtC/yr projected by EIA for 2020 (EIA 1998).

Benchmark Scenario (solar, wind electricity and petroleum transportation)

The benchmark scenario assumes that all electricity demand is met by a mixture of solar thermal, wind, and photovoltaic (PV), instead of natural gas, as in the Reference Scenario. To meet a 1 TW capacity requirement, 0.85 TW of wind and 0.35 TW of solar thermal are assumed, as well as 0.15 TW (combined) of hydroelectric and nuclear. These capacities were chosen to match transmission and distribution capacity. A relatively small balance of electricity demand is supplied by distributed PV (0.05 TW). Utility energy storage is accomplished with steam electrolysis (Quandt 1986), and compressed or liquid hydrogen storage, as well as fuel cells.

Transportation demand was met by petroleum, exactly as in the reference scenario. Carbon emissions were 370 mmtc/yr.

Target Scenario (solar, wind electricity and hydrogen transportation)

The benchmark scenario assumes that all electricity demand is met by a mixture of solar thermal, wind, and photovoltaic (PV), instead of natural gas, as in the Reference Scenario. To meet a 1 TW capacity requirement, 0.85 TW of wind and 0.85 TW of solar thermal are assumed, as well as 0.15 TW (combined) of hydroelectric and nuclear. These capacities were chosen to match transmission and distribution capacity. A relatively small balance of electricity demand is supplied by distributed PV (1.8 TW). Utility energy storage, is accomplished with steam electrolysis, and compressed or liquid hydrogen storage, as well as fuel cells. Hydrogen not needed for electricity production is used as transportation fuel. Compressed hydrogen was used for 85% of light-duty vehicle fuel demand and all commercial trucking, while liquid hydrogen was used in aircraft and for long distance light-duty vehicle trips. As an efficiency measure liquid hydrogen was only converted from ortho to para phases when necessary for long-term storage. Carbon emissions from transportation and electricity production were, of course, zero for this scenario.

Scenario Results

Summary energy balances, costs and emissions results from each scenario's computer model runs are given below. Detailed assumptions and output parameters are given in Table 1.

Reference Scenario (natural gas electricity and petroleum transportation)

In the 2020 reference scenario, assuming utility natural gas prices are $ 3.05/GJ, the U.S. can meet its 5 trillion kWh/yr electric demand (1 TW peak) with efficient combined cycle natural gas turbines at a cost of $192 billion/yr, and utility carbon emissions of 490 mmtC/yr. Land and air transportation demands are all met with only 144 billion gallons of petroleum/yr (due to PNGV light-duty vehicles) with attendant with carbon emissions of 370 millon metric tonnes per year (mmtC/yr). Fuel costs @1.50/gallon would be another $216 billion/yr. The vast majority of petroleum demand is shared roughly equally between commercial trucks and aircraft. Passenger cars and trucks only account for <10% of petroleum use.

Total annual cost is ~$420 billion/yr with total carbon emissions of 0.86 GtC/yr.

Benchmark Scenario (solar, wind electricity and petroleum transportation)

In the 2020 benchmark scenario, U.S. electric generation is completely carbonlesss relying on small amounts of remaining hydroelectric and nuclear capacity, 850 GW of wind, 330 GW of solar thermal plants and 50 GW of photovoltaics to meet the same 5 trillion kWh/yr electric demand (1 TW peak). Daily and seasonal energy storage is accomplished using 1.5 billion kWh of compressed hydrogen and 275 billion kWh of liquid hydrogen storage. Roughly 7% of all electricity is lost in energy storage and reconversion. the capital investment for electric generation and hydrogen storage is estimated to be $ 3.2 trillion, resulting in annual electric costs of $290 billion. All land and air transportation fuel demands are met by petroleum, just as in the reference scenario, with petroleum costs of $216 billion/yr (@$1.50/gallon) emitting 370 million metric tonnes of carbon annually.

Total annual cost is therefore ~$506 billion/yr with carbon emissions of 0.37 GtC/yr.

Target Scenario (solar, wind electricity and hydrogen transportation)

In the 2020 target scenario, U.S. electric generation and transportation by car, truck and aircraft are completely carbonless. The electric generation system postulated in the benchmark scenario is augmented in the target scenario to provide electricity for additional hydrogen production, storage, and use. Solar thermal capacity is tripled to 0.85 TW, and photovoltaic capacity is expanded dramatically to 1.8 TW to meet additional electricity demands without transmission and distribution expansion. Two-thirds of electricity production is from solar thermal central receivers and distributed photovoltaics. Daily and seasonal energy storage is accomplished using 4 billion kWh of compressed hydrogen storage at refueling stations and 750 billion kWh of liquid hydrogen storage at stations and utilities. 11 trillion kWh of electricity is produced annually, of which 5 trillion kWh is used directly, less than 1% of end-use electricity is lost through storage and reconversion by fuel cells. The remaining 7 trillion kWh of electricity are used to produce 4.6 trillion kWh of hydrogen for transportation use, meeting transportation demands identical to the reference case. Roughly half of hydrogen is liquefied for aircraft and long car trips, while half is used in commercial trucks and for short distance urban trips (<75 miles one-way) in light-duty vehicles.

The estimated $6.6 trillion coupled carbonless electricity and transportation fuel system has levelized costs (combined for both electricity and hydrogen fuel supply) of ~$550 billion/yr and produces no carbon emissions (offsetting 860 million metric tonnes of carbon from the reference scenario).

Key Results, Conclusions, and Recommendations

Key Results

The three scenario model runs summarized earlier, when taken and compared together, yield two key results:

1) It appears that, given inexpensive long-term oil and gas prices, improved natural gas electricity sources and very efficient (~80 mpg) passenger cars and trucks can be very competitive, producing lower carbon emissions in 2020 (0.86 GtC/yr than the same sectors do today (0.98 GtC/yr) in spite of 50% higher electricity and travel demand. However, even given this extremely aggressive fossil scenario, it will be difficult to reduce carbon emissions below 0.86 GtC/yr without sequestration (likely creating a hydrogen transportation sector), improved electric generation efficiency (likely requiring utility fuel cells), improved aircraft and freight transportation efficiency (reducing the fuel cost barrier to hydrogen use), and/or widespread use of renewable electricity sources (creating a surplus for hydrogen production)

2) If such deep carbon reductions are needed, it appears coupling electrolytic hydrogen fuel production to solar and wind electricity can achieve much greater carbon reductions more cost-effectively than solar and wind electricity alone. Given petroleum fuel prices of $1.50/gallon in 2020 the hydrogen-based target scenario reduced 75% more carbon emissions than the benchmark scenario for only ~10% higher cost. These results are more striking because they illustrate the potential advantages of hydrogen-fueled vehicles even in scenarios where most carbon reductions are made in the electric sector, and PNGV light-duty vehicles (the likeliest market for hydrogen fuel to penetrate) are only 1/3 of transportation carbon reductions.

These results are likely dependent upon solar, wind, and hydrogen cost assumptions as well as fossil fuel prices and carbon taxes or credits.. The figure below plots the estimated annual cost and carbon emissions of all three scenarios for petroleum fuel prices of $1.50-$2.00/gallon.

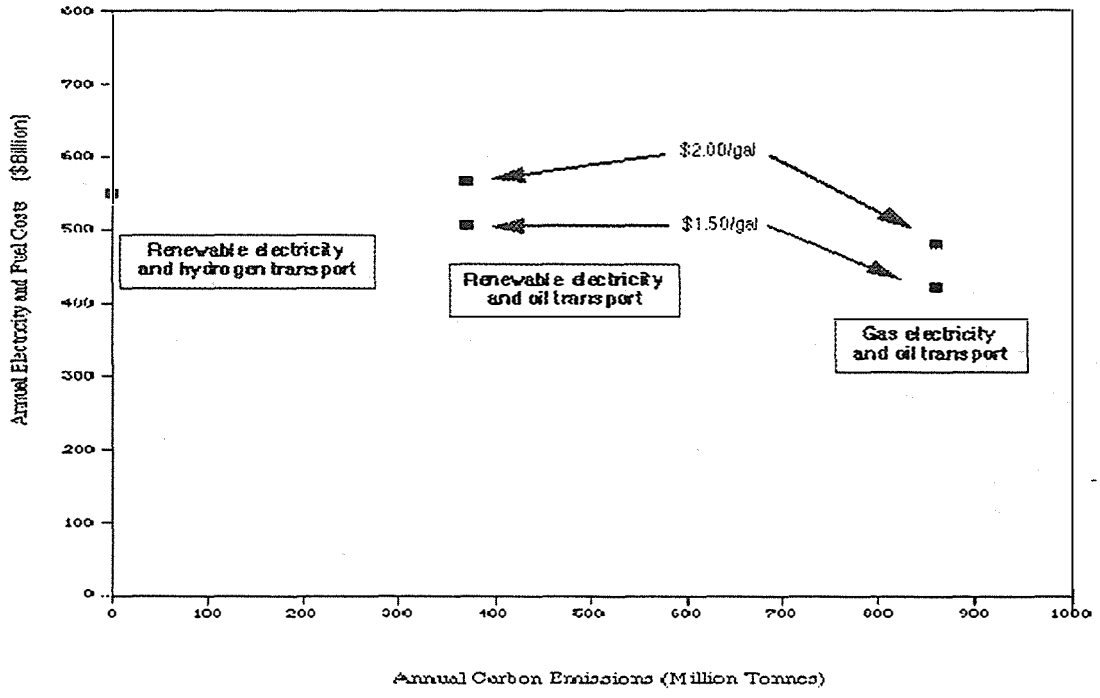

Annual cost vs. emissions for reference, benchmark, and target scenario model runs and long-term petroleum fuel prices ranging $1.50-2.00/gallon.

Key Results (Con't)

The previous plot shows that for long-term petroleum fuel prices comparable to $1.50/gal, renewable hydrogen and electricity is more cost-effective at carbon reduction than renewable electricity alone, even given optimistic renewable electricity costs and low discount rates (6%). If future petroleum fuel prices rise high enough (to ~$2.00/gal) using hydrogen vehicles could actually lower the effective cost of renewable electricity while reducing carbon emissions. The previous plot also indicates carbon reduction differences between scenarios are much greater than cost differences.

Cost differences are greatest between the fossil reference scenario and the others. These differences are principally dependent on fuel price assumptions ($3.05/GJ for natural gas and $1.50/gal for transportation petroleum) and efficiencies. It should be emphasized that no efficiency advantage was presumed for hydrogen vehicles (except for aircraft) in comparison to their petroleum-powered counterparts, and no upstrea,m carbon emissions or methane leakage were accounted for in the reference scenario.

Cost differences between the scenarios with hydrogen transportation (target scenario) and without it (benchmark)are again influenced somewhat by fuel prices, but this sensitivity is lessened due to the common technology assumptions employed in both (e.g. low-cost, efficient electrolyzers, advanced wind electricity etc.). Only under the unlikely conditions of simultaneously low oil prices and high interest (discount) rates, would the two cases compare substantially differently.

Interestingly, even though the renewable and hydrogen intensive target scenario has a greater proportion of high cost renewable electricity sources (e.g. solar) and greater energy storage rquirements than the benchmark scenario, it still had lower overall (combined transportation and electricity) costs. This supports the synergy hypothesis for the target scenario: that hydrogen fuel demand by vehicles can be a net benefit for renewable electricity systems. This also indicates that integrated hydrogen transportation/utility systems may be more attractive than stationary hydrogen utility storage alone.

Conclusions

High efficiency and coupling vehicles to utilities are most important

Although further sensitivity analyses and other refinements, such as new, nearer-term scenarios should provide an even clearer picture, two conclusions can be drawn from the results so far:

1) Super efficient hydrogen production and storage, and use are necessary for hydrogen to compete in both utility and transportation markets, even if optimistic renewable electricity targets are met. All of the efficiencies (liquefaction, electrolysis etc.) used in the hydrogen scenarios were best case. For reasons of end-use efficiency compressed hydrogen was used in the simulations wherever possible, as was only partially para converted liquid hydrogen.

2) Unless long term fossil fuel prices are very low *and* hydrogen vehicles have no efficiency advantage over fossil vehicles, coupling hydrogen fuel production to carbonless sources can be a substantial benefit. Carbon taxes would be reduced, and might even be eliminated depending upon relative hydrogen/fossil fuel prices and efficiencies.

Recommendations

Technology Development Needs

High efficiency, electrolysis, in some cases distributed on a small scale, is crucial. Cost targets for electrolysis of ~$500/kW and efficiencies of at least 90% are likely necessary. Hydrogen storage is secondary but still of significant importance. Light-duty vehicles and commercial trucks which could use compressed hydrogen as much as possible would be an important efficiency step. Bulk hydrogen storage cost targets (e.g. liquid hydrogen) for very large vessels, of ~$10/kg H2 stored are necessary, unless future demand and supply patterns can be better matched than in the scenarios used here. Compressed hydrogen storage costs projected by others (Thomas 1998) of $100-150/kg H2 were sufficient.

Systems Analysis Needs

This analysis has shown that significant environmental and economic advantages can exist for renewable electricity sources, when coupled with hydrogen fuel production for vehicles. The next step is a clearer understanding of these advantages, their requirements, and their limitations, under economic optimization conditions. A wide range of future analysis directions are possible. Hydrogen technology cost benchmarks can be determined as a function of fossil fuel prices and allowable carbon taxes. A determination of the importance of small amounts dispatchable carbonless electricity sources in the generation mix can be made. Transition scenarios for hydrogen vehicles and renewable electricity sources can be examined. LLNL plans to further develop its equilibrium optimization code to be able to answer these and similar questions.

Some new technical options could also be very important to examine in the future. One promising candidate would be a close-coupled steam electrolyzer/fuel cell using natural gas to produce electricity at night, storing waste heat to improve electrolysis efficiency during the day, when solar electricity is available, and in turn storing oxygen to improve fuel cell efficiency during the night. This could dramatically enhance the attractiveness of hydrogen production from renewable electricity, while providing a very efficient synergy with both fuel cells and natural gas utilities.

The most important market options to analyze will likely be the impact of small changes in seasonal demand patterns upon energy storage requirements, as well hydrogen fuel use in individual sectors of the transportation market.

Acknowledgments

I gratefully acknowledge the helpful suggestions of Joe Iannucci and Susan Horgan of Distributed Utilities Associates (DUA) as well as copious amounts of useful utility and renewable energy data. I would also like to thank Alan Lamont and Thomas Gilmartin of LLNL for assistance modifying LLNL's existing energy modeling capabilities for this effort.

References

Berry, Gene D. March 1996. *Hydrogen as a Transportation Fuel: Costs and Benefits*. Final Report Presented at the DOE Hydrogen Annual Review Meeting Miami, FL, Apr. 29-May 3, 1996; Lawrence Livermore National Laboratory Report UCRL-ID-123465.

"Behind the Wheel in Honda's New Gasoline-Powered ULEV Accord EX," *Green Car Journal* **4** (Apr. 1995) pp. 37–39.

Iannucci, Joseph. Personal Communication April 1998. Distributed Utility Associates, Livermore, CA 94550

Klinger, Dieter and J. Richard Kuzmyak *Personal Travel in the United States, Vol I 1983-1984 Nationwide Personal Transportation Study* for U.S. Department of Transportation, Office of Highway Information Management Washington D.C. 20590. PB89-235378.

Lamont, Alan. November 1994. *User's Guide to the METAnet Economic Modelling System version 1.2*. Lawrence Livermore National Laboratory Report UCRL-ID-122511.

Molter, T. 1994. *SPE Water Electrolyzers for Commercial Hydrogen Production.* Hamilton Standard Division of United Technologies, Space and Sea Systems, Windsor Locks, CT.

Ogden, Joan M. and R.H. Williams, 1989. *Solar Hydrogen: Moving Beyond Fossil Fuels.* World Resources Institute New York, NY.

Ogden, Joan M., E. Dennis, M. Steinbugler, and J. Strohbehn. Jan. 18, 1995. *Hydrogen Energy Systems Studies,* Final Report to NREL for Contract No. XR-11265-2, Center for Energy and Environmental Studies, Princeton University, Princeton, NJ.

Quandt, K.H. and R. Streicher, 1986."Concept and Design of a 3.5 MW Pilot Plant for High Temperature Electrolysis of Water Vapor," *International Journal of Hydrogen Energy* **11,** No. 5 pp. 309–315.

Thomas, C.E. Brian D. James, Franklin D. Lomax Jr. and Ira F. Kuhn Jr. March 1998. *Integrated Analysis of Hydrogen Passenger Vehicle Transportation Pathways,* Draft Final Report for National Renewable Energy Laboratory under subcontract AXE-6-16685-01. Directed Technologies, Inc. 4001 North Fairfax Drive Arlington, VA 22203.

U.S. Energy Information Administration (1998) *Annual Energy Outlook 1998: with projections through 2020.* DOE/EIA-03383(98),

U.S. Energy Information Administration (1998) *Monthly Energy Review: April 1998.* DOE/EIA-0035(98/04),

Winter, C-J and J. Nitsch (1988) *Hydrogen as an Energy Carrier.* Springer, Berlin

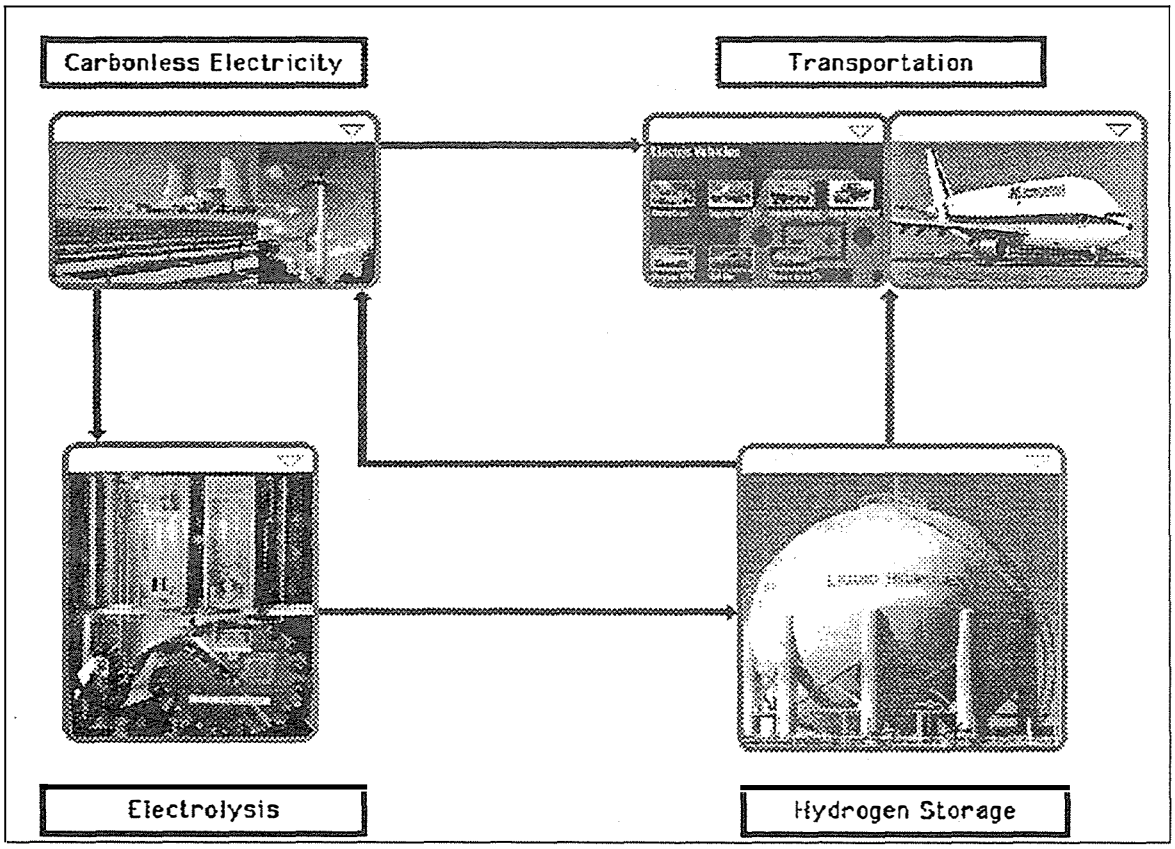

Figure 1. Conceptual representation of a coupled carbonless electricity and hydrogen transportation system and flows of electricity and hydrogen. Electricity generated from nuclear, solar, wind, or other carbonless electricity sources meets electricity grid needs first. Surplus electricity can either directly fuel batteries or other electric storage on vehicles or produces hydrogenfor ultiimate storage and use on vehicles. In periods of low solar and wind availability, stored hydrogen can be reconverted to electricity for use on conventional electricity grid.

Note: A number of additional options are not pictured. These include: hydroelectric and biomass generation, as well as mixed systems of compressed and liquid hydrogen storage, and hydrogen use by commercial trucks, in addition to aircraft and light duty vehicles.

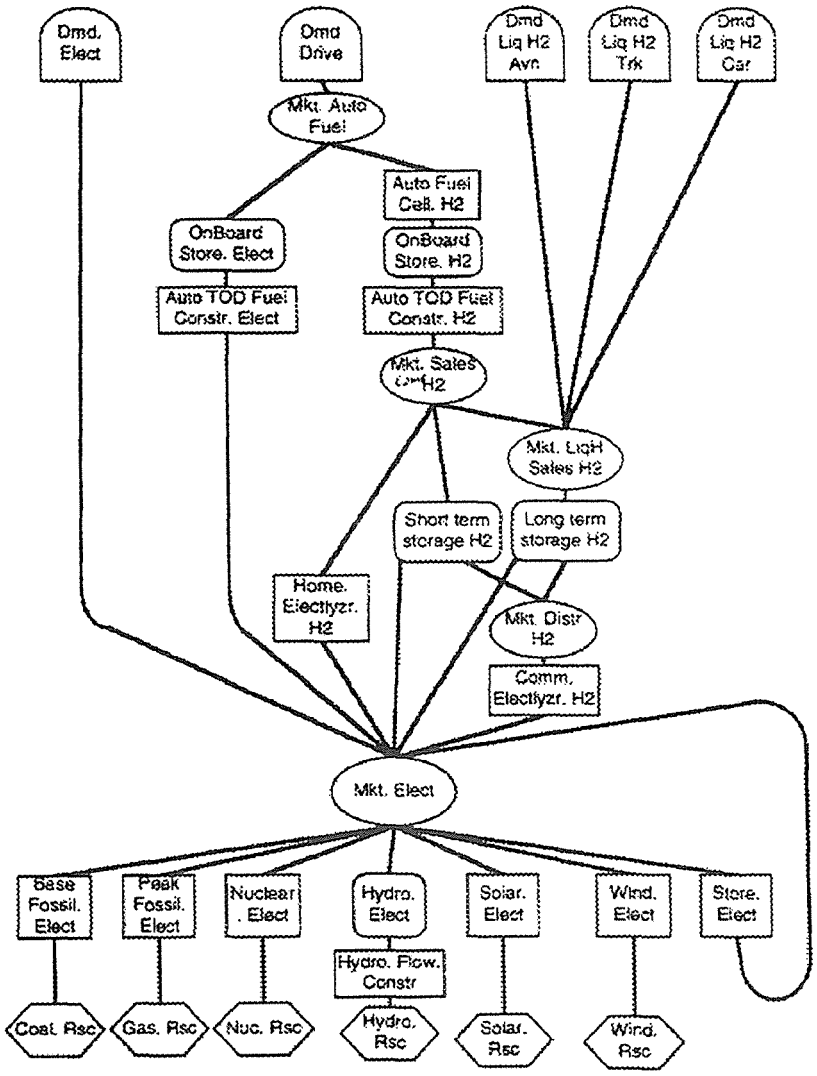

Figure 2. Conceptual schematic of a network optimization model approach to electricity and transportation systems. Electricity and hydrogen demand nodes (top) send demand quantities down through the network which are met from a number of sources supplying market nodes (e.g. Mkt. Elect.) these sources are technologies with costs and technical capabilities (capacity, efficiency etc.) of converting available resources (e.g. sun, wind, coal, gas etc. depicted as resource nodes at bottom) which are used according to resource prices and availability. These prices are then sent back up the network to the demand and storage nodes, which can adjust demand to repsond to availability and prices. This cycle is iterative, converging to a lowest cost equilibrium between supplies and demands.

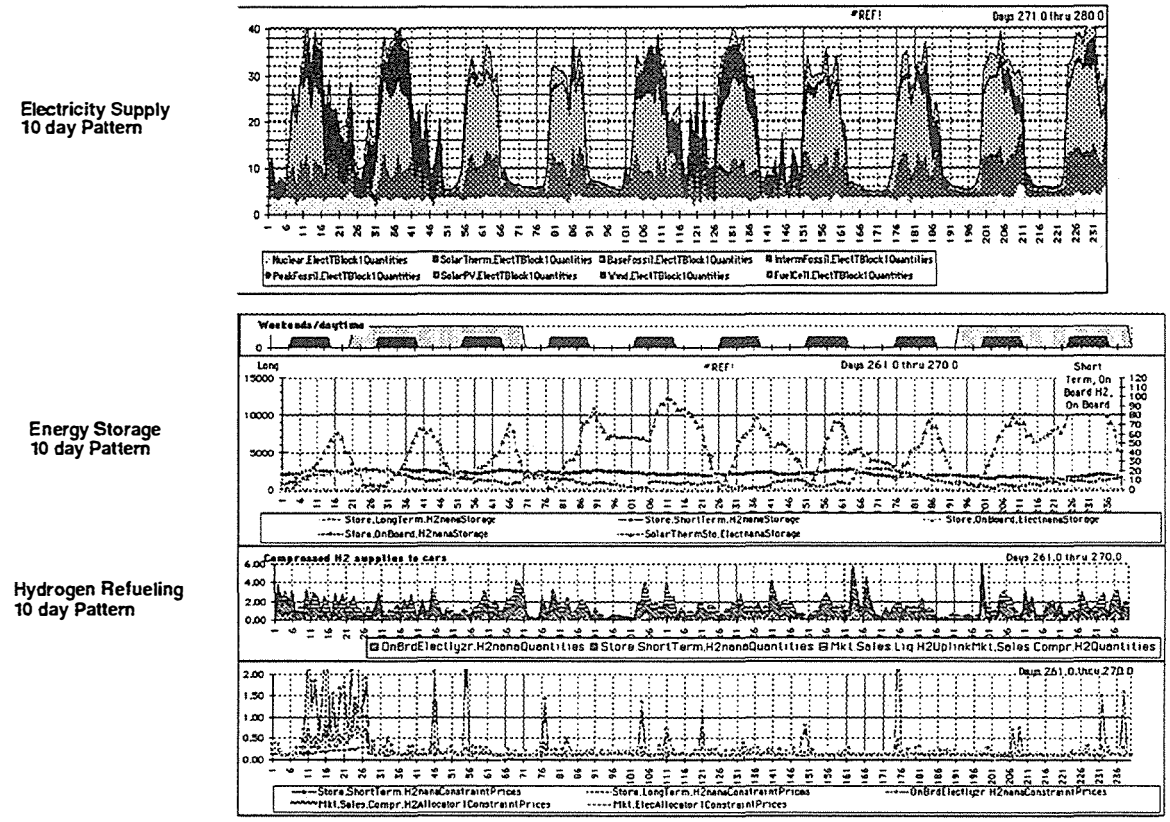

Figure 3. Typical output from LLNL's METAnet equilibrium network model. A 10 day period of hourly electric generation,, stationary and onboard energy storage, and refueling and prices are shown. A scenario run typically covers an entire year (36 of the above periods), Many runs are used to arrive at optimal capacities of electricity and hydrogen production and storage.

Table 1. System parameters used in computer model scenarios

Scenario		Reference		Benchmark		Target	
Electricity Demand (trillion kWh/yr)			5		5		5
Electric Supply (TW, trillion kWh/yr)			5		5.8		11
Natural Gas	($600/kW, $3.05/GJ)	1.0	5	-	-	-	-
Nuclear	($2000/kW)	-	-	0.05	0.44	0.05	.44
Hydroelectric	($2000/kW)	-	-	0.10	0.90	0.10	.90
Wind	($655/kW)	-	-	0.85	3.2	0.85	3.2
Solar Thermal	($2510/kW)	-	-	0.35	1.1	0.85	2.4
Solar Photovoltaic	($1110/kW)	-	-	0.05	0.12	1.8	4.3
Fuel Cells *	($200/kW)	-	-	1.0	(0.48)	1.0	(0.06)
Transportation Demand (trillion kWh/yr)		oil		oil		hydrogen	
Light-duty vehicles (urban)		1.16		1.16		1.16	
Light-duty vehicles (highway)		0.20		0.20		0.20	
Commercial trucks & rail		1.64		1.64		1.64	
Aircraft		1.45		1.45		1.63	
Hydrogen Supply (TW, kWh/yr)							
Electrolysis ($500/kW, 92% eff)		-	-		1.0		1.2
Compression ($100/kw 92%)		-	-		1.0		1.2
Liquefaction ($500/kW, 78 eff%)		-	-		1.0		1.0
Hydrogen Storage (kWh LHV H2)							
Onboard light-duty fleet ($150/kg H2)			-		-		15 billion
Stationary Compressed ($150/kg H2			-		1.5 billion		4 billion
Stationary liquid hydrogen ($10/kg H2)			-		275 billion		750 billion
End-use Electricity Cost ($Billion/yr) (@6% discount rate)		192		290		225	
Transportation Fuel Cost (@$1.50/gal petroleum fuel)		216		216		225	
Electricity Carbon Emissions (GtC/yr)		.49		0		0	
Transportation Carbon Emissions (GtC/yr)		.37		.37		0	
Total Annual Carbon Emissions		.86		.37		0	
Total Cost ($Billion/year)		$420		$506		$550	
Breakeven Carbon Tax ($/tonneC)		-		$175		$150	